Supramolecular Networks Responsive to Proteins and Small Molecules

Angerani, Simona

UNIVERSITÉ DE GENÈVE FACULTÉ DES SCIENCES

Section de chimie et biochimie
Département de chimie organique Professeur N. Winssinger

Supramolecular Networks Responsive To Proteins And Small Molecules

THÈSE

présentée à la Faculté des sciences de l'Université de Genève
pour obtenir le grade de Docteur ès sciences, mention chimie

par

Simona ANGERANI

de

Spino d'Adda (Italy)

Thèse Nº 5559

GENÈVE

Centre d'Impression de l'Unige

2021

UNIVERSITÉ DE GENÈVE
FACULTÉ DES SCIENCES

DOCTORAT ÈS SCIENCES, MENTION CHIMIE

Thèse de Madame Simona ANGERANI

intitulée :

«Supramolecular Networks Responsive to Proteins and Small Molecules»

La Faculté des sciences, sur le préavis de Monsieur N. WINSSINGER, professeur ordinaire et directeur de thèse (Département de chimie organique), Monsieur S. MATILE, professeur ordinaire (Département de chimie organique), Monsieur F. RICCI, professeur (Department of Chemical Science and Technologies,Via della Ricerca Scientifica 000133 Roma, Italy), autorise l'impression de la présente thèse, sans exprimer d'opinion sur les propositions qui y sont énoncées.

Genève, le 21 mai 2021

Thèse - 5559 -

Le Doyen

N.B. - La thèse doit porter la déclaration précédente et remplir les conditions énumérées dans les "Informations relatives aux thèses de doctorat à l'Université de Genève".

PhD Director:

Professor Nicolas Winssinger
University of Geneva
Department of Organic Chemistry
Quai Ernest-Ansermet 30
CH-1211 Geneva 4
Switzerland

Internal jury member:

Professor Stefan Matile
University of Geneva
Department of Organic Chemistry
Quai Ernest-Ansermet 30
CH-1211 Geneva 4
Switzerland

External jury member:

Professor Francesco Ricci
University of Rome Tor Vergata
Department of Scienze e Technologie Chimiche
Via della Ricerca Scientifica 1
00133 Rome
Italy

Résumé

Cette thèse est composée de cinq projets visant à développer des outils de détection applicable en milieu biologique. Les quatre premiers projets implique le design et l'application de réseau supramoléculaire capable de traduire des entrants biologiques, tel que la présence de protéines membranaires, des luciférases ou des séquences miARN, en sorties fonctionnelles. La construction des réseaux repose sur la technologie des acides nucléiques peptidiques (PNA), et plus particulièrement sur des templated réactions PNA s'appuyant sur la photoréduction catalysée au Ruthénium de linkers immolatif de picolinium. Le dernier projet décrit la découverte d'un fluorophore encagé interagissant avec la protéine moteur kinesin-1 et provoque une réponse fluorescente.

Le premier projet de cette thèse est basé sur le développement d'un réseau supramoléculaire basé sur des PNA qui agissent de manière identique aux outils theragnostic par relarguage d'agents thérapeutiques sur le site cible en réponse à la reconnaissance de la protéine cible « carbonic anhydrase IX » (CA IX), un récepteur homodimeric situé à la surface des cellules et est utlisé en tant que marqueur biologique pour le cancer. Le reseau s'assemble à la surface des cellules surexprimant CA IX comme résultant de l'interaction coopérative entre le site de binding proximal de la protéine cible et les brins de PNA fonctionnalisé avec le ligand. Une fois assemblés, les duplex de PNA affichent un surplomb pour les templated réactions qui sont ainsi capable de relarguer les molécules effecteurs de manière similaire aux fluorophores et des drogues cytotoxiques, avec une amplification signalétique, qui ainsi autorise le relarguage ciblé sur les cellules cancéreuses surexprimant CA IX. Le réseau répond au level d'expression de la protéine d'intérêt en culture cellulaire et peut être désassemblé en l'absence de cible.

Le deuxième projet vise à amplifier le signal de sortie des réseaux oligonucléotides en couplant le circuit ADN sur des PNA templated réactions afin d'obtenir une réponse quadratique. Le circuit ADN repose sur l'ouverture de deux épingles métastables fonctionnalisées au Ruthénium par un signal de sortie catalytique d'oligonucléotides qui conduit à la formation d'un duplex AND affichant un court surplomb (4 mer) aux extrémités. Les courts brins d'ADN déliés peuvent en retour avoir un rôle de sites pour les templated réactions avec des compléments PNAs portant un linker picolinium immolatif et une cage de molécule effecteur. Le système a montré l'achèvement de l'amplification du signal quadratique en réponse aux différentes concentrations d'analytes avec une limite de détection de l'ordre du femtomolaire. Le réseau a été utilisé pour délivrer des agents cytotoxiques en réponse à la présence de séquences miARN oncogéniques.

Le troisième projet réingienérie une technologie bien établie basée sur l'ADN, l'hybridation de réaction de chaine (HCR), mettant en perspective les propriétés avantageuses des PNA afin

d'obtenir un système minimaliste entièrement basé sur les PNAs. En dépit de l'exigence de longues séquences pour accorder la metastabilité des épingles dans la version original de l'ADN, l'interaction plus forte entre PNAs autorise le fait de générer des assemblements même sur de courtes séquences. Ce projet décrit le design d'un réseau de PNA-HCR basé sur des épingles à tiges 5-mer et des boucles/toehold 5-mer, qui s'est montré convenable pour l'accomplissement de l'amplification rapide d'un signal fluorescent en réponse à la détection de biomarqueurs cancéreux CA IX sur des cellules vivantes.

Le quatrième projet fût inspiré par le transfert d'énergie par résonance bioluminescente (BRET) de capteurs semisynthetiques pour la détection de médicaments et réutilise le système pour harnacher une réaction photochimique et ainsi relarguer des molécules effecteurs. Ce réseau BRET consiste en une protéine fusion SNAP-NanoLuc-DHFR qui peut être marquée avec un linker synthétique décoré avec un dérivé du complexe $[Ru(bpy)_2phen]^{2+}$ adjacent à un brin de PNA. Le chevauchement spectral entre spectre d'émission de la luciférase NanoLuc et le spectre d'absorption du complexe au Ruthénium, couplé à la proximité entre le couple donneur-accepteur accompli le marquage de la construction de la protéine et génère un BRET efficace. Cet état excité du complexe de Ruthénium peut être capturé par le linker picolinium immolatif affiché sur un PNA encagé effecteur conjugué pour un relarguage de molécules fonctionnelles. Le réseau a montré être opérationnel pour le relarguage d'agents cytotoxiques dans des environnement cellulaires avec d'une manière dépendante du substrat de la luciférase.

Le dernier projet diffère des précédents en minimisant le système de réponse à une petite molécule, QPD-OTf, précurseur du colorant quinazolinone QPD. Il a été montré que QPD-OTf interagit avec la fraction fonctionnelle active de la protéine kinesin-1 dans les cellules, suivant le mouvement de la protéine sur les microtubules en générant des cristaux de QPD fluorescents. Dans les cellules, les cristaux sont centrés dans l'appareil de Golgi et montre des fibres filamenteuses correspondant au sous ensemble de microtubules utilisé par kinesin-1 pour le traffic Golgi à ER. Une série d'expériences *in vitro* et *in cellulo* ont été réalisé pour évaluer la formation de cristaux sur l'activité de kinesin-1. De plus, il a été possible de suggérer un mécanisme d'action pour le retrait du groupement triflate comme résultat de l'activité ATP-ase du domaine moteur de la kinesin-1. QPD-OTf permet pour la première fois la visualisation de l'activité native d'une protéine moteur dans un environnement cellulaire.

Enfin, cette thèse décrit une large gamme d'outils de réponse à l'échelle nano et leur application aux systèmes biologiques. Les systèmes décrit ici permettent la visualisation d'importants procédés biologiques comme les mouvements de protéines moteurs, ainsi que la détection et le relarguage de drogues sur des cellules cancéreuses et, par ce moyen, ajoute une gamme disponible d'outils moléculaire pour étudier ces systèmes.

Summary

This thesis is composed of five projects aiming to develop responsive devices applicable in biological settings. The first four projects involve the design and application of supramolecular networks able to translate biological inputs, such as the presence of membrane proteins, luciferases or miRNA sequences, into functional outputs. The construction of the networks relies on peptide nucleic acid (PNA) technology, with a focus on PNA templated reactions capitalizing on the ruthenium catalysed photoreduction of picolinium immolative linkers. The last project describes the discovery of a small-molecule caged fluorophore that interacts with the motor protein kinesin-1 and responds by eliciting a fluorescent output.

The first project of this thesis is based on the development of a PNA-based supramolecular network that acts similarly to theragnostic devices, by releasing therapeutic agents at the target site in response to the recognition of the target protein carbonic anhydrase IX (CA IX), a homodimeric cell surface receptor which serves as a cancer biomarker. The network assembles on the surface of cells overexpressing CA IX as a result of cooperative interaction between the proximal binding sites of the target protein and PNA strands functionalized with protein ligands. Upon assembly, the resulting PNA duplex displays an overhang for templated reactions that enables the release of effector molecules, such as fluorophores and cytotoxic drugs, with signal amplification, thereby allowing targeted release on cancer cells overexpressing CA IX. The network responds to the expression level of the protein of interest in cell cultures and can disassemble in the absence of the target.

The second project aims to further improve the output amplification of oligonucleotide-based networks by coupling a DNA circuit to PNA templated reactions to yield a quadratic response. The DNA circuit relies on the opening of two ruthenium-functionalized metastable hairpins by a catalytic oligonucleotide input that leads to the formation of a DNA duplex displaying short overhangs (4-mers) at the extremities. The unpaired short DNA stretches can in turn function as sites for templated reactions with complementary PNAs bearing a picolinium immolative linker and a caged effector molecule. The system was shown to achieve quadratic signal amplification in response to different concentrations of analytes with a detection limit in the femtomolar range. The network was used to uncage cytotoxic agents in response to the presence of oncogenic miRNA sequences.

The third project reengineers a well-established DNA-based technology, the hybridization chain reaction (HCR), in light of the advantageous properties of peptide nucleic acids to afford a minimal system entirely based on PNAs. Despite the requirement of long sequences to grant hairpin metastability in the original DNA version, the stronger interaction between PNAs allows

to generate stable assemblies even with very short sequences. This project describes the design of a PNA-HCR network based on 5-mer stem and 5-mer loop/toehold hairpins, that were found suitable for the achievement of rapid amplification of fluorescent signal in response to the detection of the cancer biomarker CA IX on live cells.

The fourth project takes inspiration from bioluminescence resonance energy transfer (BRET)-based semisynthetic sensors for the detection of drugs and repurposes the system to harness a photochemical reaction for the release of effector molecules. This BRET network consists of a SNAP-NanoLuc-DHFR fusion protein that can be labelled with a synthetic linker decorated with a $[Ru(bpy)_2phen]^{2+}$ complex derivative adjacent to a PNA strand. The spectral overlap between the emission spectrum of the NanoLuc luciferase and the absorption spectrum of the ruthenium complex, coupled to the close proximity between the donor-acceptor couple achieved upon labelling of the protein construct allows for efficient BRET. The resulting excited state of the ruthenium complex can be captured by the picolinium immolative linker displayed on a PNA-caged effector conjugate for the templated release of functional molecules. The network proved to be suitable for the release of cytotoxic agents in cellular environments in a luciferase substrate dependent manner.

The last project differs from the previous ones by minimizing the responsive system to a small molecule, QPD-OTf, precursor of the well established quinazolinone precipitating dye QPD. QPD-OTf was found to interact with the functionally active fraction of the motor protein kinesin-1 in live cells, tracking the motion of the protein on microtubules by generating fluorescent QPD crystals. In cells, the crystals are centred in the Golgi apparatus and display filamentous fibers staining the subset of microtubules used by kinesin-1 for Golgi-to-ER trafficking. A series of *in cellulo* and *in vitro* experiments were employed to recapitulate the formation of the crystals to the activity of kinesin-1. In addition, it was possible to suggest a mechanism of action for the removal of the triflate group as a result of the ATP-ase activity of the motor domain of kinesin-1. QPD-OTf allowed for the first time the visualization of the native activity of a motor protein in a cellular environment.

Overall, this thesis describes a broad range of responsive nanoscale devices and their application to biological systems. The systems described herein enable the visualisation of important biological processes such as motor protein movement, as well as cancer cell detection and targeted drug release, thereby adding to the available range of molecular tools to study such systems.

Table of contents

Introduction

Life has evolved to accomplish complex operations from very simple building blocks. From this bottom-up point of view, all sorts of functions are hierarchically built from essential units that interact dynamically. Under this light, the complexity of Nature can be rationalized by simple and strong laws.[1] This concept has allowed not only to understand Nature's processes by means of deconvoluting complex systems into simple building blocks, but also to provide a method to generate new ones. The possibility to create programmable systems that respond to basic inputs represents the core of the development of electronic devices. The same reasoning can be translated to chemistry and biology, where basic modules (small molecules, proteins, nucleic acids, etc.) can be assembled into elaborated supramolecular constructs able to perform innovative functions, as well as to rewire existing ones. The design of supramolecular networks responding to biological inputs will be the focus of this thesis. The projects here discussed will explore semi-synthetic devices able to respond to biological stimuli eliciting output functions. These systems will mainly leverage on peptide nucleic acids (PNAs) as platform to harness templated reactions photocatalyzed by $[Ru(bpy)_3]^{2+}$ complexes.

Biosupramolecular Networks

This section is adapted from Watson E. E., Angerani S., Sabale P. M. and Winssinger N. "Biosupramolecular Systems: Integrating Cues into responses", Journal of the American Chemical Society, 143, 4467-4482 (2021)[2]

Being capable of manipulating biological systems with synthetic tools has attracted the interest of scientists for decades. The possibility to engineer responsive devices with customed features represents an appealing approach not only to understand the processes governing biological systems, but most importantly to redirect existing functions and generate new ones.

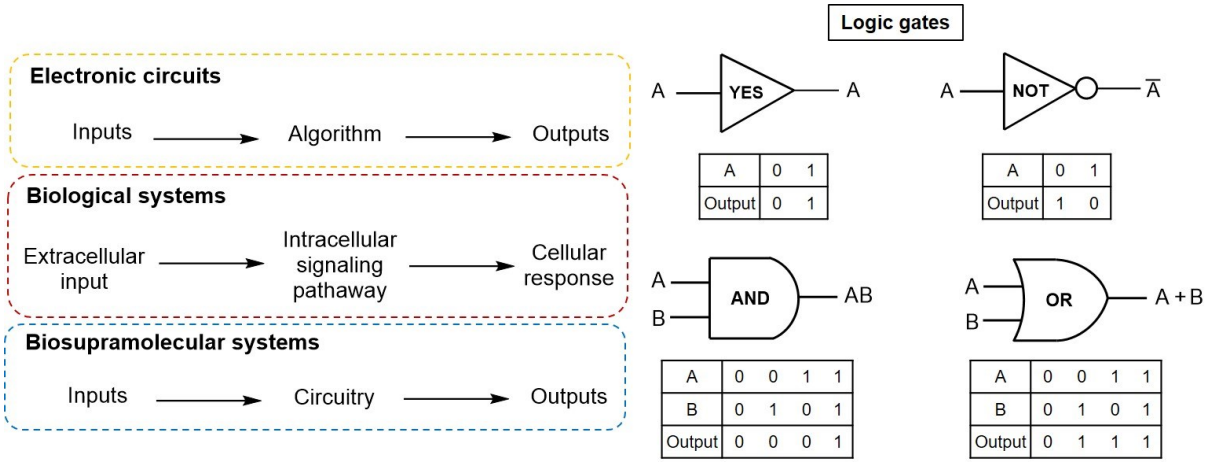

Figure 1. Modular representation of electronic, biological and biosupramolecular systems (left). Basic logic gates with corresponding truth table (right).

With the aim of schematizing biological systems, a clear parallelism has been postulated with electronic circuits, which rely on the translation of inputs into outputs through algorithms (Figure 1). One fundamental example is represented by the machine model of the cell.[3] As for electronic and cellular models, biosupramolecular systems can be fragmented into simple modules (*i.e.* inputs-circuitry-outputs) (Figure 1). The relation between different components can be defined by logic operations described by Boolean algebra (Figure 1, logic gates). The power of this categorization relies on the possibility to provide a set of simple functional modules that can be assembled by the user in a plug and play way.

Within the context of supramolecular networks, oligonucleotides play a central role. The modularity and ease of programmability offered by oligonucleotides renders them a powerful tool to wire complex operations. Not surprisingly, some of the first circuitry examples accounts for DNA-based circuits. Since the pioneering work of Adleman and Lipton,[4, 5] the field has grown exponentially, expanding to logic systems based on small molecules, proteins and cellular entities per se or to combinations of them.[2] Therefore, to date a myriad of input, circuitry and output types have been explored; the designer can envision innovative systems by picking the suitable ensemble of basic components.

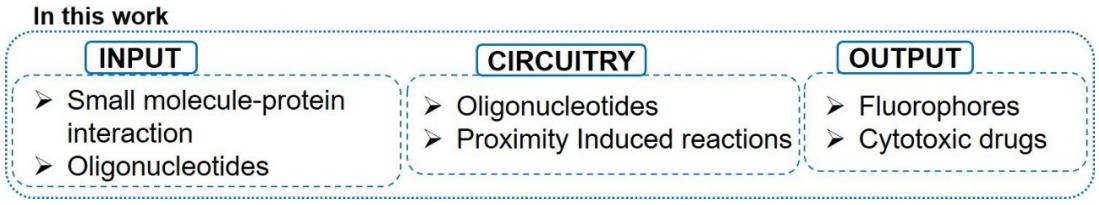

Figure 2. Scheme of inputs, circuitry and outputs used in the projects developed within this thesis.

In the context of this thesis, particularly relevant will be inputs based on small molecules and oligonucleotides sequences (receptor binding, miRNAs). Regarding the circuitry part, nucleic acids coupled to proximity induced reactions were chosen as main motive. As for the outputs, the release of small molecules (fluorophores and cytotoxics) or a fluorescence turn-on were predilected (Figure 2).

Inputs

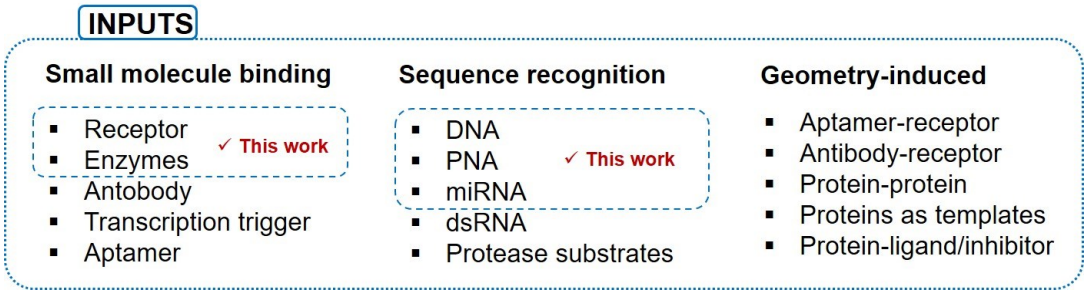

Figure 3. Summary of inputs employed in supramolecular networks; the boxes highlight the input types utilized in this thesis.

As mentioned, in this work will be described examples of networks that made use of small molecules binding to receptors or interactions between oligonucleotide sequences as source of inputs (Figure 3). Regarding small molecule binding, the interaction between receptors such as carbonic anhydrase and dihydrofolate reductase and their respective small-molecule ligands, acetazolamide and methotrexate respectively, were exploited as triggering event in the networks (*vide infra*). In literature, a variety of examples employing small molecule ligands has been reported, exploiting both the high affinity for the corresponding partner and the capacity to induce conformational changes. Notable cases comprise binding to surface receptors (CD19),[6] enzymes (hepatisis C protease),[7] antibodies (Hemagglutinin, anti-digoxigenin, anti-dinitrophenol),[8-10] and transcription triggers.[11, 12] Regarding the possibility to induce conformational changes, small molecules binding to aptamers (ATP)[13] and dimerizers (rapamycin, abscisic acid)[14-16] have been reported.

Concerning oligonucleotides sequences, this work will describe the design of networks responding to microRNAs and peptide nucleic acids (PNA) (*vide infra*). Literature examples have vastly explored DNAs,[17-28] RNAs[29-34] and PNAs[34-36] sequences recognition as triggers, but oligonucleotides assemblies (three-way junctions,[37] polymeric supports[24, 38]) and more complex oligonucleotide-based supramolecular structures (G-quadruplexes,[39] DNA origami[40]) have also been employed. Alternatively to oligonucleotides, the recognition of a peptidic sequence by the corresponding protease could be envisioned.[14, 41, 42]

Moreover, a thoroughly exploited class of input signals involves specific interaction governed by geometry. Within this class fall interactions between aptamers,[43-48] antibodies[45, 49-51] or proteins[52, 53] to their cognate receptor, as well as the effect of protein templation[53-55] and the conformational changes induced by ligand or inhibitor binding.[22, 23, 30, 36, 56-58]

Circuitry

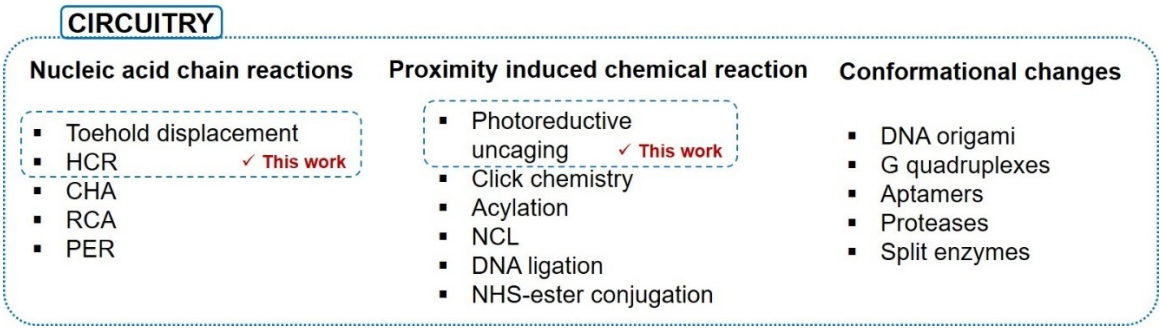

Figure 4. Summary of circuitry types employed in supramolecular networks; the boxes highlight the circuitries utilized in this thesis.

If the input module allows for the networks to be assembled and triggered, the circuitry component enables the elaboration and processing of the information. Once again, infinite options can be envisioned, with the fantasy of the designer being the only limiting factor.

However, circuits are usually following the operation of Boolean logic,[59] with AND gates being probably the most broadly used example, together with modulators such as amplifiers.

Entering the specifics of circuitry types, three main categories, namely nucleic acid chain reactions, proximity induced chemical reactions and conformational changes can be identified (Figure 4). Nucleic acid chain reactions are probably the most exploited, benefitting from the programmability and modularity offered by such systems. Within this group, toehold displacement, thanks to its simplicity and versatility, perhaps represents the most used nucleic acid-based reaction. Since the seminal examples from Gadhiri, that used toehold displacement to turn on and off enzymes,[22, 23] the field has evolved to more and more complex architectures that found applications for *in vitro* and *in cellulo* systems. The concept of Gadhiri's work used enzymes (proteases) conjugated to a DNA strand initially hybridized to a complementary sequence linked to an enzyme inhibitor. The activity of the enzyme could be modulated by addition of an invading strand that would displace the inhibitor upon toehold displacement.[22, 23, 57] Our group has recently revived this approach to restore the activity of a bioluminescent protein (HLuc) in response to mRNA.[36] The Merkx team also employed toehold displacement to regulate the activity of proteins (TEM1-β-lactamase), this time in response to a supramolecular polymer platform.[38] In addition, toehold reactions have been exploited to sense the presence or modulate the activity of proteins.[28, 55] Moreover, toehold displacement events were triggered in response to receptor dimerization on the cell surface.[43] [13, 46] Antibodies have also been used as scaffolds to trigger toehold displacement; in this context the Merkx and Ricci groups have developed several networks, in which the toehold reaction leads to bivalent interactions with the antibody.[8-10, 60] Furthermore, toehold displacement events were chosen to control three dimensional structures, such as the assembly of a nanotube[9, 61] and the opening-closing of a DNA nanovault.[18]

Continuing on circuitry types based on nuclei acid chain reactions, few other approaches play a strategic role in supramolecular networks. These approaches are namely: catalytic hairpin assembly (CHA), hybridization chain reaction (HCR), rolling circle amplification (RCA), and primer exchange reaction (PER). While the CHA and HCR do not require any external enzymatic activity to proceed, RCA and PER rely on polymerases.

As for CHA, this technique requires two metastable hairpins and an initiator strand. Upon hairpin opening by the initiator, an overhang is displayed on the opened hairpin, which in turn triggers opening of the second hairpin with concomitant displacement of the initiator strand. In this way, the initiator is regenerated and can be engaged in several hairpin opening cycles. This strategy has been used to sense proteins utilizing split input strands conjugated to protein binding motives, so that the hairpin opening event could be triggered only after input reconstitution upon protein binding.[45] In addition, a CHA system was designed to interact with 10-mer handles immobilized on a supramolecular polymer, to benefit from the resulting

increased effective concentration and hence accelerate the reaction.[24] Moreover, CHA was utilized for FRET amplification.[28]

HCR shares with CHA the requirement of two metastable hairpins and an initiator strand; however, instead of recycling the initiator for subsequent cycles, HCR enables the linear growth of an oligonucleotide assembly in which the two hairpins are alternated. Since the seminal work reported by Pierce and co-workers,[62] HCR has been employed for biosensing, bioimaging, and biomedicine.[63] To allow for facile readout, hairpins are often decorated with fluorescent moieties[32, 47, 49] or coupled to peroxidases.[64-66] Thanks to the generation of elongated products that remain co-localized with the input strands, HCR allows for clear imaging of targets on the surface of cells.[32, 47, 49, 67, 68] Likewise, HCR has been used for detection of cancer cells.[47] Moreover, the biocompatibility of the HCR process enabled the use of such technique for *in situ* hybridization.[69-74] Recently, an HCR system was used to trigger the release of small molecules.[75] To this end, one hairpin was conjugated to a disulfide and a cargo molecule, and the second hairpin to a thiol. When the initiator is added and the hairpins opened, the thiol and disulphide-cargo moieties find themselves in close proximity; the thiol can thus displace the disulfide, releasing the cargo molecule.[75]

Regarding nucleic acid chain reactions that require the use of an enzyme (polymerase), RCA replicates an oligonucleotide strand around a circular template. This technique has been used for sensing purposes,[48] for fuelling the movement of a molecular walker[27] and to sense the recognition of cell surface receptors.[76]

Yet another circuitry module is represented by primer exchange reaction, PER. In this case, given a DNA primer and catalytic hairpin mediators, custom-designed ssDNAs are produced with the help of a strand-displacing polymerase.[77] This technique has been applied to the analysis of COVID-19 genome in cell lysates with a CRISPR array[78] and to RNA degradation.[79]

Another method to wire a network is represented by proximity induced reactions. This approach is particularly relevant to this work and its application to photoreductive uncaging reactions will be described in the next chapters. As indicated by the name, such approach enables to obtain the required proximity between reaction partners to facilitate product formation. In this context oligonucleotides, acting as templates, represent a powerful platform to bring reactive moieties in close contact, with distance that can be modulated by tuning the interactions between oligonucleotide strands. However, the same effect can be obtained using antibodies and proteins as scaffolds. The chemistries span from click reaction[50, 80] to acylation,[53] native chemical ligation,[81, 82] enzymatic DNA ligation,[44] NHS-ester conjugation.[20]

Moreover, the circuitry module can engage conformational changes, including DNA suprastructures (origami,[17, 18] G-quadruplexes[39]), aptamers,[83] proteases[7, 14, 84] and split enzymes.[15, 30]

As for this work, circuitries based on toehold displacement, HCR and proximity induced chemistry techniques will be employed in the projects developed (Figure 4).

Outputs

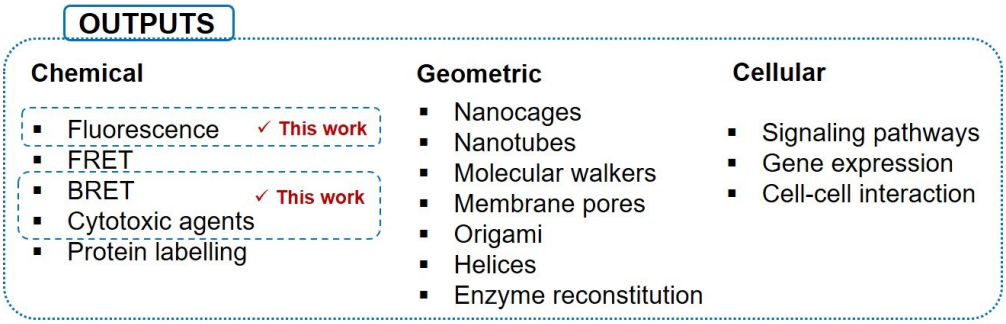

Figure 5. Summary of outputs employed in supramolecular networks; the boxes highlight the outputs utilized in this thesis.

The output represents the final event generated by a network and can be either a reporting or a functional event. Outputs can be categorized into three major groups, consisting in chemical, geometric and cellular outputs (Figure 5). Regarding the chemical group, probably the most exploited output is represented by fluorescence techniques, thanks to the easy and quantitative readout. The most commonly used fluorescence-based approaches include fluorescence turn-on upon quencher displacement,[9, 19, 29, 43, 45, 51, 53, 55, 85] FRET[9, 18, 24, 28, 32, 46, 56] or BRET[36, 58, 86] techniques, and fluorophore release as a result of chemical reaction.[33, 75, 87, 88] In addition, release of small molecule effectors was envisioned.[75, 87, 89] In alternative, tags could be appended to target proteins.[90] Concerning geometric outputs, these include the assembly of supramolecular structures (nanocages,[91] nanotubes,[9, 61] molecular walkers,[27] membrane pores,[92] functionalized origami,[93] helices[26]), or the reconstitution of enzymes and receptors.[7, 13-15, 18, 21-23, 28, 30, 36, 38, 41, 46, 58, 84] Cellular outputs are also contemplated and are mainly directed to the triggering of signalling pathways[13, 17, 50, 76, 94] and gene expression,[11, 15, 31, 95] together with the modulation of cell-cell interaction.[6, 96]

The project showcased in this work will capitalize on the release of reporting molecules, such a fluorophores, and functional molecules, such as cytotoxic agents.[97-99]

Peptide nucleic acid (PNA)

Properties and applications

As mentioned in the introduction paragraph, most of the projects discussed within this thesis rely on Peptide Nucleic Acids (PNAs) as scaffolds to generate cooperative assemblies and to perform templated reactions. PNA is a DNA mimic in which the phosphoribosyl backbone is replaced by a peptidic one consisting of N-(2-aminoethyl)-glycine monomers decorated with a nucleobase (Figure 6).[35, 100] PNA, thanks to its neutral backbone, does not suffer from electrostatic repulsion when hybridized to complementary PNA or DNA/RNA strands, leading to more stable duplexes with DNA and RNA than the corresponding homoduplexes.[101] This feature also confers hybridization independency from salt concentration.[102, 103] In heteroduplexes, PNA adopts the conformation of the nucleic acid partner (A-conformation with RNA; B-conformation with DNA); PNA homoduplexes instead adopt a characteristic P-conformation, displaying a 28 Å-wide helix with 18 base pairs per turn.[101] However, the neutral backbone can limit the solubility in aqueous buffers and cause aggregation; to overcome these drawbacks, modifications have been envisioned both at the alpha position (arginine) and at the gamma position (mini-PEGs and serine).[35] Other modifications at the γ-position, including lysine or cysteine side chains, can be included to provide further conjugation sites.[104] Moreover, the chirality introduced with γ-substituents elicits helicity (L-stereoisomers induce right-handed helices and *vice versa*). This induced preorganization can be exploited to improve hybridization to DNA and RNA, benefitting from a more favourable entropic term than achiral PNA.[105] In addition, since only L-PNA can bind to natural nucleic acids,[106] D-PNA could be employed to generate completely orthogonal systems.[107, 108]

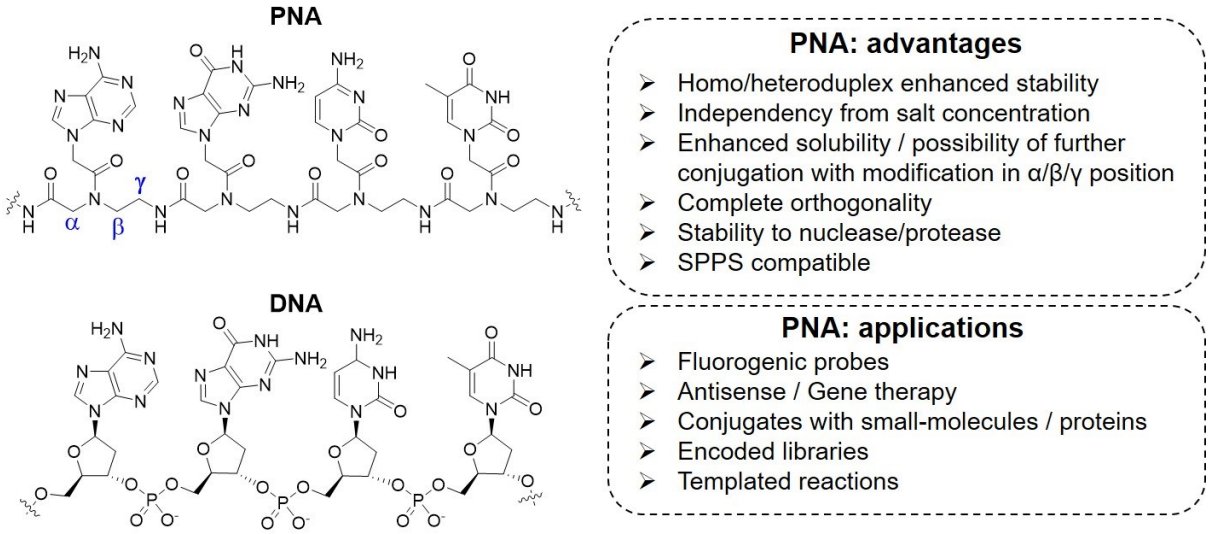

Figure 6. Structures of PNA and DNA (left); highlights on advantages and applications of PNAs (right).

Another advantage over natural oligonucleotides is represented by the stability in biological environments; in fact, PNAs are not substrates for serum nucleases and proteases,[109] making them attractive tool for *in vivo* applications.[110-112]

Regarding the synthesis, PNA strands can be obtained on solid support starting from monomers in which the nucleobase and the N-terminus bear orthogonal protecting groups, a characteristic that has been exploited to generate PNA encoded libraries.[113] PNA has also proven to be suitable for conjugation with proteins. [114-117]

Taking advantage from the properties summarized above (Figure 6), PNAs have been employed for sensing purposes, either in the context of fluorogenic probes that turn on upon hybridization or exploiting templated reactions to release fluorophores (*vide infra*).[104] Antisense and gene editing represent other fields of application for PNAs. In the first case, PNA has been employed to affect the expression of growth factors,[118] to inhibit mRNA[119] and miRNA.[120] In the case of gene editing, PNAs make good candidates thanks to their ability to perform dsDNA invasion, resulting in stable complexes;[104] the technology has been utilized to correct mutations[121, 122] or to introduce modifications.[123] The ability to invade dsDNA can also be rendered irreversible by crosslinking.[104] Moreover, PNAs can be complemented with small molecules,[124, 125] proteins[126, 127] and antibody fragments[115] to build fluorescent probes or supramolecular drugs with enhanced efficacy by means of multivalency effect. Furthermore, PNA has found multiple purposes in templated reactions.[33, 34, 87, 108, 128, 129]

Thanks to the multiple advantages and possibility of application in biological systems, PNA was chosen as suitable platform to build the networks herein discussed.

PNA-based templated ligations and transformations.

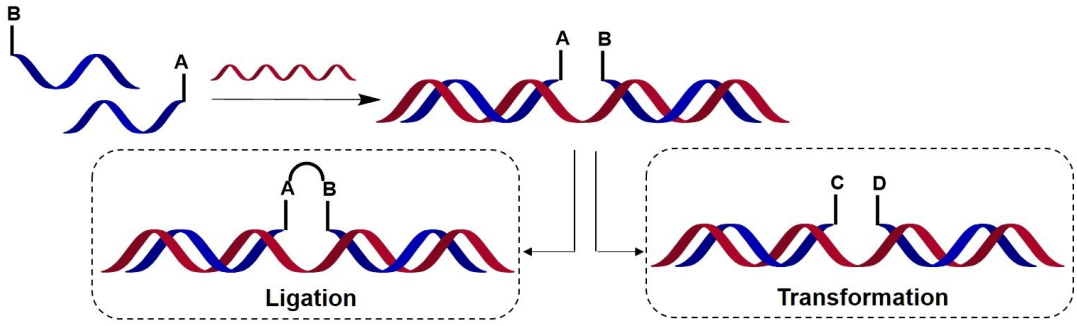

Figure 7. Scheme of oligonucleotide templated reactions.

Oligonucleotide templated reactions leverage on substrate and guide strands predisposition dictated by hybridization to achieve the effective concentration required for the reaction to proceed (Figure 7). Regarding templated ligations, one of the first examples exploited the hybridization to a DNA strand to enhance the coupling between PNA 2-mers.[130] Similar approaches have been used to build PNA oligomers with other chemistries, including reductive amination,[131-133] click reactions,[134] native chemical ligation,[82, 135] aldol condensation.[39, 136, 137]

Despite the relatively wide scope, templated ligations suffer from product inhibition, since the ligated product has higher affinity for the template than the substrate fragments.

About templated transformations, some of the chemistries already used for ligations can be reengineered to perform with substrate turnover. Accordingly, NCL-based systems could be employed to transfer a fluorophore quencher,[138] a biotin tag[139] or a bioactive peptide.[140] Other methodologies, such as Wittig olefination,[141] Staudinger reaction[142-147] and photocatalysis (*vide infra*) have been explored. In particular, the application of azide reduction chemistry proved to be proficient for the detection of mRNA[148] or miRNA *in cellulo*[128] and as a tool to release bioactive molecules.[149]

Ruthenium photocatalyzed reactions in biological systems

This section is adapted from Angerani S. and Winssinger N. "Visible Light Photoredox Catalysis Using Ruthenium Complexes in Chemical Biology, 25, 6661-6672 (2019)[150]

The projects presented within this work capitalize on reactions photocatalyzed by ruthenium tris bipyridine complexes. The non-cytotoxicity up to micromolar concentrations[151] and the absorption in the visible region of light render such complexes attractive for applications in biological systems.[150] In fact, visible light as external trigger allows for spatiotemporal control and benefits from better tissue penetration[152] and lower phototoxicity[153] than ultraviolet light.

$[Ru(bpy)_3](PF_6)_2$ has a relative absorption maximum at 452 nm (extinction coefficient ~13000 M^{-1} cm^{-1}), corresponding to the metal-to-ligand charge transfer (MLCT); excitation by visible blue light generates a triplet excited state upon intersystem crossing (ISC).[154] The excited state is relatively long lived (~800 ns) and relaxes to the ground state by phosphorescence (λ_{max} = 620 nm; quantum yield = 2.8%).[155] However, in the presence of a reactant (electron donors D, electron acceptors A), ruthenium complexes can undergo either oxidative (Ru^{2+*}/Ru^{3+}) or reductive (Ru^{2+*}/Ru^{+}) cycles (Figure 8). The systems used in this work will rely on the reductive cycle. In details, with an electron donor (i.e. tertiary amines, Hantzsch ester, NADPH, ascorbic acid, etc.), $Ru(bpy)_3^{2+}$ is reduced to $Ru(bpy)_3^{+}$ upon single electron transfer; the catalyst can then be regenerated by SET to an electron acceptor (Figure 8).[150]

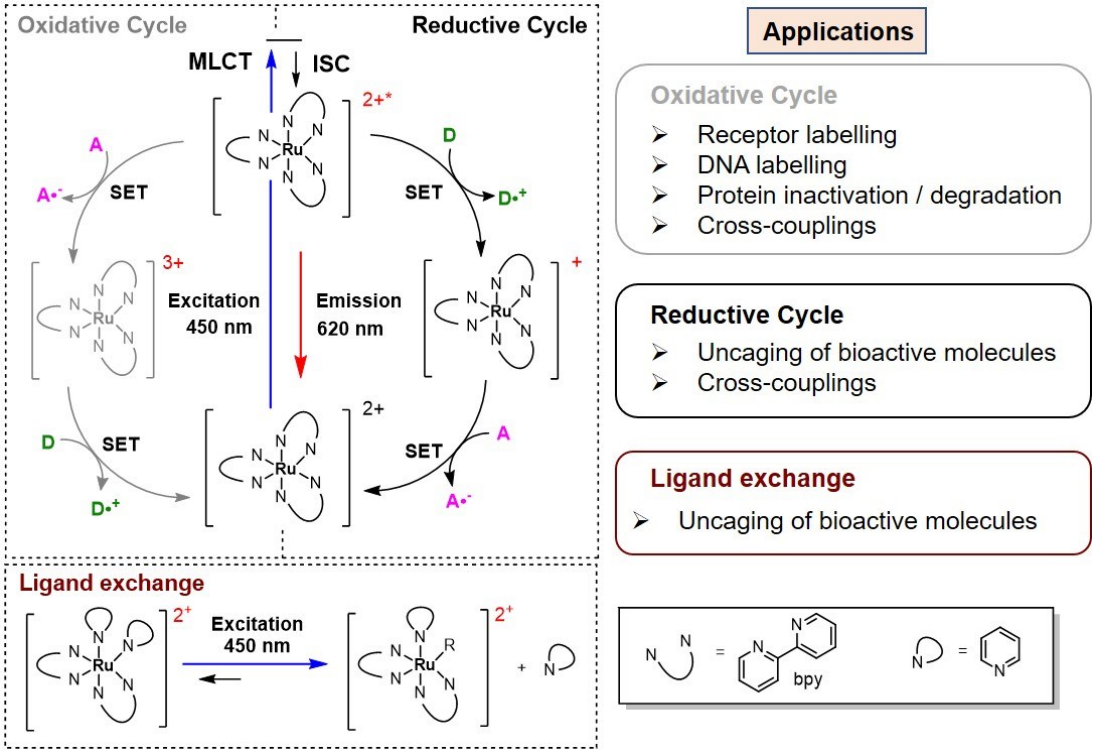

Figure 8. Schematic representation of oxidative/reductive cycles and ligand exchange of ruthenium tris bipyridine complexes and corresponding applications in biological systems.

Ruthenium tris bipyridine complexes have been employed in chemical biology in several different contexts (Figure 8).[150] One major application is represented by receptor labelling reactions, which includes crosslinking strategies as well as additional reactive probes. In the first case, the groups of Kodadek and Bonnafous explored the oxidative cycle (using ammonium persulfate as oxidant) to crosslink domains of transcription factors or GPCRs to their peptidic ligands upon formation of tyrosyl radicals that can react with proximal nucleophiles, such as tyrosines, tryptophanes, cysteines and methionines.[156-158] Cross-linking products can also involve the ruthenium complex directly, yielding adducts with DNA (guanines) or tryptophane; however, for these reactions to happen ligands more electron deficient than bipyridines are required.[159] The second case, developed by the Nakamura group, employs phenylenediamine or 1-methyl-4-arylazole derivatives as tyrosyl trapping agents; also this approach uses ($(NH_4)_2S_2O_8$) as oxidant;[90, 160] this method allows for the selective labelling of a protein of interest even in cell lysates. In addition, $[Ru(bpy)_3]^{2+}$ can be used as sensitizer to generate singlet oxygen and induce protein inactivation and degradation.[161-164] Moreover, a cross coupling methodology compatible with cell lysates has been developed.[165]

Another area that sees the employment of ruthenium complexes is the caging of bioactive molecule. This approach exploits the lability of monodentate ligands under photoexcitation (Figure 8). To this end, complexes of the type $[Ru(bpy)_2X_2]^{2+}$, where X represents the molecule to uncage can be envisioned.[166] Examples of this strategy include the release of small-molecules[167, 168] and the activation of oligonucleotides for antisense purposes.[169]

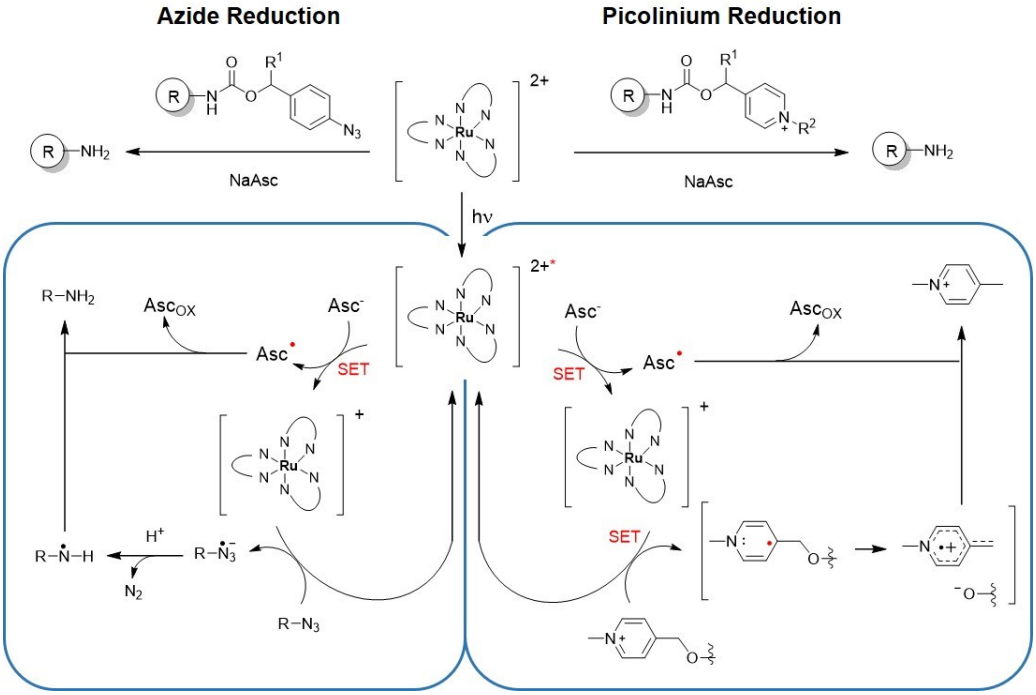

Figure 9. Scheme of ruthenium photoreduction of azides and picolinium derivatives with relative reaction mechanisms.

Besides being employed to catalyse the formation of new bonds, ruthenium complexes have been used to cleave bonds with photocatalysis under reductive conditions (Figure 8).[150] In this context, photocatalyzed reduction of azides and picolinium derivatives have been used to harness the release of a variety of bioactive compounds. Regarding the azide, such moiety was known to be involved in photosensitized reactions since the 1960s[170] and the methodology was integrated with ruthenium polypyridyl complexes in more recent reports.[171, 172] In particular, Liu's group achieved azide photoreduction to amine with $Ru(bpy)_3Cl_2$ in the presence of a reducing agent (formic acid, Hantzsch ester, NADH, sodium ascorbate) in good yields and in a completely biorthogonal fashion.[172] The reaction involves the formation of a nitrene specie upon energy transfer from the ruthenium complex and nitrogen evolution (Figure 9). Capitalizing on proximity induced reactions, our group has employed this chemistry to develop systems able to respond to target receptors *in cellulo*.[173, 174] Notably, performing the photocatalytic reaction in live cells does not require external reducing agents, affirming that the endogenous NADH/NADPH is sufficient to keep the system working.[174, 175] On the other hand, 4-pyridylmethyl groups were initially used as protecting groups in solid phase peptide synthesis;[176] the possibility to deprotect such group under electrolytic reduction paved the way for the use of picolinium esters as cleavable moiety under $[Ru(bpy)_3]^{2+}$ catalysed photoreduction.[177] In details, photoexcited $[Ru(bpy)_3]^{2+}$ is first reduced to $[Ru(bpy)_3]^{+}$ by sodium ascorbate ($k = 3.84 \times 10^7\ M^{-1}\ s^{-1}$);[177] then, single electron transfer (SET) from the ruthenium to the pyridinium ($k = 1.77 \times 10^9\ M^{-1}\ s^{-1}$) regenerates the catalyst $[Ru(bpy)_3]^{2+}$ while leading to fragmentation of the C-O bond on the picolinium ester.[177, 178] This approach has been expanded to carbamates[179] (Figure 9) and phenolic ethers.[108] Our group has applied this chemistry as reporting modality to assess the performance of ruthenium pre-catalysts[129] and for reactions templated by kinase receptors.[54]

PNA templated ruthenium photocatalysis

The projects that will be discussed within this thesis rely on the combination between $Ru(bpy)_3^{2+}$ photocatalyzed reactions and peptide nucleic acid templated transformations. PNA templates represent a platform for the design of proximity induced chemical reactions, leveraging on the high effective concentration of reagents achieved upon probes-template interaction; in addition, the complementarity to natural nucleic acids opens the way to the design of sensing devices. At the same time, the use of catalytic processes allows for output amplification. Moreover, as mentioned in the previous sections, the biocompatibility of both PNA and $Ru(bpy)_3^{2+}$ -based photocatalysis enables the application of such technology to *in vivo* systems. Taking advantage from these features, our group has tailored a variety of responsive devices. Entering into the details, these systems make use of a $[Ru(bpy)_2phen]^{2+}$ complex, in which the phenantroline ligand is functionalized with an amine group that serves

as conjugation site to the PNA component (Figure 10). Notably, the photophysical properties of $[Ru(bpy)_2phen]^{2+}$ and $[Ru(bpy)_3]^{2+}$ are equal.[180] From the first example of PNA templated release of a fluorophore upon immolation of an azide-based linker (Figure 10),[181] the scope of this system was expanded to miRNA detection in live cells[182] and live vertebrates (zebrafish).[33] Recently, the efficiency of the templated release was implemented by replacing the azide moiety with pyridinium-based linkers (Figure 10); the photocatalytic reaction was found to proceed with the fastest rate for templated reactions reported to date (k_{app} = 138 × 10^{-3} s^{-1}).[108] The length of the PNA strands could be tuned to achieve dissociation rates comparable to the rate of the photocatalytic reaction, and therefore allowed to develop a system whose efficiency is not precluded by product dissociation (Figure 10). Remarkably, a PNA templated system based on 5-mer strands reached catalytic efficiency of 10^5 M^{-1} s^{-1} and turnover frequency >100 h^{-1}.[108] On the same line, a three-way junction construct in which the product has lower affinity for the template than the substrate was developed.[37] Moreover, capitalizing on Hoogsteen base-pair interactions, PNA templated reactions have been employed for dsRNA detection.[34] Photocatalytic release of fluorophores could be also adapted for detection of single nucleobase mutations.[25] Furthermore, PNA templation served to reconstitute the ruthenium catalyst *in situ* as a result of target miRNA recognition.[129] Taken together, the advantages offered by PNA-templated ruthenium photocatalyzed reactions were considered an asset for the development of supramolecular network.

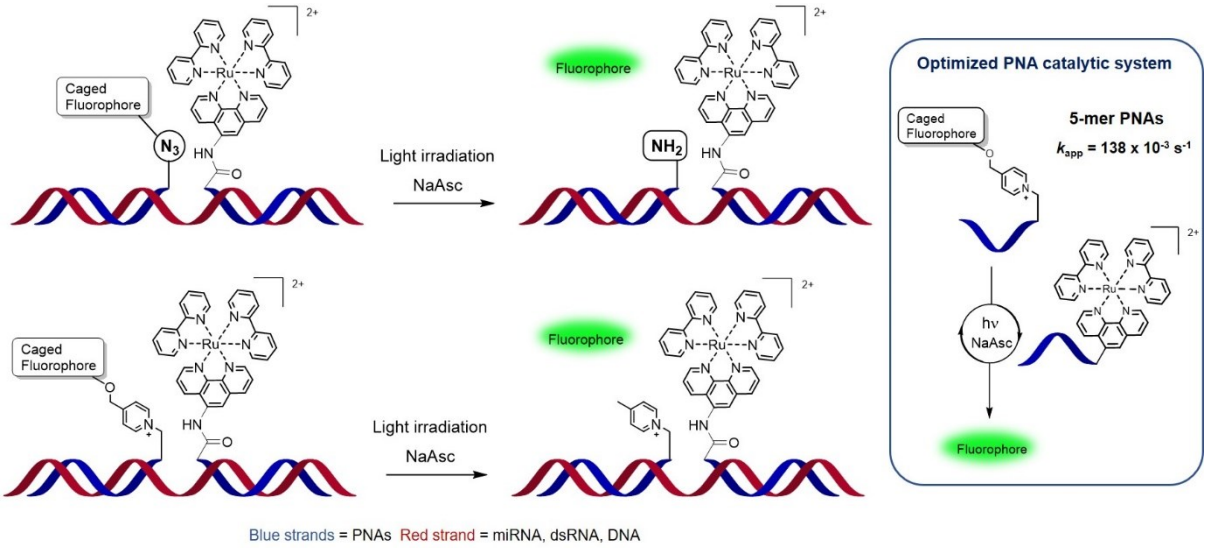

Figure 10. Schematic representation of PNA templated photoreductive uncaging. Blue box describes the optimized system for efficient substrate turnover.

Chapter I

Supramolecular network responsive to carbonic anhydrase IX

The content of this chapter is adapted from *Angerani S. and Winssinger N. "Sense-and-Release Logic-Gated Molecular Network Responding to Dimeric Cell Surface Proteins." Journal of the American Chemical Society 142, 12333-12340 (2020).*[98]

Introduction

The design of supramolecular networks represents an attractive platform to engineer responsive systems. The interest for this approach relies on the possibility to start from basic modules that can be assembled in an additive manner to generate devices with multiple layers of complexity; another key advantage is the adaptivity of such systems, that can be tailored to fulfill potentially any task envisioned by the user. In this context, nucleic acid-based assemblies combine ease of programmability, through sequence dependent interaction (hybridization), and versatility, thanks to their compatibility with biological settings. In addition, proximity induced chemistry well applies to oligonucleotides-based systems and introduces a simple way to provide the network with an output signal. Another interesting aspect is the possibility to generate oligonucleotides-based systems with enhanced affinity towards a selected target as a result of a binding event to proximal binding sites.[125]

Therapeutically, there is a constant interest for targeting agents, in order to direct the therapeutic entities selectively to the site of interest and thus avoid off-target effects. Theragnostic devices combine the sensing properties of a diagnostic tool to the healing properties of a therapeutic. This concept has been practically applied to cancer therapy through nuclear medicine, in which radionuclides labelled with ligands for cancer biomarkers are utilized. Both antibodies and small-molecules have been employed as targeting agents; remarkable example are respectively the Yttrium-90 (^{90}Y)-Tiuxetan-Ibritumomab conjugate for the treatment of refractory B-cell non-Hodgkin's lymphoma[183] and the Lutetium-177 (^{177}Lu)-Dotatate-Somatostatin conjugate against gastroenteropancreatic neuroendocrine tumors.[184]

A receptor that has raised attention as cancer biomarker, and in turn, led to the development of several theragnostic agents is carbonic anhydrase IX (CA IX).[185] CA IX is a homodimeric cell surface receptor that exhibits the active site on its the extracellular domain. CA IX is a metalloenzyme that contains a Zn^{2+} ion in the catalytic site.[186] As for the other 15 carbonic anhydrase isoforms, CA IX catalyses the conversion of carbonic anhydride to bicarbonate.[187] Despite the other isoforms are constitutively expressed in every cell, CA IX is overexpressed in response to hypoxia, a typical condition displayed by solid tumors; in addition, several cancer cell lines (especially renal cancer cells) constitutively express this receptor.[185, 187, 188]

As the name indicates, hypoxia is a condition characterised by low oxygen levels that arises as a consequence of poor vascularisation in solid tumors.[188] Under this condition, the aberrant metabolism of cancer cells is pushed towards glycolysis, with the consequent production of an excess of glycolysis metabolites, including lactic acid, protons and CO_2 (Figure 11).[188, 189] To overcome the resulting acidosis, cells respond by overexpressing CA IX, which concurs in the regulation of intracellular pH by generating bicarbonate ions (Figure 11).[188, 189] The overexpression of CA IX correlates with tumor progression and poor prognosis.[190-192] Given the interest in identifying CA IX expression levels, a variety of products that target such protein have been developed, form antibodies to small molecules, including sulfonamides, inorganic anions, phenols and coumarins.[187, 193] Sulfonamide-based inhibitors have been employed in therapy; however, the lack of isoform specificity represents an issue.[186, 187] In this context, the group of Neri developed CA IX ligands based on the small molecule inhibitor acetazolamide (AAZ)[194] that resulted effective for targeted drug delivery.[195, 196] In particular, it has been shown that AAZ-based bivalent ligands are superior to monovalent ones in terms of retention at the tumor site.[197]

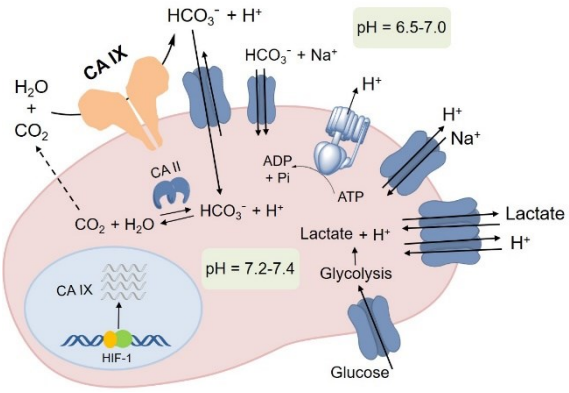

Figure 11. Schematic view of the metabolism of a cancer cell under hypoxic conditions.

Network design

Inspired by the dual action of theragnostics and spurred by the clinical relevance of carbonic anhydrase IX as cancer biomarker, a PNA-based cooperative network that assembles on carbonic anhydrase IX expressing cells was envisioned. The network capitalizes on a symbiotic relationship between the hybridization of the PNA components and the binding of small-molecule ligands to vicinal binding sites (ca. 30 Å) on the target protein, which provide sufficient stabilization to the supramolecular assembly to yield an output signal. The network can be represented as two consecutive AND gates, the first resulting in the assembly of two partially complementary PNA-AAZ strands on the surface of CA IX expressing cells; the second AND gate allows for the ruthenium-catalyzed photoreductive uncaging of small molecules, mediated by an amplifier module represented by a third complementary PNA strand bearing a pyridinium immolative linker (Figure 12). The release reaction is triggered by irradiation with visible blue light (Figure 12).

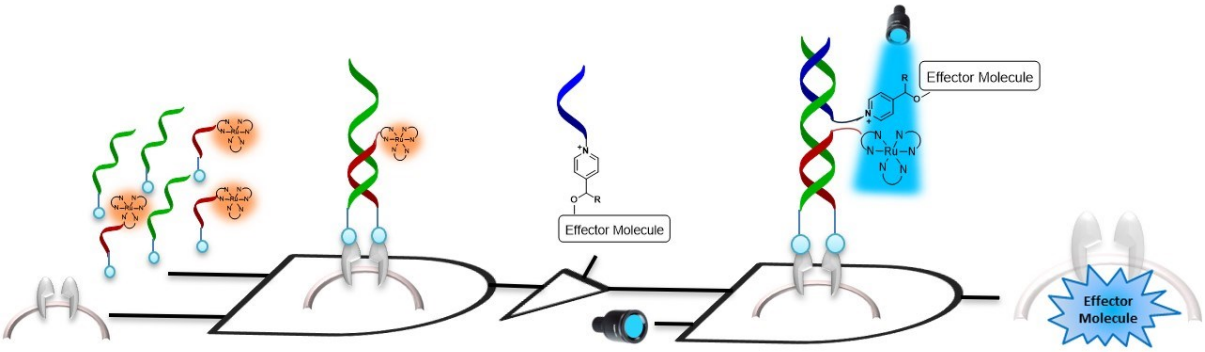

Figure 12. Schematic representation of CA IX responsive PNA network as consecutive AND gates with amplification module. The network operates on the surface of CA IX expressing cells releasing effector molecules that can be uptaken by the cells.

Results and discussion

First, to validate the possibility to selectively target CA IX in cell cultures, a fluorescently labelled AAZ-based bivalent ligand (**1**, Cy3-tagged) was prepared (Figure 13a, Figure I-S1 for extended structures). For this study, two model cell lines were employed: HT-29, a colorectal adenocarcinoma cell line that overexpresses CA IX under hypoxic conditions (1% O_2); and SKRC52,[198] a metastatic renal carcinoma cell line, constitutively expressing CA IX. Confocal microscopy revealed excellent discrimination between hypoxic and normoxic conditions, with exclusive membrane staining in hypoxic HT-29 cells (CA IX (+)) (Figure 13a), and membrane targeting in SKRC52 cells (Figure I-S2). Colocalization with the membrane dye Flipper-TR[199] further confirmed selective membrane staining (Figure I-S3). In addition, the selectivity of the bivalent ligand was assessed in a mix culture of SKRC52 (CA IX (+)) and HeLa-GFP (CA IX (-)) cells, resulting in unique membrane staining of CA IX positive cells (Figures 13b and I-S4).

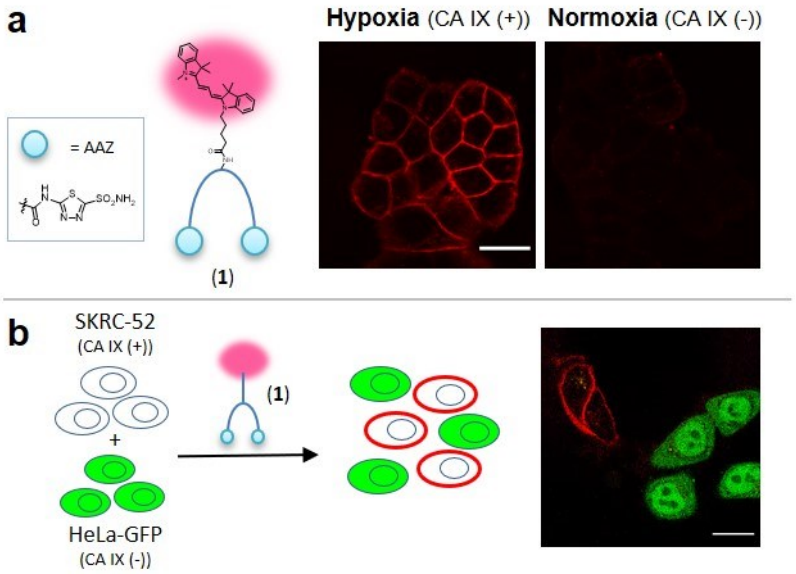

Figure 13. (a) Schematic representation of fluorescent bivalent ligand **1** (left), confocal fluorescence images of HT-29 cells labelled with the bivalent ligand **1** (100 nM; 30 min) under hypoxic (CA IX (+)) or normoxic (CA IX (-)) conditions (right). (b) Selective membrane staining of SKRC52 cells with **1** (100 nM, 30 min) in co-cultures of SKRC52 (CA IX (+)) and HeLa-GFP (CA IX (-)) cells. Scale bar 20 µm.

With the aim of coupling the binding event to a PNA templated reaction, the AAZ-based bivalent ligand was conjugated to a 5-mer PNA linked to the ruthenium photocatalyst. The length of the PNA was selected based on previous results demonstrating that a 5-mer strand is optimal for substrate turnover in templated reactions.[108] On the other hand, the complementary 5-mer PNA is conjugated to a pyridinium immolative linker attached to a caged molecule that will be released in response to ruthenium photocatalysis controlled by external light irradiation. Since the templated reaction will take place extracellularly, the 5-mer-pyridinium construct was functionalized with a cell impermeable moiety (a bis-sulfonated aryl) (Figure I-S1 for structures) to prevent premature internalization. To assess the reaction course in cellular environments, the release of fluorescent molecules was initially assayed, thanks to the immediate readout and possibility to visualize the outcome by microscopy imaging. To this end, a caged rhodamine that displays a 200-fold turn-on of fluorescence when the aniline moiety is unmasked was selected.[54] To perform the templated reaction, CA IX expressing cells (hypoxic HT-29) were preincubated with a bivalent ligand-PNA conjugate bearing the ruthenium catalyst (**2**, 100 nM, 30 min); after a washing step to remove excess ligand, the complementary strand **3** was added (5 μM) and cells were irradiated with 1 W collimated LED (455 nm; 30 min) in the presence of NaAsc (10 mM) as sacrificial reducing agent for the catalytic cycle of ruthenium (Figure 14a). As negative control, the reaction was performed without LED irradiation. Further controls were carried out with irradiating a system lacking the catalyst-bearing conjugate (BG) or just incubating the cells with the caged-fluorophore (PNA) (Figure 14b). Gratifyingly, signal quantification on microscopy images revealed a 40-fold increase in fluorescence for the sample in which all the components of the network are present (LED), demonstrating the successful release and consequent cellular uptake of the fluorophore; no fluorescent signal was detected in the control samples, indicating that the network is responsive to the external irradiation input and that no background release is observed in cellular environment in the absence of the ruthenium catalyst (Figure 14c).

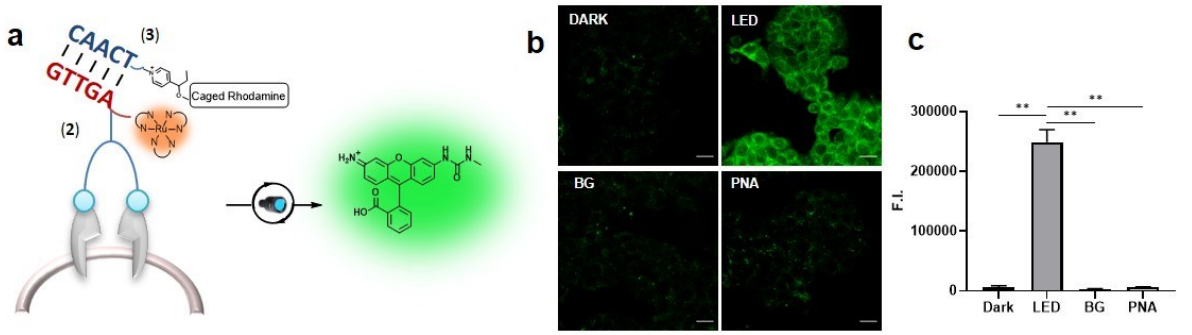

Figure 14. a) Schematic representation of PNA templated photoreductive uncaging of a fluorophore on CA IX expressing cells. b) Confocal fluorescence images of fluorophore release in hypoxic HT-29 cells; conditions: LED/DARK: CAIX-bivalent ligand-5mer-Ru (**2**), 100 nM, 30 min; wash; 5mer-py$^+$-caged-rhodamine (**3**) 5 μM, 10 mM NaAsc, 30 min 450 nm LED irradiation/dark; background (BG)/PNA: wash; 5mer-py$^+$-caged-rhodamine (**3**) 5 μM, 10 mM NaAsc, 30 min 450 nm LED irradiation/dark. c) Quantification of fluorescence of conditions shown in b. Scale bar 20 μm. Statistics were calculated using unpaired *t*-test. **p<0.01.

The same reaction was carried out on SKRC52 cells (Figure 15a), with similar results. However, the higher autofluorescence of this cell line in the rhodamine channel (Figure I-S5) diminished the overall difference in fluorescence between irradiated and not irradiated samples to 6-fold (LED *vs* DARK, Figure 15b, c).

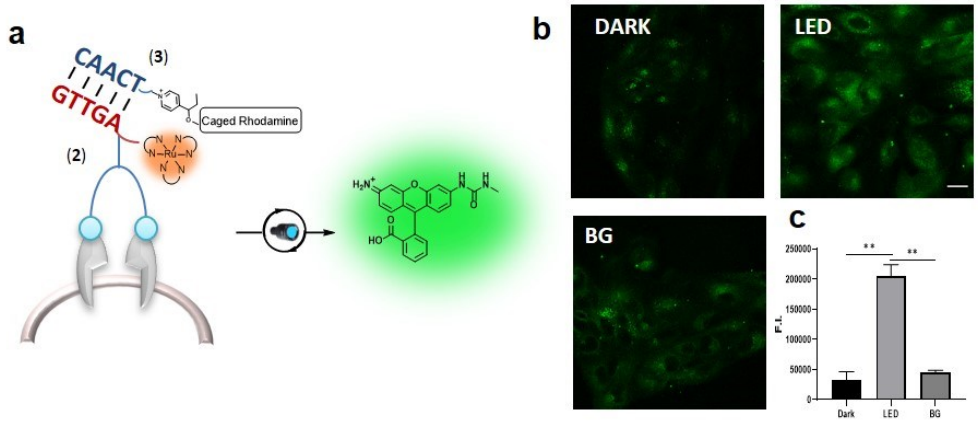

Figure 15. a) Schematic representation of PNA templated photoreductive uncaging of a fluorophore on CA IX expressing cells. b) Confocal fluorescence images of fluorophore release SKRC52 cells; conditions: LED/DARK: CAIX-bivalent ligand-5mer-Ru (**2**), 100 nM, 30 min; wash; 5mer-py$^+$-caged-rhodamine (**3**) 5 µM, 10 mM NaAsc, 30 min 450 nm LED irradiation/dark; background BG: wash; 5mer-py$^+$-caged-rhodamine (**3**) 5 µM, 10 mM NaAsc, 30 min 450 nm LED irradiation/dark. c) Quantification of fluorescence of conditions shown in b. Scale bar 20 µm. Statistics were calculated using unpaired *t*-test. **p<0.01.

Having demonstrated that it was feasible to trigger PNA templated reactions in response to CA IX expression on the surface of living cells, the cooperative effect between the protein binding event and the PNA hybridization event was investigated. To this end, the bivalent CA IX ligand was split into two monovalent ligands, each of which was conjugated to a 4-mer PNA strand. In fact, PNA 4-mers have dissociation constants in the micromolar range (K_D > 1 µM at 25 °C);[108, 125] thus, at nanomolar concentrations the interaction between 4-mers is not strong enough to yield a stable duplex in solution. However, if cooperativity is envisioned, the binding event to the membrane protein should provide the required additional stabilization for the system to remain assembled on the cell surface. In other words, once assembled on CA IX overexpressing cells, the ligand-PNA adduct should behave as the bivalent ligand. To validate this concept, the affinity of the bivalent ligand (**1**) was compared to the monomeric ligands; the latter were either conjugated to complementary PNA sequences (**4**+**5**) or to noncomplementary 4-mers (**4**+**6**) (Figure 16a). Confocal microscopy of CA IX expressing cells incubated with either of these constructs (100 nM, 30 min) showed no significant difference between the intensity of the fluorescent signal of the bivalent ligand and the complementary PNA adduct (Figure 16b); instead, the noncomplementary sequence displayed an 8-fold less intense signal (Figure 16b), confirming the cooperative contribution of the binding event and the PNA hybridization to the overall stability of the supramolecular assembly. Moreover, it has to be noticed that the assembly remains localized at the cell membrane; controls carried out at 37 °C and at 4 °C showed marginal internalization (Figure I-S6).

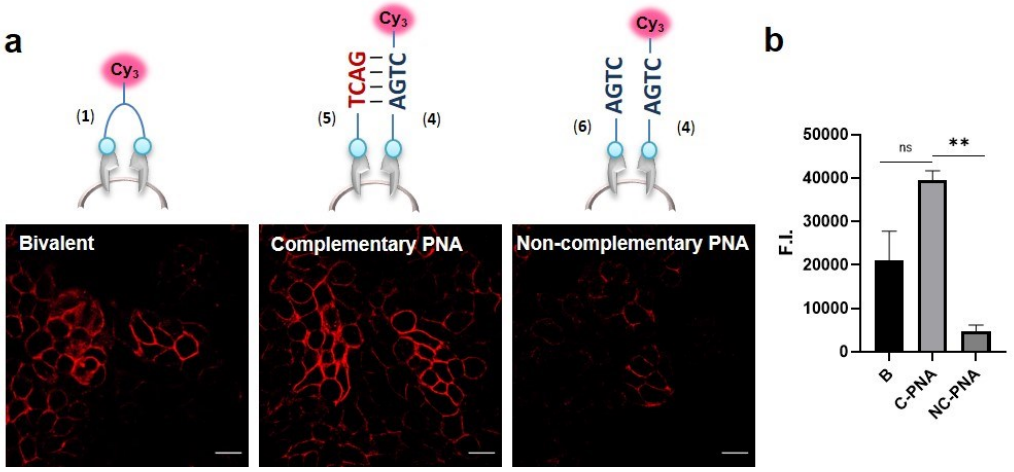

Figure 16. a) Comparison of different CA IX-PNA assemblies on the cell membrane. Conditions: hypoxic HT-29 cells treated with bivalent CAIX ligand (**1**) 100 nM or 4mers-CAIX ligand-Cy3 (**4**+**5** or **4**+**6**) 100 nM duplex, 30 min; wash and imaging. b) Fluorescence quantification of images in a). B: bivalent ligand; C-PNA: complementary PNAs; NC-PNA: non-complementary PNAs. Scale bar 20 μM. Statistics were calculated using unpaired *t*-test. **p<0.01.

Having demonstrated that cooperative events can generate a stable assembly on the cell surface, the possibility to exploit such assembly to perform chemistry was assessed. The two complementary 4mer-PNA-CA IX ligand stands were decorated with the ruthenium catalyst or the pyridinium immolative linker conjugated to a Cy3 dye respectively (**8**, **7**), incubated with CA IX (+) cells (100 nM, 30 min) and irradiated with 450 nm light (30 min; NaAsc 10 mM) (Figure 17a). In this case, the reaction can be followed over time by observing the change in localization of the Cy3 dye: before irradiation, the dye will be localized at the cell membrane; upon light irradiation and pyridinium immolation, the released Cy3 can diffuse into the cytosol (the Cy3 dye used for these experiments is not sulfated and thus cell permeable). As shown by fluorescence imaging, this is indeed the behaviour observed in cellular settings, with a clear change in localization of the signal in the Cy3 channel (Figure 17b).

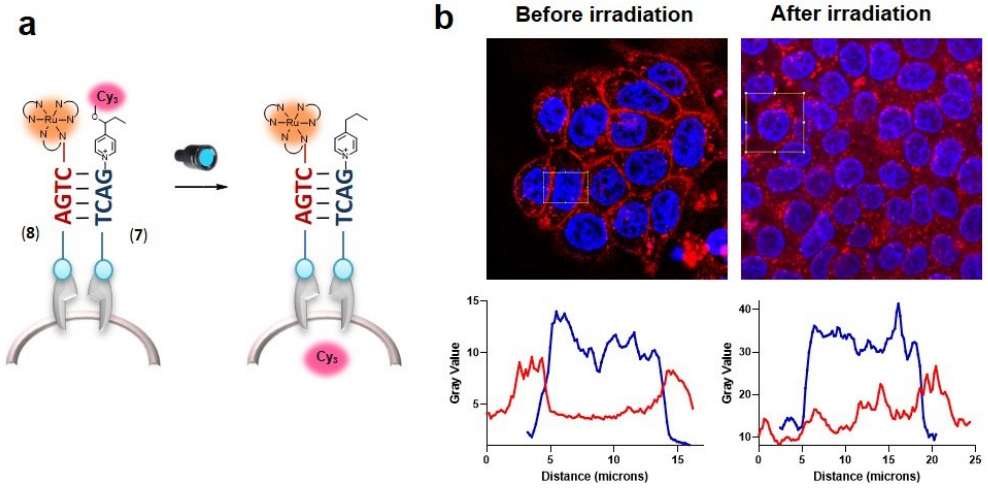

Figure 17. a) Schematic representation of the cooperative assembly for the photocatalyzed release of fluorophore from 4-mer PNA duplex anchored to a dimeric receptor. b) Confocal images show Cy3 localization in hypoxic HT-29 cells before and after photocatalyzed reaction (top), and plot profiles of the areas defined by the boxes (bottom). Conditions: CA IX ligand-4mer-py$^+$-Cy3 (**7**) + Ru-4mer-CA IX ligand (**8**) (100 nM duplex), 30 min; wash; 450 nm led irradiation, 30 min; wash; imaging. Red: Cy3; blue: Hoechst33342 (nuclei).

So far, the system proved to be selective towards the protein of interest, cooperative and able to perform chemical reactions to release a small molecule in a cellular environment in response to ruthenium photocatalysis. However, the system tested so far does not allow for signal amplification. To address this point, a three components architecture was envisioned. The system would consist of a CA IX ligand-9mer PNA (**14**) and a complementary CA IX ligand-4mer PNA bearing the ruthenium complex (**8**); upon cooperative receptor binding and PNA hybridization, the 9-mer strand displays a 5-mer overhang that can be exploited for templated reaction with a 5-mer-pyridinium bearing a caged effector molecule (**3**) (Figure 18). Upon hybridization to the overhang, the immolative linker and the ruthenium catalyst are brought in close proximity to allow for efficient energy transfer. As already mentioned, 5-mer PNA represents the optimal length for substrate turnover.[108] In addition, since the template strand does not contain the catalyst, the release reaction should occur only as a result of interaction with the preformed assembly on the cell surface, thus avoiding background release.

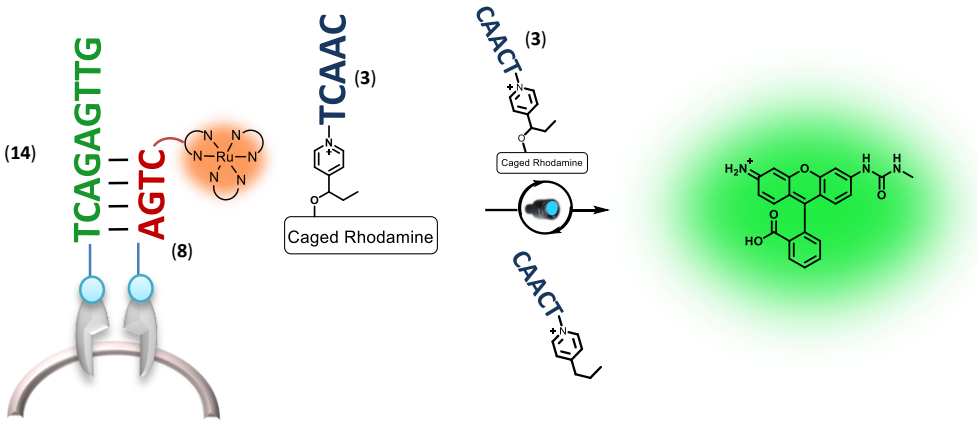

Figure 18. Schematic representation of the three components system assembling on dimeric receptor expressing cell; release of rhodamine as result of PNA-templated photoreductive uncaging.

However, to confirm that transient interactions in solution would not lead to significant reaction, the kinetics of the templated release were studied *in vitro*. Two PNA assemblies were employed to this end: the first one (**i**) consisting of a 9-mer template strand + 4-mer-Ru + 5-mer-pyridinium-caged fluorophore to mimic the background reaction (Figure 19a); the second one (**ii**) constituted by a 14-mer template strand + 9-mer-Ru + 5-mer-pyridinium-caged fluorophore to recapitulate the stable assembly generated upon CA IX binding (Figure 19a). The photocatalytic reaction was followed over time monitoring the release of a coumarin fluorophore.[108] As predicted, assembly (**i**) did not yield significant reaction either in a stoichiometric (1:1:1) or in a catalytic (1:1:10) setting (Figure 19b). On the contrary, assembly (**ii**) confirmed its superiority, with a rate constant k = 0.495 min^{-1} (1:1:1 case) and allowing for signal amplification in the catalytic setting (1:1:10), in which the concentration of the released molecule exceeds the concentration of the template already after three minutes (Figure 19b).

It has to be noted that the results of this kinetic studies are in agreement with previous reports.[108]

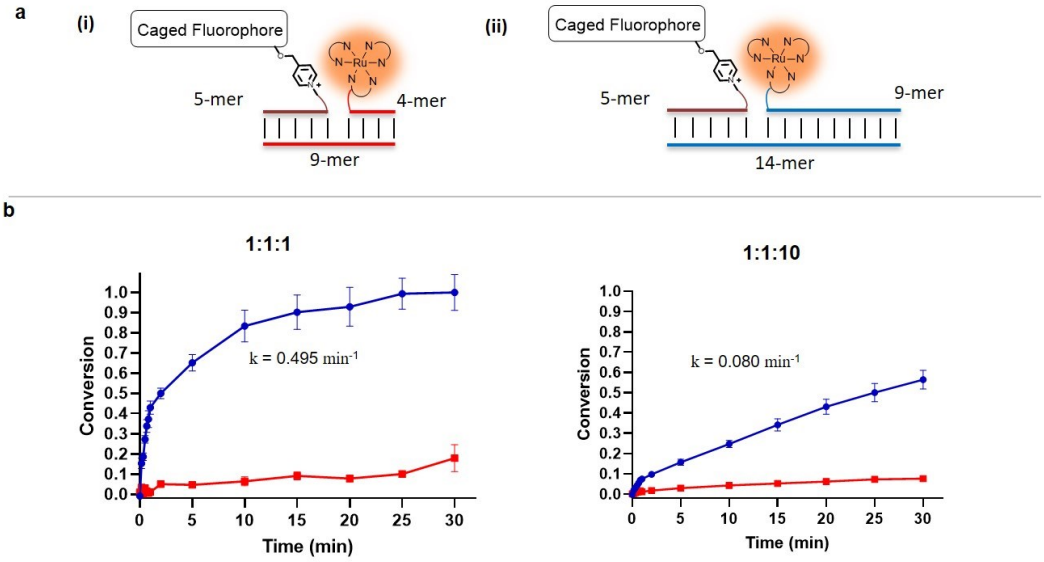

Figure 19. a) Schematic representation of PNA assemblies used for kinetic study. b) Reaction conversion over time under 455 nm LED irradiation for systems (**i**) and (**ii**) in 1:1:1 stoichiometry at 10 nM (left) and in the catalytic version (1:1:10) (right) (10 nM 14mer/9mer-Ru or 9mer/4mer-Ru; 100 nM 5mer-py$^+$-caged-fluorophore) in PBS pH 7.4 + 0.05 % tween20 + 10 mM NaAsc at 37 °C.

Overall, this data confirmed that the additional stabilisation deriving from the binding to the membrane receptor is fundamental to generate a system able to perform efficient release of effector molecules. In this light, the designed system could perform similarly to theragnostic agents, combining a first targeted recognition event to the release of therapeutic molecules. To assess the targeted release with the three components system in a cellular setting, the uncaging of a fluorophore (*i.e.* rhodamine) was evaluated in HT-29 cells either under hypoxic or normoxic conditions. To allow for duplex formation, cells were first incubated with CA IX-ligand-9-mer + CA IX-ligand-4-mer-Ru (100 nM duplex (**8**+**14**), 30 min), then washed to remove excess of ligands and treated with an excess of 5-mer-pyridinium-caged rhodamine (**3**, 5 μM). LED irradiation (30 min) in presence of sodium ascorbate (10 mM) yielded a 20-fold increase in fluorescence in hypoxic respect to normoxic cells (Figure 20a, b, CA IX (+) LED / CA IX (-) LED), confirming the potential of the system as reporting agent. Further controls, lacking light irradiation (Figure 20a, b, CA IX (+) DARK) or the ruthenium catalyst (Figure 20, CA IX (+) BG) resulted in no significant output. As evidenced by the logic gate representation of the network (Figure 20a), this experiment highlights the contribution of each basic module to the generation of the output signal: the CA IX (-) LED *vs* CA IX (+) BG settings underline the response of the first AND gate, while the CA IX (+) DARK condition show the contribution of the second AND gate (Figure 20a, logic gates schemes).

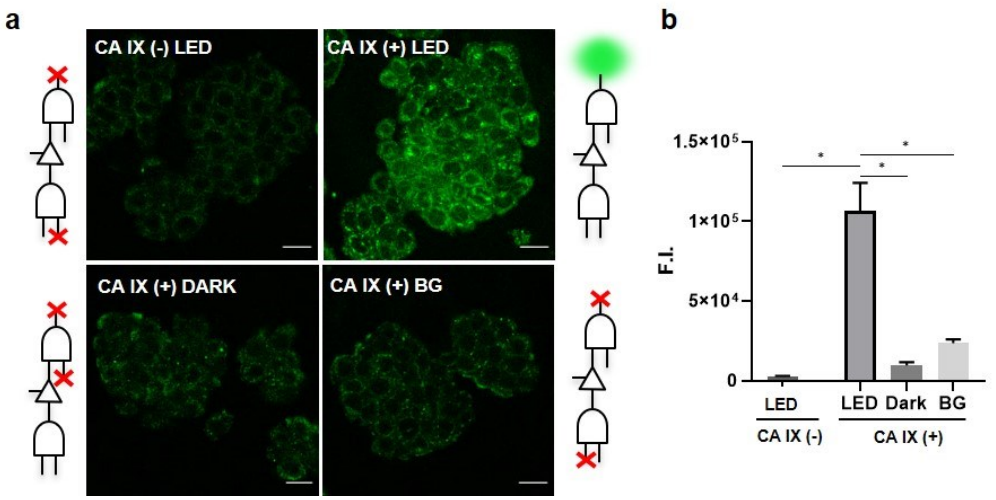

Figure 20. a) Confocal fluorescence images of rhodamine release in HT-29 cells treated with the network shown in figure 18 under normoxia (CA IX (-)) or hypoxia (CA IX (+)) and relative logic gate schemes. Conditions: CAIX-ligand-4mer-Ru (**8**), CAIX-ligand-9mer (**14**) (100 nM duplex, 30 min); wash; 5mer-py$^+$-Rho (**3**) (5 μM), 450 nm irradiation/dark (30 min); wash, imaging. Background reaction (BG): CAIX-ligand-4mer (**6**), CAIX-ligand-9mer (**14**) (100 nM duplex, 30 min); wash; 5mer-py$^+$-Rho (**3**) (5 μM), 450 nm irradiation (30 min); wash, imaging. b) Quantification of fluorescence of shown in a. Scale bar 20 μm. Statistics were calculated using unpaired *t*-test. *p<0.05.

Having demonstrated the successful generation of an output signal in response to the PNA supramolecular network and intrigued by the idea of exploiting the system as a theragnostic-like device, the application of the network for the release of a cytotoxic agent was assayed. To this end, Monomethyl-auristatin E (MMAE) was selected as model cytotoxic to release. In fact, MMAE is a well-established antimitotic that acts as microtubule destabiliser (low nM affinity for tubulin)[200] that is employed as payload in antibody-drug conjugates used for cancer therapy.[201] To evaluate the cytotoxic effect as a result of network output, a 5-mer-pyridinium conjugated to MMAE (**15**) was synthesized; in order to avoid background toxicity by means of cellular uptake, this construct was also functionalized with a cell impermeable moiety (as it was previously done for the caged fluorophore conjugates). The effect in cells of the PNA-MMAE conjugate *vs* free MMAE was evaluated by cytotoxicity assay; the result showed a difference in toxicity >100 fold (Figure I-S7).

The response of the network to the expression level of CA IX was evaluated by growth inhibition in HT-29 cells treated under hypoxia or normoxia. In details, upon treatment with the network for MMAE release (Figure 21a, b), cells were incubated for 48 hours before being stained with the nuclear dye Hoechst33342 and imaged with a high throughput microscope (Figure 21d for representative images); the acquired images were then processed, and nuclei count was considered to estimate growth inhibition. The quantification clearly indicates an effect on growth inhibition upon light irradiation when the network is assembled (Figure 21c, **8**+**14**+ 500/250 nM **15**); however, the three components alone or the network incubated in the dark did not affect cell viability (Figure 21c, d). Moreover, the same conditions tested in HT-29 under normoxic condition (i.e. not expressing CA IX) did not affect cellular growth,

demonstrating the dependence of the network response to the presence of the cancer biomarker (Figure 21c, d).

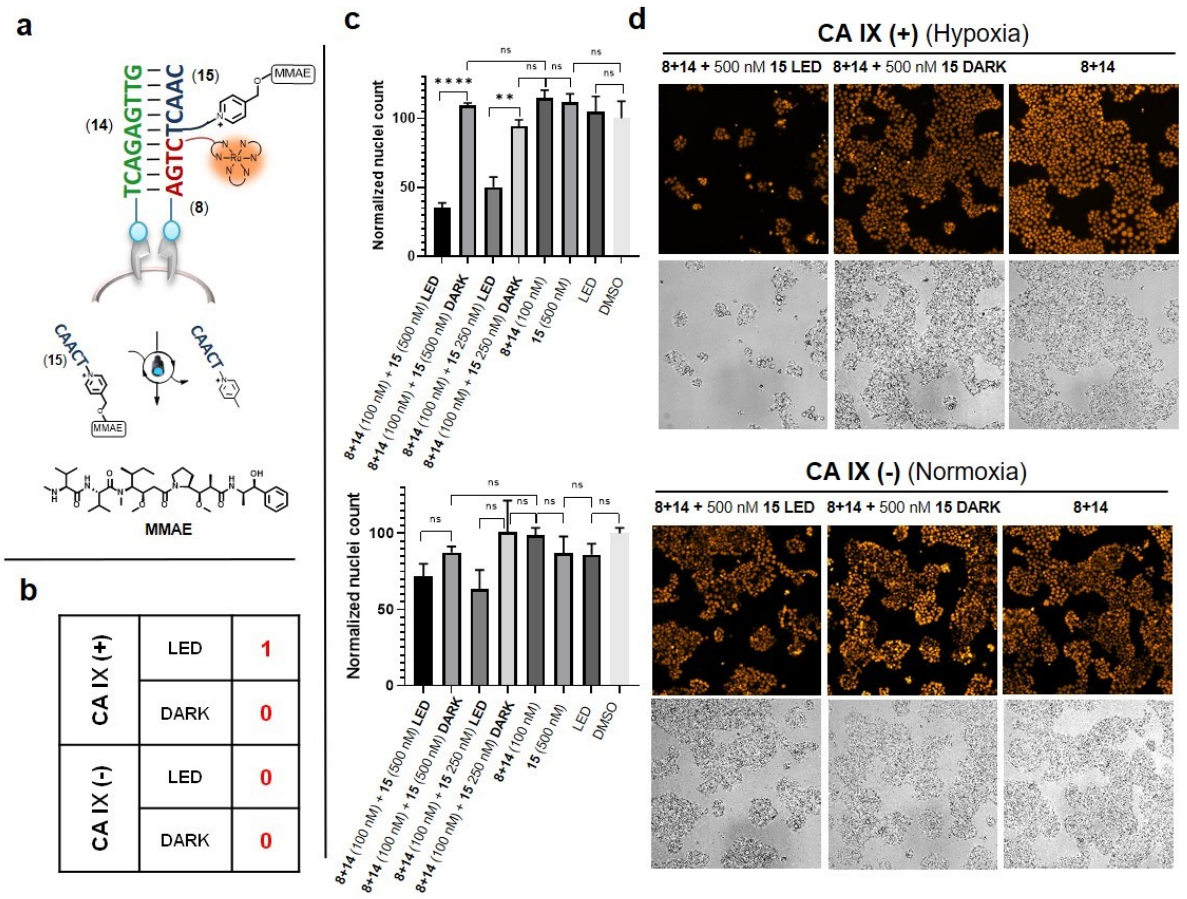

Figure 21. a) Schematic representation of the components interacting in the logic-gated network (3 strands system) to release a cytotoxic drug (MMAE). b) Truth table for the system shown in a. c) Quantification of cytotoxic effect based on nuclei count upon treatment with the network shown in a. d) Nuclear staining (Hoechst 33342) and bright field representative pictures of treatment conditions shown in c. Conditions: cell treated with CA IX-ligand(s)-PNA (**8** and **14**) (100 nM, 30 min); wash; 5mer-py+-MMAE (**15**) at concentrations reported in c; 455 nm led irradiation/dark (30 min); incubation (1 hour); wash; incubation for 48 hours; staining and acquisition. Scale bar 200 µm. Statistics were calculated using unpaired *t*-test. $^{ns}p>0.05$, $^{**}p<0.01$, $^{****}p<0.0001$.

The effect elicited by MMAE release can also be amplified by performing a second treatment with the network (Figure 22a): MMAE release was repeated after 48 hours from the first treatment. Nuclei count performed after 96 hours from the first treatment revealed higher discrimination between samples irradiated and samples kept in the dark (up to 70-fold difference for 250 nM **15**) (Figure 22b, c).

Furthermore, to prove the contribution of the first AND gate to the targeted release reaction, growth inhibition was assessed upon treatment with the two components system (**2**+**15**) (Figure 23a). In this case, a clear response was observed for cells irradiated *vs* treated in the dark, but no discrimination between hypoxic (CA IX (+)) and normoxic (CA IX (-)) was observed suggesting the expected independency of the templated release from the first AND gate (Figure 23b, c, d).

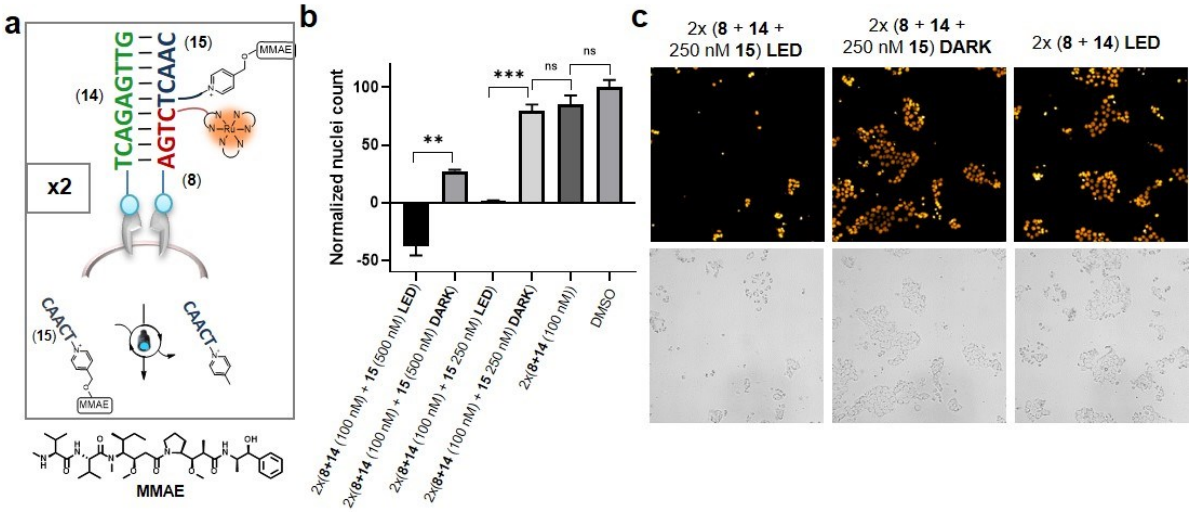

Figure 22. a) Schematic representation of PNA supramolecular assembly to release Monomethyl auristatin E (MMAE). b) Quantification of cytotoxic effect based on nuclei count for double treatment of hypoxic HT-29 cells (CA IX (+)) with construct in a. c) Nuclear staining (top) and bright field (bottom) representative images of treated cells. Conditions: cells treated with CAIX-ligand(s)-PNA (**8** and **14**) (100 nM, 30 min); wash; 5mer-py$^+$-MMAE (**15**) at concentrations reported in b; 455 nm led irradiation/dark (30 min); incubation (1 hour); wash; incubation for 48 hours; repeat treatment; incubation for 48 hours; staining and acquisition. Statistics were calculated using unpaired *t*-test. ^{ns}p>0.05, **p<0.01, ***p<0.01.

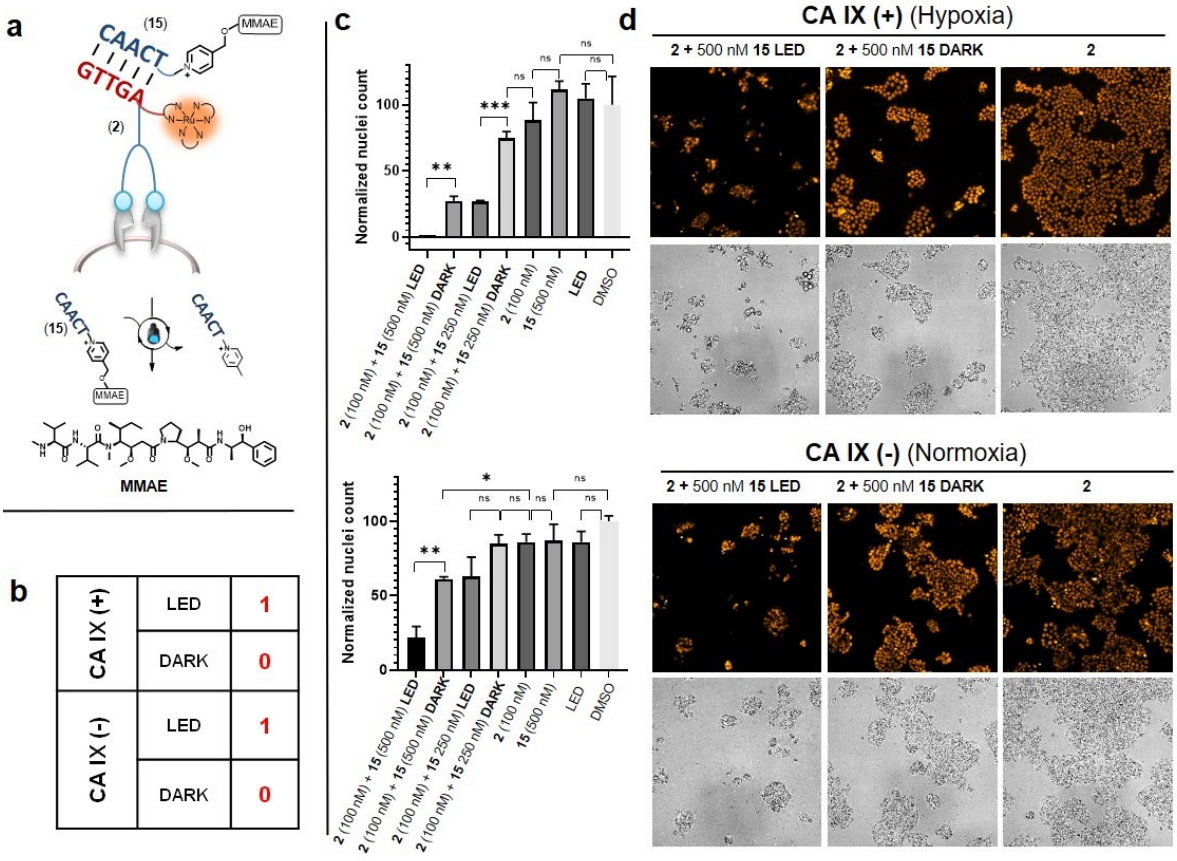

Figure 23. a) Schematic representation of PNA network (2 strands system) to release a cytotoxic drug (MMAE). b) Truth table for the system shown in a. c) Quantification of cytotoxic effect based on nuclei count upon treatment with constructs in a. d) Nuclear staining (Hoechst 33342) and bright field representative pictures of treatment conditions. Conditions: cell treated with CA IX-ligand(s)-PNA (**2**) (100 nM, 30 min); wash; 5mer-py$^+$-MMAE (**15**) at concentrations reported in c; 455 nm led irradiation/dark (30 min); incubation (1 hour); wash; incubation for 48 hours; staining and acquisition. Scale bar 200 µm. Statistics were calculated using unpaired *t*-test. ^{ns}p>0.05, *p<0.05, **p<0.01, ***p<0.001.

Conclusions

In summary, a PNA-based network composed of a three components system that responds to the cancer biomarker CA IX was developed. The system consists of two consecutive AND gates mediated by an amplifier module. The network can assemble on the surface of CA IX expressing cells and allows for the release of effector molecules in an amplified fashion thanks to the use of PNA templated reactions. The system capitalizes on the cooperative assembly of PNA components binding to proximal sites on the target receptor under thermodynamic equilibrium. This feature renders the system sensitive to the expression level of the target and grants reversibility (i.e. system disassembly) upon target disappearance. This property makes this network different from irreversible systems driven by a toe-hold displacement event. The employment of visible light as additional trigger for the $[Ru(bpy)_3]^{2+}$ catalysed uncaging reaction provides the opportunity to restrict the release only to an area of interest, overcoming any off-target effect. The compatibility of the network with *in cellulo* sense and release actions suggests the possibility to use these systems as theragnostic devices. Moreover, while this network is specific towards CA IX, the development of similar system responding to other dimeric receptors can be envisioned.

Chapter II

Supramolecular network coupling a DNA circuit to templated reactions for quadratic amplification.

This project was carried out in collaboration with KiTae Kim and Dalu Chang. The content of this chapter is adapted from *Kim, K. T., Angerani S., Chang D. and Winssinger N. "Coupling of DNA Circuit and Templated Reactions for Quadratic Amplification and Release of Functional Molecules." Journal of the American Chemical Society 141, 16288-16295 (2019).*[99]

Introduction

The wide use of oligonucleotides for the design of responsive devices has been already anticipated in the introduction of this work.[2] Leveraging on the ease of programmability, these systems can be easily customised and have proven capable of complex operations.[202] In parallel, the power of templated reactions to yield output amplification has been successfully applied to several systems,[19, 108] including the CA IX responsive network described in Chapter I.[98] An interesting area of application for these systems is the detection of endogenous nucleic acids, such as miRNAs. In fact, miRNAs have been identified as cancer biomarkers.[203] However, since miRNA are present at subnanomolar levels,[204] systems able to generate an amplified readout are necessary. Based on these premises, combining a DNA-based circuit and a PNA templated reaction represented an attractive way to harness a sensing operation coupled to the release of functional molecules. To this end, a network that generates an assembly able to perform catalytic transformations as a result of a triggering event initiated by a miRNA sequence was envisioned (Figure 24).

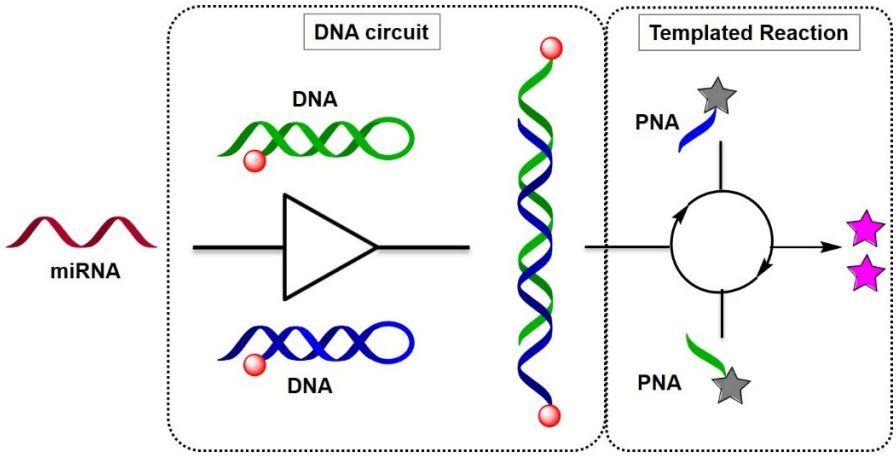

Figure 24. Schematic representation of miRNA triggered network coupling a DNA circuit to a PNA templated reaction.

Network Design

The network is designed so that the input strand can act catalytically (first amplification), and the resulting product is competent for templated transformations with substrate turnover (second amplification). In details, the network requires an initiator strand (I) and two metastable hairpins functionalized with a $[Ru(bpy)_2phen]^{2+}$ catalyst (RuA and RuB); at this stage, the ruthenium catalyst is shielded by the geometry of the hairpin, and thus not available for templated reactions (Figure 25). Once the initiator strand (I) triggers the opening of the metastable hairpin (RuA) by toehold displacement, the second Ru-hairpin (RuB) can hybridize to the overhang displayed by RuA and displace the initiator strand (Figure 25). The resulting RuA:RuB adduct exhibits two hybridization sites to enable templated reaction with complementary 4-mer PNAs conjugated to a pyridinium immolative linker and a caged effector (Output). In this way, the templated reaction can perform under 455 nm light irradiation in the presence of sodium ascorbate as sacrificial reducing agent (Figure 25).

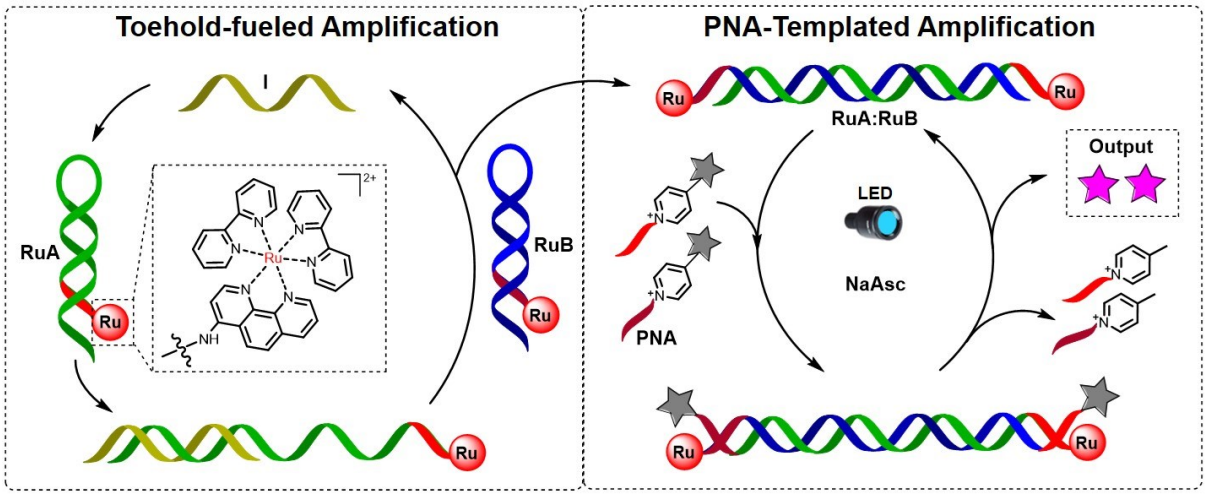

Figure 25. Schematic representation of the toehold-fuelled DNA circuit coupled to the PNA/DNA-templated photoreductive uncaging of output molecules.

Results and discussion

The system was designed to be triggered by miR-21; for the characterization of the system, the corresponding DNA (miR-21-5p DNA) was used as initiator strand (I). First, the hairpin sequence was optimized to show metastability in the absence of the initiator strand; at the same time, the length of stem and loop was adjusted in order not to limit the rate of the circuit. Among the different couples of hairpins tested (Figure II-S1, Table II-S1 for sequence information), hairpins with 7-mer overhangs, 14-mer stems and 9-mer loops (Figure 26a) performed better, showing no leakage and >90% conversion to the hairpin duplex (50 nM hairpins, 0.125 eq. initiator, Figure 26b). With this system in hand, the corresponding hairpins pair bearing the ruthenium complex at the 5' position was prepared, and the efficiency of the RuAB duplex formation was evaluated by electrophoresis. In this case poor conversion was

observed in tris buffer (Figure 26c top), probably due to the additional hairpin stabilization originating from electrostatic interactions between DNA and the positively charged ruthenium complex. To overcome this issue, magnesium chloride (12 mM) was added to the system, restoring the efficiency of the circuit (Figure 26c bottom, Figure II-S2 for other $MgCl_2$ concentrations).

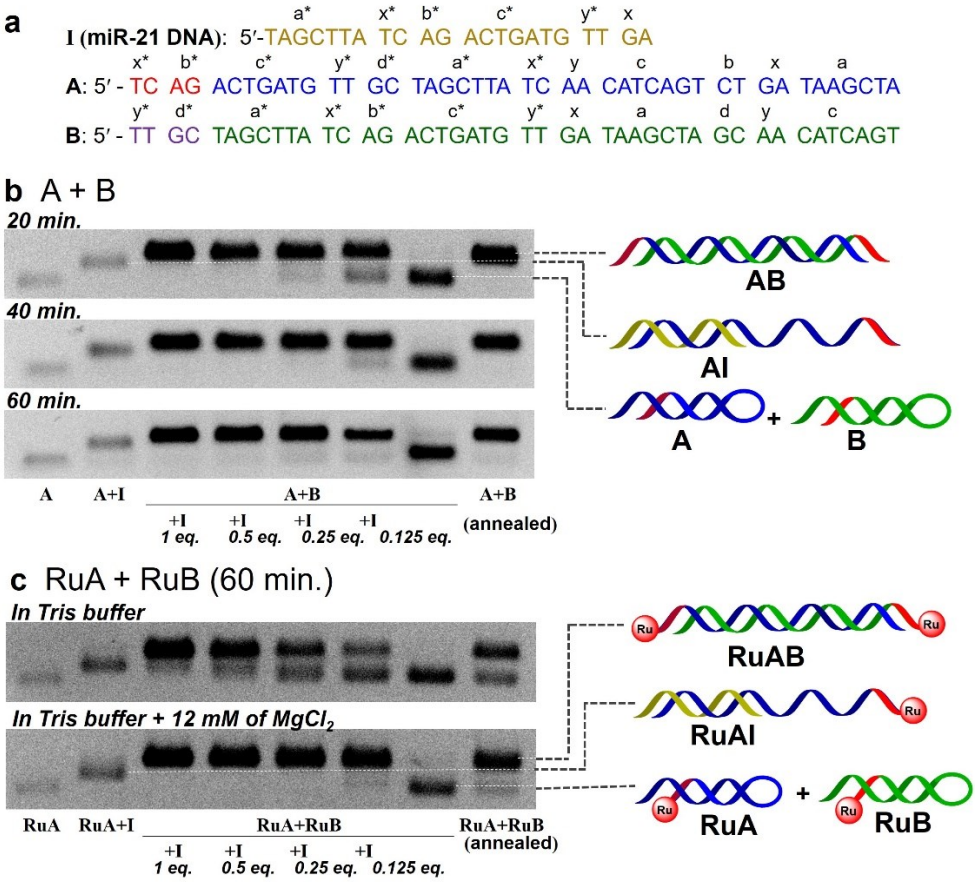

Figure 26. a) Sequences of A, B, and I with segment names. RuA and RuB have the same sequence of A and B, respectively. DNA-fuelled amplification of (b) AB or (c) RuAB duplexes bearing two sticky-ends, the sites for templated reaction, monitored by 2 % agarose gel electrophoresis. The RuAB circuitry is accelerated by addition of 12 mM $MgCl_2$. Tris buffer conditions: 20 mM pH 7.5 Tris, 140 mM NaCl, 5 mM KCl, 12 mM $MgCl_2$, 0.02 % tween-20, 37 °C.

In order to measure the kinetics of the network, one hairpin was conjugated to a dabcyl quencher (Dab-A), while the initiator was attached to fluorescein (FAM-I) (Figure 27); in this way the first step of the network, the formation of I:A, can be monitored by following the fluorescence quenching of fluorescein, while the second step, the formation of A:B, would result in FAM fluorescence recovery. These measurements revealed rate constants k_A = 2.3×10^6 M^{-1} s^{-1} and k_B = 5.1×10^5 M^{-1} s^{-1} at 37 °C (approximation pseudo-first order reaction, e.g. [Dab-A >> FAM-I]) (Figure 27, Figure II-S3), which result faster than the one observed in a circuit reported by Pierce *et al*. that employs a 6-mer toehold.[205] The kinetics were also confirmed assuming second order kinetics (Figure II-S4).

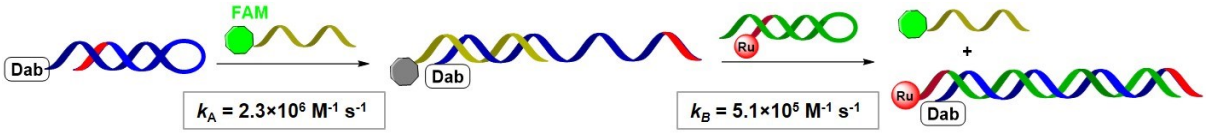

Figure 27. Fluorescence quenching experiments for determination of kinetic parameters (k_A and k_B) of DNA circuit by pseudo-first order kinetics. Conditions: 20 mM pH 7.5 Tris, 140 mM NaCl, 5 mM KCl, 12 mM $MgCl_2$, 0.02 % tween-20, 37 °C (reaction performed at 10 nM or reagents). Dab: dabcyl quencher; FAM: fluorescein.

The resulting RuA:RuB duplex is equipped with two 4-mers at the 5'-ends that can be further employed as sites for hybridization with complementary PNA strands for templated reactions. Even though the unveiling of unpaired overhangs is relatively common in DNA circuits, the impact of short sticky ends in templated reactions had not been assessed before. Despite 4-mer strands are usually too short to yield efficient templated reactions, the length limitation may be compensated by additional base stacking upon hybridization at the sticky-end. In order to quantify this effect, the catalytic sites were evaluated individually by following the uncaging of a coumarin fluorophore with truncated versions of the RuA:RuB duplex (i.e. RuS1:PC and RuS2:PC) (Figure 28).

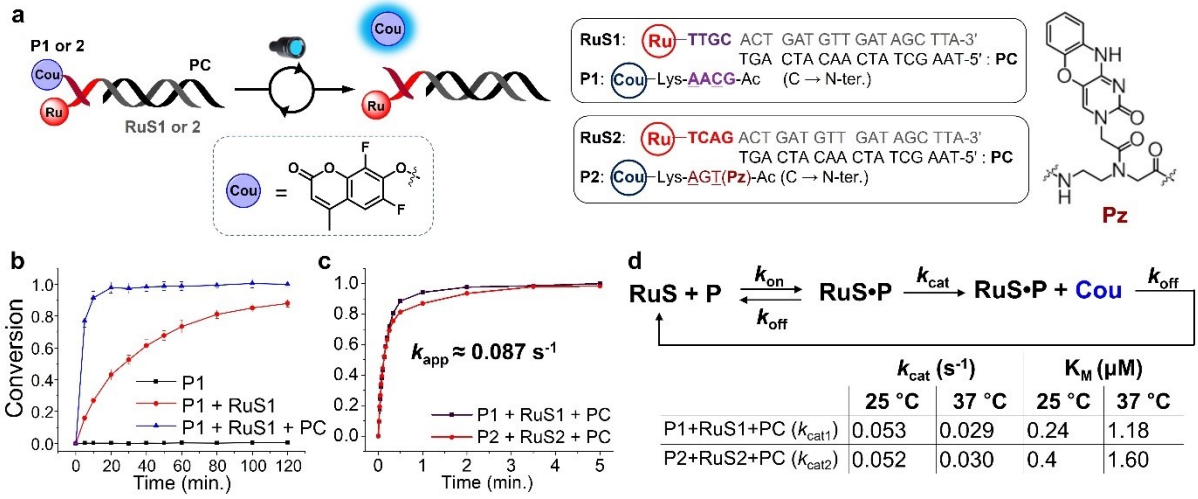

	k_{cat} (s^{-1})		K_M (μM)	
	25 °C	37 °C	25 °C	37 °C
P1+RuS1+PC (k_{cat1})	0.053	0.029	0.24	1.18
P2+RuS2+PC (k_{cat2})	0.052	0.030	0.4	1.60

Figure 28. a) Schematic representation of templated reaction on DNA sticky-ends using truncated versions of the RuA:RuB duplex and relative sequences used; underlined residues represent serine-modified PNA. b) Templated reaction between P1 and RuS1 using 1:1 stoichiometry (50 nM) at 25 °C in the presence or absence of PC strand. c) k_{app} of P1 and P2 with RuS1:PC and RuS2:PC respectively (6 μM, 1:1 stoichiometry). d) Catalytic performance of RuS and measurements of k_{cat} and K_M from Lineweaver–Burk plot.

Several PNA modifications were tested (Figure II-S5), with N-acetylated serine-modified PNA 4-mers resulting the better performing, yielding templated conversion with half-life < 3 min (P1+RuS1+PC, Figure 28b), which is significantly superior to the case in which the sticky end is absent ($t_{1/2}$ ≈ 40 min, P1+RuS1, Figure 28b). The positive contribution of the base stacking was further confirmed by the improved kinetics obtained by substituting the pyrimidine base cytosine with a phenoxazine (Pz), displaying an extended π-surface area ($t_{1/2}$ > 30 min, P2'+RuS2+PC *vs* $t_{1/2}$ ~ 3 min, P2+RuS2+PC) (Figure 28, Figure II-S6). The reaction outcome resulted also strictly connected to sequence specificity (Figure II-S7). The importance of the sticky end presence was confirmed by running the reaction with DNA strands lacking the short

overhang (Figure II-S8). Additionally, templated reactions benefiting from a sticky end hybridization resulted 38-fold faster (k_{app} = 0.087 s^{-1}) (Figure 28c, Figure II-S9) than PNA-PNA templated reactions with 4-mers.[108] Moreover, since the network was designed to sense targets present at low concentrations, the catalytic and Michaelis constants were calculated for systems in which RuA:RuB is present in catalytic amount; these experiments showed k_{cat} ~ 0.03 s^{-1} and K_M ~ 1 μM at 37 °C (Figure 28d, Figure II-S10).

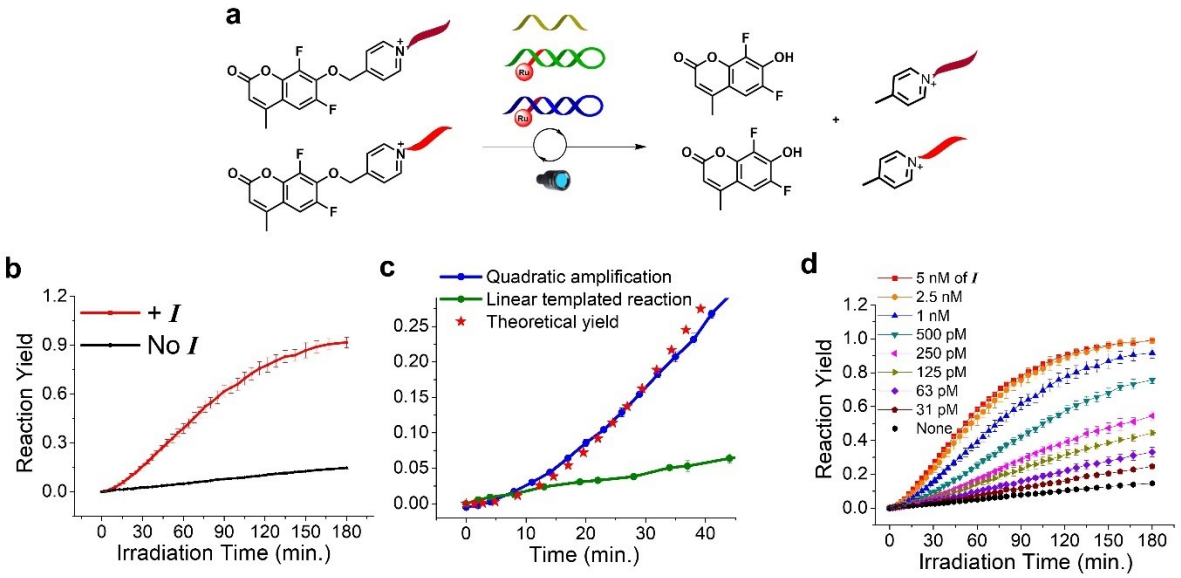

Figure 29. a) Schematic representation of quadratic templated release of coumarin. b) Templated reaction performed with or without 0.2 eq. of I at 25 °C. c) Initial stage of the quadratic (5 nM of RuA and RuB) and linear templated reaction (1 nM of RuA and RuB) in the presence of 1 nM of I. d) Release over a range of concentrations of I (1 nM, 90 min of irradiation time). General conditions: 150 nM of PNAs, 5 nM of DNAs, 20 mM pH 7.5 Tris, 140 mM NaCl, 5 mM KCl, 12 mM $MgCl_2$, 0.02 % tween-20, 5 mM sodium ascorbate, 25 °C, 200 μL, data was taken right after adding I.

Having characterized the single components of the network, the overall circuit output was investigated (Figure 29a). As anticipated, this system is designed to yield quadratic amplification upon accumulation of the RuA:RuB duplex and templated reaction. Incubation of 0.2 eq. of initiator respect to RuA and RuB (5 nM) in the presence of excess PNA 4-mers (150 nM, 30-fold excess) (Figure 29b, Figure II-S11) indeed showed exponential signal amplification, reaching maximum a 6-fold faster reaction than in the linear case, and affording > 80 nM output from 1 nM input (Figure 29c). The quadratic trend was confirmed across a range of initiator concentration (31 pM - 5 nM, Figure 29d, Figure II-S12), with the system reaching up to 3500-fold amplification with 5 μM PNAs after 80 min irradiation (10 nM RuA, RuB, 1 nM I, 37 °C) (Figure II-S13E). These results convert to >195 turnovers for each catalytic site and >9 turnovers of initiator.

Moreover, the selectivity of the network and the quadratic trend were tested at 37 °C over the target miR21 sequence (Figure 30b, c) or other sequences, including different DNA and RNA, proving to be able to discriminate even a single mismatch (Figure 30a, d). Accordingly, the

system responds to the target sequence across a range of concentrations (Figure 30e, Figure II-S13F).

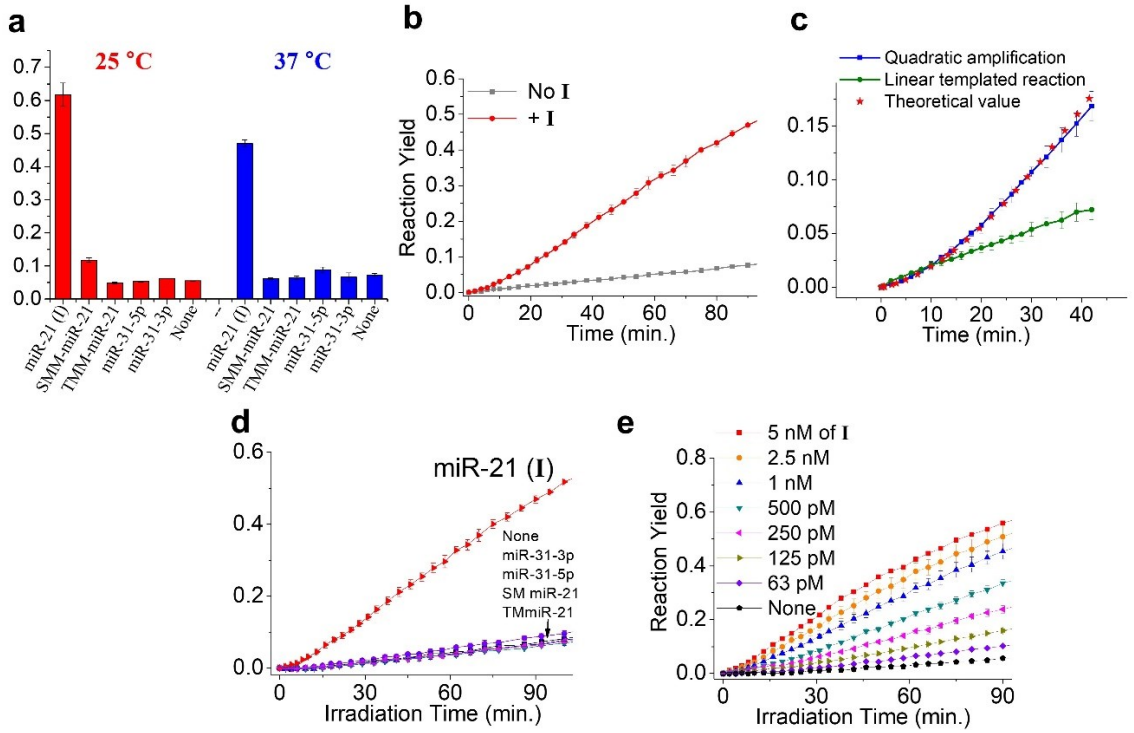

Figure 30. a) Templated reaction yield in the presence of different types of oligonucleotide sequences (1 nM, 90 min of irradiation time). b) Reaction with or without 0.1 eq. of I. c) Initial stage of the quadratic (10 nM of RuA and RuB) and linear templated reaction (1 nM of RuA and RuB) in the presence of 1 nM of I. Templated reaction yield in the presence of different d) types of mismatched sequences or e) concentration of I. General conditions: 150 nM of PNAs, 5 nM of DNAs, 20 mM pH 7.5 Tris, 140 mM NaCl, 5 mM KCl, 12 mM $MgCl_2$, 0.02 % tween-20, 5 mM sodium ascorbate, 37 °C, 200 µL, data was taken right after adding I. miR-21, SMM-miR-21, and TMM-miR-21 are DNA sequences. miR-31-5p and 3p are RNA sequences.

Furthermore, to investigate the sensitivity of the system, the detection limit was calculated (Figure 31, Figures II-S14, II-S15, II-S16). The network is able to sense the presence of initiator down to 8 pM (1.6 fmol) at 37 °C after 3 hours irradiation (Figure 31a); the limit can be further pushed to subpicomolar levels in case of preincubation (24 hours) before irradiation (8 hours) (Figure 31b).

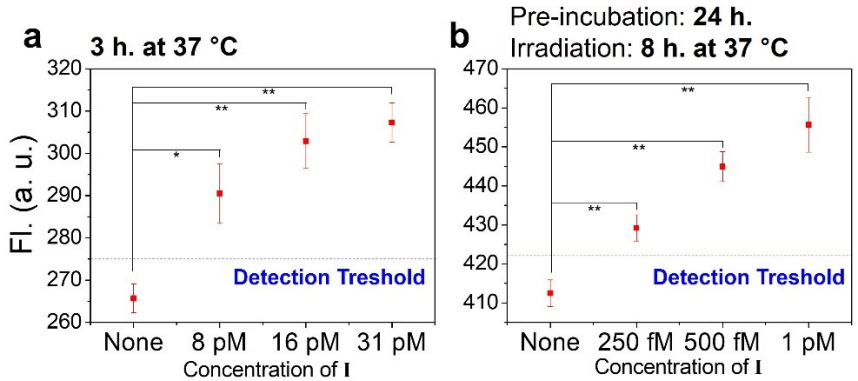

Figure 31. a) Detection threshold of quadratic amplification reaction tested at 3 hours irradiation time or b) at 24 hours pre-incubation and 8 hours irradiation time. Experiments were performed in general conditions. Statistics were calculated using an unpaired two-sample *t*-test (*p < 0.05, **p < 0.01). The detection threshold was defined as the average of no initiator (None) plus three times the standard deviation.

The characterization of the system components demonstrated that the network is competent for the release of output molecules in the micromolar range (Figure II-S13), thus the release of biologically effective molecules could be envisioned. In this context, 5-fluorouracyl (5FU) was selected as model substrate to release. In fact, 5FU is a well established anticancer drug[206] with IC_{50} between low micromolar and high nanomolar range.[207, 208] 5FU-PNA conjugates (5FUP1 and 5FUP2) were prepared by attaching the pyridinium linker at the oxygen of 5FU (O2 position) to yield a caged prodrug (Figure 32). The cytotoxicity of the 5FU-pyridinium-PNA conjugates *vs* free drug was tested in HT-29 cells towards a range of concentrations after 144 hours treatment; while the free drug showed IC_{50} of 350 nM, the PNA conjugate did not show observable toxicity up to 10 μM (Figure 32).

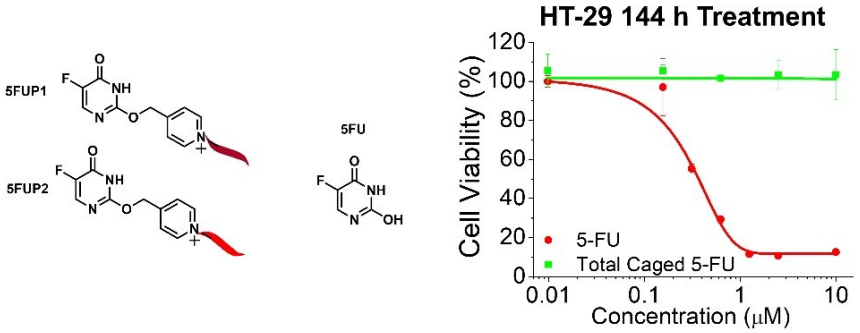

Figure 32. Left) Schematic representation of 5FU-PNA conjugates and 5FU free drug. Right) Dose-response curve for 5FUP1/5FUP2 and 5FU in HT-29 cells after 144 hours treatment.

Established the window of concentration useful to elicit an effect in a cellular setting, the release of 5FU by the network was first evaluated *in vitro* by HPLC quantification (Figure 33b).

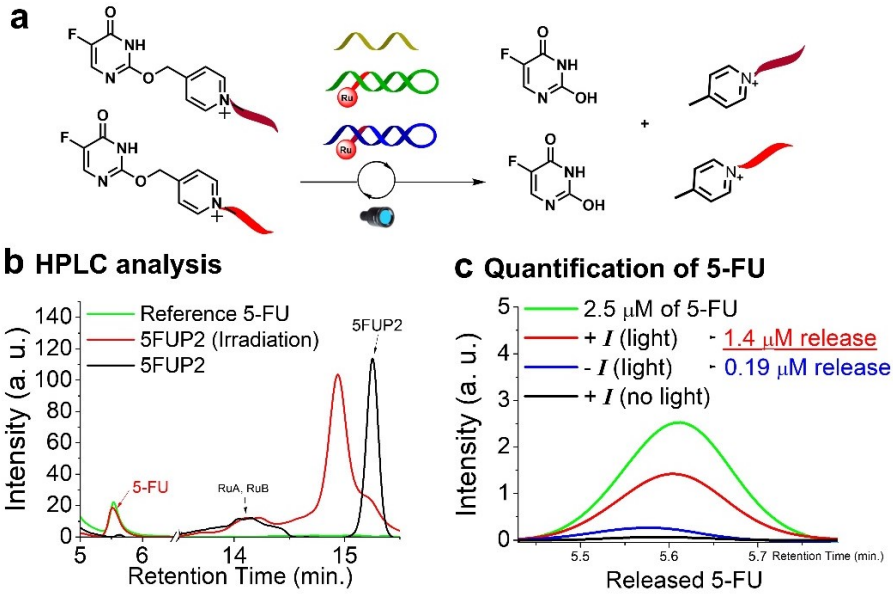

Figure 33. a) Schematic representation of quadratic release of 5FU. b) HPLC analysis of released 5FU from templated reaction. Conditions: 2 hours irradiation, 20 μM of 5FUP2, 1 μM of RuA and RuB, 100 nM of I, 5 mM sodium ascorbate, total V. 100 μL in general buffer. c) HPLC analysis of 5-FU released in the presence of 1 nM of miR-21-5p with irradiation (light) or without irradiation (no light). The area of 0.25 μM 5FU (0.25 nmol / 100 μL) was used as the reference. Reaction conditions before direct injection: 0.5 h of irradiation, 4 h of pre-incubation, 5 μM of each 5FUP1 and 5FUP2, 60 nM of RuA and RuB, 1 nM of miR-21-5, 5 mM of sodium ascorbate, total V. 100 μL in general buffer.

Similarly, the release reaction was carried out using the mature bioactive form of miR21, microRNA-21-5p, under conditions that mimic the triggering of the network by circulating miRNA. In this way, miR21-5p (1 nM) was incubated with RuA and RuB (60 nM) for 4 hours, followed by addition of PNAs-pyridinium-5-FU (5FUP1, 5FUP2, 5 μM each) and 30 min irradiation with 455 nm LED (5 mM NaAsc) or incubation in the dark; the chromatogram clearly showed the possibility to yield concentration of released drug above the IC_{50} value (1.4 μM) in the presence of initiator (Figure 33c), revealing a >1000-fold amplification. On the other hand, without initiator the amount of released product was significantly lower than the IC_{50} value (0.19 μM) (Figure 33c).

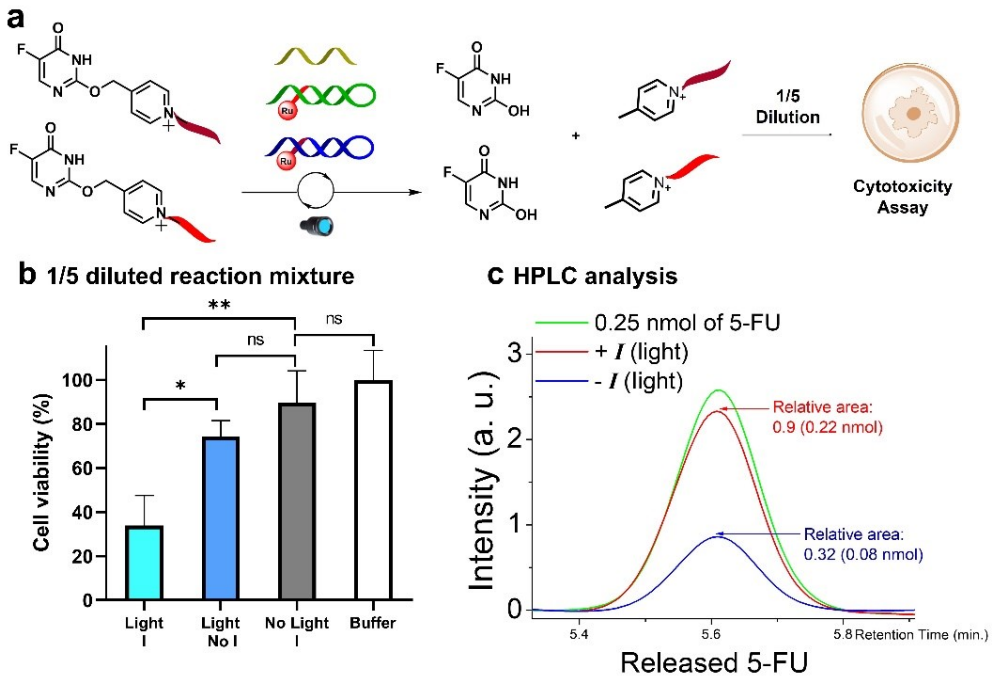

Figure 34. a) Schematic representation of 5FU release for cytotoxicity assay. b) Quantification of cell viability in HT-29 cells treated with 5FU released by the coupled system in the presence or absence of 1 nM of I with irradiation (+light) or without irradiation (no light). The viability of Tris buffer-treated cells was used as control (Buffer). Reaction conditions before treatment to cells: 3 h of irradiation, 5 μM of each 5FUP1 and 5FUP2, 10 nM of RuA and RuB, 1 nM of I, 5 mM of sodium ascorbate, total V. 140 μL in general buffer. 1/5-diluted samples were used to treat cells. Statistics were calculated using an unpaired two-sample *t*-test ($^{ns}p \geq 0.05$; *p < 0.05; **p < 0.01). c) HPLC analysis of the reaction performed in the same conditions (100 μL scale, no dilution).

Finally, the effect of the network release was evaluated in HT-29 cells: the reaction mixture was diluted into cell media and cells were incubated for 144 hours and viability was evaluated with a WST-1 assay (Figure 34a; Figure 34c, Figure II-S17 for HPLC confirmation of 5FU release). The results of the assay confirm the cytotoxic effect of the network (Light, I), while samples missing either the initiator input (Light, No I) or LED irradiation (No light, I) showed cell viability ≥ 75% (Figure 34b). Even though the release reaction was not performed entirely *in cellulo*, the results serve as proof of concept for the successful release of bioactive molecules by a DNA-based network responding to biologically relevant inputs.

Conclusions

In summary, a DNA/PNA-based network able to perform quadratic output amplification was developed. The network can respond to biologically relevant inputs, such as miR-21, sensing the analyte down to subpicomolar concentrations and being able to discriminate sequences that differ just by one nucleobase. The circuit can in turn translate the input signal to output by releasing effector molecules up to micromolar concentrations starting with 1 nM of input strand, achieving > 1000-fold amplification. The power of the network relies on two sequential amplification steps, the first one based on a toehold displacement process yielding a DNA duplex that acts catalytically in the following step, which is represented by a DNA/PNA templated reaction enhanced by sticky-end hybridization. In this context, the contribution of π-stacking interactions at the sticky ends site was investigated, resulting in improved reaction with purine nucleobases or with pyrimidine surrogates displaying a larger π-surface area. The benefits of sticky-end interactions allowed to perform extremely fast (k_{cat} ~ 0.05 s^{-1}) templated reactions even at very short PNA length (4-mers). The application of this network can be potentially extended to any oligonucleotide sequence for sensing purposes. In addition, the possibility to release biologically active output molecules enables to elicit an effect in cellular environment in response to a circulating biomarker.

Chapter III

Minimal PNA-based hybridization chain reaction (HCR) network.

This project was carried out in collaboration with KiTae Kim.

Introduction

As highlighted in the introduction section regarding biosupramolecular networks, HCR systems generate polymeric elongated products from the alternate assembly of two hairpins in response to the presence of a triggering strand.[205] This technology has been widely used for sensing purposes,[63] spanning from miRNA detection[69-74] to the recognition of target receptors on cell surface.[32, 47, 49, 67, 68] Recently, HCR has been employed to trigger the release of functional molecules,[75] and it was further coupled to logic gated operations thanks to the use of split initiators[47, 49] (Figure 35).

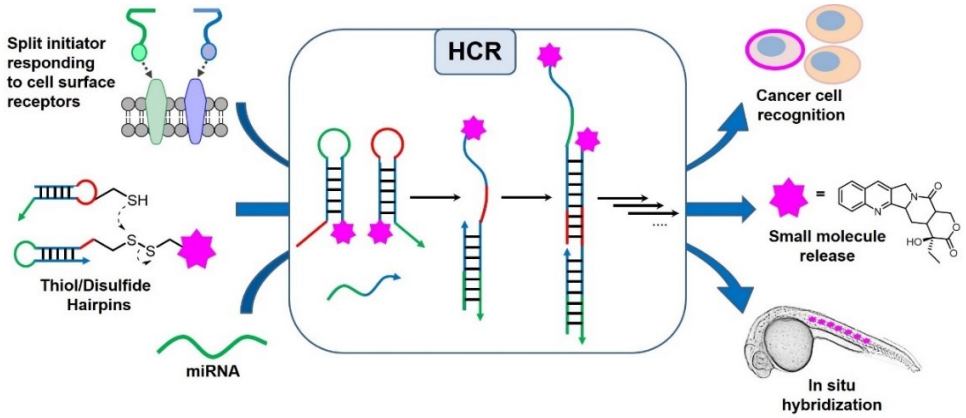

Figure 35. Schematic representation of different inputs and outputs of HCR.

A key aspect to grant effective HCR is represented by the metastability of the hairpin components, which must avoid untriggered hybridization in the absence of the initiator strand. On the other hand, presence of the trigger strand should allow for efficient elongation. For these requirements to be fulfilled, HCR systems require long DNA sequences (≥30-mers);[205] to maintain hairpin metastability, the shortest stem region lengths vary between 12 and 18 nucleotides, with toehold regions of length comprised between 6- and 12-mers.[62, 209, 210] Moreover, to grant metastability the length of toeholds needs to remain shorter than the length of stem regions, or, if similar lengths are present, a higher GC content in the stem is preferable.[209] Furthermore, it has been demonstrated that HCR systems with hairpins containing shorter stems (12-mers) show faster kinetics (10-fold).[209]

Network Design

Although the low metastability of DNA hairpins with very short lengths precludes their employment in HCR systems, the performances of DNA mimics have yet to be explored. With the aim of developing minimal HCR systems, peptide nucleic acids (PNAs), thanks to the high sequence specificity and duplex stability even at short lengths,[35] represented a promising candidate. In fact, PNA was adopted for the formation of hairpin structures comprised of a 4-mer PNA stem with short peptide loops.[211] The high thermal stability of such hairpins indicated that PNA would be a suitable candidate for the construction of metastable hairpins with short stem/loop length to be employed in HCR. Moreover, modified monomers can further tune the PNA properties,[101] for example conferring enhanced solubility and cell permeability,[104, 106, 118] or modulating the strength of interaction with complementary PNA and DNA strands.[106] In addition, the enzymatic stability of PNA against nucleases and proteases offers an advantage to naturally occurring oligonucleotides when considering its application in biological environments. Based on these premises, a PNA-based minimal HCR system was developed. The network utilizes 5-mer stems and 5-mer toehold/loops PNA hairpins, constituted of γ-modified PNA monomers (Figure 36). Using an initiator strand conjugated to a ligand able to bind a protein of interest, a network adapted to the detection of cell surface receptors could be envisioned.

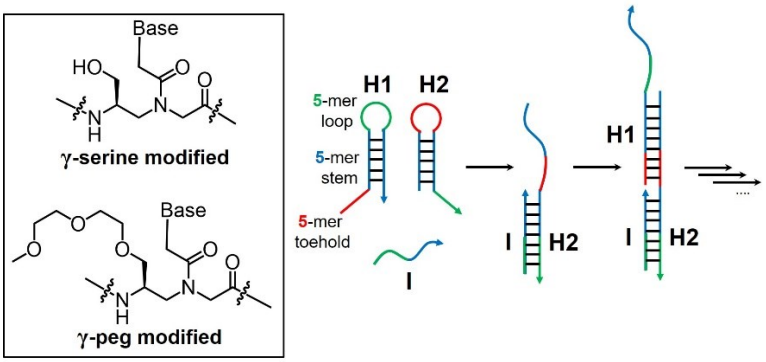

Figure 36. Basic design of minimal PNA-HCR network; the box indicates the modified PNA monomers employed.

Results and discussion

First, the design of PNA hairpins for efficient HCR was investigated. In order to establish the optimal hairpin structure, different lengths of stem and loop were tested. Since previous reports showed that stable hairpins can be obtained with four G:C pairs,[211] PNA hairpins having 3-mer loop and 4-mer stem (3,4-system), 4-mer loop and 5-mer stem (4,5-system), and 5-mer loop and 5-mer stem (5,5-system) were initially considered as HCR scaffolds (Figure 37; see Table III-S1 for full sequence information). To benefit from the improved solubility and duplex stability compared to unmodified PNAs,[105, 212] γ-serine modified PNA monomers were first employed. Ideally, the hairpins should display enough stability to maintain

the closed conformation in the absence of the initiator strand; on the other hand, strong hybridization between the initiator and the first hairpin should enable the formation of the I:H2 adduct, necessary to open the second hairpin and thus allow for the formation of elongation products. The properties of the hairpins, with and without the presence of the initiator were assessed by polyacrylamide gel electrophoresis (PAGE). Since the PNA backbone is neutral, charged fluorophores (FITC or Cy3) were introduced on hairpins and initiator to enable migration in gel. Gel analysis of FITC labelled HCR components revealed that while the three systems (3,4; 4,5; 5,5) showed hairpin stability in absence if I, together with the yield of elongated products, the I:H2 adduct for the 3,4- and 4,5-systems was either not detectable (3,4), or only partially formed (4,5) (Figure 37). On the other hand, the 5,5-system showed >90% conversion to the I:H2 duplex (Figure 37). Based on these results, the 5,5-system was selected as model design for further studies.

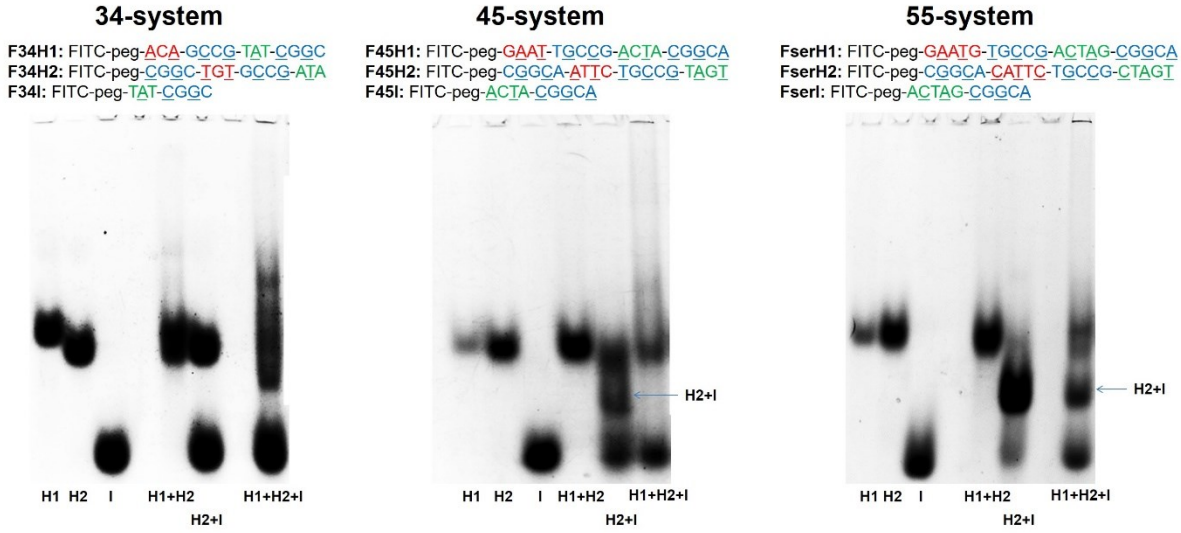

Figure 37. 5 % PAGE analysis of HCR using FITC-labelled γ-serine modified-PNAs. Conditions for reaction: pH 7.5 0.1X PBS, 0.02 % tween-20, 1 μM of each component, 20 μL, r.t., 2 h. of incubation.

In details, gel scans of the 5,5-system highlighted that the hairpins (FserH2) plus 1 eq. of initiator (FserI) yielded a clearly observable H2+I product (Figure 37 55-system, H2+I). As expected, addition of I to the hairpin mixture (FserH1+FserH2) produced elongated PNA HCR products, observed as a smear band appearing at higher position in the gel respect to the original hairpins (Figure 38a, H1+H2+1 eq. of I). Moreover, precipitation of bigger size products was observed at the loading zone of the gel, possibly due to the low solubility of PNA elongated products (Figure 38a, red box). These results suggested that the I strand produces desired HCR products comprised of I and at least three hairpins (H2+I+H1+H2). However, the elongation yield of HCR seemed to be not very efficient (estimated less than 10-fold); product precipitation could prevent the formation of longer size HCR products. Even in case of 1:1 stoichiometry the initiator strand was not completely consumed. In contrast, in the presence of 0.1 eq. or 0.01 eq. of I, the bands corresponding to I and H2+I were fully consumed, but the

ones corresponding to H1 and H2 were still present (Figure 38a, H1+H2+I). These results imply that the kinetics of the hairpin elongation step are comparable to H2+I formation.

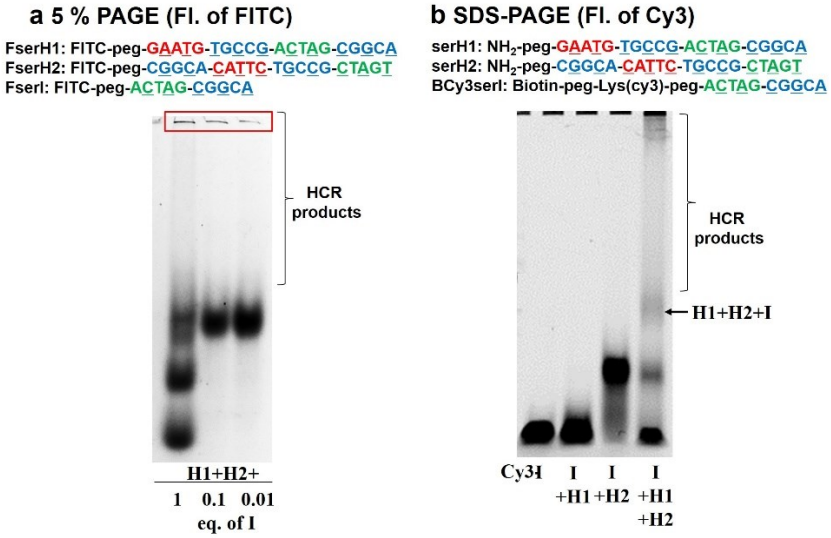

Figure 38. a) Titration of initiator analysed by 5 % PAGE of HCR using FITC-labelled γ-serine modified-PNAs. Reaction conditions: pH 7.5 0.1X PBS, 0.02 % tween-20, 1 μM of each component, 20 μL, r.t., 2 h incubation. b) SDS-PAGE analysis of HCR using γ-serine modified-PNAs, BCy3serI, serH1, and serH2. Reaction conditions: pH 7.5 0.1X PBS, 0.02 % tween-20, 1 μM of each component, 15 μL, r.t., 3 h. of incubation.

To verify the results obtained by PAGE, demonstrating that the system was competent in forming elongated products, the reaction was ulteriorly analysed by SDS-PAGE gel electrophoresis. This time the initiator sequence was labelled with Cy3 (BCy3serI). The gel confirmed the formation of the I:H2 complex, as well as the production of elongated products (Figure 38b). Although γ-serine modified-PNAs exhibited HCR behaviour, fluorescence quantification in a model system involving elongation of HCR products on streptavidin beads yielded 5.2-fold of elongation maximum (Figure 39). The limited performances are possibly due to the low solubility of high molecular weight species generated upon elongation.

To overcome these issues, a γ-peg modified-PNA was assayed; in fact, such modification is known to confer low aggregation and water solubility.[213] The PNA sequences previously used for the 5,5-system were maintained, this time utilizing γ-peg modified-monomers in place of γ-serine modified monomers. PAGE analysis of FITC-labelled PNAs (FpegH1, FpegH2, FpegI) demonstrated the formation of HCR products in the presence of the I sequence, as well as the metastability of the hairpins (Figure 40a). However, 0.13-0.063 eq. of I were not able to consume all the hairpins after 2 hours of incubation (Figure 40a, lane H1+H2+ 1/8 and 1/16 eq. of I), which suggested less than 16-fold elongation yield of PNA HCR. A similar pattern was observed for SDS-PAGE with γ-peg modified-PNA hairpins (Figure 40b, Figure III-S1). Since the reaction is expected to slow down as H1 and H2 are consumed, a beneficial effect from a longer reaction time could be speculated.

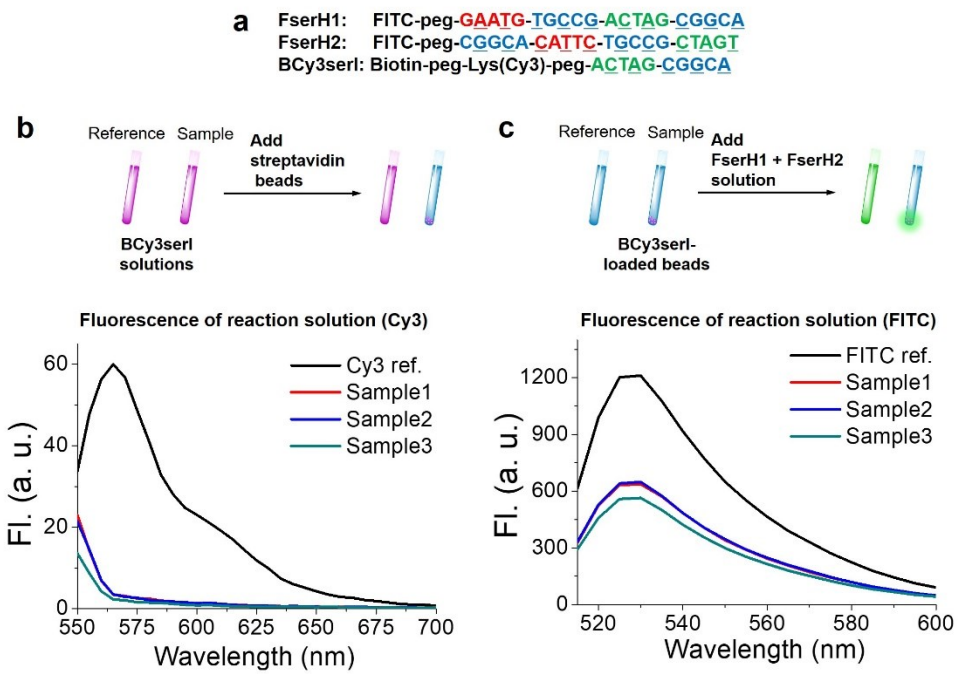

d

Consumed FITC hairpins (pmol)	Loaded BCy3serI (pmol)	Ratio		
141.5	28.5	5.0	Average	5.2
141.1	28.3	5.0		
161.5	29.0	5.6		

Figure 39. a) Sequences of PNA used. b) Quantification of loaded initiator sequence based on fluorescence measurement of BCy3serI in solution; 30 pmol of BCy3serI was used; streptavidin beads loading was found to be >95%. c) Quantification of hairpins participating in HCR based on fluorescence measurements of the solution after reaction. 150 pmol of each FserH1 and FserH2 (total 300 pmol of hairpin / 150 µL) was added to pre-loaded beads. Fluorescence of the resulting solution was measured after 2 h of incubation. d) The result showed that 5.2 eq. of hairpins are consumed for HCR. Reaction conditions: pH 7.5 0.1X PBS, 0.02 % tween-20.

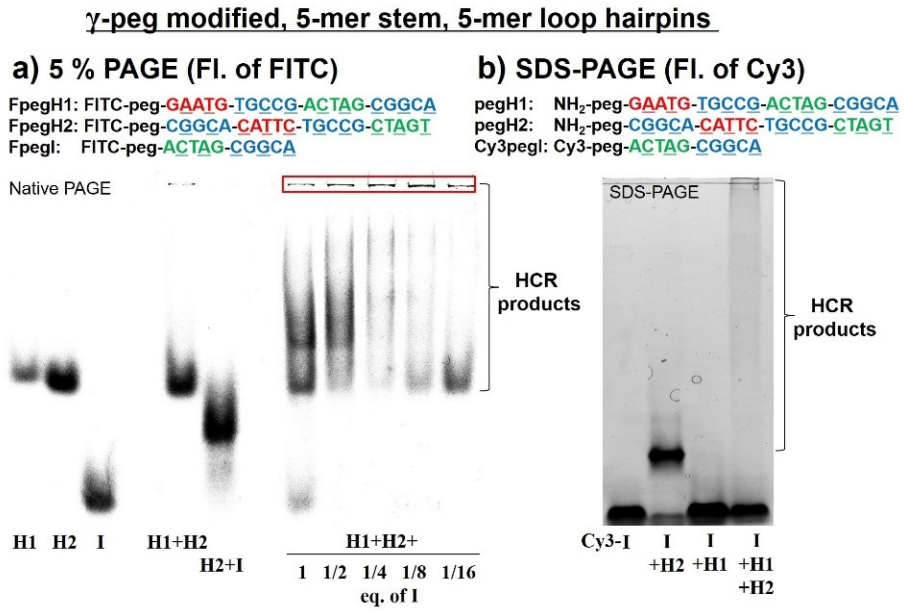

Figure 40. a) 5 % PAGE analysis of HCR using FITC-labelled γ-peg modified-PNAs. Reaction conditions: pH 7.5 0.1X PBS, 0.02 % tween-20, 500 nM of each component, 20 µL, r.t., 2 h incubation. b) SDS-PAGE analysis of HCR using γ-peg modified-PNAs, Cy3pegI, pegH1, and pegH2. Reaction conditions: pH 7.5 0.5X PBS, 0.02 % tween-20, 500 nM of each component, 15 µL, r.t., 2 h incubation.

Next, the performances of the γ-peg-PNA HCR were assessed by fluorescence. In a first approach, streptavidin beads were loaded with a biotin-labelled initiator (BpegI) and mixed with a solution of the hairpins (Cy3pegH2 + pegH1); in this way the HCR products will remain attached to the beads. Upon 4 hours incubation, the fluorescence of the supernatant was measured to quantify the amount of consumed hairpins, revealing the consumption of 90 pmol of Cy3pegH2 by 15 pmol of BpegI, which indicates 6-fold increase of fluorescence and, in turn, 12-fold of HCR elongation (Figure 41a). A sample missing the initiator strand was used as reference.

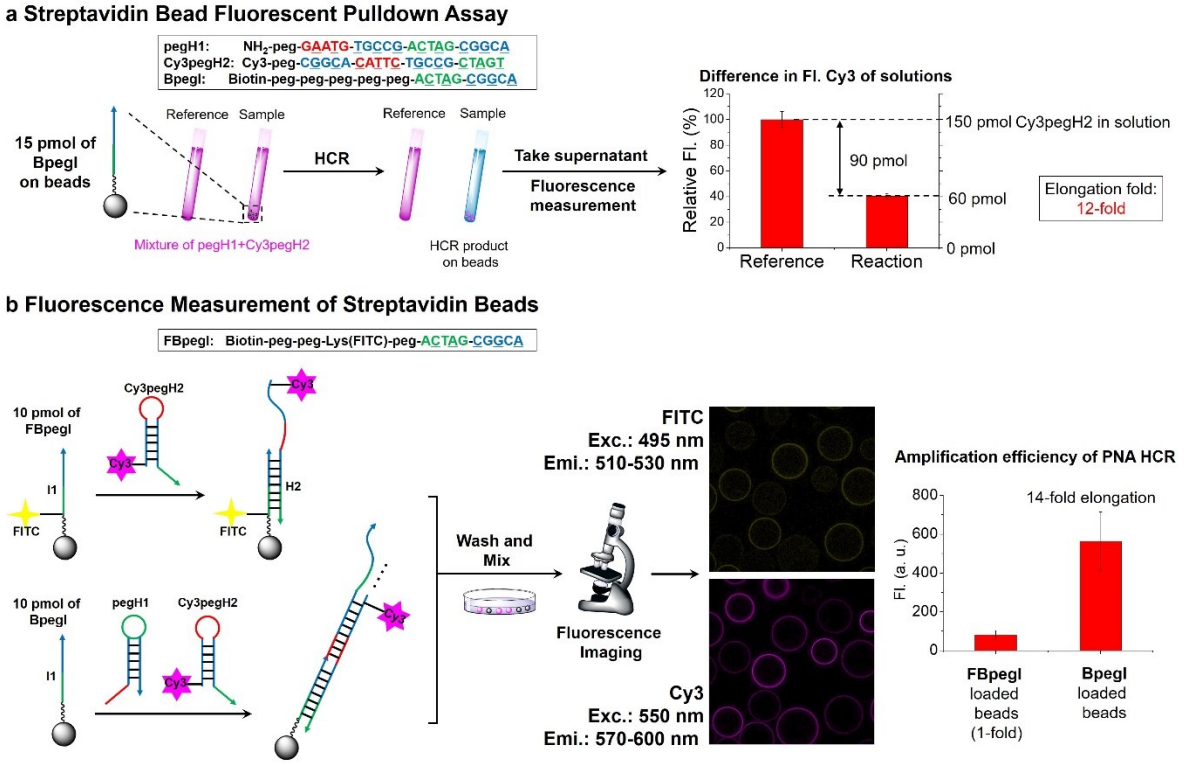

Figure 41. a) Scheme and result of streptavidin bead fluorescent pulldown assay. Reaction conditions: pH 7 1X SSC, 0.02 % tween-20, 15 pmol of BpegI, 1 μM (150 pmol) of pegH1 and Cy3pegH2, 4 h reaction. b) Fluorescent microscopy analysis for estimation of HCR elongation. Reaction conditions: pH 7 1X SSC, 0.02 % tween-20, 10 pmol of FBpegI or BpegI were loaded, 1 μM (200 pmol) of pegH1 and Cy3pegH2, 4 h reaction. Yellow: FITC; magenta: Cy3.

Moreover, the amount of hairpins involved in HCR products was evaluated by fluorescence imaging of streptavidin beads. In this case, two different biotinylated initiators (BpegI and FBpegI) were prepared; each initiator was loaded on separated beads and submitted to HCR reaction with pegH1+Cy3pegH2 (Figure 41b). As control, initiator-loaded beads (FBpegI) were treated with an excess amount of Cy3-labelled hairpin H2 (Cy3pegH2) (1-fold of elongation (H2+I)) (to allow for fluorescence microscopy detection the control beads are loaded with FITC-labelled initiator). After incubation and washing the beads from each reaction were mixed and screened with a confocal microscope. A clear discrimination based on fluorescence intensity in the Cy3 channel was observed, with beads treated for HCR displaying stronger fluorescence. In details, beads treated for HCR yielded 7-fold higher fluorescence compared

to the control (Figure 41b). This result indicates a 14-fold elongation yield, which is consistent with previous quantification accomplished by fluorescent pulldown assay (Figure 41a). In addition, experiments carried out at different concentration of reagents and reaction time confirmed similar elongation efficiency (Figure III-S2). Furthermore, the size of HCR products was established by size-exclusion chromatography (SEC); these experiments reinforced previous results obtained by fluorescent techniques, by confirming the formation of HCR products with estimated size around 57 kDa (~8-fold elongation) (Figure III-S3).

Having established that peg-modified PNA monomers enabled the formation of HCR products with up to 10-fold elongation, the kinetics of hairpin hybridization were measured. FITC or Dabcyl modified hairpin/initiator were used to monitor the dissociation constants and the rate constants of the first (H2+I) and second (H2+I+H1) hybridization steps (Figure 42, Figure III-S4). The first step of the HCR process, I:H2 formation, was followed using a FITC labelled initiator (FpegI) and a dabcyl-modified H2 (DpegH2) (Figure 42a). Approximating the reaction to pseudo-first-order kinetics (Dabcyl-PNA in excess) a rate constant of 4.5×10^4 M^{-1} s^{-1} (k_{on}, Figure 42b) (half-life = 78 s; $k_{obs} = 8.9 \times 10^{-3}$ s^{-1}, Figure III-S4) was calculated. Interestingly, the second step (H2:I+H1) revealed a 2.6-fold faster reaction rate constant (1.2×10^5 M^{-1} s^{-1}, Figure 42c) (half-life = 30 s; $k_{obs} = 2.3 \times 10^{-2}$ s^{-1}, Figure III-S4). These kinetic reflect previous data reported for DNA HCR systems.[209] The faster reaction for the second step can be attributed to additional base stacking interactions between pegIF and DpegH1, mediated by the formation of pegIF:pegH2 duplex.[214] These results are in line with previous data observed by PAGE, showing that the initiator was not fully consumed even in HCR using a stoichiometric ratio of reagents (Figure 40a, lane H1+H2+1 eq. of I). The dissociation constant of the two steps were found to be similar and in the low nanomolar range (Figure III-S4).

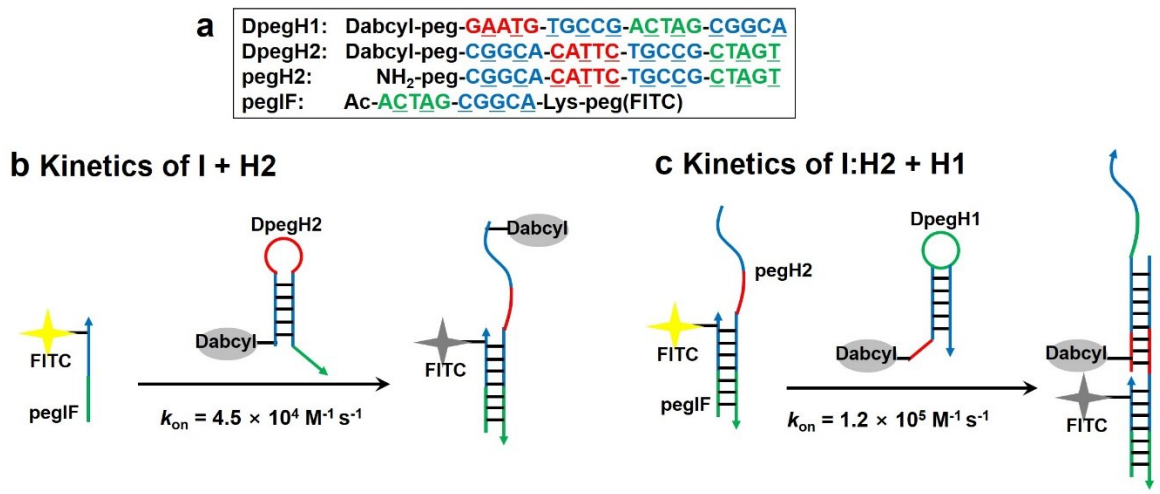

Figure 42. a) Sequences used. b) Kinetic analysis of first initiation step and c) elongation step of PNA HCR calculated using pseudo-first order reaction kinetic model. On-rate constant (k_{on}) are reported.

Moreover, the HCR product reached maximum elongation within 4 h of reaction time (4 h. reaction and 24 hours reaction yield similar amount of HCR elongation, see Figure III-S3).

These data may suggest that the intrinsic properties of this system prevent further elongation; improvement of the elongation efficiency can be speculated by utilizing a longer toehold on the hairpin structure.

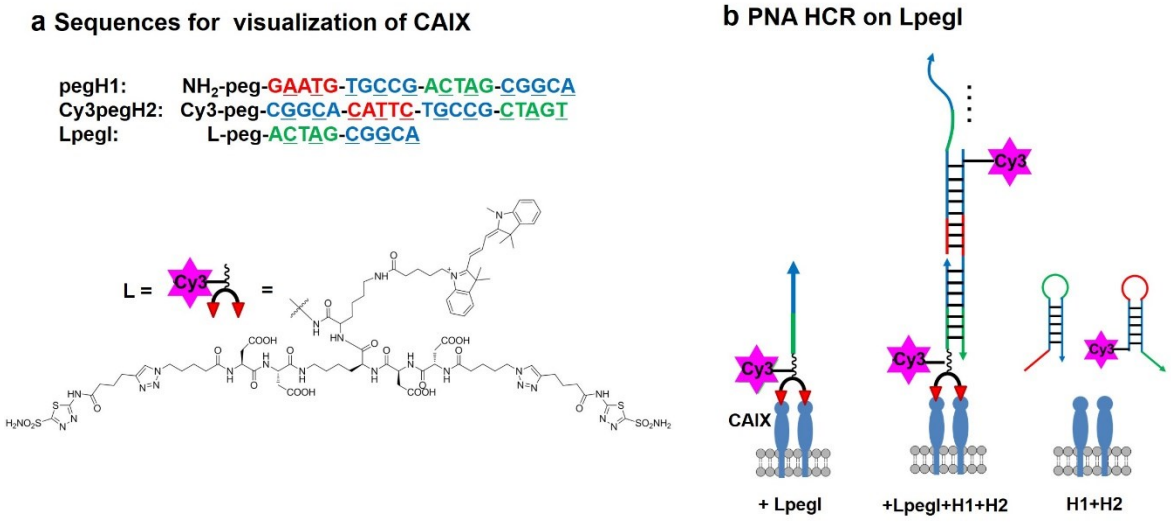

Figure 43. a) Sequences used. b) Conceptual image of PNA HCR using LpegI. CA IX visualization model using 1:1 assembly with LepgI, PNA HCR (LpegI+pegH1+Cy3pegH2), or only hairpins (pegH1+Cy3pegH2).

Having characterised the PNA HCR system and encouraged by the successful visualization of PNA HCR products on the surface of initiator-loaded beads, the application of the PNA HCR network for the detection of biomarkers expressed on the surface of cancer cells was envisioned. In this context, carbonic anhydrase IX (CA IX) was once again chosen as protein of interest. HT-29 cells were selected as a model cell line for the expression of CA IX under hypoxic conditions. To allow for selective binding to the target protein, the initiator strand was conjugated to an acetazolamide-based bivalent ligand[197] (LpegI) (Figure 43a). In addition, a Cy3 tag was introduced to allow for the monitoring of the fluorescence signal arising from 1:1 binding between the initiator strand and CA IX (Figure 43b). Hypoxic HT-29 cells were treated with LpegI (100 nM, 30 min, hypoxic conditions), followed by incubation with hairpins pegH1+Cy3pegH2 (1 μM, 1 hour, hypoxic conditions) (Figure 44a). Confocal fluorescence imaging revealed a 6-fold increase of Cy3 fluorescent signal (corresponding to 12-fold elongation efficiency) localized on the cell membrane (Figure 44a, b). Cells treated with hairpins pegH1+Cy3pegH2 (1 μM, 1 hour, hypoxic conditions) but lacking the initiator strand were used as control, and showed no fluorescence upon washing (Figure 44a, b), highlighting the fact that the PNA HCR is suitable for the recognition of biological markers, and that the system is specifically responsive to the initiator trigger. Once again, this result was consistent with the previous experiments using loaded beads. Accordingly, the results demonstrate that the PNA HCR system can be used to readily visualize CA IX in cellulo. The advantage of an amplified fluorescence signals makes this setup particularly appealing for the imaging of cellular targets with low expression level.

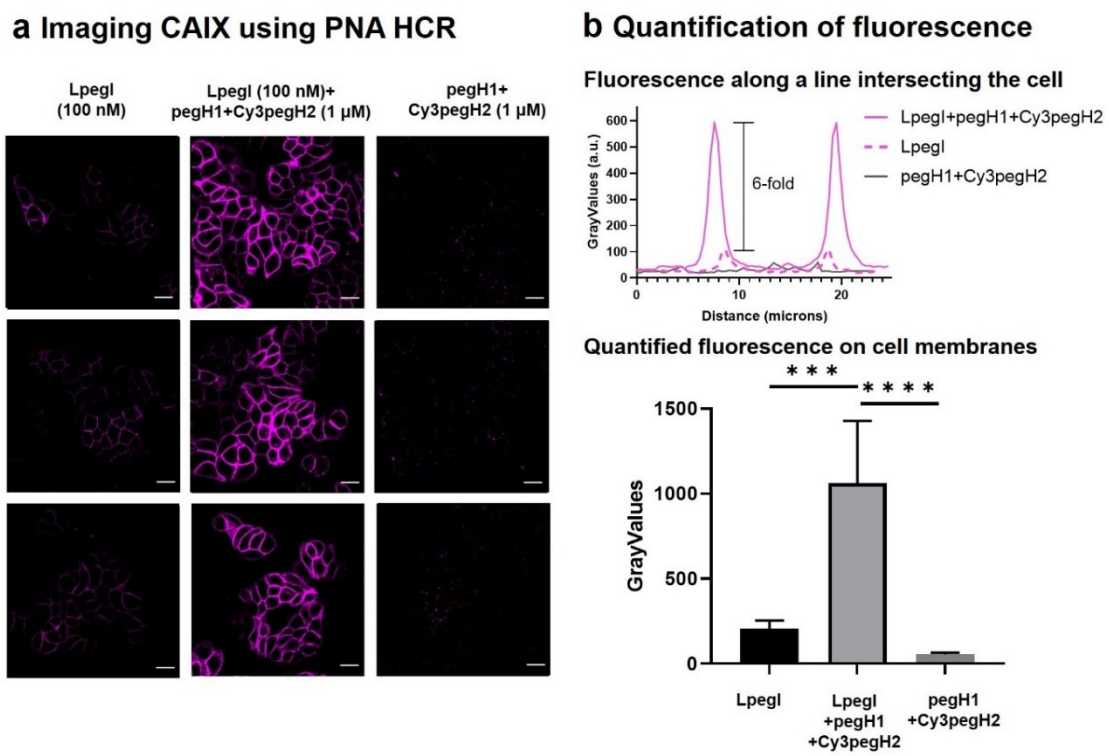

Figure 44. a) Fluorescence pictures of hypoxic HT-29 cells treated with LpegI (left); LpegI+pegH1+Cy3pegH2 (center); pegH1+Cy3pegH2 (right). b) Fluorescence intensity profiles measured along a line intersecting the cell and quantification of fluorescence on cell membranes. Error bars represent standard error of the mean. Statistics were calculated using a *t*-test. *** p<0.001; **** p<0.0001.

Conclusions

In conclusion, a minimal HCR system based on γ-modified PNAs (including L-serine or peg modification) was described. Among the screened options, γ-peg-modified 5-mer stem and 5-mer toehold/loop hairpins were found to be the beneficial, showing hairpin metastability together with fast (k_{on} = 1.2 × 10^5 M^{-1} s^{-1}) and strong hybridization (K_d 18 nM). The elongation efficiency for PNA HCR was improved to >10-fold by using γ-peg-modified PNA, thanks to the increased solubility of HCR products. The optimized 5,5-system was finally applied to signal amplification and distinct visualization of the cancer biomarker CA IX in live cells by fluorescence. Classic DNA HCR systems require long sequences to allow for the formation of elongated products without leakage (hairpin metastability is lost with stems below 12 nucleobase length); this work demonstrates that PNA represents a valuable alternative for the design of minimal systems. Moreover, the results suggest the suitability of PNA HCR for the detection of targets in biological environments. Additionally, the design of customed systems can be envisioned by exploring further modifications to grant the tunability of the PNA HCR performances.

Overall, PNA HCR could serve as tool for the detection of cellular targets. Moreover, the versatility of PNA, together with the advantageous properties (chemical and enzymatic stability, strong hybridization, etc.) respect to DNA may envisage its employment in more complex and biocompatible architectures or in DNA-PNA hybrid systems. To this end, further modifications aiming to enhance the performance of PNA HCR will have to be explored.

Chapter IV

BRET-based Supramolecular network

This project was carried out in collaboration with Eric Lindberg and Marcello Anzola. The content of this chapter is adapted from *Lindberg E., Angerani S., Anzola M., and Winssinger N. "Luciferase-induced photoreductive uncaging of small-molecule effectors." Nature Communications 9:3539 (2018).*[97]

Introduction

Bioluminescence is a naturally occurring phenomenon that involves the oxidation of a luciferase cofactor with the resulting emission of photons.[215] Several species use bioluminescence, mostly as a defence mechanism, emitting light with a spectrum that spans from blue to red.[216, 217] To date, a variety of native luciferases, together with engineered versions have been studied and employed for sensing purposes.[215, 217] In fact, bioluminescence offers different advantages in comparison to techniques based on fluorescence. For instance, bioluminescence overcomes the issues related to the use of external illumination, removing background fluorescence, photobleaching, light scattering, and adverse effects deriving from sample heating by external light sources.[217] For these reasons, bioluminescence imaging represents a very powerful tool that can be exploited in reporting assays with exceptional sensitivity.[217] The compatibility of bioluminescence-based devices for *in vivo* imaging[218, 219] has been applied to freely moving organisms; remarkably, these systems can be implanted in mammals and remain functional for months post implantation.[220]

In addition, analogously to FRET, the bioluminescent signal can be transferred to proximal acceptors, represented by either fluorescent proteins,[218, 221] small-molecule fluorophores[222, 223] or quantum dots.[224] Bioluminescence resonance energy transfer (BRET) has become an emerging reporting modality to study dynamic biological events, such as protein-protein[221, 225] and protein-ligand interactions,[221, 226, 227] receptor trafficking,[228] and intracellular inorganic ions.[229]

A very proficient field is represented by BRET-based semisynthetic sensors for point of care analyte detection, extensively explored by the work of Kai Johnsson's group. These systems rely on BRET originating from the proximity of a bright engineered luciferase (NLuc) to an acceptor fluorophore and provide a colorimetric readout that can be easily captured by a commercial camera. These devices were customized to respond to several metabolites[230] and drugs,[231] by equipping the sensor with either modified receptors[230, 231] or antibodies.[232]

Another successful approach to design BRET sensors relies on the reconstitution of split luciferases, which was applied to the detection of antibodies.[233, 234]

In addition to the development of sensors, bioluminescence was reported to trigger a signalling event, such as the modulation of neurons.[235, 236]

Network design

Following the idea of exploiting a BRET-based system to harness a chemical transformation, a BRET controlled supramolecular network was envisioned by combining the basic design of Kai Johnsson's semisynthetic sensors to ruthenium catalysed PNA-templated reactions. In this way, BRET would act as triggering event for the release of effector molecules, to ideally induce a response in biological systems. Interestingly, NanoLuc (NLuc),[237] a luciferase derived from the deep-sea shrimp *Olophorus gracilirostris* and optimized by Promega, has an emission spectrum that almost perfectly overlaps with the absorption spectrum of $[Ru(bpy)_2phen]^{2+}$ (Figure 45). In principle, if NLuc and the ruthenium complex are brought in close proximity, the spectral overlap should allow for bioluminescence resonance energy transfer, resulting in the excitation of $[Ru(bpy)_2phen]^{2+}$. The excited state of the ruthenium complex can be then engaged in the PNA-templated photoreductive uncaging of small-molecule effectors, as already discussed in previous chapters.

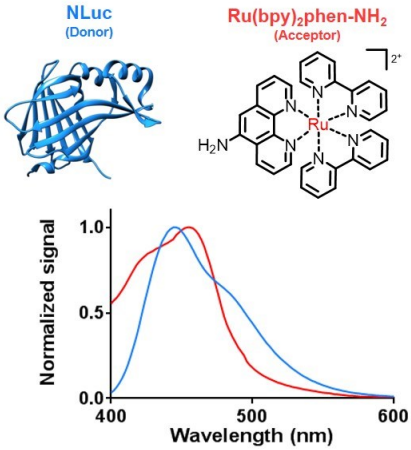

Figure 45. Structure of the NLuc luciferase and ruthenium complex; overlapped emission spectrum of NLuc (blue) and absorption spectrum of the ruthenium complex (red).

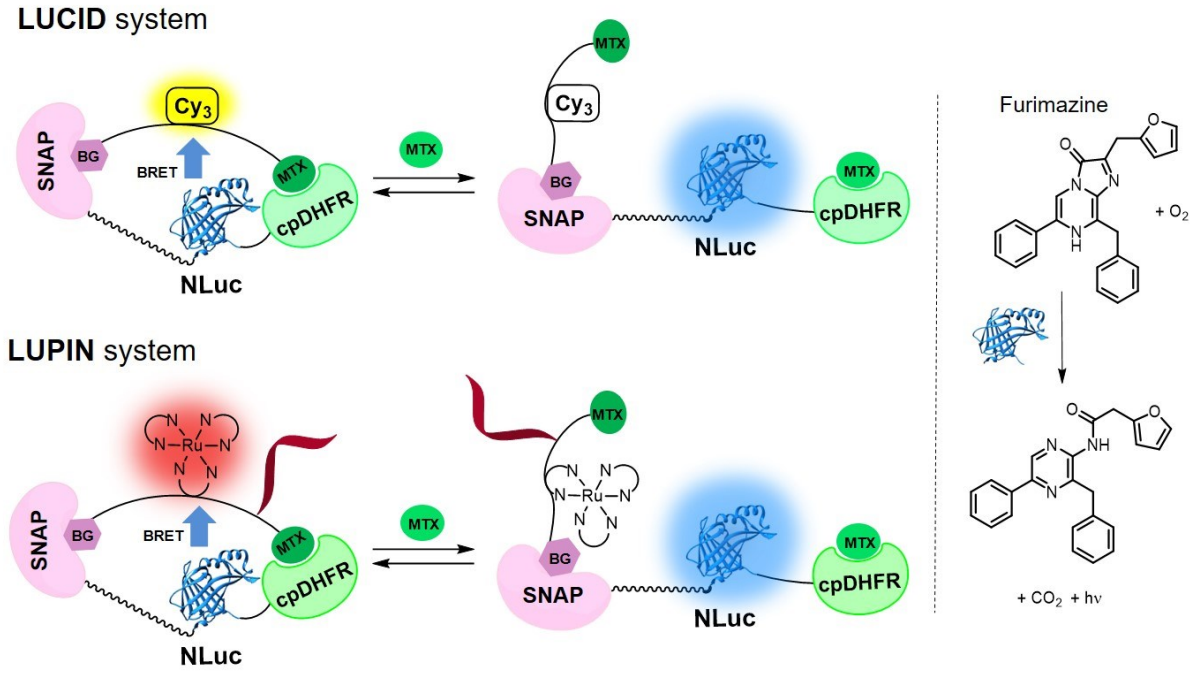

Figure 46. Schematic representation of the LUCID and LUPIN systems (left); Reaction scheme for the conversion of luciferase substrate furimazine (right).

Regarding the network design, the luciferase-based indicator of drugs (LUCID)[231] sensor for methothrexate (Mtx) was taken as model system (Figure 46). LUCID-Mtx employs a fusion protein consisting of SNAP-tag, NanoLuc and a circularly permuted dihydro folate reductase (cpDHFR) receptor. The protein component can be labelled with a synthetic linker containing a benzylguanine (BG), for the covalent labelling of SNAP-tag, and methotrexate, for the binding to DHFR, located at opposite ends of the linker; in addition, the middle part bears a Cy3 fluorophore.[231] Upon labelling, Cy3 is brought in proximity to NLuc, where it acts as BRET acceptor (Figure 46).[231] Addition of external methotrexate shifts the sensor to the open conformation by displacing the Mtx attached to the linker, resulting in decreased BRET[231] (Figure 46). In analogy to the LUCID systems, a modified synthetic linker, in which the acceptor fluorophore is replaced with a ruthenium complex was designed (Figure 46). Moreover, the linker would be decorated with a 5-mer PNA for templated reaction. In this way, a Luciferase-based Photocatalysis Induced via Nucleic acid template system (LUPIN) was designed (Figure 46).

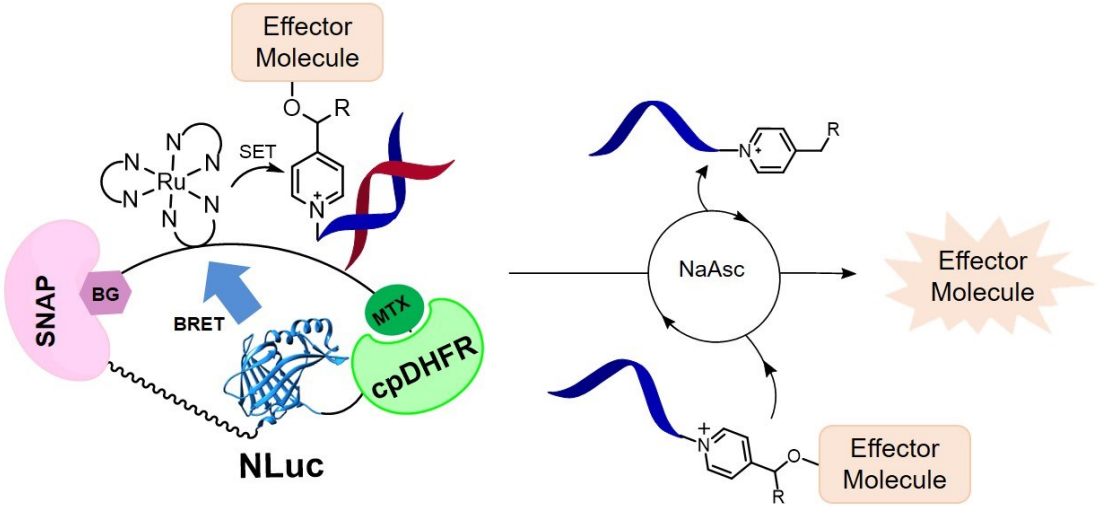

Figure 47. Schematic representation of the templated release of effector molecules by LUPIN upon BRET and single electron transfer (SET) from the ruthenium complex to the pyridinium immolative linker.

Addition of luciferase substrate, furimazine (Figure 46), would trigger photon emission from NLuc and consequent BRET to the ruthenium complex; addition of a complementary PNA strand bearing the pyridinium immolative linker derived with a caged effector molecule in presence of a sacrificial reducing agent (NaAsc) would allow for templated release with output amplification (Figure 47).

Results and discussion

First, the synthetic linker bearing the ruthenium complex adjacent to a 5-mer PNA was prepared (**16**, Figure IV-S1 for extended structure). Upon labelling of the SNAP-NLuc-DHFR protein system, the luminescence emission spectrum of the LUPIN system was measured

either in presence or absence of external methotrexate to assess the BRET efficiency (Figure 48, Figures IV-S2, IV-S3, IV-S4). Gratifyingly, in absence of external methotrexate, the luminescence spectrum showed the appearance of a band at 610 nm, corresponding to the emission of the ruthenium complex (Figure 48, red), confirming the successful energy transfer from the NLuc luciferase when the system exists predominantly in the close conformation. On the other hand, addition of Mtx led to disappearance of the 610 nm band, confirming the reduction of BRET as a consequence of the Ru-NLuc proximity disruption (Figure 48, black). Since LUCID-Mtx has an EC_{50} of 85 μM,[231] 100 μM methotrexate was added to LUPIN to ensure a shift of the system to the open conformation. From these data it was possible to calculate an energy transfer efficiency of 64%. Moreover, based on the spectral overlap between NLuc and the ruthenium complex, the Forster distance was found to be 16 Å (see Supplementary Materials of chapter IV for detailed formula). The energy transfer efficiency exceeding 50% suggests that the system has an average distance <16 Å.

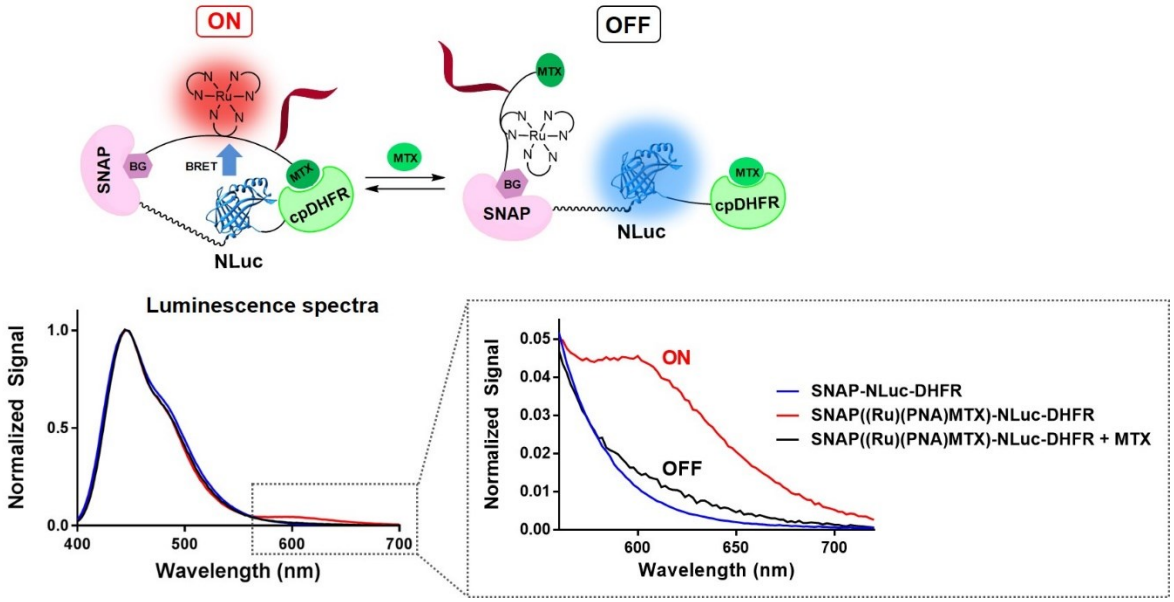

Figure 48. Luminescence emission spectra of the LUPIN system in the absence (red) or presence (black) of methotrexate; spectra of SNAP-NLuc-DHFR (blue).

Despite the LUCID sensors capitalize on the shift from close to open conformations to exert their function, the LUPIN system benefits from the closed state to harness a chemical reaction. Therefore, having confirmed the proximity-induced BRET between the luciferase and ruthenium, the possibility to translate the energy transfer into the photocatalytic release of molecules caged by pyridinium linkers was assessed. For simplicity, the release reaction was first tested with a caged rhodamine-pyridinium-5mer PNA construct *in vitro* (Figure 49a). LUPIN (50 nM) was treated with Rho-py^{+}-5-mer (**17**, 500 nM) in presence of furimazine (100 μM) and sodium ascorbate (10 mM), and the rhodamine release was followed by fluorescence measurements over time. Fluorescence increase was observed, yielding 65 nM of Rhodamine

(1.3 turnover) (Figure 49b, green), demonstrating that the BRET system can successfully induce chemical transformations. As control, the LUPIN network supplemented with Mtx (100 μM) resulted in a release reaction reduced by half (Figure 49b black, Figure IV-S5), which reflected the shift of the system to the open conformation. Moreover, the effect of random interactions between NLuc and the ruthenium complex, and between the ruthenium and the pyridinium immolative linker were respectively evaluated. In the first case, the SNAP protein was pre-saturated with benzyl guanine to prevent labelling with the synthetic linker (Figure 49b, blue); in the second scenario, a linker lacking the PNA component was employed (Figure 49b, beige). Release reaction conducted in both setups resulted in only marginal fluorescence, corroborating the importance of geometric proximity and templation for the efficient performance of the network.

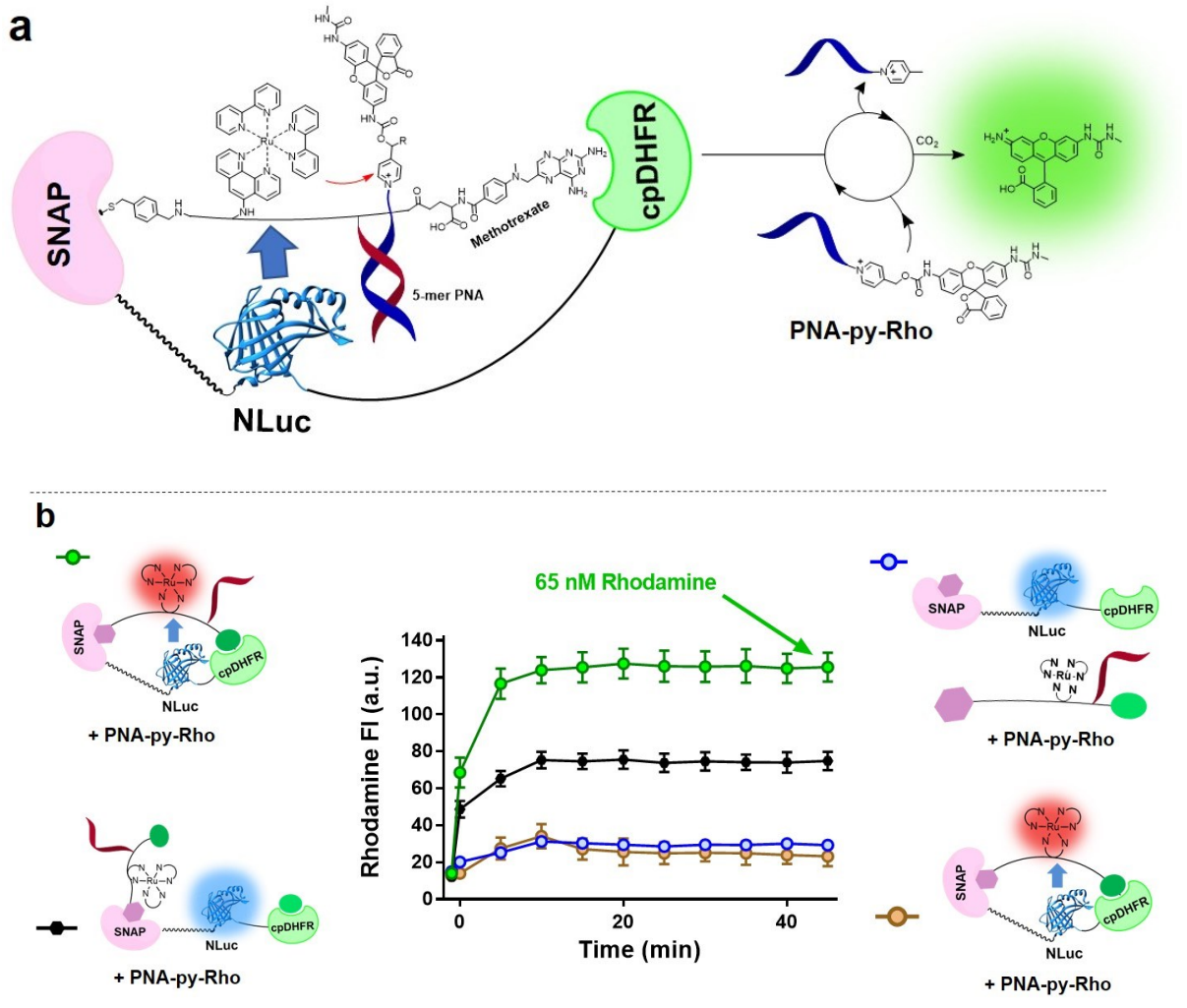

Figure 49. a) Schematic representation of the LUPIN system for the release of Rhodamine. b) Fluorescence enhancement due to rhodamine uncaging by the LUPIN system (green). In the presence of methotrexate, the reaction is partially inhibited due to lower BRET efficiency (black). In the absence of nucleic acid template (beige), or in the absence of a covalent link between the synthetic linker and the protein construct (blue), the reaction is marginal. Reaction conditions: SNAP-NLuc-DHFR labeled with BG-(Ru)(PNA)-MTX (**16**, 50 nM), PNA-PyRho (**17**, 0.5 μM), sodium ascorbate (10 mM), furimazine (100 μM), and methotrexate (100 μM).

However, the profile of rhodamine fluorescence over time reached plateau already after 15 min (Figure 49b), indicating that the reaction stops due to the fast consumption of luciferase substrate (furimazine). With the intent to prolong the bioluminescence emission, and in turn improve the release reaction, the concentration of LUPIN was titrated down (50 nM, 10 nM, 2 nM), keeping the concentration of furimazine (100 μM) and of Rho-py$^+$-PNA (**17**, 5 μM) constant. Both the luminescence decay of NLuc and the rhodamine fluorescence increase were monitored over time. While at 50 nM LUPIN the reaction plateaued after 10 min (360 nM released rhodamine; turn over number (TON = 7) and the luminescence half life is *ca*. 8 min (Figure 50left), decreasing the concentration of the system to 10 nM extended the luminescence $t_{1/2}$ to ~21 min, and the release reaction reached 630 nM of rhodamine, corresponding to a TON of 64 in 2 hours (Figure 50centre). Reducing further the concentration to 2 nM resulted in even longer luminescence half life (~78 min), but the rhodamine release decreased to 130 nM (TON 64) (Figure 50right). Interestingly, the TON increased lowering the concentration of the LUPIN system; this effect might be explained by a faster bioluminescence rate respect to the rate of photoreduction. Moreover, the release reaction was found to correlate with furimazine and Rho-py$^+$-PNA concentration (Figures IV-S6, IV-S7). Consistently with the near diffusion control of the ruthenium reduction step, the system performances are independent from NaAsc concentration down to 0.1 mM (Figure IV-S8).

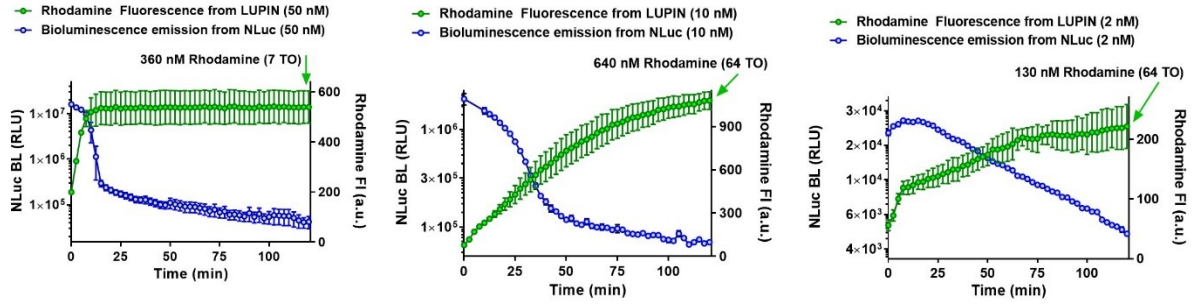

Figure 50. Rhodamine fluorescence (green) and bioluminescence emission spectra (blue) over time for the LUPIN system at different concentrations (50, 10, and 2 nM).

Overall, these data depict the possibility to uncage small molecules at concentrations within the effective range of several drugs from a system operating at low nanomolar levels. To this end, two small molecule drugs, ibrutinib, a covalent kinase inhibitor clinically used for the treatment of lymphoma and leukemia,[238] and a duocarmycin analogue, a highly potent DNA-alkylating cytotoxic prodrug,[239] were chosen as prototypical drugs to be released by the BRET-based network. To obtain caged prodrugs (**18**, **19**), the two drugs were strategically conjugated to the pyridinium immolative linker-5mer PNA *via* a heteroatom involved in the binding to the target (Figure 51). Having previously established that the photocatalyzed templated reaction with blue LED irradiation was yielding clean and almost quantitative release (Figure 51), the uncaging of ibrutinib by LUPIN was evaluated.

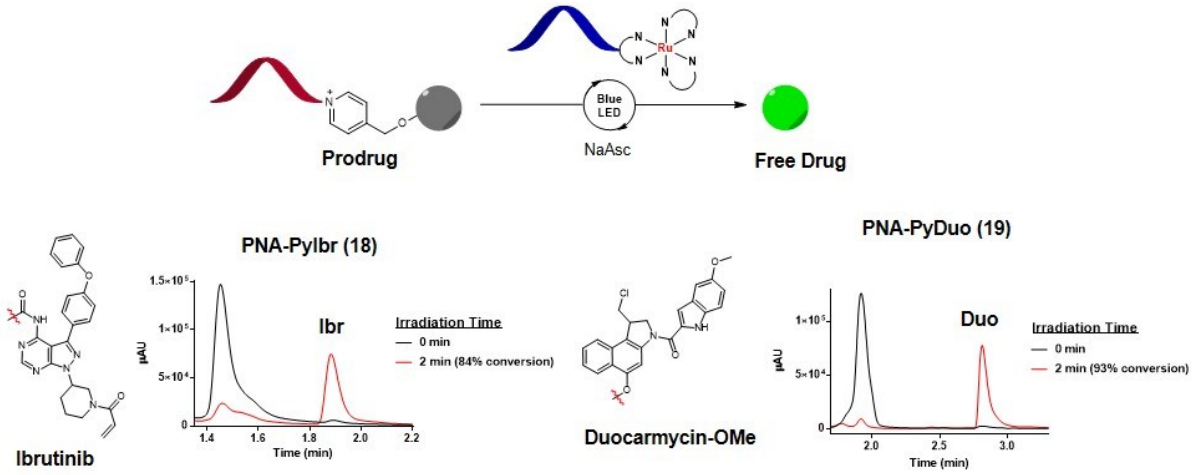

Figure 51. Schematic representation of the prodrug templated release of caged drugs (top). Structure of caged drugs and HPLC traces of the reaction mixture before (black) and after irradiation (red).

Since ibrutinib covalently binds ErbB2 in SKRB3 cells, the efficacy of release was assessed by fluorescent imaging through a competition experiment (Figure 52). To this end, an ibrutinib-Cy3 conjugate (**20**) was prepared; ErbB2 labelling by the Cy3 derivative (50 nM, 30 min), together with target saturation with free drug (1 μM ibrutinib) was confirmed in a cell assay (Figures IV-S9, IV-S10). Then, the release reaction was performed either in presence or absence of LUPIN (10 nM, 2 hours) and the reaction mixture was added to SKBR3 cells (30 min). Following treatment with ibrutinib-Cy3 (**20**, 50 nM, 30 min), cells were imaged with a confocal microscope. In the absence of LUPIN, cells show strong fluorescent signal from ibrutinib-Cy3 labelling (Figure 52), indicating that the Ibrutinib-py$^+$-PNA conjugate is indeed unable to bind the target. On the other hand, in the presence of LUPIN, the labelling was drastically reduced (Figure 52, Figure IV-S11), confirming that the ibrutinib released was sufficient to saturate the target.

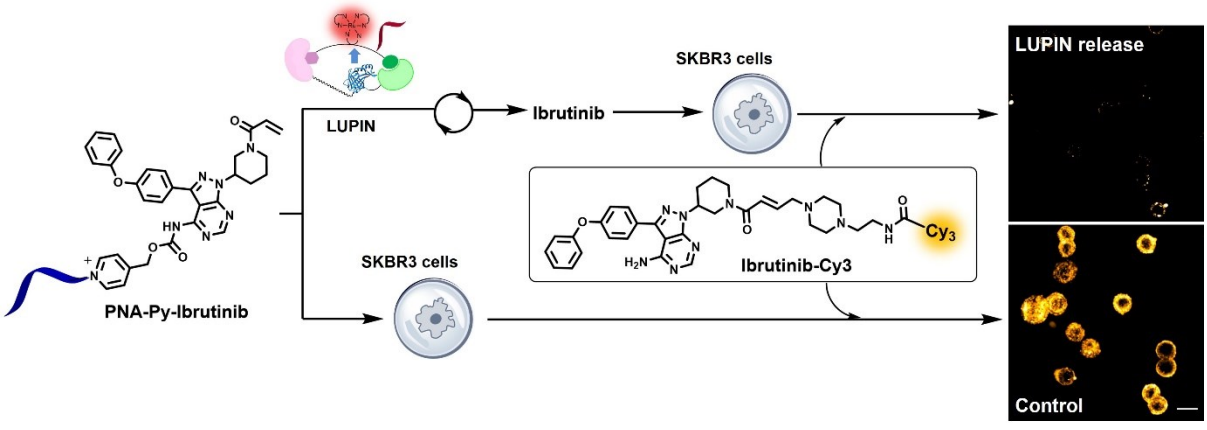

Figure 52. Ibrutinib release by LUPIN. Competition with ibrutinib-Cy3 derivative in SKBR3 cells overexpressing ErbB2. SKBR3 cells were treated with either the prodrug alone (PNA-Py-Ibrutinib) or prodrug + LUPIN for 30 min; then the cells were treated with ibrutinib-Cy3. The lower fluorescence observed for the LUPIN-uncaged product population indicates that the ErbB2 was saturated with the uncaged prodrug. Conditions for LUPIN release: SNAP-NLuc-DHFR labelled with BG-(Ru)(PNA)-MTX (**16**, 10 nM), PNA-Py-Ibrutinib (**18**, 5 μM), sodium ascorbate (10 mM), furimazine (100 μM), and Ibrutinib-Cy3 (**20**, 50 nM). Scale bar: 20 μm.

Moreover, the efficacy of LUPIN-induced drug release was envisioned by cytotoxicity assay utilizing the duocarmycin derivative-PNA conjugate (**19**). In this case, the phenolic oxygen of the duocarmycin is attached to the pyridinium linker through a primary benzylic ether (Figure 51). In fact, it is well established that the activity of the drug is remarkably reduced as far as the heteroatom is engaged in a covalent bond; upon bond cleavage, the free phenol triggers an intramolecular cyclopropanation under physiological conditions that leads to the formation of the potent DNA-alkylating product.[239-242] However, during the assessment of cytotoxicity of free drug *vs* prodrug, low levels of background immolation of the pyridinium linker were observed; given the subnanomolar toxicity of the duocarmycin drug, even this marginal release elicited partial cytotoxicity, reducing the therapeutic window. Therefore, the background release was measured by fluorescence from a caged rhodamine incubated in cell media (Figure IV-S12), resulting in 0.6% immolation after 12 hours; assuming first-order rate of decomposition, the half life of the linker is 1005 hours. In order to overcome this issue, two modified pyridinium linkers, one using a 2,6-lutidine (PNA-Lut-Rho **21**) and the other using a secondary benzylic ether (PNA-py^2-Rho **22**), were tested in cell media: both showed no background release (Figure IV-S12). When the kinetics of templated release were measured, the derivative with the secondary benzylic ether performed better (Figure IV-S13); thus, a PNA-py^2-Duocarmycin conjugate (PNA-py^2-Duo **23**) (Figure 53a) was used for further cytotoxicity experiments.

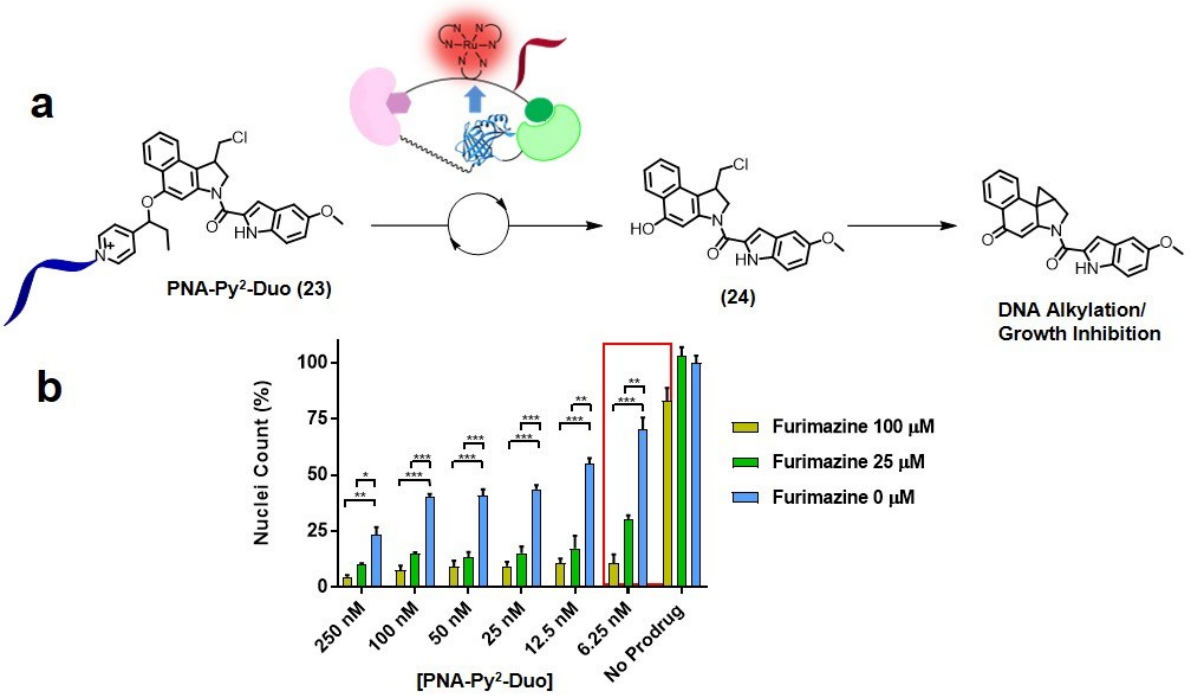

Figure 53. a) Schematic representation of Duocarmycin-OMe release by LUPIN with furimazine to generate DNA alkylating agent. b) Quantification of cellular growth (MCF-7) by nuclei count. Bar graph of nuclei count across different furimazine and prodrug (PNA-Py^{2}Duo **23**) concentrations. Representative images of the conditions highlighted by the red box are shown in Figure 54. The bar graph is the average of three independent experiments ran in triplicates. Error bars show ± 1 standard deviation from the mean. Statistics were calculated using a two-tailed *t*-test with unequal variances (Welch's unpaired *t*-test). *p < 0.05, **p < 0.01, ***p < 0.001.

First, the cytotoxicity of the free duocarmycin derivative (**24**) and of the duocarmycin-py^2-PNA conjugate (**23**) was measured in MCF-7 cells, revealing a therapeutic window of >100 folds (Figure IV-S14). Then, the release was performed with LUPIN (10 nM) over a range of duocarmycin-py^2-PNA concentrations (**23**, 250 nM – 6.25 nM) and the cytotoxic effect was measured after 3 hours treatment and 72 hours incubation by staining and counting nuclei. While the LUPIN system and the PNA-prodrug construct alone did not show significant effect on cell growth (Figure 53b; Figure 54, No Prodrug and PNA-py^{2}Duo), a clear dose-response effect was observed in the presence of the whole network (Figure 53; Figure 54, LUPIN release). The cytotoxicity effect nicely correlates with the furimazine concentration (Figures 53, 54, Figure IV-S15), confirming that the release reaction is a result of BRET. In addition, the evidence that the release reaction performs even at low nanomolar concentrations of substrate (6.25 nM) (Figure 53b) highlights the key role of PNA templation.

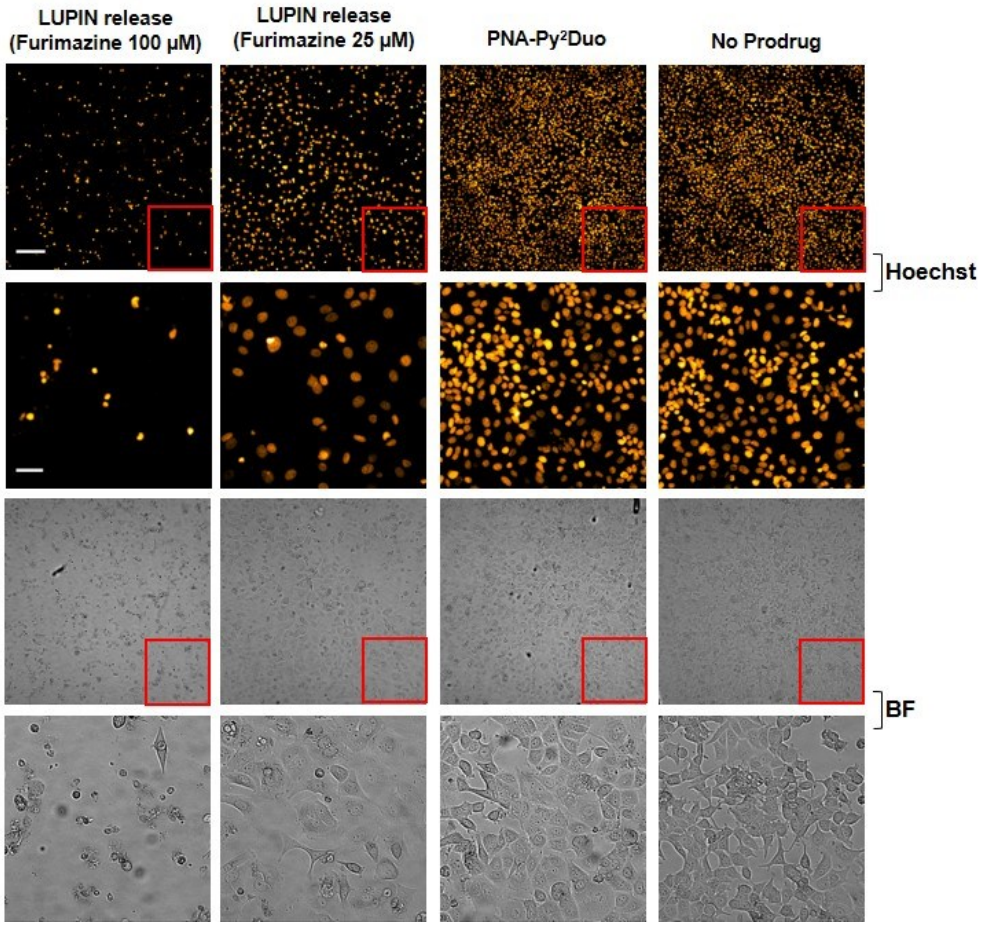

Figure 54. Representative images of cytotoxicity assay reported in Figure 53b. Nuclear Hoechst33342 staining (gold) and bright field (BF) images of MCF-7 treated with LUPIN components. The red squares indicate the zoomed-in area below it.

Conclusions

In summary, the design and application of a BRET-based semisynthetic network (LUPIN) was achieved. The LUPIN system takes inspiration from BRET-based sensors, with which shares the fusion protein component (*i.e.* SNAP-NanoLuc-receptor), and couples the BRET event to a chemical reaction for the release of effector molecules. A synthetic linker functionalized with a ruthenium complex and a PNA strand enables the templated release from conjugates bearing a pyridinium immolative linker. The system can operate at low nanomolar concentrations reaching up to 64 turnovers for the release of caged small molecules. The network proved to be suitable for the release of potent cytotoxics in cellular environments. The release reaction can be modulated by tuning the concentration of luciferase substrate, and the system can be further controlled by the addition of receptor ligand, behaving similarly to allosterically controlled enzymes. In addition, the use of bioluminescence overcomes the limitation deriving from external light irradiation in the context of biological applications. Moreover, even though the LUPIN network makes use of a ruthenium photocatalyst, the use of different pairs of luciferase-photocatalyst can be anticipated. Furthermore, the possibility to genetically encode the luciferase component could allow the release of effector molecules at a specific location within biological systems. Recent advances in the filed of BRET-based systems demonstrate the successful application of this technology to other chemical systems.[223, 243]

Chapter V

QPD-OTf: a precipitating dye tracking kinesin-1 activity in living cells

This project was carried out in collaboration with Eric Lindberg, Nikolai Klena, Christopher Bleck and Charlotte Aumeier. The content of this chapter is adapted from *Angerani S., Lindberg E., Klena N., Bleck C. K. E., Aumeier C., and Winssinger N. "Kinesin-1 activity recorded in living cells with a precipitating dye." Nature Communications 12:1463 (2021).*[244]

Introduction

QPD[245] is a quinazolinone-based precipitating dye that fluoresces as a result of an excited-state intramolecular proton transfer (ESIPT)[246] between the phenolic group and the quinazolinone (Figure 55). The fluorescence can be completely quenched disrupting the ESIPT system by functionalizing the phenolic moiety, and in turn freeing the aryl group out planarity with the quinazolinone. This feature allows for the design of pro-fluorophores responsive to customable inputs (Figure 55). In addition, the high photostability and low autofluorescence as result of a large Stoke shift (ex: 365 nm; em: 540 nm) render this fluorophore a desirable candidate for *in cellulo* applications. In fact, a variety of QPD derivatives has been developed for the visualization of enzymatic activity in biological settings.[245, 247] Probably the most widely utilized is the commercial ELF-97®, a phosphate QPD derivative used to label different cytological targets, including cytoskeletal elements and organelles, with high spatial resolution in response to phosphatase activity.[248] Following this lead, other caged fluorophores have been developed to respond to alternative chemistries, including protease activity (carbamate derivative),[249] hydrogen peroxide (boronic acid derivative)[250] and metal catalysed photochemistry (azide[174] or picolinium[129] derivatives); all these derivatives can localize the fluorescent signal at the site of cleavage *in cellulo*.

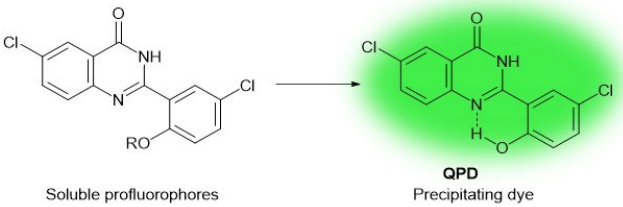

Input	Caging group R
Phosphatase	Phosphate
β-Glucoronidase	Glucoronide
Protease	Peptidic carbamates
Hydrogen peroxide	Boronic acid
$[Ru(bpy)_3]^{2+}$ photocatalysis	Azide Picolinium derivative

Figure 55. Structure of QPD profluorophores and of fluorescent precipitating dye (top). Summary of inputs and respective caging groups used to trigger dye precipitation.

The visualization of cytoskeleton related proteins, such as motor proteins, offers the possibility to gain insights on cellular trafficking. In fact, these proteins transport cargoes by walking on microtubules (MTs) or actin filaments using the energy derived from ATP hydrolysis as propellent.[251] In this context, kinesins and dyneins regulate the transport on MTs, directing

their motion towards their plus-end or minus-end respectively.[251] Regarding the kinesin family, these proteins display motor domains for the binding to MTs and responsible for the ATP-ase activity, and light chains that respond to cargo binding.[252] Among other members, kinesin-1 is a tetrameric motor protein constituted of heavy (Figure 56, brown) and light chains (Figure 56, blue); the heavy chains include the motor domains responsible for microtubule binding. Kinesin-1 is involved in Golgi-to-ER and ER-to-Golgi trafficking by interacting with pre-Golgi and Golgi membranes.[253, 254] In the absence of cargoes, kinesin-1 assumes a folded conformation (Figure 56) that inhibits ATP hydrolysis;[255] cargo binding induces a conformational switch, allowing to restore the hydrolytic activity of the protein, and resulting in motion along microtubules (Figure 56). In particular, kinesin-1 results functionally active during Golgi-to-ER transport, walking on MTs for significant distances.[256, 257] The most accredited mechanism for the motion of kinesins on MTs is the hand-over-hand model.[258] According to a recent report, kinesin-1 motion on MT proceeds through two 4-nm sub-steps.[259] Starting from the motor domains bound to MT, with the front motor domain without nucleotide and the rear one binding ADP + Pi, the first sub-step happens as a consequence of ATP binding to the front motor and Pi release from the rear on; at this stage the two motor domains align.[259] The second sub-step is triggered by ATP hydrolysis in the front domain and ADP release from the former back one.[259] Moreover, it has been observed that kinesin-1 walks preferentially on highly stable microtubules, such as acetylated and detyrosinated MTs.[260-262]

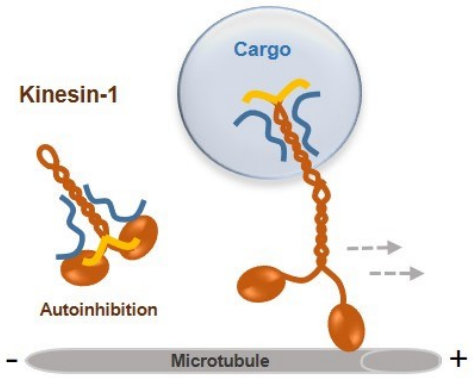

Figure 56. Kinesin-1 autoinhibition state and active state walking on microtubule upon cargo binding. Blue: light chains; brown: heavy chains and motor domains; yellow: tails.

Since kinesin-1 has been associated with different pathologies, such as cancer,[263] neurological disorders[264] and infection,[265] being able to track this motor protein in cells might help understand and overcome deleterious functions. So far, monitoring motor proteins in cells has relied on techniques involving antibodies, quantum dots or fluorescently labelled modified proteins.[266-271] However, these methods necessitate extensive sample treatment, by fixation and staining steps, or manipulation, requiring transfection. Moreover, these techniques are unable to discriminate proteins based on their motility, rather staining the total protein expression. Considering that only a fraction of kinesin-1 (~30%) is active in cells,[272] distinguishing the signal arising from the protein moving on MTs from the high background signal belonging to the immotile fraction is extremely complicated.[260] Thus, the advent of fluorophores able to track the endogenous activity of kinesin-1 would be beneficial.

Project approach

Since this project originates from serendipitous findings, the discussion will not be focused on the design of the system but will treat instead the approach employed to recapitulate the observed output to the responsible triggering event. In a network context, the project differs from the previous ones described within this work since it does not build form the rational design of a responsive network but makes use of a deconvolution process to disclose the key modules of an existing responsive system.

The project is based on the quinazolinone precipitating dye derivative QPD-OTf, that generates aster-like fluorescent crystals in living cells over time (Figure 57).

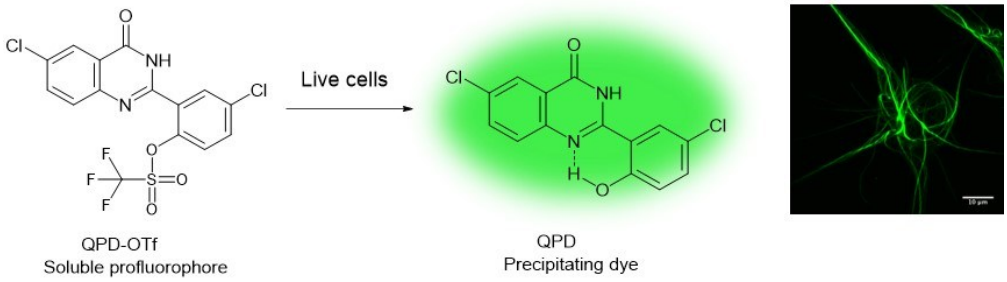

Figure 57. Structure of the profluorophore QPD-OTf (left); green fluorescent QPD crystals imaged in live cells (right).

Despite QPD and several pro-fluorophore analogues are well established products,[129, 174, 245, 247-250] frequently used to visualize specific entities *in cellulo*,[248] none of the reported derivatives shows aggregation into supramolecular structures resembling the shapes that were observed with QPD-OTf. The exquisite behaviour of this molecule in a cellular setting pointed towards the involvement of a specific biological event rather than a fortuitus dye uncaging from the triflate derivate. Thus, the study evolved from the critical analysis of preliminary cellular imaging data to more specific experiments involving cellular function manipulation and *in vitro* assays with purified proteins.

Results and discussion

QPD-OTf was initially designed to respond to superoxide, thus envisioning a tool for the detection of oxidative stress in cells. This molecule was inspired by a reported double triflated fluorescein derivative, which undergoes triflate cleavage upon nucleophilic attack by superoxide ion.[273] Surprisingly, attempts to precipitate QPD from QPD-OTf by treatment with $O_2^{\cdot -}$ *in vitro* led to no observable reaction. However, macrophage cells (RAW264.7) stimulated with zymosan and treated with QPD-OTf yielded dotted fluorescent precipitate within 10 min; over time the dots evolved into fibers (Figure 58).

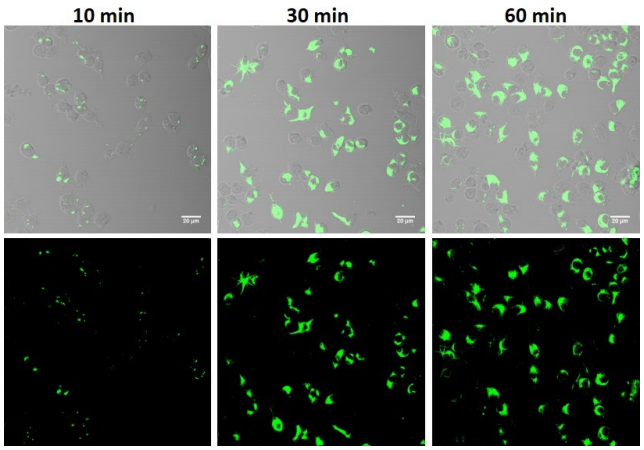

Figure 58. Confocal images of RAW264.7 cells treated with QPD-OTf. QPD fluorescence (green). Scale bar 20 μM.

Intrigued by this behaviour, QPD-OTf (20 μM, 4 hours) was incubated with several human and mammalian cell lines (U2OS, HeLa, HEK293, MCF-7, PTK2) with the formation of filamentous, aster-like crystals spanning through the cell (Figure 59).

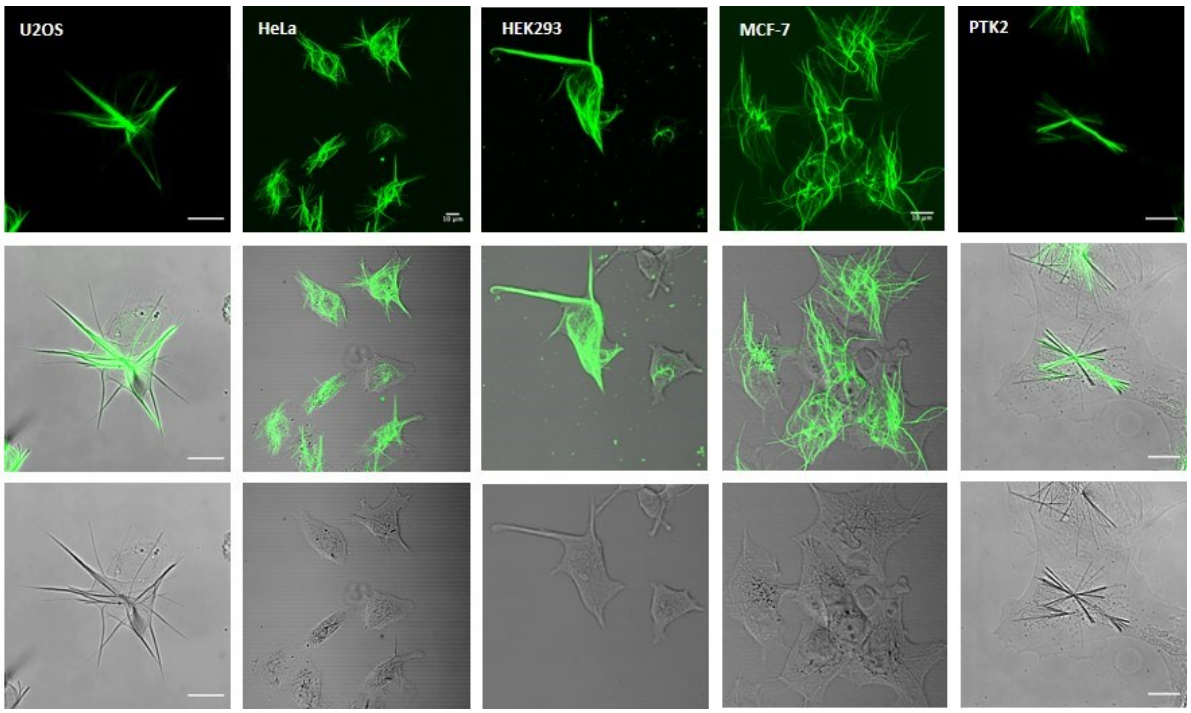

Figure 59. Fluorescent crystals in a panel of cell lines treated with QPD-OTf (20 μM, 4 hours). Scale bar 10 μm.

Even though different cell lines require slightly different timeframes to develop crystals, fluorescent fibers are already observable under a microscope (63X objective) after 30 min treatment and reach considerable size within 2-4 hours (easily recognizable with a 20X objective) (Figure 60), with the fibers even able to induce cell membrane deformation (Figure 59).

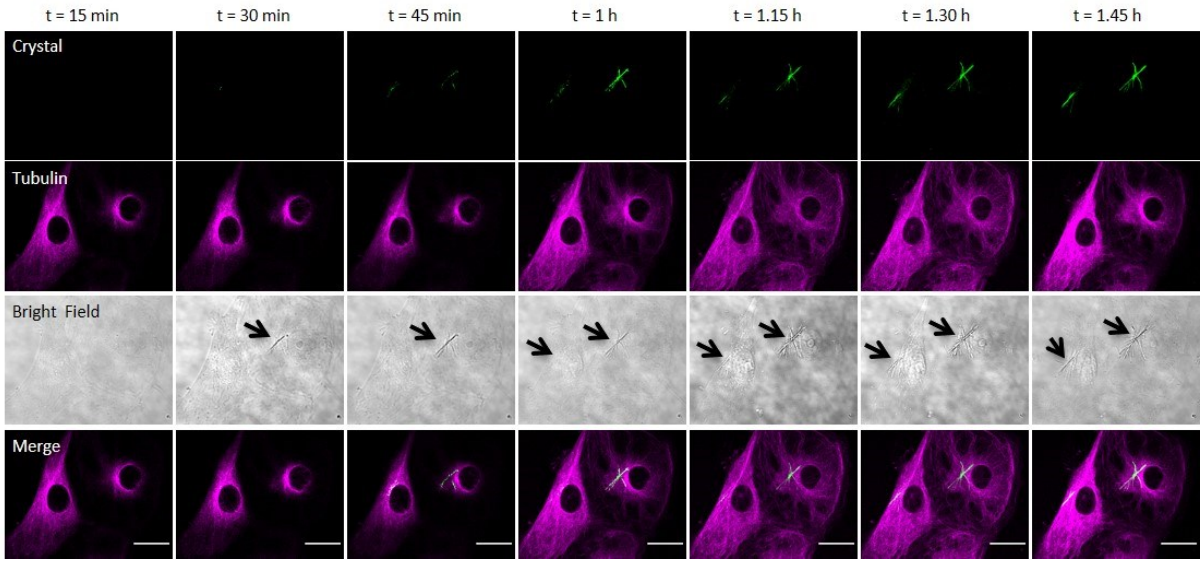

Figure 60. Crystal formation over time in PTK2-GFP-Tubulin cells treated with QPD-OTf (20 μM) imaged over time. Green: QPD fluorescence; magenta: GFP-tubulin. Black arrows indicate the position of crystals. Scale bar 20 μM.

The structure of the crystals was further confirmed by FIB-SEM analysis of QPD-OTf treated HeLa cells (20 μM, 4 hours) (Figure 61): the crystal fibers have a well-defined structure, with rotational symmetry order 3-like and hexagonal cross-section (100 to 700 nm size); in addition, all the fibers emanate from a common central point.

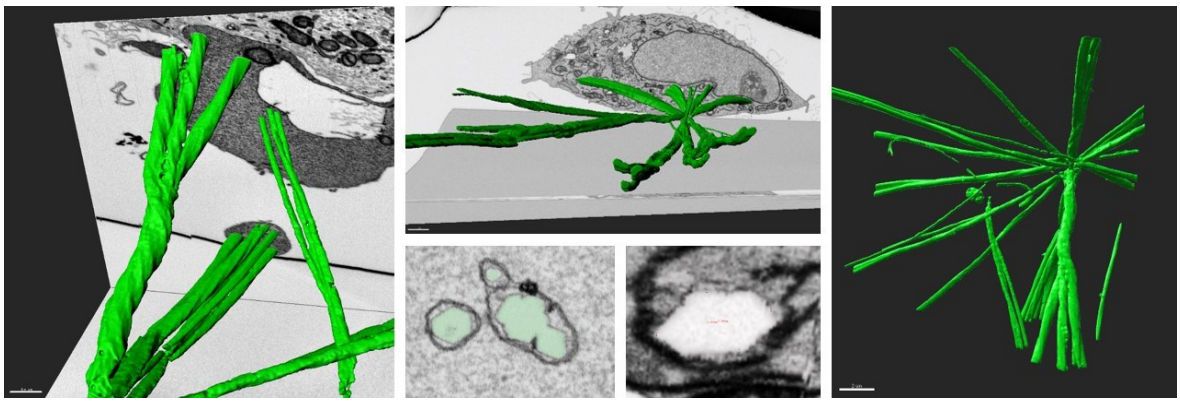

Figure 61. FIB-SEM 3D-reconstruction of crystal inside HeLa cells and respective cross-sections of fibers; green: crystal. Scale bar 0.4 μM.

Even tough prolonged incubation time (16 hours, 10-20 μM QPD-OTf) leads to cell death, cell viability can be preserved almost completely upon temporary treatment and fresh media replacement (Figure V-S1), and crystal dissolution can be monitored over time (Figure V-S2).

The filamentous nature of the crystals led to hypothesize a potential association with cytoskeletal elements. Importantly, since triflate removal and restoration of the QPD ESIPT system is a prerogative for fluorescence, a cleavage event in the cellular environment must be considered. First, immunostaining of actin and tubulin in cells treated with QPD-OTf

showed alignment of the crystal fibers with microtubules, and no colocalization with actin (Figure 62).

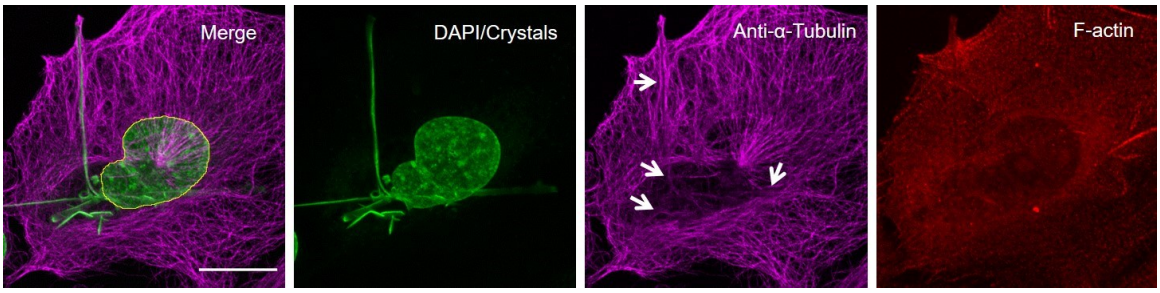

Figure 62. Immunofluorescence of U2OS cells treated with QPD-OTf. Fixed U2OS treated with QPD-OTf and stained with DAPI, α-tubulin immunostaining and actin immunostaining. White arrows indicate colocalization with crystal fibres. Green: DAPI/Crystals; magenta: anti-α-tubulin; red: F-actin. Scale bar 20 μM.

Confocal fluorescence microscopy of live cells stably expressing GFP-tubulin (PTK2-GFP-tubulin and HeLa-GFP-tubulin cells) treated with QPD-OTf confirmed the colocalization of the crystals with microtubules (Figure 63, Figure V-S3). A similar pattern was observed in cells stained with SiR-Tubulin,[274] a Taxol based fluorescent probe (Figure V-S4). However, the crystals colocalized with a discrete subset of MTs within a cell.

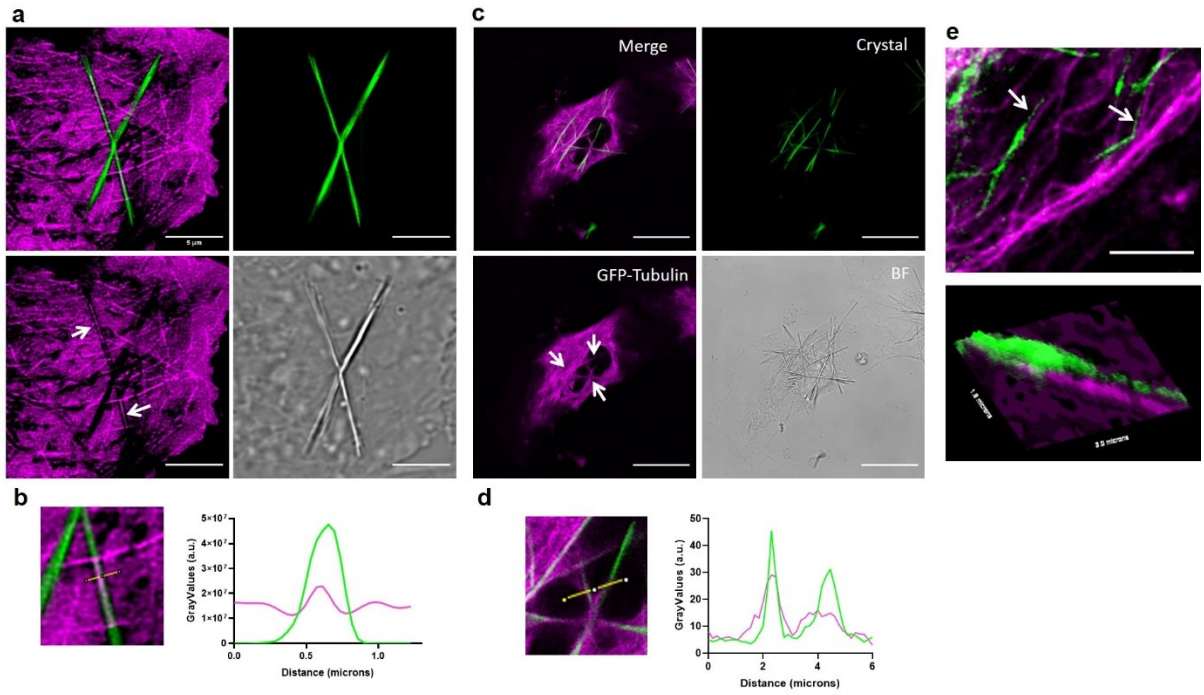

Figure 63. a) Super-resolution imaging of HeLa-GFP-Tubulin live cells treated with QPD-OTf (20 μM; 2 hours); white arrows indicate colocalization with crystals (GFP-tubulin: magenta; crystal: green). Scale bar 5 μM. b) Live cell imaging of PTK2-GFP-Tubulin treated with QPD-OTf (20 μM; 2 hours); white arrows indicate colocalization with crystals (GFP-tubulin: magenta; crystal: green). Scale bar 20 μM. b), d) Plot profiles of tubulin channel (magenta) and QPD channel (green). Yellow lines represent the sections plotted in the graphs. e) Super-resolution image of live HeLa-GTP-Tubulin cells treated with QPD-OTf at early time point (QPD-OTf 20 μM; 20 min) (top); white arrows indicate colocalization with crystals; scale bar 5 μM. Surface plot of crystal and MT signal (bottom) (GFP-tubulin: magenta; crystal: green); surface section: 1.8x3.0 microns.

Interestingly, cells pre-treated with SiR-Tubulin (1 μM, 30 min) did not form crystals upon incubation with QPD-OTf. Since Taxol is a well characterized MT stabilizer that leads to suppression of the dynamic behaviour of microtubules,[275] the involvement of MT dynamics in crystal formation was considered.

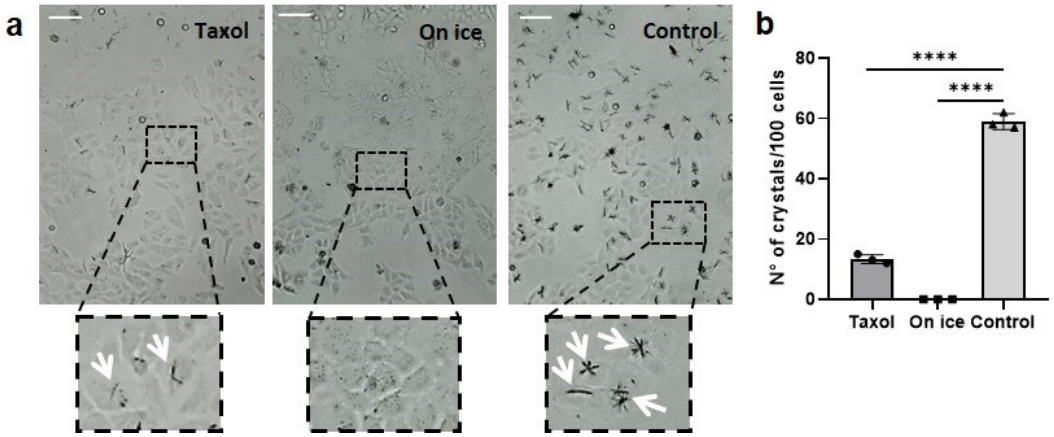

Figure 64. a) Representative images of crystal formation in cells treated (left) with 1 μM Taxol for 1 hour and 20 μM QPD-OTf for 4 hours at 37 C; (middle) on ice for 1 hour and with 20 μM QPD-OTf for 4 hours on ice; and (right) with 20 μM QPD-OTf for 4 hours at 37 °C. (Bottom) Zoomed-in images of cells in the black squares; white arrows indicate crystals. Scale bar 100 μM. b) Quantification of number of crystals for conditions reported in a; n= 100; data are presented as mean value +/- the standard deviation (SD); data are the average of three independent experiments; statistics were calculated using a two-tailed *t*-test; **** $p < 0.0001$.

Thus, the MT dynamic was systematically affected, and the number of crystals was quantified. First, the dynamicity of the microtubule network was inhibited with Taxol (1 μM, 1 hour); following treatment with QPD-OTf (20 μM, 4 hours) resulted in a 75% reduction in crystal formation respect to the control sample (Figure 64); additionally, the few crystals present showed thinner fibers (Figure 64a). Second, total depolymerization of the MT network by incubation on ice completely prevented crystal formation (Figure 64). These experiments highlighted that a dynamic microtubule network is a prerequisite for crystal formation. Moreover, incubation of QPD-OTf with cell lysates yielded no crystals, further strengthening the data supporting microtubules dynamics as necessary condition for crystal formation.

However, as previously mentioned, not the entire MT skeleton is interested by crystal fibers. In order to investigate the reason behind the selective staining of microtubule subsets, the attention was directed to the centre of the crystals. In fact, cells in interphase show a single crystal, with the centre usually located close to the nucleus. Thus, the possibility to have colocalization with a microtubule organizing centre was considered. In a cell MTs can generate from the centrosome, the Golgi apparatus,[276, 277] or from spontaneous nucleation sites in the cytosol,[278] with the centrosome being the main MT organizing centre; however, the involvement of the centrosome in crystal location was ruled out by imaging experiments on GFP-tubulin cells treated with QPD-OTf, which showed no colocalization between the centrosome and the centre of crystals (Figure 65).

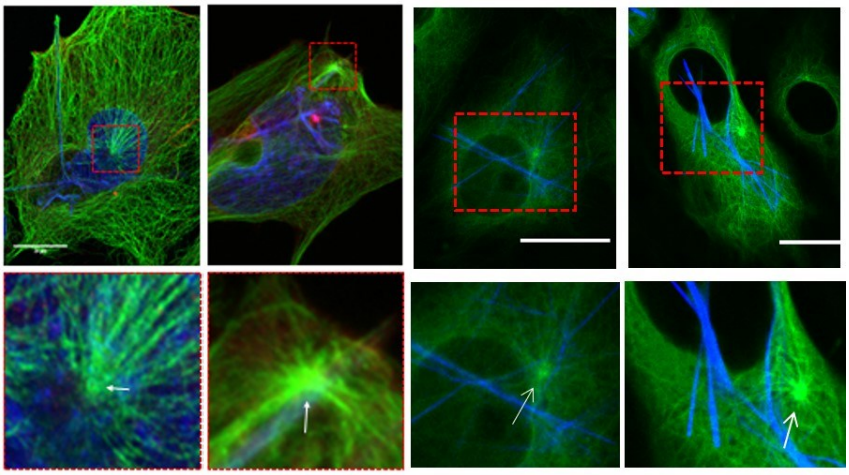

Figure 65. Representative images of U2OS or PTK2-GFP-Tubulin treated with QPD-OTf (2 hours, 20 μM). Green: tubulin; blue: crystal/DAPI. Arrows indicate the position of the centrosome. Red dotted-boxes indicate the zoomed-in area of the pictures shown in the bottom panels. Scale bar 20 μM.

Then, cells were transfected with mCherry-Giantin to be able to visualize the Golgi apparatus. Upon QPD-OTf treatment, good colocalization between the Golgi and the centre of the crystals was observed (Figure 66a, U2OS cells; Figure V-S5, PTK2-GFP-Tubulin cells), suggesting a potential correlation between crystals and Golgi-derived microtubules. In addition, Golgi elements were found to strictly correlate with growing crystal fibers (Figure V-S6). Moreover, since the Golgi apparatus is responsible for protein transport, playing a key role in the secretory pathway,[279] the effect of Golgi trafficking inhibition on the localization of crystal was investigated. To this end, Brefeldin A (BFA), a fungal metabolite responsible for the inhibition of protein secretion that causes the disassembly of the Golgi complex[280, 281] was used to treat cells before addition of QPD-OTf. While the Golgi apparatus appears as a compact complex in U2OS cells in interphase, treatment with BFA (20 μM) showed the expected scattered Golgi (Figure V-S7). Adding QPD-OTf to BFA treated cells resulted in thinner crystals, with fiber thickness reduced by 58% compared to the control sample (Figure 66c); in addition, crystals were spread throughout the cell and generating from multiple nucleation sites (Figure 66b).

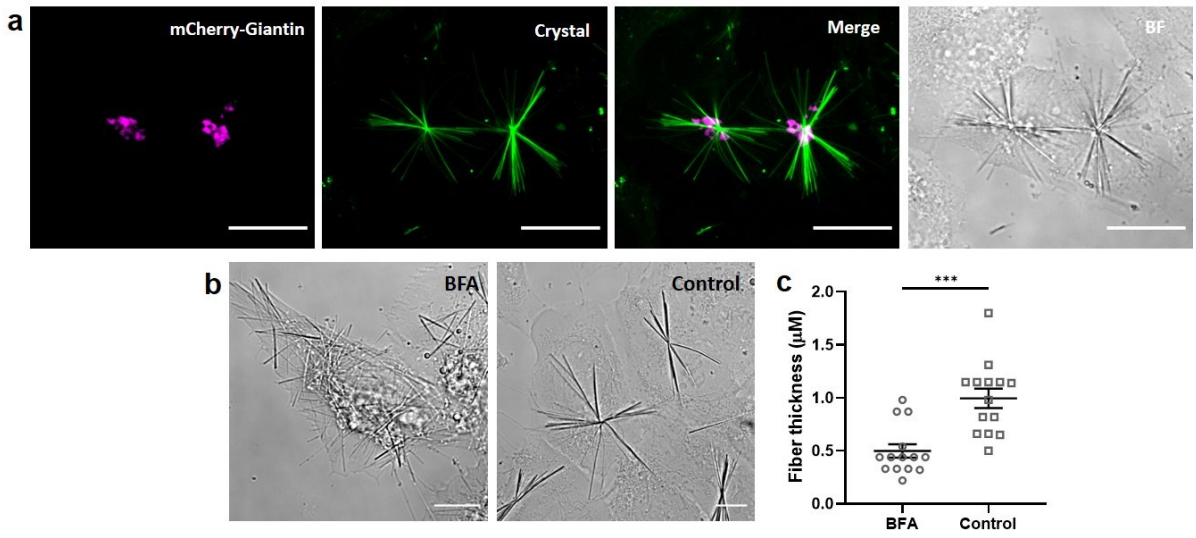

Figure 66. a) Representative images of mCherry-Giantin transfected U2OS cells treated with QPD-OTf (20 µM 3 hours). Crystals (green), mCherry-Giantin (magenta). Scale bar 20 µM. b) Representative images showing the effect of brefeldin A (BFA) on crystal morphology and location. BFA treated cells (20 µM BFA 4 hours + 20 µM QPD-OTf 2.5 hours) (top). Control (20 µM QPD-OTf 2.5 hours) (bottom); scale bar 10 µM. c) Quantification of images reported in b; n=14 fibers; data are presented as mean value +/- the standard error of the mean (SEM); statistics were calculated using a two-tailed *t*-test; ***p=0.0001.

Interestingly, the crystals remain centred on Golgi vesicles (Figure 67), suggesting that the Golgi apparatus is strictly related to crystal formation and that modifications at the Golgi structure correlate with crystals morphology and location.

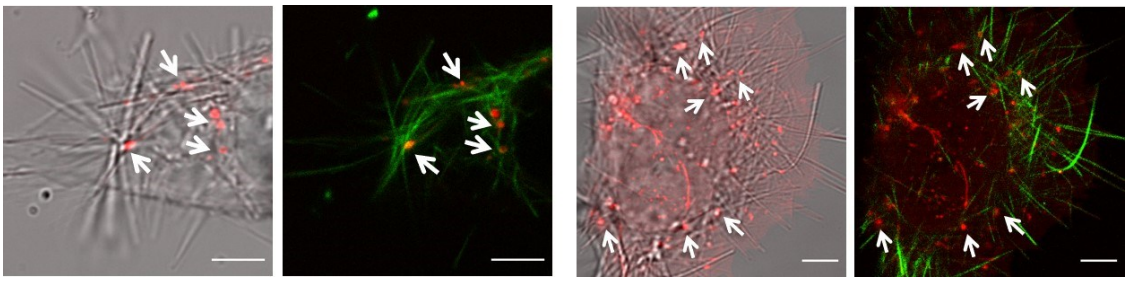

Figure 67. Localization of crystals and Golgi vesicles after BFA treatment; Golgi (red) crystals (bright field) (left); Golgi (red) crystals (green) (right); arrows indicate centres of crystal; scale bar 5 µM.

So far, both microtubule dynamics and Golgi elements, known to act as MTs nucleating sites, resulted strictly connected to crystal formation. To establish whether tubulin polymerization was sufficient to generate QPD crystals, Taxol stabilized MTs or dynamic microtubules elongating from stabilized seeds were treated with QPD-OTf *in vitro* and the mixture was imaged over time with a TIRF microscope. Even after 2 hours of incubation, neither crystals nor QPD fluorescent signal was detected (Figure V-S8), indicating that the tubulin polymerization event is not sufficient and suggesting that crystal formation might depend on the activity of additional MTs related enzymes. In addition, to exclude spontaneous nucleation of QPD crystals on other fibrillar structures, QPD-OTf was incubated with methyl-cellulose, resulting in no fluorescence or crystals observed.

Reasoning that QPD precipitation requires an enzymatic event strictly connected to microtubules but not necessary for MTs proliferation, and simultaneously related to Golgi trafficking, the attention was directed towards motor proteins. In fact, these proteins exert their function of cargo transport moving along microtubules using ATP hydrolysis as source of energy.[252] Among motor proteins, the kinesin family transports cargoes to the cell periphery walking on microtubules towards their (+)-end.[282] Kinesin-1 is present both in pre-Golgi and Golgi membranes, and it cycles between ER and Golgi.[253, 254] It is functionally active only during Golgi-to-ER transport despite being able to move in both directions.[254] In addition, Taxol is known to inhibit the motion of kinesin-1.[283] These prerequisites were in line with the experimental data observed so far, and thus encouraged to focus on kinesin-1. To circle back to the effect of MT dynamics on crystal formation, this time in the context of kinesin-1, QPD-OTf was added to cells transfected with Kin330-GFP or Kin560-GFP, two truncated versions of kinesin-1 displaying no ability to walk on microtubules, and enhanced motion on MTs respectively.[284, 285]

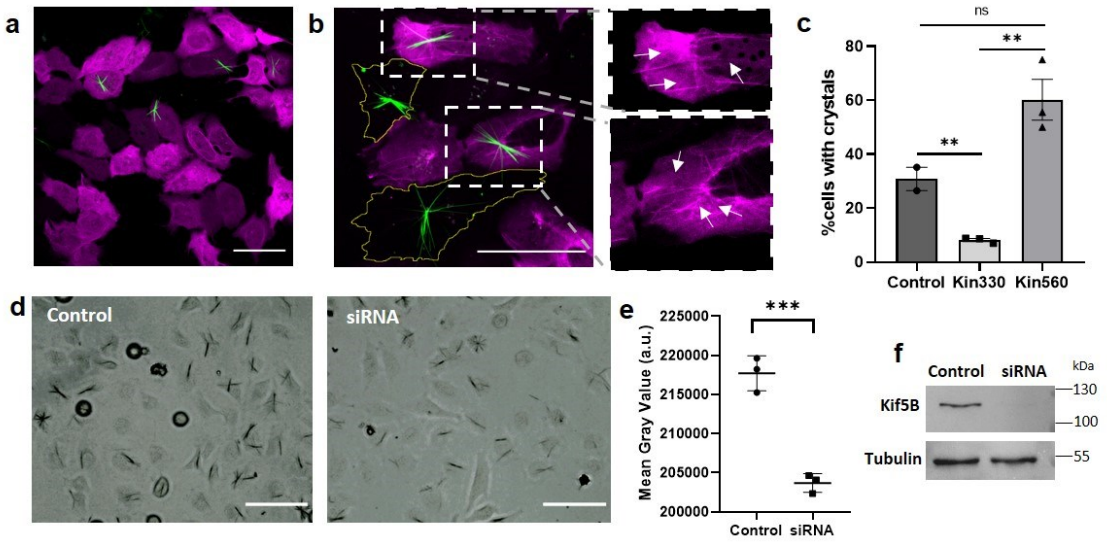

Figure 68. a) U2OS transfected with Kin330-GFP plasmid and treated with QPD-OTf (20 μM, 2.5 hours); green: crystals, magenta: Kin330-GFP. b) U2OS transfected with Kin560-GFP plasmid and treated with QPD-OTf (20 μM, 2.5 hours) (left); zoom of highlighted boxes, arrows indicate stabilized MTs correlating with crystals (right); green: crystals, magenta: kinesin. Scale bar 50 μm. c) Quantification of crystal formation in transfected cells *vs* control; n= 20; average of three independent experiments; data are presented as mean value +/- the standard error of the mean (SEM). Statistics calculated using a two-tailed *t*-test; **p=0.0064 (Control *vs* Kin330), **p=0.0024 (Kin330 *vs* Kin560); ns p=0.065. d) Kinesin-1 knockdown experiment. Representative images of HeLa-GFP-Tubulin treated with RNA control sequence + QPD-OTf (20 μM, 2 hours) (left) or with kinesin-1 siRNA + QPD-OTf (20 μM, 2 hours) (right). Scale bar 100 μM. e) Quantification of crystal intensity for kinesin-1 knockdown experiment. n = 30; data are the average of three independent experiments; data are presented as mean value +/- the standard deviation (SD); Statistics were calculated using a two-tailed *t*-test; *** p = 0.0007. f) Kif5B and Tubulin bands from Western Blot assay for the kinesin-1 knockdown experiment in HeLa cells.

In cells transfected with Kin330-GFP the number of crystals was significantly reduced (by 87%) compared to non-transfected cells (Figure 68a; 68c for quantification). The residual formation of some crystals could be attributed to the activity of wildtype cellular kinesin-1. On the other hand, cells transfected with Kin560-GFP showed unaltered crystal formation (Figure

68b, c, Figure V-S9); in addition, it was possible to correlate the crystal filaments to the signal of Kin560-GFP on specific MTs (Figure 68b zoom). Moreover, siRNA knockdown of kinesin-1 demonstrated a significant reduction of crystal intensity (Figure 68d, e; Western Blot confirming efficient Kif5B knockdown, Figure 68f), confirming the involvement of kinesin-1 in crystal formation.

To gain further insight regarding the role of kinesin-1 on crystal formation, the effect of kinesore, a small-molecule activator of kinesin-1,[286] was assessed in cells. Kinesore interacts with kinesin-1 at the kinesin light chain-cargo interface (K_i = 49 μM for aiKLC2TPR: SKIPWD complex), mimicking the effect of cargo binding and resulting in kinesin-1 over activity.[286] In fact, in the absence of cargo binders, kinesin-1 is autoinhibited; in cells, only a small fraction of kinesin-1 is active[287, 288] (*vide supra*). The enhanced motion induced by kinesore extensively rearranges the microtubule network.[286] When QPD-OTf was added to U2OS cells pre-treated with kinesore (100 μM, 2 hours) no crystals formed, yet a diffused QPD fluorescence was observed (Figure 69). This result confirmed the involvement of kinesin-1 activity in QPD precipitation; however, the resulting over activity of the motor protein might compromise the formation of a compact tridimensional structure, such as crystal fibers. Moreover, since QPD is still generated in presence of kinesore, which interacts at the kinesin-1-light chain-cargo interface, binding of QPD-OTf at the cargo binding site of kinesin-1 should be discarded.

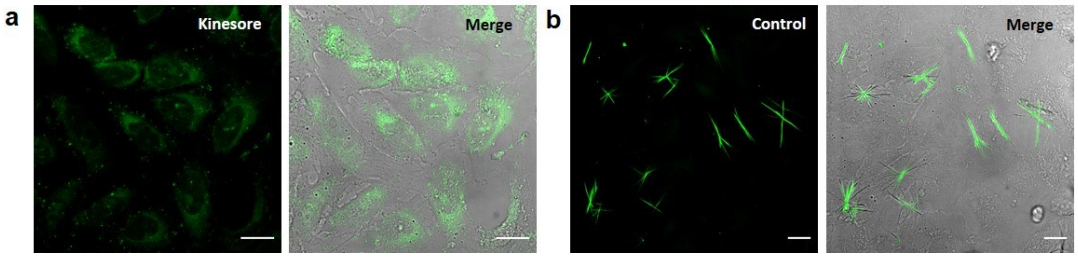

Figure 69. a) U2OS treated with kinesore (100 μM) in Ringer's buffer + QPD-OTf (20 μM); green: QPD fluorescence. b) Control conditions for experiment reported in a (QPD-OTf 20 μM, 2 hours in Ringer's buffer); green: crystals. Scale bar 20 μM.

To further understand the interaction between QPD-OTf and kinesin-1, and possibly shine light on the mechanism of QPD generation, an *in vitro* system employing purified proteins was screened. Since kinesin-1 walks processively on microtubules upon hydrolysis of ATP by the motor domains,[289] crystal formation was analysed under several conditions in presence of kinesin-1, +/- tubulin, MTs, ATP, GTP, AMP-PNP in BRB80 buffer. Samples containing both kinesin and microtubules appeared to generate significant QPD fluorescence (Figure 70a-c, samples 3,4,5), with the most intense signal deriving from the sample containing QPD-OTf, kinesin-1 and microtubules (Figure 70a-c, sample 4). Moreover, the presence of a non-hydrolysable version of ATP (AMP-PNP), causing reduced motility of kinesin-1 bound to microtubules,[290, 291] reduced the fluorescent precipitate (Figure 70a-c, sample 3). Presence of ATP also slightly reduced the formation of the precipitate (Figure 70a-c, sample 5). In addition,

confocal microscopy revealed the presence QPD-fluorescent filamentous structures in the MT/kinesin/QPD-OTf samples (Figure 70d).

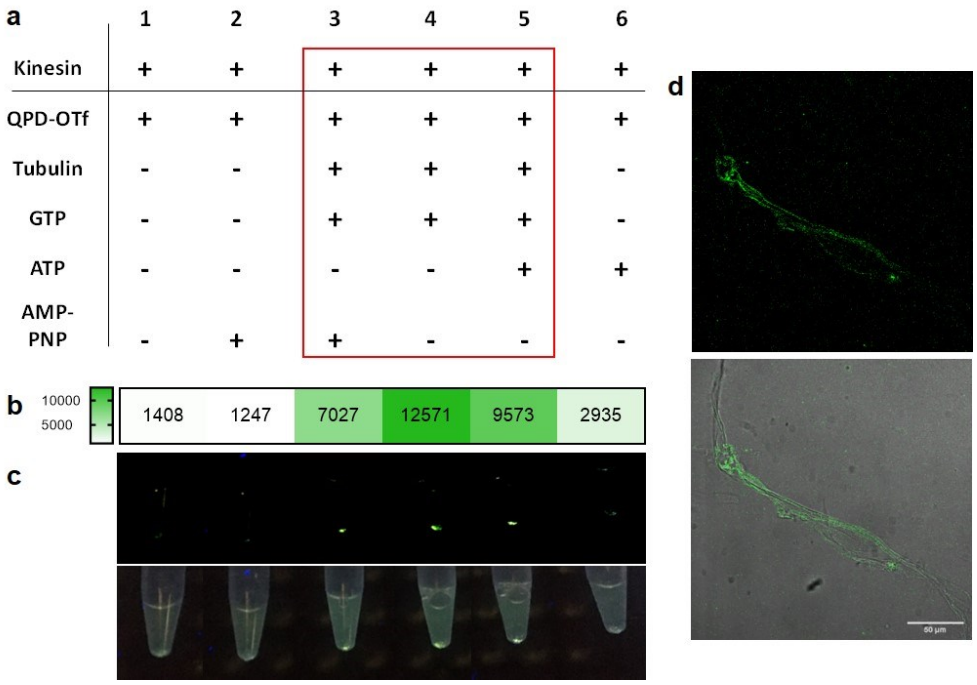

Figure 70. a) In vitro precipitation of QPD; table of conditions for the samples reported in c; red square indicates the samples that gave detectable QPD-fluorescence. b) Intensity map of emitted light by samples 1-6 under 366 nm excitation; intensity values are expressed as grey values from the green channel of an RGB picture acquired with a smartphone camera. c) Samples under 366 nm light: green channel (top); original picture (bottom). d) Confocal imaging of fluorescent filaments contained in sample 4; green: crystal. Scale bar 50 µm.

These results corroborated the correlation between kinesin-1 activity and QPD precipitation already observed with the transfection assays; in addition, the precipitate reduction in presence of AMP-PNP suggested a potential competition of QPD-OTf for the ATP binding site of kinesin-1. Furthermore, since QPD precipitate was formed even in the absence of ATP, the role of QPD-OTf as substrate analogue was hypothesized. In this way, the triflate group of QPD-OTf might behave as the ATP-phosphate group. To prove the viability of this hypothesis, molecular docking of QPD-OTf into the ATP binding pocket of the kinesin-1 motor domain was performed using Autodock Vina[292]. Fitting into the human kinesin-1 in the ATP state (PDB: 3J8Y) gave a best calculated pose (-8.3 kcal/mol), where the triflate moiety well correlates with the positioning of the phosphate group of ATP (Figure 71a). Moreover, Ispinesib,[293] a known allosteric inhibitor of the motor domain of kinesin Eg5 shares with QPD-OTf the quinazolinone core. Since the motor domains of kinesin-1 and Eg5 show high structural similarity,[294] docking calculations for QPD-OTf in the Ispinesib-like binding site of both Eg5 (PDB:4AP0) and kinesin-1 were performed (Figure 71b, c). QPD-OTf shows good affinity for Eg5 (-9.3 kcal/mol) and good pose correlation with Ispinesib; however, this binding mode positions the molecule too far from the nucleotide binding site, thus preventing triflate hydrolysis. Less favourable binding was calculated for the allosteric site of kinesin-1 (-5.8

kcal/mol), in which the molecule accommodates only in a solvent exposed area of the protein (Figure 71c, Figure V-S10).

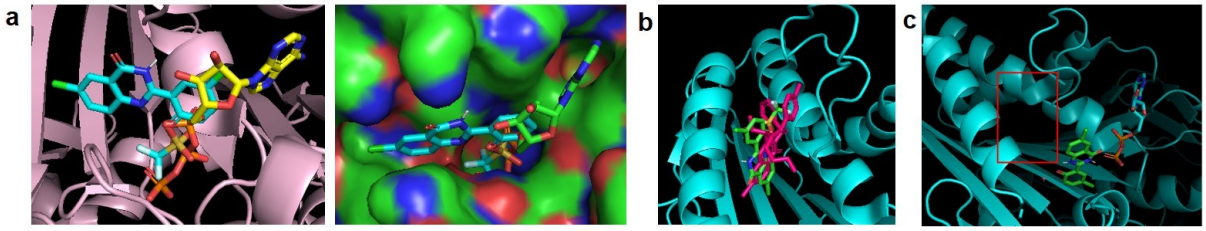

Figure 71. a) Docking of QPD-OTf into ATP binding site of kinesin-1. Left: QPD-OTf (cyan), ATP (yellow), kinesin-1 (pink); right: QPD-OTf (cyan), ATP (green), kinesin-1 (polarized surface). b) QPD-OTf docking into the Ispinesib binding site of Eg-5. Superposition of Ispinesib (magenta) and QPD-OTf (green) into Eg5 protein (cyan). c) docking into the Ispinesib binding site of kinesin-1 co-crystallized with ADP. QPD-OTf (green), ADP (cyan backbone; orange phosphate groups) into kinesin-1 (cyan). Red box indicates the "Ispinesib-like" binding site.

Overall, the docking studies suggest the hydrolysis of the triflate of QPD-OTf in the nucleotide binding pocket of kinesin-1. In addition, the calculations offer an explanation for the selectivity of the molecule for kinesin-1 over Eg5. Since Eg5 is associated to the mitotic spindle,[295, 296] to further validate the docking results with *in cellulo* evidence, the effect of QPD-OTf was assessed in mitotic cells. In this way, involvement of Eg5 in QPD precipitation should yield crystals colocalizing with the mitotic spindle. Imaging of mitotic HeLa-GFP-tubulin treated with QPD-OTf revealed no association with the mitotic spindle, yet generated crystals compatible with Golgi transport (Figure 72).

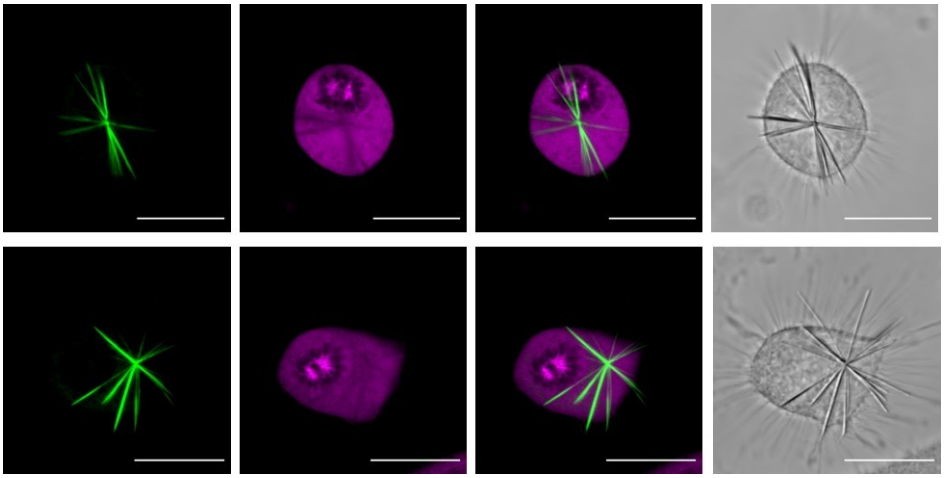

Figure 72. Mitotic HeLa-GFP-Tubulin cells treated with QPD-OTf (20 μM). Green: crystal; magenta: tubulin. Scale bar 20 μm.

Conclusions

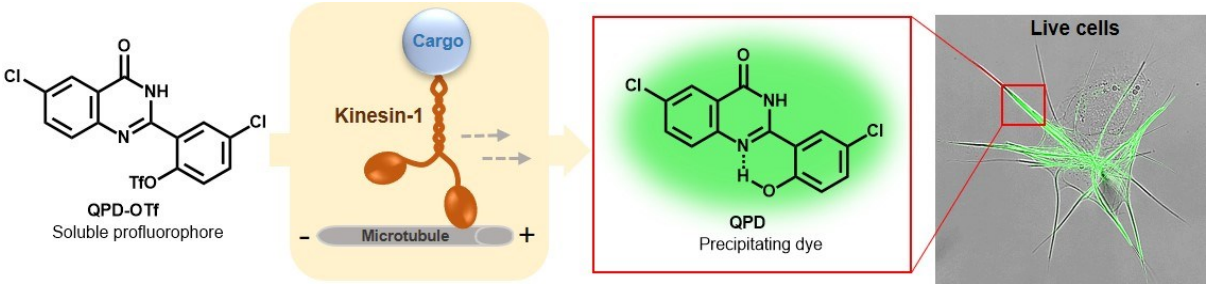

In summary, the characterization and application of a precipitating dye that produces fluorescent crystals in response to kinesin-1 activity on microtubules generating from the Golgi apparatus is disclosed. The centre of the crystals reflects the location of Golgi elements; the number of crystals per cell and their thickness well correlates with Golgi compactness/fragmentation. The crystal formation is sensitive to kinesin-1 motility and kinesin-1 inhibitors or protein depletion disrupt the formation of the crystals. In addition, the presence of microtubules is required to generate QPD fluorescence *in vitro*. The data suggest that QPD crystals form upon triflate cleavage after QPD-OTf binding to the ATP binding pocket of the kinesin-1 motor domain. Acting as an ATP-ase substrate, QPD-OTf is therefore able to track the motility of kinesin-1 on MTs. QPD-OTf offers for the first time the possibility to record the native activity of a motor protein in cellular environments. The possibility to dissolve the crystals in cell media after staining provides a non-destructive method to visualize the motion of kinesin-1 on Golgi derived microtubules. While general methods to report motor proteins *in cellulo* relying on modification with fluorescent tags stain the global content of protein,[270] QPD-OTf allows to track specifically the portion of active motor. This approach allows to recognize specific subsets of microtubules used for transport. In addition to the advantages offered by the precise visualization of endogenous activity of motor protein, these findings pave the way for the development of QPD derivatives as ATP-ase substrates.

Conclusions

This thesis focuses on the design, characterization, and application of responsive devices able to translate a biological input into a functional output. This work explores the development of supramolecular networks with modular architectures, using peptide nucleic acids (PNA) as technology to generate key supramolecular interactions. Particular credit is given to the employment of PNA templated reactions capitalizing on the ruthenium catalysed photoreduction of picolinium immolative linkers to obtain amplified output signals. The devices are designed to respond to the presence of biological entities, such as proteins and oligonucleotide sequences, and proved to successfully perform in cellular settings.

Regarding protein-responsive devices, four systems were developed. The first network capitalizes on the cooperative interaction between proximal binding sites of the cell membrane protein carbonic anhydrase IX (CA IX, a cancer biomarker) and PNA strands functionalized with small-molecule CA IX ligands. This cooperation allows for the assembly of a supramolecular system able to release output molecules (fluorophores, cytotoxic agents) in an amplified fashion thanks to the employment of PNA templated transformations. The network performs similarly to theragnostic devices, coupling the recognition of the target protein to the release of therapeutic agents in a CA IX-expression dependent manner.

A second example uses the recognition of the CA IX target protein to elicit a hybridization chain reaction (HCR) process. In this case, the HCR technology was reengineered to perform with a system entirely constituted of PNAs. Leveraging on the advantageous properties of peptide nucleic acids, in particular the possibility to generate stable assemblies even with short sequences, a minimal PNA-HCR network based on 5-mer stem and 5-mer loop/toehold hairpins was developed. The system offers an alternative to the well-established DNA-HCR version, overcoming the requirement of long sequences to grant hairpin metastability. The PNA-HCR device represents a useful reporting tool that yields amplified fluorescent signal in response to the detection of a target protein on living cells.

Moreover, a bioluminescence resonance energy transfer (BRET)-based network is illustrated. With the aim of generating a system capitalizing on the spatiotemporal control offered by photo-controlled devices, and at the same time overcoming the tissue penetration limitation arising from external light irradiation, a network responsive to a luciferase protein was developed. The system geometry allows for efficient BRET from the bright luciferase NanoLuc to a $[Ru(bpy)_2phen]^{2+}$ complex derivative, which fuels a PNA templated transformation for the release of effector molecules (fluorophores, small molecule cytotoxics).

A further example minimizes the responsive system to a small molecule, QPD-OTf, precursor of the well established quinazolinone precipitating dye QPD. QPD-OTf, eliciting a fluorescent response by generating fluorescent crystals upon interaction with the motor protein kinesin-1

in living cells, allowed for the first time the visualization of the native activity of a motor protein in a cellular environment.

In the context of oligonucleotides-responsive devices, a network that couples the performances of a DNA fuelled circuit to PNA templated reaction to yield an output signal with quadratic amplification was developed. The system responds to biologically relevant oligonucleotide targets, such as miRNAs, with a remarkably low detection limit (in the femtomolar range). In addition, the network can be adapted to the release of therapeutic agents, once again providing a dual system that combines a diagnostic event (target detection) and a therapeutic one (drug release).

Overall, this thesis describes a broad range of responsive nanoscale devices and their application to biological settings. The systems described herein enable the visualisation of important biological processes such as motor protein movement, as well as cancer cell detection and targeted drug release, thereby adding to the available portfolio of molecular tools to study such systems.

References

1. Woodward, J. Simplicity in the Best Systems Account of Laws of Nature. *The British Journal for the Philosophy of Science* **65**, 91 - 123 (2014).
2. Watson, E.E., Angerani, S., Sabale, P.M. & Winssinger, N. Biosupramolecular Systems: Integrating Cues into Responses. *Journal of the American Chemical Society* (2021).
3. Jacob F Fau - Monod, J. & Monod, J. Genetic regulatory mechanisms in the synthesis of proteins.
4. Adleman, L.M. Molecular Computation of Solutions to Combinatorial Problems. *Science* **266**, 1021-1024 (1994).
5. Lipton, R.J. DNA Solution of Hard Computational Problems. *Science* **268**, 542-545 (1995).
6. Roybal, Kole T. et al. Precision Tumor Recognition by T Cells With Combinatorial Antigen-Sensing Circuits. *Cell* **164**, 770-779 (2016).
7. Cunningham-Bryant, D. et al. A Chemically Disrupted Proximity System for Controlling Dynamic Cellular Processes. *Journal of the American Chemical Society* **141**, 3352-3355 (2019).
8. Engelen, W., Meijer, L.H.H., Somers, B., de Greef, T.F.A. & Merkx, M. Antibody-controlled actuation of DNA-based molecular circuits. *Nat Commun* **8** (2017).
9. Ranallo, S., Sorrentino, D. & Ricci, F. Orthogonal regulation of DNA nanostructure self-assembly and disassembly using antibodies. *Nat Commun* **10** (2019).
10. Porchetta, A. et al. Programmable Nucleic Acid Nanoswitches for the Rapid, Single-Step Detection of Antibodies in Bodily Fluids. *Journal of the American Chemical Society* **140**, 947-953 (2018).
11. Schaerli, Y., Gili, M. & Isalan, M. A split intein T7 RNA polymerase for transcriptional AND-logic. *Nucleic Acids Res* **42**, 12322-12328 (2014).
12. Williams, J.Z. et al. Precise T cell recognition programs designed by transcriptionally linking multiple receptors. *Science* **370**, 1099 (2020).
13. Li, H. et al. A DNA-Mediated Chemically Induced Dimerization (D-CID) Nanodevice for Nongenetic Receptor Engineering To Control Cell Behavior. *Angew Chem Int Edit* **57**, 10226-10230 (2018).
14. Fink, T. et al. Design of fast proteolysis-based signaling and logic circuits in mammalian cells. *Nat Chem Biol* **15**, 115-+ (2019).
15. Gramespacher, J.A., Burton, A.J., Guerra, L.F. & Muir, T.W. Proximity Induced Splicing Utilizing Caged Split Inteins. *Journal of the American Chemical Society* **141**, 13708-13712 (2019).
16. Wu, C.-Y., Roybal, K.T., Puchner, E.M., Onuffer, J. & Lim, W.A. Remote control of therapeutic T cells through a small molecule–gated chimeric receptor. *Science* **350**, aab4077 (2015).
17. Douglas, S.M., Bachelet, I. & Church, G.M. A Logic-Gated Nanorobot for Targeted Transport of Molecular Payloads. *Science* **335**, 831-834 (2012).
18. Grossi, G., Jepsen, M.D.E., Kjems, J. & Andersen, E.S. Control of enzyme reactions by a reconfigurable DNA nanovault. *Nat Commun* **8** (2017).
19. Velema, W.A. & Kool, E.T. Fluorogenic Templated Reaction Cascades for RNA Detection. *Journal of the American Chemical Society* **139**, 5405-5411 (2017).
20. Yan, X.W. et al. Quantitative synthesis of protein-DNA conjugates with 1: 1 stoichiometry. *Chem Commun* **54**, 7491-7494 (2018).
21. Rosier, B.J.H.M. et al. Proximity-induced caspase-9 activation on a DNA origami-based synthetic apoptosome. *Nat Catal* **3**, 295-306 (2020).
22. Gianneschi, N.C. & Ghadiri, M.R. Design of molecular logic devices based on a programmable DNA-regulated semisynthetic enzyme. *Angew Chem Int Edit* **46**, 3955-3958 (2007).
23. Mukherjee, P., Leman, L.J., Griffin, J.H. & Ghadiri, M.R. Design of a DNA-Programmed Plasminogen Activator. *Journal of the American Chemical Society* **140**, 15516-15524 (2018).

24. Engelen, W., Wijnands, S.P.W. & Merkx, M. Accelerating DNA-Based Computing on a Supramolecular Polymer. *Journal of the American Chemical Society* **140**, 9758-9767 (2018).
25. Kim, K.T. & Winssinger, N. Enhanced SNP-sensing using DNA-templated reactions through confined hybridization of minimal substrates (CHOMS). *Chem Sci* **11**, 4150-4157 (2020).
26. Lou, C.G. et al. Peptide-oligonucleotide conjugates as nanoscale building blocks for assembly of an artificial three-helix protein mimic. *Nat Commun* **7** (2016).
27. Valero, J. & Famulok, M. Regeneration of Burnt Bridges on a DNA Catenane Walker. *Angew Chem Int Edit* **59**, 16366-16370 (2020).
28. Chen, R.P., Blackstock, D., Sun, Q. & Chen, W. Dynamic protein assembly by programmable DNA strand displacement. *Nat Chem* **10**, 474-481 (2018).
29. Groves, B. et al. Computing in mammalian cells with nucleic acid strand exchange. *Nat Nanotechnol* **11**, 287-+ (2016).
30. Furman, J.L. et al. Toward a General Approach for RNA-Templated Hierarchical Assembly of Split-Proteins. *Journal of the American Chemical Society* **132**, 11692-11701 (2010).
31. Green, A.A. et al. Complex cellular logic computation using ribocomputing devices. *Nature* **548**, 117-+ (2017).
32. Wang, J., Wang, D.X., Ma, J.Y., Wang, Y.X. & Kong, D.M. Three-dimensional DNA nanostructures to improve the hyperbranched hybridization chain reaction. *Chem Sci* **10**, 9758-9767 (2019).
33. Holtzer, L. et al. Nucleic Acid Templated Chemical Reaction in a Live Vertebrate. *Acs Central Sci* **2**, 394-400 (2016).
34. Kim, K.T., Chang, D.L. & Winssinger, N. Double-Stranded RNA-Specific Templated Reaction with Triplex Forming PNA. *Helv Chim Acta* **101** (2018).
35. Barluenga, S. & Winssinger, N. PNA as a Biosupramolecular Tag for Programmable Assemblies and Reactions. *Accounts of Chemical Research* **48**, 1319-1331 (2015).
36. Chang, D.L., Kim, K.T., Lindberg, E. & Winssinger, N. Smartphone DNA or RNA Sensing Using Semisynthetic Luciferase-Based Logic Device. *Acs Sensors* **5**, 807-813 (2020).
37. Chang, D.L., Kim, K.T., Lindberg, E. & Winssinger, N. Accelerating Turnover Frequency in Nucleic Acid Templated Reactions. *Bioconjugate Chem* **29**, 158-163 (2018).
38. Wijnands, S.P.W., Engelen, W., Lafleur, R.P.M., Meijer, E.W. & Merkx, M. Controlling protein activity by dynamic recruitment on a supramolecular polymer platform. *Nat Commun* **9** (2018).
39. Meguellati, K., Koripelly, G. & Ladame, S. DNA-Templated Synthesis of Trimethine Cyanine Dyes: A Versatile Fluorogenic Reaction for Sensing G-Quadruplex Formation. *Angew Chem Int Edit* **49**, 2738-2742 (2010).
40. Andersen, E.S. et al. Self-assembly of a nanoscale DNA box with a controllable lid. *Nature* **459**, 73-76 (2009).
41. Stein, V. & Alexandrov, K. Protease-based synthetic sensing and signal amplification. *P Natl Acad Sci USA* **111**, 15934-15939 (2014).
42. Holt, B.A. & Kwong, G.A. Protease circuits for processing biological information. *Nat Commun* **11**, 5021 (2020).
43. Liang, H. et al. Nongenetic Approach for Imaging Protein Dimerization by Aptamer Recognition and Proximity-Induced DNA Assembly. *Journal of the American Chemical Society* **140**, 4186-4190 (2018).
44. Fredriksson, S. et al. Protein detection using proximity-dependent DNA ligation assays. *Nat Biotechnol* **20**, 473-477 (2002).
45. Tang, Y.N. et al. Universal Strategy To Engineer Catalytic DNA Hairpin Assemblies for Protein Analysis. *Anal Chem* **87**, 8063-8066 (2015).
46. Chen, S. et al. Logic-Gate-Actuated DNA-Controlled Receptor Assembly for the Programmable Modulation of Cellular Signal Transduction. *Angew Chem Int Edit* (2019).

47. Chang, X. et al. Construction of a Multiple-Aptamer-Based DNA Logic Device on Live Cell Membranes via Associative Toehold Activation for Accurate Cancer Cell Identification. *Journal of the American Chemical Society* **141**, 12738-12743 (2019).
48. Zhang, D. et al. Equipping Natural Killer Cells with Specific Targeting and Checkpoint Blocking Aptamers for Enhanced Adoptive Immunotherapy in Solid Tumors. *Angew Chem Int Edit* **59**, 12022-12028 (2020).
49. Koos, B. et al. Proximity-dependent initiation of hybridization chain reaction. *Nat Commun* **6** (2015).
50. Komatsu, T. et al. Antibody Clicking as a Strategy to Modify Antibody Functionalities on the Surface of Targeted Cells. *Journal of the American Chemical Society* **142**, 15644-15648 (2020).
51. Rudchenko, M. et al. Autonomous molecular cascades for evaluation of cell surfaces. *Nat Nanotechnol* **8**, 580-586 (2013).
52. Miller, L.W., Cai, Y., Sheetz, M.P. & Cornish, V.W. In vivo protein labeling with trimethoprim conjugates: a flexible chemical tag. *Nat Methods* **2**, 255-257 (2005).
53. Koshi, Y. et al. Target-specific chemical acylation of lectins by ligand-tethered DMAP catalysts. *Journal of the American Chemical Society* **130**, 245-251 (2008).
54. Saarbach, J. et al. Kinase-templated abiotic reaction. *Chem Sci* **8**, 5119-5125 (2017).
55. Li, F. et al. Dynamic DNA Assemblies Mediated by Binding-Induced DNA Strand Displacement. *Journal of the American Chemical Society* **135**, 2443-2446 (2013).
56. Bertucci, A. et al. Protein-Controlled Actuation of Dynamic Nucleic Acid Networks by Using Synthetic DNA Translators. *Angew Chem Int Edit* **59**, 20577-20581 (2020).
57. Saghatelian, A., Guckian, K.M., Thayer, D.A. & Ghadiri, M.R. DNA detection and signal amplification via an engineered allosteric enzyme. *Journal of the American Chemical Society* **125**, 344-345 (2003).
58. Meijer, L.H.H. et al. Hierarchical control of enzymatic actuators using DNA-based switchable memories. *Nat Commun* **8** (2017).
59. Szacilowski, K. Digital information processing in molecular systems. *Chem Rev* **108**, 3481-3548 (2008).
60. Mocenigo, M. et al. Rapid, Cost-Effective Peptide/Nucleic Acid-Based Platform for Therapeutic Antibody Monitoring in Clinical Samples. *Acs Sensors* **5**, 3109-3115 (2020).
61. Green, L.N., Amodio, A., Subramanian, H.K.K., Ricci, F. & Franco, E. pH-Driven Reversible Self-Assembly of Micron-Scale DNA Scaffolds. *Nano Lett* **17**, 7283-7288 (2017).
62. Dirks, R.M. & Pierce, N.A. Triggered amplification by hybridization chain reaction. *Proc Natl Acad Sci U S A* **101**, 15275-15278 (2004).
63. Bi, S., Yue, S. & Zhang, S. Hybridization chain reaction: a versatile molecular tool for biosensing, bioimaging, and biomedicine. *Chem Soc Rev* **46**, 4281-4298 (2017).
64. Lu, S., Hu, T., Wang, S., Sun, J. & Yang, X. Ultra-Sensitive Colorimetric Assay System Based on the Hybridization Chain Reaction-Triggered Enzyme Cascade Amplification. *ACS Appl Mater Interfaces* **9**, 167-175 (2017).
65. Wang, F., Elbaz, J., Orbach, R., Magen, N. & Willner, I. Amplified analysis of DNA by the autonomous assembly of polymers consisting of DNAzyme wires. *J Am Chem Soc* **133**, 17149-17151 (2011).
66. Shimron, S., Wang, F., Orbach, R. & Willner, I. Amplified detection of DNA through the enzyme-free autonomous assembly of hemin/G-quadruplex DNAzyme nanowires. *Anal Chem* **84**, 1042-1048 (2012).
67. Zhu, G. et al. Building fluorescent DNA nanodevices on target living cell surfaces. *Angew Chem Int Ed Engl* **52**, 5490-5496 (2013).
68. Li, Z., He, X., Luo, X., Wang, L. & Ma, N. DNA-Programmed Quantum Dot Polymerization for Ultrasensitive Molecular Imaging of Cancer Cells. *Anal Chem* **88**, 9355-9358 (2016).

69. Choi, H.M., Beck, V.A. & Pierce, N.A. Next-generation in situ hybridization chain reaction: higher gain, lower cost, greater durability. *ACS Nano* **8**, 4284-4294 (2014).
70. Choi, H.M. et al. Programmable in situ amplification for multiplexed imaging of mRNA expression. *Nat Biotechnol* **28**, 1208-1212 (2010).
71. Cheglakov, Z., Cronin, T.M., He, C. & Weizmann, Y. Live Cell MicroRNA Imaging Using Cascade Hybridization Reaction. *J Am Chem Soc* **137**, 6116-6119 (2015).
72. Wu, Z., Liu, G.Q., Yang, X.L. & Jiang, J.H. Electrostatic nucleic acid nanoassembly enables hybridization chain reaction in living cells for ultrasensitive mRNA imaging. *J Am Chem Soc* **137**, 6829-6836 (2015).
73. Li, L. et al. Two-color imaging of microRNA with enzyme-free signal amplification via hybridization chain reactions in living cells. *Chem Sci* **7**, 1940-1945 (2016).
74. Ge, Z. et al. Hybridization chain reaction amplification of microRNA detection with a tetrahedral DNA nanostructure-based electrochemical biosensor. *Anal Chem* **86**, 2124-2130 (2014).
75. Prinzen, A.L. et al. Amplified Self-Immolative Release of Small Molecules by Spatial Isolation of Reactive Groups on DNA-Minimal Architectures. *Angew Chem Int Edit* **59**, 12900-12908 (2020).
76. Gao, Q.Q. et al. Highly Specific, Single-step Cancer Cell Isolation with Multi-Aptamer-Mediated Proximity Ligation on Live Cell Membranes. *Angew Chem Int Edit* **59**, 23564-23568 (2020).
77. Hollenstein, M. DNA Synthesis by Primer Exchange Reaction Cascades. *Chembiochem* **19**, 422-424 (2018).
78. Dai, Y.F. et al. An Integrated Multi-Function Heterogeneous Biochemical Circuit for High-Resolution Electrochemistry-Based Genetic Analysis. *Angew Chem Int Edit* **59**, 20545-20551 (2020).
79. Kishi, J.Y., Schaus, T.E., Gopalkrishnan, N., Xuan, F. & Yin, P. Programmable autonomous synthesis of single-stranded DNA. *Nat Chem* **10**, 155-164 (2018).
80. Rouhanifard, S.H. et al. ClampFISH detects individual nucleic acid molecules using click chemistry-based amplification (vol 37, pg 84, 2018). *Nat Biotechnol* **37**, 102-102 (2019).
81. Ficht, S., Dose, C. & Seitz, O. As Fast and Selective as Enzymatic Ligations: Unpaired Nucleobases Increase the Selectivity of DNA-Controlled Native Chemical PNA Ligation. *Chembiochem* **6**, 2098-2103 (2005).
82. Sayers, J., Payne, R.J. & Winssinger, N. Peptide nucleic acid-templated selenocystine–selenoester ligation enables rapid miRNA detection. *Chem Sci* **9**, 896-903 (2018).
83. Wang, L. et al. Bispecific Aptamer Induced Artificial Protein-Pairing: A Strategy for Selective Inhibition of Receptor Function. *Journal of the American Chemical Society* **141**, 12673-12681 (2019).
84. Gao, X.J., Chong, L.S., Kim, M.S. & Elowitz, M.B. Programmable protein circuits in living cells. *Science* **361**, 1252-1258 (2018).
85. Widen, J.C. et al. AND-gate contrast agents for enhanced fluorescence-guided surgery. *Nat Biomed Eng* (2020).
86. Engelen, W., van de Wiel, K.M., Meijer, L.H.H., Saha, B. & Merkx, M. Nucleic acid detection using BRET-beacons based on bioluminescent protein-DNA hybrids. *Chem Commun* **53**, 2862-2865 (2017).
87. Gorska, K. & Winssinger, N. Reactions Templated by Nucleic Acids: More Ways to Translate Oligonucleotide-Based Instructions into Emerging Function. *Angew Chem Int Edit* **52**, 6820-6843 (2013).
88. Di Pisa, M. & Seitz, O. Nucleic Acid Templated Reactions for Chemical Biology. *Chem Med Chem* **12**, 872-882 (2017).

89. Morihiro, K., Ankenbruck, N., Lukasak, B. & Deiters, A. Small Molecule Release and Activation through DNA Computing. *Journal of the American Chemical Society* **139**, 13909-13915 (2017).
90. Sato, S. & Nakamura, H. Ligand-Directed Selective Protein Modification Based on Local Single-Electron-Transfer Catalysis. *Angew Chem Int Edit* **52**, 8681-8684 (2013).
91. Bhatia, D., Surana, S., Chakraborty, S., Koushika, S.P. & Krishnan, Y. A synthetic icosahedral DNA-based host-cargo complex for functional in vivo imaging. *Nat Commun* **2** (2011).
92. Kurokawa, T. et al. DNA Origami Scaffolds as Templates for Functional Tetrameric Kir3 K+ Channels. *Angew Chem Int Edit* **57**, 2586-2591 (2018).
93. Hong, F., Zhang, F., Liu, Y. & Yan, H. DNA Origami: Scaffolds for Creating Higher Order Structures. *Chem Rev* **117**, 12584-12640 (2017).
94. Ueki, R. et al. DNA aptamer assemblies as fibroblast growth factor mimics and their application in stem cell culture. *Chem Commun* **55**, 2672-2675 (2019).
95. Chen, Z.B. et al. De novo design of protein logic gates. *Science* **368**, 78-+ (2020).
96. Lajoie, M.J. et al. Designed protein logic to target cells with precise combinations of surface antigens. *Science* **369**, 1637-+ (2020).
97. Lindberg, E., Angerani, S., Anzola, M. & Winssinger, N. Luciferase-induced photoreductive uncaging of small-molecule effectors. *Nat Commun* **9** (2018).
98. Angerani, S. & Winssinger, N. Sense-and-Release Logic-Gated Molecular Network Responding to Dimeric Cell Surface Proteins. *Journal of the American Chemical Society* **142**, 12333-12340 (2020).
99. Kim, K.T., Angerani, S., Chang, D.L. & Winssinger, N. Coupling of DNA Circuit and Templated Reactions for Quadratic Amplification and Release of Functional Molecules. *Journal of the American Chemical Society* **141**, 16288-16295 (2019).
100. Nielsen, P.E., Egholm, M., Berg, R.H. & Buchardt, O. Sequence-Selective Recognition of DNA by Strand Displacement with a Thymine-Substituted Polyamide. *Science* **254**, 1497-1500 (1991).
101. Nielsen, P.E. & Egholm, M. An introduction to peptide nucleic acid.
102. Egholm, M. et al. PNA hybridizes to complementary oligonucleotides obeying the Watson–Crick hydrogen-bonding rules. *Nature* **365**, 566-568 (1993).
103. Tomac, S. et al. Ionic effects on the stability and conformation of peptide nucleic acid complexes. *Journal of the American Chemical Society* **118**, 5544-5552 (1996).
104. Saarbach, J., Sabale, P.M. & Winssinger, N. Peptide nucleic acid (PNA) and its applications in chemical biology, diagnostics, and therapeutics. *Curr Opin Chem Biol* **52**, 112-124 (2019).
105. Dragulescu-Andrasi, A. et al. A Simple γ-Backbone Modification Preorganizes Peptide Nucleic Acid into a Helical Structure. *Journal of the American Chemical Society* **128**, 10258-10267 (2006).
106. Manicardi, A. & Corradini, R. Effect of chirality in gamma-PNA: PNA interaction, another piece in the picture.
107. Sacui, J., Hsieh, W.C., Manna, A., Sahu, B. & Ly, D.H. Gamma Peptide Nucleic Acids: As Orthogonal Nucleic Acid Recognition Codes for Organizing Molecular Self-Assembly. *Journal of the American Chemical Society* **137**, 8603-8610 (2015).
108. Chang, D., Lindberg, E. & Winssinger, N. Critical Analysis of Rate Constants and Turnover Frequency in Nucleic Acid-Templated Reactions: Reaching Terminal Velocity. *Journal of the American Chemical Society* **139**, 1444-1447 (2017).
109. Buchardt, O., Egholm, M., Berg, R.H. & Nielsen, P.E. Peptide Nucleic-Acids and Their Potential Applications in Biotechnology. *Trends Biotechnol* **11**, 384-386 (1993).
110. Mardirossian, G. et al. In Vivo Hybridization of Technetium-99m-Labeled Peptide Nucleic Acid (PNA). *Journal of Nuclear Medicine* **38**, 907 (1997).
111. Westerlund, K. et al. Site-specific conjugation of recognition tags to trastuzumab for peptide nucleic acid-mediated radionuclide HER2 pretargeting. *Biomaterials* **203**, 73-85 (2019).

112. Myrhammar, A. et al. Evaluation of an antibody-PNA conjugate as a clearing agent for antibody-based PNA-mediated radionuclide pretargeting. *Sci Rep-Uk* **10** (2020).
113. Zambaldo, C., Barluenga, S. & Winssinger, N. PNA-encoded chemical libraries. *Curr Opin Chem Biol* **26**, 8-15 (2015).
114. Lovrinovic, M. et al. Synthesis of protein-nucleic acid conjugates by expressed protein ligation. *Chem Commun*, 822-823 (2003).
115. Kazane, S.A. et al. Self-Assembled Antibody Multimers through Peptide Nucleic Acid Conjugation. *Journal of the American Chemical Society* **135**, 340-346 (2013).
116. Gholami, Z. & Hanley, Q. Controlled Assembly of SNAP-PNA-Fluorophore Systems on DNA Templates To Produce Fluorescence Resonance Energy Transfer. *Bioconjugate Chem* **25**, 1820-1828 (2014).
117. Flory, J.D. et al. Low Temperature Assembly of Functional 3D DNA-PNA-Protein Complexes. *Journal of the American Chemical Society* **136**, 8283-8295 (2014).
118. Thomas, S.M. et al. Antitumor Effects of EGFR Antisense Guanidine-Based Peptide Nucleic Acids in Cancer Models. *Acs Chem Biol* **8**, 345-352 (2013).
119. Endoh, T., Hnedzko, D., Rozners, E. & Sugimoto, N. Nucleobase-Modified PNA Suppresses Translation by Forming a Triple Helix with a Hairpin Structure in mRNA InVitro and in Cells. *Angew Chem Int Edit* **55**, 899-903 (2016).
120. Cheng, C.J. et al. MicroRNA silencing for cancer therapy targeted to the tumour microenvironment. *Nature* **518**, 107-+ (2015).
121. Schleifman, E.B. et al. Targeted Disruption of the CCR5 Gene in Human Hematopoietic Stem Cells Stimulated by Peptide Nucleic Acids. *Chem Biol* **18**, 1189-1198 (2011).
122. Bahal, R. et al. In vivo correction of anaemia in beta-thalassemic mice by gamma PNA-mediated gene editing with nanoparticle delivery. *Nat Commun* **7** (2016).
123. McNeer, N.A. et al. Systemic delivery of triplex-forming PNA and donor DNA by nanoparticles mediates site-specific genome editing of human hematopoietic cells in vivo. *Gene Ther* **20**, 658-669 (2013).
124. Bandlow, V. et al. Spatial Screening of Hemagglutinin on Influenza A Virus Particles: Sialyl-LacNAc Displays on DNA and PEG Scaffolds Reveal the Requirements for Bivalency Enhanced Interactions with Weak Monovalent Binders. *Journal of the American Chemical Society* **139**, 16389-16397 (2017).
125. Machida, T. et al. Dynamic Cooperative Glycan Assembly Blocks the Binding of Bacterial Lectins to Epithelial Cells. *Angew Chem Int Edit* **56**, 6762-6766 (2017).
126. Englund, E.A. et al. Programmable multivalent display of receptor ligands using peptide nucleic acid nanoscaffolds. *Nat Commun* **3** (2012).
127. Gavins, G.C. et al. Live cell PNA labelling enables erasable fluorescence imaging of membrane proteins. *Nat Chem* **13**, 15-23 (2021).
128. Gorska, K., Keklikoglou, I., Tschulena, U. & Winssinger, N. Rapid fluorescence imaging of miRNAs in human cells using templated Staudinger reaction. *Chem Sci* **2**, 1969-1975 (2011).
129. Anzola, M. & Winssinger, N. Turn On of a Ruthenium(II) Photocatalyst by DNA-Templated Ligation. *Chem-Eur J* **25**, 334-342 (2019).
130. Bohler, C., Nielsen, P.E. & Orgel, L.E. Template Switching between Pna and Rna Oligonucleotides. *Nature* **376**, 578-581 (1995).
131. Rosenbaum, D.M. & Liu, D.R. Efficient and sequence-specific DNA-templated polymerization of peptide nucleic acid aldehydes. *Journal of the American Chemical Society* **125**, 13924-13925 (2003).
132. Brudno, Y., Birnbaum, M.E., Kleiner, R.E. & Liu, D.R. An in vitro translation, selection and amplification system for peptide nucleic acids. *Nat Chem Biol* **6**, 148-155 (2010).
133. Kleiner, R.E., Brudno, Y., Birnbaum, M.E. & Liu, D.R. DNA-templated polymerization of side-chain-functionalized peptide nucleic acid aldehydes. *Journal of the American Chemical Society* **130**, 4646-4659 (2008).

134. Chouikhi, D., Barluenga, S. & Winssinger, N. Clickable peptide nucleic acids (cPNA) with tunable affinity. *Chem Commun* **46**, 5476-5478 (2010).
135. Ficht, S., Mattes, A. & Seitz, O. Single-nucleotide-specific PNA-peptide ligation on synthetic and PCR DNA templates. *Journal of the American Chemical Society* **126**, 9970-9981 (2004).
136. Koripelly, G., Meguellati, K. & Ladame, S. Dual Sensing of Hairpin and Quadruplex DNA Structures Using Multicolored Peptide Nucleic Acid Fluorescent Probes. *Bioconjugate Chem* **21**, 2103-2109 (2010).
137. Sleiman, M.H. & Ladame, S. Synthesis of squaraine dyes under mild conditions: applications for labelling and sensing of biomolecules. *Chem Commun* **50**, 5288-5290 (2014).
138. Grossmann, T.N. & Seitz, O. DNA-catalyzed transfer of a reporter group. *Journal of the American Chemical Society* **128**, 15596-15597 (2006).
139. Grossmann, T.N., Roglin, L. & Seitz, O. Target-catalyzed transfer reactions for the amplified detection of RNA. *Angew Chem Int Edit* **47**, 7119-7122 (2008).
140. Erben, A., Grossmann, T.N. & Seitz, O. DNA-Triggered Synthesis and Bioactivity of Proapoptotic Peptides. *Angew Chem Int Edit* **50**, 2828-2832 (2011).
141. Chen, X.H., Roloff, A. & Seitz, O. Consecutive Signal Amplification for DNA Detection Based on De Novo Fluorophore Synthesis and Host-Guest Chemistry. *Angew Chem Int Edit* **51**, 4479-4483 (2012).
142. Cai, J.F., Li, X.X., Yue, X. & Taylor, J.S. Nucleic acid-triggered fluorescent probe activation by the staudinger reaction. *Journal of the American Chemical Society* **126**, 16324-16325 (2004).
143. Pianowski, Z.L. & Winssinger, N. Fluorescence-based detection of single nucleotide permutation in DNA via catalytically templated reaction. *Chem Commun*, 3820-3822 (2007).
144. Franzini, R.M. & Kool, E.T. 7-Azidomethoxy-Coumarins as Profluorophores for Templated Nucleic Acid Detection. *Chembiochem* **9**, 2981-2988 (2008).
145. Franzini, R.M. & Kool, E.T. Efficient Nucleic Acid Detection by Templated Reductive Quencher Release. *Journal of the American Chemical Society* **131**, 16021-+ (2009).
146. Abe, H. et al. A reduction-triggered fluorescence probe for sensing nucleic acids. *Bioconjugate Chem* **19**, 1219-1226 (2008).
147. Shibata, A., Ito, Y. & Abe, H. RNA-templated molecule release induced protein expression in bacterial cells. *Chem Commun* **49**, 270-272 (2013).
148. Pianowski, Z., Gorska, K., Oswald, L., Merten, C.A. & Winssinger, N. Imaging of mRNA in Live Cells Using Nucleic Acid-Templated Reduction of Azidorhodamine Probes. *Journal of the American Chemical Society* **131**, 6492-6497 (2009).
149. Gorska, K., Manicardi, A., Barluenga, S. & Winssinger, N. DNA-templated release of functional molecules with an azide-reduction-triggered immolative linker. *Chem Commun* **47**, 4364-4366 (2011).
150. Angerani, S. & Winssinger, N. Visible Light Photoredox Catalysis Using Ruthenium Complexes in Chemical Biology. *Chem-Eur J* **25**, 6661-6672 (2019).
151. Schatzschneider, U. et al. Cellular Uptake, Cytotoxicity, and Metabolic Profiling of Human Cancer Cells Treated with Ruthenium(II) Polypyridyl Complexes [Ru(bpy)2(N⌑N)]Cl2 with N⌑N=bpy, phen, dpq, dppz, and dppn. *Chemmedchem* **3**, 1104-1109 (2008).
152. Avci, P. et al. Low-Level Laser (Light) Therapy (LLLT) in Skin: Stimulating, Healing, Restoring. *Semin Cutan Med Surg* **32**, 41-52 (2013).
153. Khoshakhlagh, P., Bowser, D.A., Brown, J.Q. & Moore, M.J. Comparison of visible and UVA phototoxicity in neural culture systems micropatterned with digital projection photolithography. *J Biomed Mater Res A* **107**, 134-144 (2019).
154. Arias-Rotondo, D.M. & McCusker, J.K. The photophysics of photoredox catalysis: a roadmap for catalyst design. *Chem Soc Rev* **45**, 5803-5820 (2016).
155. Nakamaru, K. Synthesis, Luminescence Quantum Yields, and Lifetimes of Trischelated Ruthenium(Ii) Mixed-Ligand Complexes Including 3,3'-Dimethyl-2,2'-Bipyridyl. *B Chem Soc Jpn* **55**, 2697-2705 (1982).

156. Fancy, D.A. & Kodadek, T. Chemistry for the analysis of protein-protein interactions: Rapid and efficient cross-linking triggered by long wavelength light (vol 96, pg 6020, 1999). *P Natl Acad Sci USA* **97**, 1317-1317 (2000).
157. Fancy, D.A. et al. Scope, limitations and mechanistic aspects of the photo-induced cross-linking of proteins by water-soluble metal complexes. *Chem Biol* **7**, 697-708 (2000).
158. Duroux-Richard, I. et al. Crosslinking photosensitized by a ruthenium chelate as a tool for labeling and topographical studies of G-protein-coupled receptors. *Chem Biol* **12**, 15-24 (2005).
159. Estalayo-Adrian, S., Garnir, K. & Moucheron, C. Perspectives of ruthenium(II) polyazaaromatic photo-oxidizing complexes photoreactive towards tryptophan-containing peptides and derivatives. *Chem Commun* **54**, 322-337 (2018).
160. Sato, S., Hatano, K., Tsushima, M. & Nakamura, H. 1-Methyl-4-aryl-urazole (MAUra) labels tyrosine in proximity to ruthenium photocatalysts. *Chem Commun* **54**, 5871-5874 (2018).
161. Lee, J.Y., Yu, P., Xiao, X.S. & Kodadek, T. A general system for evaluating the efficiency of chromophore-assisted light inactivation (CALI) of proteins reveals Ru(II) tris-bipyridyl as an unusually efficient "warhead". *Mol Biosyst* **4**, 59-65 (2008).
162. Lee, J.Y., Udugamasooriya, D.G., Lim, H.S. & Kodadek, T. Potent and selective photo-inactivation of proteins with peptoid-ruthenium conjugates. *Nat Chem Biol* **6**, 258-260 (2010).
163. Sato, S., Morita, K. & Nakamura, H. Regulation of Target Protein Knockdown and Labeling Using Ligand-Directed Ru(bpy)(3) Photocatalyst. *Bioconjugate Chem* **26**, 250-256 (2015).
164. Sato, S., Tsushima, M. & Nakamura, H. Target-protein-selective inactivation and labelling using an oxidative catalyst. *Org Biomol Chem* **16**, 6168-6179 (2018).
165. Huang, H.C., Zhang, G.J., Gong, L., Zhang, S.Y. & Chen, Y.Y. Visible-Light-Induced Chemoselective Deboronative Alkynylation under Biomolecule-Compatible Conditions. *Journal of the American Chemical Society* **136**, 2280-2283 (2014).
166. Salassa, L., Garino, C., Salassa, G., Gobetto, R. & Nervi, C. Mechanism of Ligand Photodissociation in Photoactivable [Ru(bpy)2L2]2+ Complexes: A Density Functional Theory Study. *Journal of the American Chemical Society* **130**, 9590-9597 (2008).
167. Zayat, L., Salierno, M. & Etchenique, R. Ruthenium(II) bipyridyl complexes as photolabile caging groups for amines. *Inorg Chem* **45**, 1728-1731 (2006).
168. van Rixel, V.H.S. et al. Photo-Uncaging of a Microtubule-Targeted Rigidin Analogue in Hypoxic Cancer Cells and in a Xenograft Mouse Model. *Journal of the American Chemical Society* **141**, 18444-18454 (2019).
169. Griepenburg, J.C., Rapp, T.L., Carroll, P.J., Eberwine, J. & Dmochowski, I.J. Ruthenium-caged antisense morpholinos for regulating gene expression in zebrafish embryos. *Chem Sci* **6**, 2342-2346 (2015).
170. Lewis, F.D. & Saunders, W.H. Intermediates in Direct Photolysis of Alkyl Azides. *Journal of the American Chemical Society* **90**, 7031-& (1968).
171. Farney, E.P. & Yoon, T.P. Visible-Light Sensitization of Vinyl Azides by Transition-Metal Photocatalysis. *Angew Chem Int Edit* **53**, 793-797 (2014).
172. Chen, Y.Y., Kamlet, A.S., Steinman, J.B. & Liu, D.R. A biomolecule-compatible visible-light-induced azide reduction from a DNA-encoded reaction-discovery system. *Nat Chem* **3**, 146-153 (2011).
173. Sadhu, K.K., Eierhoff, T., Romer, W. & Winssinger, N. Photoreductive Uncaging of Fluorophore in Response to Protein Oligomers by Templated Reaction in Vitro and in Cellulo. *Journal of the American Chemical Society* **134**, 20013-20016 (2012).
174. Sadhu, K.K., Lindberg, E. & Winssinger, N. In cellulo protein labelling with Ru-conjugate for luminescence imaging and bioorthogonal photocatalysis. *Chem Commun* **51**, 16664-16666 (2015).

175. Blacker, T.S. & Duchen, M.R. Investigating mitochondrial redox state using NADH and NADPH autofluorescence. *Free Radical Biology and Medicine* **100**, 53-65 (2016).
176. Camble, R., Garner, R. & Young, G.T. Amino-acids and peptides. Part XXX. Facilitation of peptide synthesis by the use of 4-picolyl esters for carboxy-group protection. *Journal of the Chemical Society C: Organic*, 1911-1916 (1969).
177. Borak, J.B. & Falvey, D.E. A New Photolabile Protecting Group for Release of Carboxylic Acids by Visible-Light-Induced Direct and Mediated Electron Transfer. *The Journal of Organic Chemistry* **74**, 3894-3899 (2009).
178. Sundararajan, C. & Falvey, D.E. C-O bond fragmentation of 4-picolyl- and N-methyl-4-picolinium esters triggered by photochemical electron transfer. *J Org Chem* **69**, 5547-5554 (2004).
179. Edson, J.B., Spencer, L.P. & Boncella, J.M. Photorelease of Primary Aliphatic and Aromatic Amines by Visible-Light-Induced Electron Transfer. *Org Lett* **13**, 6156-6159 (2011).
180. Yoshikawa, N. et al. Transition states of the 3MLCT to 3MC conversion in Ru(bpy)2(phen derivative)2+ complexes. *Journal of Molecular Structure* **1094**, 98-108 (2015).
181. Rothlingshofer, M., Gorska, K. & Winssinger, N. Nucleic Acid Templated Uncaging of Fluorophores Using Ru-Catalyzed Photoreduction with Visible Light. *Org Lett* **14**, 482-485 (2012).
182. Sadhu, K.K. & Winssinger, N. Detection of miRNA in Live Cells by Using Templated RuII-Catalyzed Unmasking of a Fluorophore. *Chem-Eur J* **19**, 8182-8189 (2013).
183. Wiseman, G.A. & Witzig, T.E. Yttriutm-90 (Y-90) ibritumomab tiuxetan (Zevalin (R)) induces long-term durable responses in patients with relapsed or refractory B-cell non-Hodgkin's lymphoma. *Cancer Biother Radio* **20**, 185-188 (2005).
184. Maqsood, M.H., Din, A.T.U. & Khan, A.H. Neuroendocrine Tumor Therapy with Lutetium-177: A Literature Review. *Cureus* **11** (2019).
185. Lau, J., Lin, K.S. & Benard, F. Past, Present, and Future: Development of Theranostic Agents Targeting Carbonic Anhydrase IX. *Theranostics* **7**, 4322-4339 (2017).
186. Supuran, C.T. Carbonic anhydrases: novel therapeutic applications for inhibitors and activators. *Nat Rev Drug Discov* **7**, 168-181 (2008).
187. Tafreshi, N.K., Lloyd, M.C., Bui, M.M., Gillies, R.J. & Morse, D.L. in Carbonic Anhydrase: Mechanism, Regulation, Links to Disease, and Industrial Applications. (eds. S.C. Frost & R. McKenna) 221-254 (Springer Netherlands, Dordrecht; 2014).
188. Pastorekova, S. & Gillies, R.J. The role of carbonic anhydrase IX in cancer development: links to hypoxia, acidosis, and beyond. *Cancer Metast Rev* **38**, 65-77 (2019).
189. Parks, S.K., Cormerais, Y. & Pouyssegur, J. Hypoxia and cellular metabolism in tumour pathophysiology. *J Physiol-London* **595**, 2439-2450 (2017).
190. Maseide, K. et al. Carbonic anhydrase IX as a marker for poor prognosis in soft tissue sarcoma. *Clin Cancer Res* **10**, 4464-4471 (2004).
191. Kon-No, H. et al. Carbonic anhydrase IX expression is associated with tumor progression and a poor prognosis of lung adenocarcinoma. *Lung Cancer* **54**, 409-418 (2006).
192. Choi, S.W. et al. Expression of carbonic anhydrase IX is associated with postoperative recurrence and poor prognosis in surgically treated oral squamous cell carcinomas. *Hum Pathol* **39**, 1317-1322 (2008).
193. Wichert, M. & Krall, N. Targeting carbonic anhydrase IX with small organic ligands. *Curr Opin Chem Biol* **26**, 48-54 (2015).
194. Ahlskog, J.K.J., Dumelin, C.E., Trussel, S., Marlind, J. & Neri, D. In vivo targeting of tumor-associated carbonic anhydrases using acetazolamide derivatives. *Bioorg Med Chem Lett* **19**, 4851-4856 (2009).
195. Krall, N. et al. A Small-Molecule Drug Conjugate for the Treatment of Carbonic Anhydrase IX Expressing Tumors. *Angew Chem Int Edit* **53**, 4231-4235 (2014).

196. Cazzamalli, S., Dal Corso, A., Widmayer, F. & Neri, D. Chemically Defined Antibody- and Small Molecule-Drug Conjugates for in Vivo Tumor Targeting Applications: A Comparative Analysis. *Journal of the American Chemical Society* **140**, 1617-1621 (2018).
197. Krall, N., Pretto, F. & Neri, D. A bivalent small molecule-drug conjugate directed against carbonic anhydrase IX can elicit complete tumour regression in mice. *Chem Sci* **5**, 3640-3644 (2014).
198. van Schaijk, F.G. et al. Pretargeting with Bispecific Anti-Renal Cell Carcinoma x Anti-DTPA(In) Antibody in 3 RCC Models. *Journal of Nuclear Medicine* **46**, 495 (2005).
199. Dal Molin, M. et al. Fluorescent Flippers for Mechanosensitive Membrane Probes. *Journal of the American Chemical Society* **137**, 568-571 (2015).
200. Waight, A.B. et al. Structural Basis of Microtubule Destabilization by Potent Auristatin Anti-Mitotics. *Plos One* **11** (2016).
201. Doronina, S.O. et al. Development of potent monoclonal antibody auristatin conjugates for cancer therapy. *Nat Biotechnol* **21**, 778-784 (2003).
202. Zhang, D.Y. & Seelig, G. Dynamic DNA nanotechnology using strand-displacement reactions. *Nat Chem* **3**, 103-113 (2011).
203. Mitchell, P.S. et al. Circulating microRNAs as stable blood-based markers for cancer detection. *P Natl Acad Sci USA* **105**, 10513-10518 (2008).
204. Dong, H.F. et al. MicroRNA: Function, Detection, and Bioanalysis. *Chem Rev* **113**, 6207-6233 (2013).
205. Yin, P., Choi, H.M.T., Calvert, C.R. & Pierce, N.A. Programming biomolecular self-assembly pathways. *Nature* **451**, 318-322 (2008).
206. Longley, D.B., Harkin, D.P. & Johnston, P.G. 5-Fluorouracil: Mechanisms of action and clinical strategies. *Nat Rev Cancer* **3**, 330-338 (2003).
207. Wiebke, E.A., Grieshop, N.A., Loehrer, P.J., Eckert, G.J. & Sidner, R.A. Antitumor effects of 5-fluorouracil on human colon cancer cell lines: Antagonism by levamisole. *J Surg Res* **111**, 63-69 (2003).
208. Violette, S. et al. Resistance of colon cancer cells to long-term 5-fluorouracil exposure is correlated to the relative level of Bcl-2 and Bcl-x(L) in addition to Bax and p53 status. *Int J Cancer* **98**, 498-504 (2002).
209. Ang, Y.S. & Yung, L.Y.L. Rational design of hybridization chain reaction monomers for robust signal amplification. *Chem Commun* **52**, 4219-4222 (2016).
210. Tsuneoka, Y. & Funato, H. Modified in situ Hybridization Chain Reaction Using Short Hairpin DNAs. *Front Mol Neurosci* **13** (2020).
211. Machida, T., Dutt, S. & Winssinger, N. Allosterically Regulated Phosphatase Activity from Peptide-PNA Conjugates Folded Through Hybridization. *Angew Chem Int Edit* **55**, 8595-8598 (2016).
212. Vieville, J.M.P., Barluenga, S., Winssinger, N. & Delsuc, M.A. Duplex formation and secondary structure of gamma-PNA observed by NMR and CD. *Biophys Chem* **210**, 9-13 (2016).
213. Sahu, B. et al. Synthesis and characterization of conformationally preorganized, (R)-diethylene glycol-containing gamma-peptide nucleic acids with superior hybridization properties and water solubility. *J Org Chem* **76**, 5614-5627 (2011).
214. Yuan, B.F., Zhuang, X.Y., Hao, Y.H. & Tan, Z. Kinetics of base stacking-aided DNA hybridization. *Chem Commun (Camb)*, 6600-6602 (2008).
215. Syed, A.J. & Anderson, J.C. Applications of bioluminescence in biotechnology and beyond. *Chem Soc Rev* (2021).
216. De Niz, M., Stanway, R.R., Wacker, R., Keller, D. & Heussler, V.T. An ultrasensitive NanoLuc-based luminescence system for monitoring Plasmodium berghei throughout its life cycle. *Malaria Journal* **15**, 232 (2016).

217. Kaskova, Z.M., Tsarkova, A.S. & Yampolsky, I.V. 1001 lights: luciferins, luciferases, their mechanisms of action and applications in chemical analysis, biology and medicine. *Chem Soc Rev* **45**, 6048-6077 (2016).
218. Schaub, F.X. et al. Fluorophore-NanoLuc BRET Reporters Enable Sensitive In Vivo Optical Imaging and Flow Cytometry for Monitoring Tumorigenesis. *Cancer Res* **75**, 5023-5033 (2015).
219. Saito, K. et al. Luminescent proteins for high-speed single-cell and whole-body imaging. *Nat Commun* **3** (2012).
220. Iwano, S. et al. Single-cell bioluminescence imaging of deep tissue in freely moving animals. *Science* **359**, 935-939 (2018).
221. Dragulescu-Andrasi, A., Chan, C.T., De, A., Massoud, T.F. & Gambhir, S.S. Bioluminescence resonance energy transfer (BRET) imaging of protein-protein interactions within deep tissues of living subjects. *P Natl Acad Sci USA* **108**, 12060-12065 (2011).
222. Hiblot, J. et al. Luciferases with Tunable Emission Wavelengths. *Angew Chem Int Edit* **56**, 14556-14560 (2017).
223. Chang, D. et al. Luciferase-Induced Photouncaging: Bioluminolysis. *Angewandte Chemie International Edition* **58**, 16033-16037 (2019).
224. Zhang, Y. et al. HaloTag protein-mediated site-specific conjugation of bioluminescent proteins to quantum dots. *Angew Chem Int Edit* **45**, 4936-4940 (2006).
225. Machleidt, T. et al. NanoBRET-A Novel BRET Platform for the Analysis of Protein-Protein Interactions. *Acs Chem Biol* **10**, 1797-1804 (2015).
226. De, A., Loening, A.M. & Gambhir, S.S. An improved bioluminescence resonance energy transfer strategy for imaging intracellular events in single cells and living subjects. *Cancer Res* **67**, 7175-7183 (2007).
227. Stoddart, L.A., Kilpatrick, L.E. & Hill, S.J. NanoBRET Approaches to Study Ligand Binding to GPCRs and RTKs. *Trends Pharmacol Sci* **39**, 136-147 (2018).
228. Namkung, Y. et al. Monitoring G protein-coupled receptor and β-arrestin trafficking in live cells using enhanced bystander BRET. *Nat Commun* **7**, 12178 (2016).
229. Aper, S.J.A., Dierickx, P. & Merkx, M. Dual Readout BRET/FRET Sensors for Measuring Intracellular Zinc. *Acs Chem Biol* **11**, 2854-2864 (2016).
230. Yu, Q.Y. et al. Semisynthetic sensor proteins enable metabolic assays at the point of care. *Science* **361**, 1122-1125 (2018).
231. Griss, R. et al. Bioluminescent sensor proteins for point-of-care therapeutic drug monitoring. *Nat Chem Biol* **10**, 598-603 (2014).
232. Xue, L., Yu, Q.L.Y., Griss, R., Schena, A. & Johnsson, K. Bioluminescent Antibodies for Point-of-Care Diagnostics. *Angew Chem Int Edit* **56**, 7112-7116 (2017).
233. Ni, Y., Arts, R. & Merkx, M. Ratiometric Bioluminescent Sensor Proteins Based on Intramolecular Split Luciferase Complementation. *Acs Sensors* **4**, 20-25 (2019).
234. Tenda, K. et al. Paper-Based Antibody Detection Devices Using Bioluminescent BRET-Switching Sensor Proteins. *Angew Chem Int Edit* **57**, 15369-15373 (2018).
235. Berglund, K., Birkner, E., Augustine, G.J. & Hochgeschwender, U. Light-Emitting Channelrhodopsins for Combined Optogenetic and Chemical-Genetic Control of Neurons. *Plos One* **8**, e59759 (2013).
236. Park, S.Y. et al. Novel luciferase–opsin combinations for improved luminopsins. *Journal of Neuroscience Research* **98**, 410-421 (2020).
237. Hall, M.P. et al. Engineered Luciferase Reporter from a Deep Sea Shrimp Utilizing a Novel Imidazopyrazinone Substrate. *Acs Chem Biol* **7**, 1848-1857 (2012).
238. Wang, Y., Zhang Ll Fau - Champlin, R.E., Champlin Re Fau - Wang, M.L. & Wang, M.L. Targeting Bruton's tyrosine kinase with ibrutinib in B-cell malignancies.

239. Tietze, L.F. et al. Selective Treatment of Cancer: Synthesis, Biological Evaluation and Structural Elucidation of Novel Analogues of the Antibiotic CC-1065 and the Duocarmycins. *Chemistry – A European Journal* **13**, 4396-4409 (2007).
240. Tietze, L.F., Schuster, H.J., Hampel, S.M., Rühl, S. & Pfoh, R. Enantio- and Diastereoselective Synthesis of Duocarmycine-Based Prodrugs for a Selective Treatment of Cancer by Epoxide Opening. *Chemistry – A European Journal* **14**, 895-901 (2008).
241. Vielhauer, G.A. et al. Evaluation of a reductively activated duocarmycin prodrug against murine and human solid cancers. *Cancer Biol Ther* **14**, 527-536 (2013).
242. Nani, R.R. et al. In Vivo Activation of Duocarmycin–Antibody Conjugates by Near-Infrared Light. *Acs Central Sci* **3**, 329-337 (2017).
243. Chang, D., Feng, S., Girik, V., Riezman, H. & Winssinger, N. Luciferase Controlled Protein Interactions. *Journal of the American Chemical Society* **143**, 3665-3670 (2021).
244. Angerani, S. et al. Kinesin-1 activity recorded in living cells with a precipitating dye. *Nat Commun* **12**, 1463 (2021).
245. Naleway, J.J. et al. Synthesis and use of new fluorogenic precipitating substrates. *Tetrahedron Letters* **35**, 8569-8572 (1994).
246. Heller, A. & Williams, D.L. Intramolecular proton transfer reactions in excited fluorescent compounds. *The Journal of Physical Chemistry* **74**, 4473-4480 (1970).
247. Diwu, Z. et al. Fluorescent molecular probes I. The synthesis and biological properties of an ELF® β-glucuronidase substrate that yields fluorescent precipitates at the enzymatic activity sites. *Tetrahedron* **53**, 7159-7164 (1997).
248. Paragas, V.B., Kramer, J.A., Fox, C., Haugland, R.P. & Singer, V.L. The ELF®-97 phosphatase substrate provides a sensitive, photostable method for labelling cytological targets. *Journal of Microscopy* **206**, 106-119 (2002).
249. Thorn-Seshold, O., Vargas-Sanchez, M., McKeon, S. & Hasserodt, J. A robust, high-sensitivity stealth probe for peptidases. *Chem Commun* **48**, 6253-6255 (2012).
250. Lindberg, E. & Winssinger, N. High Spatial Resolution Imaging of Endogenous Hydrogen Peroxide in Living Cells by Solid-State Fluorescence. *Chembiochem* **17**, 1612-1615 (2016).
251. Lamond, A.I. Molecular biology of the cell, 4th edition. *Nature* **417**, 383-383 (2002).
252. Sweeney, H.L. & Holzbaur, E.L.F. Motor Proteins. LID - 10.1101/cshperspect.a021931 [doi] LID - a021931.
253. Lippincottschwartz, J., Cole, N.B., Marotta, A., Conrad, P.A. & Bloom, G.S. Kinesin Is the Motor for Microtubule-Mediated Golgi-to-Er Membrane Traffic. *Journal of Cell Biology* **128**, 293-306 (1995).
254. Gupta, V., Palmer, K.J., Spence, P., Hudson, A. & Stephens, D.J. Kinesin-1 (uKHC/KIF5B) is Required for Bidirectional Motility of ER Exit Sites and Efficient ER-to-Golgi Transport. *Traffic* **9**, 1850-1866 (2008).
255. Yip, Y.Y. et al. The light chains of kinesin-1 are autoinhibited. *Proceedings of the National Academy of Sciences* **113**, 2418 (2016).
256. Block, S.M., Goldstein, L.S.B. & Schnapp, B.J. Bead movement by single kinesin molecules studied with optical tweezers. *Nature* **348**, 348-352 (1990).
257. Hancock, W.O. & Howard, J. Processivity of the motor protein kinesin requires two heads. *The Journal of cell biology* **140**, 1395-1405 (1998).
258. Yildiz, A., Tomishige, M., Vale, R.D. & Selvin, P.R. Kinesin Walks Hand-Over-Hand. *Science* **303**, 676 (2004).
259. Sudhakar, S. et al. Germanium nanospheres for ultraresolution picotensiometry of kinesin motors. *Science* **371**, eabd9944 (2021).
260. Cai, D.W., McEwen, D.P., Martens, J.R., Meyhofer, E. & Verhey, K.J. Single Molecule Imaging Reveals Differences in Microtubule Track Selection Between Kinesin Motors. *Plos Biol* **7** (2009).

261. Reed, N.A. et al. Microtubule acetylation promotes kinesin-1 binding and transport. *Curr Biol* **16**, 2166-2172 (2006).
262. Dunn, S. et al. Differential trafficking of Kif5c on tyrosinated and detyrosinated microtubules in live cells. *J Cell Sci* **121**, 1085-1095 (2008).
263. Moamer, A. et al. A role for kinesin-1 subunits KIF5B/KLC1 in regulating epithelial mesenchymal plasticity in breast tumorigenesis.
264. Morihara, T. et al. Transcriptome analysis of distinct mouse strains reveals kinesin light chain-1 splicing as an amyloid-β accumulation modifier. *Proceedings of the National Academy of Sciences* **111**, 2638 (2014).
265. Strunze, S. et al. Kinesin-1-Mediated Capsid Disassembly and Disruption of the Nuclear Pore Complex Promote Virus Infection. *Cell Host & Microbe* **10**, 210-223 (2011).
266. Courty, S., Luccardini, C., Bellaiche, Y., Cappello, G. & Dahan, M. Tracking Individual Kinesin Motors in Living Cells Using Single Quantum-Dot Imaging. *Nano Lett* **6**, 1491-1495 (2006).
267. Pfister, K.K., Wagner, M.C., Stenoien, D.L., Brady, S.T. & Bloom, G.S. Monoclonal antibodies to kinesin heavy and light chains stain vesicle-like structures, but not microtubules, in cultured cells. *Journal of Cell Biology* **108**, 1453-1463 (1989).
268. Endow, S.A. in Kinesin Protocols. (ed. I. Vernos) 123-131 (Humana Press, Totowa, NJ; 2001).
269. Tanenbaum, M.E., Gilbert, L.A., Qi, L.S., Weissman, J.S. & Vale, R.D. A Protein-Tagging System for Signal Amplification in Gene Expression and Fluorescence Imaging. *Cell* **159**, 635-646 (2014).
270. Tas, R.P. et al. Differentiation between Oppositely Oriented Microtubules Controls Polarized Neuronal Transport. *Neuron* **96**, 1264-+ (2017).
271. Katrukha, E.A. et al. Probing cytoskeletal modulation of passive and active intracellular dynamics using nanobody-functionalized quantum dots. *Nat Commun* **8** (2017).
272. Hollenbeck, P.J. The Distribution, Abundance and Subcellular-Localization of Kinesin. *Journal of Cell Biology* **108**, 2335-2342 (1989).
273. Hu, J.J. et al. Fluorescent Probe HKSOX-1 for Imaging and Detection of Endogenous Superoxide in Live Cells and In Vivo. *Journal of the American Chemical Society* **137**, 6837-6843 (2015).
274. Lukinavicius, G. et al. Fluorogenic probes for live-cell imaging of the cytoskeleton. *Nat Methods* **11**, 731-U168 (2014).
275. Xiao, H. et al. Insights into the mechanism of microtubule stabilization by Taxol. *Proceedings of the National Academy of Sciences* **103**, 10166 (2006).
276. Chabin-Brion, K. et al. The Golgi complex is a microtubule-organizing organelle. *Mol Biol Cell* **12**, 2047-2060 (2001).
277. Sanders, A.A.W.M. & Kaverina, I. Nucleation and Dynamics of Golgi-derived Microtubules. *Front Neurosci-Switz* **9** (2015).
278. Toya, M. & Takeichi, M. Organization of Non-centrosomal Microtubules in Epithelial Cells.
279. Arvan, P., Zhao, X., Ramos-Castaneda, J. & Chang, A. Secretory Pathway Quality Control Operating in Golgi, Plasmalemmal, and Endosomal Systems. *Traffic* **3**, 771-780 (2002).
280. Fujiwara, T., Oda, K., Yokota, S., Takatsuki, A. & Ikehara, Y. Brefeldin-a Causes Disassembly of the Golgi-Complex and Accumulation of Secretory Proteins in the Endoplasmic-Reticulum. *J Biol Chem* **263**, 18545-18552 (1988).
281. Lippincott-Schwartz, J., Yuan, L.C., Bonifacino, J.S. & Klausner, R.D. Rapid redistribution of Golgi proteins into the ER in cells treated with brefeldin A: Evidence for membrane cycling from Golgi to ER. *Cell* **56**, 801-813 (1989).
282. Woehlke, G. & Schliwa, M. Directional motility of kinesin motor proteins. *Bba-Mol Cell Res* **1496**, 117-127 (2000).
283. LaPointe, N.E. et al. Effects of eribulin, vincristine, paclitaxel and ixabepilone on fast axonal transport and kinesin-1 driven microtubule gliding: Implications for chemotherapy-induced peripheral neuropathy. *Neurotoxicology* **37**, 231-239 (2013).

284. Inoue, Y. et al. Movements of truncated kinesin fragments with a short or an artificial flexible neck. *Biophys J* **72**, Mp211-Mp211 (1997).
285. Romberg, L., Pierce, D.W. & Vale, R.D. Role of the kinesin neck region in processive microtubule-based motility. *Journal of Cell Biology* **140**, 1407-1416 (1998).
286. Randall, T.S. et al. A small-molecule activator of kinesin-1 drives remodeling of the microtubule network. *P Natl Acad Sci USA* **114**, 13738-13743 (2017).
287. Cockburn, J.J.B. et al. Insights into Kinesin-1 Activation from the Crystal Structure of KLC2 Bound to JIP3. *Structure* **26**, 1486-1498.e1486 (2018).
288. Verhey, K.J. & Hammond, J.W. Traffic control: regulation of kinesin motors. *Nat Rev Mol Cell Bio* **10**, 765-777 (2009).
289. Cross, R.A. Mechanochemistry of the Kinesin-1 ATPase. *Biopolymers* **105**, 476-482 (2016).
290. Vugmeyster, Y., Berliner, E. & Gelles, J. Release of Isolated Single Kinesin Molecules from Microtubules. *Biochemistry* **37**, 747-757 (1998).
291. Hancock, W.O. & Howard, J. Kinesin's processivity results from mechanical and chemical coordination between the ATP hydrolysis cycles of the two motor domains. *P Natl Acad Sci USA* **96**, 13147-13152 (1999).
292. Trott, O. & Olson, A.J. Software News and Update AutoDock Vina: Improving the Speed and Accuracy of Docking with a New Scoring Function, Efficient Optimization, and Multithreading. *J Comput Chem* **31**, 455-461 (2010).
293. Luo, L. et al. ATP-competitive inhibitors of the mitotic kinesin KSP that function via an allosteric mechanism. *Nat Chem Biol* **3**, 722-726 (2007).
294. Muretta, J.M. et al. The structural kinetics of switch-1 and the neck linker explain the functions of kinesin-1 and Eg5. *Proceedings of the National Academy of Sciences* **112**, E6606 (2015).
295. Castillo, A. & Justice, M.J. The kinesin related motor protein, Eg5, is essential for maintenance of pre-implantation embryogenesis. *Biochem Bioph Res Co* **357**, 694-699 (2007).
296. Wojcik, E.J. et al. Kinesin-5: Cross-bridging mechanism to targeted clinical therapy. *Gene* **531**, 133-149 (2013).

Experimental Section

Supplementary materials of Chapter I

CA-IX bivalent ligand-Ru-5mer-Cy3 **(1)** 	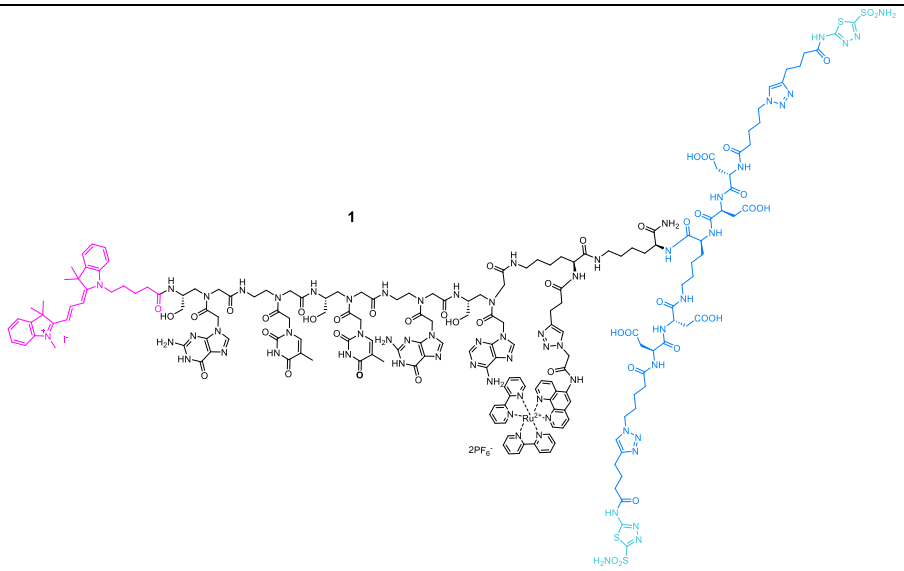
CA-IX bivalent ligand-Ru-5mer **(2)** 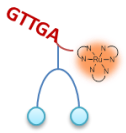	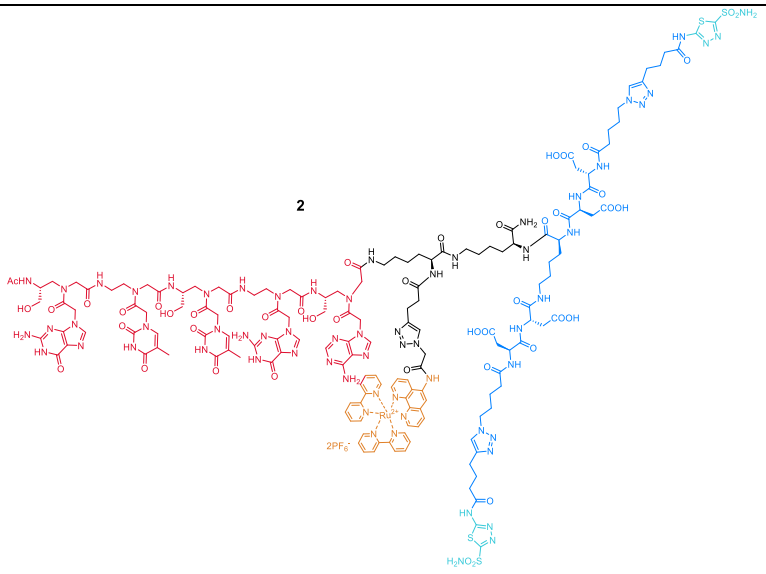
5mer-sulfonate-py^{+}-Rho **(3)** 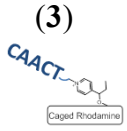	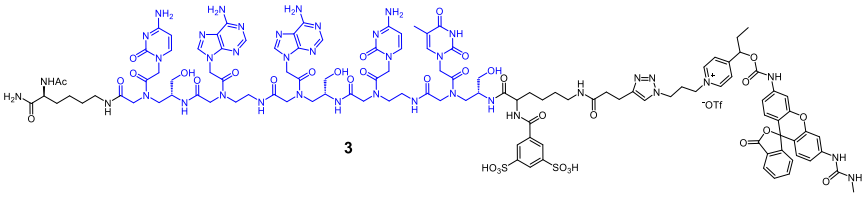

Cy3-4mer-CAIX ligand (**4**) 	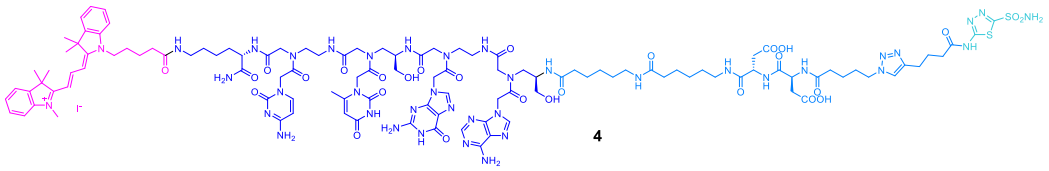
CAIX ligand-4mer (**5**) 	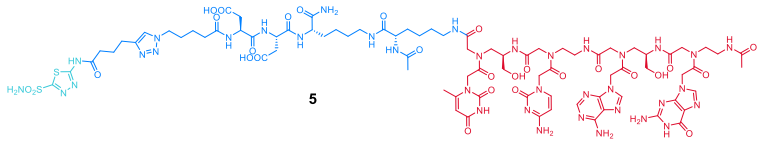
4mer-CAIX ligand (**6**) 	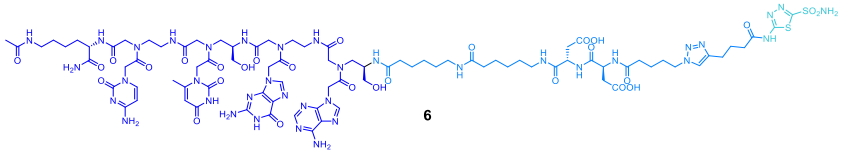
CAIX ligand-4mer-py^{+}-Cy$_3$ (**7**) 	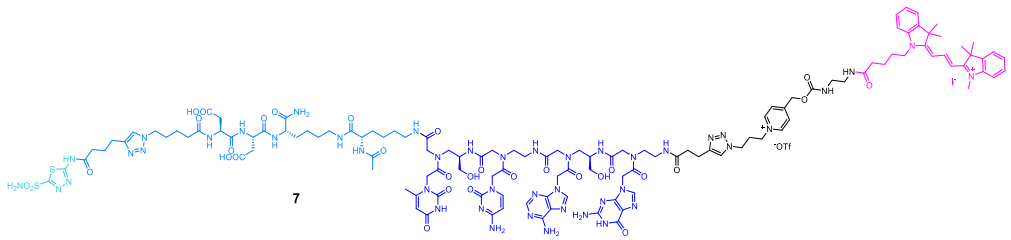
Ru-4mer-CAIX ligand (**8**) 	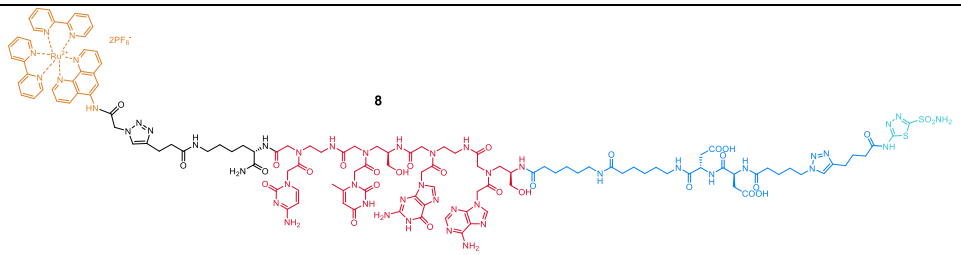
14mer (**9**)	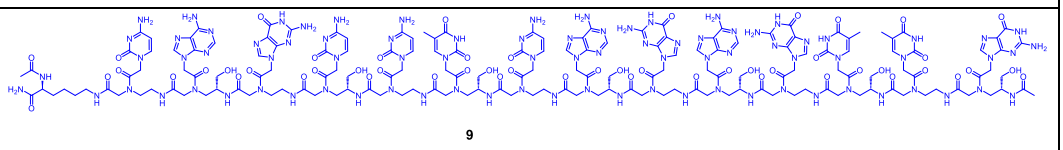
Ru-9mer (**10**) 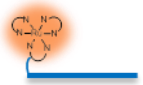	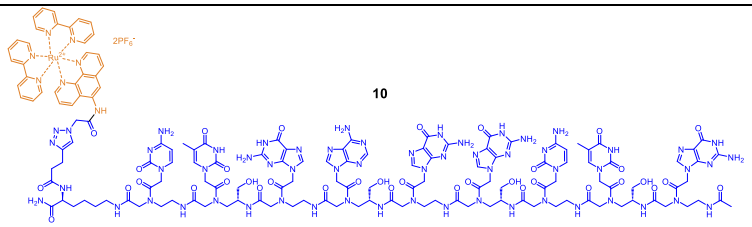

5mer-py$^+$-Cou (**11**) 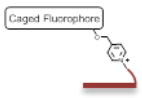	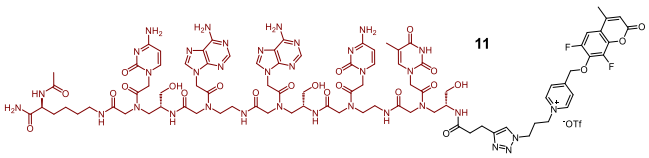
9mer (**12**)	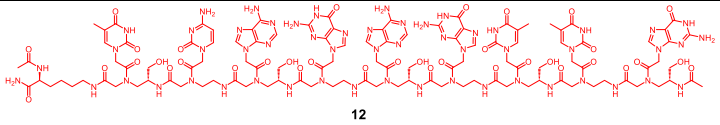
Ru-4mer (**13**) 	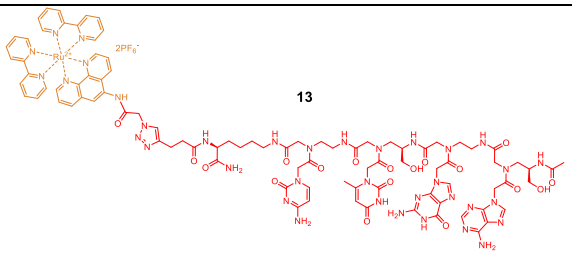
CAIX ligand-9mer (**14**) 	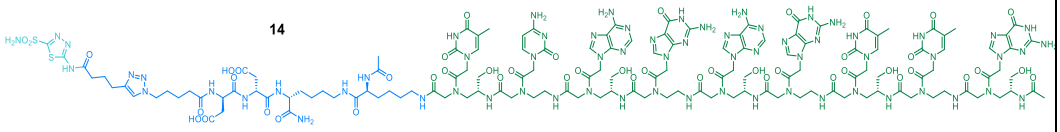
Sulphonate-5mer-py$^+$-MMAE (**15**) 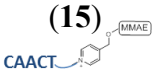	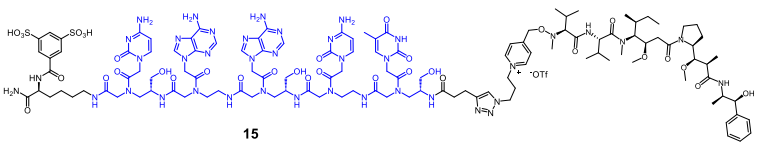

Figure I-S1. Summary of compounds used in this study.

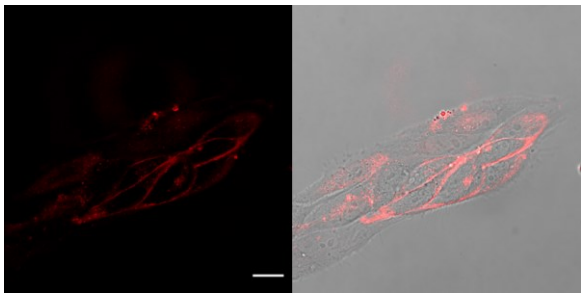

Figure I-S2. Confocal fluorescence images of SKRC-52 cells labelled with bivalent ligand (**1**) (100 nM, 30 min). Scale bar 20 μM.

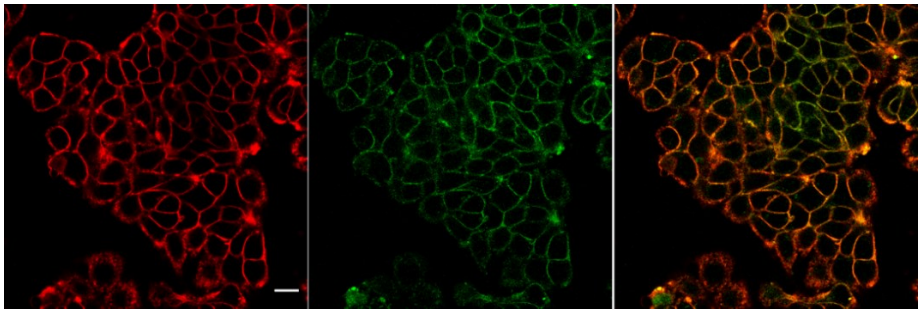

Figure I-S3. Confocal fluorescence images of HT-29 cells labelled with bivalent ligand (**1**) (red), Flipper-TR® (green), and merge channels. Scale bar 20 μM.

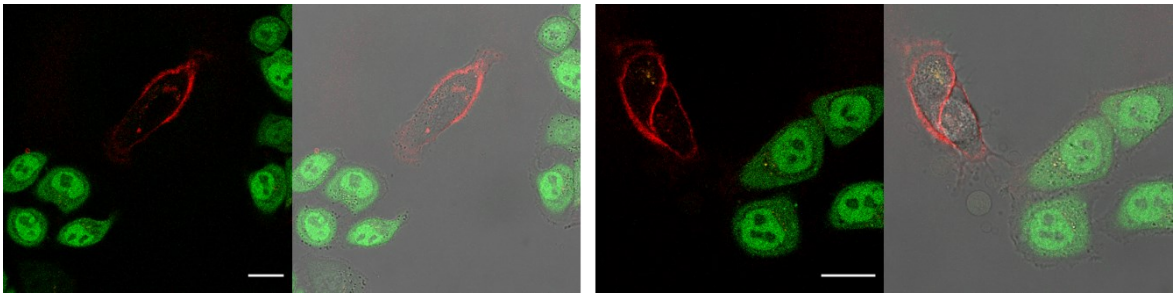

Figure I-S4. Confocal fluorescence images of SKRC-52 co-cultured with HeLa-GFP cells labelled with bivalent ligand (**1**) (red). Scale bar 20 μM.

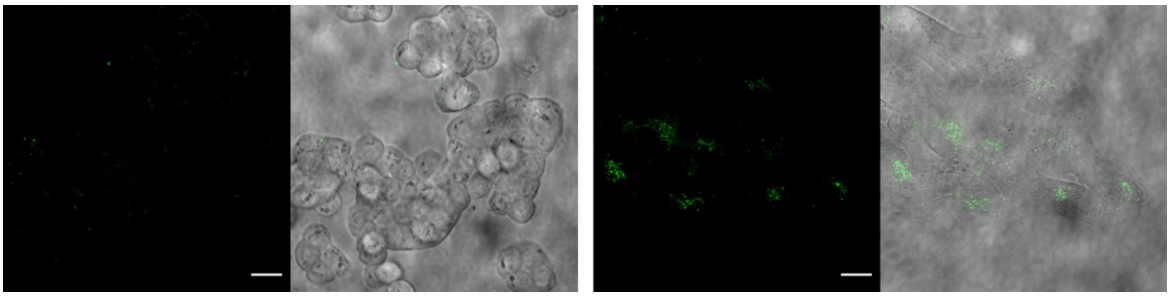

Figure I-S5. Confocal fluorescence images of non-treated HT-29 (left) and SKRC-52 cells (right) under 488 nm laser illumination. Scale bar 20 μM.

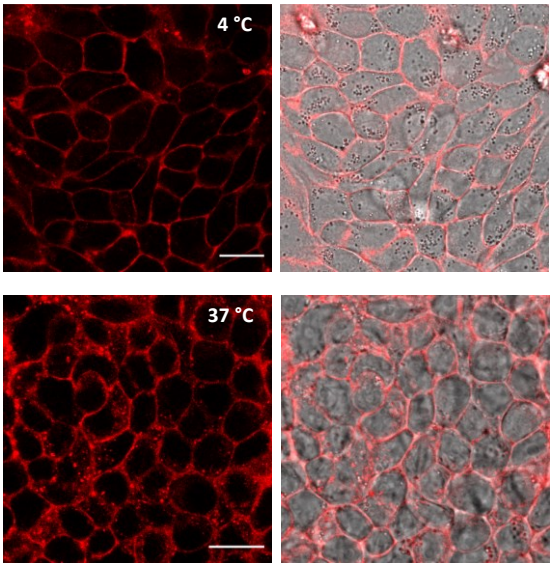

Figure I-S6. Confocal fluorescence images of hypoxic HT-29 treated with **8**+**7** (100 nM duplex) for 1.5 hours; top: incubation at 4 °C; bottom: incubation at 37 °C. Scale bar: 20 μM; red: Cy_3.

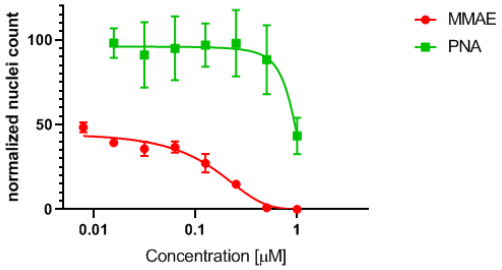

Figure I-S7. Dose response curves for HT-29 hypoxic cells after 1.5 hours treatment with MMAE or 5mer-py$^+$-MMAE (**15**) at different concentrations, and 48 hours incubation. Relative toxicity was then evaluated via Hoechst staining, fluorescence imaging and nuclei count for each condition. Error bars represent standard deviation.

Materials and methods

Each reaction in an organic solvent was performed in anhydrous conditions under N_2. All reagents and solvents were purchased from commercial sources and were used without any further purification. Anhydrous solvents were obtained by passing them through commercially available alumina column (Innovative Technology, Inc., ® VA). Reverse phase column chromatography was performed using Isolera Biotage using SNAP Cartridge KP-C18-HS of 60 g or 12 g. HPLC purification was performed with an Agilent Technologies 1260 infinity HPLC using a ZORBAX 300SB-C18 column (9.4 x 250 mm). For confirmation of synthesized compound, ^{1}H NMR spectra were recorded on AVANCE 3 HD for 400 MHz and Bruker 500 UltraShield for 500 MHz using DMSO-d_6, as solvent, with residual solvent peaks (δ = 2.50 ppm; δ = 39.52 ppm). LC-MS spectra were recorded by using a DIONEX Ultimate 3000 UHPLC coupled with a Thermo LCQ Fleet Mass Spectrometer System (electrospray ionization (ESI)) operated in positive mode (condition for elution gradient: 0 min, A:B = 100:0; 4 min, A:B = 10:90; solution A: 0.01% aqueous TFA solution; solution B, 0.01 % TFA in HPLC grade acetonitrile; flow rate: 0.750 mL/min.). MALDI-TOF mass spectra were measured using a Bruker Daltonics Autoflex spectrometer. Fluorescence intensities were measured using a Molecular Devices Spectra Max M5. Automated solid phase synthesis was carried out on an Intavis AG Multipep RS instrument. Fluorescence imaging was carried out using a Leica SP8. For compounds containing Cy_3 a 530 nm laser was used for fluorophore excitation; for compounds containing Rhodamine a 488 nm laser was used for excitation. All fluorescence images were analysed with Image J. Cell counting and imaging of cells was carried out using a Molecular Devices™ ImageXpress Micro (IXM) XL automated microscope with DAPI settings. Excitation = 100 ms. Objective 20×. Fluorescence images were analyzed using MetaXpress® software by using a nuclei count protocol were the particle mask size was width = 10 µm; height = 25 µm; fluorescence cutoff threshold = 1000. Each well was analysed by the acquisition of matrix of images covering the well (16 tiles). Azido-pyridinium-coumarin, Azido-pyridinium-Rhodamine $[Ru(bpy)_2(phenNHCOCH_2Br)](PF_6)_2$, were synthesized according to our previous synthetic procedures.[1,2,3] Flipper-TR® was a kind gift of prof. Stefan Matile group.

Automated PNA synthesis.[4] Solid phase syntheses were performed with NovaPEG Rink amide resin obtained from EMD Millipore. PNAs were synthesized in 500 µL fritted tubes by using an Intavis MultiPep instrument in a fully automated fashion. The resin (5 mg 0.44 mmol/g, 2.2 µmol) was swollen in DCM (300 µL) for 20 min then washed with DMF and DCM and treated with a pre-activated (5 min) solution of the corresponding Mtt-protected PNA monomer (5 equiv), HATU (4 equiv), DIPEA (5 equiv), and 2,6-lutidine(7.5 equiv) for 20 min in NMP. This process was repeated once (double couplings). Each coupling was

followed by a capping step with Ac_2O (5.3 equiv) and 2,6-lutidine (6.4 equiv) in DMF (150 µL per column).

Fmoc deprotection resin was treated with 20% piperidine in DMF (10 min x 2) followed by washing of resin with DCM, DMF and DCM.

Mtt deprotection.
The resin was treated with a solution of HOBt in a 1:1 mixture of hexafluoroisopropanol and 1,2-dichloroethane (200 µL / column) for 3 min, washed with DCM, this process was repeated 3 times after which the resin was washed with DCM, DMF and DCM.

General method for coupling of primary amine with carboxylic acid.
Carboxylic acid (5 eq.) was pre-activated in NMP with HATU (4.5 eq.), DIPEA (4 eq.) and 2,6-lutidine (4 eq.) for 10 mins. The activated carboxylic acid was then added to the resin and left for 10 min after which the coupling was repeated. The resin was then washed with DCM, DMF and DCM, followed by capping for 5 min and washed again with DCM, DMF and DCM.

General method for click reaction on solid phase.
PNAs derivatized with 4-pentynoic acid were treated with a solution of azide-derivatized small molecule (S1, S5, S7, azido-pyridinium-Coumarin, azido-pyridinium-Rhodamine) (1.5 equiv in 200 µL of NMP), followed by a solution of sodium ascorbate in H_2O (16.6 µL, 198 mg/mL, 16.5 µmol, 7.5 equiv), a solution of $CuSO_4$ in H_2O (4.2 µL, 21.4 mg/mL 0.55 µmol, 0.25 equiv) and TBTA (0.6 mg, 0.5 equiv). After 16 hours swirling at room temperature, the resin was washed with H_2O (6 x 250 µL), DMF (6 x 250 µL), and DCM (6 x 250 µL).

Cleavage from resin
PNA derivatives were cleaved suspending the resin in neat TFA (200 µL) and shaking at room temperature for 2 hours. The solution was filtered and the product precipitated with diethyl ether (2 mL, 10 times of the volume of TFA). The precipitate was pelleted by centrifugation and the supernatant was removed. The pellet was washed with diethyl ether then dissolved in 400 µL H_2O for HPLC purification as described in the general technique for PNA purification.

General technique for PNA purification. Final compounds were purified using an Agilent 1100 series HPLC equipped with DAD and with a Agilent ZORBAX Eclipse XDB-C18 column (4.6 x 250 mm, 5µm); linear gradient from 100% H_2O 0.1% TFA to 100% MeCN 0.1% TFA with a flow rate of 3 mL/min).

Preparation of sulfonated PNA-Pyridinium derivative 3. PNA (5 mg 0.44 mmol/g, 2.2 μmol) with C-terminal Lysine was treated with a solution of 20% piperidine in DMF (200 μL, 2 x 5 min), washed and then capped with Ac_2O (5.3 equiv) and 2,6-lutidine (6.4 equiv) in DMF (150 μL per column, 2 x 5 min). Mtt protecting group was removed upon treatment with HOBt in a 1:1 mixture of HFIP and DCE (200 μL) for 3 min (x 2) and then the resin was washed and treated with a pre-activated (5 min) solution of Fmoc-Lys(Mtt)OH (5 equiv), HATU (4 equiv), DIPEA (5 equiv) and 2,6-lutidine (7.5 equiv) for 1 hour in NMP. Mtt protecting group was removed upon treatment with HOBt in a 1:1 mixture of HFIP and DCE (200 μL) for 3 min (x 2) and then the resin was washed and treated with a pre-activated (5 min) solution of 4-pentynoic acid (5 equiv), HATU (4 equiv), DIPEA (5 equiv) and 2,6-lutidine (7.5 equiv) for 1 hour in NMP. After the reaction, the resin was washed with DMF and DCM. The Fmoc group was removed with a solution of 20% piperidine in DMF (200 μL, 30 min). 3,5-disulfobenzoic acid (11 μmol, 5 equiv), HATU (4 equiv), DIPEA (5 equiv) and 2,6-lutidine (7.5 equiv) in 150 μL of DMF was added to the resin and swirled for 1 hour. After washings with H_2O, DMF and DCM, a solution of small molecule (Rhodamine-py$^+$-azide) (1.5 equiv in 200 μL of NMP) was added to the resin followed by a solution of sodium ascorbate in H_2O (16.6 μL, 198 mg/mL, 16.5 μmol, 7.5 equiv), a solution of $CuSO_4$ in H_2O (4.2 μL, 21.4 mg/mL 0.55 μmol, 0.25 equiv) and TBTA (0.6 mg, 0.5 equiv). After 16 hours, the resin was washed with H_2O (6 x 250 μL), DMF (6 x 250 μL), and DCM (6 x 250 μL). The resin was suspended in TFA (200 μL) for 2 h; the solution was filtered and the product precipitated with diethyl ether (2 mL, 10 times of the volume of TFA). The precipitate was pelleted by centrifugation and the supernatant was removed. The pellet was washed with diethyl ether, then dissolved in 400 μL H_2O for HPLC purification as described in the general technique for PNA purification.

Preparation of PNA-Pyridinium derivative 11. PNA (5 mg 0.44 mmol/g, 2.2 μmol) with C-terminal Lysine was treated with a solution of 20% piperidine in DMF (200 μL, 2 x 5 min), washed and then capped with Ac_2O (5.3 equiv) and 2,6-lutidine (6.4 equiv) in DMF (150 μL per column, 2 x 5 min). Mtt protecting group was removed upon treatment with HOBt in a 1:1 mixture of HFIP and DCE (200 μL) for 3 min (x 2) and then the resin was washed and treated with a pre-activated (5 min) solution of 4-pentynoic acid (5 equiv), HATU (4 equiv), DIPEA (5 equiv) and 2,6-lutidine (7.5 equiv) for 1 hour in NMP. After the reaction, the resin was washed with DMF and DCM. After washings, a solution of small molecule (Coumarine-py$^+$-azide) (1.5 equiv in 200 μL of NMP) was added to the resin followed by a solution of sodium ascorbate in H_2O (16.6 μL, 198 mg/mL, 16.5 μmol, 7.5 equiv), a solution of $CuSO_4$ in H_2O (4.2 μL, 21.4 mg/mL 0.55 μmol, 0.25 equiv) and TBTA (0.6 mg, 0.5 equiv). After 16 hours, the resin was washed with H_2O (6 x 250 μL), DMF (6 x 250 μL), and DCM

(6 x 250 µL). The resin was suspended in TFA (200 µL) for 2 h; the solution was filtered and the product precipitated with diethyl ether (2 mL, 10 times of the volume of TFA). The precipitate was pelleted by centrifugation and the supernatant was removed. The pellet was washed with diethyl ether, then dissolved in 400 µL H_2O for HPLC purification as described in the general technique for PNA purification.

Preparation of sulfonated PNA-Pyridinium derivative 15. PNA (5 mg 0.44 mmol/g, 2.2 µmol) with C-terminal Lysine was treated with HOBt in a 1:1 mixture of HFIP and DCE (200 µL) for 3 min (x 2) to remove the Mtt protecting group, then the resin was washed with DMF and DCM and treated with a pre-activated (5 min) solution of 4-pentynoic acid (5 equiv), HATU (4 equiv), DIPEA (5 equiv) and 2,6-lutidine (7.5 equiv) for 1 hour in NMP. After the reaction, the resin was washed with DMF and DCM. Fmoc protecting group was then removed by treatment with a solution of 20% piperidine in DMF (200 µL, 2 x 5 min); the resin was washed and 3,5-disulfobenzoic acid (11 µmol, 5 equiv), HATU (4 equiv), DIPEA (5 equiv) and 2,6-lutidine (7.5 equiv) in 150 µL of DMF was added to the resin and swirled for 1 hour. After washings with H_2O, DMF and DCM, a solution of small molecule (MMAE-py$^+$-azide (**S7**)) (1.5 equiv in 200 µL of NMP) was added to the resin followed by a solution of sodium ascorbate in H_2O (16.6 µL, 198 mg/mL, 16.5 µmol, 7.5 equiv), a solution of $CuSO_4$ in H_2O (4.2 µL, 21.4 mg/mL 0.55 µmol, 0.25 equiv) and TBTA (0.6 mg, 0.5 equiv). After 16 hours, the resin was washed with H_2O (6 x 250 µL), DMF (6 x 250 µL), and DCM (6 x 250 µL). The resin was suspended in TFA (200 µL) for 2 h; the solution was filtered and the product precipitated with diethyl ether (2 mL, 10 times of the volume of TFA). The precipitate was pelleted by centrifugation and the supernatant was removed. The pellet was washed with diethyl ether, then dissolved in 400 µL H_2O for HPLC purification as described in the general technique for PNA purification.

Preparation of CAIX ligand derivatives

Bivalent CAIX ligand was synthesized following procedures previously reported[5] and adapted to be compatible with NovaPEG Rink amide resin.

Procedure for kinetic measurements

Templated reactions and kinetic values were obtained according to our previously reported procedure.[1]

Cell culture

HT-29 cell lines were obtained from the American Type Culture Collection (ATCC) and expanded following their instructions. Cells were grown in McCoy's 5A (modified) medium (Gibco) containing 10% FCS and 1% pen-strep at 37 °C under 5% CO_2 in a humidified incubator. SKRC52 cells were obtained from the Memorial Sloan Kettering Cancer Center and cultured in RPMI medium (Gibco) containing 10% FCS and 1% pen-strep at 37 °C under 5% CO_2 in a humidified incubator. HeLa Kyoto GFP-chmp4b cells were obtained from Prof. Roux group (University of Geneva, Switzerland) and cultured in DMEM (Gibco) containing 10% FCS and 1% pen-strep at 37 °C under 5% CO_2 in a humidified incubator. Cells were regularly tested for mycoplasma contamination by staining with Hoechst 33342. Experiments under hypoxic conditions were conducted in an Eppendorf® Galaxy® 48R CO_2 incubator at 37 °C with 1% O_2, 5% CO_2 and 94% N_2 settings.

Photocatalysed reactions on cells

Cell culture dishes were irradiated with a collimated LED light 7.5 cm above the plate (455 nm, 1W: Thorlabs, part number M455L2-C1 – www.thorlabs.com). The experiments were protected from external light by performing the experiments inside a protected enclosure.

CA IX staining with bivalent ligand-Cy_3

HT-29 cells ($2x10^5$) were seeded into 3.5 cm glass bottom dishes with 10 mm microwell (Mattek); cells were incubated in McCoy's 5A medium at 37 °C under 5% CO_2 in a humidified incubator for 48 hours. Medium was replaced with fresh one and cells were transferred into the hypoxia incubator (1% O_2) for 24 hours. Cells were treated with CA IX-bivalent ligand-Cy3 (**1**) (100 nM) and incubated under hypoxic conditions (30 min), then washed three times with HBSS buffer and immediately imaged with a SP8 microscope with Cy_3 settings. Control cells were submitted to the same protocol, but kept at 37 °C, 5% CO_2, air.

Rhodamine release with bivalent ligand in CA IX expressing cells

HT-29 cells ($2x10^5$) were seeded into 3.5 cm glass bottom dishes with 10 mm microwell (Mattek); cells were incubated in McCoy's 5A medium at 37 °C under 5% CO_2 in a humidified incubator for 48 hours. Medium was replaced with fresh one and cells were transferred into the hypoxia incubator (1% O_2) for 24 hours. Cells were treated with CA IX-bivalent ligand-5mer-Ru (**2**) (100 nM) and incubated under hypoxic conditions (30 min), then washed three times with HBSS; complementary 5mer-sulfonate-py^+-Rho (**3**) (5 µM) in HBSS supplemented with 10 mM NaAsc (100 µL total volume) was added to cells, the dish was immediately sealed and irradiated with a 450 nm LED or kept in the dark (30 min). After irradiation cells were incubated for additional 30 min before being washed three

times with HBSS and imaged with a Leica SP8 microscope.
The same experiment was carried out with SKRC52 cells; these cells do not require hypoxic conditions to express CA IX, though they were kept at 37 °C under 5% CO_2 in a humidified incubator.

4-mer-Duplex assembly on CA IX expressing cells

HT-29 cells ($2x10^5$) were seeded into 3.5 cm glass bottom dishes with 10 mm microwell (Mattek); cells were incubated in McCoy's 5A medium at 37 °C under 5% CO_2 in a humidified incubator for 48 hours. Medium was replaced with fresh one and cells were transferred into the hypoxia incubator (1% O_2) for 24 hours. Cells were treated with Cy3-4mer-CAIX ligand (**4**) + CAIX ligand-4mer (**5**) or Cy3-4mer-CAIX ligand (**4**) + 4mer-CAIX ligand (**6**) (100 nM duplex) and incubated under hypoxic conditions (30 min), then washed with HBSS and immediately imaged with a Leica SP8 microscope.

Cy_3 release from 4-mers duplex on CA IX expressing cells

HT-29 cells ($2x10^5$) were seeded into 3.5 cm glass bottom dishes with 10 mm microwell (Mattek); cells were incubated in McCoy's 5A medium at 37 °C under 5% CO_2 in a humidified incubator for 48 hours. Medium was replaced with fresh one and cells were transferred into the hypoxia incubator (1% O_2) for 24 hours. Cells were treated with CAIX ligand-4mer-py^+-Cy_3 (**7**) + Ru-4mer-CAIX ligand (**8**) (100 nM duplex) and incubated under hypoxic conditions (30 min), then washed with HBSS. HBSS supplemented with 10 mM NaAsc (100 µL total volume) was added to cells, the dishes were immediately sealed and irradiated with a 450 nm LED or kept in the dark (30 min). After irradiation cells were incubated for additional 30 min under hypoxic conditions before being washed three times with HBSS and imaged with a Leica SP8 microscope. Hoechst 33342 (5 µg/mL) was added 15 min before imaging.

Evaluation of internalization

HT-29 cells ($2x10^5$) were seeded into 3.5 cm glass bottom dishes with 10 mm microwell (Mattek); cells were incubated in McCoy's 5A medium at 37 °C under 5% CO_2 in a humidified incubator for 48 hours. Medium was replaced with fresh one and cells were transferred into the hypoxia incubator (1% O_2) for 24 hours. Cells were treated with CAIX ligand-4mer-py^+-Cy_3 (**7**) + Ru-4mer-CAIX ligand (**8**) (100 nM duplex) and incubated under hypoxic conditions (1.5 hours) at 4 °C or at 37 °C in the dark, then washed with HBSS and imaged with a Leica SP8 microscope.

Rhodamine release with 3 components PNA assembly in CA IX expressing cells

HT-29 cells ($2x10^5$) were seeded into 3.5 cm glass bottom dishes with 10 mm microwell (Mattek); cells were incubated in McCoy's 5A medium at 37 °C under 5% CO_2 in a

humidified incubator for 48 hours. Medium was replaced with fresh one and cells were transferred into the hypoxia incubator (1% O_2) for 24 hours. Cells were treated with CAIX ligand-9mer (**14**) + Ru-4mer-CAIX ligand (**8**) (100 nM duplex) and incubated under hypoxic conditions (30 min), then washed with HBSS; complementary 5mer-sulfonate-py$^+$-Rho (**3**) (5 μM) in HBSS supplemented with 10 mM NaAsc (100 μL total volume) was added to cells, the dish was immediately sealed and irradiated with a 450 nm LED or kept in the dark (30 min). After irradiation cells were incubated for additional 30 min before being washed three times with HBSS and imaged with a Leica SP8 microscope.

MMAE and 5mer-py$^+$-MMAE effect in HT-29 hypoxic cells

HT-29 cells (8x10^3) were seeded into 96-well plates (Ibidi) and incubated in McCoy's 5A medium at 37 °C under 5% CO_2 in a humidified incubator for 48 hours. Medium was replaced with fresh one and cells were transferred into the hypoxia incubator (1% O_2) for 24 hours. Then, media was removed and replaced with MMAE or 5mer-py$^+$-MMAE (**15**) at different concentrations in HBSS supplemented with 10 mM NaAsc. The plate was incubated for 1.5 hours at 37 °C. Then media was replaced with fresh McCoy's 5A (with 10% FCS, 1% pen-strep) and the plate was placed under hypoxic conditions for 48 hours. Cells were washed with DMEM (-) (Gibco), Hoechst 33342 stain was added to a final concentration of 1 μg/μL followed by incubation for 30 min at 37 °C and 5% CO_2. Bright field and fluorescence images were then acquired using a HTS IXM-XL microscope with DAPI settings at 37 °C and 5% CO_2; subsequent image analysis and nuclei count was achieved by using MetaXpress® software. Drug effect was expressed as normalized nuclei count. Sigmoidal curve fits of normalized nuclei count *vs*. concentration data was obtained using Graph-Pad Prism 8.

MMAE release in HT-29 cells

HT-29 cells (8x10^3) were seeded into 96-well plates (Ibidi) and incubated in McCoy's 5A medium at 37 °C under 5% CO_2 in a humidified incubator for 48 hours. Medium was replaced with fresh one and cells were transferred into the hypoxia incubator (1% O_2) for 24 hours. CA IX-bivalent-5merRu (**2**) (100 nM) or CAIX ligand-9mer (**14**) + Ru-4mer-CAIX ligand (**8**) (100 nM duplex) were added to cells and incubated under hypoxic conditions (30 min). Then, media was removed and replaced with Sulphonate-5mer-py$^+$-MMAE (**15**) at 500 or 250 nM in HBSS supplemented with 10 mM NaAsc. The plate was sealed, irradiated with a 450 nm LED or kept in the dark (30 min), followed by incubation for 1.5 hours at 37 °C. Then media was replaced with fresh McCoy's 5A (with 10% FCS, 1% pen-strep) and the plate was placed under hypoxic conditions for 48 hours. After that cells were washed with DMEM (-) (Gibco), Hoechst 33342 stain was added to a final concentration of 1 μg/μL followed by incubation for 30 min at 37 °C and 5% CO_2. Bright field and

fluorescence images were then acquired using a HTS IXM-XL microscope with DAPI settings at 37 °C and 5% CO_2. Nuclei count was normalized considering MMAE 1 μM as maximum effect (0 % nuclei count) and DMSO as no effect (100 % nuclei count). Drug effect was expressed as normalized nuclei count *vs* concentration data using GraphPad Prism 8. For the equivalent experiment carried out under normoxia, HT-29 cells were kept at 37 °C under 5% CO_2 in a humidified incubator.

Double MMAE release in HT-29 cells

HT-29 cells ($8x10^3$) were seeded into 96-well plates (Ibidi) and incubated in McCoy's 5A medium at 37 °C under 5% CO_2 in a humidified incubator for 48 hours. Medium was replaced with fresh one and cells were transferred into the hypoxia incubator (1% O_2) for 24 hours. CAIX ligand-9mer (**14**) + Ru-4mer-CAIX ligand (**8**) (100 nM duplex) were added to cells and incubated under hypoxic conditions (30 min). Then, media was removed and replaced with Sulphonate-5mer-py$^+$-MMAE (**15**) at 500 or 250 nM in HBSS supplemented with 10 mM NaAsc. The plate was sealed, irradiated with a 450 nm LED or kept in the dark (30 min), followed by incubation for 1.5 hours at 37 °C. Then media was replaced with fresh McCoy's 5A (with 10% FCS, 1% pen-strep) and the plate was placed under hypoxic conditions for 48 hours. After 48 hours the treatment with **14**, **8**, **15** was repeated as in the first treatment and cells were incubated under hypoxia for additional 48 hours. Then cells were washed with DMEM (-) (Gibco), Hoechst 33342 stain was added to a final concentration of 1 μg/μL followed by incubation for 30 min at 37 °C and 5% CO_2. Bright field and fluorescence images were then acquired using a HTS IXM-XL microscope with DAPI settings at 37 °C and 5% CO_2. Nuclei count was normalized considering MMAE 1 μM as maximum effect (0 % nuclei count) and DMSO as no effect (100 % nuclei count). Drug effect was expressed as normalized nuclei count *vs* concentration data using GraphPad Prism 8.

Synthesis of small molecules

Synthesis of Ruthenium derivative

Compound S1

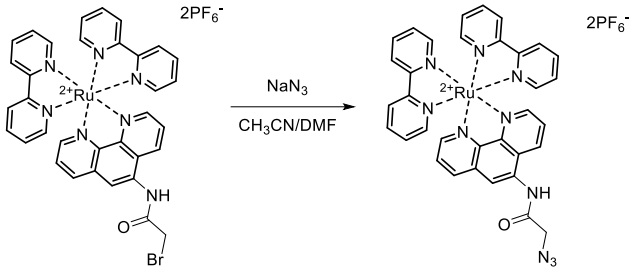

$[Ru(bpy)_2(phenNHCOCH_2Br)](PF_6)_2$ (24 mg, 0.033 mmol, 1 eq) was dissolved in acetonitrile/DMF 2:1 (1.5 mL, 0.02 M); sodium azide (6.5 mg, 0.099 mmol, 3 eq) was added and the mixture was stirred at room temperature in the dark for 4 hours. Then acetonitrile was removed under reduced pressure and the residue was loaded into an Isolera Biotage using SNAP Cartridge KP-C18-HS 12 g column (linear gradient from 100% H_2O to 60% MeCN). The fraction containing the desired product were collected and lyophilized to afford **S1** as an orange solid (28 mg, 85% yield). Expected mass: 692.132. LC-MS (ESI^+): RT= 1.41 min. m/z found: 691.1 $[M]^{2+}$, 346.1 $[M+H]^{3+}$, 804.5 $[M+TFA]^{2+}$. ^1H NMR (500 MHz, DMSO-d_6) δ 10.74 (s, 1H), 8.91 (dd, *J* = 8.6, 1.2 Hz, 1H), 8.88 (d, *J* = 8.2 Hz, 2H), 8.84 (d, *J* = 8.3 Hz, 2H), 8.79 (dd, *J* = 8.3, 1.2 Hz, 1H), 8.66 (s, 1H), 8.24 – 8.19 (m, 2H), 8.16 (dd, *J* = 5.2, 1.1 Hz, 1H), 8.14 – 8.09 (m, 2H), 8.05 (dd, *J* = 5.3, 1.2 Hz, 1H), 7.92 (dd, *J* = 8.6, 5.2 Hz, 1H), 7.86 – 7.81 (m, 3H), 7.61 – 7.55 (m, 4H), 7.39 – 7.34 (m, 2H), 4.35 (s, 2H). ^{13}C NMR (126 MHz, DMSO) δ 168.56, 157.28, 157.04, 157.02, 152.92, 151.95, 151.92, 151.88, 147.69, 145.23, 138.45, 138.33, 136.91, 133.56, 133.07, 130.62, 128.32, 128.29, 128.22, 127.08, 126.84, 126.30, 124.96, 124.87, 120.45, 51.73.

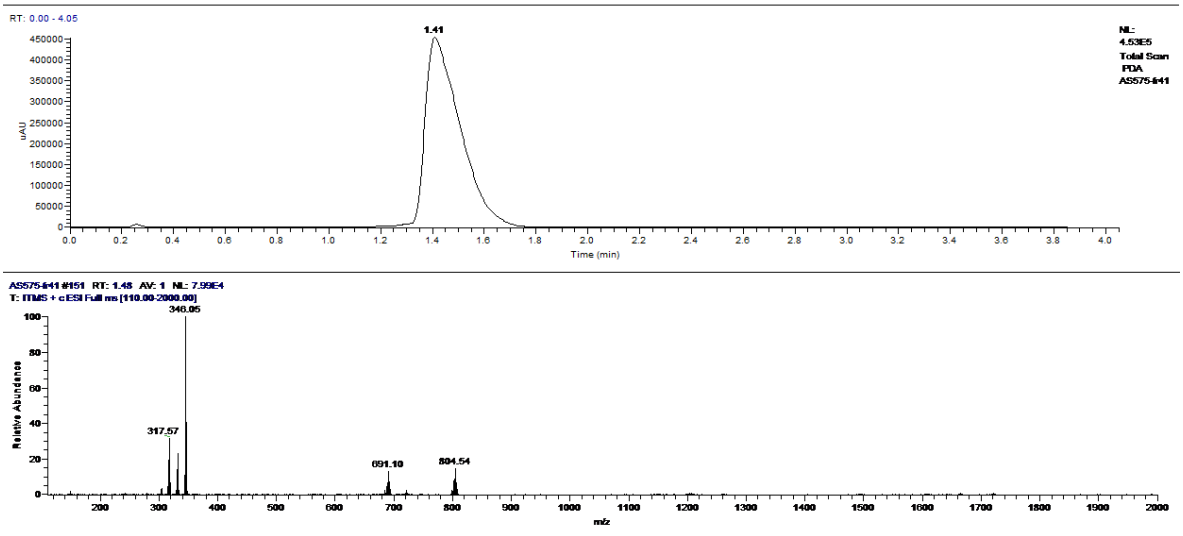

LC-MS trace of **S1**.

Synthesis of Cy3 derivative

Compound S2

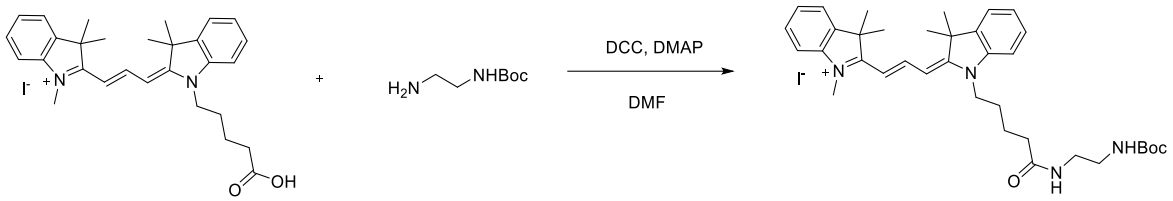

Cy3-COOH (50 mg, 0.088 mmol, 1 eq) was dissolved in dry DMF (1.8 mL, 0.05 M); then tert-butyl (2-aminoethyl)carbamate (14 mg, 0.088 mmol, 1 eq), DCC (20 mg, 0.097 mmol, 1.1 eq) and DMAP (1 mg, 0.009 mmol, 0.1 eq) were added and the mixture was stirred at room temperature overnight. DMF was removed under reduced pressure and the crude residue was loaded on silica and purified by flash column chromatography (dry load, DCM/methanol 95:5). Fractions containing the desired product were collected concentrated under reduced pressure to afford **S2** as a purple solid (30 mg, 48% yield). Expected mass: 585.379. LC-MS (ESI^+): RT= 2.68 min. m/z found: 585.40 $[M]^+$.

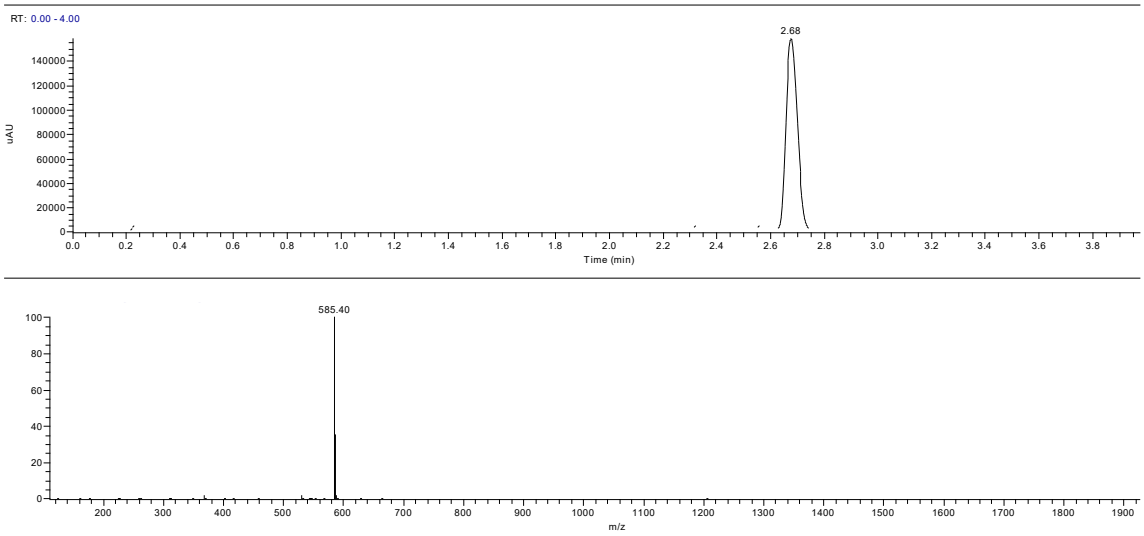

LC-MS trace of **S2**.

Compound S3

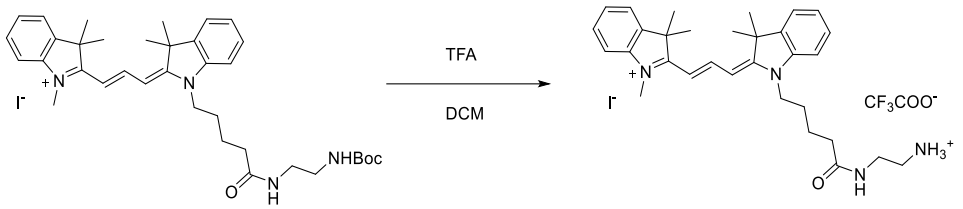

S2 (30 mg, 0.042 mmol, 1 eq) was dissolved in dry DCM (850 µL, 0.05 M). TFA (320 µL, 0.42 mmol, 100 eq) was added dropwise at room temperature. The mixture was stirred for 1 hour, then the solvent was removed and the residue dried under reduced pressure.

Expected mass: 485.328. LC-MS (ESI$^+$): RT= 2.09 min. m/z found: 485.38 $[M]^+$ 243.22 $[M+H]^{2+}$. ^{1}H NMR (400 MHz, DMSO-d_6) δ 8.34 (t, J = 13.5 Hz, 1H), 8.09 (t, J = 5.7 Hz, 1H), 7.82 (s, 2H), 7.64 (d, J = 6.5 Hz, 2H), 7.48 – 7.42 (m, 4H), 7.30 (dtd, J = 7.5, 6.2, 2.5 Hz, 2H), 6.49 (dd, J = 13.5, 11.8 Hz, 2H), 4.12 (t, J = 7.1 Hz, 2H), 3.66 (s, 3H), 3.26 (q, J = 6.3 Hz, 2H), 2.82 (q, J = 6.1 Hz, 2H), 2.19 (t, J = 7.0 Hz, 2H), 1.69 (d, J = 1.6 Hz, 16H).

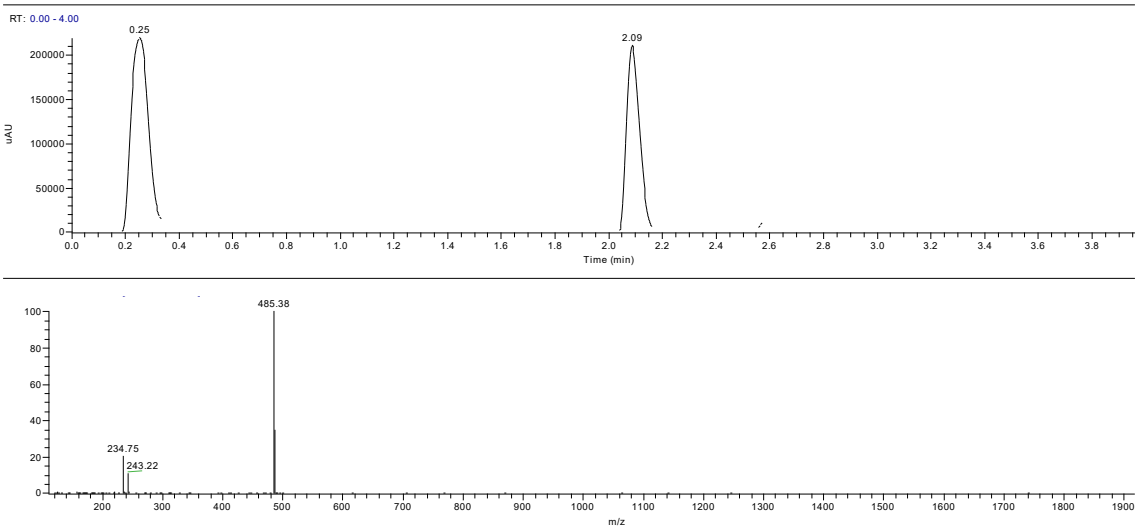

LC-MS trace of **S3**.

Compound S4

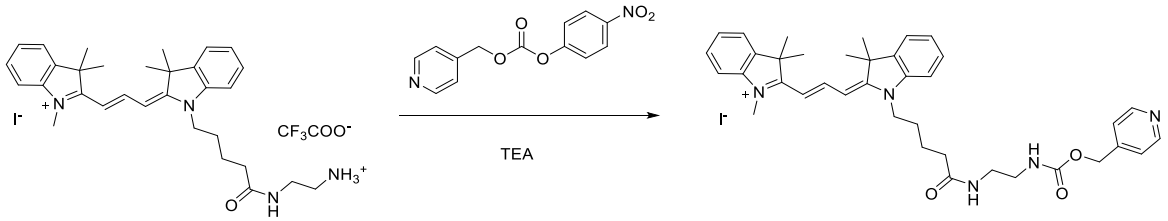

S3 (8 mg, 0.011 mmol, 1 eq) was dissolved in dry DCM (220 µL, 0.05 M) and cooled to 0 °C; then TEA (5 µL, 0.033 mmol, 3 eq) was added and the mixture was stirred 15 min at 0 °C. The mixture was then allowed to reach room temperature and 4-nitrophenyl (pyridin-4-ylmethyl) carbonate (5 mg, 0.017 mmol, 1.5 eq) was added; the mixture was stirred at room temperature for 2 hours. DCM was removed under reduced pressure and the crude residue was loaded on

silica and purified by flash column chromatography (dry load, DCM/methanol 95:5). Fractions containing the desired product were collected concentrated under reduced pressure to afford **S4** as a purple solid (6 mg, 73% yield). Expected mass: 620.359. LC-MS (ESI^+): RT= 2.14 min. m/z found: 620.37 $[M]^+$, 310.84 $[M+H]^{2+}$. ^1H NMR (500 MHz, DMSO-d_6) δ 8.54 (s, 2H), 8.32 (t, *J* = 13.5 Hz, 1H), 7.90 (t, *J* = 5.7 Hz, 1H), 7.62 (d, *J* = 7.4 Hz, 2H), 7.47 – 7.38 (m, 5H), 7.33 – 7.26 (m, 4H), 6.46 (dd, *J* = 14.9, 13.5 Hz, 2H), 5.01 (s, 2H), 4.09 (t, *J* = 7.2 Hz, 2H), 3.64 (s, 3H), 3.08 (q, *J* = 6.5, 5.8 Hz, 2H), 3.04 – 2.99 (m, 2H), 2.12 (t, *J* = 7.0 Hz, 2H), 1.74 – 1.58 (m, 16H). ^{13}C NMR (126 MHz, DMSO) δ 174.49, 173.67, 171.89, 157.53, 155.82, 149.68, 149.24, 142.64, 141.95, 140.58, 128.65, 128.59, 125.28, 125.13, 122.54, 122.42, 121.68, 111.52, 111.45, 102.91, 102.38, 63.46, 48.87, 43.52, 38.45, 34.82, 31.36, 27.47, 27.24, 26.49, 22.34, 22.34.

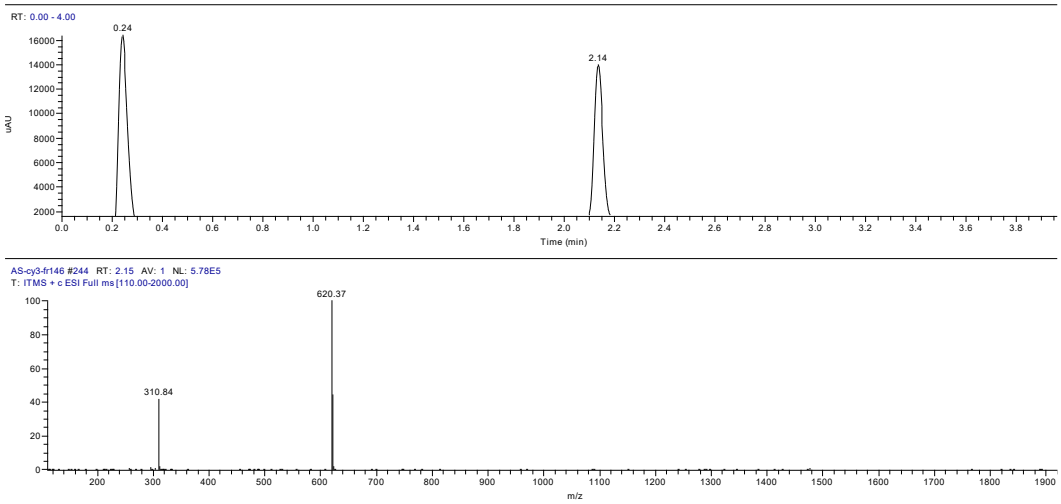

LC-MS trace of **S4**.

Compound S5

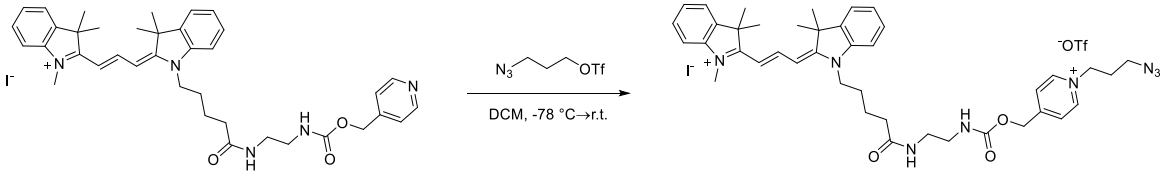

S4 (6 mg, 0.008 mmol, 1 eq) was dissolved in dry DCM (160 µL, 0.05 M) and cooled to -78 °C. Then 3-azidopropyl trifluoromethanesulfonate (2 mg, 0.008 mmol, 1 eq), dissolved in 100 µL of DCM, was added dropwise to **S4** solution. The mixture was allowed to reach room temperature and stirred for 2 hours. The reaction was monitored by LC-MS. DCM was removed under reduced pressure upon addition of 200 µL of DMSO to the mixture. The crude residue was directly injected in reverse phase HPLC and purified. Fractions containing the desired product were collected and lyophilized to afford **S5** as a purple solid (4 mg, 53% yield).

Expected mass: 704.415. LC-MS (ESI$^+$): RT= 2.23 min. m/z found: 703.29 $[M]^+$, 352.37 $[M+H]^{2+}$. ^{1}H NMR (400 MHz, DMSO) δ 9.03 (d, *J* = 6.5 Hz, 2H), 8.34 (t, *J* = 13.5 Hz, 1H), 7.98 (t, *J* = 6.5 Hz, 3H), 7.64 (d, *J* = 7.5 Hz, 3H), 7.44 (dd, *J* = 14.1, 7.5 Hz, 4H), 7.36 – 7.25 (m, 2H), 6.48 (dd, *J* = 13.4 Hz, 2H), 5.30 (s, 2H), 4.63 (t, *J* = 7.2 Hz, 2H), 4.12 (t, *J* = 6.8 Hz, 2H), 3.65 (s, 4H), 3.16 – 2.97 (m, 4H), 2.23 – 2.11 (m, 4H), 1.78 – 1.59 (m, 16H). 13C NMR (126 MHz, DMSO) δ 174.94, 174.11, 172.37, 158.48, 158.21, 157.96, 155.79, 150.12, 145.15, 143.07, 142.37, 141.03, 141.01, 129.07, 129.03, 125.73, 125.57, 125.00, 122.99, 122.86, 111.96, 111.87, 103.35, 102.81, 63.41, 58.56, 49.32, 49.30, 48.03, 43.97, 38.77, 35.28, 31.82, 30.05, 27.92, 27.69, 26.99, 22.79.

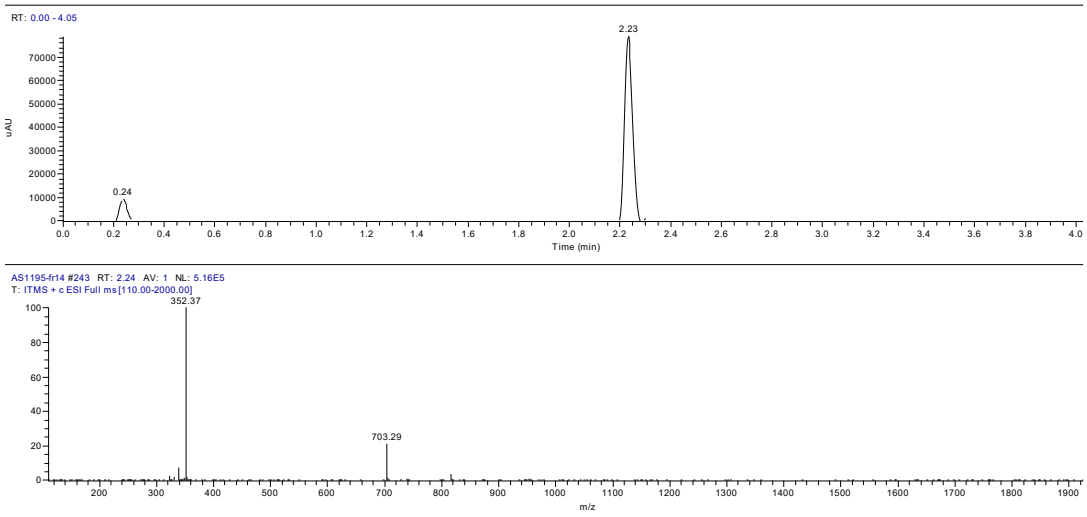

LC-MS trace of **S5**

Synthesis of MMAE derivatives

Compound S6

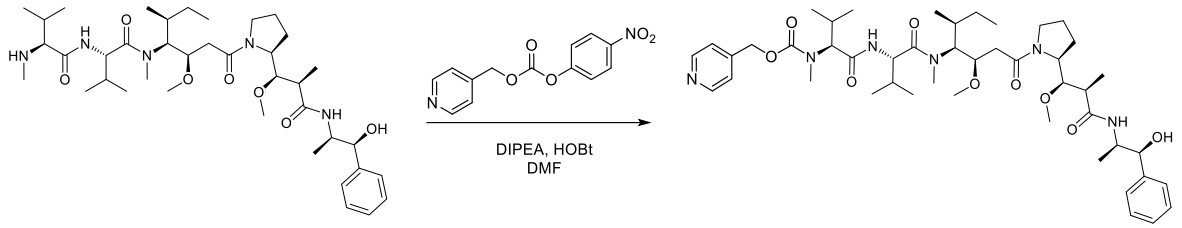

Mono-methyl auristatin-E (MMAE) (4 mg, 0.006 mmol, 1 eq) was dissolved in dry DMF (600 µL, 0.01 M); then DIPEA (2 µL, 0.012 mmol, 2 eq), HOBt (0.75 mg, 0.006 mmol, 1 eq) and pyridine-*p*-nitro phenyl carbonate (1.5 mg, 0.006 mmol, 1 eq) were added at room temperature. The mixture was stirred for 8 hours and monitored by LC-MS. The crude mixture was directly injected into reverse phase HPLC and purified. Fractions containing the desired product were collected and lyophilized.

Expected mass: 852.536. LC-MS (ESI$^+$): RT= 2.20 min. m/z found: 853.5 $[M+H]^+$, 427.6 $[M+2H]^{2+}$. ^{1}H NMR (500 MHz, DMSO-d_6) δ 8.64 (s, 2H), 8.47 – 8.40 (m, 0.5H), 8.18 – 8.11 (m, 0.5H), 7.89 (d, *J* = 8.7 Hz, 1H), 7.62 (d, *J* = 8.5 Hz, 1H), 7.60 – 7.54 (m, 1H), 7.52 – 7.45 (m, 1H), 7.33 – 7.24 (m, 4H), 7.20 – 7.13 (m, 1H), 5.29 – 5.14 (m, 2H), 4.78 – 4.70 (m, 0.5 H), 4.56 – 4.23 (m, 3H), 4.06 – 3.90 (m, 2H), 3.78 (dd, *J* = 9.4, 2.4 Hz, 0.5H), 3.62 – 3.52 (m, 1H), 3.36 – 3.10 (m, 6H), 3.08 – 2.95 (m, 3H), 2.93 – 2.86 (m, 1H), 2.45 – 2.38 (m, 1H), 2.32 – 2.22 (m, 1H), 2.19 – 2.08 (m, 2H), 2.05 – 1.93 (m, 1H), 1.87 – 1.66 (m, 3H), 1.59 – 1.42 (m, 2H), 1.36 – 1.23 (m, 1H), 1.07 – 0.72 (m, 30H).

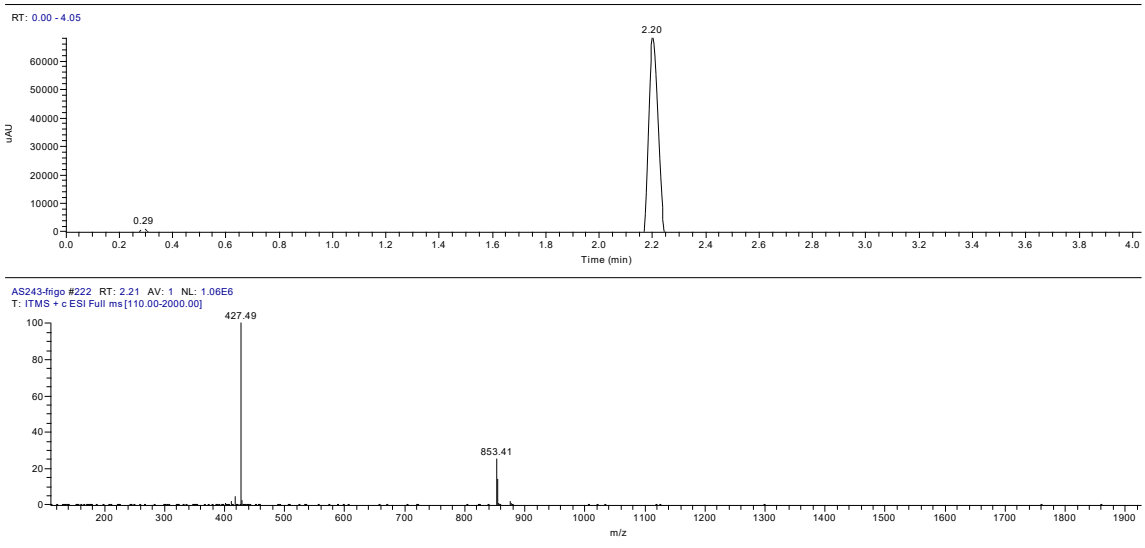

LC-MS trace of **S6**.

Compound S7

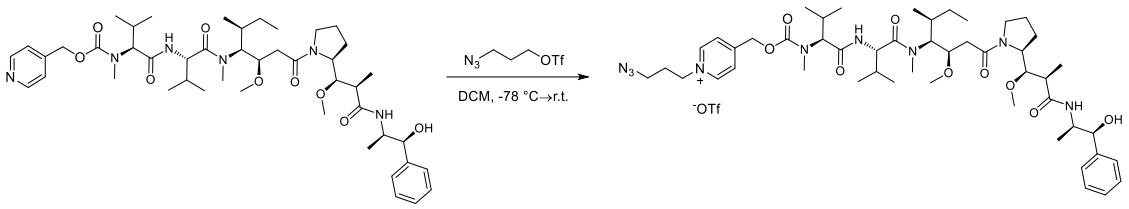

Compound **S6** (1.1 mg, 0.0013 mmol, 1 eq) was dissolved in DCM (250 µL, 0.005 M) and cooled to -78 °C; then 3-azidopropyl trifluoromethanesulfonate (0.35 mg, 0.0013 mmol, 1 eq), dissolved in 100 µL of DCM, was added dropwise to the MMAE solution. The mixture was allowed to reach room temperature and stirred for 2 hours. The reaction was monitored by LC-MS. DCM was removed under reduced pressure upon addition of 200 µL of DMSO to the mixture. The crude residue was directly injected in reverse phase HPLC and purified. Fractions containing the desired product were collected and lyophilized to afford **S7** as a white solid (1 mg, 80% yield). Expected mass: 936.591. LC-MS (ESI$^+$): RT= 2.30 min. m/z found: 936.5 $[M]^+$, 469.0 $[M+H]^{2+}$. ^{1}H NMR (500 MHz, DMSO-d_6) δ 9.09 – 9.03 (m, 2H), 8.53 (d, *J* = 9.7 Hz, 0.5H), 8.22 (d, *J* = 8.4 Hz, 1H), 8.16 – 8.11 (m, 1H), 8.09 – 8.03 (m, 1H), 7.92 (d, *J* = 8.3 Hz, 1H), 7.64 (d, *J* = 8.4 Hz, 0.5H), 7.33 – 7.22 (m, 5H), 7.17 (q, *J* = 7.0 Hz, 1H), 5.48 – 5.33 (m, 2.5H), 4.75 (s, 0.5H), 4.65 (d, *J* = 6.6 Hz, 2H), 4.58 – 4.21 (m, 3H), 4.05 – 3.91 (m, 2H), 3.78 (d, *J* = 9.3 Hz, 0.5H), 3.61 – 3.53 (m, 1H), 3.48 (d, *J* = 4.7 Hz, 1.5H), 3.26 – 3.11 (m, 2.5H), 3.07 – 2.97 (m, 2.5H), 2.92 – 2.87 (m, 1H), 2.41 (dt, *J* = 16.4, 8.6 Hz, 0.5H), 2.31 – 2.09 (m, 5.5H), 2.06 – 1.93 (m, 1H), 1.85 – 1.68 (m, 3.5H), 1.58 – 1.40 (m, 2.5H), 1.36 – 1.22 (m, 2H), 1.07 – 0.70 (m, 30H). ^{13}C NMR (126 MHz, DMSO) δ 168.68, 156.98, 144.73, 144.65, 143.67, 127.76, 127.71, 126.62, 126.48, 126.39, 124.94, 124.72, 85.38, 81.61, 76.93, 74.78, 64.24, 63.52, 60.91, 60.26, 59.21, 58.64, 58.14, 57.14, 49.74, 49.06, 47.57, 47.18, 46.23, 43.72, 43.20, 35.11, 30.22, 30.03, 29.65, 26.88, 25.32, 24.34, 23.11, 19.12, 19.00, 18.81, 18.64, 18.47, 15.47, 15.31, 15.02, 10.38, 10.27.

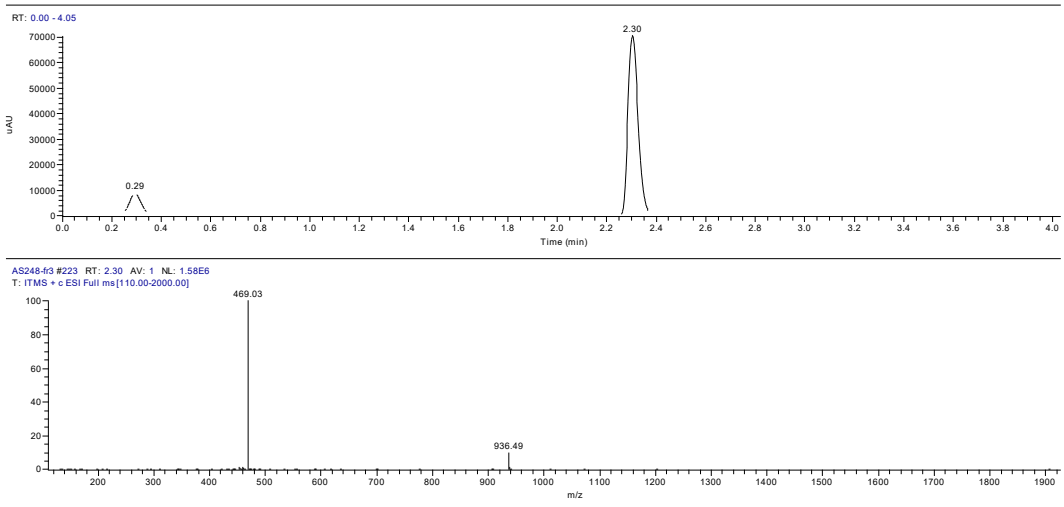

LC-MS trace of **S7**.

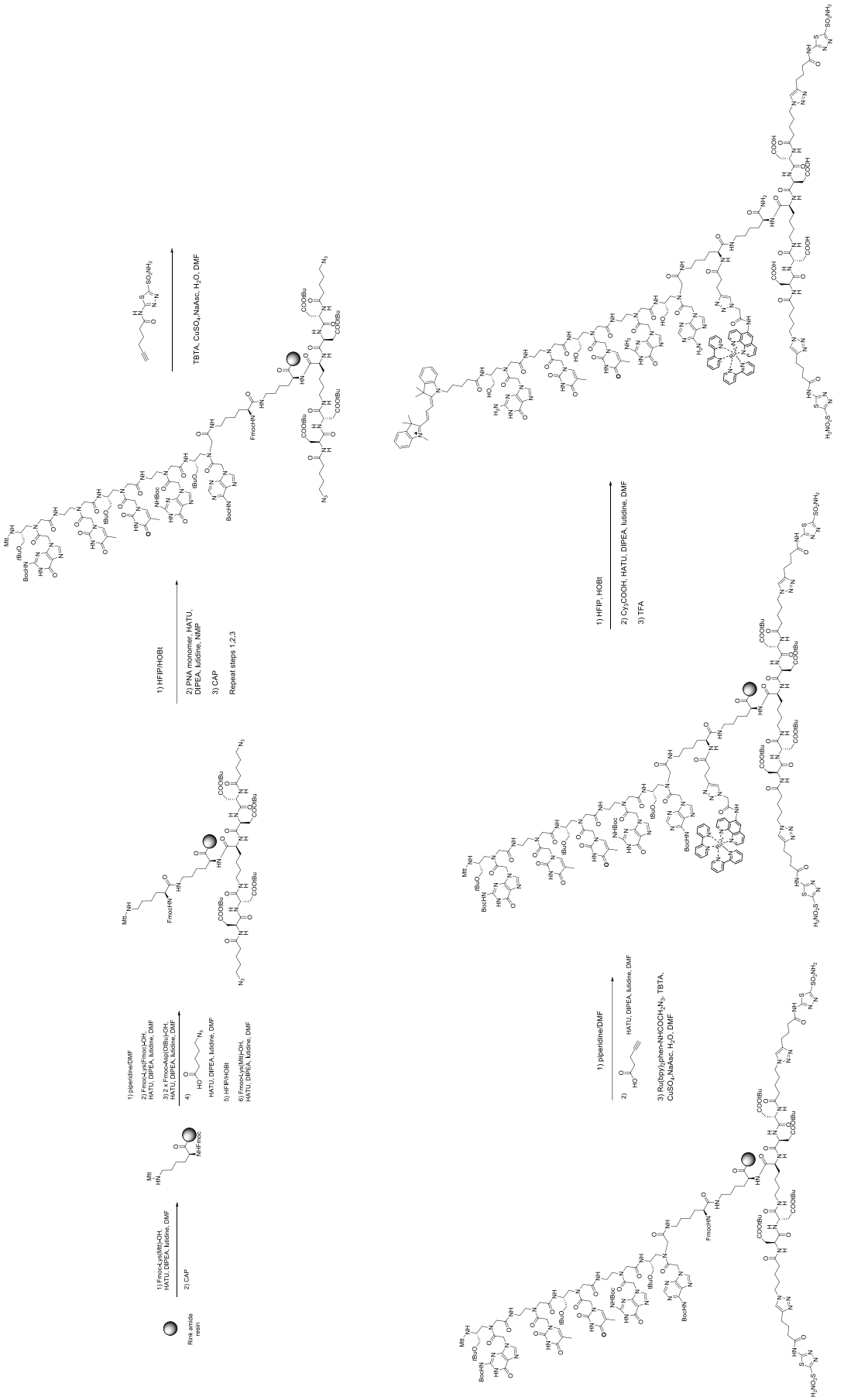

Synthetic scheme of CAIX-PNA ligand

PNA and peptide derivatives

CA-IX bivalent ligand-Ru-5mer-Cy3 (**1**)

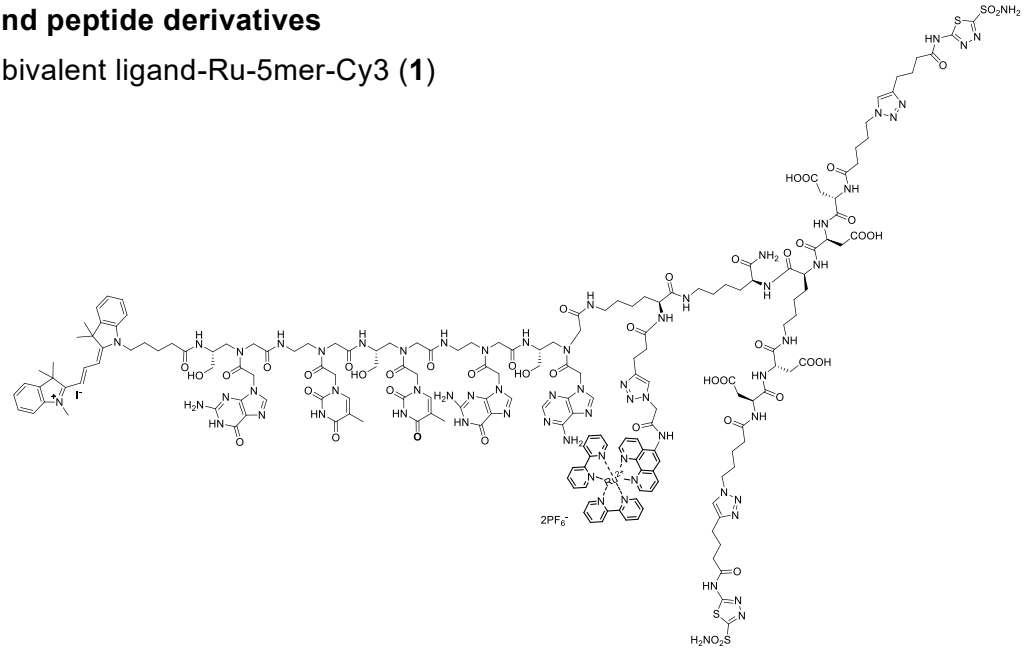

Chemical Formula: $C_{186}H_{229}N_{66}O_{45}RuS_4^{3+}$. Expected Mass: 4336.557. LC-MS (ESI^+): RT= 1.95 min. m/z found: 1446.4 $[M+H]^{3+}$, 1084.8 $[M+2H]^{4+}$, 868.7 $[M+3H]^{5+}$ Molecular Weight: 4338.5.

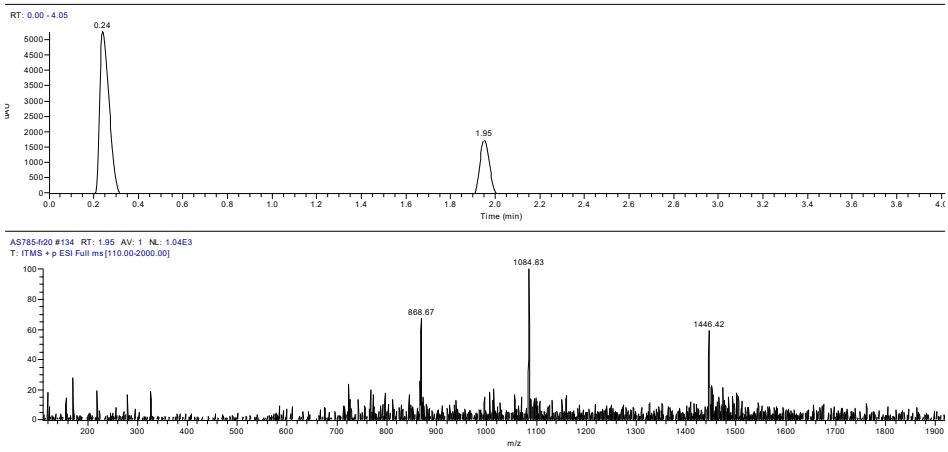

LC-MS trace of compound **1**.

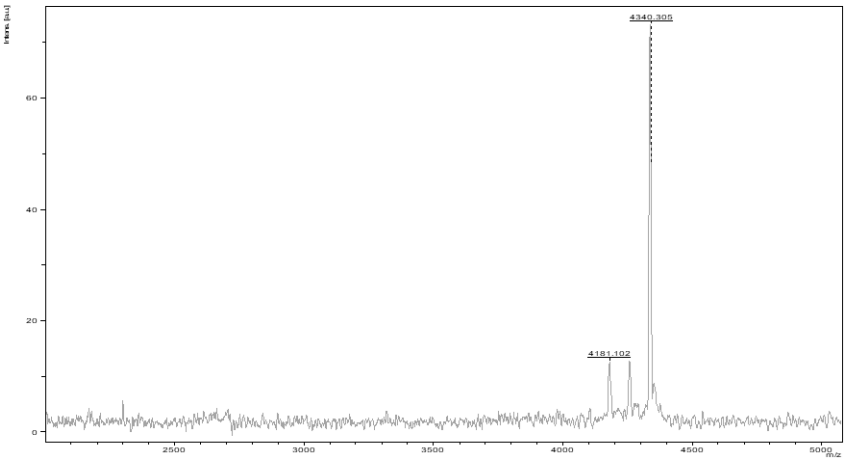

MALDI trace of compound **1**.

CA-IX bivalent ligand-5mer-Ru (**2**)

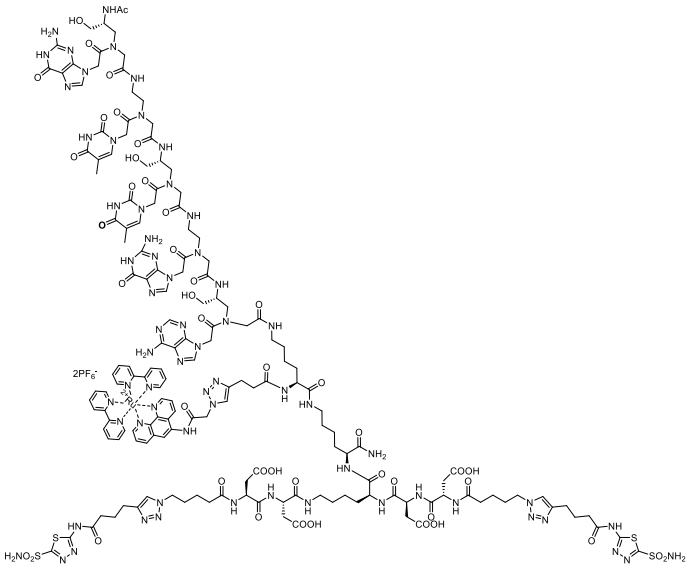

Chemical Formula: $C_{159}H_{198}N_{64}O_{45}RuS_4^{2+}$. Expected Mass: 3953.308. LC-MS (ESI^+): RT= 1.59 min. m/z found: 1977.7 $[M]^{2+}$, 798.1 $[M+H]^{3+}$ Molecular Weight: 3955.0

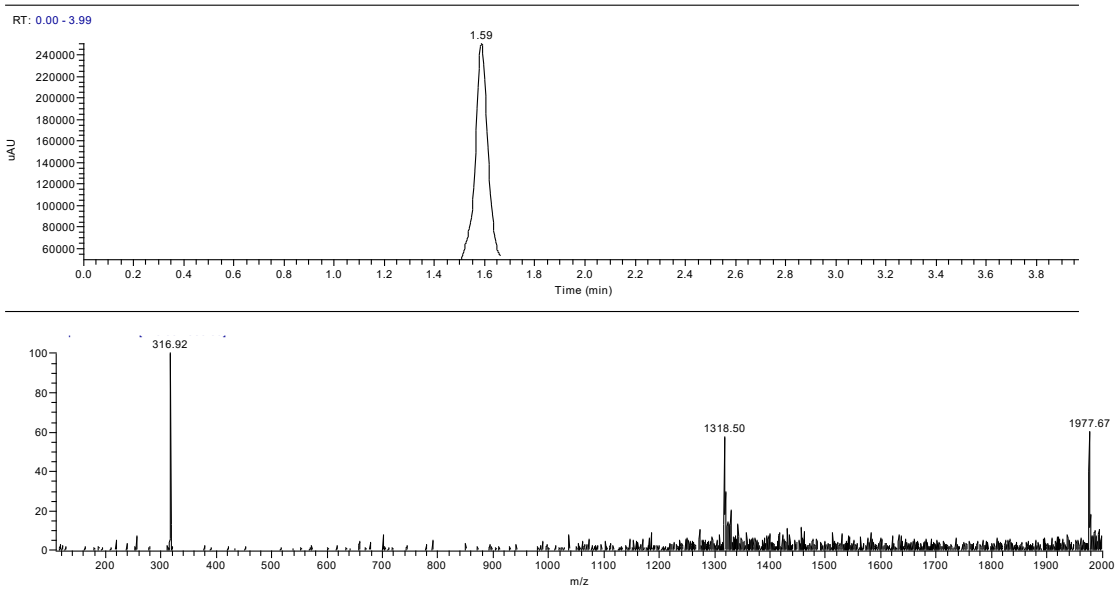

LC-MS trace of compound **2**.

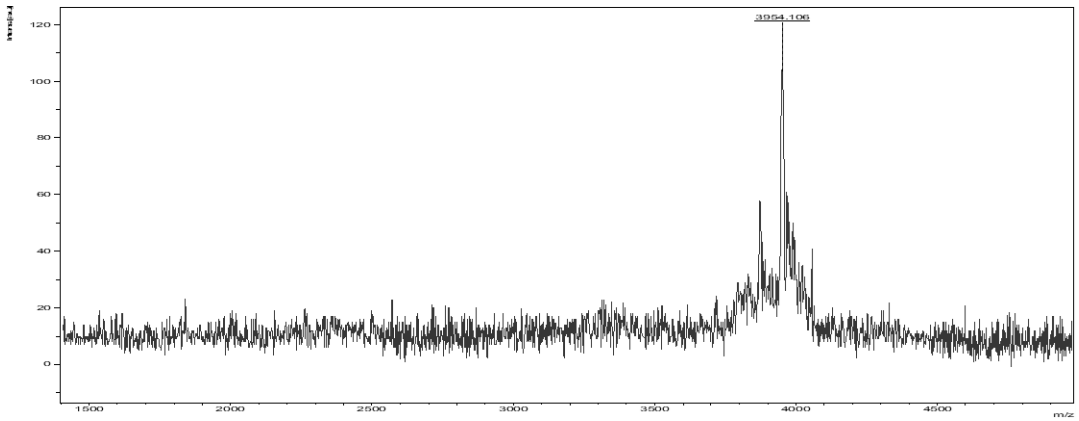

MALDI trace of compound **2**.

5mer-sulfonate-py^{+}-Rho (**3**)

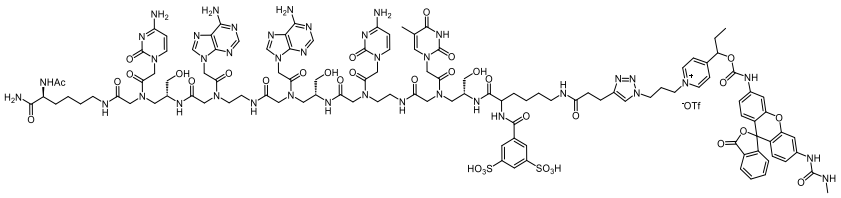

Chemical Formula: $C_{116}H_{141}N_{40}O_{34}S_2^{+}$. Expected Mass: 2701.997. LC-MS (ESI^{+}): RT= 1.69 min. m/z found: 1351.8 $[M+H]^{2+}$, 901.8 $[M+2H]^{3+}$ Molecular Weight: 2703.8

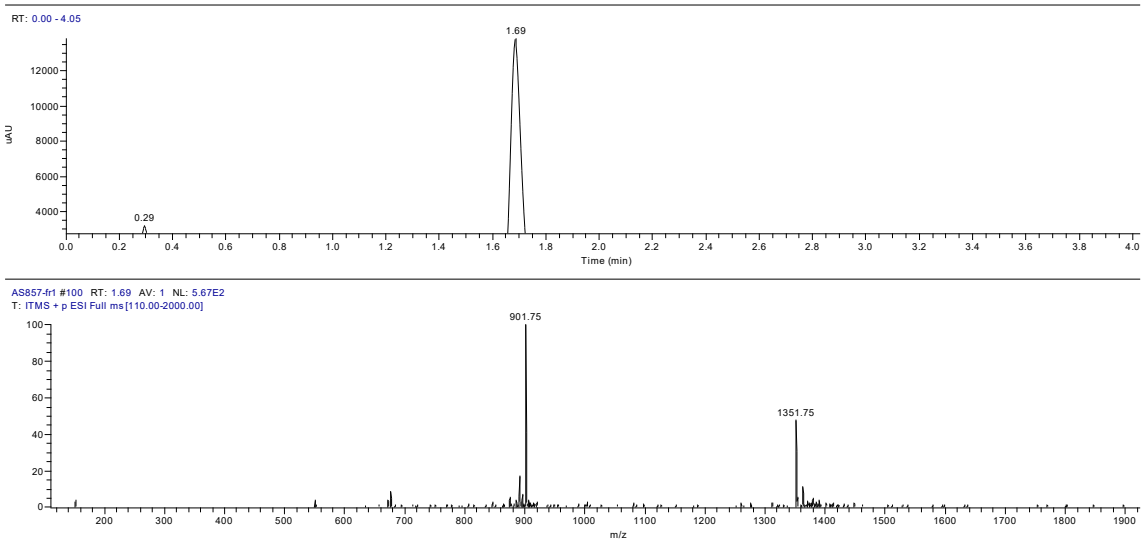

LC-MS trace of compound **3**.

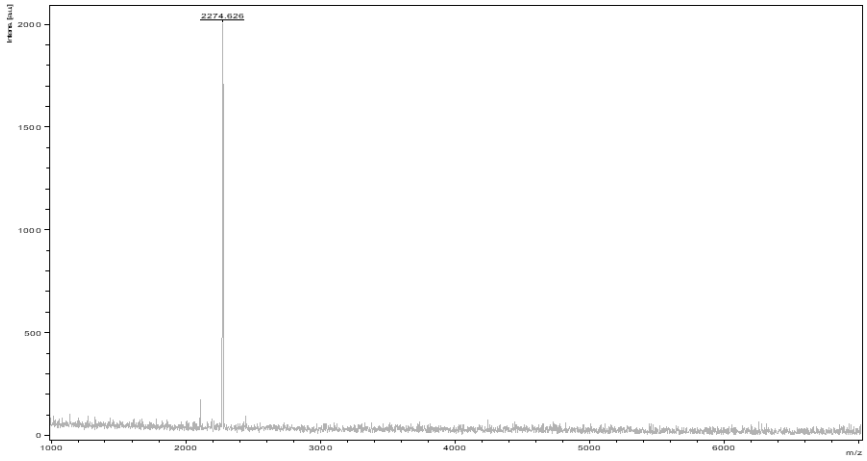

MALDI trace of compound **3**

Cy3-4mer-CAIX ligand (**4**)

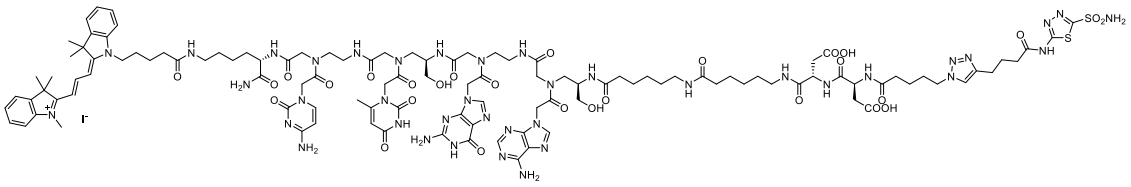

Chemical Formula: $C_{113}H_{154}N_{39}O_{28}S_2^+$. Expected Mass: 2569.126. LC-MS (ESI^+): RT= 2.00 min. m/z found: 1285.9 $[M+H]^{2+}$, 857.7 $[M+2H]^{3+}$ 643.5 $[M+3H]^{4+}$ Molecular Weight: 2570.8

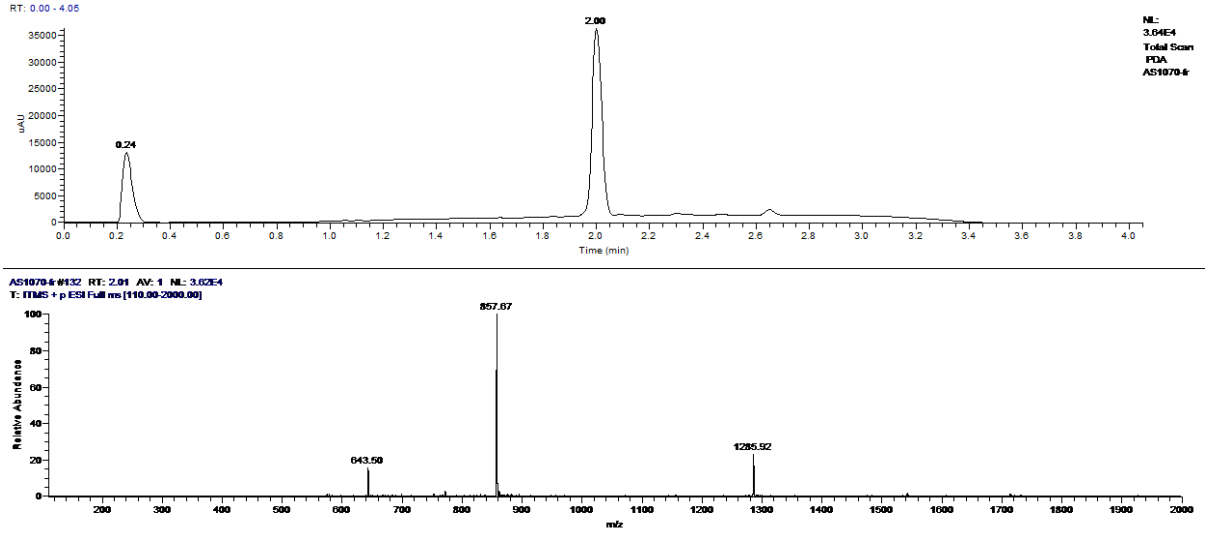

LC-MS trace of compound **4**

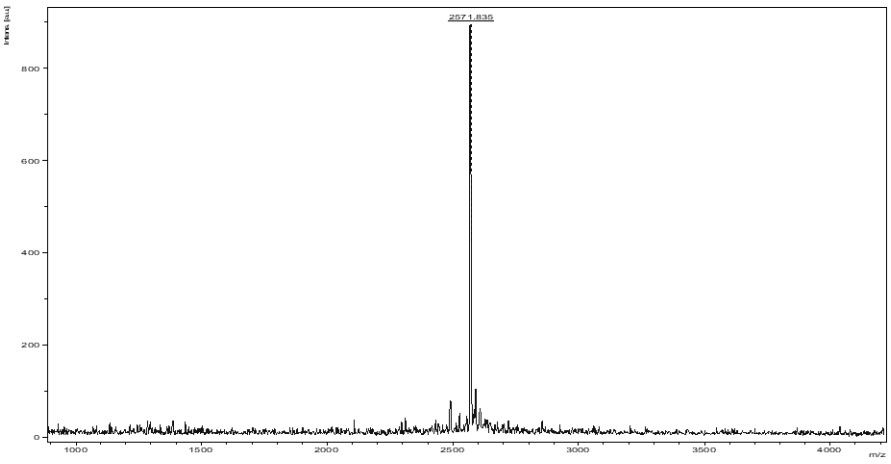

MALDI trace of compound **4**.

CAIX ligand-4mer (**5**)

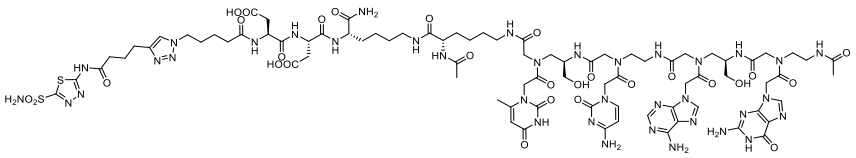

Chemical Formula: $C_{82}H_{115}N_{37}O_{28}S_2$. Expected Mass: 2129.815. LC-MS (ESI$^+$): RT= 1.37 min. m/z found: 1065.5 $[M+2H]^{2+}$, 711.3 $[M+3H]^{3+}$ Molecular Weight: 2131.1

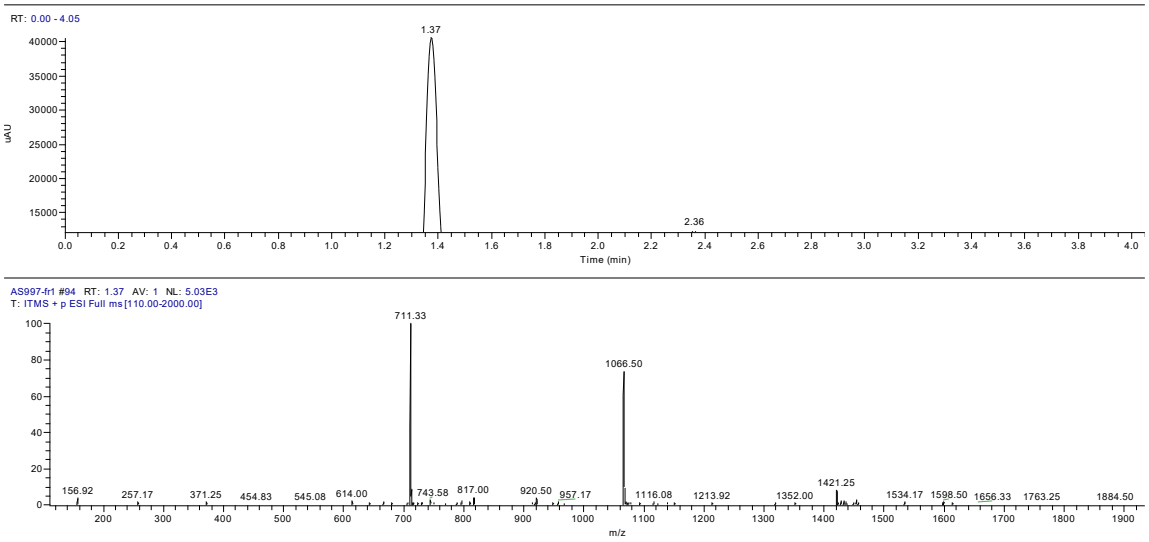

LC-MS trace of compound **5**.

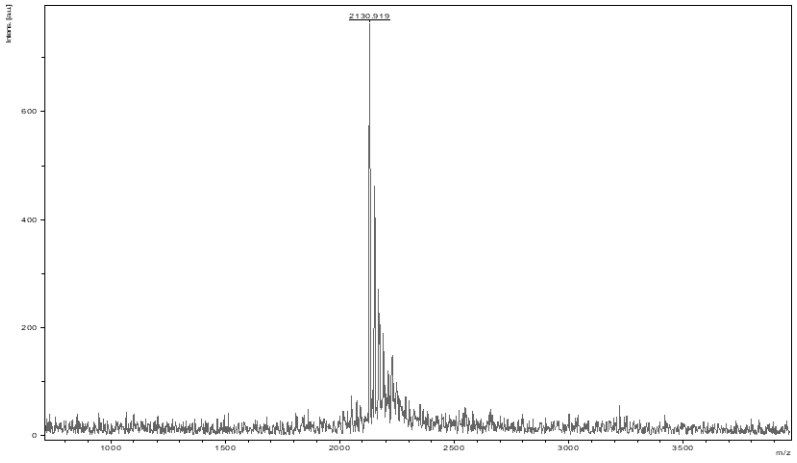

LC-MS trace of compound **5**.

4mer-CAIX ligand (**6**)

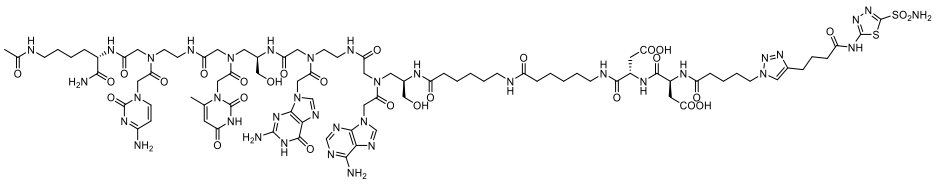

Chemical Formula: $C_{86}H_{123}N_{37}O_{28}S_2$. Expected Mass: 2185.878. LC-MS (ESI^+): RT= 1.39 min. m/z found: 1094.3 $[M+2H]^{2+}$, 730.1 $[M+3H]^{3+}$ Molecular Weight: 2187.3

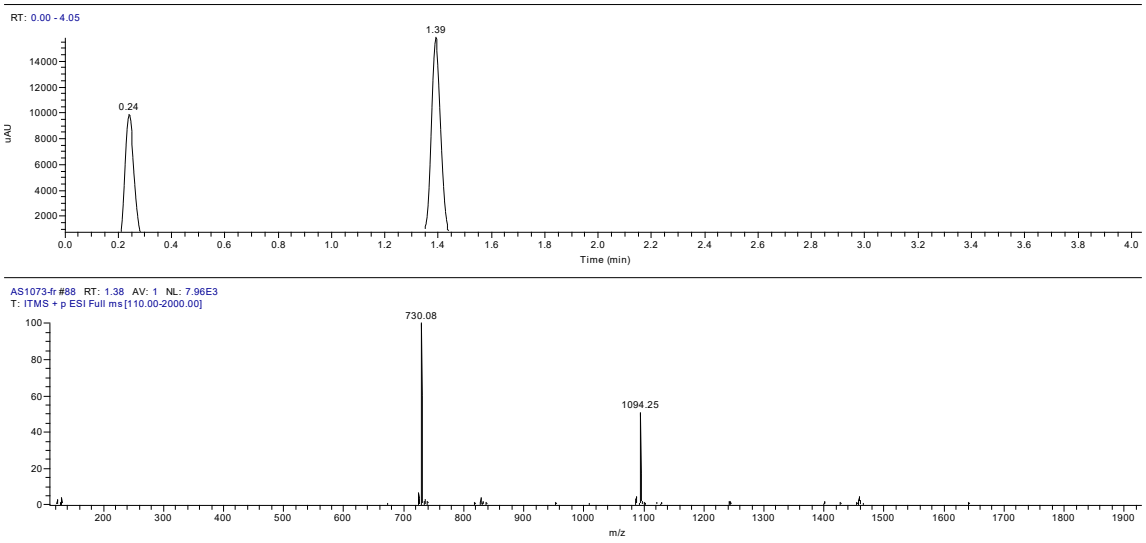

LC-MS trace of compound **6**.

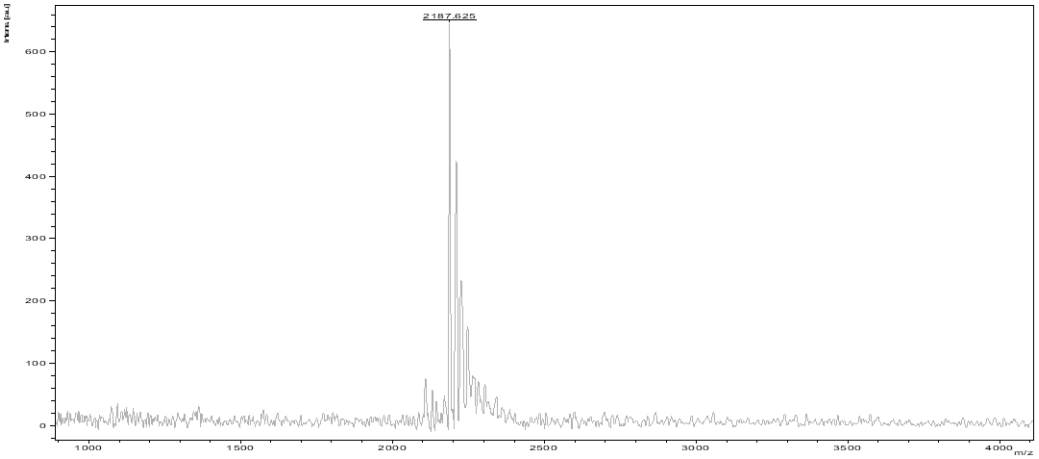

MALDI trace of compound **6**.

CAIX ligand-4mer-py^{+}-Cy$_3$ (**7**)

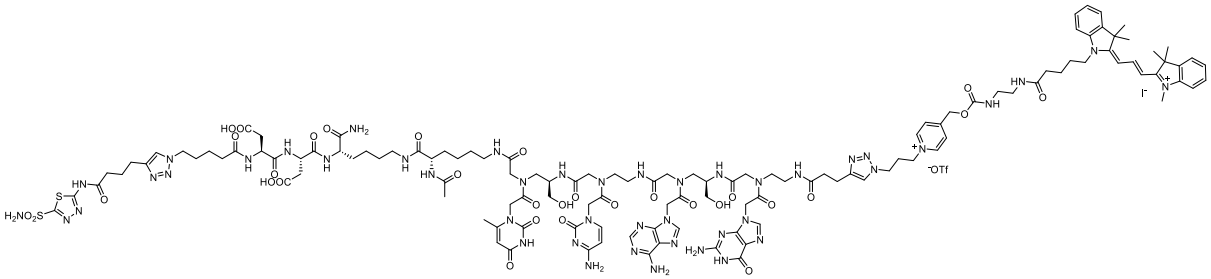

Chemical Formula: $C_{126}H_{169}N_{45}O_{31}S_2^{2+}$. Expected Mass: 2872.2462. LC-MS (ESI^{+}): RT= 2.00 min. m/z found: 1436.6 $[M]^{2+}$, 958.4 $[M+H]^{3+}$, 718.8 $[M+2H]^{4+}$ Molecular Weight: 2874.1

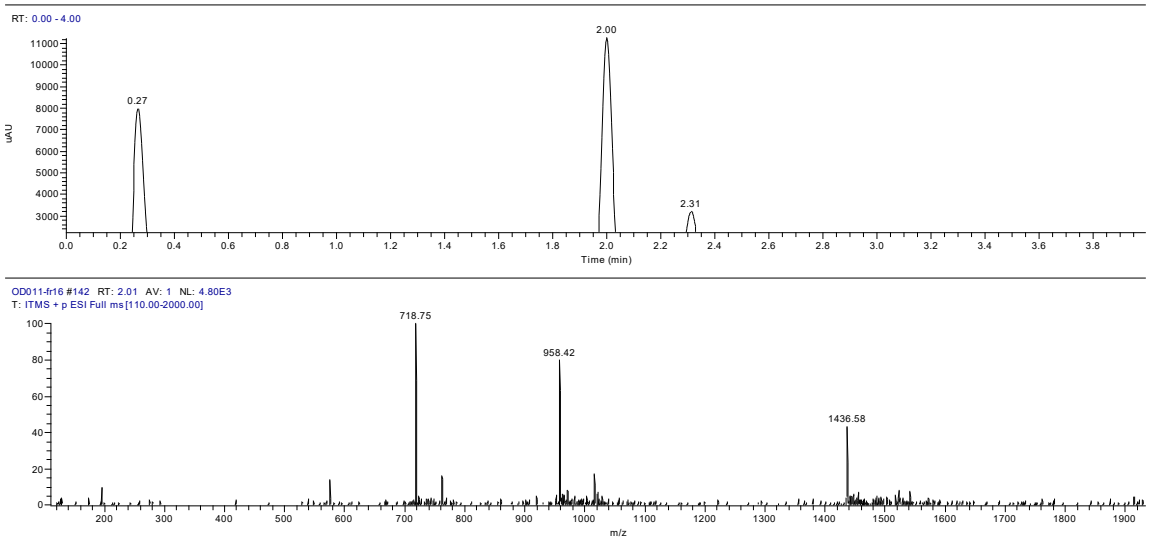

LC-MS trace of compound **7**.

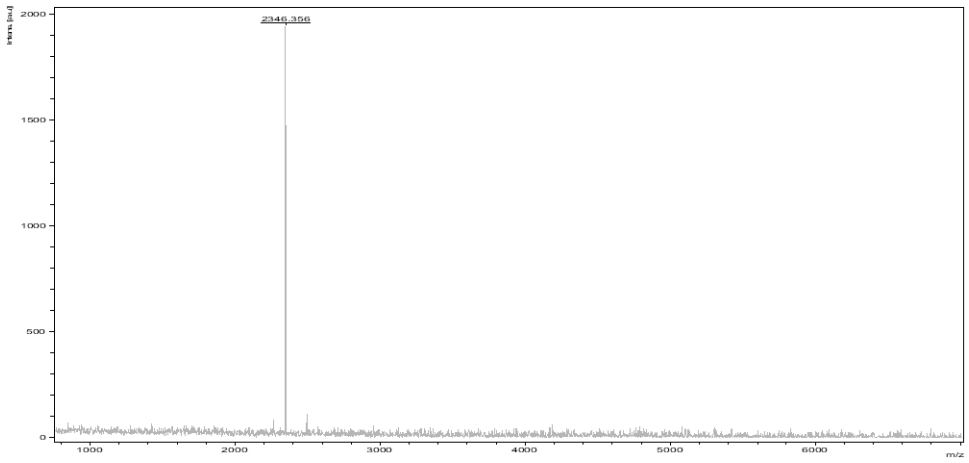

MALDI trace of compound **7**.

Ru-4mer-CAIX ligand (**8**)

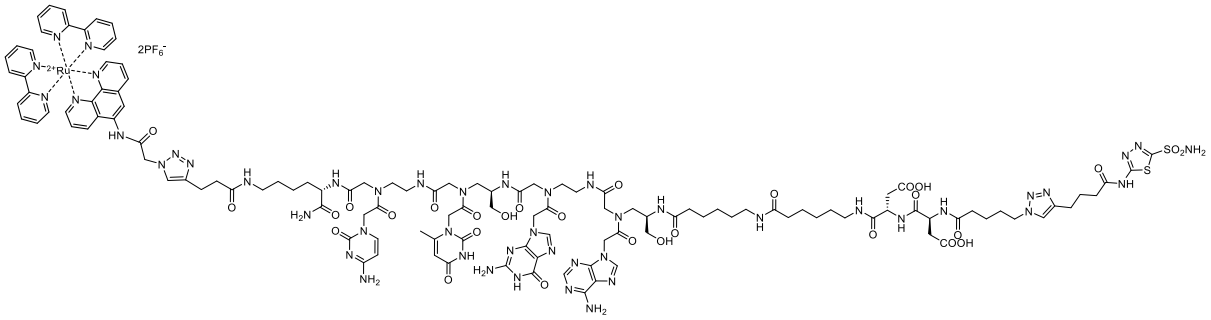

Chemical Formula: $C_{123}H_{151}N_{47}O_{29}RuS_2^{2+}$. Expected Mass: 2916.026. LC-MS (ESI^+): RT= 1.46 min. m/z found: 1459. $[M]^{2+}$, 972.8 $[M+H]^{3+}$, 792.9 $[M+2H]^{4+}$ 584.3 $[M+3H]^{5+}$ Molecular Weight: 2917.0

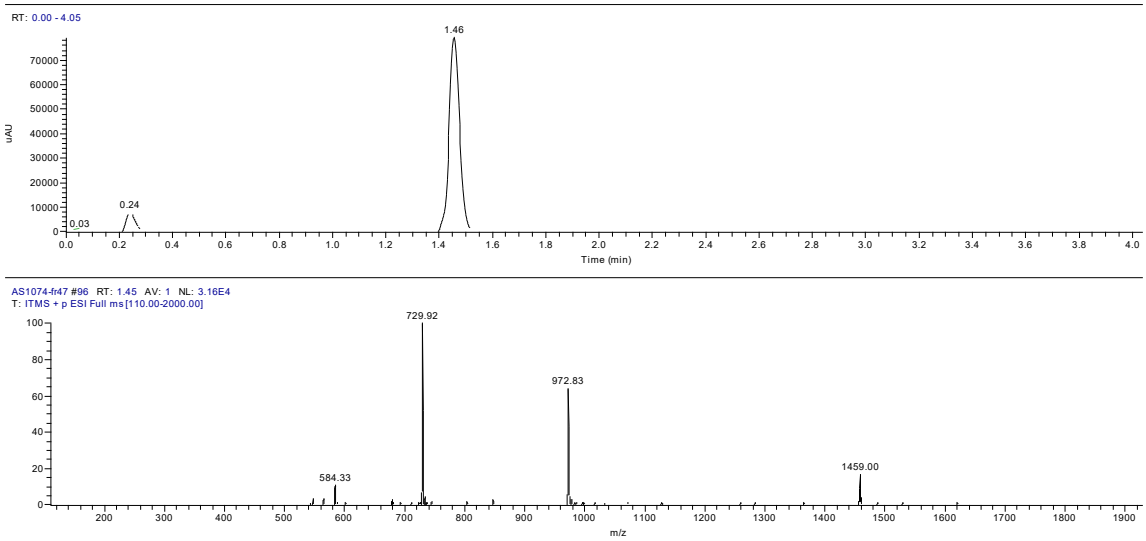

LC-MS trace of compound **8**.

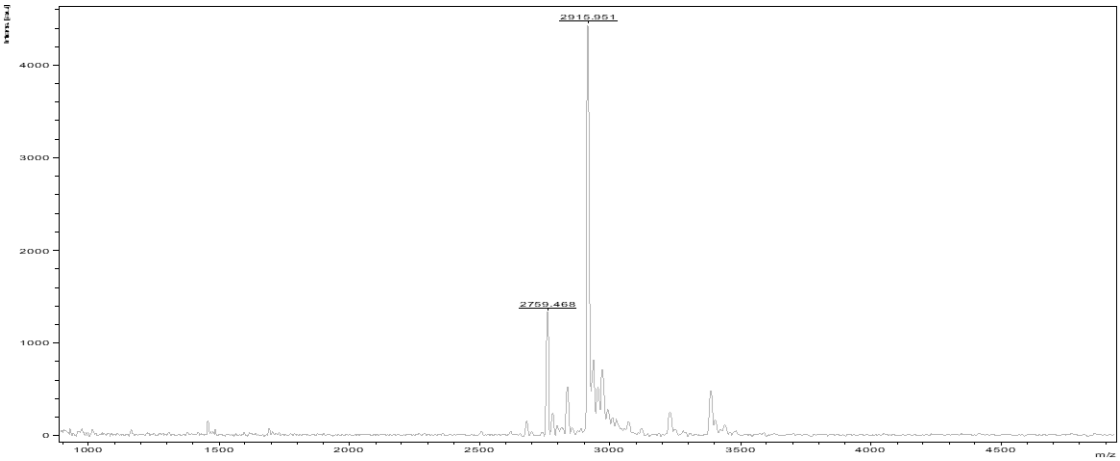

MALDI trace of compound **8**.

14mer (**9**)

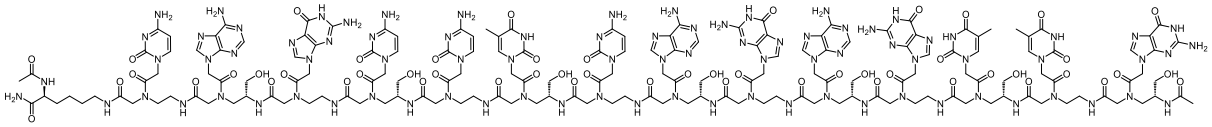

Chemical Formula: $C_{167}H_{218}N_{84}O_{52}$. Expected Mass: 4231.699. LC-MS (ESI^+): RT= 1.13 min. m/z found: 1412.3 $[M+3H]^{3+}$, 1059.5 $[M+4H]^{4+}$ 847.8 $[M+5H]^{5+}$ Molecular Weight: 4234.1

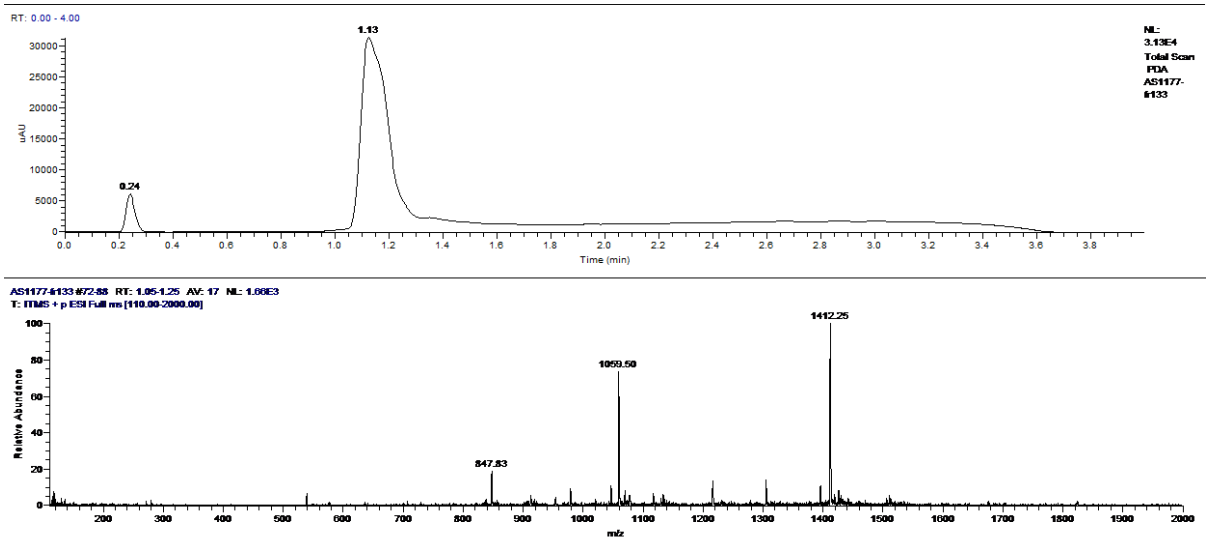

LC-MS trace of compound **9**.

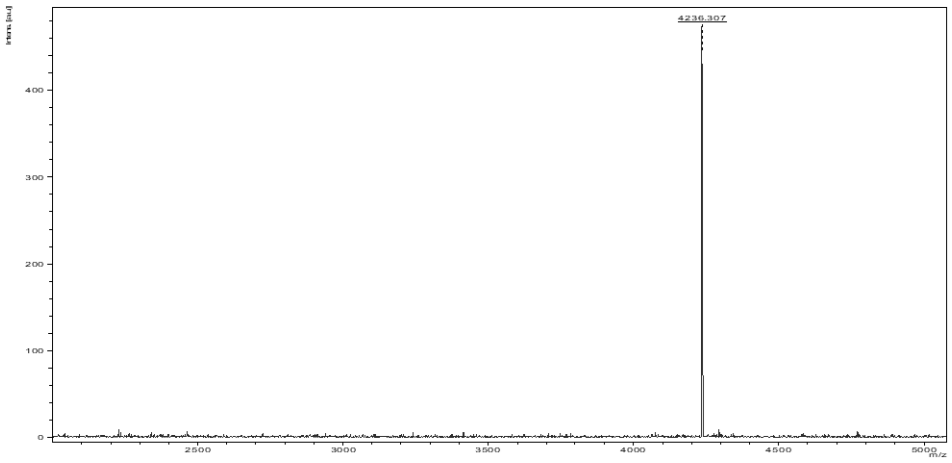

MALDI trace of compound **9**.

Ru-9mer (**10**)

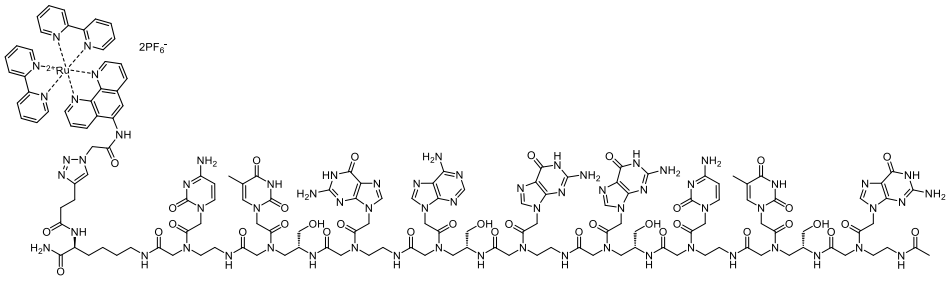

Chemical Formula: $C_{148}H_{174}N_{66}O_{36}Ru^{2+}$. Expected Mass: 3553.284. LC-MS (ESI^+): RT= 1.28 min. m/z found: 1185.7 $[M+H]^{3+}$, 889.2 $[M+2H]^{4+}$, 711.5 $[M+3H]^{5+}$ 593.1 $[M+4H]^{6+}$ Molecular Weight: 3554.5

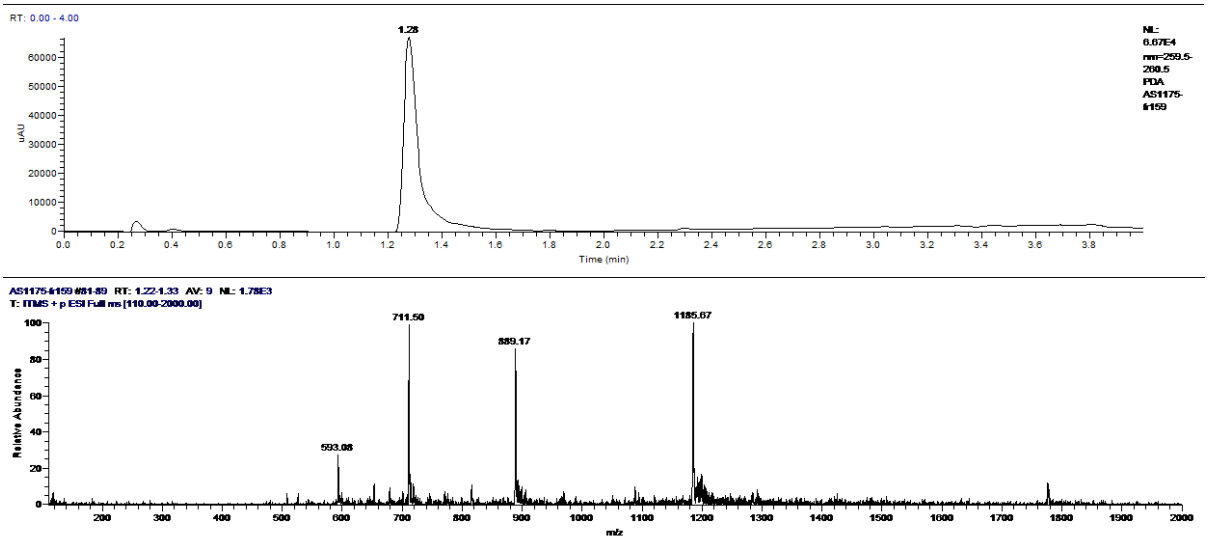

LC-MS trace of compound **10**.

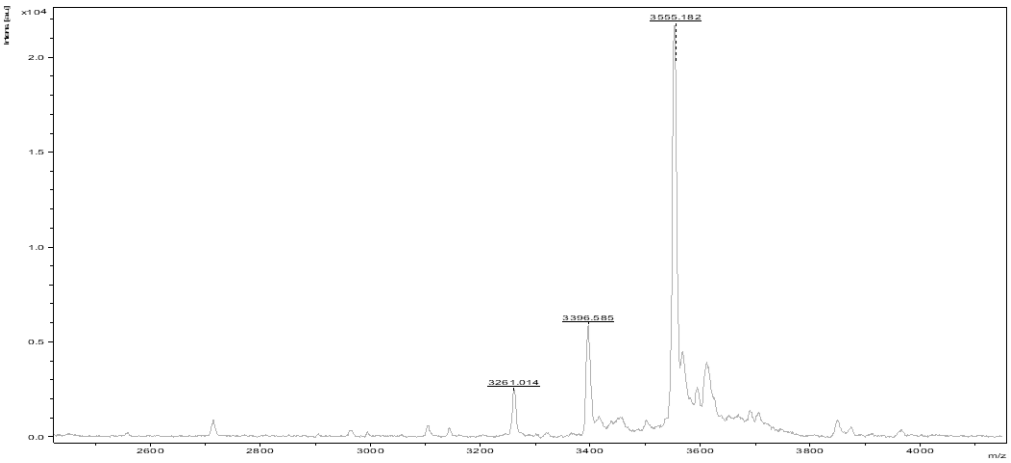

MALDI trace of compound **10**.

5mer-py^{+}-Cou (**11**)

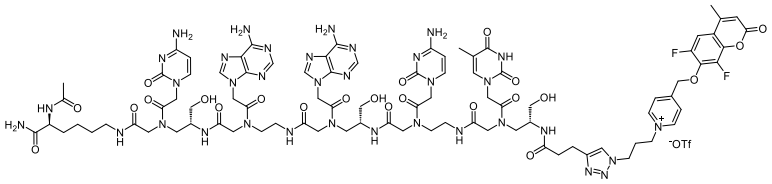

Chemical Formula: $C_{88}H_{110}F_2N_{35}O_{23}^{+}$. Expected Mass: 2062.847. LC-MS (ESI^{+}): RT= 1.37 min. m/z found: 1375.8 $[M+H]^{2+}$, 1032.0 $[M+2H]^{3+}$ 688.6 $[M+3H]^{4+}$ 517.1 $[M+4H]^{5+}$ Molecular Weight: 2064.1

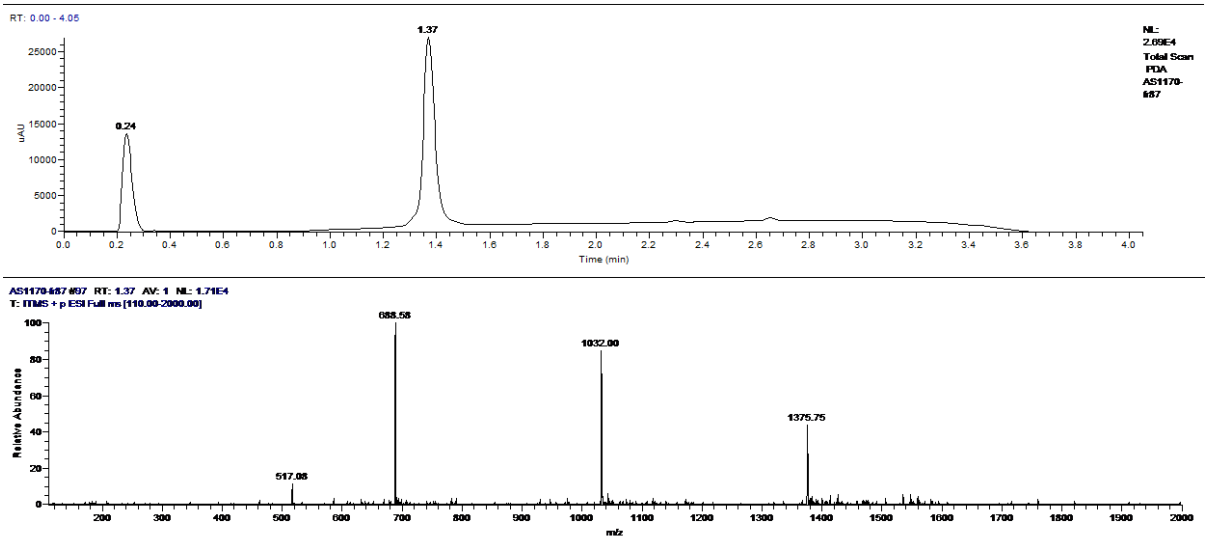

LC-MS trace of compound **11**.

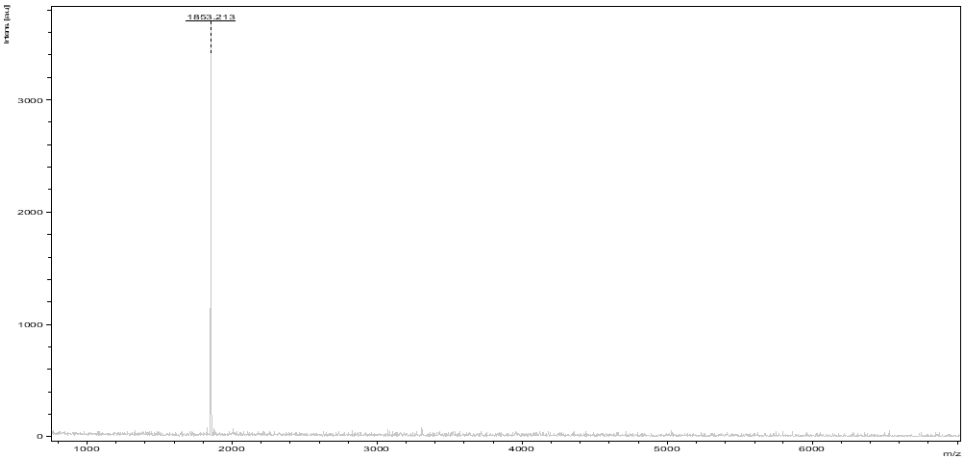

MALDI trace of compound **11**.

9mer (**12**)

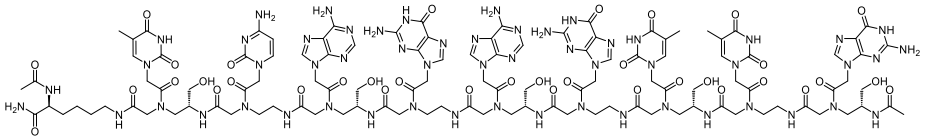

Chemical Formula: $C_{113}H_{149}N_{55}O_{36}$. Expected Mass: 2852.151. LC-MS (ESI^+): RT= 1.15 min. m/z found: 1427.5 $[M+2H]^{2+}$, 952.2 $[M+3H]^{3+}$ 714.2 $[M+4H]^{4+}$ Molecular Weight: 2853.8

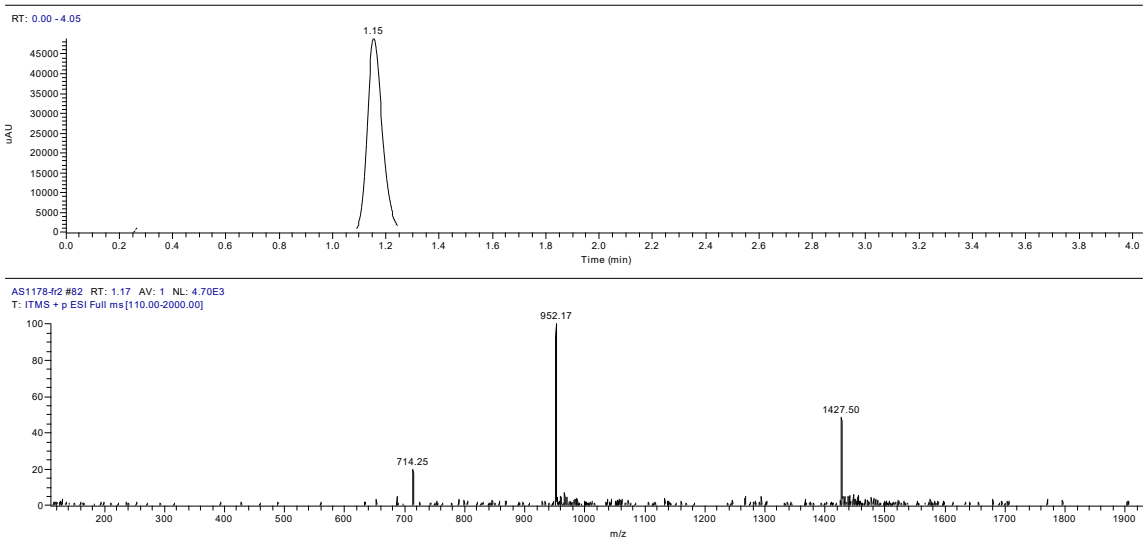

LC-MS trace of compound **12**.

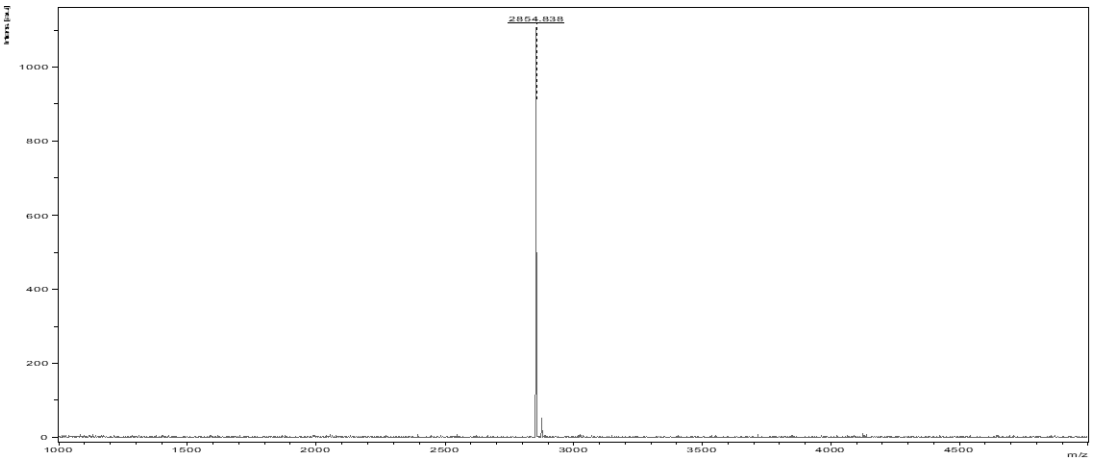

MALDI trace of compound **12**.

Ru-4mer (**13**)

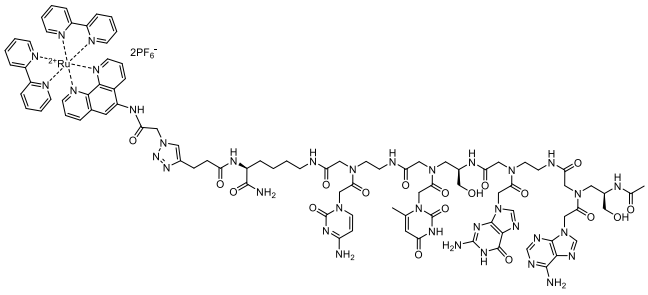

Chemical Formula: $C_{92}H_{104}N_{36}O_{18}Ru^{2+}$. Expected Mass: 2102.736. LC-MS (ESI^+): RT= 1.31 min. m/z found: 1051.4 $[M+]^{2+}$, 701.4 $[M+H]^{3+}$, 526.4 $[M+2H]^{4+}$ Molecular Weight: 2103.1

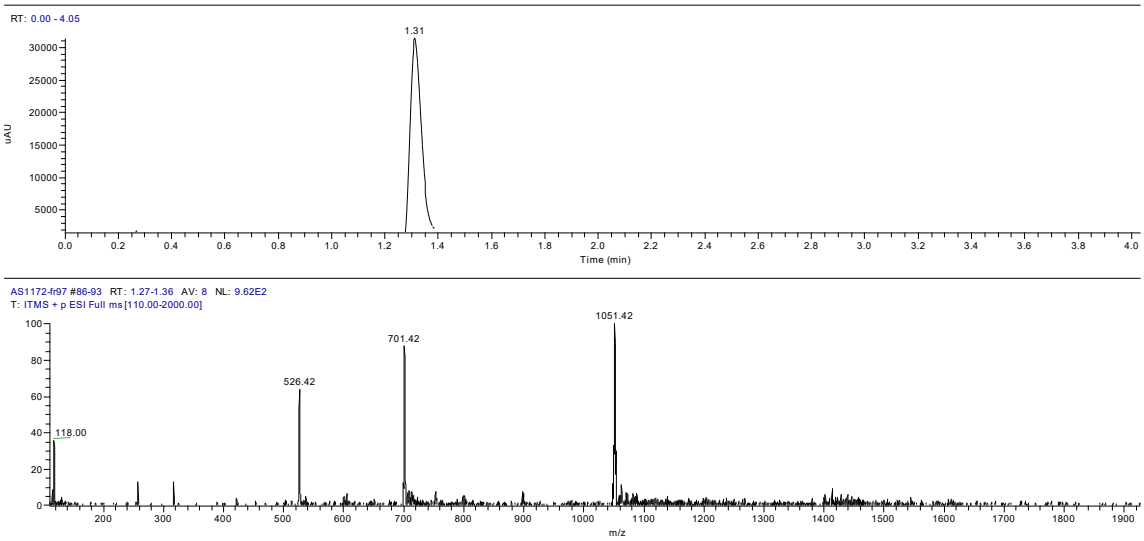

LC-MS trace of compound **13**.

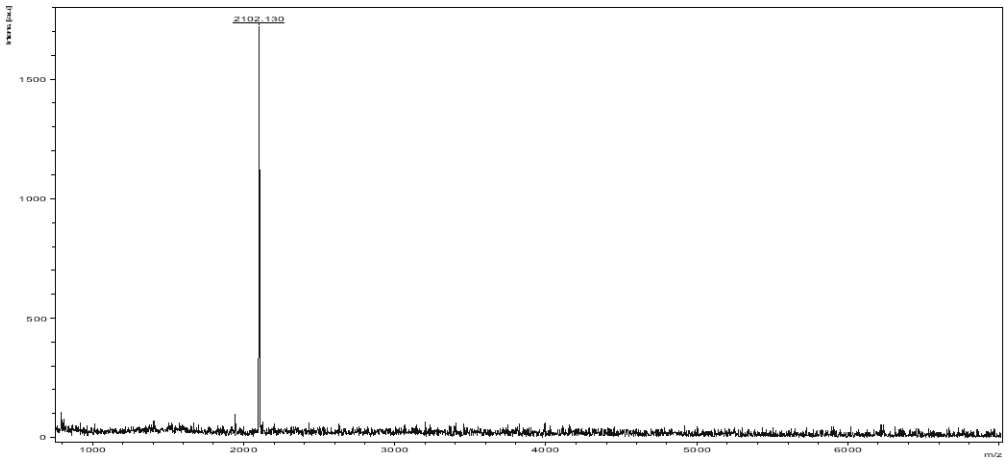

LC-MS trace of compound **13**.

CAIX ligand-9mer (**14**)

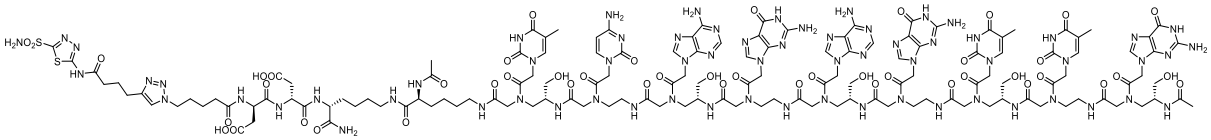

Chemical Formula: $C_{140}H_{188}N_{66}O_{47}S_2$. Expected Mass: 3609.379. LC-MS (ESI^+): RT= 1.36 min. m/z found: 1806.2 $[M+2H]^{2+}$, 1204.8 $[M+3H]^{3+}$ 903.8 $[M+4H]^{4+}$ Molecular Weight: 3611.6y

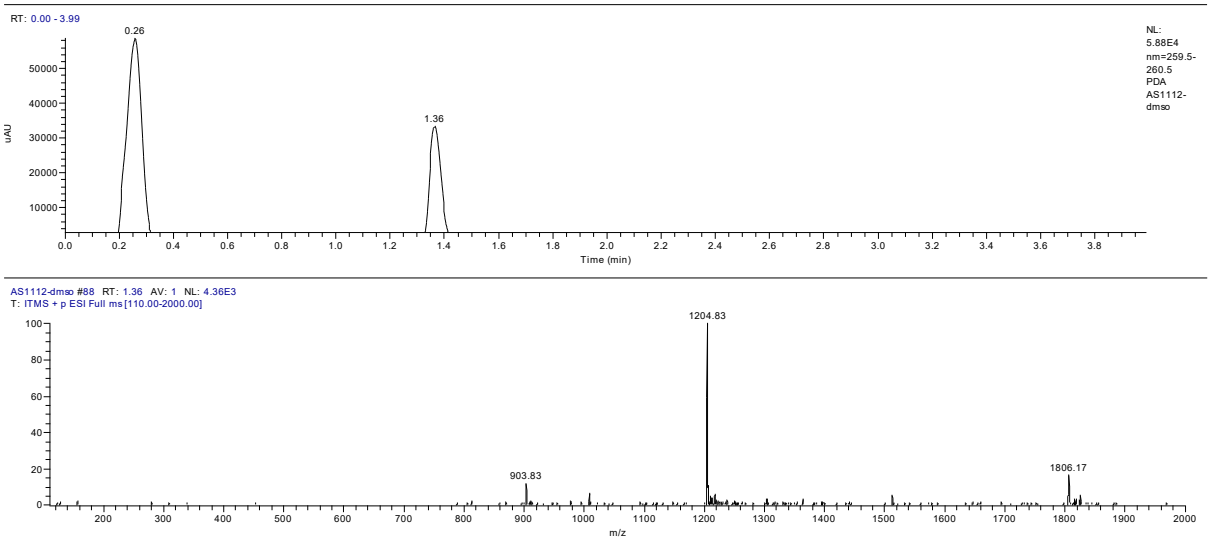

LC-MS trace of compound **14**.

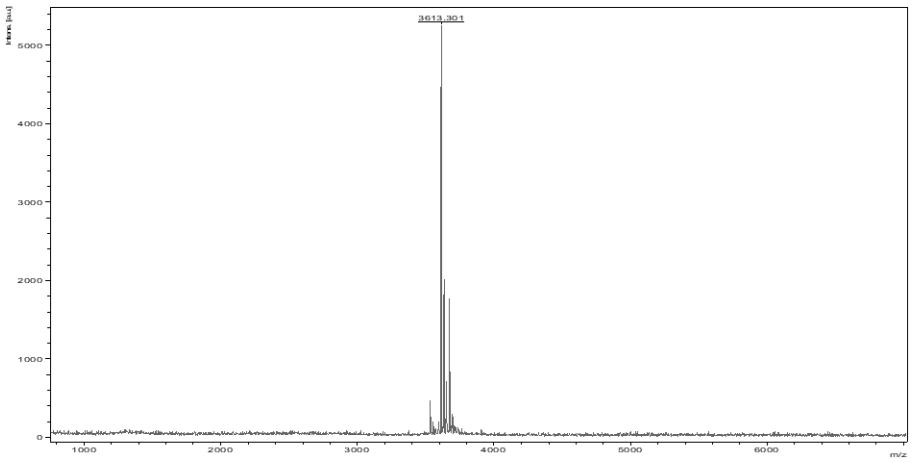

LC-MS trace of compound **14**.

Sulphonate-5mer-py^{+}-MMAE (**15**)

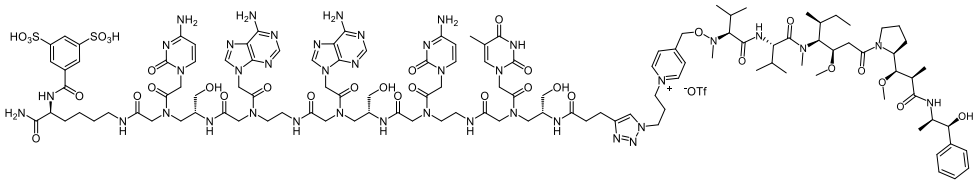

Chemical Formula: $C_{122}H_{173}N_{40}O_{34}S_2^{+}$. Expected Mass: 2806.247. LC-MS (ESI^{+}): RT= 1.88 min. m/z found: 1418.3 $[M+H]^{2+}$, 945.9 $[M+2H]^{3+}$ Molecular Weight: 2808.1

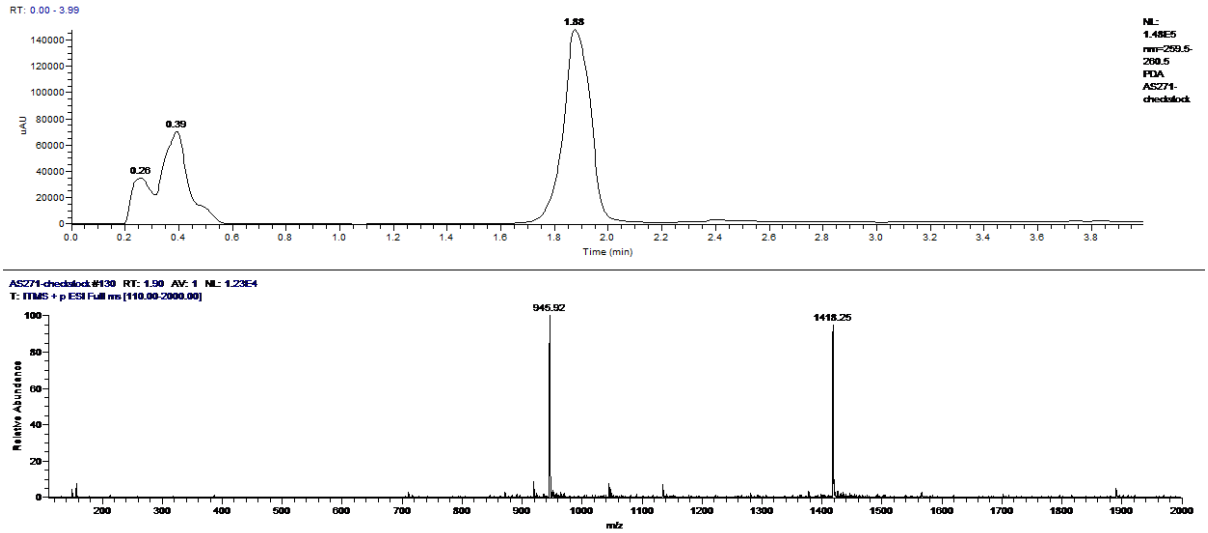

LC-MS trace of compound **16**.

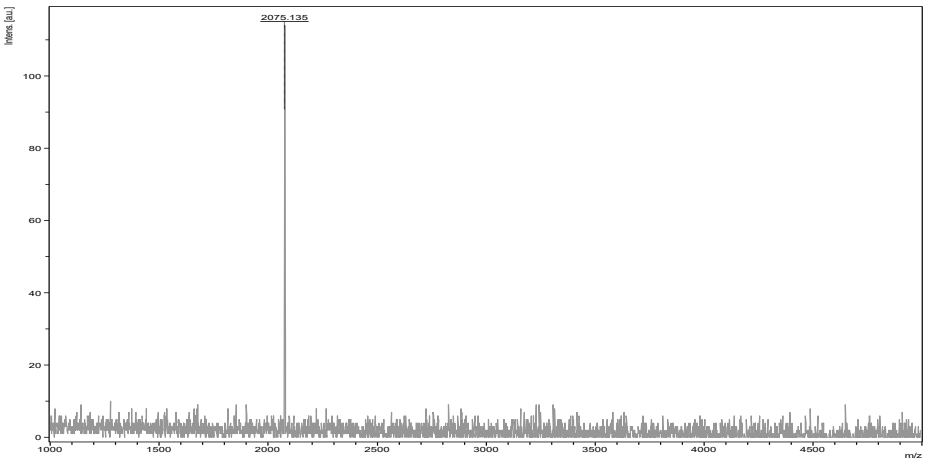

MALDI trace of compound **16**.

NMR spectra

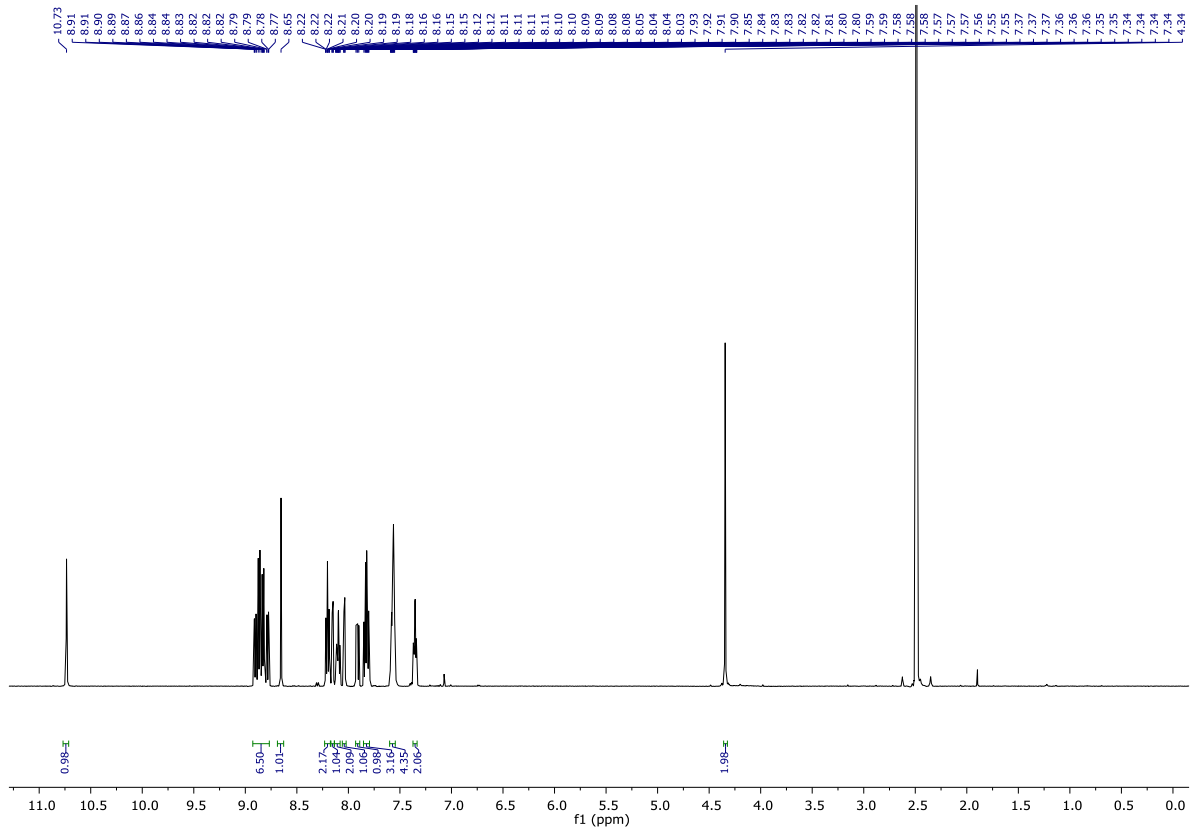

^{1}H Spectrum of **S1**

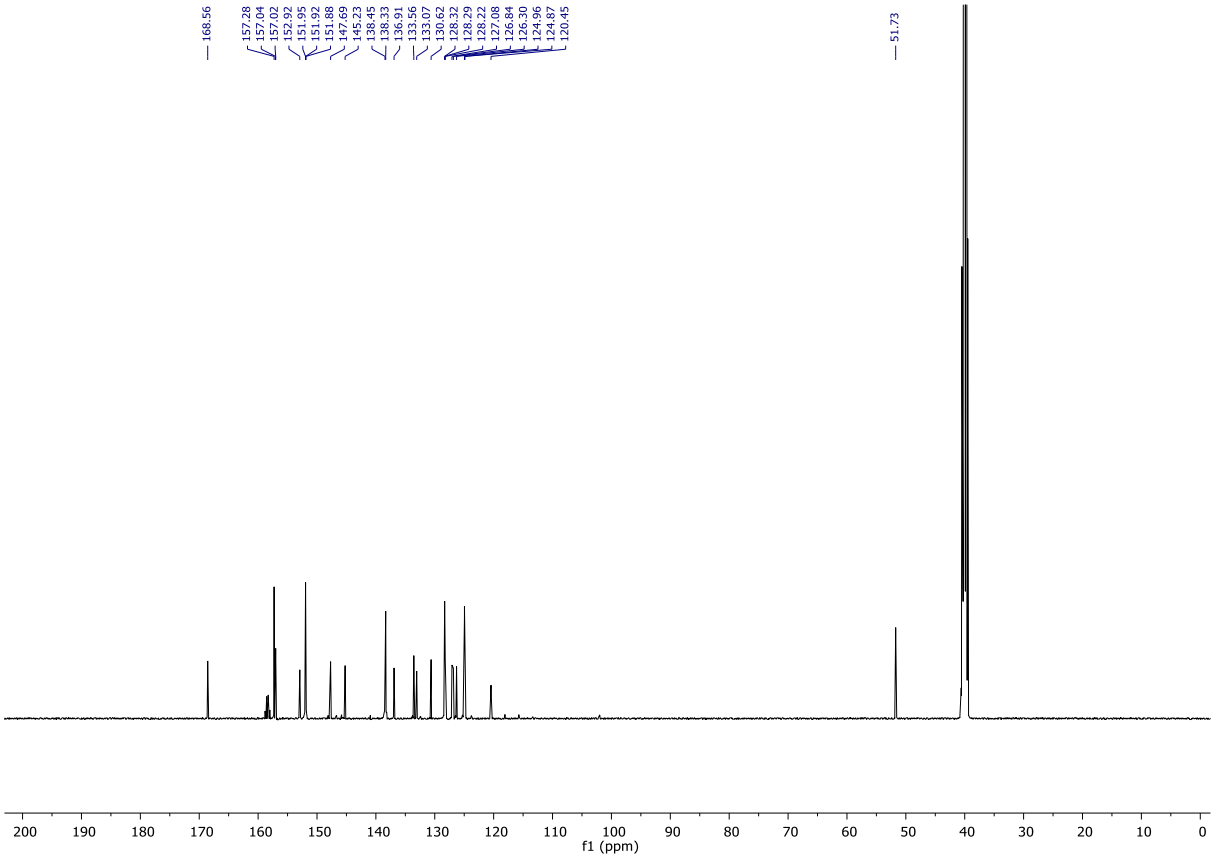

^{13}C Spectrum of **S1**

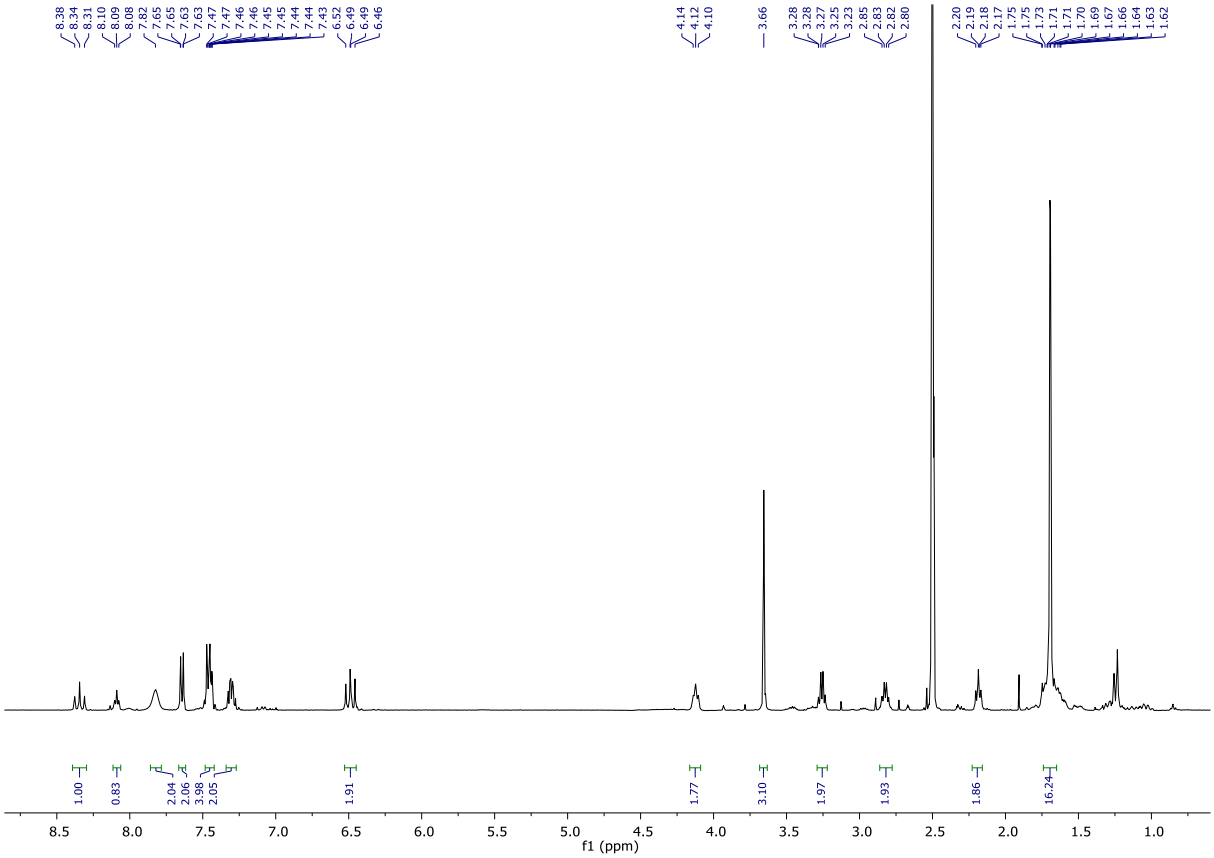

^{1}H Spectrum of **S3**

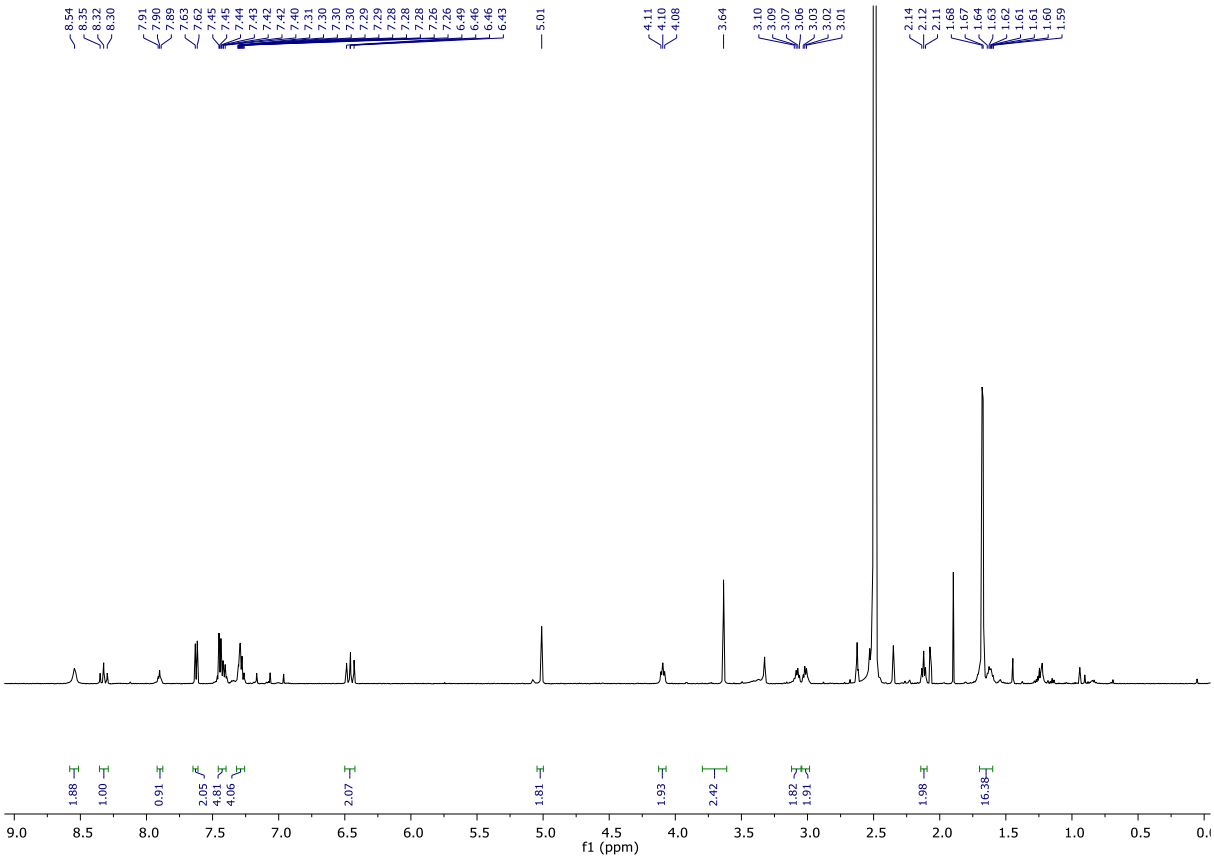

^{1}H Spectrum of **S4**

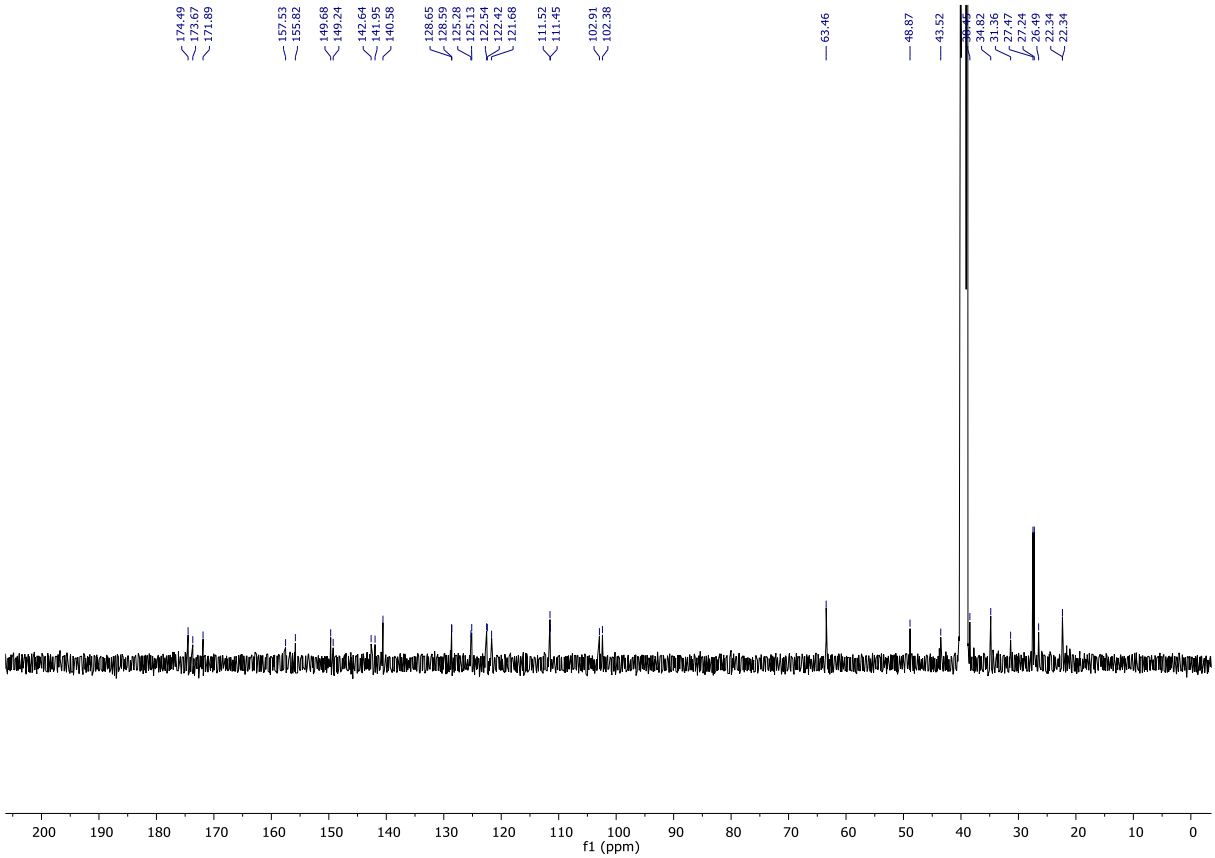

^{13}C Spectrum of **S4**

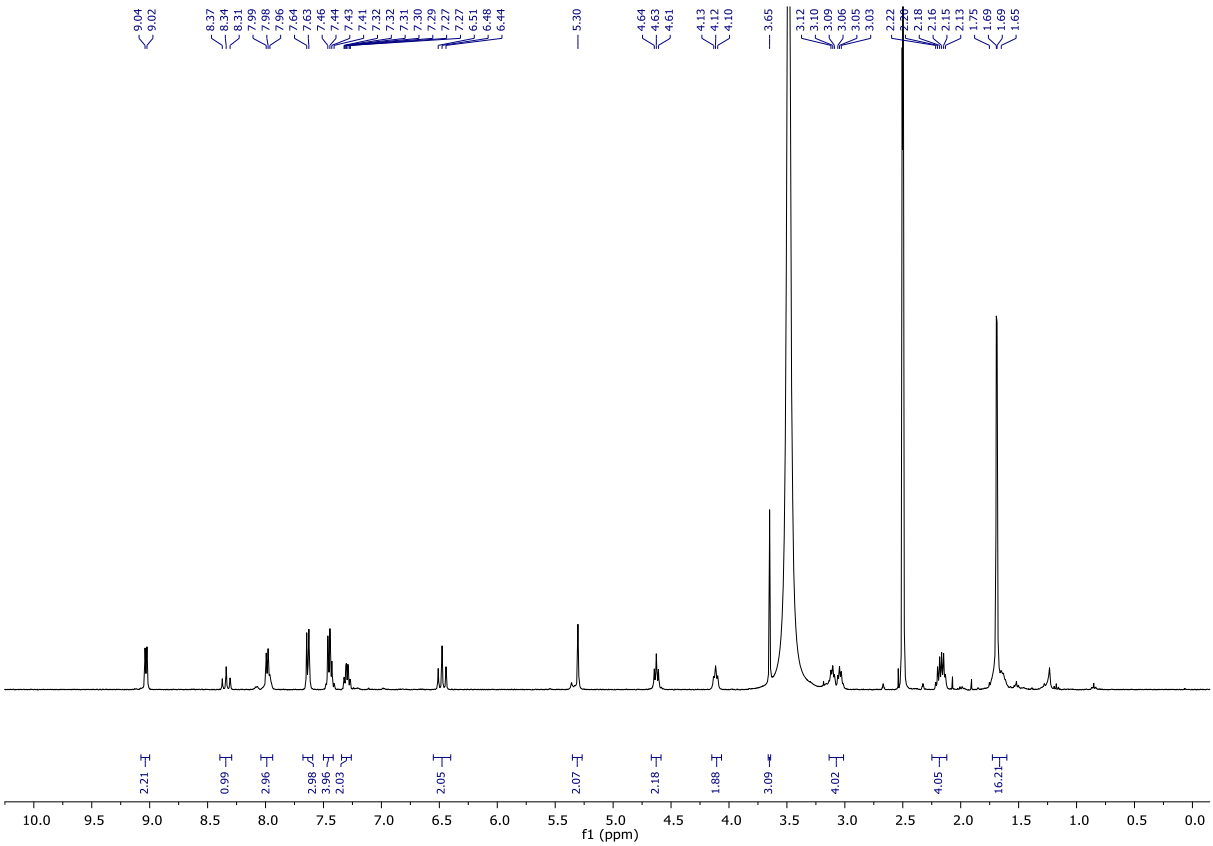

^{1}H Spectrum of **S5**

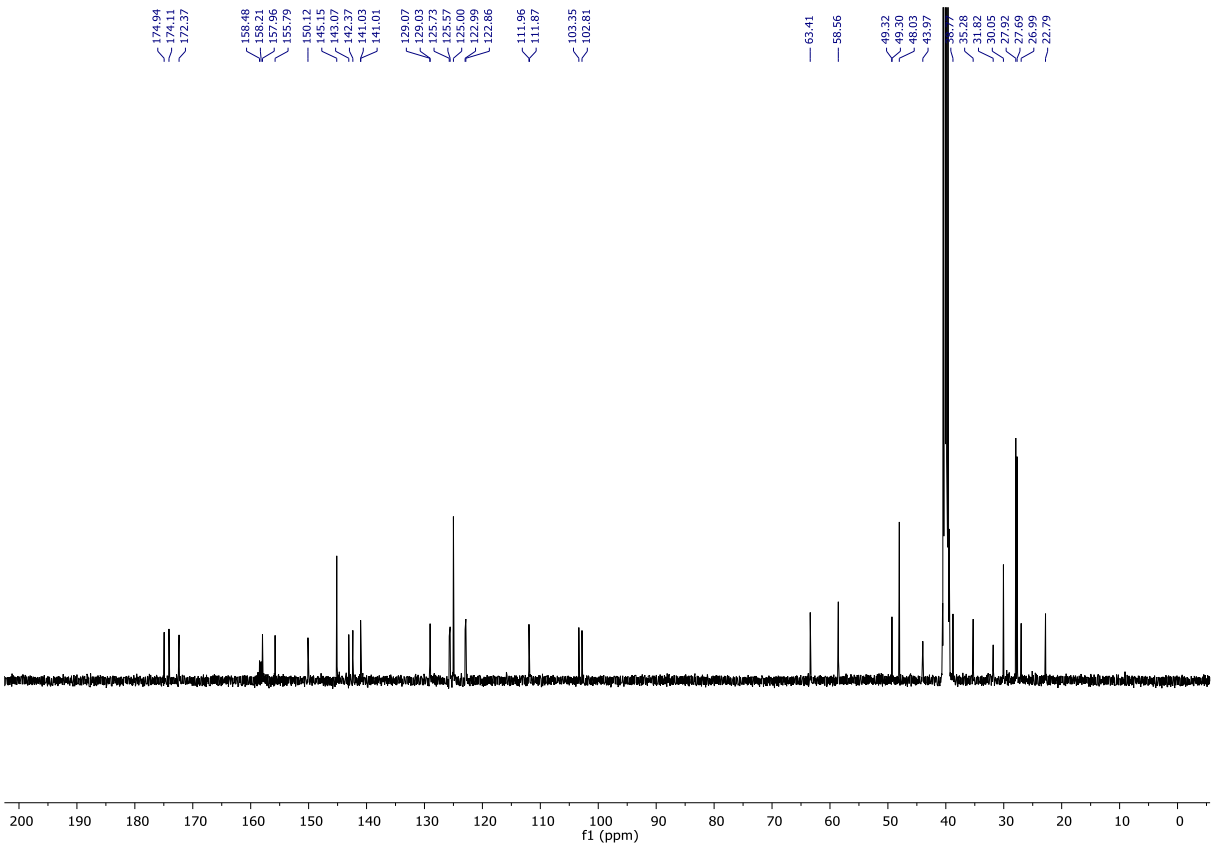

^{13}C Spectrum of **S5**

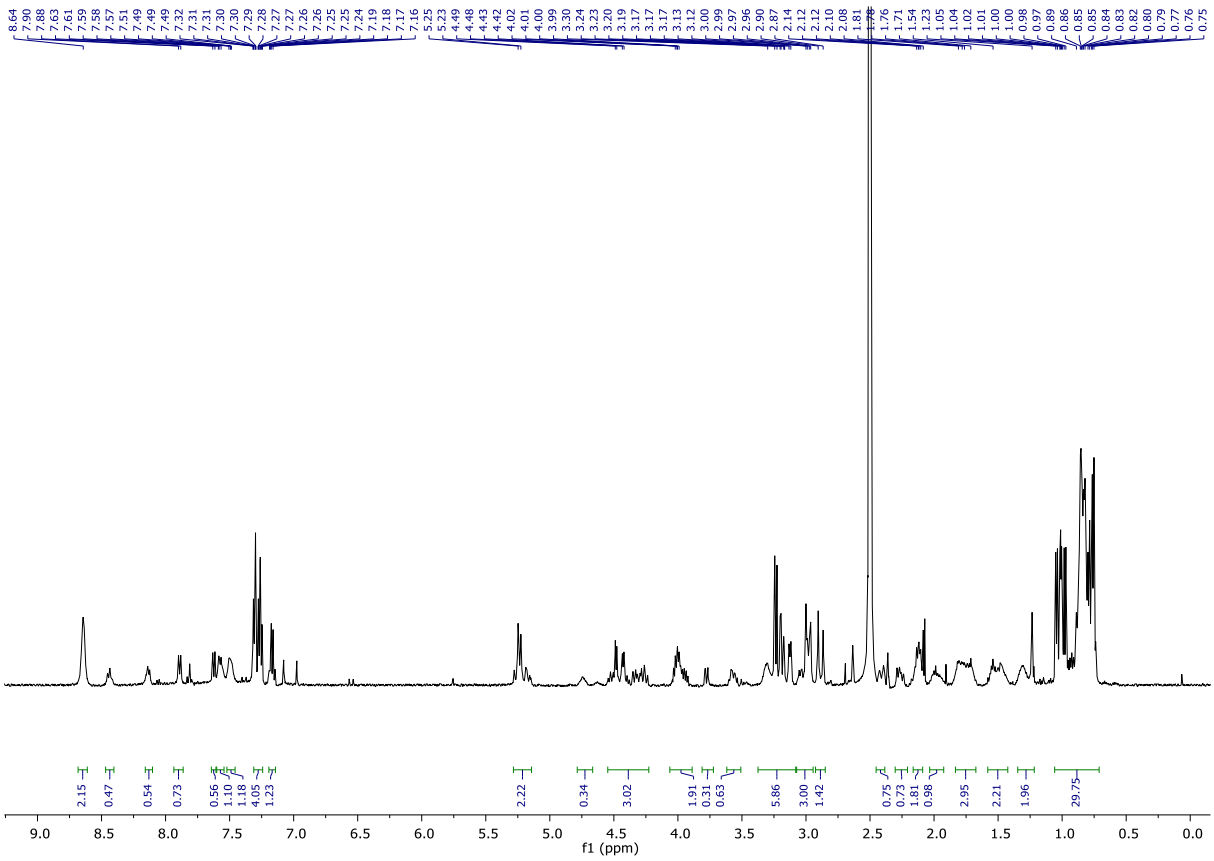

^{1}H Spectrum of **S6**

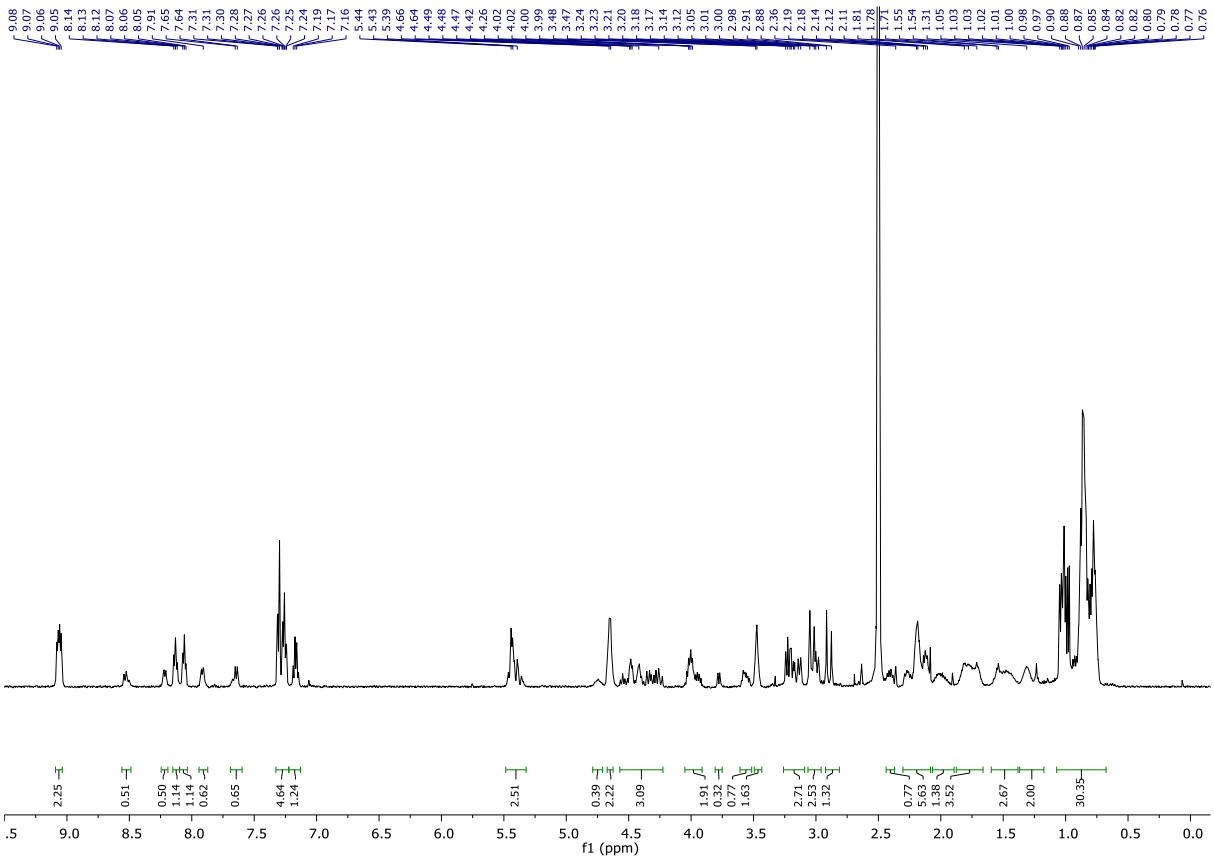

^{1}H Spectrum of **S7**

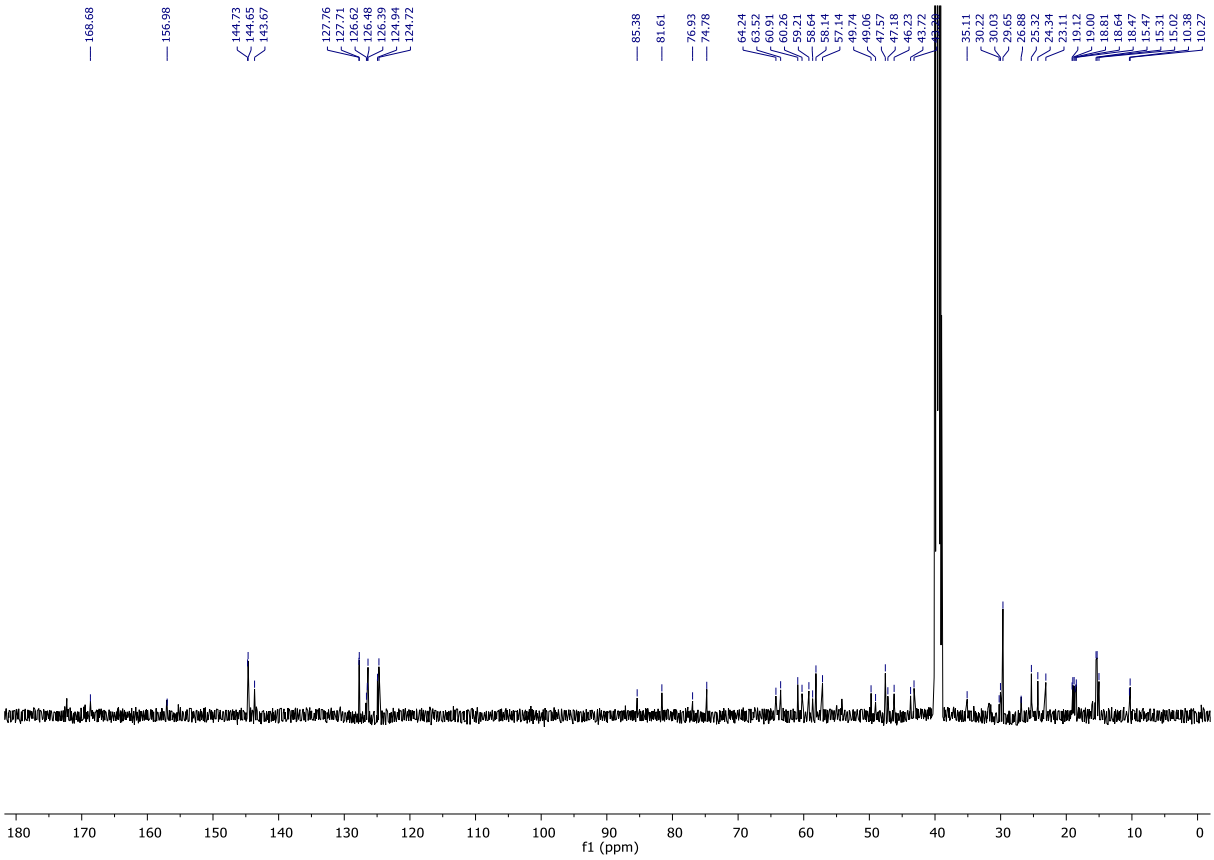

^{13}C Spectrum of **S7**

Supplementary References

1. Chang D.; Lindberg E.; Winssinger N. Critical Analysis of Rate Constants and Turnover Frequency in Nucleic Acid-Templated Reactions: Reaching Terminal Velocity. *J. Am. Chem. Soc.* **2017,** *139*, 1444-1447.

2. Lindberg, E.; Angerani, S.; Anzola, M.; Winssinger, N., Luciferase-induced photoreductive uncaging of small-molecule effectors. *Nat Commun* **2018,** *9*.

3. Keller S. *et al.* Light-driven electron injection from a biotinylated triarylamine donor to $[Ru(diimine)_3]^{2+}$-labeled streptavidin *Org. Biomol. Chem.*, **2016**, *14*, 7197-7201.

4. Chouikhi D., et al. Expanding the Scope of PNA-Encoded Synthesis (PES): Mtt-Protected PNA Fully Orthogonal to Fmoc Chemistry and a Broad Array of Robust Diversity-Generating Reactions. *Chem. Eur. J.* **2018**, *18*, 12698-12704.

5. Krall, N.; Pretto, F.; Neri, D., A bivalent small molecule-drug conjugate directed against carbonic anhydrase IX can elicit complete tumour regression in mice. *Chem Sci* **2014,** *5*, 3640-3644.

Supplementary Material of Chapter II

Materials and methods

Each reaction in an organic solvent was performed under anhydrous conditions under Ar or N_2. All reagents and solvents were purchased from commercial sources and were used without any further purification. Anhydrous solvents were obtained by passing them through commercially available alumina column (Innovative Technology, Inc., ® VA). Reverse phase column chromatography was performed using Isolera Biotage using SNAP Cartridge KP-C18-HS of 60 g or 12 g. For confirmation of synthesized compound, ^{1}H NMR spectra were recorded on Bruker 300 UltraShield for 300 MHz using $CDCl_3$, CD_3OD, or D_2O as solvent, with residual solvent peaks $CDCl_3$ (δ = 7.26) CD_3OD (δ = 3.31), D_2O (δ = 4.79). LC-MS spectra were recorded by using a DIONEX Ultimate 3000 UHPLC coupled with a Thermo LCQ Fleet Mass Spectrometer System (electrospray ionization (ESI)) operated in positive mode (condition for elution gradient: 0 min, A:B = 100:0; 4 min, A:B = 10:90; solution A: 0.01% aqueous TFA solution; solution B, 0.01 % TFA in HPLC grade acetonitrile; flow rate: 0.750 mL/min.). Azido-pyridinium-coumarin was synthesized according to our previous synthetic procedures.[1]

Synthesis and identification of DNA strands

All RNA and DNA samples were purchased from Eurogentec and re-purifed by 8M urea denaturing gel before use. For the ruthenium-conjugated DNA (**RuA** and **RuB**), 14 mM of **Ru-NHS** in DMSO, 0.091 M of pH 8.5 NaB buffer, and 400 μM of amino-modified hairpin DNA were prepared. 20 μL of DNA solution, 180 μL of NaB buffer, and 50 μL of Ru-NHS solution were mixed well in a microtube and the mixture was incubated in room temperature for 12 h. After reaction, the mixtures were directly injected into HPLC. An Agilent high-performance liquid chromatography system (1260 Series) was used to purify the labelled DNAs; Agilent, ZORBAX 300SB-C18 column (9.4 x 250 mm); gradient elution: 0 min, A:B = 100:0; 28 min, A:B = 50:50; 29 min, A:B = 0:100; 30 min, A:B = 100:0; solution A: 0.1 M pH 7.3 TEAA buffer; solution B, 0.1 % TFA in HPLC grade acetonitrile; flow rate: 3.0 mL/min; UV detection: 260 nm and 455 nm for Ruthenium complex labelled PNAs. After HPLC, samples were lyophilized and re-purified by 8M urea denaturing gel. Synthesized DNAs were identified by MALDI-TOF mass using a Bruker Daltonics Autoflex spectrometer. 3-HPA/DAC was used for MALDI-matrix.

Synthesis and identification of PNA strands

PNAs were synthesized as described in the supplementary materials section of chapter 1. The structures of PNA backbone used are shown below:

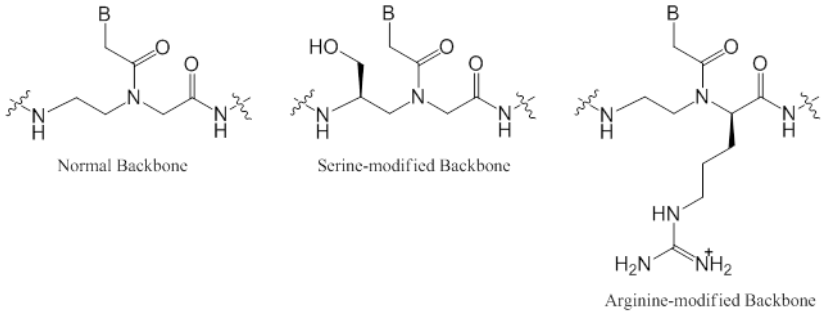

After automated synthesis of PNA parts, coumarin-PNA and 5-FUOPy-PNA conjugations were performed by click chemistry between 4-pentynoic acid and azido-pyridinium-coumarin or 5-FU-OPy. To 2.2 mg of resin in 500 µL fritted tubes, 50 µL of NMP, 20 µL of *t*-BuOH, 2 mg (3.7 µmol) of azido-pyridinium-coumarin in 50 µL of NMP, 2 mg (8 µmol) of $CuSO_4$ $5H_2O$ in 50 µL of water, and 8 mg (40.4 µmol) of sodium ascorbate in 50 µL of water were added. The reaction mixture was mixed and incubated for 3 h. After reaction, the resin was washed with water, DMF, and DCM.

PNAs were cleaved from the resin and HPLC purified as described in the supplementary methods of chapter 1.

Quantification of oligonucleotides and PNAs

Nanodrop 2000c spectrophotometer (Thermo Fisher Scientific) was used to determine the DNA, RNA, and PNA concentrations. The absorbance at 260 nm of the sample was measured. For quantification of oligonucleotides, 13700, 6600, 11700, 8800, 20900, 11100 M^{-1} were used as extinction coefficient at 260 nm for A, T, G, C, FAM, Dabcyl, respectively. For quantification of PNAs containing **Pz** and pyridinium coumarin, the absorption by natural nucleobases (A, T, G, and C) at 260 nm was calculated by followed equation: $A_{260\ (A,\ T,\ G,\ C)} = A_{260} - 1.15 \times A_{315} - A_{358}$.

Agarose gel electrophoresis for DNA circuitry

For stock solution of the hairpins, 200 nM of each hairpin in 20 mM Tris buffer pH 7.5, 140 mM NaCl, 5 mM KCl, 0.02 % tween-20, (+12 mM of $MgCl_2$ for **RuA** and **RuB**) was prepared and annealed by a snap-cooling procedure (7 min. incubation at 95 °C and cooling on ice for 5 min). 5 µL of each stock solutions and **I** were mixed in the 200 µL microtubes. Reaction mixtures (20 µL) are incubated at 37 °C for 20~60 min before addition of SYBR gold (5.2×) for DNA staining. 2 % Agarose gels and running buffers were prepared by pH 8.5 1× lithium borate (LB) buffer.

Kinetics of DNA circuitry

The kinetics were monitored in same buffer solution used for gel experiments (20 mM pH

7.5 Tris buffer, 140 mM NaCl, 5 mM KCl, 12 mM $MgCl_2$, 0.02 % tween-20). To measure the rate constants by pseudo first order kinetics, 10 µL of 20 eq. **Dab-A** (or **RuB**) were added to 0.99 mL of **FAM-I** (or **FAM-I+Dab-A** hybrid) and the mixture was mixed very quickly. Fluorescence at 530 nm was measured every 7 seconds (λ_{exc}: 485 nm, cutoff: 515 nm, λ_{emi}: 530 nm). To measure the k_A of second order kinetics, 50 µL of **Dab-A** solution (10 pmol) were added to 0.90 mL of 11.1 nM **FAM-I** (10 pmol) for the first step. When the fluorescence intensity reaches a plateau, 50 µL of 1 eq. **RuB** (10 pmol) were added to 0.95 mL of 10.5 nM **FAM-I+Dab-A** hybrid for the monitoring the second step (k_B).

DNA-templated reaction

Reactions were performed in general Tris buffer. Conditions: 20 mM pH 7.5 Tris buffer, 140 mM NaCl, 12 mM $MgCl_2$, 5 mM KCl, 0.02 % tween-20, 5 mM sodium ascorbate. Each experiment was performed in triplicates. Fluorescence intensities of released coumarin were measured using a Molecular Devices Spectra Max M5 with following parameters (λ_{ex}: 360 nm, λ_{em}: 460 nm, cutoff: 455 nm, PMT gain: medium, flash per read: 6, shake 5 sec. before first read). The plate was irradiated with a collimated LED light 15 cm above the plate (455 nm, 1W: Thorlabs, part number M455L2-C1 – www.thorlabs.com). Fluorescence intensities were measured by using a Molecular Devices Spectra Max M5. The percentage of conversion was calculated based on a titration curve of coumarin conversion. We validated that the reaction reaches a plateau and that the fluorescent units of this plateau indeed correspond to 100% yield according to the titration curve. Kinetic values (k_{app}, $t_{1/2}$) were calculated according to a previous report.[5]

Sample preparation for quadratic reactions

200 nM stock solutions of **RuA** and **RuB** were prepared according to the method used for agarose gel electrophoresis. After mixing **RuA**, **RuB**, **P1**, **P2**, and sodium ascorbate, **I** sequence was added to the final solution. For pre-incubation, sodium ascorbate was added right before irradiation.

5-FU release analysis by HPLC

The reaction for 5-FU release was done in general buffer conditions. After irradiation, the samples were directly injected into HPLC using the following conditions: elution gradient 0 min, A:B = 100:0; 7 min, A:B = 100:0; 28 min, A:B = 0:100; 29 min, A:B = 0:100; 30 min, A:B = 100:0; solution A: pH 8.0 TEAA buffer; solution B, 0.1 % TFA in HPLC grade acetonitrile; flow rate: 3.0 mL/min; UV detection: 260 nm. 5-FU was dissolved in water in injected into HPLC as a reference molecule.

Cytotoxicity test for quantification of 5-FU

Reaction mixture preparation: 5FUP1 and **5FUP2** (5 μM each), **RuA** and **RuB** (10 nM), **I** (1 nM) were incubated in 140 μL of general Tris buffer and irradiated or kept in the dark for 3 h. Afterwards the mixtures were lyophilized, dissolved in McCoy's 5A (modified) containing 10% FCS and 1% pen-strep (700 μL) and added to cells (100 μL for each well).

Cell culture: HT-29 cell lines were obtained from the American Type Culture Collection (ATCC) and expanded following their instructions. Cells were grown in McCoy's 5A (modified) medium (Gibco) containing 10% FCS and 1% pen-strep at 37 °C under 5% CO_2 in a humidified incubator. Cells were regularly tested for mycoplasma contamination by staining with Hoechst 33342.

5-FU free drug/5FUP(prodrug) toxicity in HT-29 cells: HT-29 cells were seeded into 96-well plates ($5x10^4$ cells/well) and allowed to adhere overnight. Media was replaced with 5-FU free drug/5FUP at different concentrations in McCoy's 5A containing 10% FCS, 1% pen-strep plus 0.2X of general Tris buffer; cells were incubated at 37 °C under 5% CO_2 in humidified incubator for 144 h. Fresh media (100 μL/well of DMEM, no phenol-red) was replaced and WST-1 reagent (10 μL/well) was added; cells were incubated for additional 2 h at 37 °C, 5% CO_2. Absorbance of formazan product was measured in a microplate reader (Molecular Devices Spectra Max M5) (450-690 nm). Drug effect was expressed as normalized viability; 50% viability was obtained from sigmoidal curve fits of normalized viability vs. concentration data using GraphPad Prism 8. All experiments were conducted in triplicates, with error bars representing the standard deviation.

Toxicity test in HT-29 cells for estimation of 5-FU released by the coupled system: HT-29 cells were seeded into 96-well plates ($5x10^4$ cells/well) and allowed to adhere overnight. Media was replaced with reaction mixtures in McCoy's 5A (modified) medium (Gibco) containing 10% FCS, 1% pen-strep plus 0.2X Tris buffer; cells were incubated at 37 °C under 5% CO_2 in a humidified incubator for 144 h. Fresh media (100 μL/well of DMEM, no phenol-red) was replaced and WST-1 reagent (10 μL/well) was added; cells were incubated for additional 2 h at 37 °C, 5% CO_2. Absorbance of formazan product was measured in a microplate reader (Molecular Devices Spectra Max M5) (450-690 nm). Drug effect was expressed as normalized viability; data were plotted using GraphPad Prism 8. All experiments were conducted in triplicates, with error bars representing the standard error of the mean.

Sequences information

Table II-S1 RNA, DNA and PNA sequences investigated in this study

Name	Sequence (5´ to 3´ for RNA and DNA, N- to C-terminal for PNA)
A	TCAGACTGATGTTGCTAGCTTATCAACATCAGTCTGATAAGCTA
B	TTGCTAGCTTATCAGACTGATGTTGATAAGCTAGCAACATCAGT
A2	TCAGACTGATGTTCGTAGCTTATCAACATCAGTCTGATAAGCTA
B2	TTCGTAGCTTATCAGACTGATGTTGATAAGCTACGAACATCA
B3	TTCGTAGCTTATCAGACTGATGTTGATAAGCTACGAACATCAGT
A3	TCAGACTGATGTTGATAGCTTATCAACATCAGTCTGATAAGCTA
B4	TTGATAGCTTATCAGACTGATGTTGATAAGCTATCAACATCAGT
I (miR-21)	TAGCTTATCAGACTGATGTTGA
miR-21-5p	UAGCUUAUCAGACUGAUGUUGA
RuA	Ru-TCAGACTGATGTTGCTAGCTTATCAACATCAGTCTGATAAGCTA
RuB	Ru-TTGCTAGCTTATCAGACTGATGTTGATAAGCTAGCAACATCAGT
FAM-I	FAM-TAGCTTATCAGACTGATGTTGA
Dab-A	TCAGACTGATGTTGCTAGCTTATCAACATCAGTCTGATAAGCTA-Dabcyl
RuS1	Ru-TTGCACTGATGTTGATAGCTTA
RuS2	Ru-TCAGACTGATGTTGATAGCTTA
PC	TAAGCTATCAACATCAGT
FC	TAAGCTATCAACATCAGTCTGA
P1	Ac-GCAA-Lys-pyCou
P2	Ac-**Pz**TGA-Lys-pyCou
ArgP2	Ac-CTGA-Lys-pyCou
AmiP2	NH_2-CTGA-Lys-pyCou
P1'	Ac-G**Pz**AA-Lys-pyCou
P2'	Ac-CTGA-Lys-pyCou
SMM-miR-21	TAGTTTATCAGACTGATGTTGA
TMM-miR-21	TAGTTTATTACACTGATGTTGA
miR-31-5p	GGCAAGAUGCUGGCAUAGC
miR-31-3p	GCUAUGCCAACAUAUUGCC
5FUP1	Ac-GCAA-Lys-5-FUOPy
5FUP2	Ac-**Pz**TGA-Lys-5-FUOPy

[a] L-serine modified PNA is marked with underline

Optimization of DNA circuitry

Figure II-S1. Agarose gel test of non-modified DNA hairpins.

2% Agarose gel electrophoresis test of DNA circuitry by using different combinations of hairpin sequences (**A+B**, **A2+B2**, **A2+B3**, **A3+B4**). The efficiency of the DNA circuitry was tested at 20, 40, 60 min incubation time. A longer length of stem and a shorter length of loop were used for higher meta-stability of hairpins; longer overhang length was used to increase reaction rates. Lane 1: **A**, lane 2: **A+I** (1 eq.), lane 3: **A+B+I** (1 eq.), lane 4: **A+B+I** (0.5 eq.), lane 5: **A+B+I** (0.25 eq.), lane 6: **A+B+I** (0.125 eq.), lane 7: **A+B**, lane 8: **A+B** (annealed). Sample conditions: 50 nM of DNA hairpins, 20 mM pH 7.5 Tris buffer, 140 mM NaCl, 5 mM KCl, 0.02 % tween-20, 20 µL reaction volume, 1 pmol, 37 °C, stained with SYBR gold (5.2×) before loading.

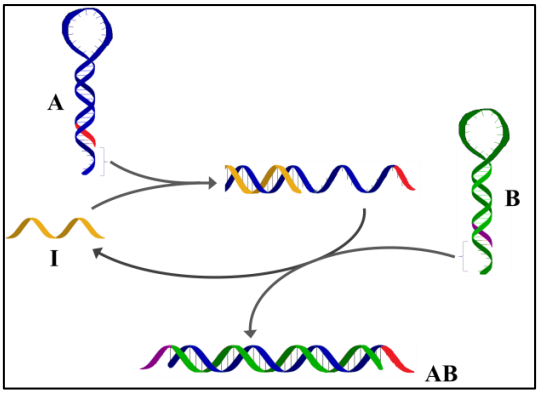

A (7-mer overhang, 14-mer stem, 9-mer loop), B (7-mer overhang, 14-mer stem, 9-mer loop)

```
          a*      x*  b*      c*      y*  x
I:  5'-TAGCTTA  TC  AG  ACTGATG  TT  GA
        x*  b*      c*      y*  d*      a*      x*  y       c       b   x       a
A: 5'- TC  AG  ACTGATG  TT  GC  TAGCTTA  TC  AA  CATCAGT  CT  GA  TAAGCTA
        y*  d*      a*      x*  b*      c*      y*  x       a       d   y       c
B: 5'- TT  GC  TAGCTTA  TC  AG  ACTGATG  TT  GA  TAAGCTA  GC  AA  CATCAGT
```

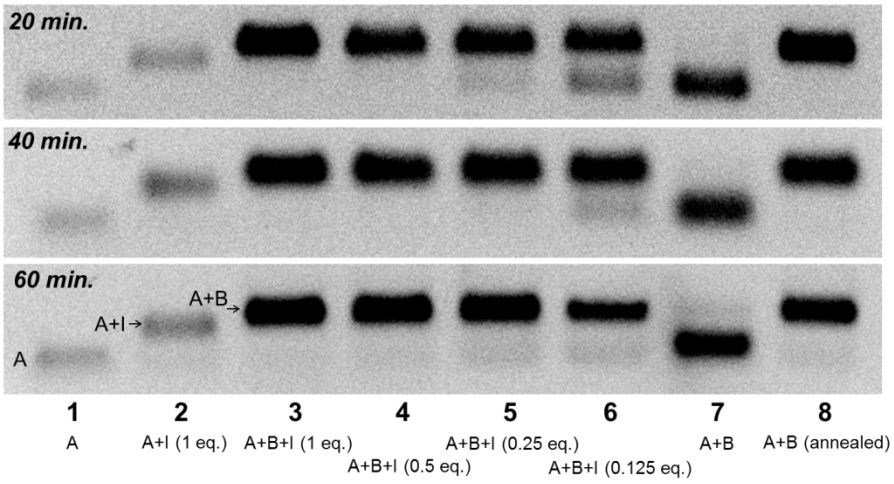

A2 (7-mer overhang, 13-mer stem, 11-mer loop), B2 (5-mer overhang, 14-mer stem, 9-mer loop)

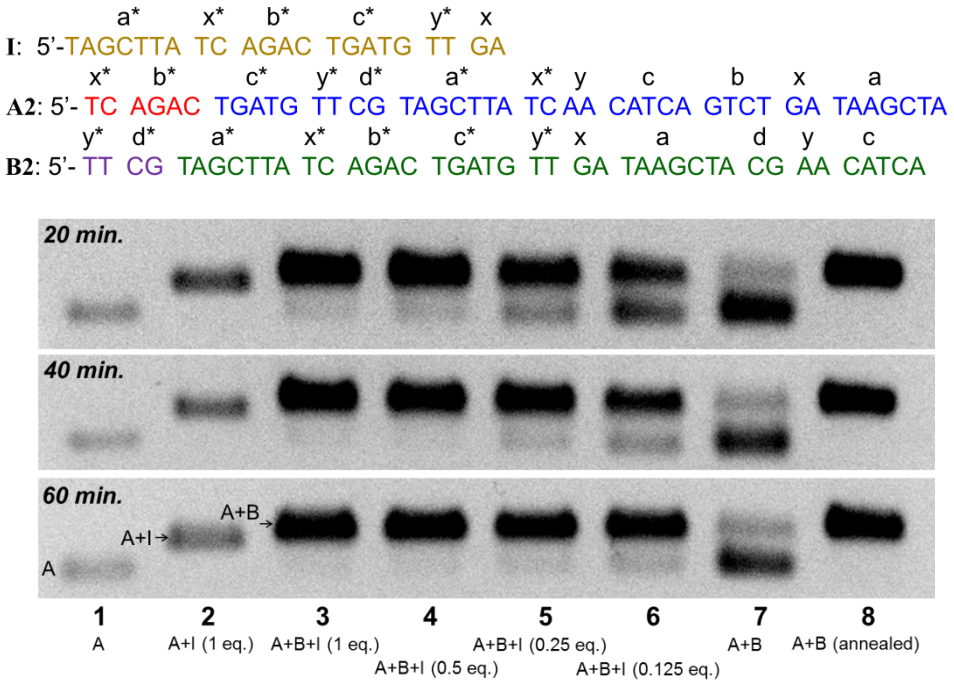

A2 (7-mer overhang, 13-mer stem, 11-mer loop), B3 (7-mer overhang, 14-mer stem, 9-mer loop)

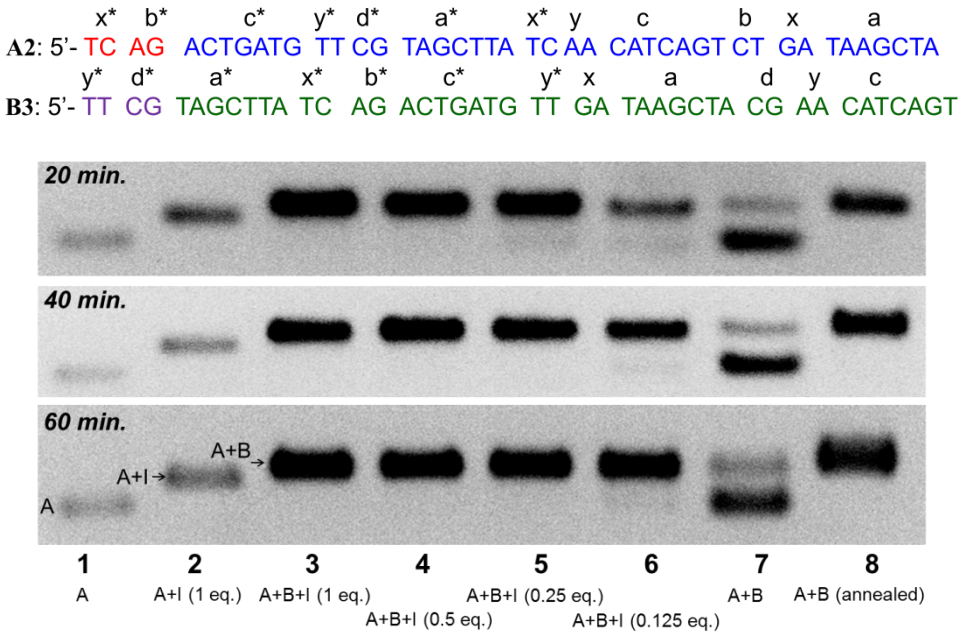

A3 (7-mer overhang, 16-mer stem, 5-mer loop), B4 (7-mer overhang, 14-mer stem, 9-mer loop)

```
          x*  b*     c*     y*  d*     a*     x*  y    c       b   x    a
A3: 5'- TC  AG ACTGATG TT GA TAGCTTA TC AA CATCAGT CT GA TAAGCTA
          y*  d*     a*     x*  b*     c*     y*  x    a       d   y    c
B4: 5'- TT  GA TAGCTTA TC   AG ACTGATG TT GA TAAGCTA TC AA CATCAGT
```

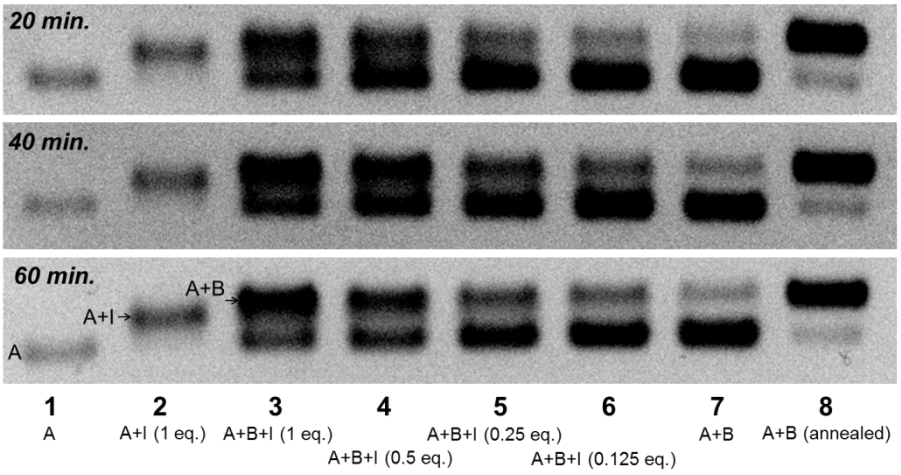

Figure II-S2. Effect of Mg^{2+} concentration on the RuA and RuB circuit.

2% Agarose gel electrophoresis test of DNA circuitry using **RuA** and **RuB**. The efficiency of the DNA circuitry was tested in presence of 0, 4, 8, 12 mM of $MgCl_2$. Lane1: **A**, lane 2: **A+I** (1 eq.), lane 3: **A+B+I** (1 eq.), lane 4: **A+B+I** (0.5 eq.), lane 5: **A+B+I** (0.25 eq.), lane 6: **A+B+I** (0.125 eq.), lane 7: **A+B**, lane 8: **A+B** (annealed). Sample conditions: 50 nM of DNA hairpins, 20 mM pH 7.5 Tris buffer, 140 mM NaCl, 5 mM KCl, 0.02 % tween-20, 20 µL reaction volume, 1 pmol, 37 °C, 1 h incubation, stained with SYBR gold (5.2×) before loading.

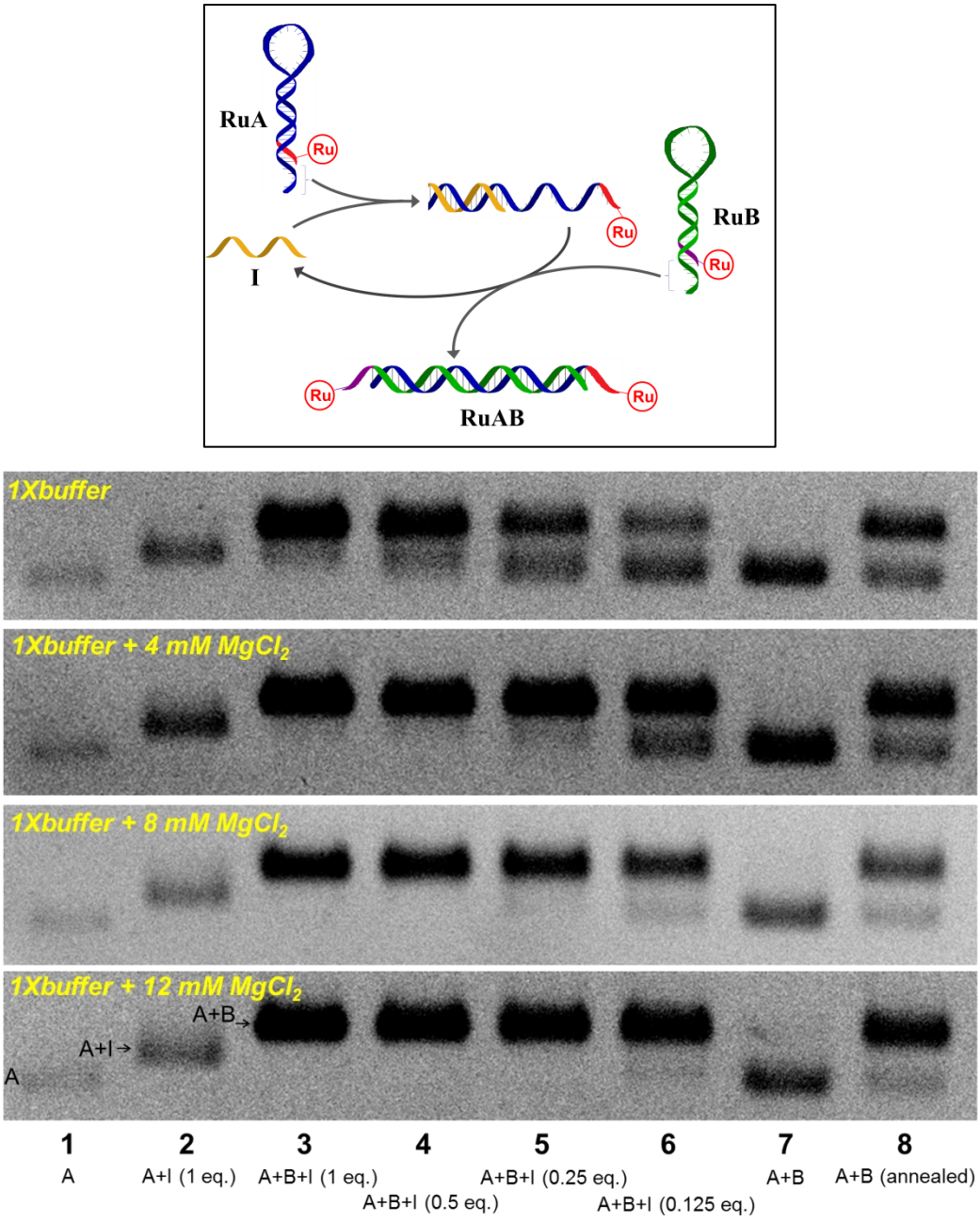

Kinetics of DNA circuit

Figure II-S3. Rate constant calculated from pseudo first order kinetics. Time-dependent fluorescence change of **FAM-I** after injection of excess **Dab-A** or **RuB**. To measure the k_A, 20 eq. of **Dab-A** (10 µL) was added to 0.99 mL solution of 0.4, 0.8, 0.4, 1.0 nM **FAM-I** with rapid agitation. To measure the k_B, 20 eq. of **RuB** (10 µL) was added to 0.99 mL solution of **FAM-I:Dab-A** duplex. Rate constants (k) were calculated from the half-life of the reaction, using $t_{1/2} = \ln 2 / k'$, $k' = k$ [**Dab-A**] or [**RuB**]. The k_A and k_B were measured at 25 °C and 37 °C.

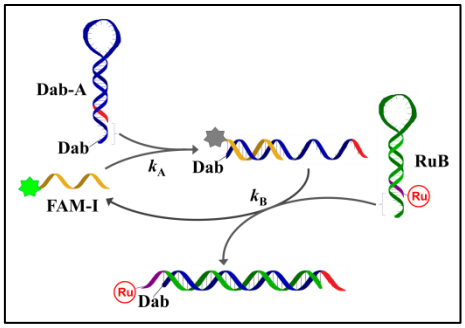

Rates at 37 °C

Dab-A + FAM-I → Dab-A•FAM-I (k_A) Dab-A•FAM-I + RuB → Dab-A•RuB + FAM-I (k_B)

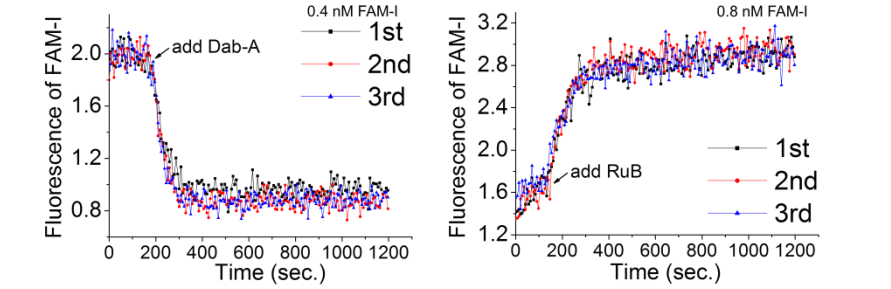

	$t_{1/2}$	k' (s^{-1})	k ($M^{-1} s^{-1}$)
k_A (37°C)	39 ± 4.0 s	0.018 ± 0.002	(2.3 ± 0.21) X 10^6
k_B (37°C)	84 ± 3.0 s	0.008 ± 0.0003	(5.1 ± 0.18) X 10^5

Rates at 25 °C

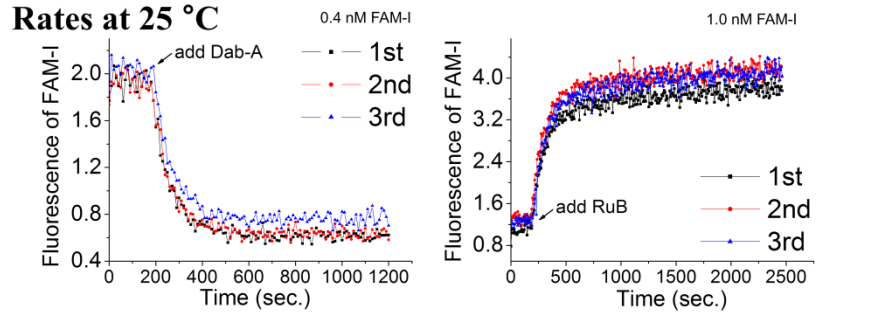

	$t_{1/2}$	k' (s^{-1})	k ($M^{-1} s^{-1}$)
k_A (25°C)	55 ± 2.0 s	0.013 ± 0.0005	(1.6 ± 0.06) X 10^6
k_B (25°C)	117 ± 5.0 s	0.0059 ± 0.0002	(3.0 ± 0.12) X 10^5

Figure II-S4. Rate constant calculated from second order kinetics.

Time-dependent fluorescence change of **FAM-I** (10 nM final concentration) after injection of 1 eq. of **Dab-A** or **RuB** or **B**. Rate constants (k) were calculated from the half-life of the second order reaction, where $[A]_0 = [B]_0 = [I]_0$, $t_{1/2} = 1 / k [\mathbf{FAM\text{-}I}]_0$. The k_A and k_B were measured at 37 °C. k_C stands for a rate constant obtained by adding hairpin **B** (50 nM of **FAM-I** was used for this reaction), instead of **RuB**. The rate constants are consistent with the values obtained from pseudo first order kinetics.

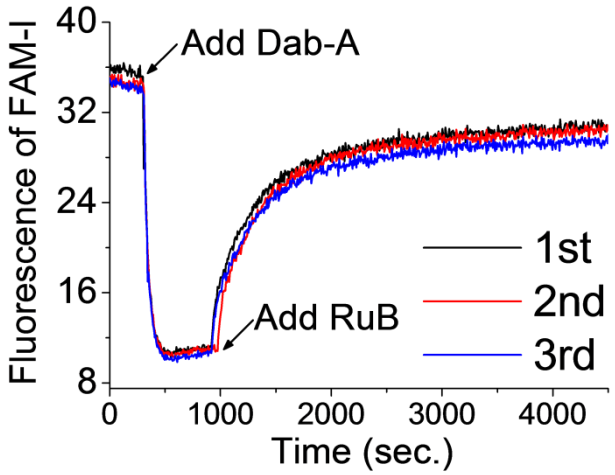

	$t_{1/2}$	k ($M^{-1} s^{-1}$)
k_A (37 °C)	34 ± 1.5 s	(2.8 ± 0.12) X 10^6
k_B (37 °C)	224 ± 5.3 s	(4.5 ± 0.10) X 10^5
k_C (37 °C)	76 ± 1.4 s	(2.6 ± 0.05) X 10^5

Optimization of 4-mer templated reaction in basic model

Figure II-S5. Test of 4-mer PNAs with different charges and backbones.

Templated reaction at the 4-mer sticky end. (A) Arginine-modified (**ArgP2**) and (B) non-acetylated-serine-modified-PNA (**AmiP2**) having additional positive charges on PNAs were tested. However, such modifications were found detrimental for the rate of the templated reaction. (C) Among three model PNAs, acetylated serine-modified PNA (**P2'**) exhibited the fastest kinetics. Underlined letters indicate the position of serine or arginine modifications. Conditions: 100 nM of each DNA or PNAs (1:1 stoichiometry) in general Tris buffer conditions at 25 °C.

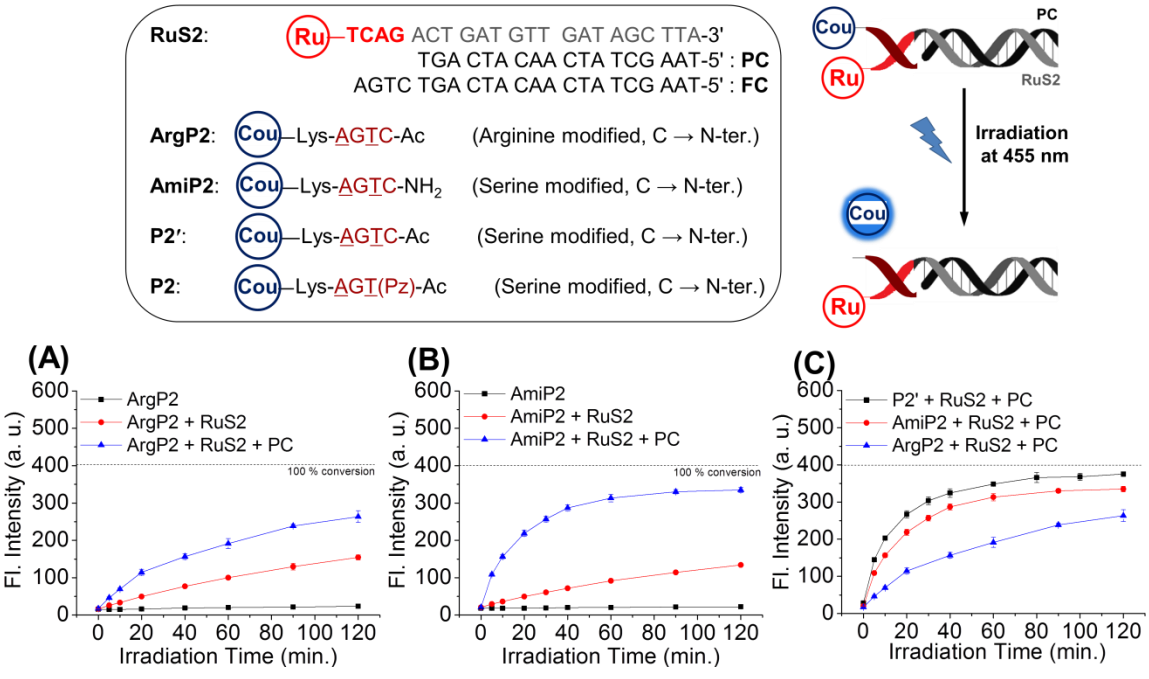

Figure II-S6. Test of 4-mer PNAs with phenoxazine nucleobase (Pz).

Templated reaction using normal 4-mer PNAs (A) **P1** and (D) **P2'** and phenoxazine (Pz)-modified PNAs (B) **P1'** and (C) **P2** in the presence and absence of **PC** sequences. Conditions: 50 nM of each DNA or PNAs (1:1 stoichiometry) in general buffer conditions at 25 °C. **P1** and **P2** showed the fastest templated reaction kinetics. The Pz nucleobase located only at the N-terminal affords additional duplex stability presumably due to bulkiness.

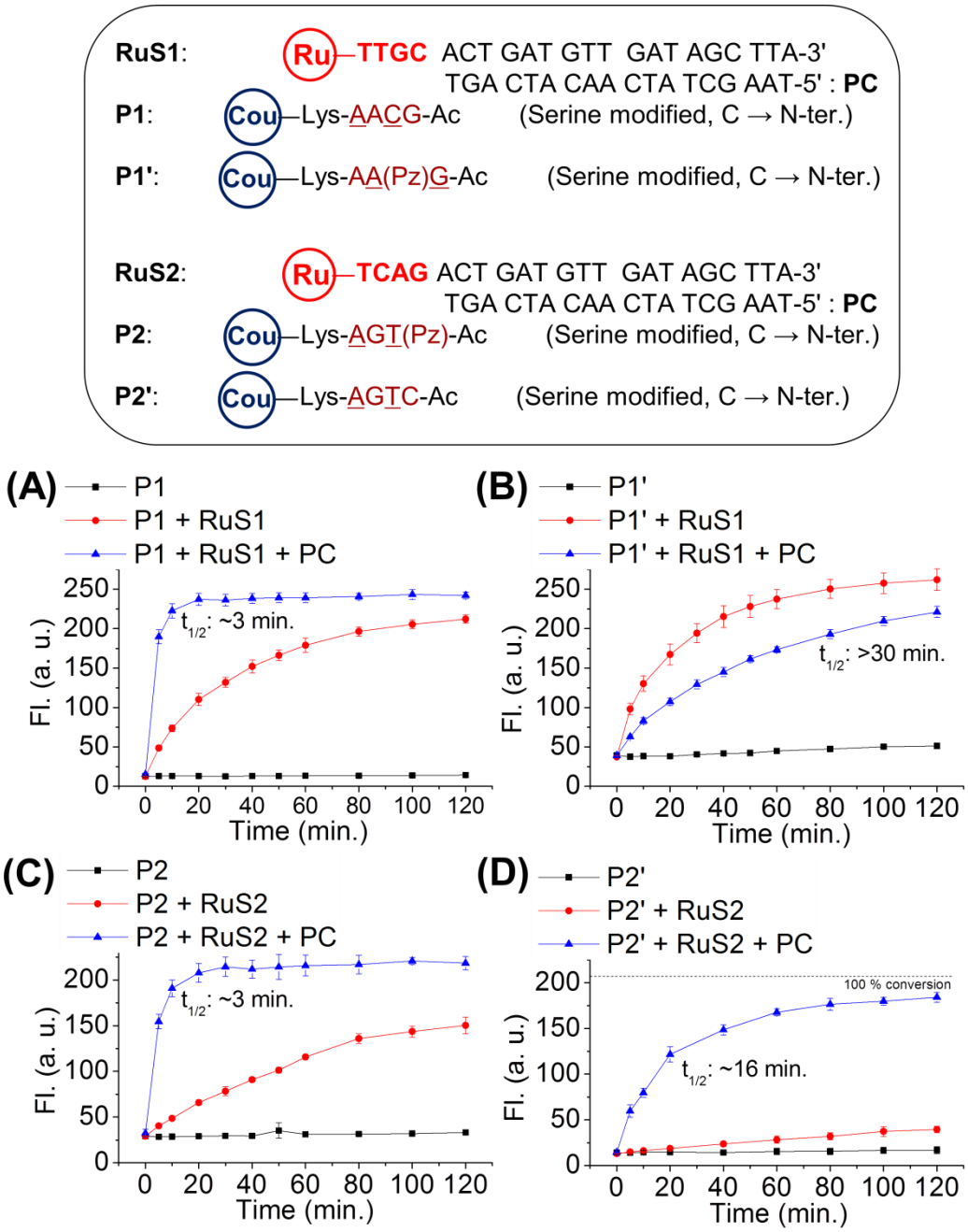

Figure II-S7. Selectivity test of 4-mer PNAs.

4-mer templated reaction with mismatched sequences. None of the mismatched PNA/DNA duplexes afforded fluorescent signal from released coumarin, which implies high sequence selectivity for 4-mer PNA/DNA binding. Conditions: 50 nM of each DNA or PNAs (1:1 stoichiometry) in general buffer conditions at 25 °C.

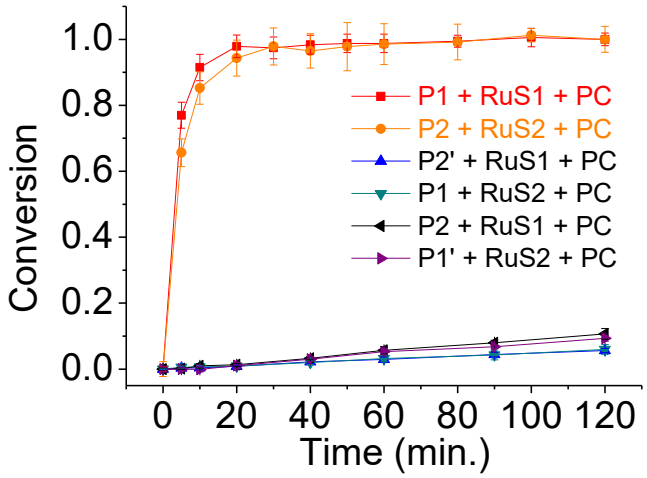

Figure II-S8. Test of 4-mer PNAs with different additives.

Kinetics of **P2** in the presence of different additives, **PC** or **FC** (see Figure II-S5 for sequence information). **PC** significantly enhances the reaction while **FC** strongly slows down the reaction. Likewise, the hairpin **RuA** does not afford a relevant signal since the 4-mer site is blocked. Conditions: 50 nM of each DNA or PNAs (1:1 stoichiometry) in general Tris buffer conditions at 25 °C.

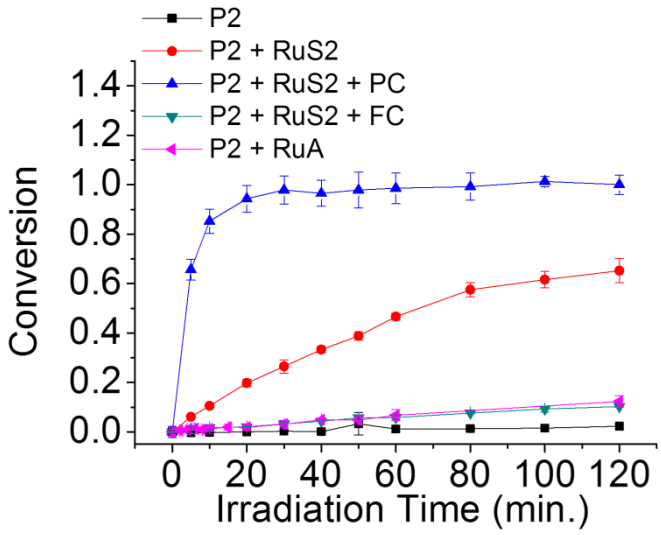

Figure II-S9. k_{app} measurement of 4-mer sticky-end templated reaction at 25 and 37 °C. (A, B) Calculated k_{app} from 4-mer templated reaction (1:1 stoichiometry) of **P1+RuS1+PC** and **P2+RuS2+PC** with different concentrations of samples (1-6 μM) at 25 and 37 °C. (C) Raw data for estimation of k_{app}.

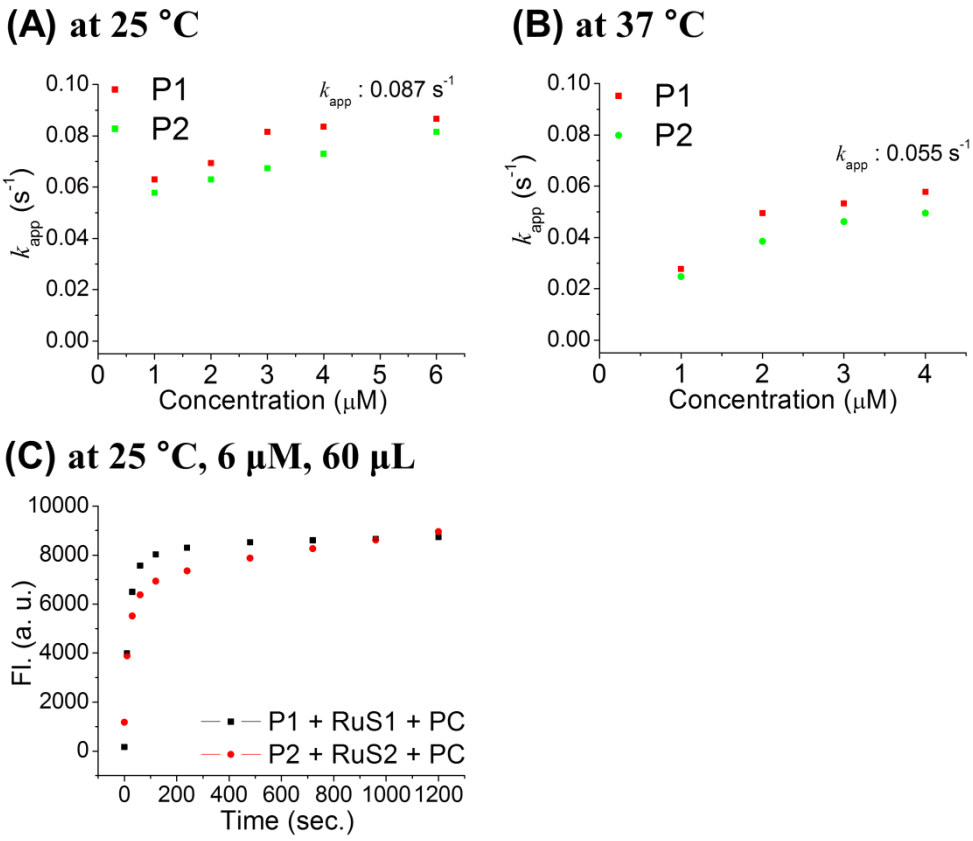

Figure II-S10. Calculation of k_{cat} from the Lineweaver-Burk equation

k_{cat} and K_M were measured from the Lineweaver-Burk equation. **P1** or **P2** was added to **RuS1+PC** or **RuS2+PC**. The V was measured from the reaction yield of the initial 5 min. The concentration of the reaction yield was calculated using a calibration value for coumarin. Data points were obtained using 175, 250, 500, 1000 nM of substrates at 25 °C and 50, 100, 250, 500 nM at 37 °C, respectively. Conditions for **P1**+**RuS1+PC**: total 200 µL, 5 nM of **RuS1+PC**, 20 mM pH 7.5 Tris, 140 mM NaCl, 5 mM KCl, 12 mM $MgCl_2$, 0.02 % tween-20, 5 mM sodium ascorbate; Conditions for **P2**+**RuS2+PC**: 5 nM or 10 nM of **RuS2+PC** was used for 25 or 37 °C, respectively.

$$\frac{1}{V} = \frac{K_M}{V_{max}} \frac{1}{[P1\ or\ P2]} + \frac{1}{V_{max}}$$

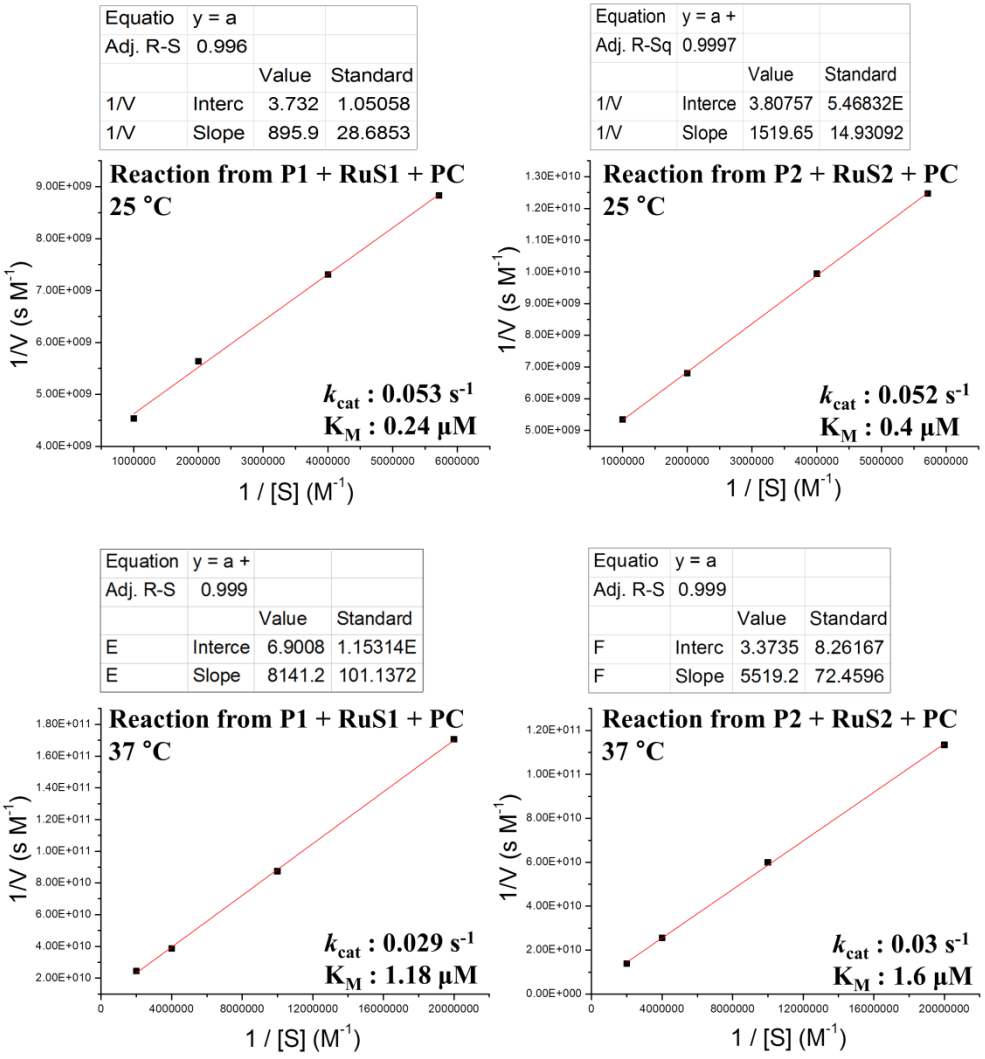

Evaluation of DNA circuit coupled to templated reaction

Figure II-S11. Quadratic amplification behavior at ambient temperature.

Templated reaction coupled with DNA circuit, using (A) 2.5 nM or (B) 5 nM of **RuA** and **RuB**. 125 nM of PNAs, 20 mM pH 7.5 Tris, 140 mM NaCl, 5 mM KCl, 12 mM $MgCl_2$, 0.02 % tween-20, 5 mM sodium ascorbate, 25 °C; data were collected right after adding **I**. (C) Acceleration of templated reaction by the DNA circuit was clearly observed by differentiation curves of (B). The time points where a maximum rate was observed in (C) are consistent with the estimated time of full conversion into **RuAB** duplexes (D).

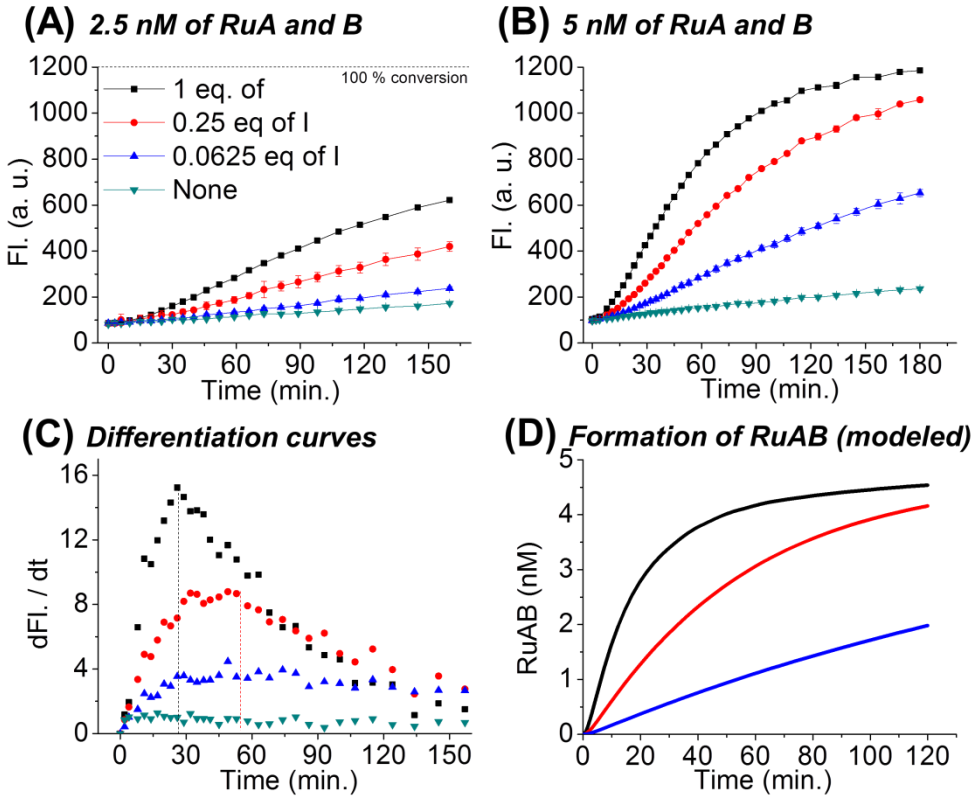

Figure II-S12. Quadratic amplification behavior at 37 °C.

(E) Fluorescence raw data of reactions at 37 °C. General conditions: 150 nM of PNAs, 10 nM of **RuA** and **RuB**, 20 mM pH 7.5 Tris, 140 mM NaCl, 5 mM KCl, 12 mM $MgCl_2$, 0.02 % tween-20, 5 mM sodium ascorbate, 37 °C, 200 µL, data were collected right after adding **I**. (F) Fluorescence raw data of Figure 29.

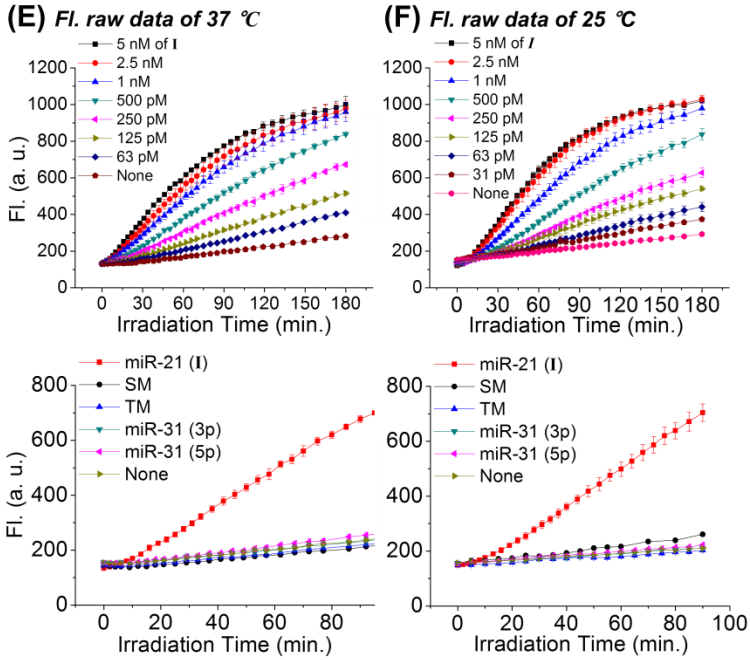

Figure II-S13. Test of coumarin release by coupled system in different conditions (37 °C). Fluorescence of released coumarin by the coupled system in different concentration. The raw fluorescence data are also shown in below. Conditions: (A) General Tris buffer (20 mM pH 7.5 Tris, 140 mM NaCl, 5 mM KCl, 12 mM $MgCl_2$, 0.02 % tween-20, 5 mM NaAsc), 5 µM of each **P1** and **P2**, 10 nM of **RuA** and **RuB**, Total V. 100 µL, 0.1 eq. of **I**, 30 min of pre-incubation; (B) general Tris buffer, 3 µM of each **P1** and **P2**, 10 nM of **RuA** and **RuB**, Total V.: 100 µL, 1 eq. of **I**, 20 min of pre-incubation; (C) general Tris buffer, 1 mM NaAsc, 0.6 µM of each **P1** and **P2**, 10 nM of **RuA** and **RuB**, Total V.: 200 µL, 0.1 eq. of **I**, 3 h of pre-incubation. 10 nM of DNA circuit provided low background signal. Notably, 3500-fold of amplification (corrected for background reaction) was measured after 80 min of irradiation for (A).

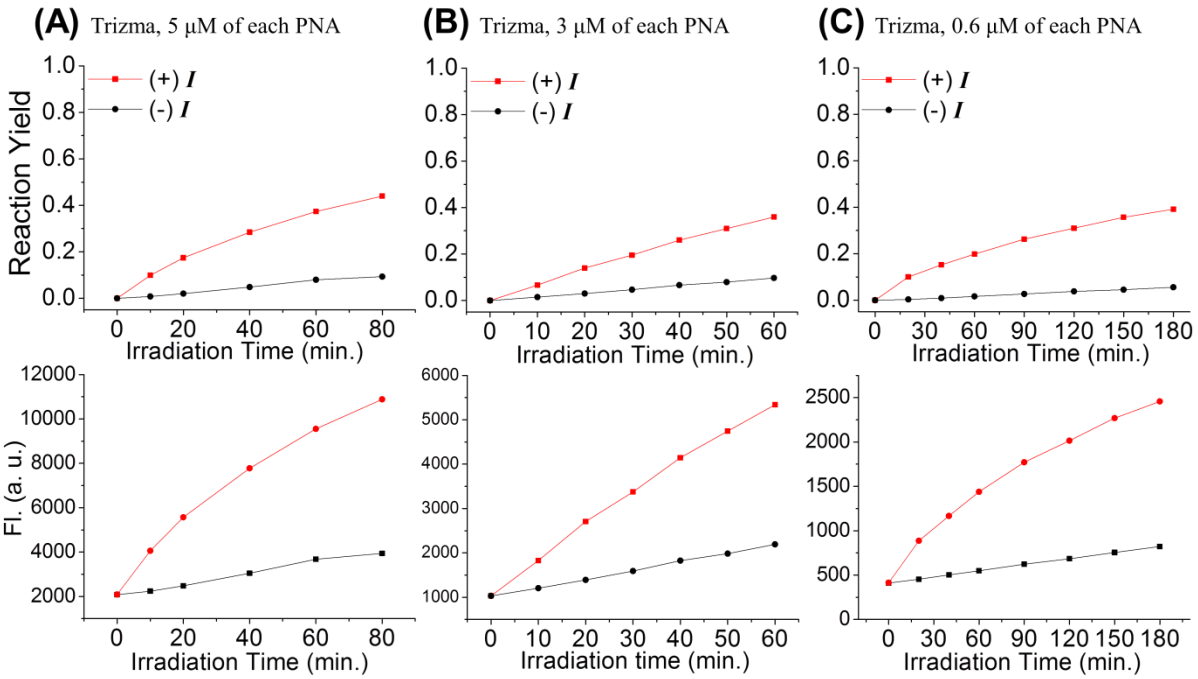

Figure II-S14. Detection threshold of quadratic amplification.

Detection threshold after 8 or 9 h of irradiation in general Tris buffer at 25 or 37 °C. In these conditions, 500 fM of **I** was detectable. General conditions: 150 nM of PNAs, 5 nM (25 °C) or 10 nM (37 °C) of **RuA** and **RuB**, 20 mM pH 7.5 Tris, 140 mM NaCl, 5 mM KCl, 12 mM $MgCl_2$, 0.02 % tween-20, 5 mM sodium ascorbate, 200 µL, data was taken right after adding **I**.

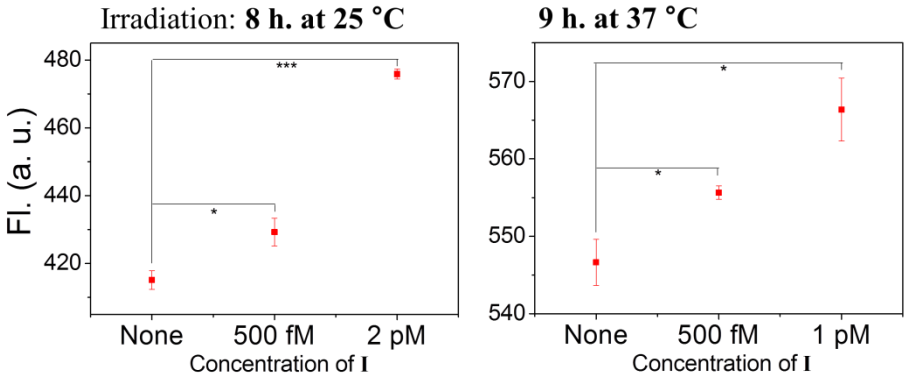

Figure II-S15. Detection threshold of quadratic amplification.

Detection threshold after 5 h of pre-incubation and 1 h or irradiation at 37 °C in general Tris buffer. In these conditions, 10 pM of **I** was detectable. The amount of released coumarin was consistent with the expected fluorescence values (background signal (none) + theoretical fluorescence enhancement) estimated from modeled kinetics calculated by wolfram mathematica.

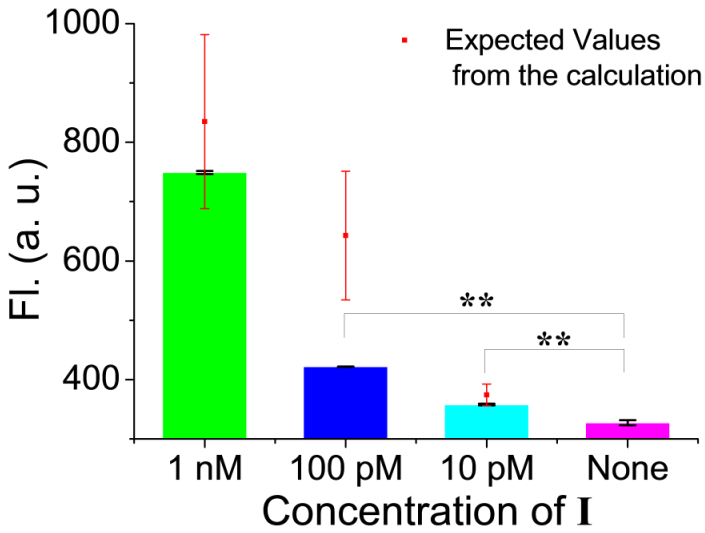

Figure II-S16. Detection threshold of 4-mer linear templated reaction.

Detection threshold of templated reaction was tested in the absence of DNA circuit. Different concentrations of **RuAB** duplexes were prepared from hybridization of **RuA** and **RuB** in the presence of 1 eq. of initiator (**I**). 25 and 150 nM of **P1** and **P2** were used for 25 and 37 °C reaction, respectively. Samples were irradiated for 2 h except the last ones. 25 pM and 63 pM detection thresholds were obtained at 25 °C and 37 °C respectively.

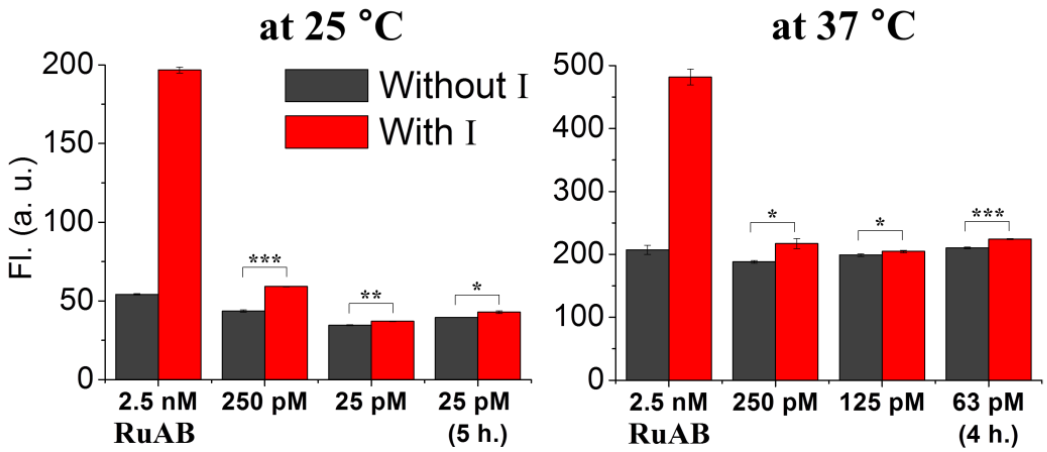

Figure II-S17. Release of functional molecules by coupled system.

HPLC analysis of 5-FU released by the coupled system using a real **miR-21-5p** sequence. As a reference, 0.25 nmol of 5-FU was injected in HPLC. The reaction sample with **I** affords a signal of 5-FU corresponding to 1.4 μM release after 0.5 h of irradiation under these conditions: 20 mM pH 7.5 Tris, 140 mM NaCl, 5 mM KCl, 12 mM $MgCl_2$, 0.02 % tween-20, 5 mM NaAsc, 4 h of pre-incubation, 10 μM of total prodrug PNAs, 60 nM of **RuA** and **RuB**, total V. 100 μL, 1 nM of **I**.

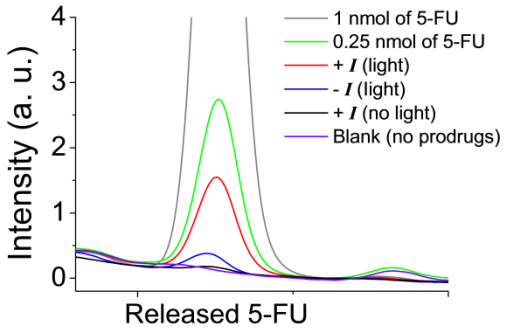

100 μL reaction	Area	Corrected Area	Conc. (μM)
0.25 nmol 5-FU	0.38	-	-
+ ***I*** (light)	0.22	0.21	1.41
- ***I*** (light)	0.037	0.029	0.19
+ ***I*** (no light)	0.0084	-	-

Figure II-S18. Kinetic modeling of the DNA circuit and templated reactions.
To predict the amount of produced **RuAB** duplex and released coumarin, numerical differential equation solver (Wolfram Mathematica 11.1) was implemented using the following chemical differential equations. For prediction of pre-incubation, the value [**RuA• RuB**] obtained from DNA circuit was adopted as an initial value (t = 0 s) for the calculation of the amount of released molecules (Coumarin) by templated reactions. Modeling of coupled reaction (150 nM of **P1** and **P2**, 10 nM of **RuA** and **RuB**, 1 nM of **I**, 3 h of reaction at 37 °C) clearly showed quadratic behavior.

Equations for DNA circuit

$d[RuA]/dt = -k_A [RuA][I]$

$d[RuB]/dt = -k_B [RuB][RuA•I]$

$d[I]/dt = -k_A [RuA][I] + k_B [RuB][RuA•I]$

$d[RuA•I]/dt = k_A [RuA][I] - k_B [RuB][RuA•I]$

$d[RuA• RuB]/dt = k_B [RuB][RuA•I]$

Equations for templated reactions

$d[P1]/dt = -(k_{cat1} [RuA• RuB][P1]) / (K_{M1} + [P1])$

$d[P2]/dt = -(k_{cat2} [RuA• RuB][P2]) / (K_{M2} + [P2])$

$d[Cou1]/dt = (k_{cat1} [RuA• RuB][P1]) / (K_{M1} + [P1])$

$d[Cou2]/dt = (k_{cat2} [RuA• RuB][P2]) / (K_{M2} + [P2])$

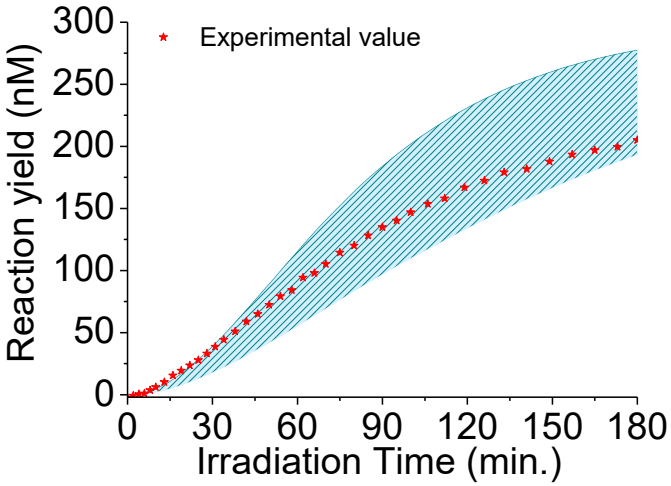

Synthesis of small molecules

Synthesis of ruthenium catalyst-*N*-hydroxysuccinimide ester for conjugation with DNA

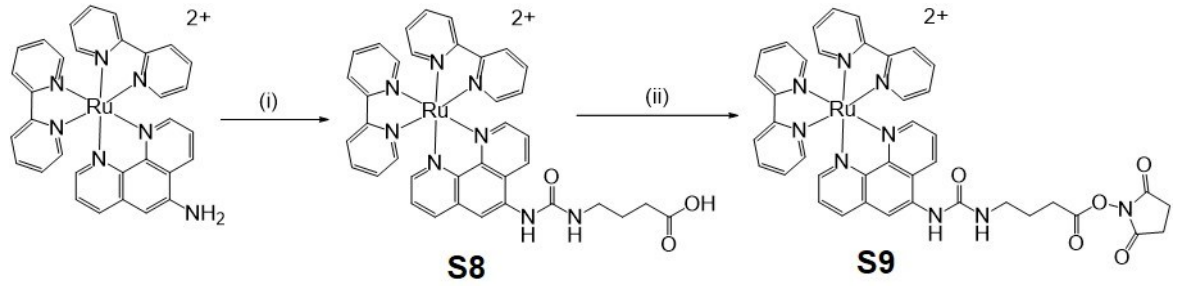

Reagents and conditions: (i) a) triphosgene (0.5 eq), diisopropylethylamine (4.0 eq), DCE, r.t., 4 h. b) γ-aminobutyric acid (3.0 eq), DMF, r.t., 12 h, 14 %; (ii) *N*-hydroxysuccinimide (1.5 eq), EDC•HCl (1.3 eq), DCM/DMF, r.t., 2 h, 95%;

Ruthenium complex (S8)

1.5 mg (0.0033 mmol) of triphosgene and 6.1 mg (0.01 mmol) of bis(2,2′-bipyridine)-(5-aminophenanthroline)ruthenium bis(hexafluorophosphate) in N_2 purged round-bottom flask were dissolved in 200 µL of 1,2-dichloroethane. The mixture was cooling down to 0 °C in ice bath and 7 µL (0.04 mmol) of diisopropylethylamine was added to the reaction mixture. The reaction mixture was vigorously stirred at r.t. After 4 h, the mixture was diluted with 1 mL of DMF and 3 mg (0.03 mmol) of γ-aminobutyric acid was added, and solution was vigorously stirred at r.t. for 12 h. The product was extracted with 10 mL of H_2O and lyophilized. The dried sample was purified by HPLC (condition for elution gradient: 0 min, A:B = 100:0; 28 min, A:B = 30:70; 29 min, A:B = 0:100; 30 min, A:B = 100:0; solution A: 0.1% aqueous TFA solution; solution B, 0.1 % TFA in HPLC grade acetonitrile; flow rate: 3.0 mL/min; UV detection: 254 and 455 nm). The product was found at R.T. 14.3 min to yield 1 mg (14 %) of **Ruthenium complex (S8)**. **^{1}H NMR** (300 MHz, DMSO-d_6) δ 9.20 (s, 1H), 8.85 (dd, *J* = 13.4, 6.0 Hz, 5H), 8.76 (s, 1H), 8.63 (dd, *J* = 8.4, 1.2 Hz, 1H), 8.27 – 8.05 (m, 5H), 7.97 – 7.87 (m, 2H), 7.86 – 7.72 (m, 3H), 7.61 – 7.52 (m, 4H), 7.36 (m, 2H), 6.93 (t, *J* = 5.8 Hz, 1H), 3.22 (t, *J* = 6.3 Hz, 2H), 2.35 – 2.22 (m, 2H), 1.74 (p, *J* = 7.0 Hz, 2H). **^{13}C NMR** (75 MHz, DMSO-d_6) δ 174.46, 162.62, 156.93, 156.70, 155.34, 151.57, 151.48, 151.45, 147.41, 143.34, 137.99, 135.82, 131.57, 131.07, 127.98, 126.57, 125.72, 125.43, 124.59, 45.97, 31.20, 25.28. **LC-MS (ESI)** RT= 1.49 min. Expected Mass: 738.1641, *m/z* found: 368.9 $[M]^{2+}$.

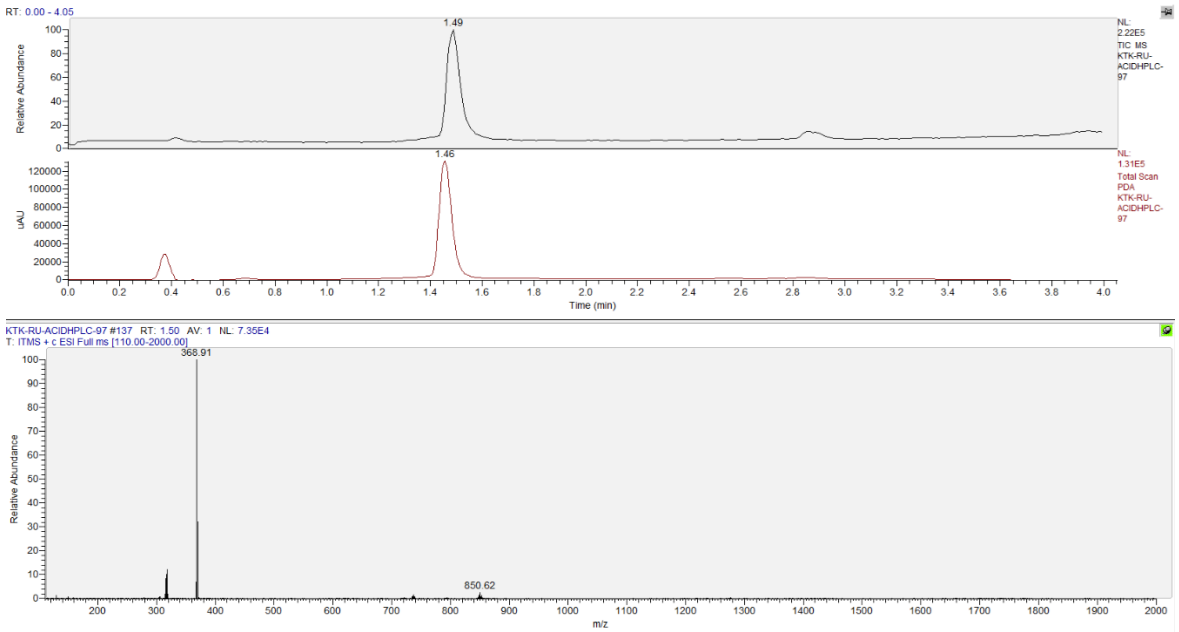

LC-MS trace of compound **S8.**

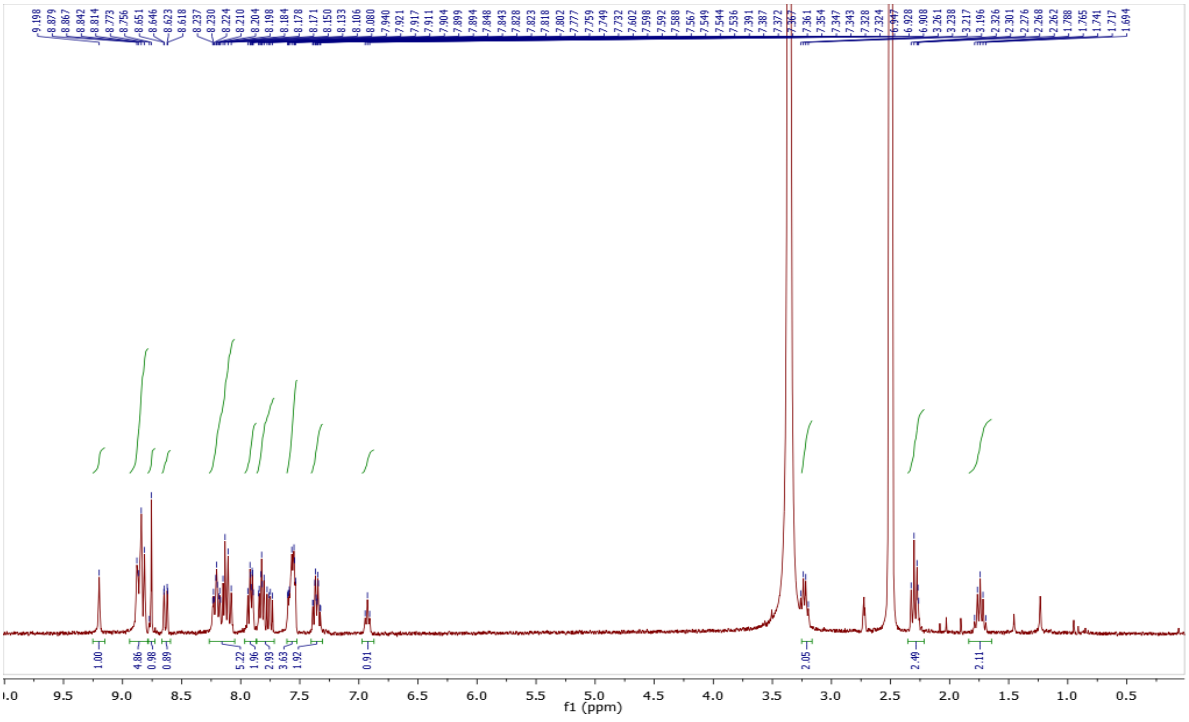

^{1}H NMR of Ruthenium complex (S8)

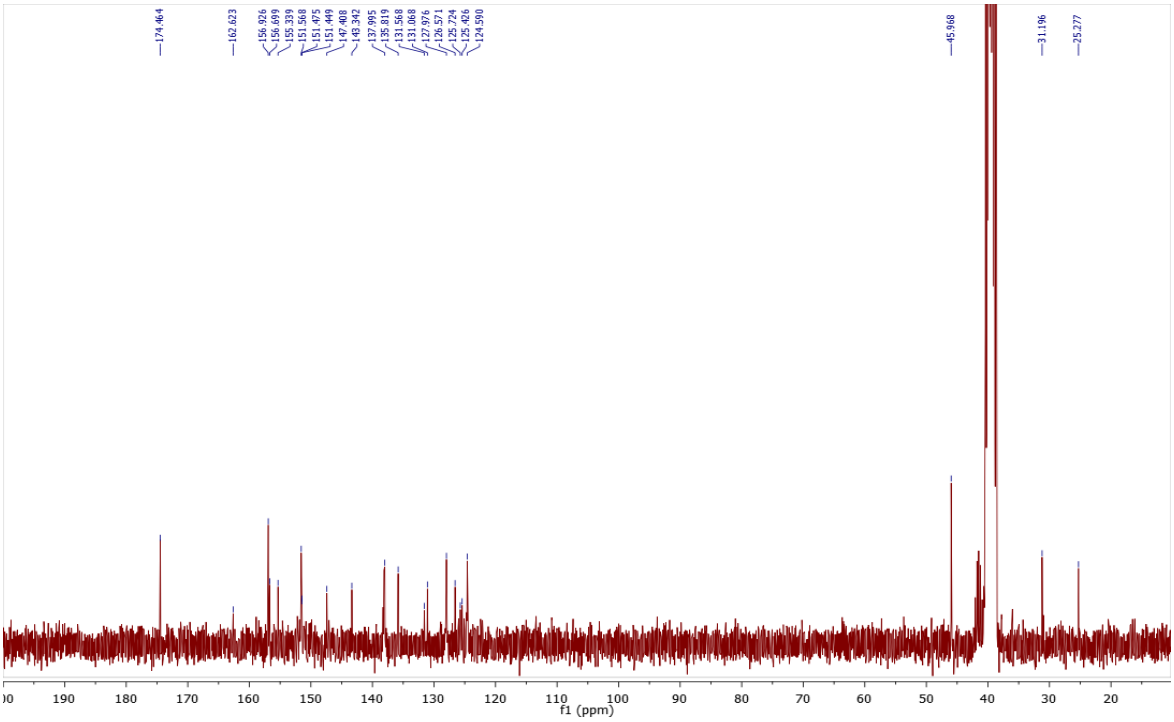

^{13}C NMR of Ruthenium complex (S8)

Ruthenium catalyst-N-hydroxysuccinimide ester (S9)

1.0 mg (0.0014 mmol) of ruthenium complex (**S8**), 0.24 mg (1.5 eq.) of *N*-hydroxysuccinimide, and 0.35 mg (1.3 eq.) of EDC•HCl were dissolved in the 1:1 mixture of DCM/DMF to be 0.05 M solution. The reaction mixture was stirred vigorously for 2 h and directly injected into HPLC (condition for elution gradient: 0 min, A:B = 100:0; 28 min, A:B = 30:70; 29 min, A:B = 0:100; 30 min, A:B = 100:0; solution A: 0.1% aqueous TFA solution; solution B, 0.1 % TFA in HPLC grade acetonitrile; flow rate: 3.0 mL/min; UV detection: 254 and 455 nm). The product was found at R.T. 15.7 min. to yield 1.1 mg (95 %) of **Ruthenium catalyst-N-hydroxysuccinimide ester (S9)**. **^{1}H NMR** (400 MHz, DMSO-d_6) δ 9.24 (s, 1H), 8.90 – 8.85 (m, 3H), 8.83 (dt, *J* = 8.3, 1.0 Hz, 2H), 8.76 (s, 1H), 8.64 (dd, *J* = 8.4, 1.2 Hz, 1H), 8.21 (m, 2H), 8.12 (m, 3H), 7.95 – 7.89 (m, 2H), 7.83 (m, 2H), 7.76 (dd, *J* = 8.3, 5.3 Hz, 1H), 7.57 (m, 4H), 7.36 (m, 2H), 7.04 (s, 1H), 3.31 (t, *J* = 6.4 Hz, 2H), 2.82 (s, 4H), 2.77 (t, *J* = 7.5 Hz, 2H), 1.94 – 1.82 (m, 2H). **^{13}C NMR** (101 MHz, DMSO-d_6) δ 170.22, 168.78, 157.63, 156.77, 151.44, 147.21, 143.14, 137.91, 135.61, 127.82, 126.40, 125.53, 125.20, 124.44, 40.14, 38.25, 27.79, 25.43, 24.96. **LC-MS (ESI)** RT= 1.55 min. Expected Mass: 835.1805, *m/z* found: 417.8 $[M]^{2+}$

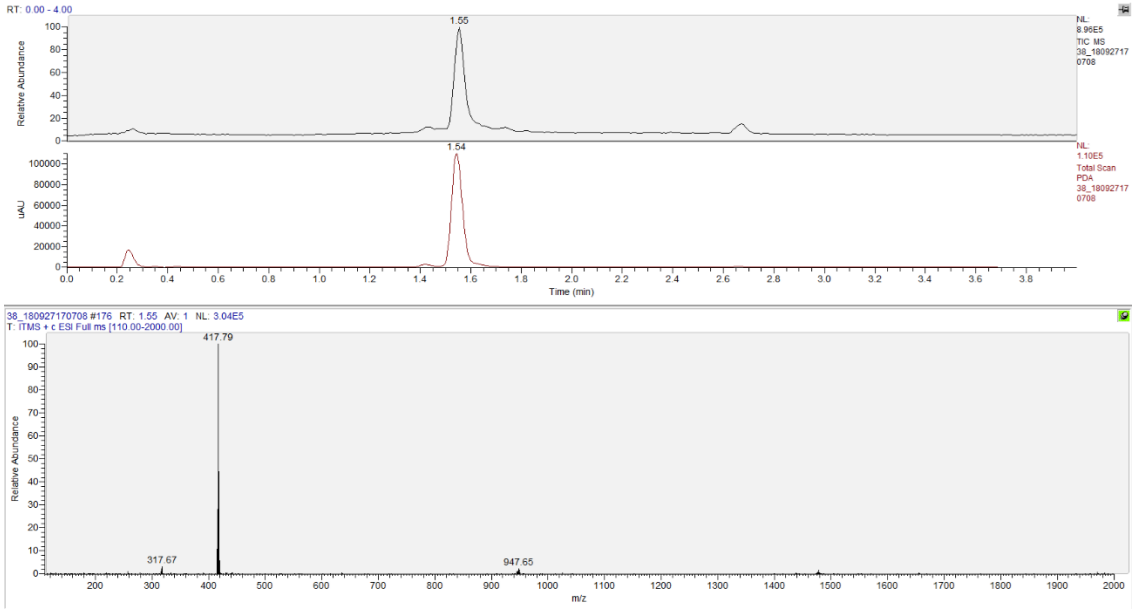

LC-MS trace of compound **S9**.

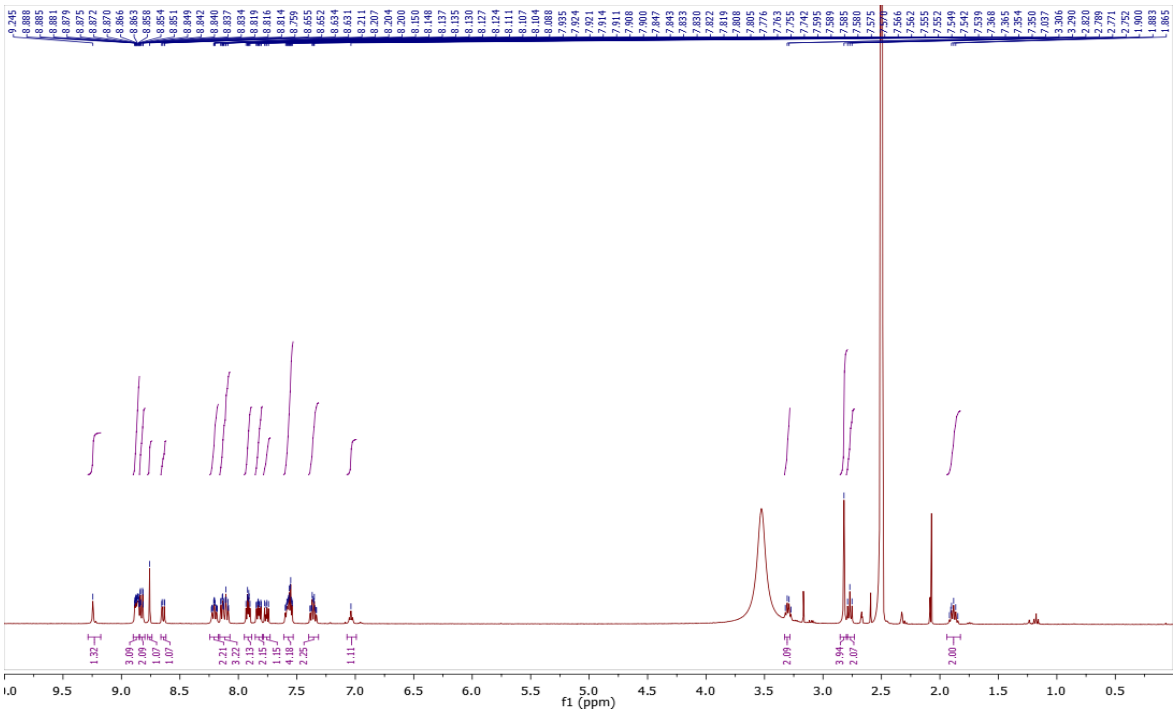

^{1}H NMR of Ruthenium catalyst-N-hydroxysuccinimide ester (S9)

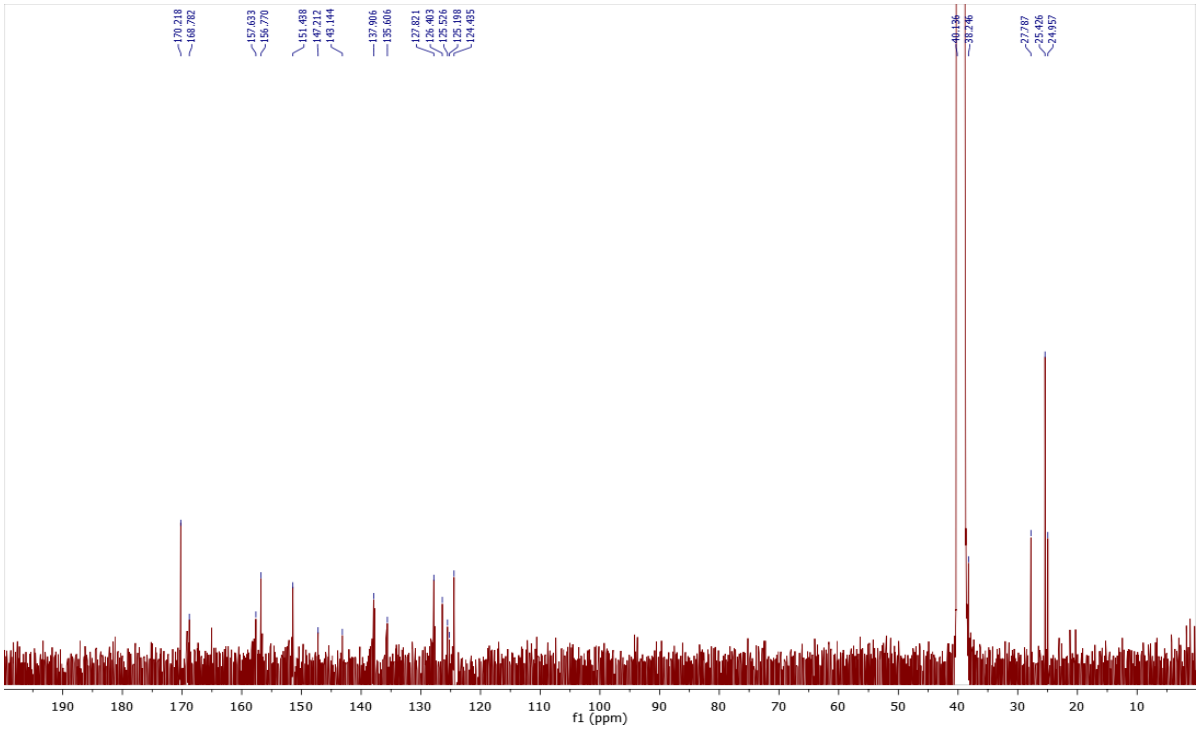

^{13}C NMR of Ruthenium catalyst-N-hydroxysuccinimide ester (S9)

Synthesis of Pz monomer

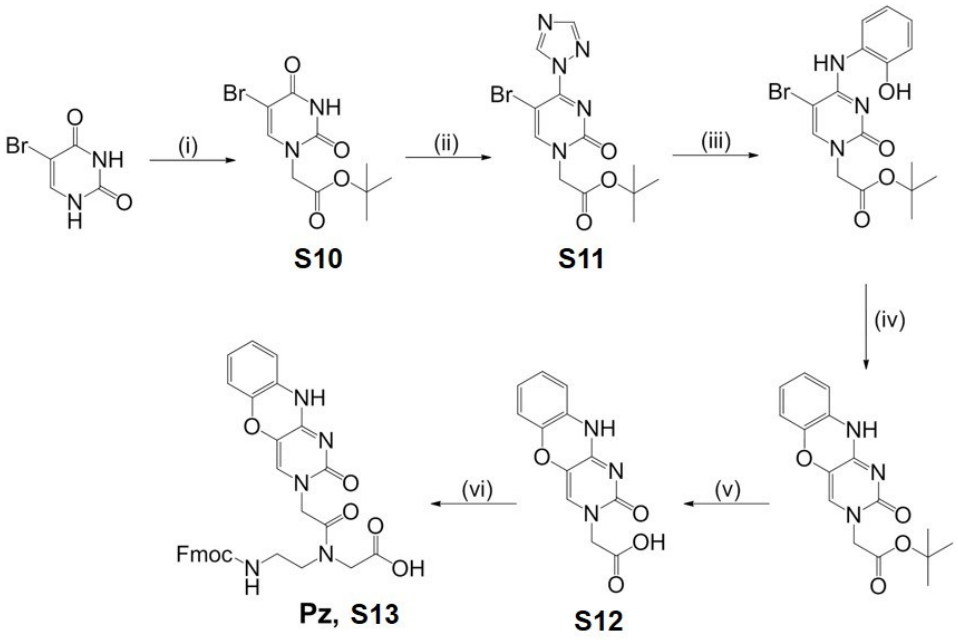

Reagents and conditions: (i) *tert*-butyl bromoacetate (1.0 eq.), K_2CO_3 (1.0 eq.), DMF, r.t. 21 h, 85 %; (ii) 1,2,4-triazole (9.0 eq.), $POCl_3$ (2.0 eq.), Triethylamine (15.0 eq.), ACN, 0 °C → r.t., 21 h, 79 %; (iii) 2-aminophenol (2.0 eq.), DBU (2.1 eq.), ACN, r.t. 20 h; (iv) KF (10.0 eq.), Ethanol, Reflux, 20 h; (v) TFA (excess), r.t., 5 h, 41 %; (vi) a) TSTU (1.0 eq.), diisopropylethylamine (1.3 eq.), DMF, r.t. 20 min. b) *N*-[2-(Fmoc-amino)-ethyl]glycine (1.0 eq.), diisopropylethylamine (3.0 eq.), DMF, r.t. 6 h, 76 %.

5-Bromo-N^1-*tert*-butoxycarbonylmethyl-uracil (S10) and **5-Bromo-N^1-(*tert*-butoxycarbonylmethyl)-4-N^1-(1,2,4-triazolyl)-uracil (S11)** were prepared according to cited procedures.[2]

Direct synthesis of precursor of Pz monomer (S12)

0.4 mL of DBU (2.1 eq.) was added to a solution of compound **S11** in ACN (50 mL/7.4 mmol of **S11**). The resulting solution was stirred at r.t. for 20 h and evaporated under vacuum. The crude was dissolved in ethyl acetate and the solution was filtered through silica gel to remove the impurities. The filtrate was evaporated to dryness for the next reaction. To the crude product, 740 mg of KF (10 eq.) and 50 mL of ethanol were added. The reaction mixture was refluxed for 20 h. After drying the reaction mixture in vacuum, the crude was filtered through silica gel and washed with 10 % MeOH/ethyl acetate solution (500 mL). The filtrate was evaporated and redissolved in a minimum amount of DCM and 2 mL of trifluoroacetic acid was added to the solution. The reaction mixture was stirred vigorously for 5 h and evaporated. The crude was injected into reverse phase column chromatography (Biotage) with condition: elution gradient: 0 min, A:B = 100:0; 28 min, A:B

= 30:70; 29 min, A:B = 0:100; 30 min, A:B = 100:0; solution A: 0.1% aqueous TFA solution; solution B, 0.1 % TFA in HPLC grade acetonitrile; flow rate: 3.0 mL/min; UV detection: 254 and 358 nm. R.T. 14.1 min. Lyophilized fractions yield 136 mg (41 % for three steps) of compound **S12**. **^{1}H NMR** (300 MHz, DMSO-d_6) δ 7.41 (s, 1H), 6.92 – 6.73 (m, 4H), 4.30 (s, 2H). **^{13}C NMR** (75 MHz, DMSO-d_6) δ 170.24, 154.53, 154.04, 142.57, 126.74, 124.10, 122.30, 115.59, 110.22, 79.43, 50.10. **LC-MS (ESI)** RT= 1.54 min. Expected Mass: 259.0593, *m/z* found: 260.04 $[M+H]^+$.

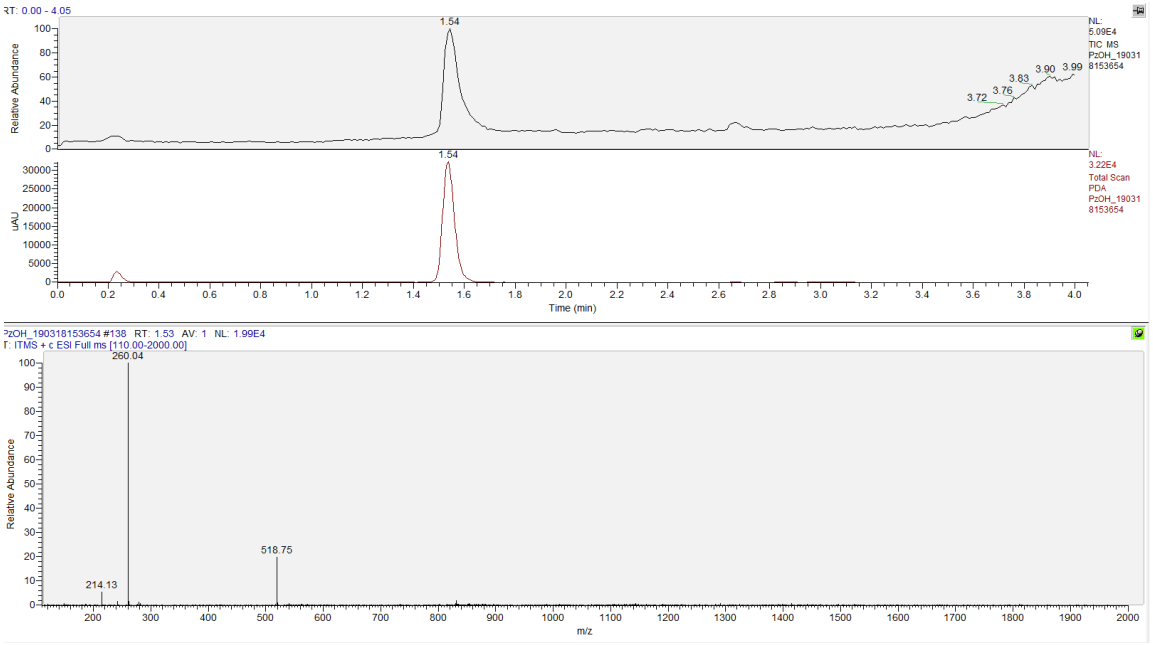

LC-MS trace of compound S12.

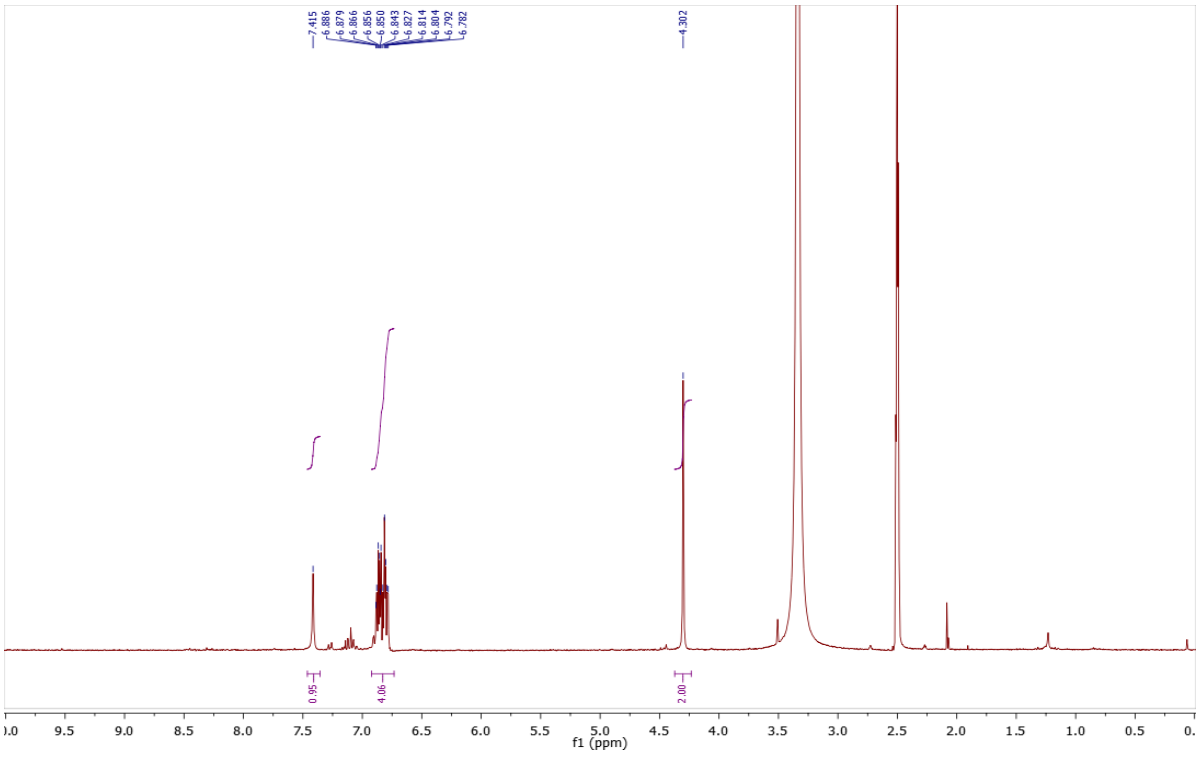

^{1}H NMR of N^{1}-(tert-Butoxycarbonylmethyl)phenoxazine (S12)

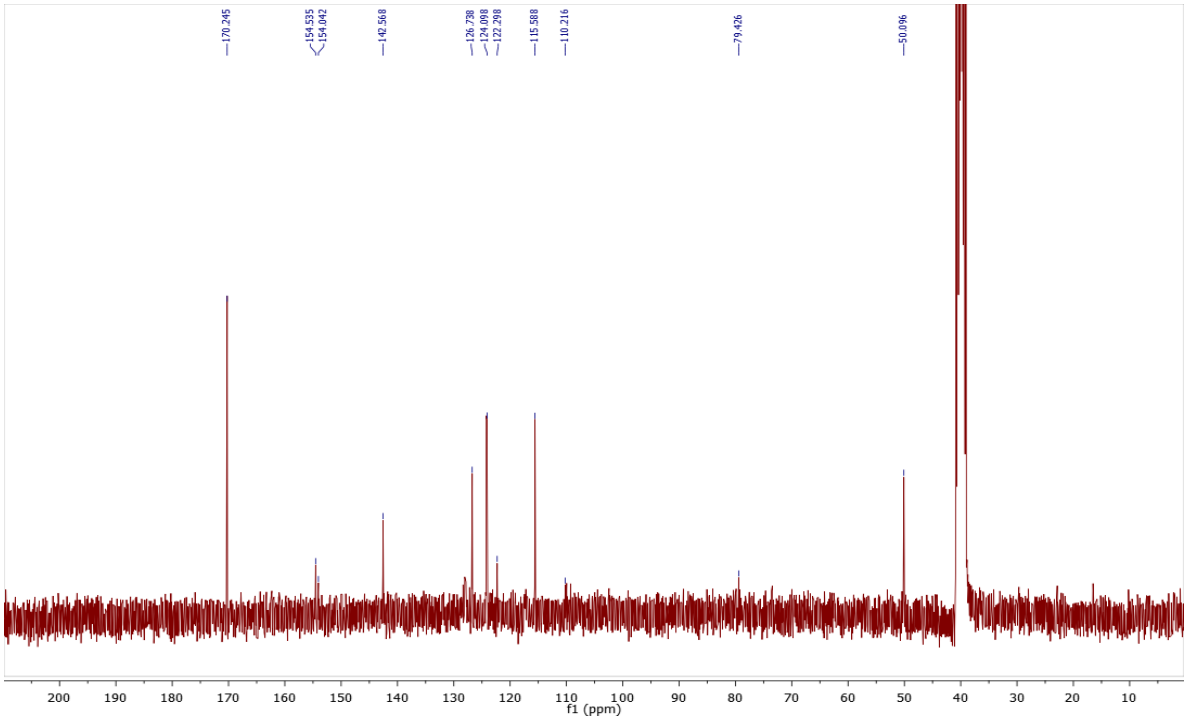

^{13}C NMR of N^{1}-(tert-Butoxycarbonylmethyl)phenoxazine (S12)

Synthesis of Pz monomer (S13)

136 mg (0.524 mmol) of compound **S12** were dissolved in 2 mL DMF. To the resulting solution, 157 mg (1.0 eq.) of TSTU and 0.12 mL (1.3 eq.) of diisoproplyethylamine were added and stirred for 20 min to pre-activate compound **S12**. 178 mg (1.0 eq.) of *N*-[2-(Fmoc-amino)-ethyl]glycine were added to the reaction mixture, followed by addition of 0.25 mL of diisopropylethylamine. After 6 h under stirring, the sample was directly injected into reverse phase column chromatography (Biotage) to obtain 230 mg (76 %) of yellowish solids, **Pz**, **S13** after lyophilization. **^{1}H NMR** (400 MHz, DMSO-d_6) δ 7.88 (d, J = 7.4 Hz, 2H), 7.72 – 7.64 (m, 2H), 7.41 (t, J = 7.3 Hz, 3H), 7.33 (td, J = 7.4, 1.1 Hz, 2H), 7.22 (s, 1H), 6.93 – 6.72 (m, 4H), 4.59 (s, 1H), 4.42 (s, 1H), 4.37 – 4.17 (m, 4H), 3.99 (s, 1H), 3.38 – 3.31 (m, 2H), 3.31 – 3.04 (m, 2H). **^{13}C NMR** (101 MHz, DMSO-d_6) δ 206.93, 171.29, 170.92, 168.40, 167.94, 159.23, 158.86, 158.49, 158.13, 156.77, 156.60, 154.37, 153.91, 144.35, 144.33, 142.62, 141.19, 141.18, 128.07, 127.53, 126.60, 125.60, 124.23, 124.08, 120.57, 117.37, 115.54, 114.48, 65.98, 49.19, 48.18, 47.36, 47.19, 31.15. **LC-MS (ESI)** RT= 2.39 min. Expected Mass: 581.1910, *m/z* found: 582.1 $[M+H]^{+}$.

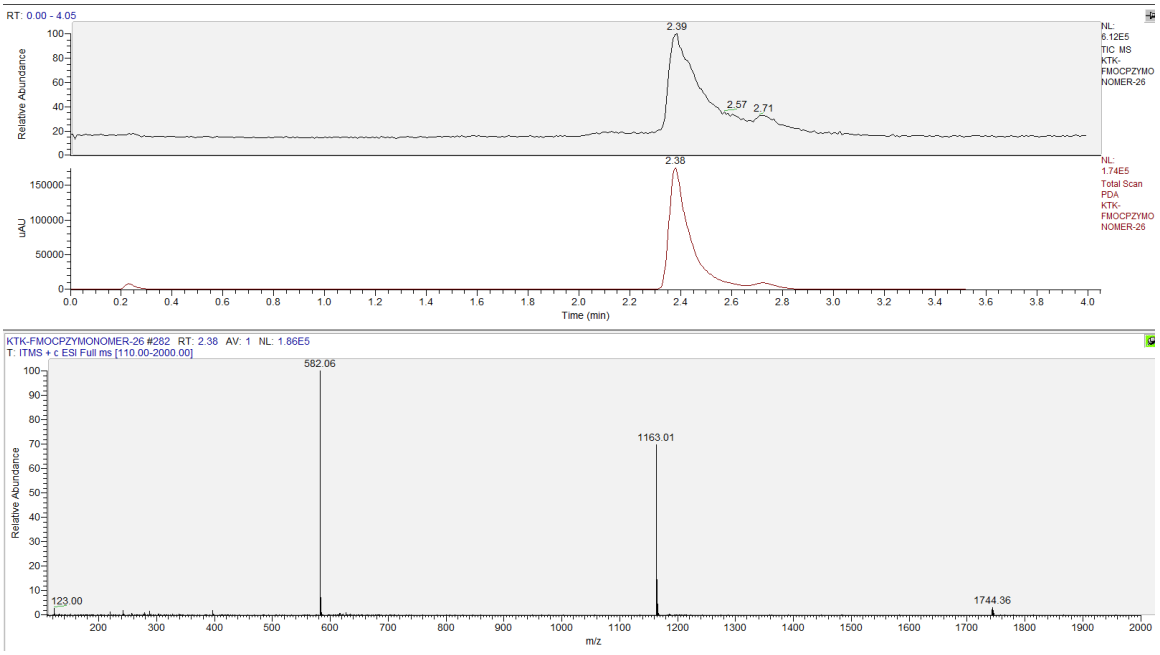

LC-MS trace of compound **S13**.

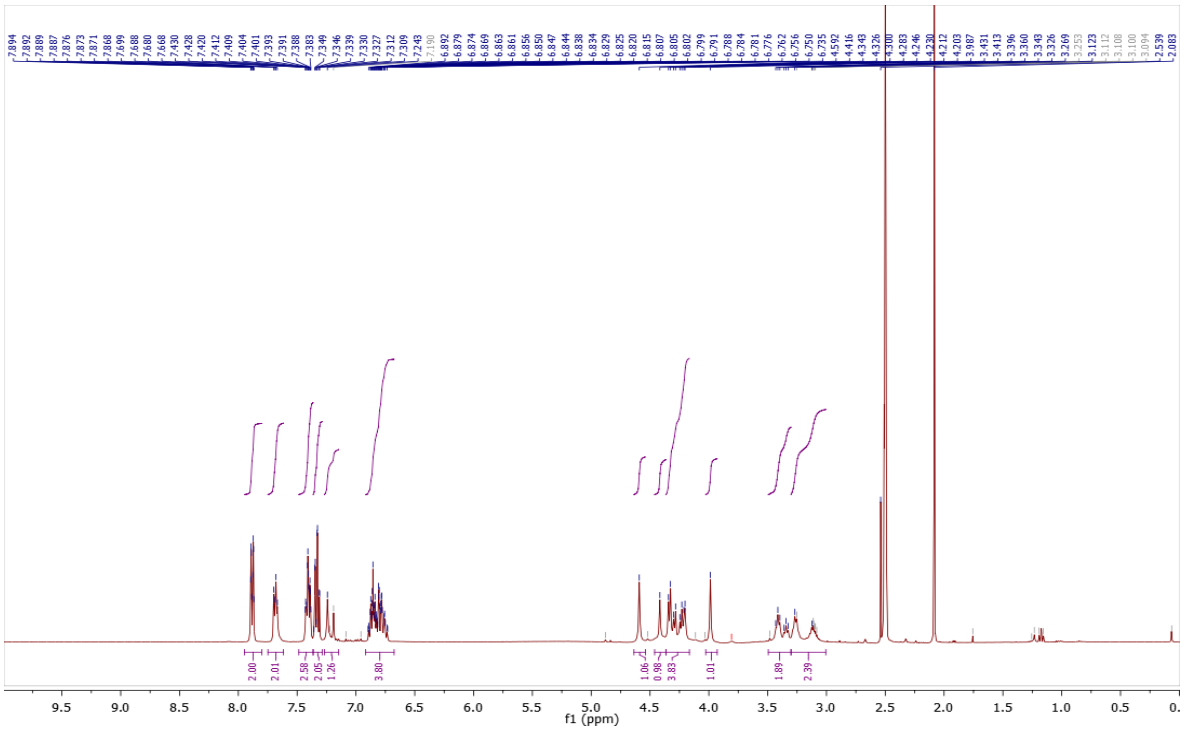

^{1}H NMR of Pz monomer (S13)

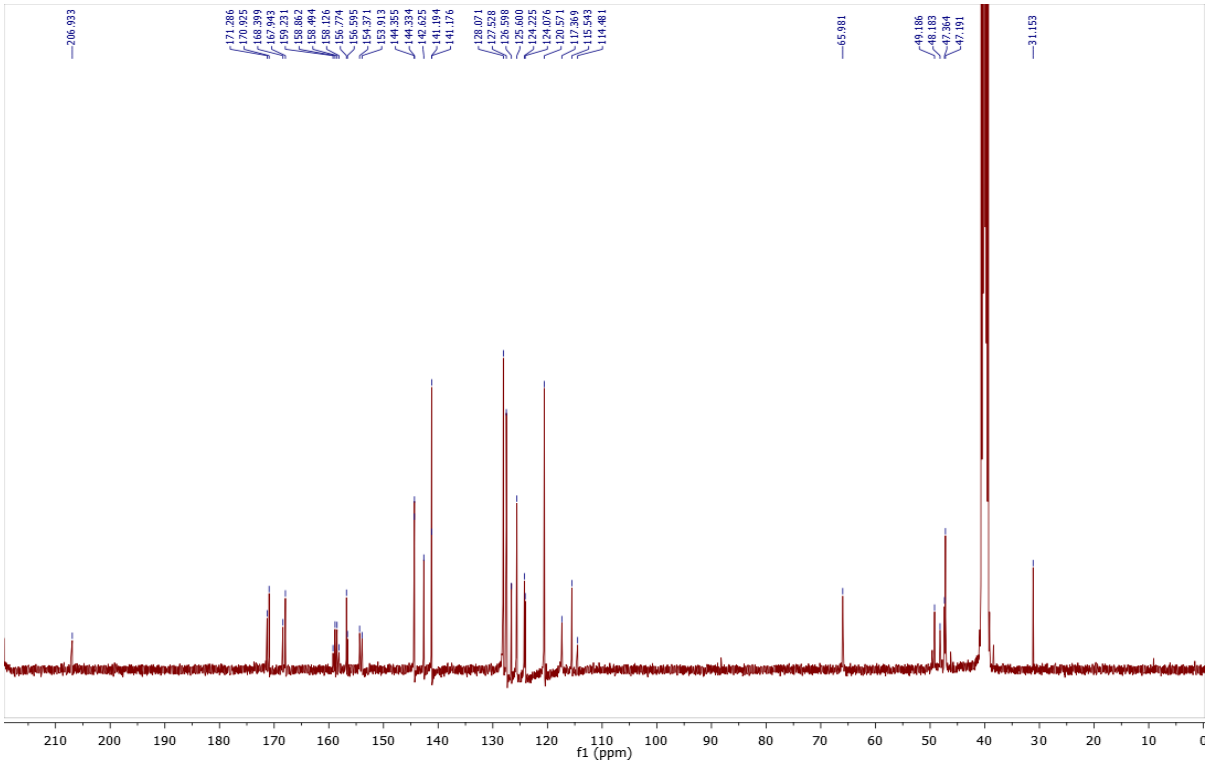

^{13}C NMR of Pz monomer (S13)

Synthesis of 5-FU prodrug (5-FUOPy)

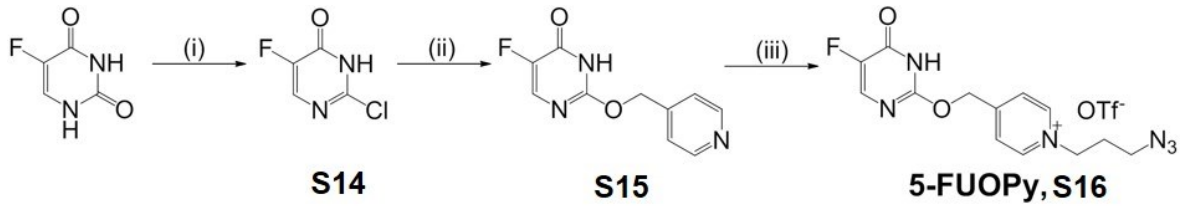

Reagents and conditions: (i) a) $POCl_3$ (10 eq.), *N*,*N*-dimethylaniline (1.5 eq.), 114 °C, 2 h, 64 % b) NaOH (1.3 eq.), THF, r.t. 3 h, 80 %; (ii) NaH (1.5 eq.), 4-pyridinemethanol (1.5 eq), toluene, 135 °C, 4 h, 26 %; (iii) 3-azidopropyl trifluoromethanesulfonate (1.1 eq.), DCM/THF, 0 °C → r.t., 3 h, 24%.

5-fluoro-2-chloro-3H-pyrimidin-4-one (S14) was prepared according to cited procedures.[3,4]

Synthesis of compound S15

123 mg (1.5 eq.) of 4-pyridinemethanol was dissolved in 10 mL of toluene and cooled down to 0 °C in an ice bath. 45 mg (1.5 eq.) of 60 % NaH (dispersion in mineral oil) was added to the solution and stirred at r.t. After 30 min, 111 mg (0.75 mmol) of compound **S14** dispersed in 10 mL of toluene was added to the solution dropwise. The reaction mixture

was refluxed at 135 °C for 4 h and quenched with a few mL of water. After evaporation of the organic solvent, the aqueous solution was adjusted to pH 7 by using conc. HCl. The product was extracted with 10 % MeOH/DCM solution (50 mL x 5). The organic layers were collected, dried with Na_2SO_4 and concentrated. The crude mixture was purified by flash column chromatography (10% MeOH/DCM) to obtain 43 mg (26 %) of **S15**. **^{1}H NMR** (400 MHz, D_2O) δ 8.87 – 8.77 (m, 2H), 8.13 (d, *J* = 6.7 Hz, 2H), 7.87 (d, *J* = 3.9 Hz, 1H), 5.78 (s, 2H). **^{13}C NMR** (75 MHz, D_2O) δ 156.98, 153.91, 144.16, 141.10, 124.38, 67.23. **^{19}F NMR** (282 MHz, D_2O) δ -162.44. **LC-MS (ESI)** RT= 0.36 min. Expected Mass: 221.0601, *m/z* found: 222.0 $[M+H]^+$.

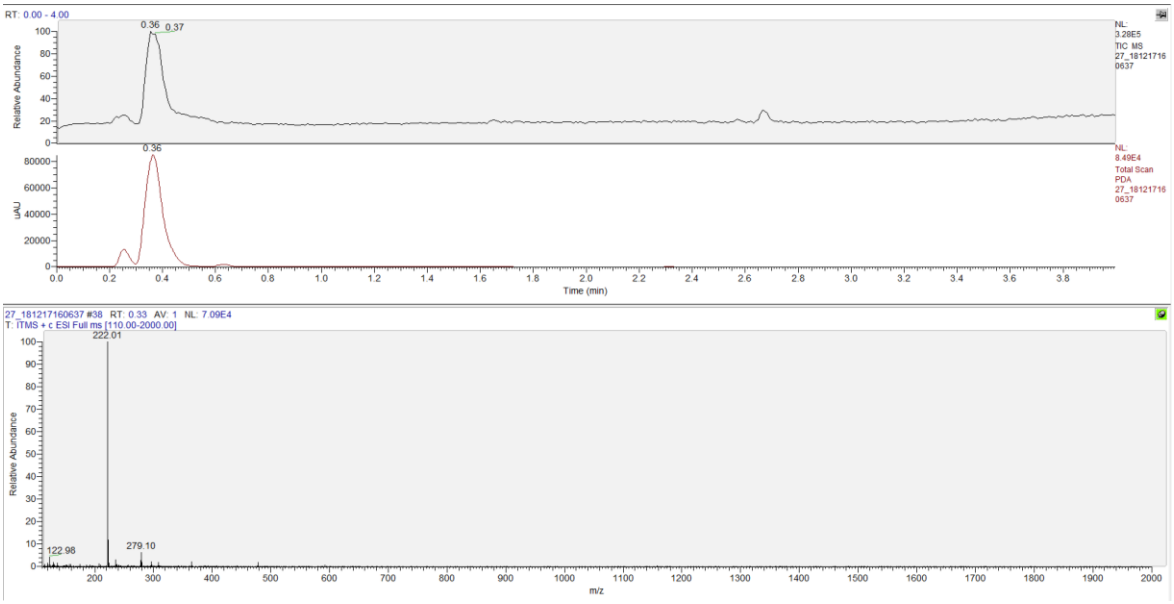

LC-MS trace of compound **S15**.

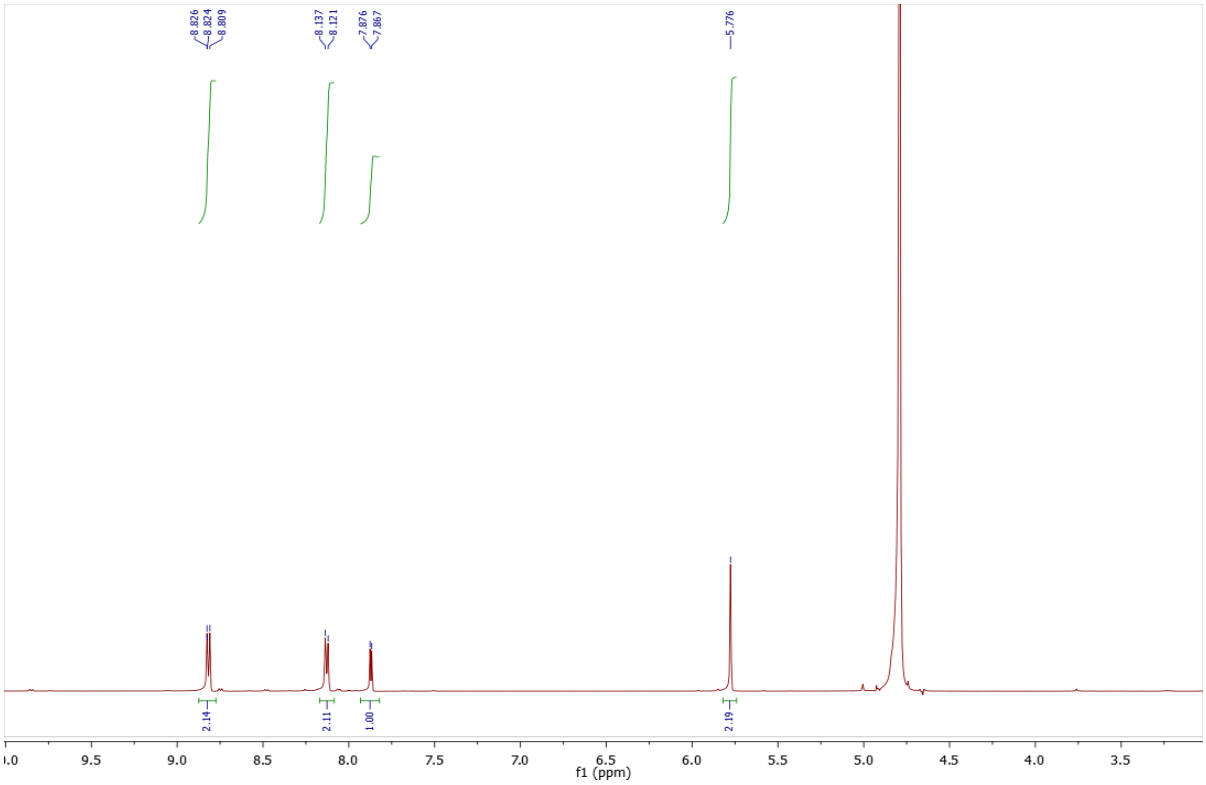

^{1}H NMR of compound **S15.**

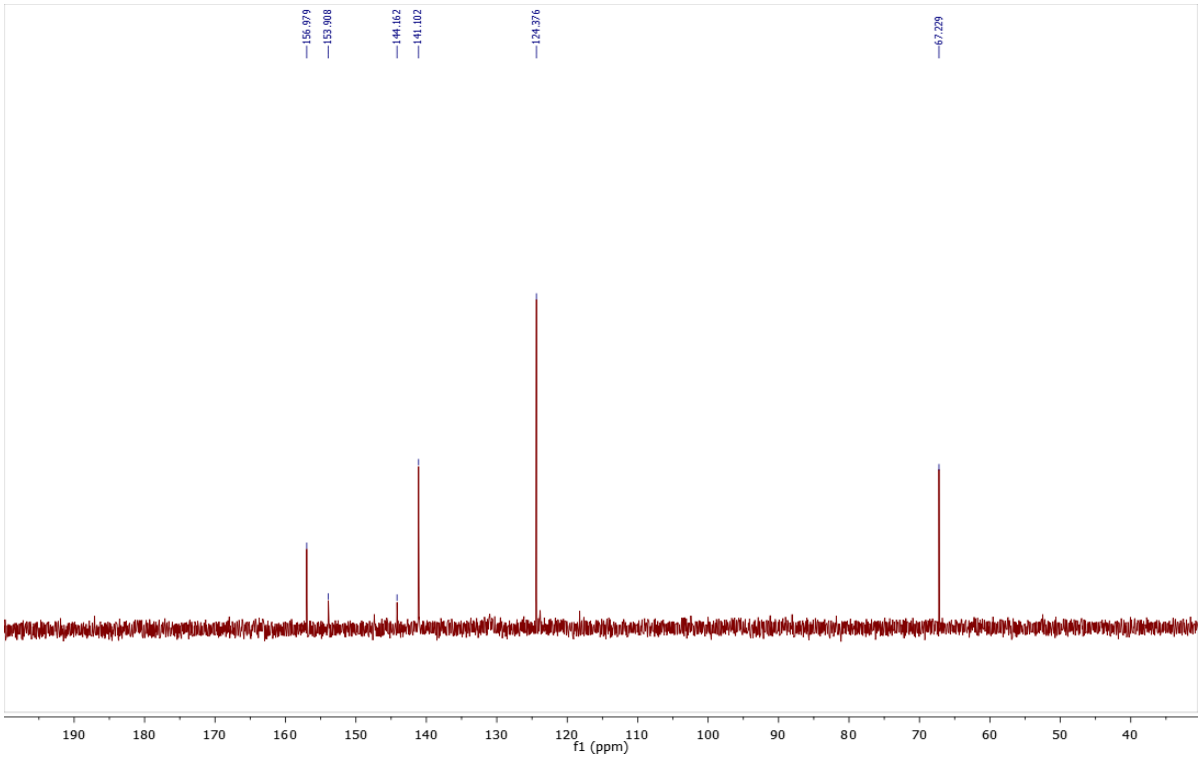

^{13}C NMR of compound **S15.**

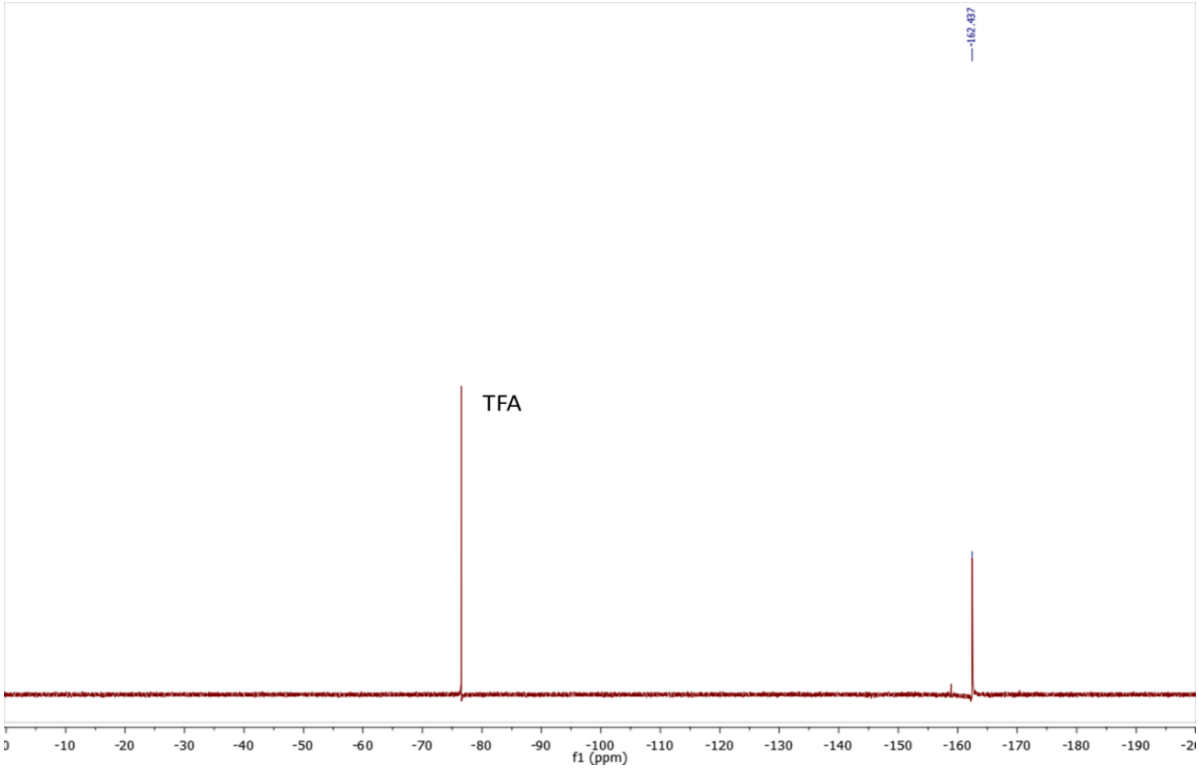

^{19}F NMR of compound **S15.**

Synthesis of 5-FUOPy (S16)

46 mg (0.21 mmol) of dried compound **S15** was dissolved in 5 mL of DCM/THF solution under N_2. The solution was cooled down to 0 °C, then 38 µL (1.1 eq.) of 3-azidopropyl trifluoromethanesulfonate were added dropwise. The reaction was stirred at r.t. for 3 h. The reaction was concentrated under reduced pressure, purified by HPLC with condition: elution gradient: 0 min, A:B = 100:0; 28 min, A:B = 30:70; 29 min, A:B = 0:100; 30 min, A:B = 100:0; solution A: 0.1% aqueous TFA solution; solution B, 0.1 % TFA in HPLC grade acetonitrile; flow rate: 3.0 mL/min; UV detection: 260 nm. The product was found at R.T. 8.8-9.2 min. Lyophilized fractions yield 22 mg (24 %) of oily compound **5-FUOPy (S16)**. **^{1}H NMR** (400 MHz, D_2O) δ 8.90 (d, *J* = 6.8 Hz, 2H), 8.13 (d, *J* = 6.6 Hz, 2H), 7.87 (d, *J* = 3.9 Hz, 1H), 5.76 (s, 2H), 4.74 (t, 2H), 3.52 (t, *J* = 6.3 Hz, 2H), 2.33 (p, *J* = 6.9 Hz, 2H). **^{13}C NMR** (75 MHz, D_2O) δ 155.88, 144.39, 125.31, 67.04, 58.92, 47.51. **^{19}F NMR** (282 MHz, D_2O) δ -160.2. **LC-MS (ESI)** RT= 0.4-0.8 min. Expected Mass: 305.1157, *m/z* found: 305.0 $[M]^+$.

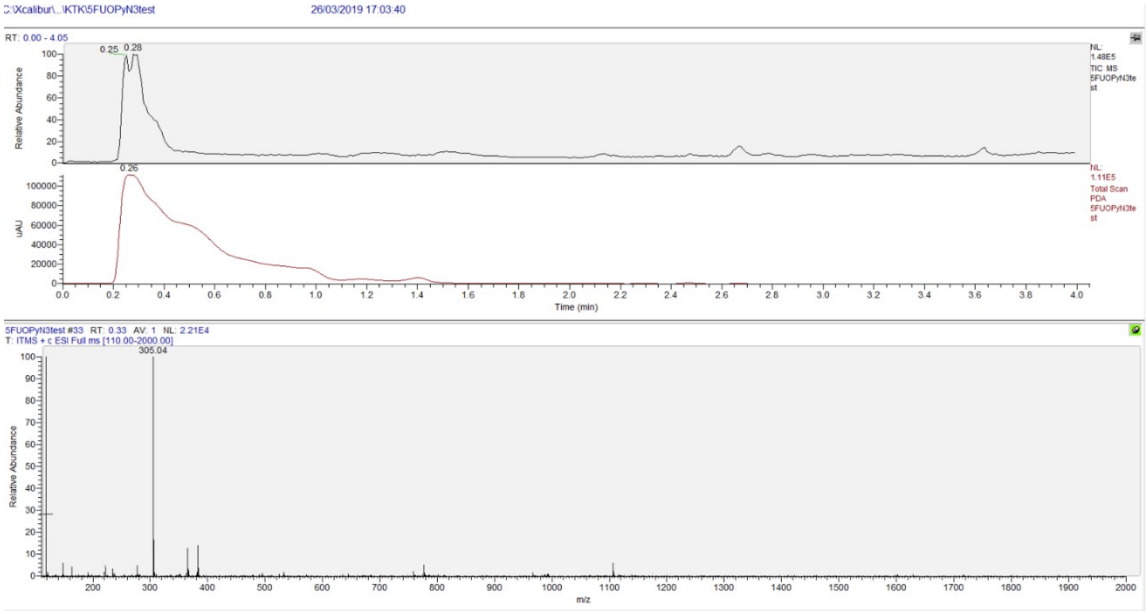

LC-MS trace of compound **S16**.

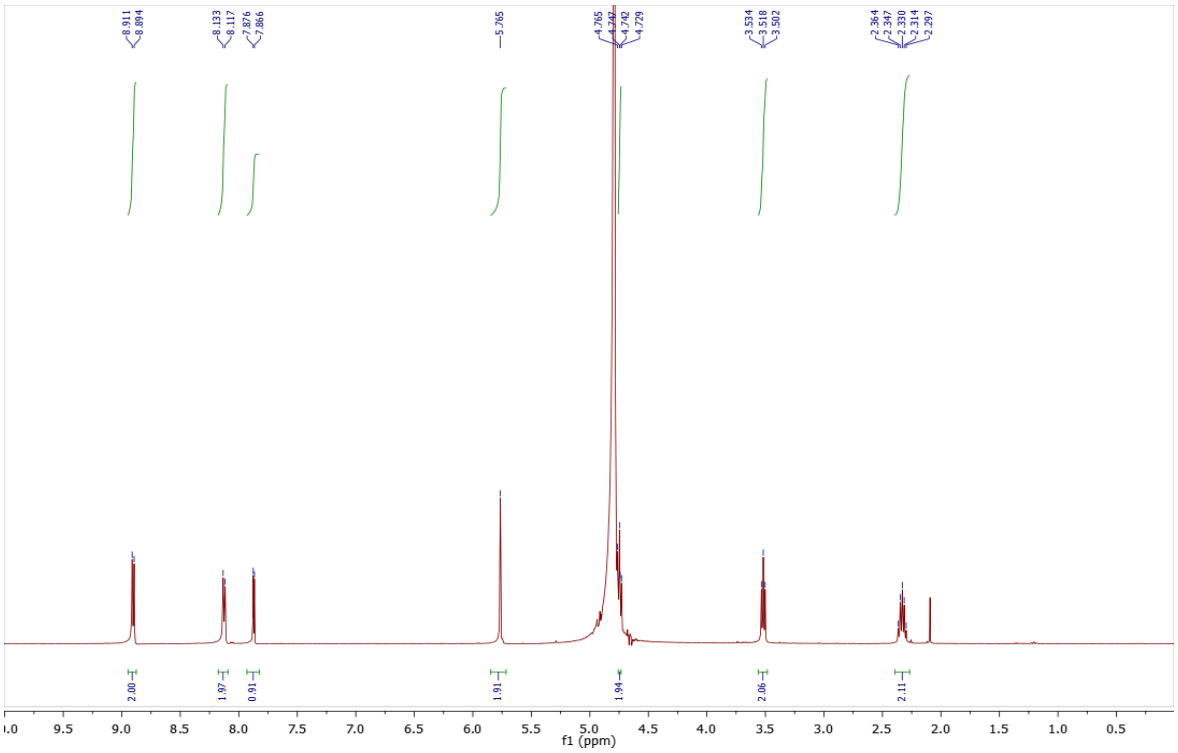

^{1}H NMR of 5-FUOPy (S16)

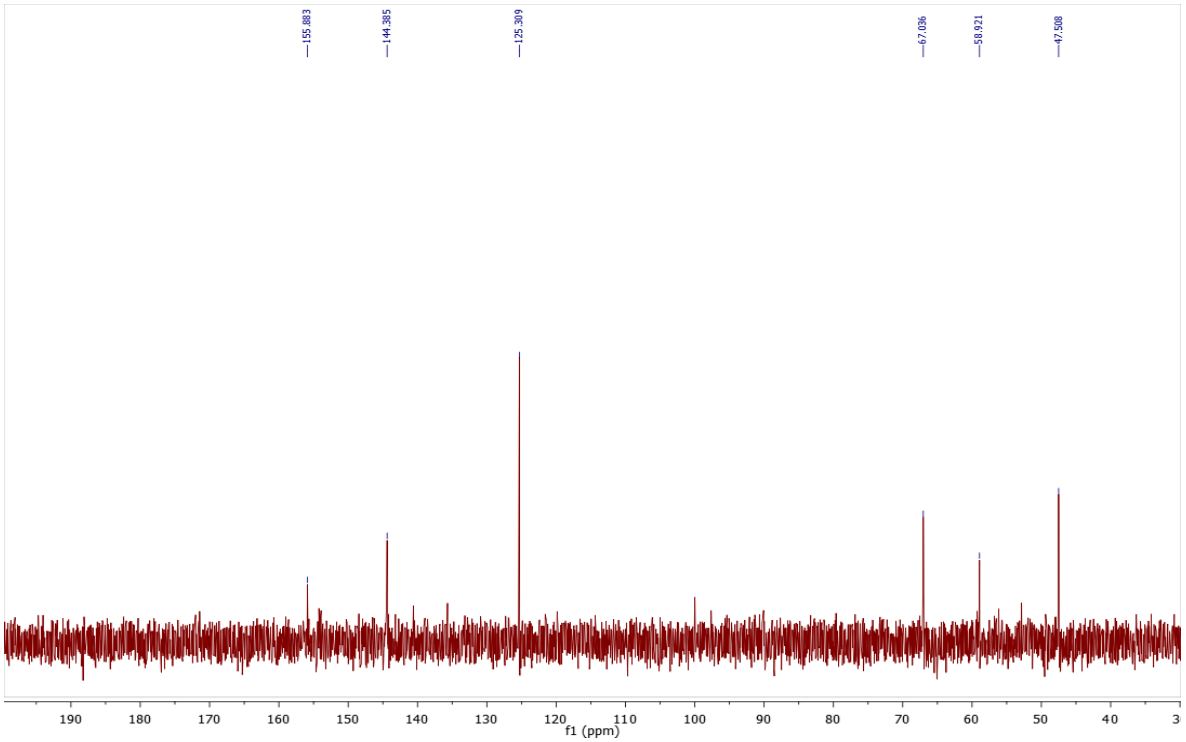

^{13}C NMR of 5-FUOPy (S16)

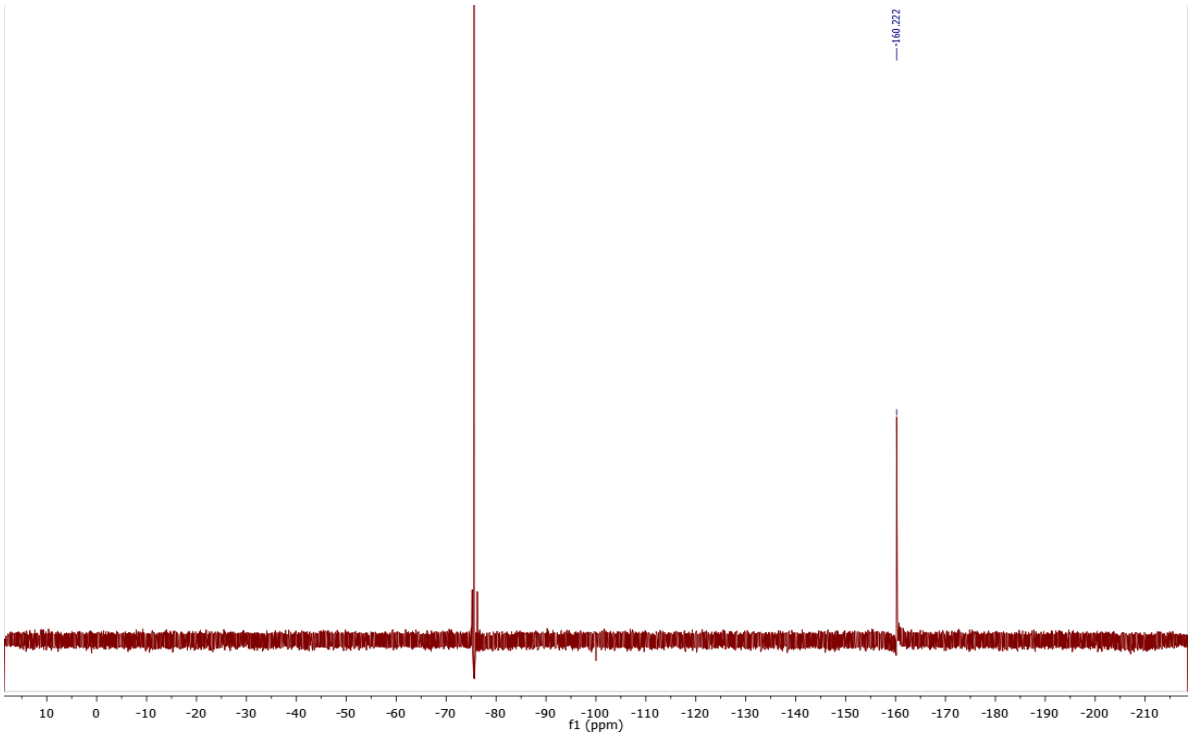

^{19}F NMR of 5-FUOPy (S16)

MALDI-TOF and LC-MS spectra of the synthesized DNAs and PNAs

RuA (Ru-TCAGACTGATGTTGCTAGCTTATCAACATCAGTCTGATAAGCTA); Expected Mass for $C_{474}H_{587}N_{169}O_{268}P_{44}Ru$: 14397.4998, MALDI-TOF m/z found: 14399.2

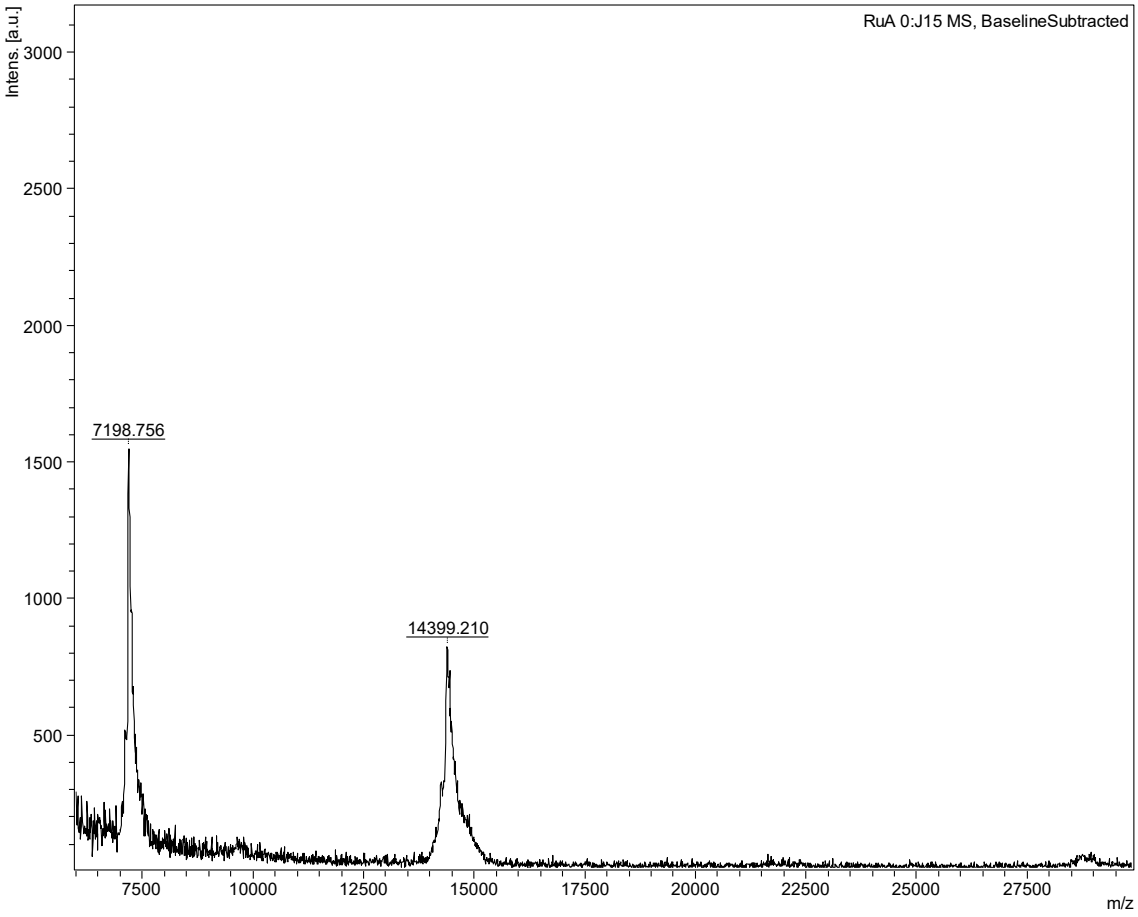

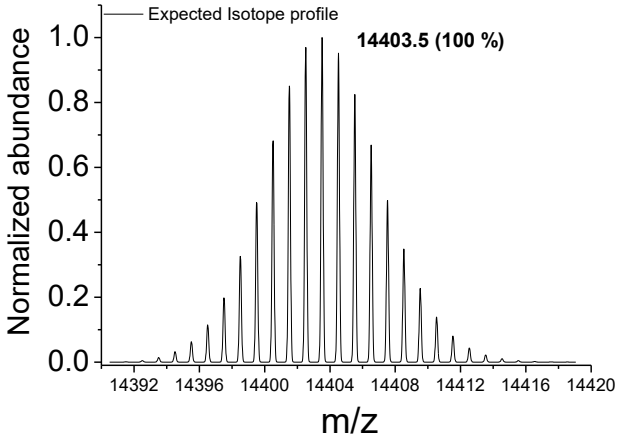

RuB (Ru-TTGCTAGCTTATCAGACTGATGTTGATAAGCTAGCAACATCAGT); Expected Mass for $C_{475}H_{587}N_{171}O_{268}P_{44}Ru$: 14437.5059, MALDI-TOF m/z found: 14437.1

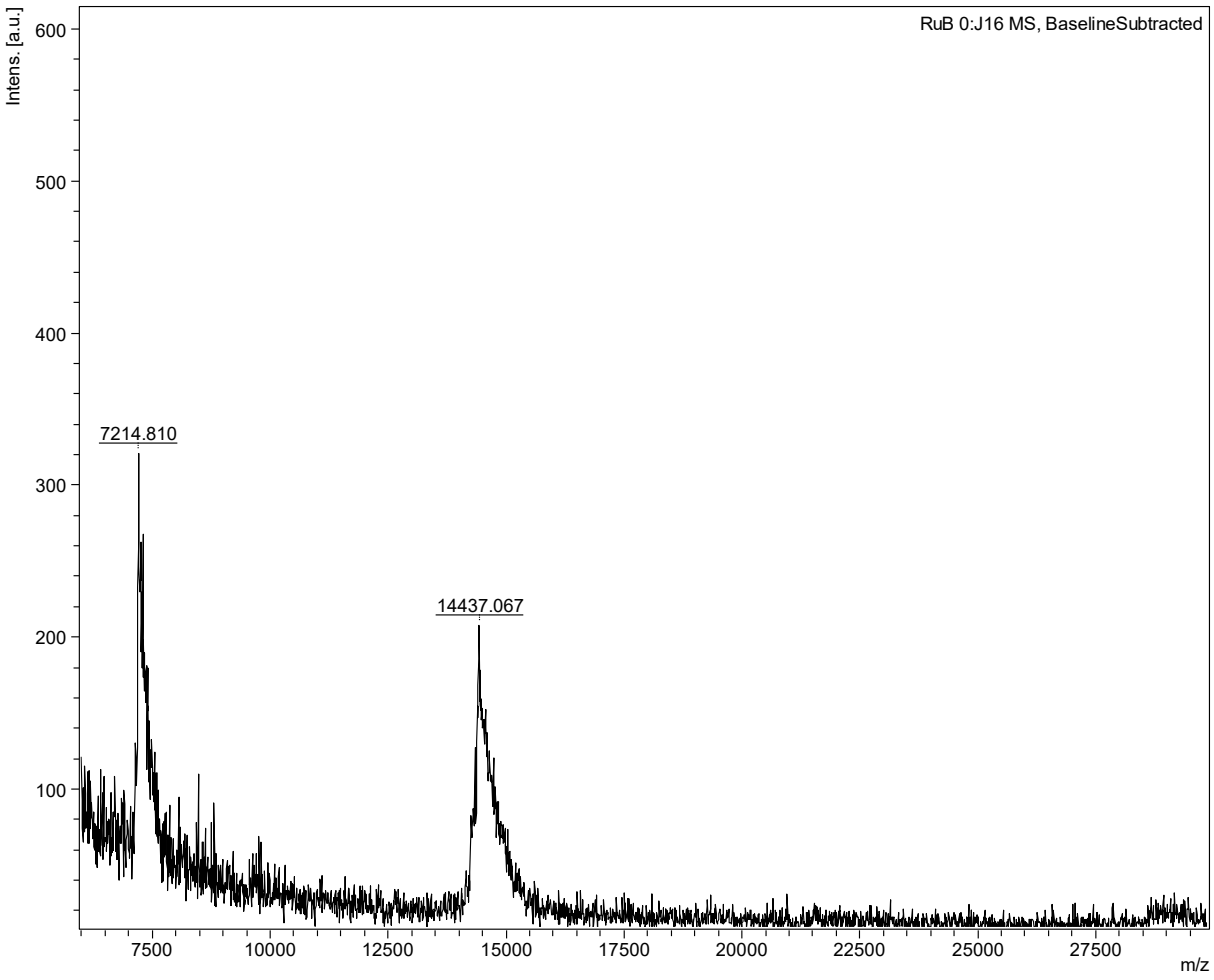

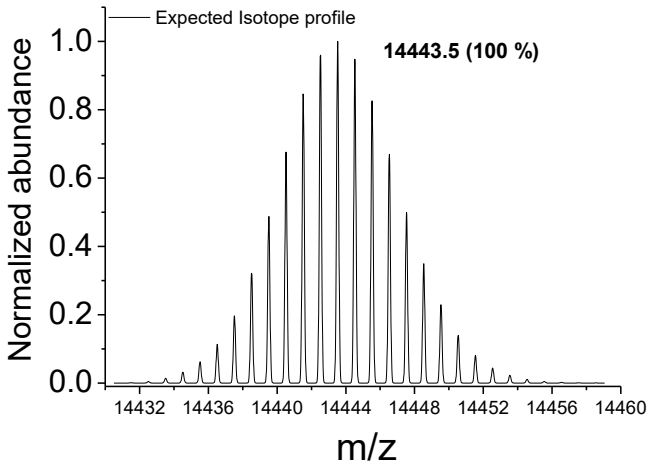

RuS1 (Ru-TTGCACTGATGTTGATAGCTTA); Expected Mass for $C_{260}H_{318}N_{86}O_{139}P_{22}Ru$: 7651.373, MALDI-TOF m/z found: 7652.4

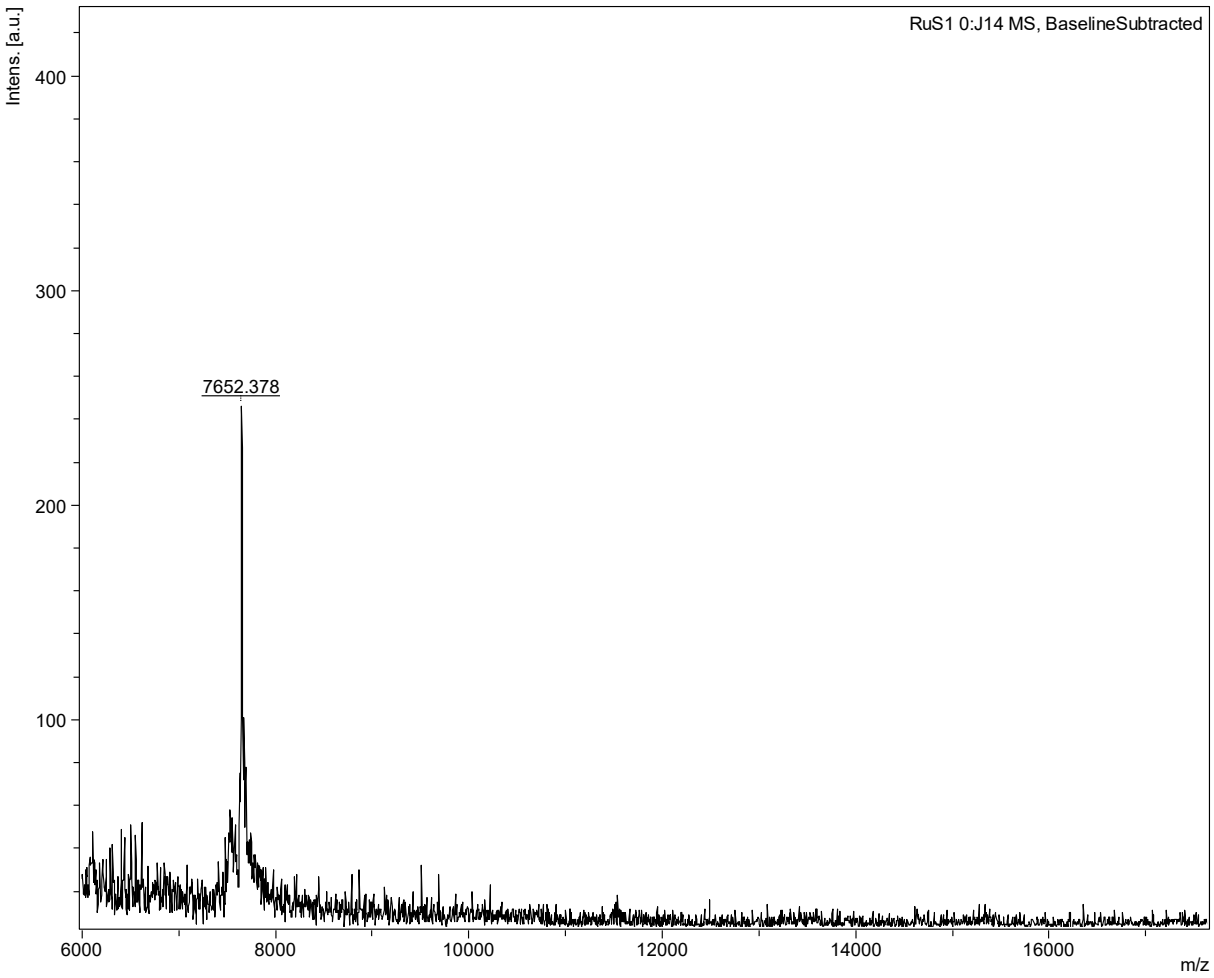

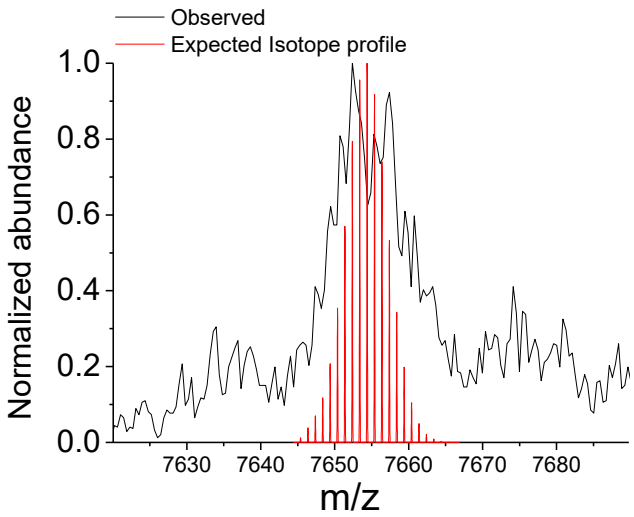

RuS2 (Ru-TCAGACTGATGTTGATAGCTTA); Expected Mass for $C_{260}H_{317}N_{89}O_{137}P_{22}Ru$: 7660.3845, MALDI-TOF m/z found: 7662.9

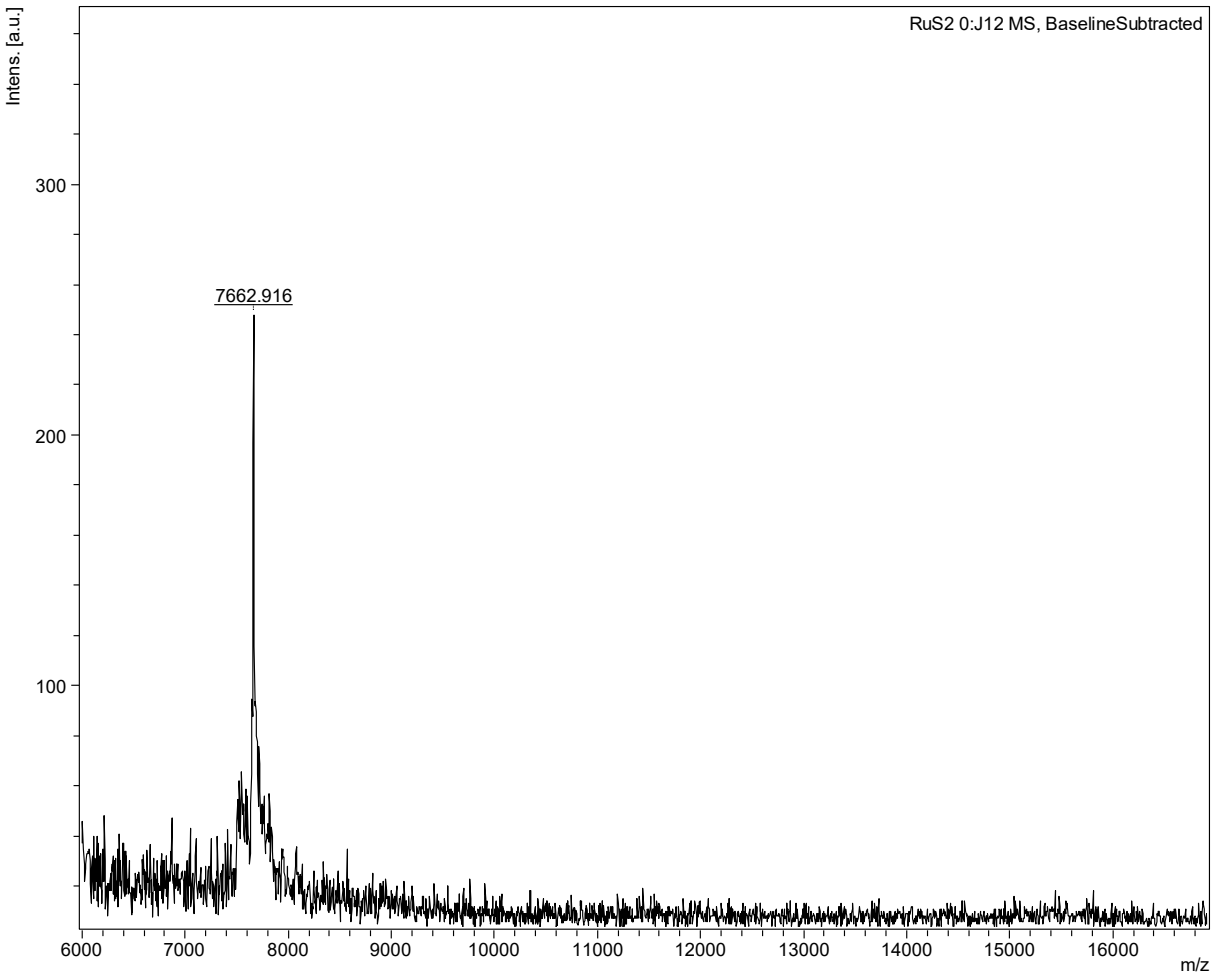

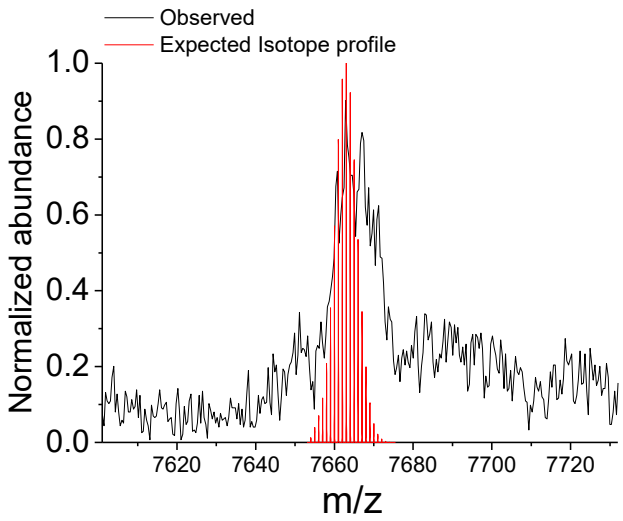

P1 (Ac-G<u>C</u>A<u>A</u>-Lys-Cou); Expected Mass for $C_{77}H_{94}F_2N_{33}O_{18}^+$: 1806.7423, LC-MS (ESI) RT= 1.48 min. m/z: 1807.5 $[M]^+$,1355.3 $[3M+H]^{4+}$, 1205.1 $[2M+H]^{3+}$, 904.4 $[M+H]^{2+}$, 603.3 $[M+2H]^{3+}$, 452.6 $[M+3H]^{4+}$; MALDI-TOF m/z found: 1598.5 $[M\text{-Coumarin}]^+$.

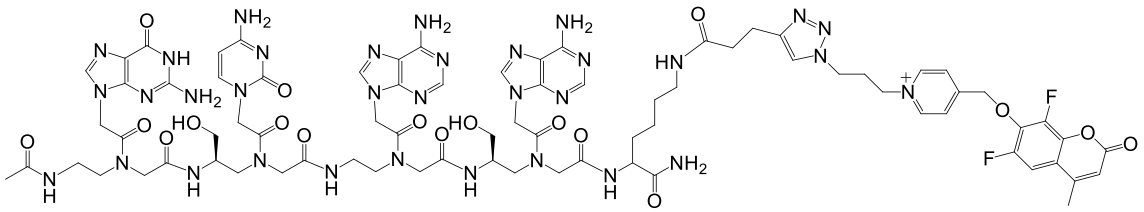

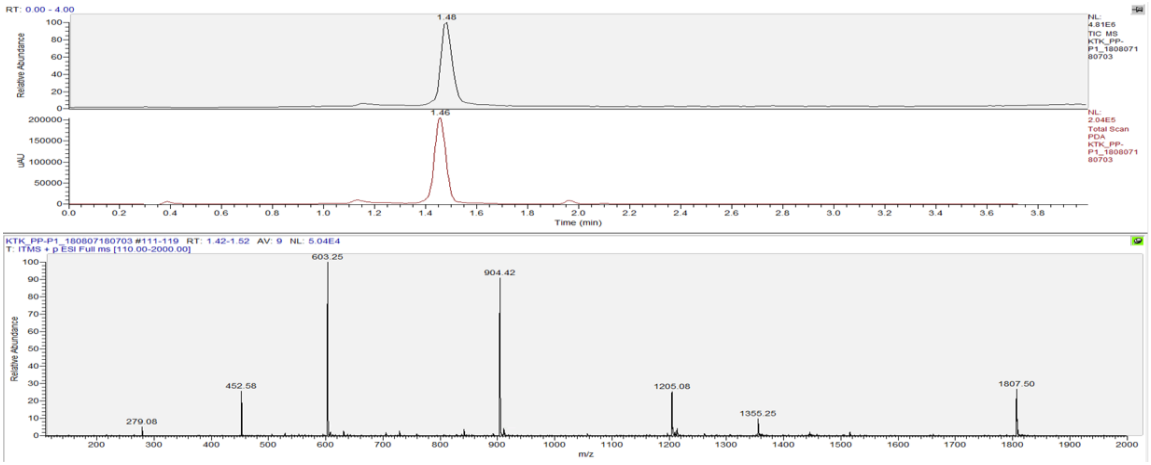

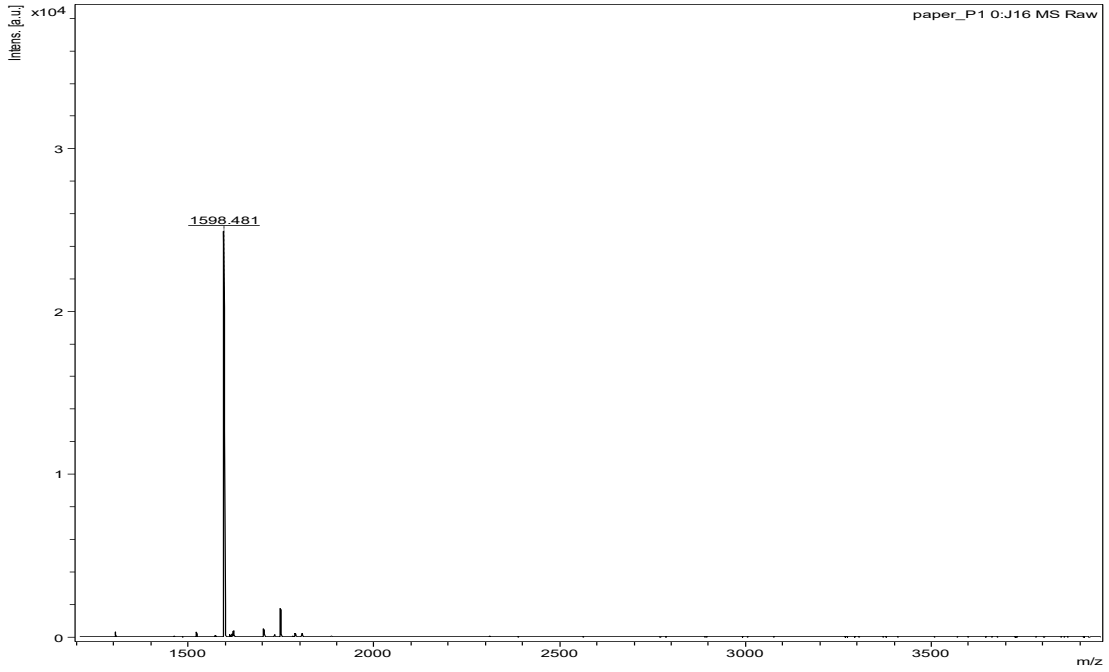

P2 (Ac-**Pz**TG**A**-Lys-Cou); Expected Mass for $C_{83}H_{97}F_2N_{30}O_{21}^+$: 1887.7413, LC-MS (ESI) RT= 1.65 min. m/z: 1888.4 $[M]^+$, 1415.9 $[3M+H]^{4+}$, 1259.1 $[2M+H]^{3+}$, 944.8 $[M+H]^{2+}$, 630.2 $[M+2H]^{3+}$; MALDI-TOF m/z found: 1677.5 $[M\text{-Coumarin}]^+$.

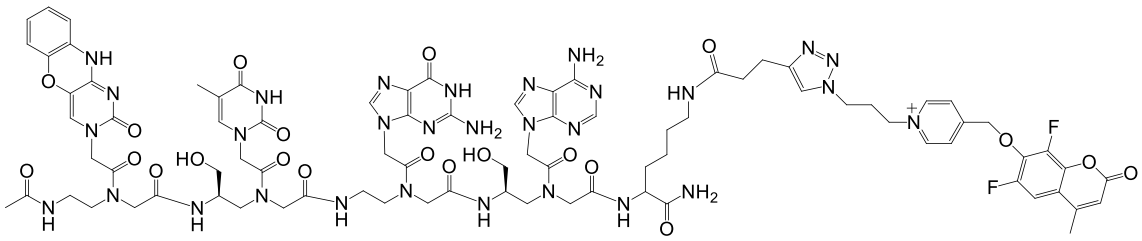

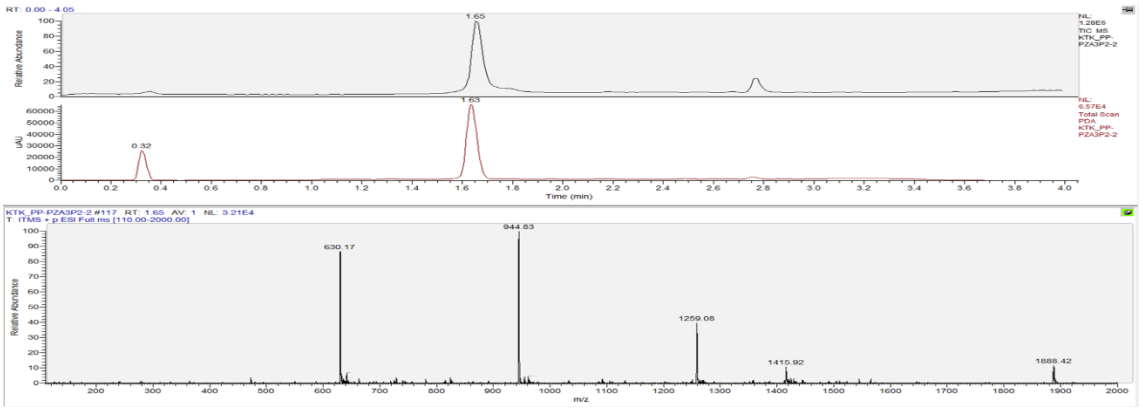

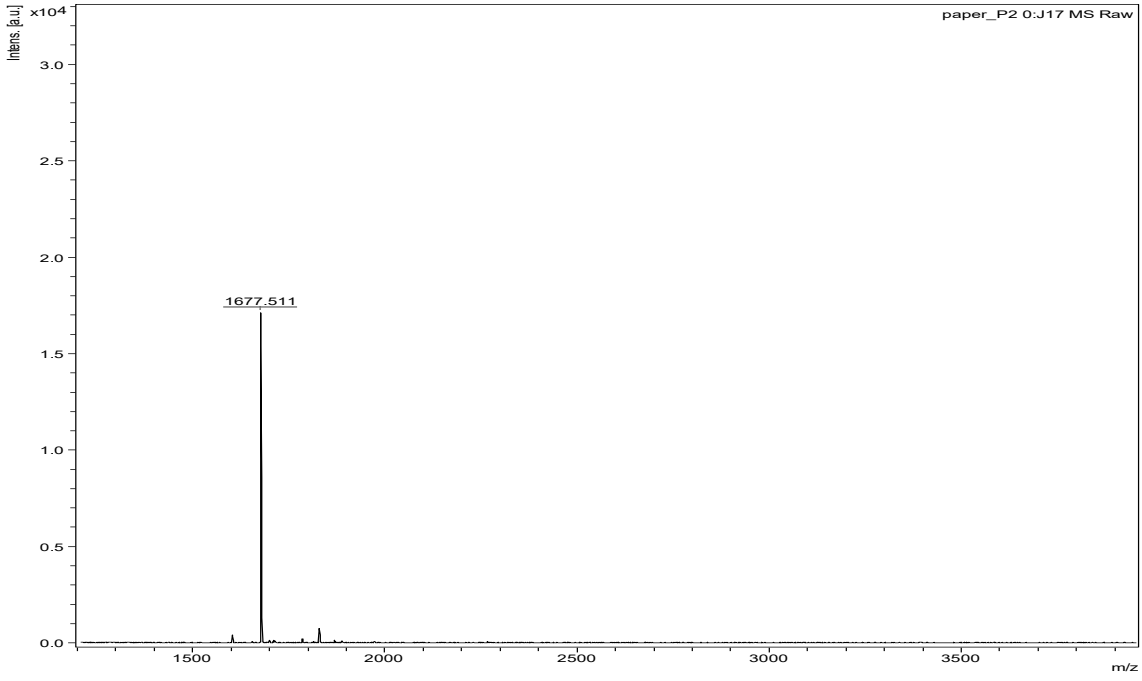

ArgP2 (Ac-CTGA-Lys-Cou); Expected Mass for $C_{83}H_{111}F_2N_{36}O_{18}^{3+}$: 1937.8834, LC-MS (ESI) RT= 1.43 min. m/z: 969.0 $[M+H]^{2+}$, 646.3 $[M+2H]^{3+}$, 484.9 $[M+3H]^{4+}$; MALDI-TOF m/z found: 1729.4 $[M\text{-Coumarin}]^{+}$.

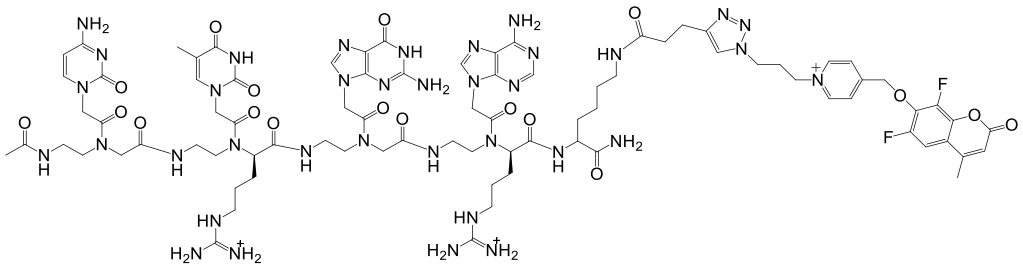

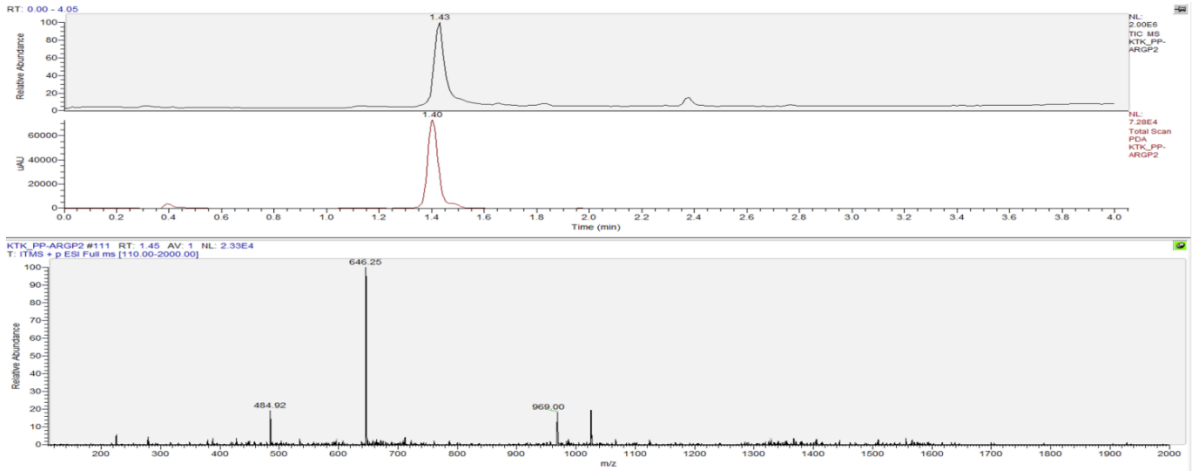

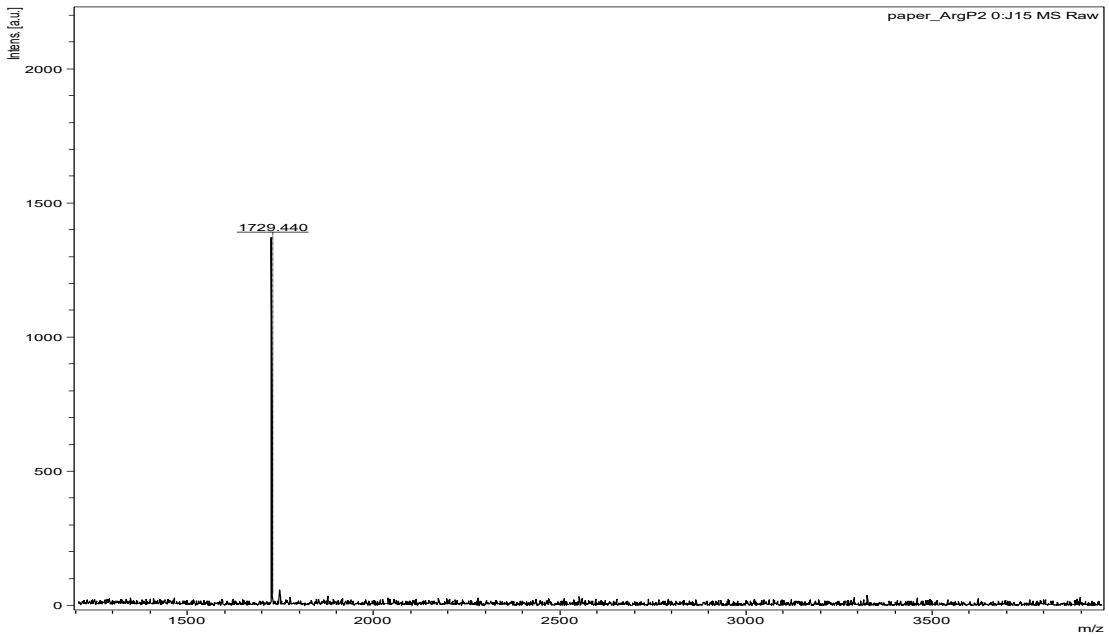

AmiP2 (NH_2-C<u>T</u>G<u>A</u>-Lys-Cou); Expected Mass for $C_{75}H_{93}F_2N_{30}O_{19}^+$: 1755.7196, LC-MS (ESI) RT= 1.46 min. m/z: 1756.3 $[M]^+$, 1316.8 $[3M+H]^{4+}$, 1170.7 $[2M+H]^{3+}$, 878.9 $[M+H]^{2+}$, 586.3 $[M+2H]^{3+}$, 440.0 $[M+3H]^{4+}$; MALDI-TOF m/z found: 1543.6 $[M\text{-Coumarin}]^+$.

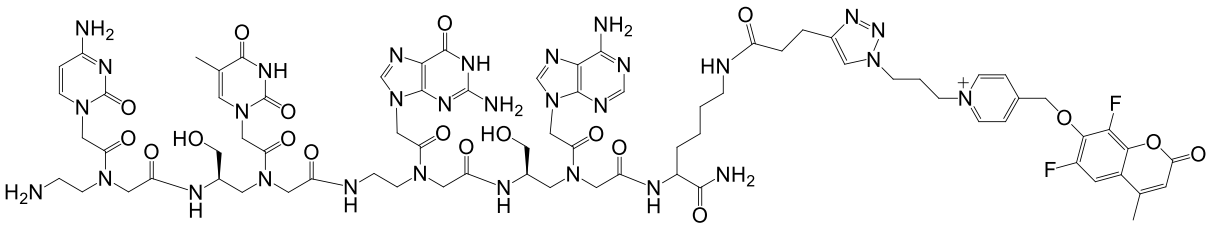

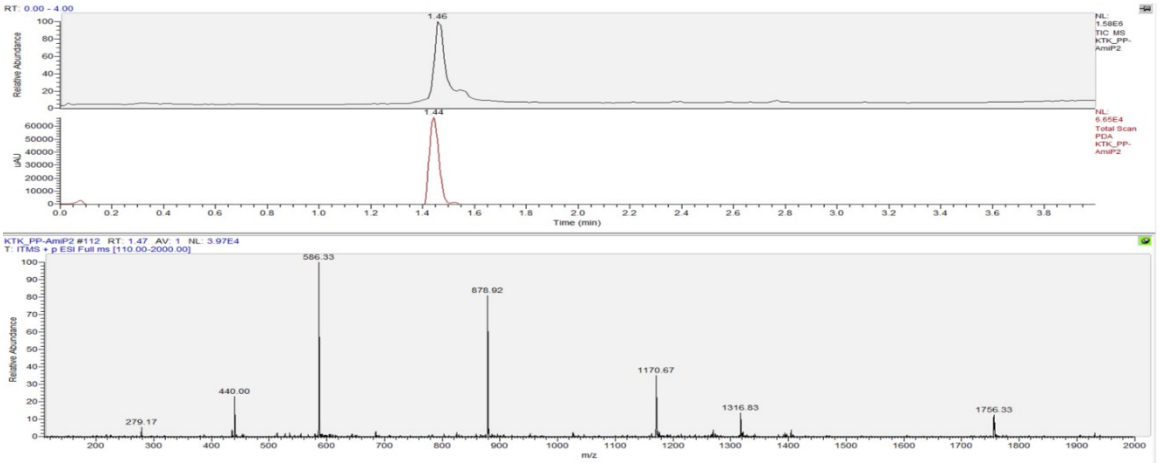

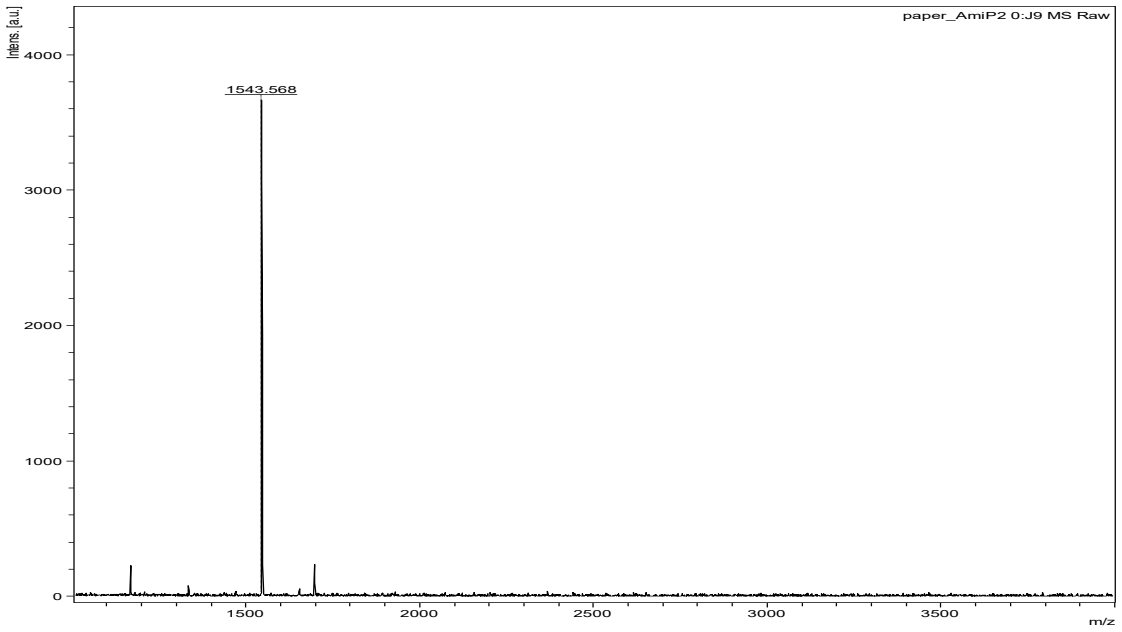

P1' (Ac-G**Pz**AA-Lys-Cou); Expected Mass for $C_{83}H_{96}F_2N_{33}O_{19}^+$: 1896.7523, LC-MS (ESI) RT= 1.56 min. m/z: 1897.6 $[M]^+$, 1423.0 $[3M+H]^{4+}$, 1264.8 $[2M+H]^{3+}$, 949.1 $[M+H]^{2+}$, 633.3 $[M+2H]^{3+}$; MALDI-TOF m/z found: 1686.7 $[M\text{-Coumarin}]^+$.

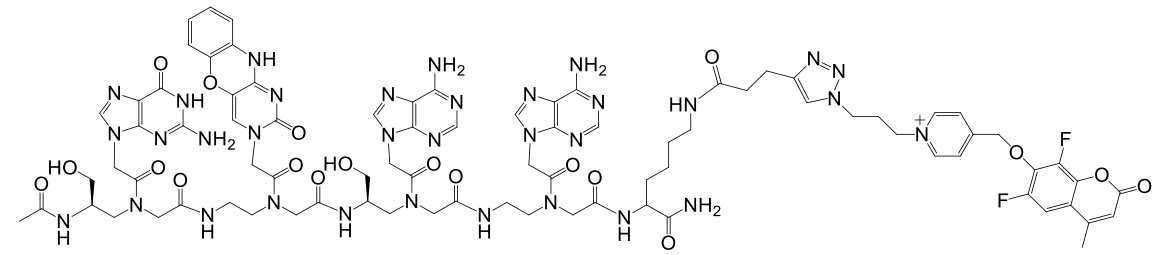

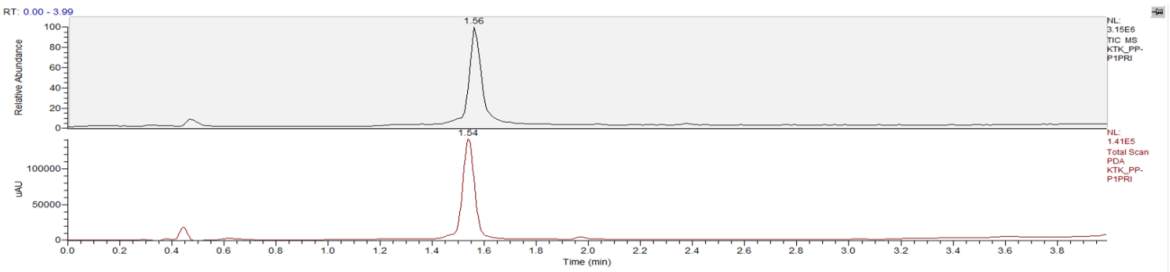

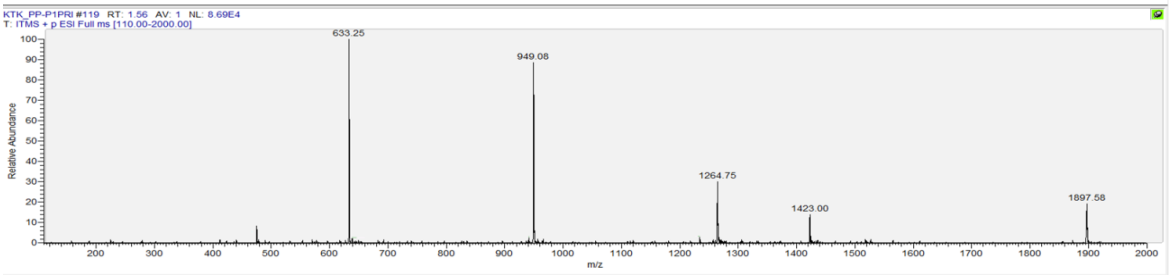

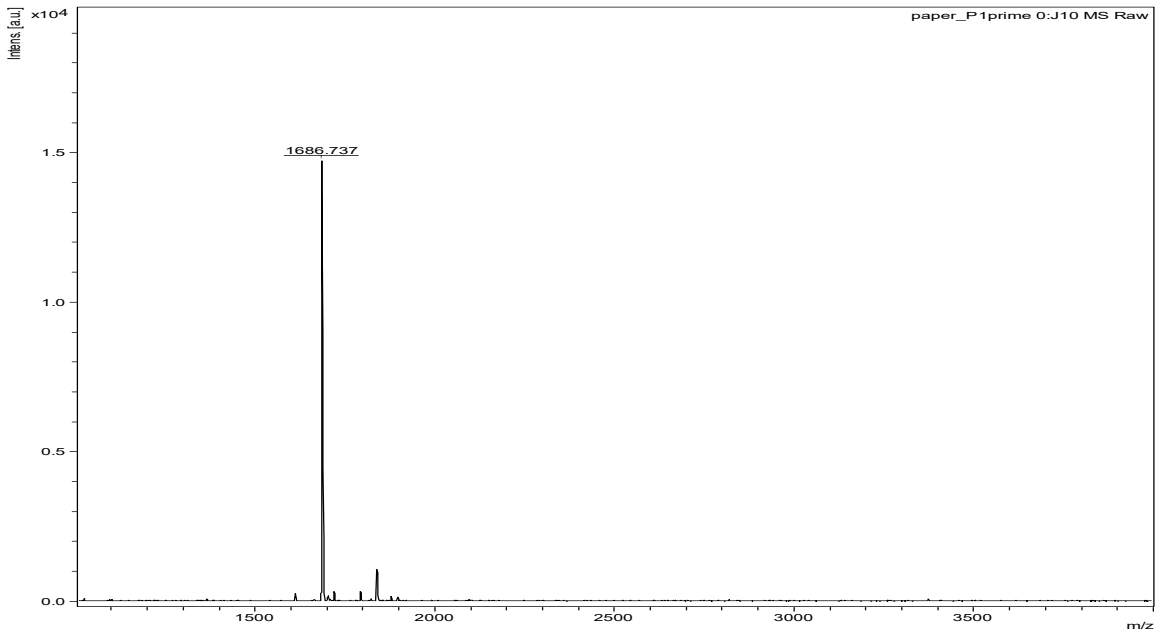

P2' (Ac-CTGA-Lys-Cou); Expected Mass for $C_{77}H_{95}F_2N_{30}O_{20}^+$: 1797.7301, LC-MS (ESI) RT= 1.50 min. m/z: 1798.5 $[M]^+$, 1348.3 $[3M+H]^{4+}$, 1198.8 $[2M+H]^{3+}$, 899.4 $[M+H]^{2+}$, 600.2 $[M+2H]^{3+}$, 450.4 $[M+3H]^{4+}$; MALDI-TOF m/z found: 1587.7 $[M\text{-Coumarin}]^+$.

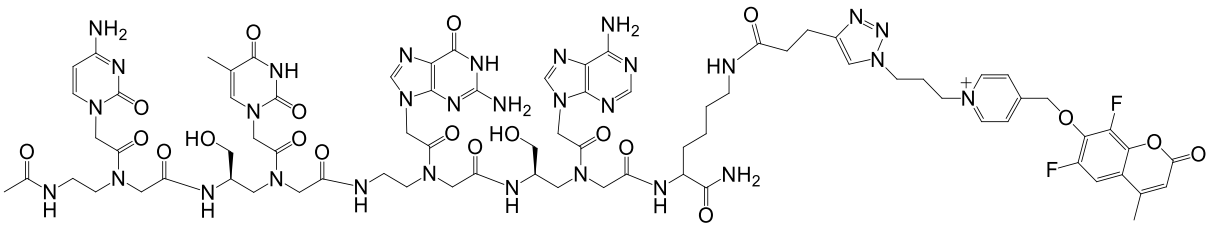

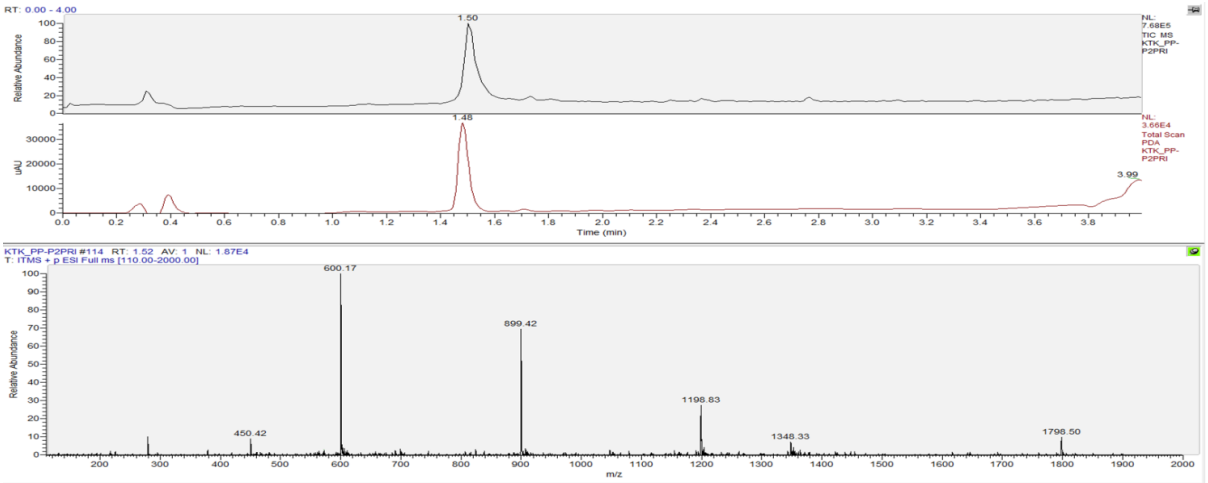

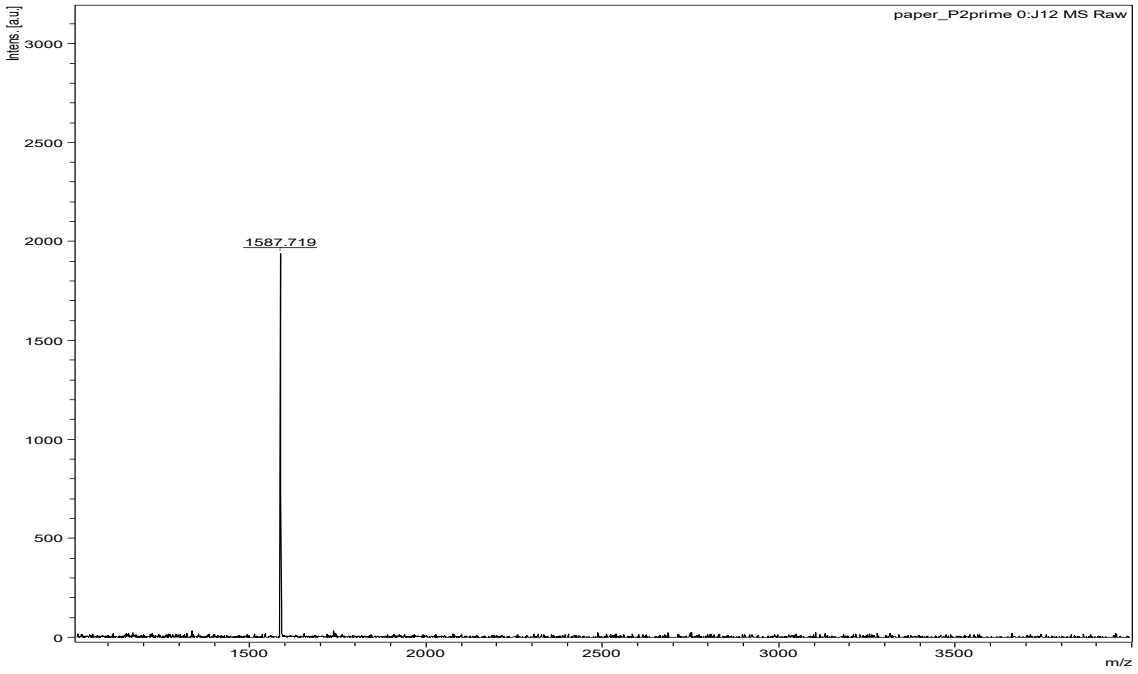

5FUP1 (Ac-GCAA-Lys-5-FUOPy); Expected Mass for $C_{71}H_{91}FN_{35}O_{17}^{+}$: 1724.7311 , LC-MS (ESI) RT= 1.09 min. m/z: 1725.3 $[M]^{+}$, 863.1 $[M+H]^{2+}$, 575.9 $[M+2H]^{3+}$; MALDI-TOF m/z found: 1594.6 $[M-5FU]^{+}$.

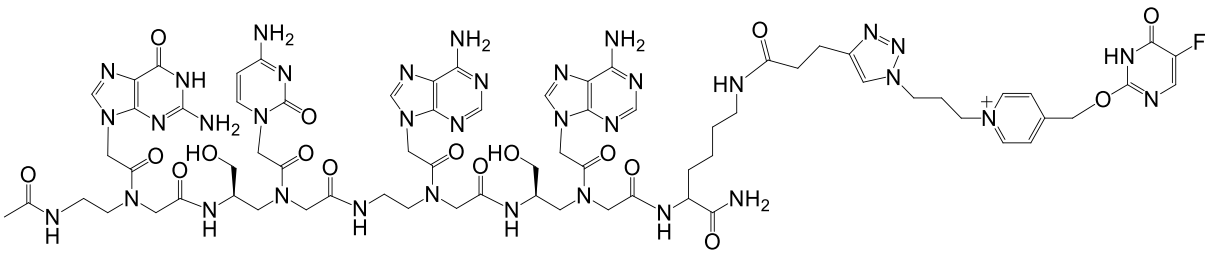

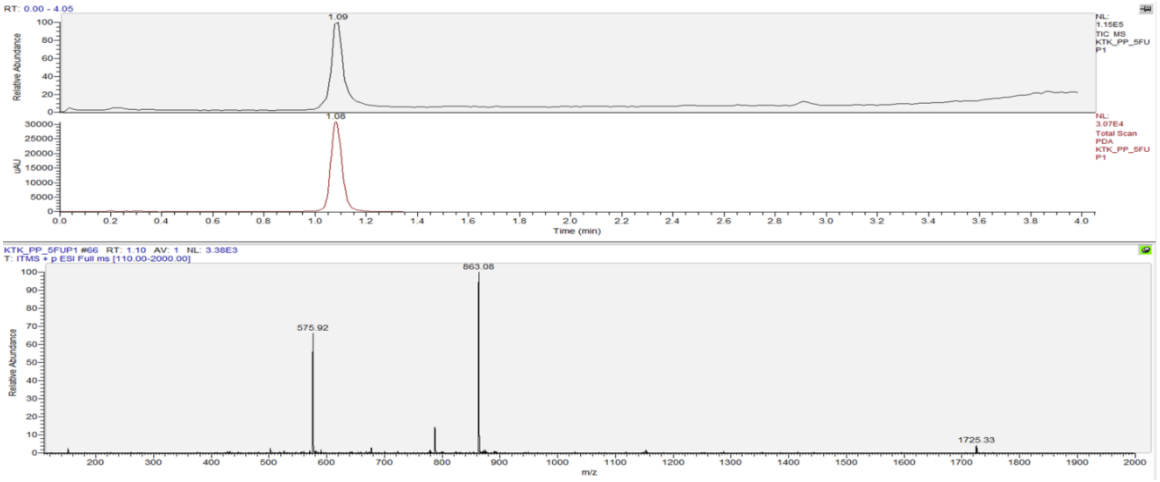

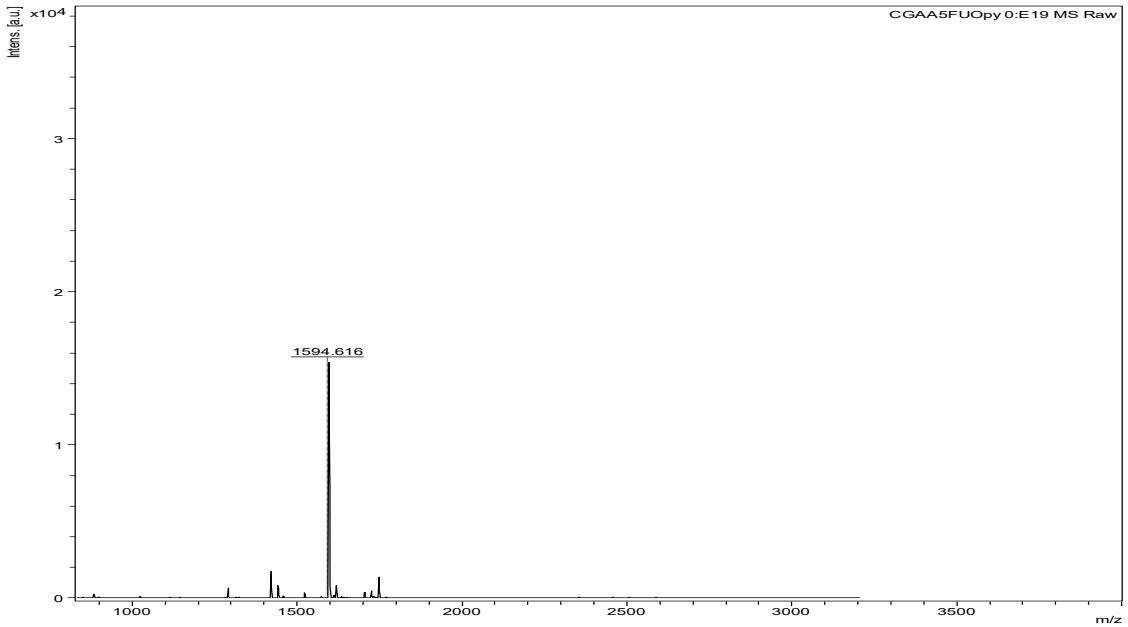

5FUP2 (Ac-**Pz**TGA-Lys-5-FUOPy); Expected Mass for $C_{77}H_{94}FN_{32}O_{20}^{+}$: 1805.7301, LC-MS (ESI) RT= 1.33 min. m/z: 1806.4 $[M]^{+}$, 903.8 $[M+H]^{2+}$, 602.8 $[M+2H]^{3+}$; MALDI-TOF m/z found: 1678.9 $[M-5FU]^{+}$.

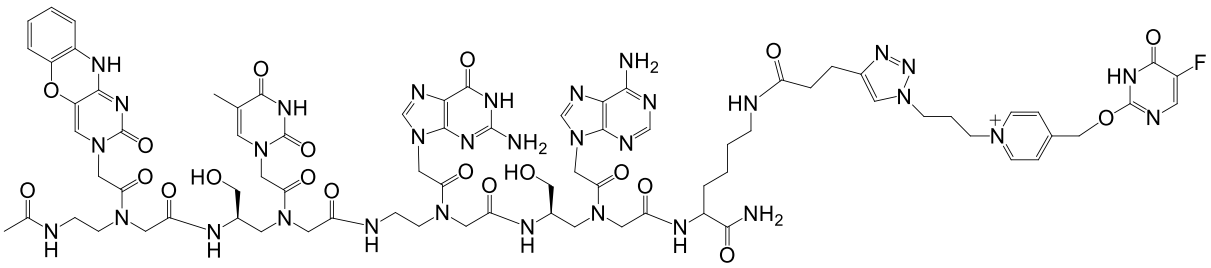

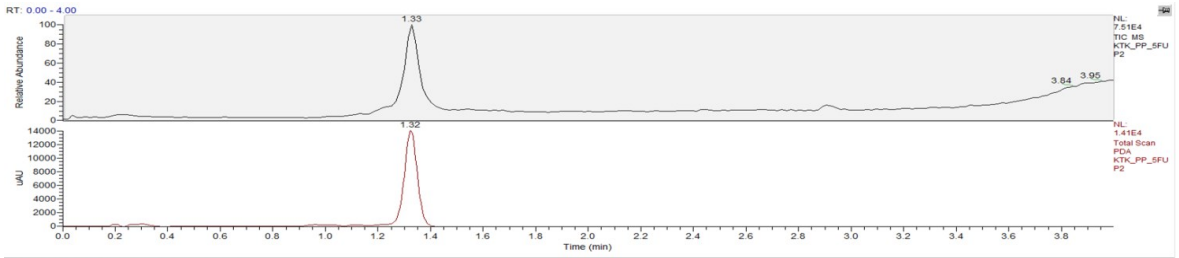

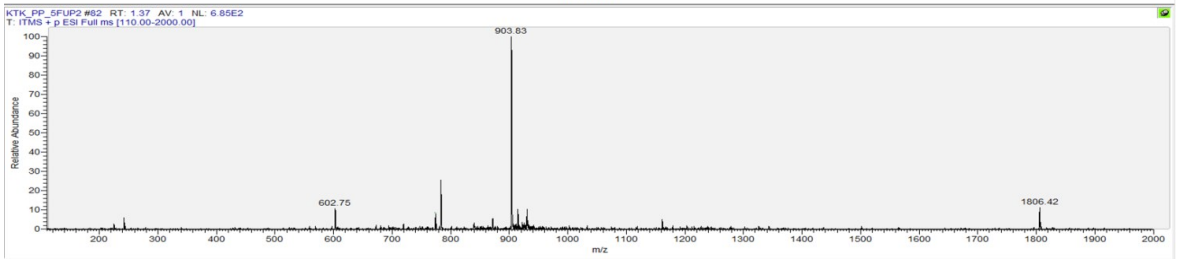

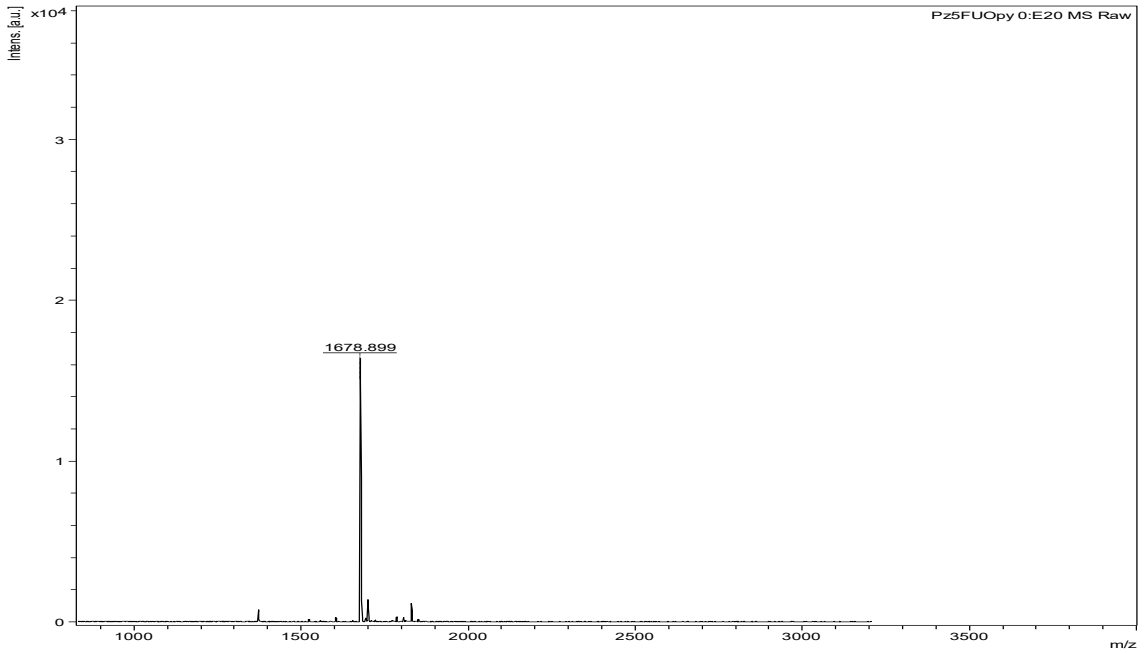

References

(1) Chang, D.; Lindberg, E.; Winssinger, N. *J. Am. Chem. Soc.* **2017**, *139*, 1444-1447.

(2) Ausin, C.; Ortega, J.-A.; Robles, J.; Grandas, A.; Pedroso, E. *Org. Lett.* **2002**, *4*, 4073-4075.

(3) Butters, M.; Ebbs, J.; Green, S. P.; MacRae, J.; Morland, M. C.; Murtiashaw, C. W.; Pettman, A. J. *Org. Proc. Res. Dev.* **2001**, *5*, 28-36.

(4) Zhang, Z.; Wallace, M. B.; Feng, J.; Stafford, J. A.; Skene, R. J.; Shi, L.; Lee, B.; Aertgeerts, K.; Jennings, A.; Xu, R.; Kassel, D. B.; Kaldor, S. W.; Navre, M.; Webb, D. R.; Gwaltney, S. L. *J. Med. Chem.* **2011**, *54,* 510-524.

Supplementary Material of Chapter III

Materials and methods

General information

PNAs were purified by HPLC and lyophilized. LC-MS spectra were recorded by using a DIONEX Ultimate 3000 UHPLC coupled with a Thermo LCQ Fleet Mass Spectrometer System (electrospray ionization (ESI)) operated in positive. A Bruker Daltonics Autoflex spectrometer was used for MALDI-TOF mass results.Nanodrop 2000c spectrophotometer (Thermo Fisher Scientific) was used to determine the DNA and PNA concentrations. The absorbance at 260 nm of the sample was measured. For quantification of oligonucleotides, 13700, 6600, 11700, 8800, 13700, 7200 M^{-1} were used as extinction coefficient at 260 nm for A, T, G, C, FITC, Dabcyl, respectively. The hairpin samples were heated at 98 °C for 6 min and cooled down on ice for 10 min before use (snap-cooling). Procedures and methods for synthesis and purification of PNA strands was carried out based on our previous report.[1]

Evaluation of PNA HCR by gel electrophoresis

For 5 % native PAGE analysis, 2~4 μM (based on final concentration) stocks of H1, H2, I were prepared in buffer pH 7.5 0.1×PBS, 0.02 % tween-20. The stocks were heated to 98 °C for 6 min and cooled down in ice for 10 min before use. H1, H2, I (5 μL each) were mixed and buffer was added to the mixture to reach the desired dilution (20 μL final sample volume). The HCR reaction was carried out for 2 h at r.t. followed by addition of 2 μL of glycerol. The sample was loaded and analyzed on 5% polyacrylamide gel (1×TBE buffer, 100~250 V) at r.t. The FITC band was visualized on a Fusion FX7.

For SDS-PAGE of PNAs, TruPAGE Precast Gel 4-12 % (12 well, PCG2003, Sigma-Aldrich) and TruPAGE™ Tris-MOPS SDS Express Running Buffer, 20× were used. 15 μL of final volume and 1 μM (0.5 μM for γ-serine modified PNAs) of reaction components were used for each reaction. The HCR reactions (pH 7.5 0.1×PBS, 0.02 % tween-20) were carried out for 2 h at r.t. 5 μL of 4×loading buffer were added to each sample for gel loading. Afterwards, the samples were loaded on gel without heating. The fluorescence of Cy3 in the gel was monitored by Fusion FX7.

Streptavidin bead fluorescent pulldown assay for estimation of HCR elongation

For Fig. 39, 4 μL of High Capacity Streptavidin Agarose beads (Thermo Scientific) in 200 μL eppendorf were washed with reaction buffer. 30 μL of 0.1 μM **BCy3serI** (3 pmol) were added to the beads and reacted for 1 h. in a rotating shaker. After initiator loading, the supernatant was taken for Cy3 fluorescence measurement to calculate the yield of initiator loaded on beads. After removing the supernatant by micropipette, the beads were treated with 30 μL of annealed 1 μM of **FserH1** and **FserH2** (30 pmol) for HCR reaction. After 2 h. of reaction, the fluorescence intensity of the supernatant of the reaction mixture was monitored by plate reader (cuvette) to calculate elongation efficiency of γ-serine-modifed PNA HCR.

For Fig. 41, 4 μL of High Capacity Streptavidin Agarose beads (Thermo Scientific) in 200 μL eppendorf were washed with reaction buffer. 150 μL of 0.1 μM **BpegI** (15 pmol) were added to the beads and reacted for 1 h. in a rotating shaker. After removing the supernatant by micropipette, the beads were treated with 75 μL of annealed 2 μM of **pegH1** and **Cy3pegH2**

(150 pmol for each) for HCR reaction. After 4 h. of reaction, the fluorescence intensity of the supernatant was monitored by plate reader (cuvette) to calculate elongation efficiency.

Fluorescence microscopy analysis for estimation of HCR elongation

Streptavidin beads (3 µL) were washed with water and 0.1 µM, 10~100 µL (1~10 pmol, 10 pmol for FITC-labelled I) of biotinylated-I in pH 7 1×SSC buffer, 0.02 % tween-20 was incubated with beads for 1 h. After removing the supernatant, HCR was initiated by adding 0.5 µM of mixture of H1 and H2 hairpins (pH 7 1×SSC buffer, 0.02 % tween-20). After 4 h. of reaction at r.t., the beads were washed with 1×SSC buffer 3 times and moved to microscopy plate using 100 µL of 1×SSC buffer. Fluorescence image of the beads were taken by Leica SP5 by using the parameters: 495 nm of excitation and 510~530 nm of emission, 20 % laser power (Argon white laser) for FITC imaging, 550 nm of excitation and 570~600 nm of emission, 3 % laser power for Cy3 imaging. Average values of fluorescence peaks were obtained from Plot profiles of surface of beads. All images were analysed in ImageJ.

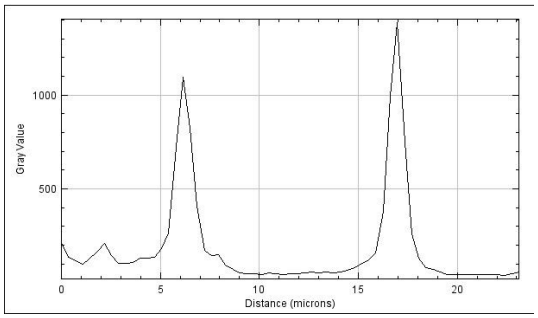

Size exclusion chromatography (SEC) of HCR product

As reference samples, 100 µL of 5 µM **Ref1+Ref2** (20-mer γ-peg-modifed PNA duplex), **Ref3+Ref4** (10-mer), or **Ref5+Ref6** (6-mer) were prepared in pH 7.5 0.1×PBS. Each sample was spiked with 0.5 µL of 360 µM of Caffeine as an internal standard. The samples were analyzed by HPLC using size exclusion column (Agilent Bio SEC-3 Columns, 100 Å, 300 mm * 4.6 mm, 0.35 mL/min., r.t., 0.5×PBS buffer). 2 µM stock sample of each pegH1, pegH2, and pegI (2 µM, 500 µL) were prepared and annealed. Reaction samples are prepared as described in the figures of the main text (100 µL of final volume) and injected into HPLC after 2 h. of reaction time for analysis. Retention time of reference PNAs were utilized to draw a standard curve for size-estimation.

Kinetics analysis of HCR

The kinetics of HCR was monitored in buffer solution (pH 7 1×SSC buffer, 0.02 % tween-20). To measure the k_{obs} of the first step by using pseudo first order kinetics, 10 pmol of **pegIF** in 800 µL of buffer was prepared. To this solution, 200 pmol of **DpegH2** in 200 µL (1 µM in 1×SSC buffer) was added and the mixture was mixed very quickly. Fluorescence at 530 nm was measured every 10 seconds before adding **DpegH2** (λ_{exc}: 485 nm, cutoff: 515 nm, λ_{emi}: 530 nm, PMT gain: medium). To measure the the k_{obs} of the second step, 20 µL of 0.5 µM **pegIF** (10 pmol) in 1×SSC buffer was mixed with 20 µL of 1 µM **pegH2** (20 pmol) and incubated. After 10 min. of incubation, 760 µL of 1×SSC buffer was added to the sample. During the fluorescence measurement of the **pegIF+pegH2** mixture, 200 pmol of **DpegH1** in

200 µL (1 µM in 1×SSC buffer) were added to monitor fluorescence changes. The fluorescence intensity after addition was corrected by dilution effect (×0.8).

Determination of K_d was done by measuring fluorescence change (λ_{exc}: 485 nm, cutoff: 515 nm, λ_{emi}: 530 nm, PMT gain: medium) of 2 nM of **pegIF** (total 1 mL) for the first step or 10 nM of **pegIF+pegH2** mixture for the second step in 1×SSC buffer at r.t.; every data point was taken after 1 min from addition to allow the solution to equilibrate.

Cell culture

HT-29 cell lines were obtained from the American Type Culture Collection (ATCC) and expanded following their instructions. Cells were grown in McCoy's 5A (modified) medium (Gibco) containing 10% FCS and 1% pen-strep at 37 °C under 5% CO_2 in a humidified incubator. Cells were regularly tested for mycoplasma contamination by staining with Hoechst 33342.

Experiments under hypoxic conditions were conducted in an Eppendorf® Galaxy® 48R CO_2 incubator at 37 °C with 1% O_2, 5% CO_2 and 94% N_2 settings.

HCR reaction on hypoxic HT-29 cells

HT-29 cells ($2x10^5$) were seeded into 3.5 cm glass bottom dishes with 10 mm microwell (Mattek); cells were incubated in McCoy's 5A medium at 37 °C under 5% CO_2 in a humidified incubator for 48 hours. Medium was replaced with fresh one and cells were transferred into the hypoxia incubator (1% O_2) for 24 hours.

Initiator-CA IX ligand (**Lpegl**): cells were treated with Initiator-CA IX ligand (100 nM; 30 min) under hypoxia; cells were washed with HBSS and imaged with a Leica SP8 microscope.

Initiator-CA IX ligand + Hairpins: cells were treated with Initiator-CA IX ligand (100 nM; 30 min) under hypoxia; cells were washed with HBSS and incubated with hairpins (1 µM) under hypoxia for 1 hour. Then cells were washed with HBSS and imaged with a Leica SP8 microscope.

Hairpins: cells were washed with HBSS and incubated with hairpins (1 µM) under hypoxia for 1 hour. Then cells were washed with HBSS and imaged with a Leica SP8 microscope.

All images were analysed in ImageJ.

Sequences informations

Table III-S1. RNA, DNA and PNA sequences investigated in this study

Name	Sequence (5´ to 3´ for RNA and DNA, N- to C-terminal for PNA)
F34H1	FITC-peg-ACA-GCCG-TAT-CGGC
F34H2	FITC-peg-CGGC-TGT-GCCG-ATA
F34l	FITC-peg-TAT-CGGC
F45H1	FITC-peg-GAAT-TGCCG-ACTA-CGGCA
F45H2	FITC-peg-CGGCA-ATTC-TGCCG-TAGT
F45l	FITC-peg-ACTA-CGGCA
FserH1	FITC-peg-GAATG-TGCCG-ACTAG-CGGCA
FserH2	FITC-peg-CGGCA-CATTC-TGCCG-CTAGT
Fserl	FITC-peg-ACTAG-CGGCA
serH1	NH_2-peg-GAATG-TGCCG-ACTAG-CGGCA
serH2	NH_2-peg-CGGCA-CATTC-TGCCG-CTAGT
BCy3serl	Biotin-peg-Lys(Cy3)-peg-ACTAG-CGGCA
FpegH1	FITC-peg-GAATG-TGCCG-ACTAG-CGGCA (peg)
FpegH2	FITC-peg-CGGCA-CATTC-TGCCG-CTAGT (peg)
Fpegl	FITC-peg-ACTAG-CGGCA-Lys-Ac (peg)
pegH1	NH_2-peg-GAATG-TGCCG-ACTAG-CGGCA (peg)
pegH2	NH_2-peg-CGGCA-CATTC-TGCCG-CTAGT (peg)
Cy3pegl	Cy3-peg-ACTAG-CGGCA (peg)
Cy3pegH2	cy3-peg-CGGCA-CATTC-TGCCG-CTAGT (peg)
pegl	NH_2-peg-ACTAG-CGGCA (peg)
Bpegl	Biotin-peg-peg-peg-peg-peg-ACTAG-CGGCA (peg)
FBpegl	Biotin-peg-peg-Lys(FITC)-peg-ACTAG-CGGCA (peg)
Ref1	NH_2-peg-AGTCTCAGTGTCAACGTACG (peg)
Ref2	NH_2-peg-CGTACGTTGACACTGAGACT (peg)
Ref3	NH_2-peg-AGTCTCAGTG (peg)
Ref4	NH_2-peg-CACTGAGACT (peg)
Ref5	NH_2-peg-GATGCT (peg)

Ref6	NH_2-peg-AGCATC (peg)
DpegH1	Dabcyl-peg-GAATG-TGCCG-ACTAG-CGGCA (peg)
DpegH2	Dabcyl-peg-CGGCA-CATTC-TGCCG-CTAGT (peg)
pegIF	Ac-ACTAG-CGGCA-Lys-peg(FITC) (peg)
LpegI	Ligand-Lys(Cy3)-peg-ACTAG-CGGCA (peg)

[a] L-serine- or peg-modified PNA is marked with underline; (peg) = peg-modified sequence

Supplementary Figures

Figure III-S1. Size analysis of PNA complexes using SDS-PAGE.

Complex of **Cy3pegI+pegH2** was found to have higher mobility than **Cy3pegH2** itself. This result indicates that H2 hairpin itself exists as monomeric state, the hairpin, not as a dimer. Conditions for reaction: pH 7.5 0.5×PBS, 0.02 % tween-20, 500 nM of each component, 15 µL, r.t., 2 h. of incubation.

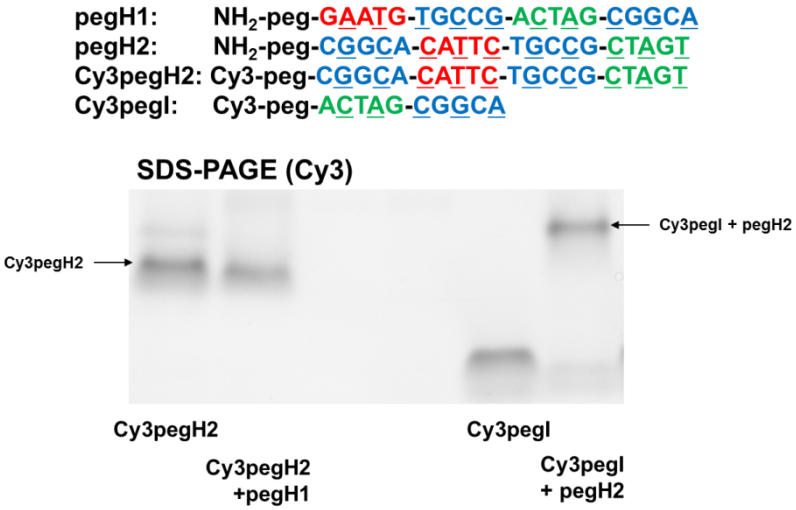

Figure III-S2 On-bead fluorescent microscopy assay.

Reaction conditions: pH 7 1×SSC buffer, 0.02 % tween-20; (A) 2 pmol of **Bpegl**, 32.5 pmol of each hairpin (0.22 µM), total 150 µL, 4 h of reaction; (B) 1 pmol of **Bpegl**, 65 pmol of each hairpin (0.43 µM), total 150 µL, 24 h of reaction. Even for long incubation time (24 h), HCR reaction afforded 12-fold of elongation yield.

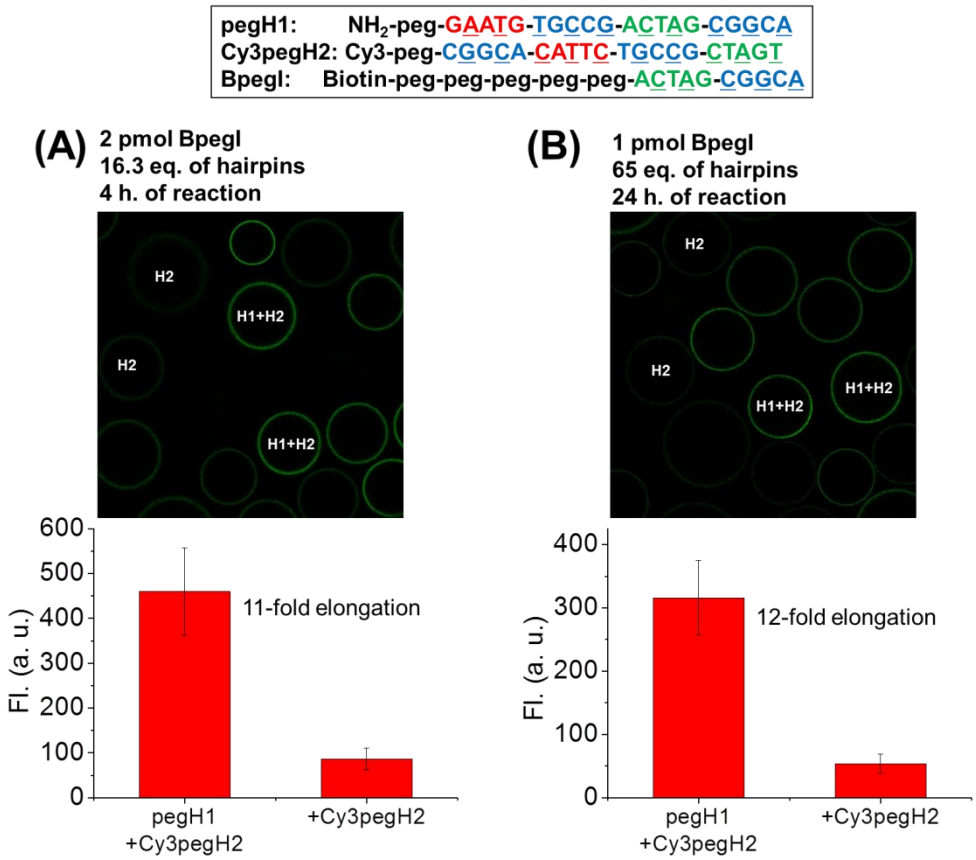

Figure III-S3 Size estimation of HCR product based on size exclusion chromatography (SEC).

(A) HPLC profile of reference 20-mer (**Ref1+Ref2**), 10-mer (**Ref3+Ref4**), 6-mer (**Ref5+Ref6**) peg-modified PNA duplexes. (B) Injection profiles of H1, H2, I, and their complexes. The major peak of HCR reaction (**pegH1**+**pegH2**+ 0.1 eq. of **pegI**) was found at 7.5 min. (C) Standard curve obtained from reference PNA duplexes in (A). The size of major peak of HCR product was estimated as 57 kDa based on the standard curve.

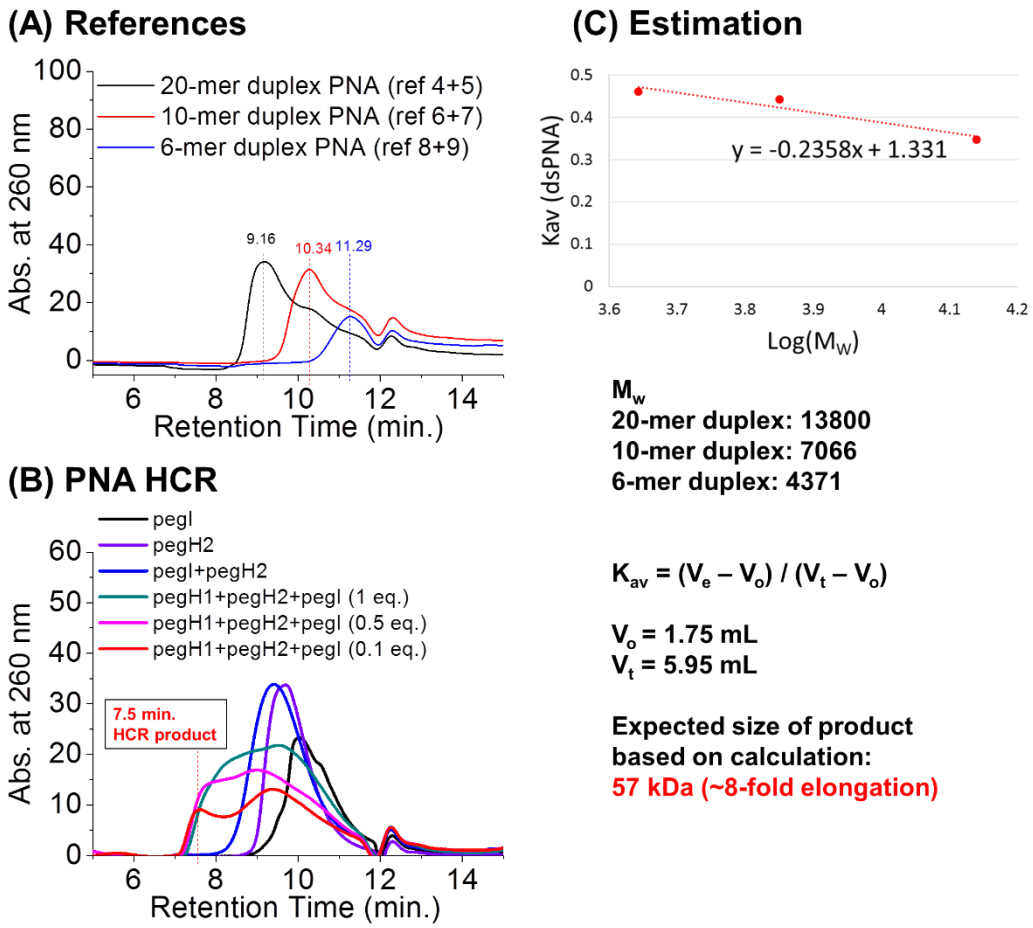

Figure III-S4 Kinetic data of each HCR step (**pegIF + DpegH2** and **pegIF:pegH2 + DpegH1**).

K_d of I + H2 (A) and I:H2 + H1 (B). Raw kinetic data of I + H2 (C) and I:H2 + H1 (D). (E and F) Half-life and reaction rate constant (Pseudo-first-order kinetics) calculated from processed data of (C) and (D). Conditions: pH 7 1×SSC buffer, 0.02 % tween-20, 2 nM of **pegIF** for (A), 10 nM of **pegIF** + 10 nM of **pegH2** for (B), 10 nM of **pegIF +** 200 nM of **DpegH2** for (C and E), 10 nM of **pegIF** + 20 nM of **pegH2 +** 200 nM of **DpegH1** for (D and F). (G) Control reaction using **pegIF + DpegH1**. **pegIF + DpegH1** showed no fluorescence quenching while fluorescence was rapidly quenched for **pegIF + DpegH2.** Conditions: 10 nM of **pegIF +** 200 nM of **DpegH1**.

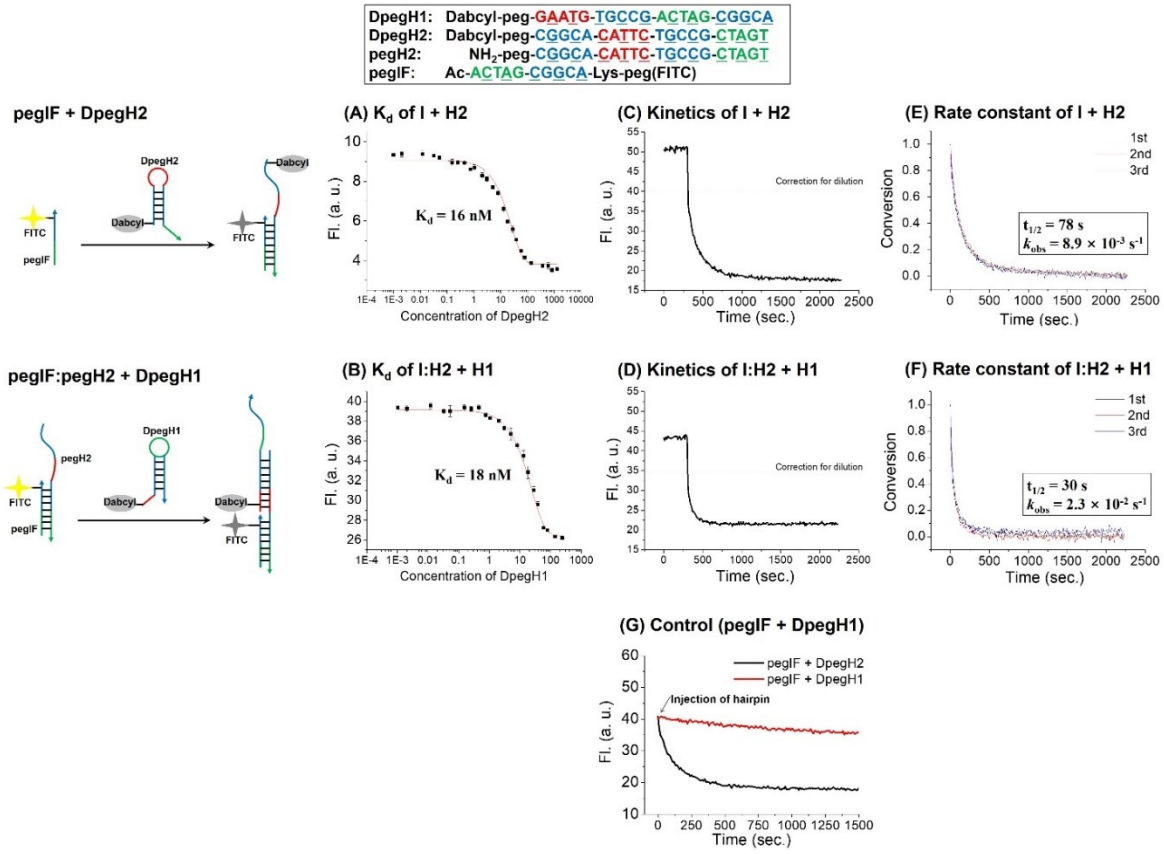

Mass spectra of the synthesized DNAs and PNAs

F34H1 (FITC-peg-ACA-GCCG-TAT-CGGC); Expected Mass for $C_{183}H_{223}N_{85}O_{56}S$: 4538.6936; isotopic mass range (green insert). LC-MS (ESI) RT= 1.47 min. m/z: 1514.7 $[M+3H]^{3+}$, 1136.3 $[M+4H]^{4+}$, 909.4 $[M+5H]^{5+}$, 758.2 $[M+6H]^{6+}$, MALDI-TOF m/z found: 4540.2.

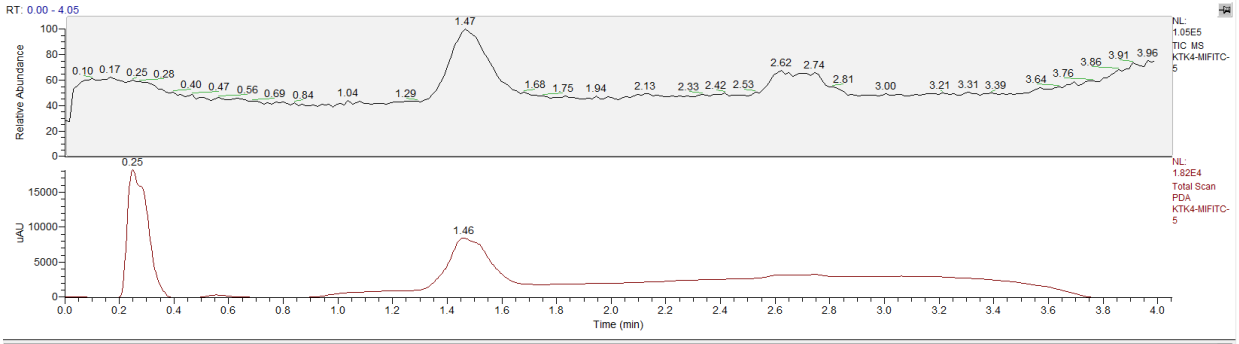

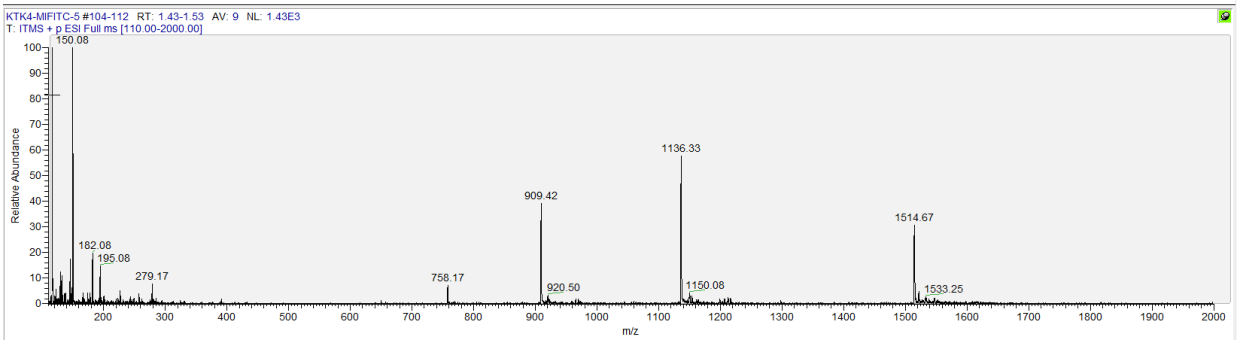

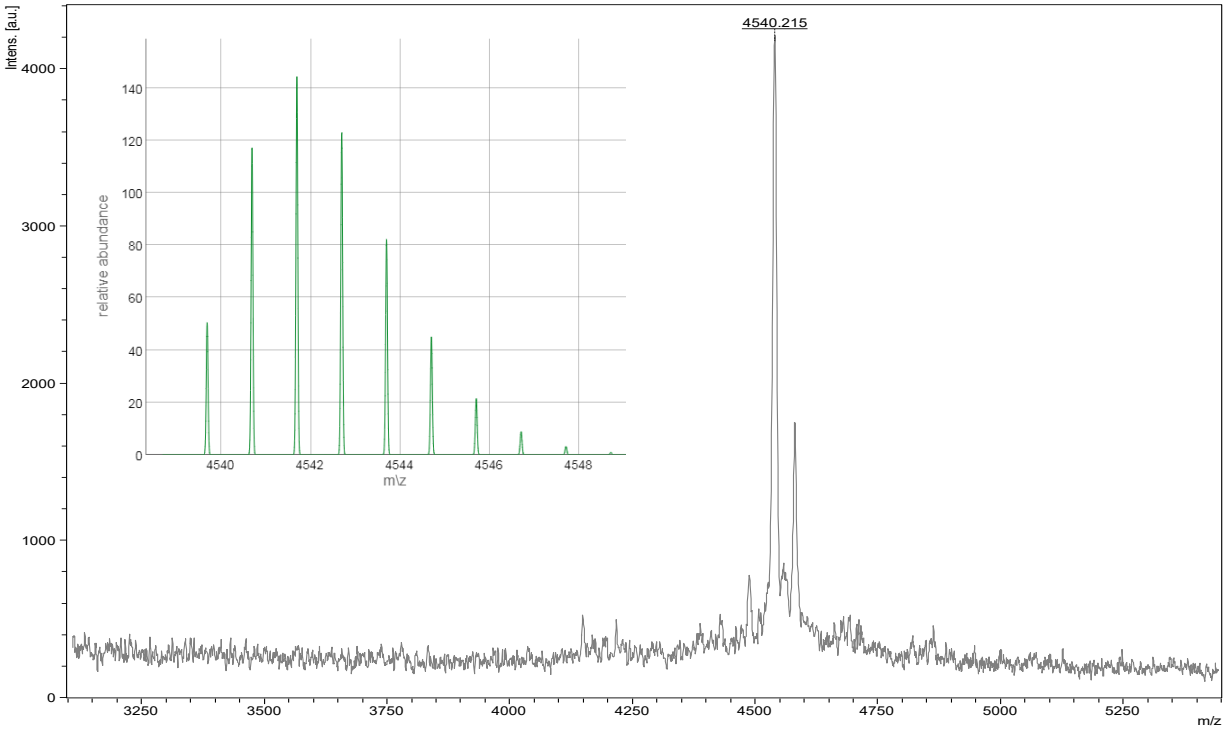

F34H2 (FITC-peg-CGGC-TGT-GCCG-ATA); Expected Mass for $C_{184}H_{224}N_{84}O_{58}S$: 4569.6881, isotopic mass range (green insert). LC-MS (ESI) RT= 1.48 min. m/z: 1524.9 $[M+3H]^{3+}$, 1144.1 $[M+4H]^{4+}$, 915.6 $[M+5H]^{5+}$, 763.3 $[M+6H]^{6+}$, MALDI-TOF m/z found: 4751.9 $[M+H]^{+}$.

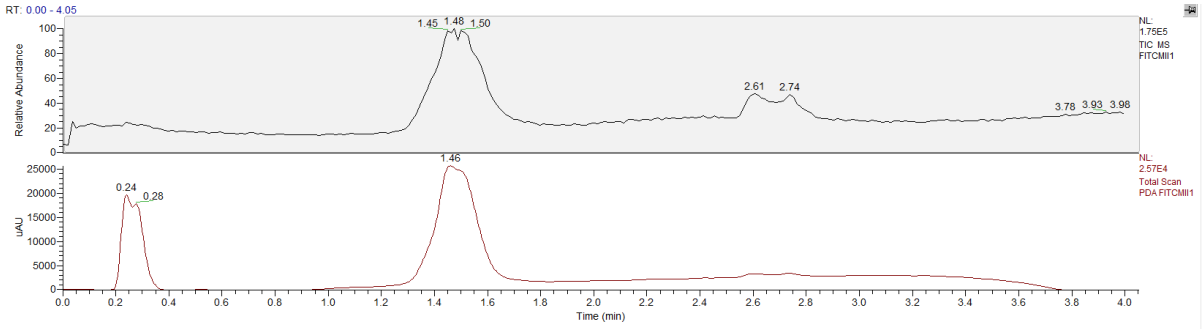

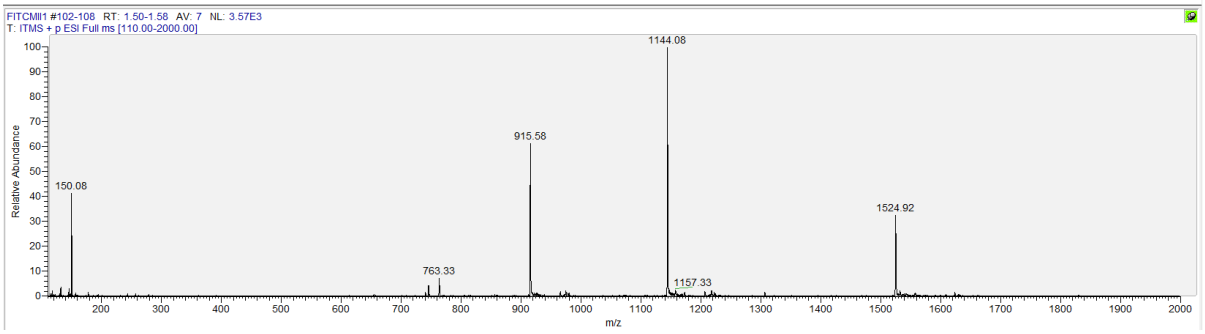

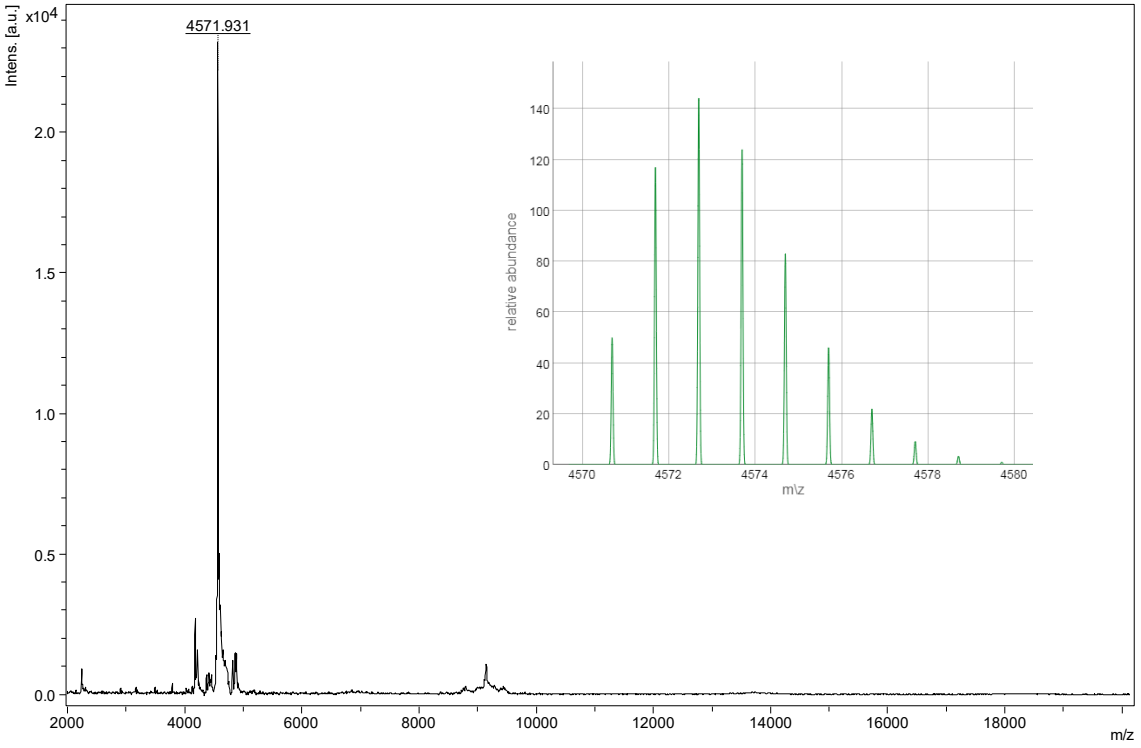

F34l (FITC-peg-TAT-CGGC); Expected Mass for $C_{105}H_{124}N_{42}O_{33}S$: 2532.9037; isotopic mass range (green insert). LC-MS (ESI) RT= 1.54 min. m/z: 1690.1 $[2M+3H]^{3+}$, 1268.1 $[M+2H]^{2+}$, 845.9 $[M+3H]^{3+}$, 634.8 $[M+4H]^{4+}$, MALDI-TOF m/z found: 2535.3 $[M+H]^{+}$

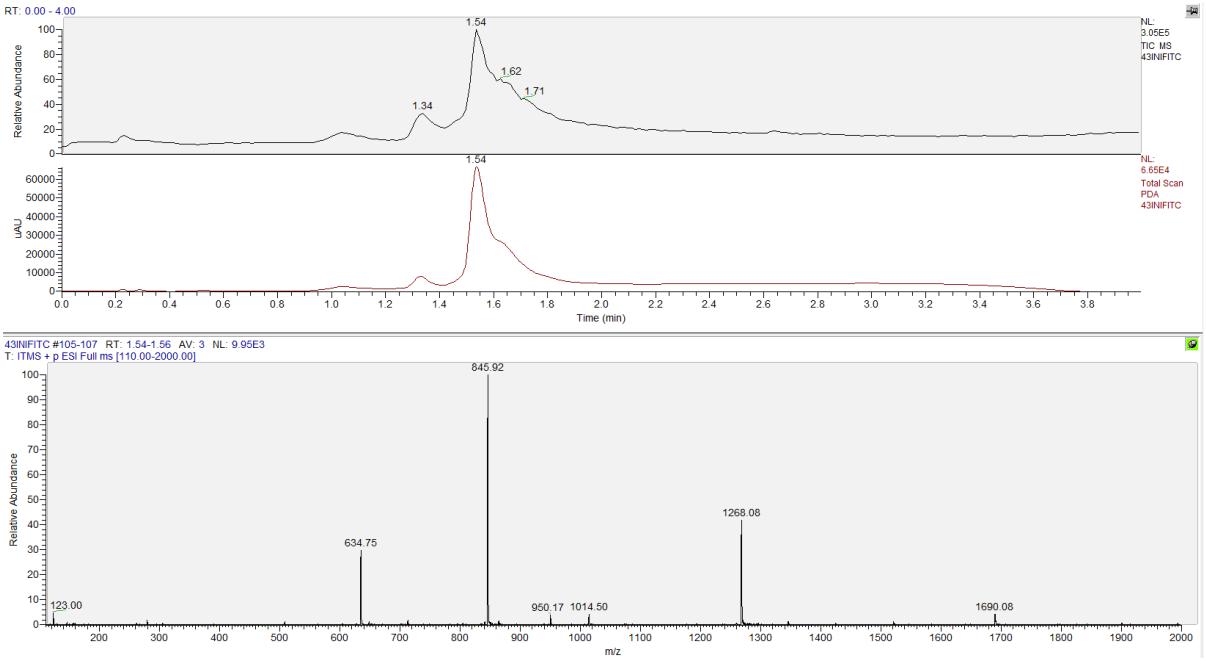

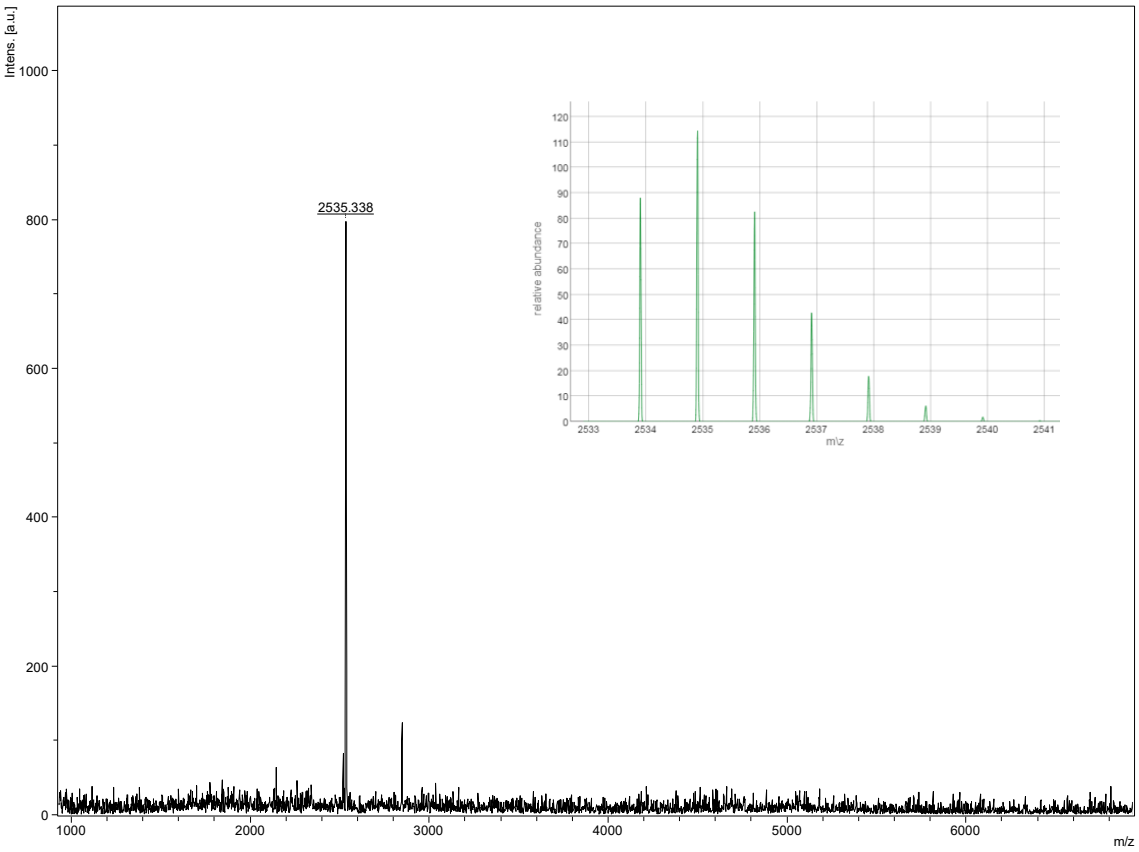

F45H1 (FITC-peg-GAAT-TGCCG-ACTA-CGGCA); Expected Mass for $C_{229}H_{280}N_{110}O_{69}S$: 5706.1503; isotopic mass range (green insert). LC-MS (ESI) RT= 1.44 min. m/z: 1428.3 $[M+4H]^{4+}$, 1142.8 $[M+5H]^{5+}$, MALDI-TOF m/z found: 5713.9 $[M+H]^{+}$

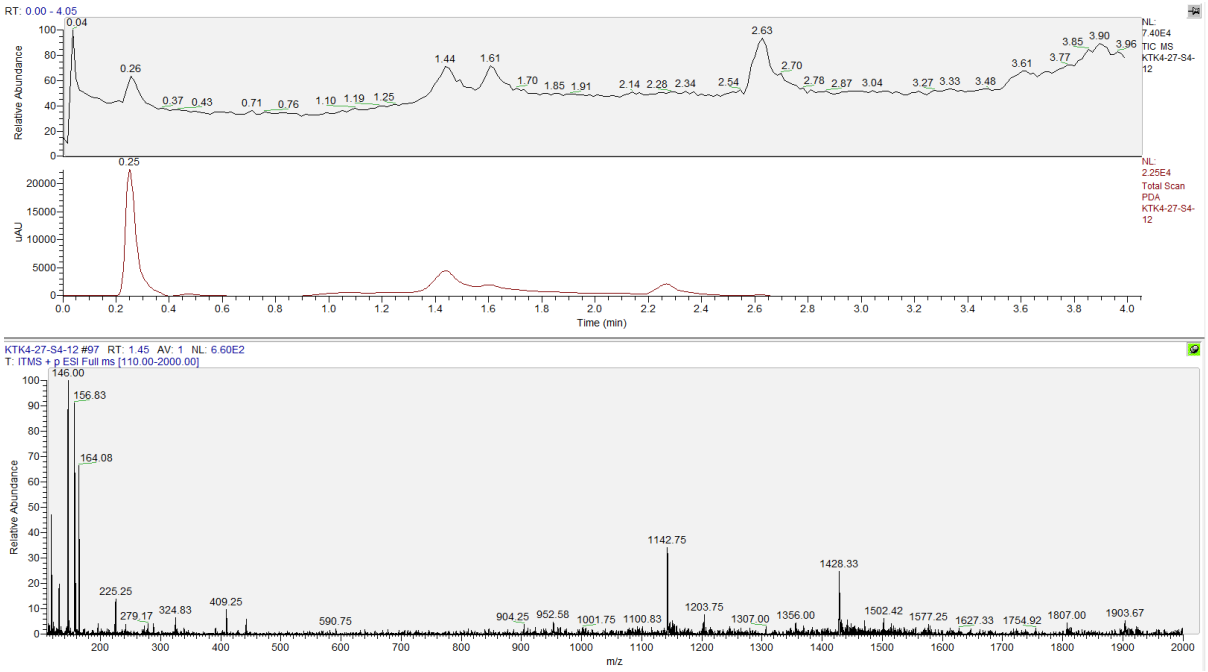

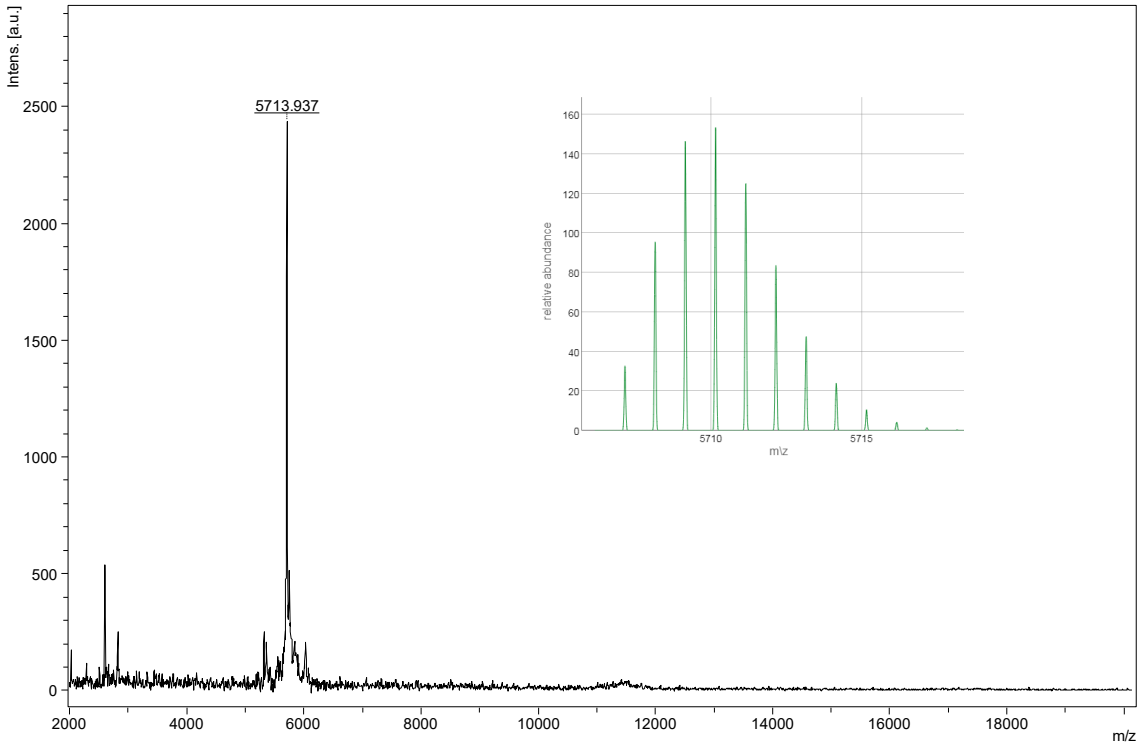

F45H2 (FITC-peg-CGGCA-ATTC-TGCCG-TAGT); Expected Mass for $C_{229}H_{282}N_{104}O_{73}S$: 5688.1272; isotopic mass range (green insert). LC-MS (ESI) RT= 1.45 min. m/z: 1897.6 $[M+3H]^{3+}$, 1424.0 $[M+4H]^{4+}$, 1139.3 $[M+5H]^{5+}$, 949.7 $[M+6H]^{6+}$, MALDI-TOF m/z found: 5693.6 $[M+H]^{+}$

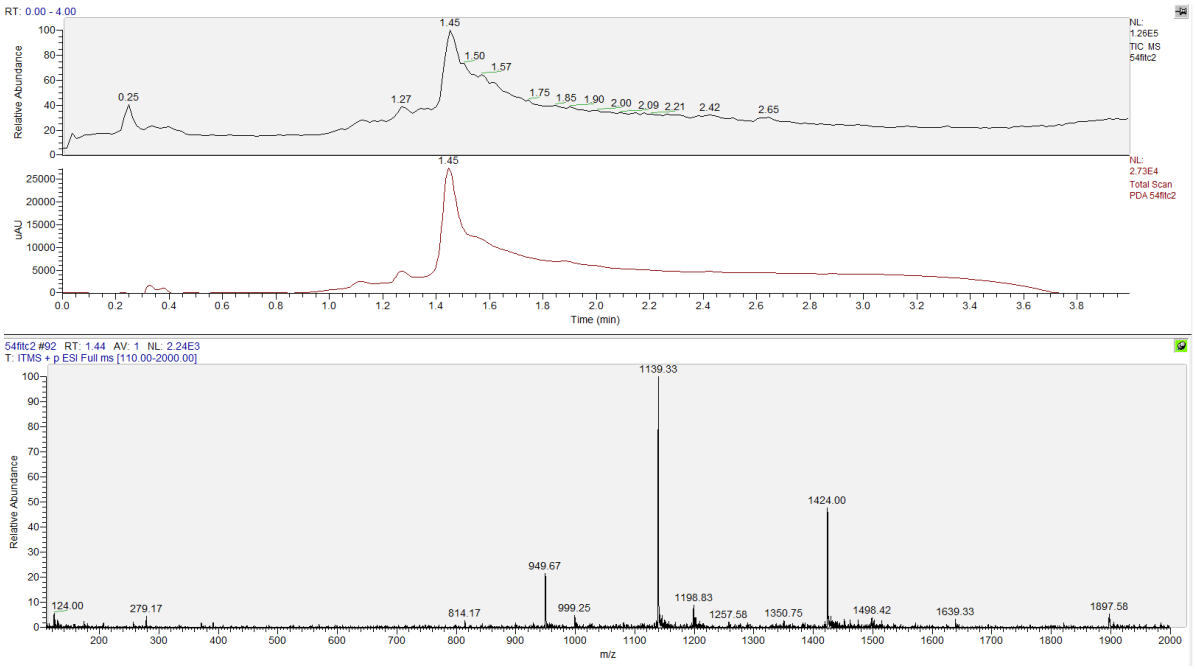

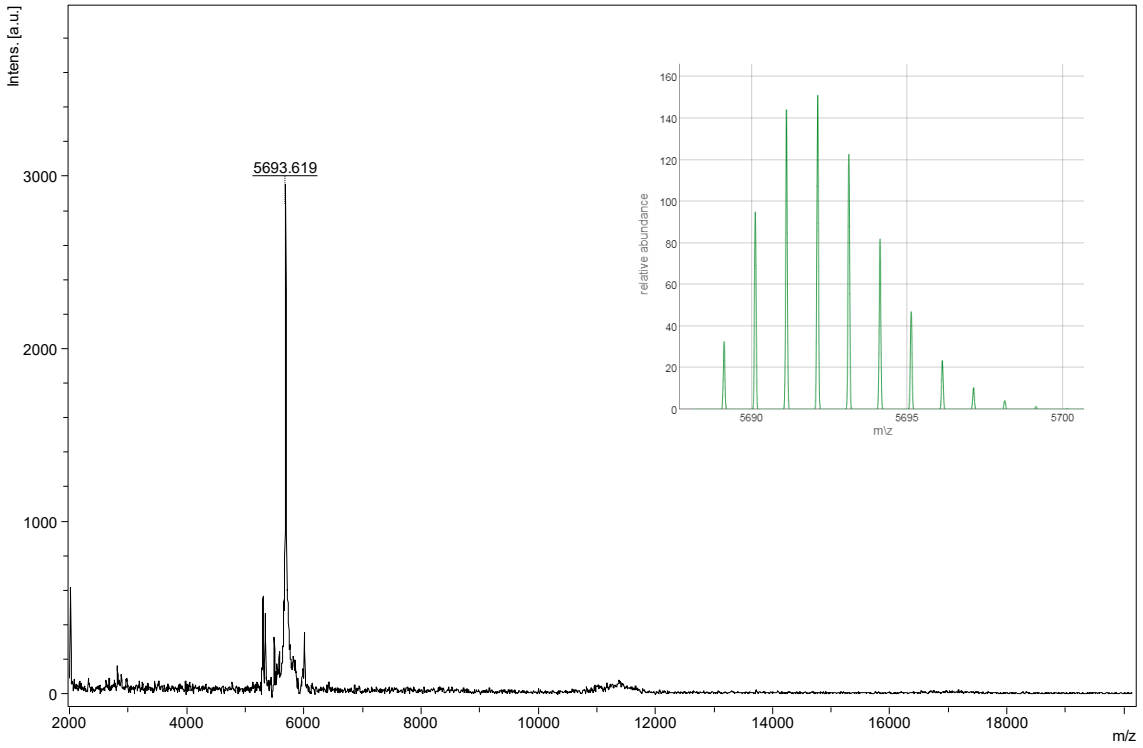

F45l (FITC-peg-ACTA-CGGCA); Expected Mass for $C_{128}H_{153}N_{57}O_{38}S$: 3128.1513; isotopic mass range (green insert). LC-MS (ESI) RT= 1.45 min. m/z: 1565.50 $[M+2H]^{2+}$, 1044.2 $[M+3H]^{3+}$, 783.4 $[M+4H]^{4+}$, 626.9 $[M+5H]^{5+}$, MALDI-TOF m/z found: 3131.9 $[M+H]^{+}$

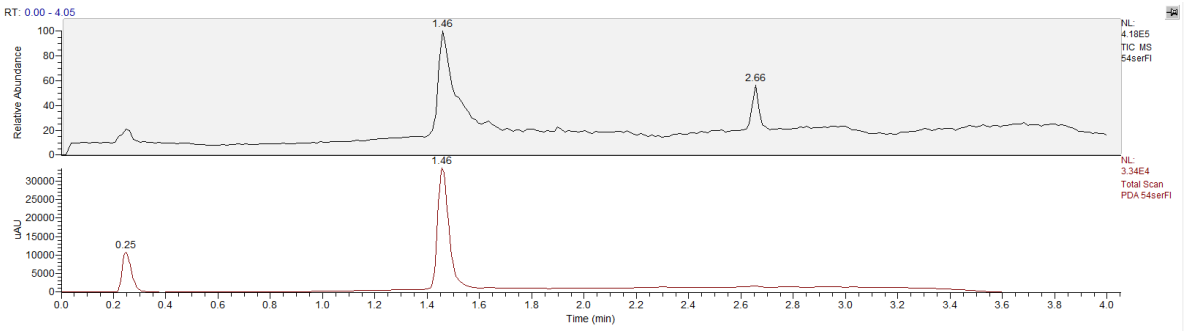

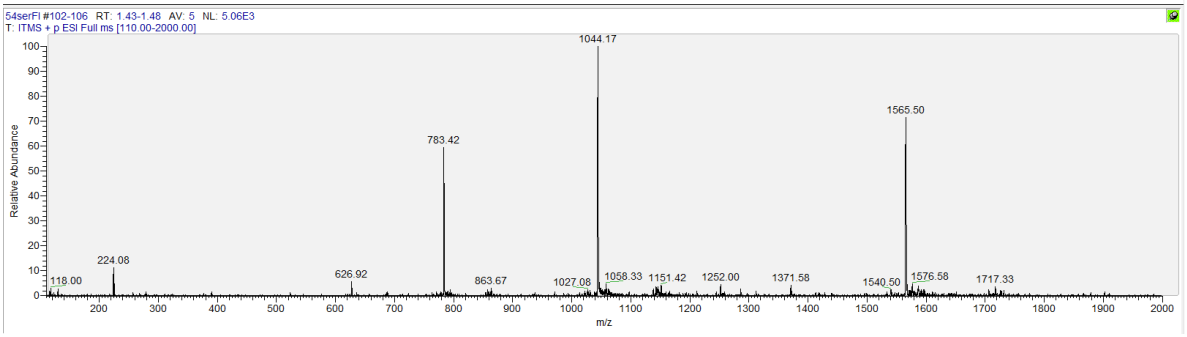

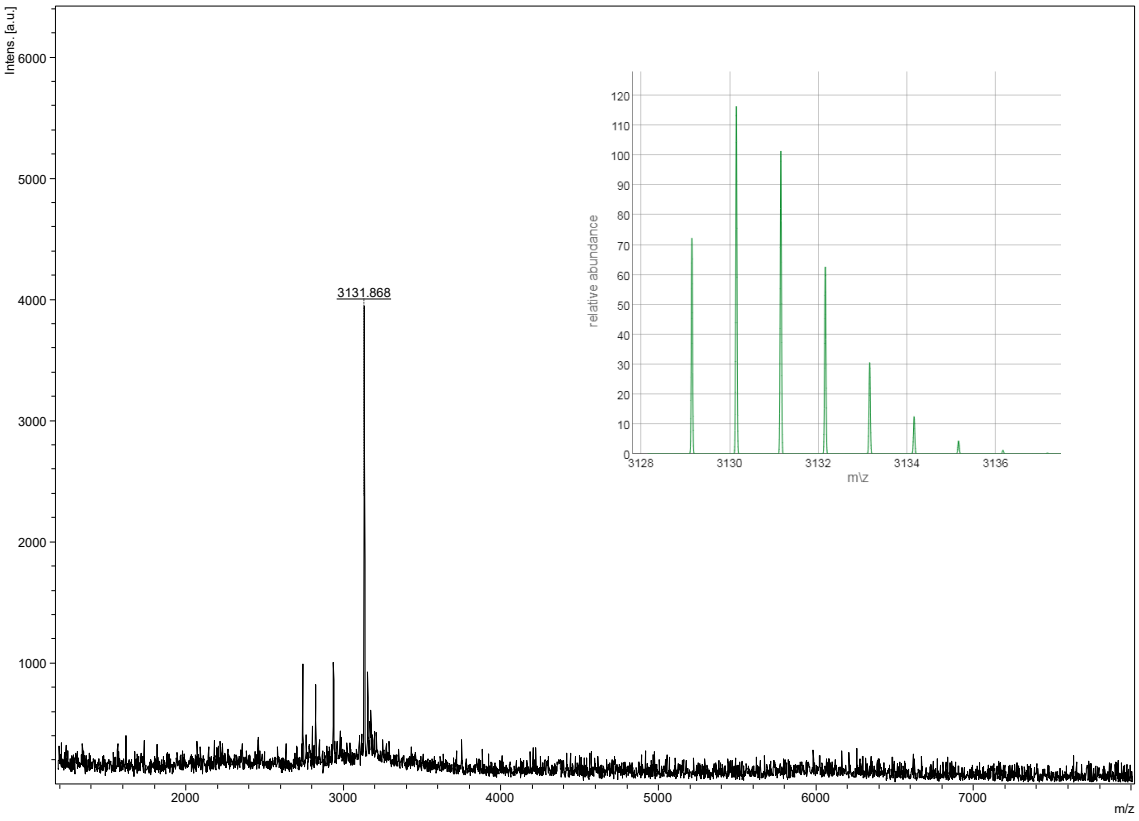

FserH1 (FITC-peg-GAATG-TGCCG-ACTAG-CGGCA); Expected Mass for $C_{252}H_{308}N_{124}O_{76}S$: 6318.3769; isotopic mass range (green insert). LC-MS (ESI) RT= 1.46 min. m/z: 1581.6 $[M+4H]^{4+}$, 1265.3 $[M+5H]^{5+}$, 1054.6 $[M+6H]^{6+}$, 904.3 $[M+7H]^{7+}$, MALDI-TOF m/z found: 6325.8 $[M+H]^{+}$

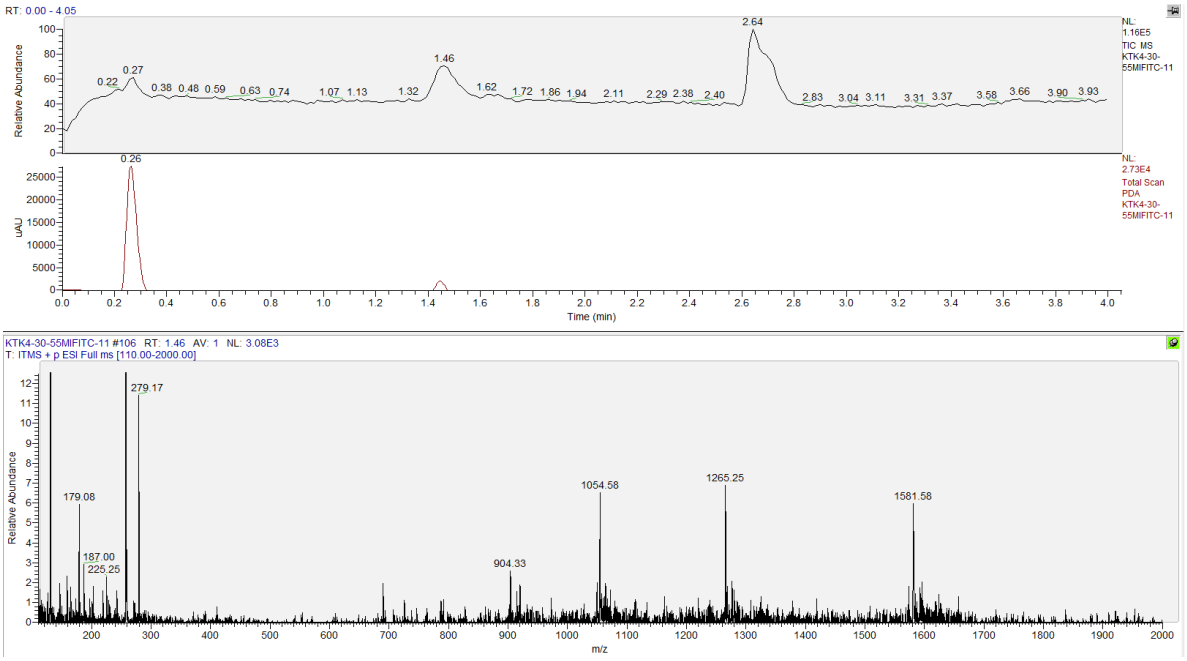

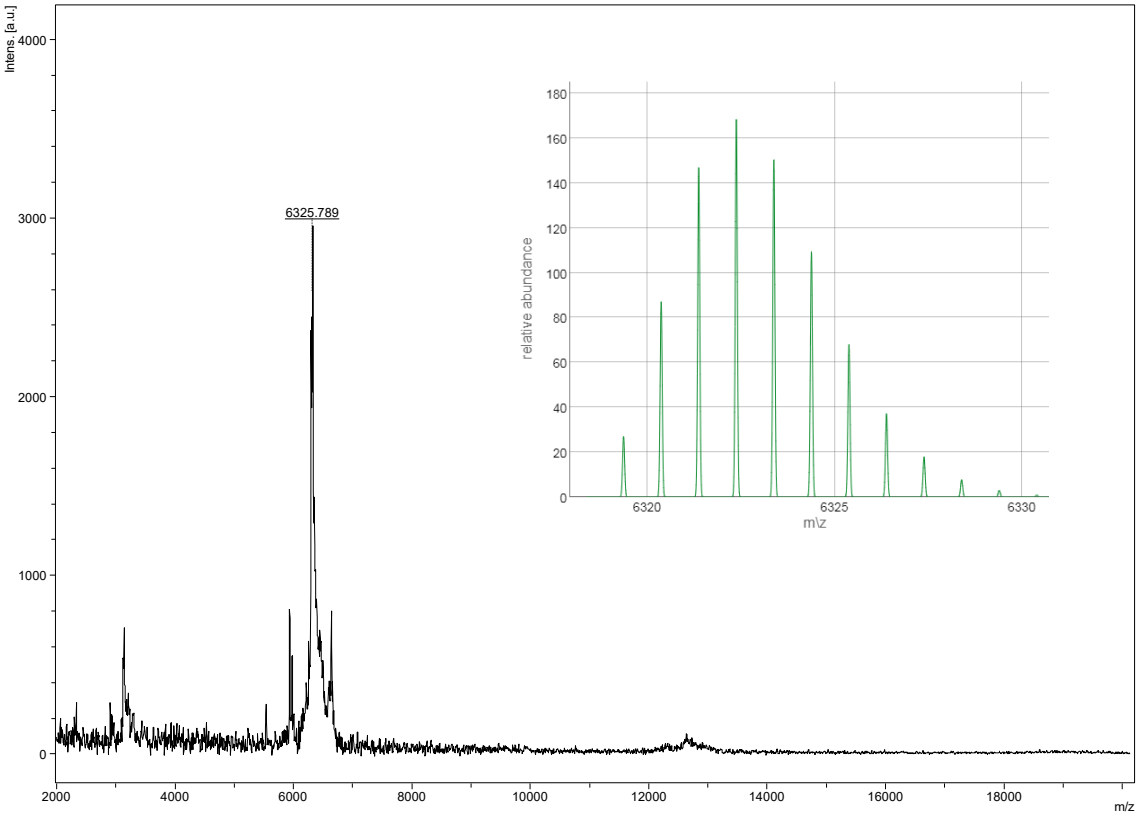

FserH2 (FITC-peg-CGGCA-CATTC-TGCCG-CTAGT); Expected Mass for $C_{250}H_{310}N_{114}O_{80}S$: 6220.3414; isotopic mass range (green insert). LC-MS (ESI) RT= 1.45 min. m/z: 1556.8 $[M+4H]^{4+}$, 1245.9 $[M+5H]^{5+}$, 1038.5 $[M+6H]^{6+}$, MALDI-TOF m/z found: 6226.9 $[M+H]^{+}$

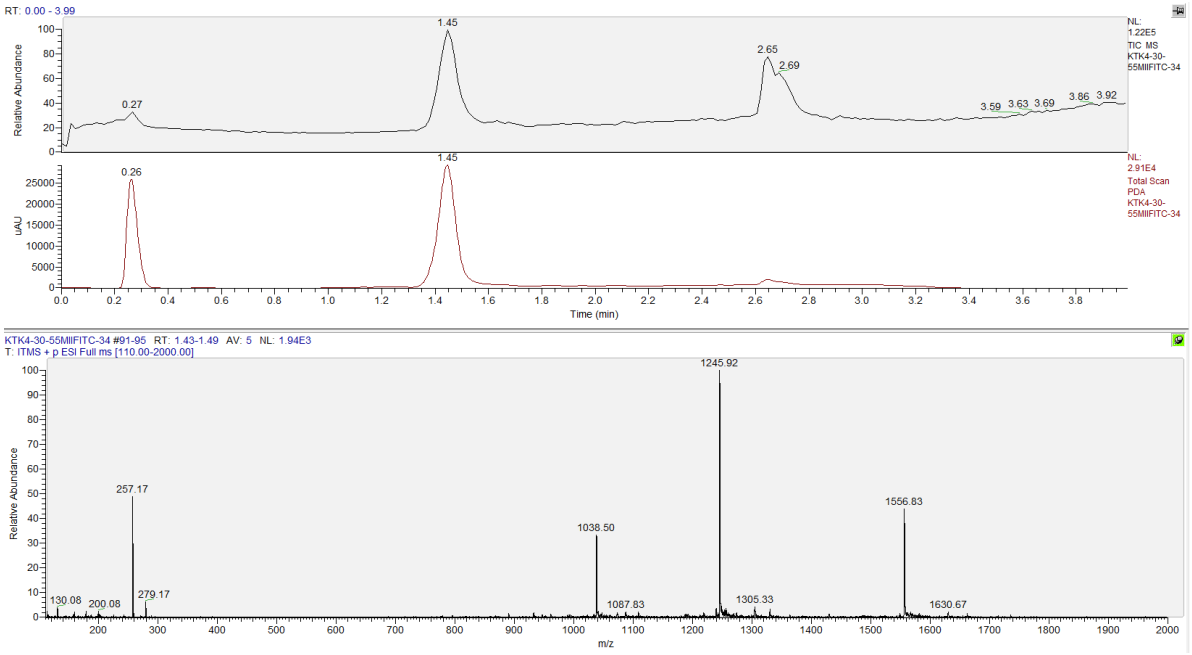

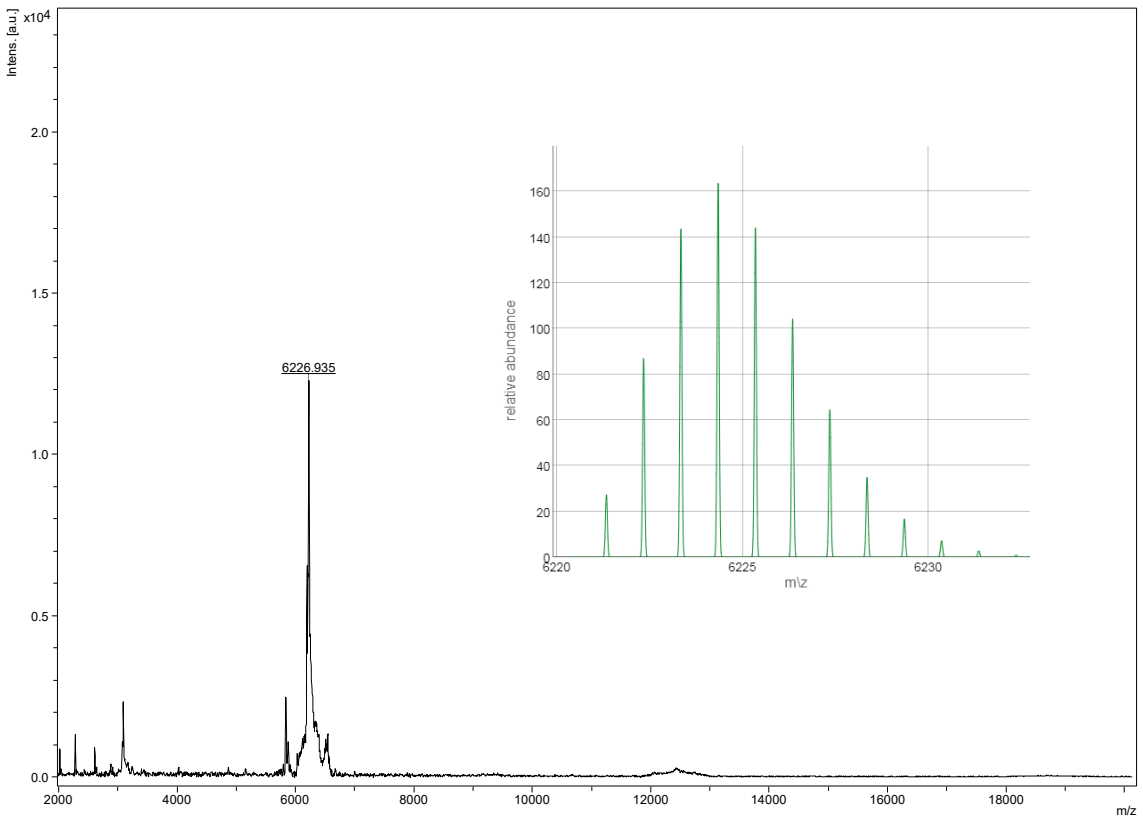

FserI (FITC-peg-ACTAG-CGGCA); Expected Mass for $C_{139}H_{166}N_{64}O_{41}S$: 3419.2593; isotopic mass range (green insert). LC-MS (ESI) RT= 1.43 min. m/z: 1711.5 $[M+2H]^{2+}$, 1141.3 $[M+3H]^{3+}$, 856.3 $[M+4H]^{4+}$, 685.4 $[M+5H]^{5+}$, MALDI-TOF m/z found: 3422.1 $[M+H]^{+}$

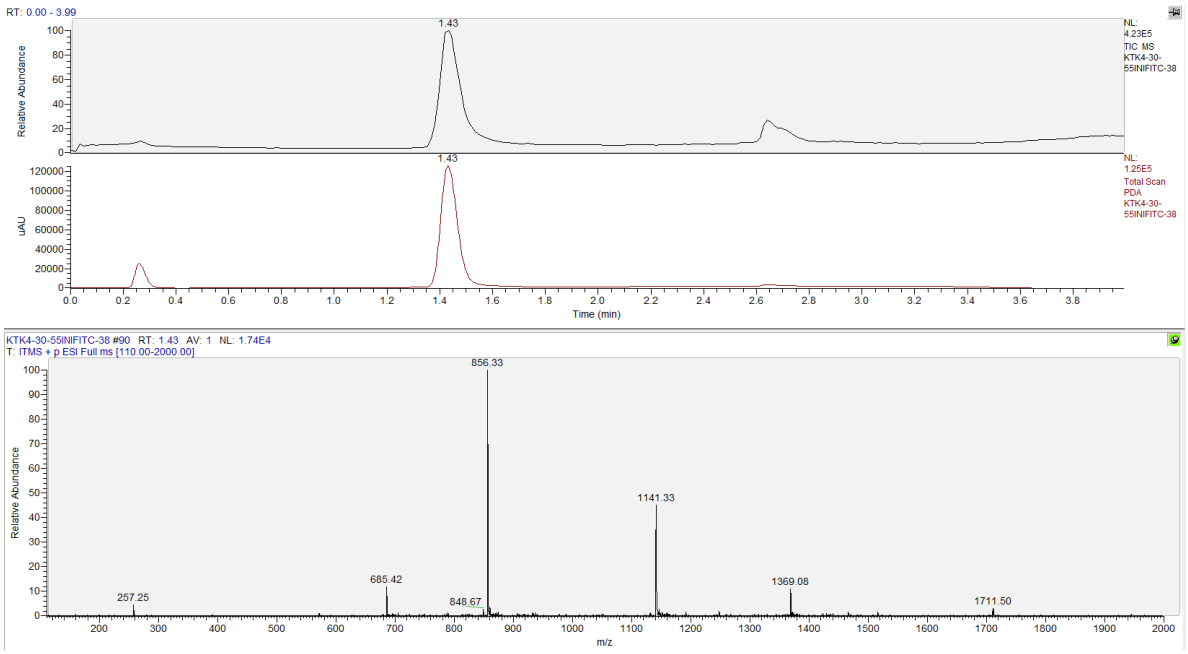

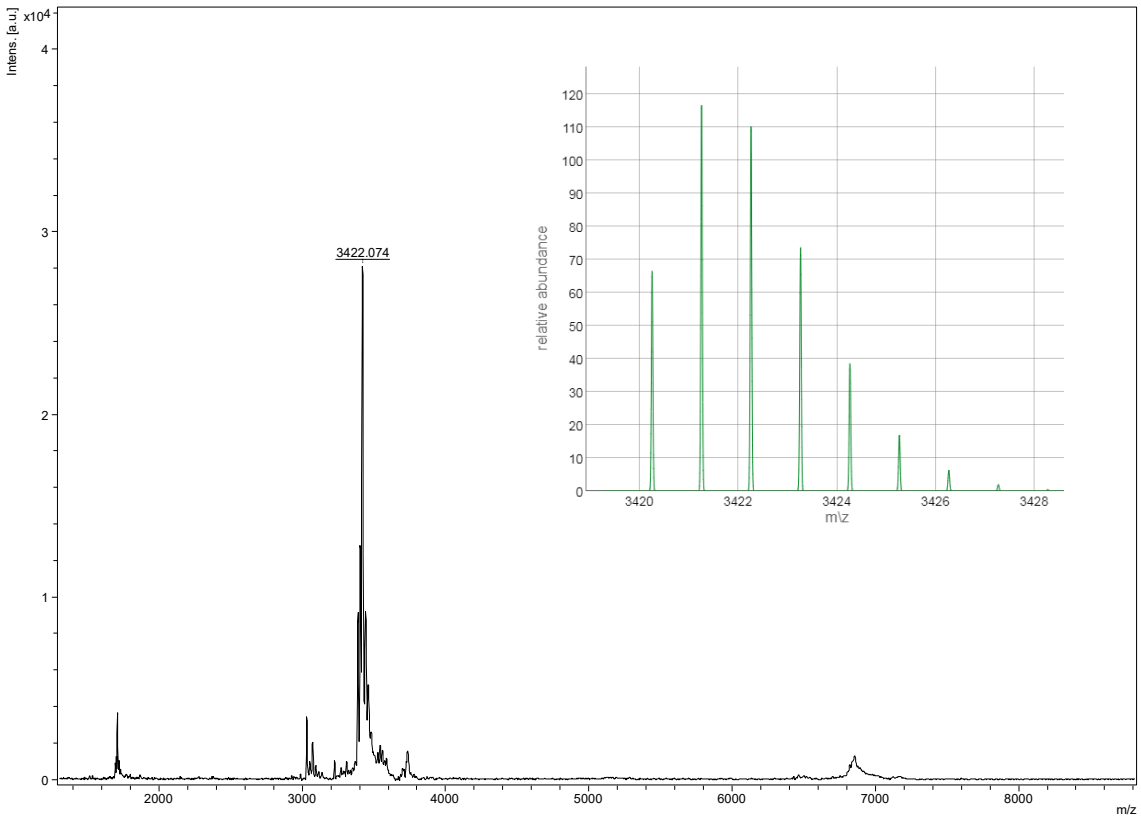

serH1 (NH_2-peg-G<u>A</u><u>A</u><u>T</u>G-<u>T</u><u>G</u><u>C</u><u>C</u><u>G</u>-<u>A</u><u>C</u><u>T</u><u>A</u><u>G</u>-<u>C</u><u>G</u><u>G</u><u>C</u><u>A</u>); Expected Mass for $C_{231}H_{297}N_{123}O_{71}$: 5929.3411; isotopic mass range (green insert). LC-MS (ESI) RT= 1.11 min. m/z: 1484.1 $[M+4H]^{4+}$, 1187.9 $[M+5H]^{5+}$, 990.2 $[M+6H]^{6+}$, MALDI-TOF m/z found: 5935.1 $[M+H]^{+}$

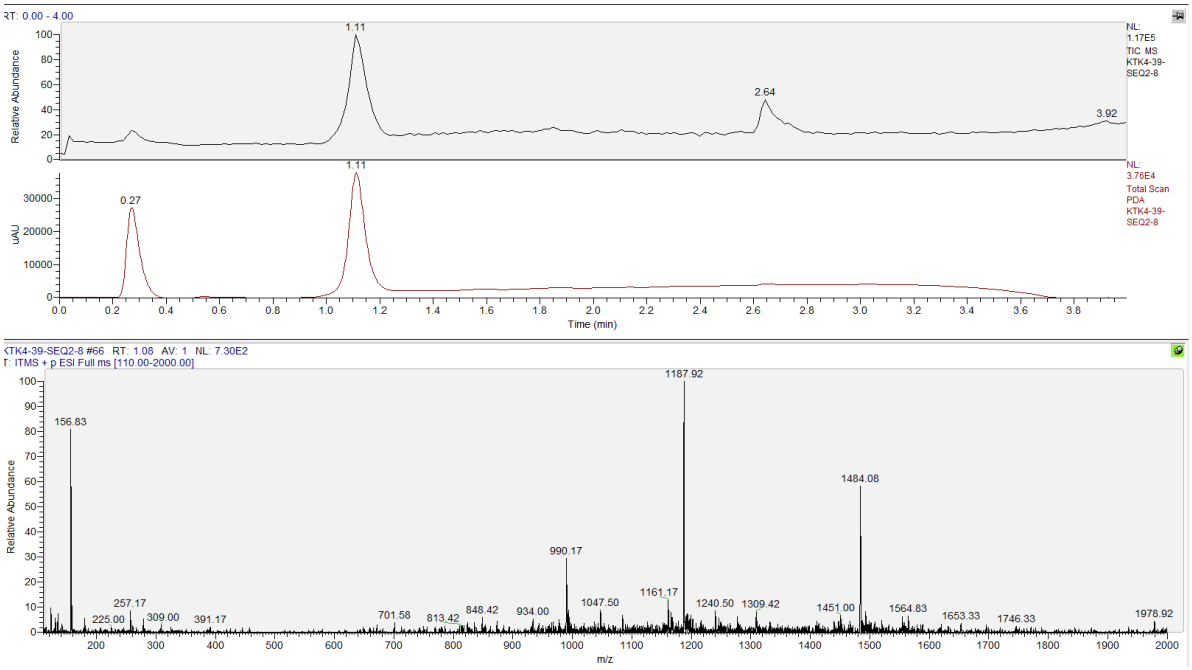

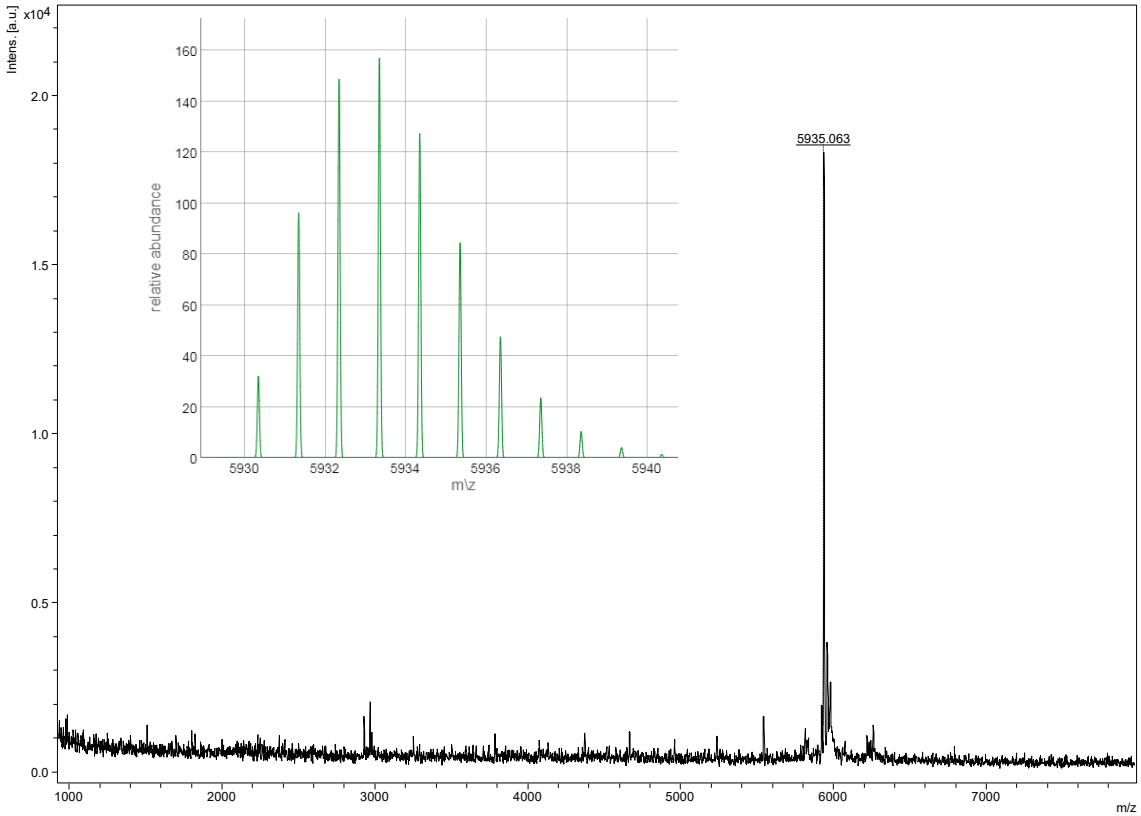

serH2 (NH_2-peg-CGGCA-CATTC-TGCCG-CTAGT); Expected Mass for $C_{229}H_{299}N_{113}O_{75}$: 5831.3056; isotopic mass range (green insert). LC-MS (ESI) RT= 1.09 min. m/z: 1459.6 $[M+4H]^{4+}$, 1168.1 $[M+5H]^{5+}$, 973.7 $[M+6H]^{6+}$, MALDI-TOF m/z found: 5836.8 $[M+H]^{+}$

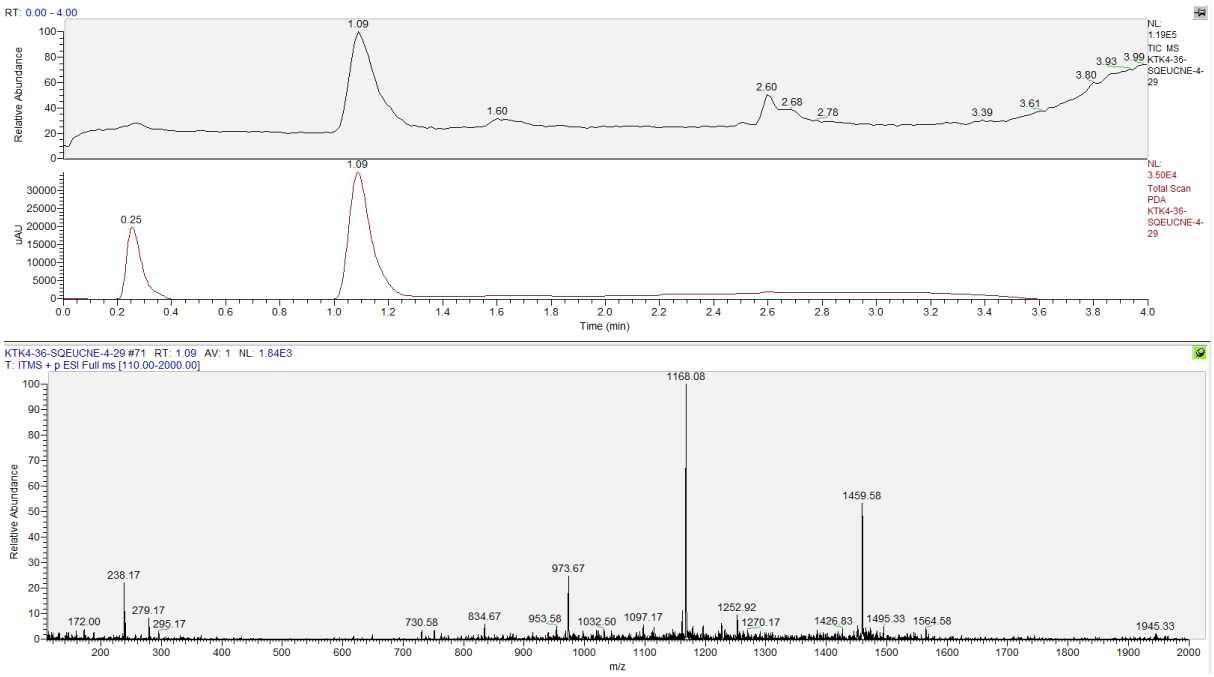

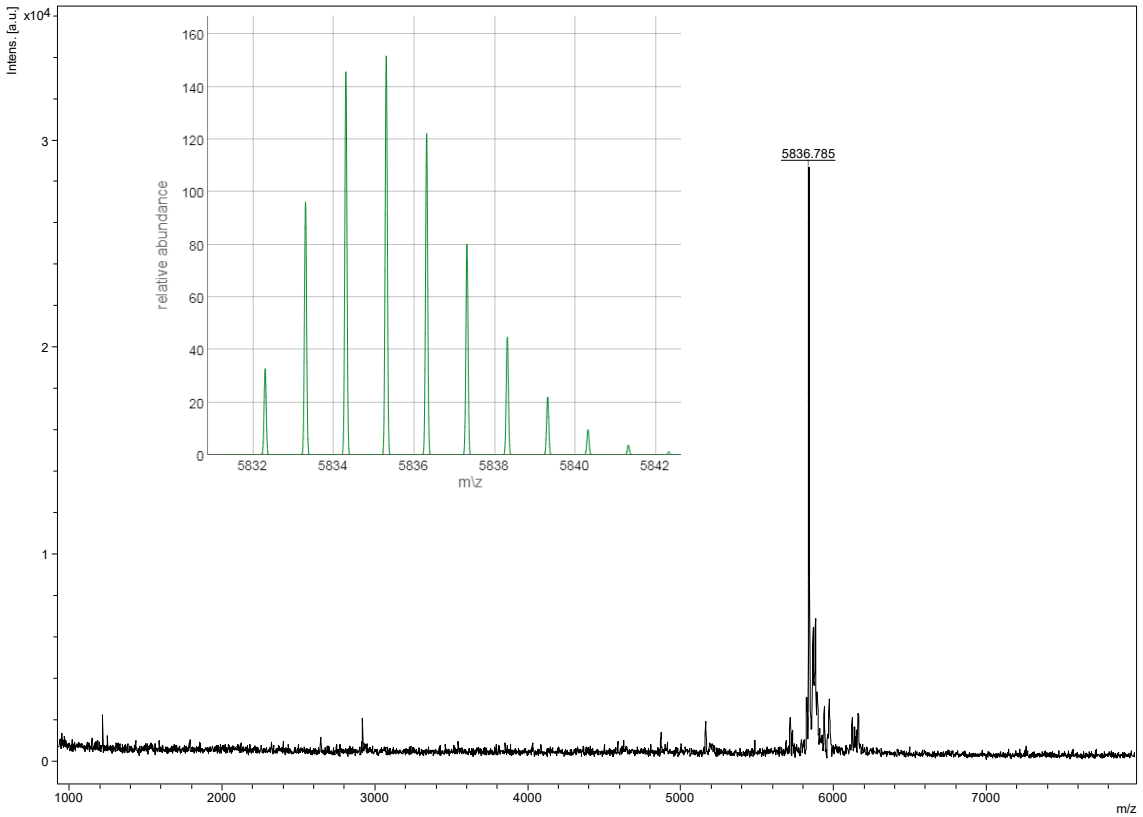

Cy3serI (biotin-peg-Lys(cy3)-peg-ACTAG-CGGCA); Expected Mass for $C_{169}H_{225}N_{70}O_{43}S^{+}$: 3954.7287; isotopic mass range (green insert). LC-MS (ESI) RT= 2.11 min. m/z: 1319.7 $[M+2H]^{3+}$, 990.0 $[M+3H]^{4+}$, 792.3 $[M+4H]^{5+}$, 660.4 $[M+5H]^{6+}$, MALDI-TOF m/z found: 3955.4 $[M]^{+}$

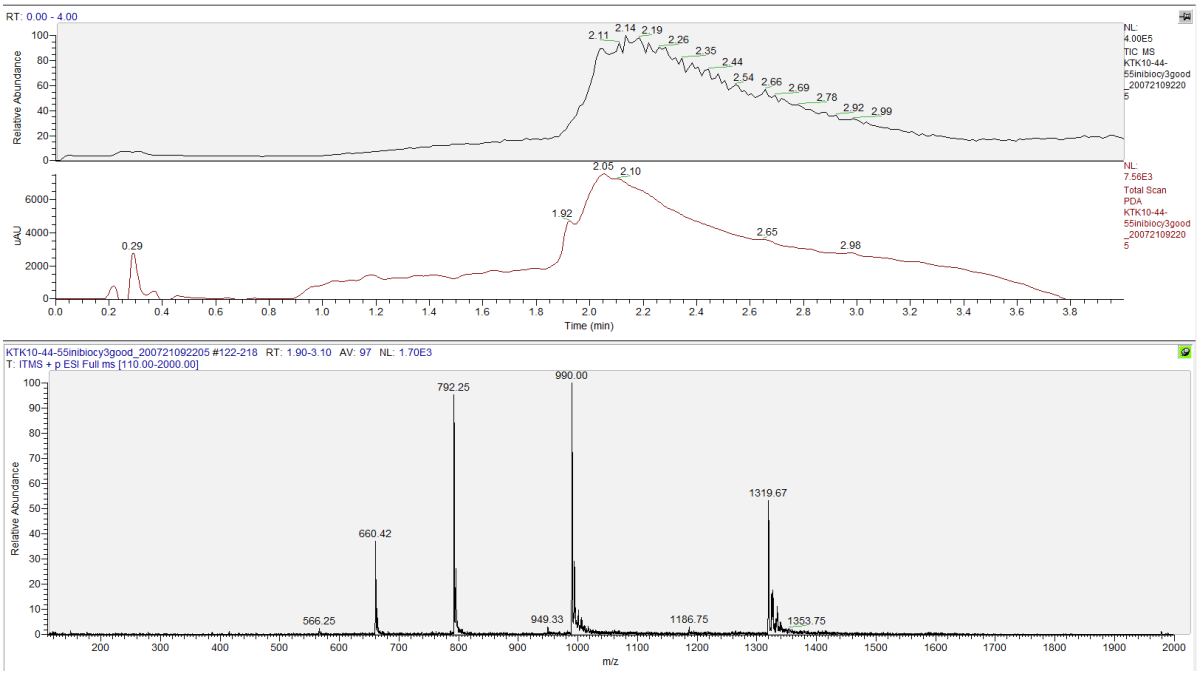

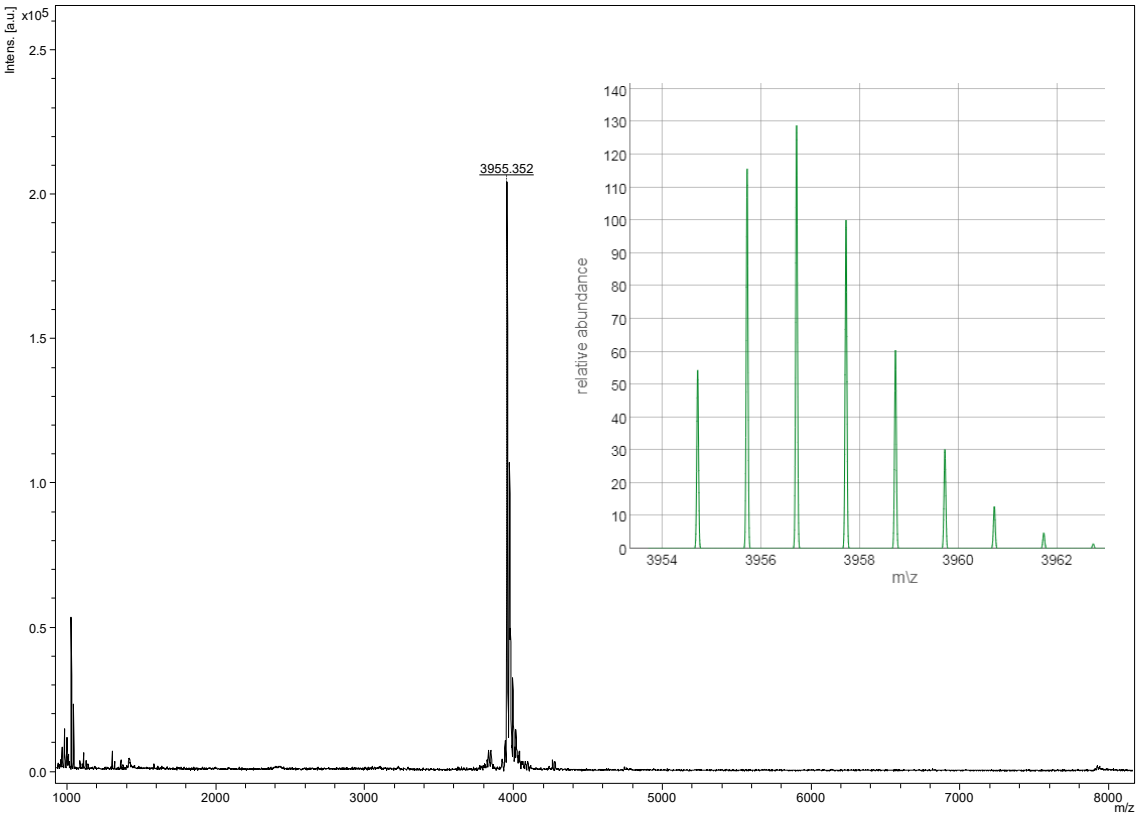

FpegH1 (FITC-peg-GAATG-TGCCG-ACTAG-CGGCA); Expected Mass for $C_{302}H_{408}N_{124}O_{96}S$: 7339.0577; isotopic mass range (green insert). LC-MS (ESI) RT= 1.93 min. m/z: 1469.6 $[M+5H]^{5+}$, 1225.0 $[M+6H]^{6+}$, 1050.1 $[M+7H]^{7+}$, 919.2 $[M+8H]^{8+}$, MALDI-TOF m/z found: 7345.5 $[M+H]^{+}$

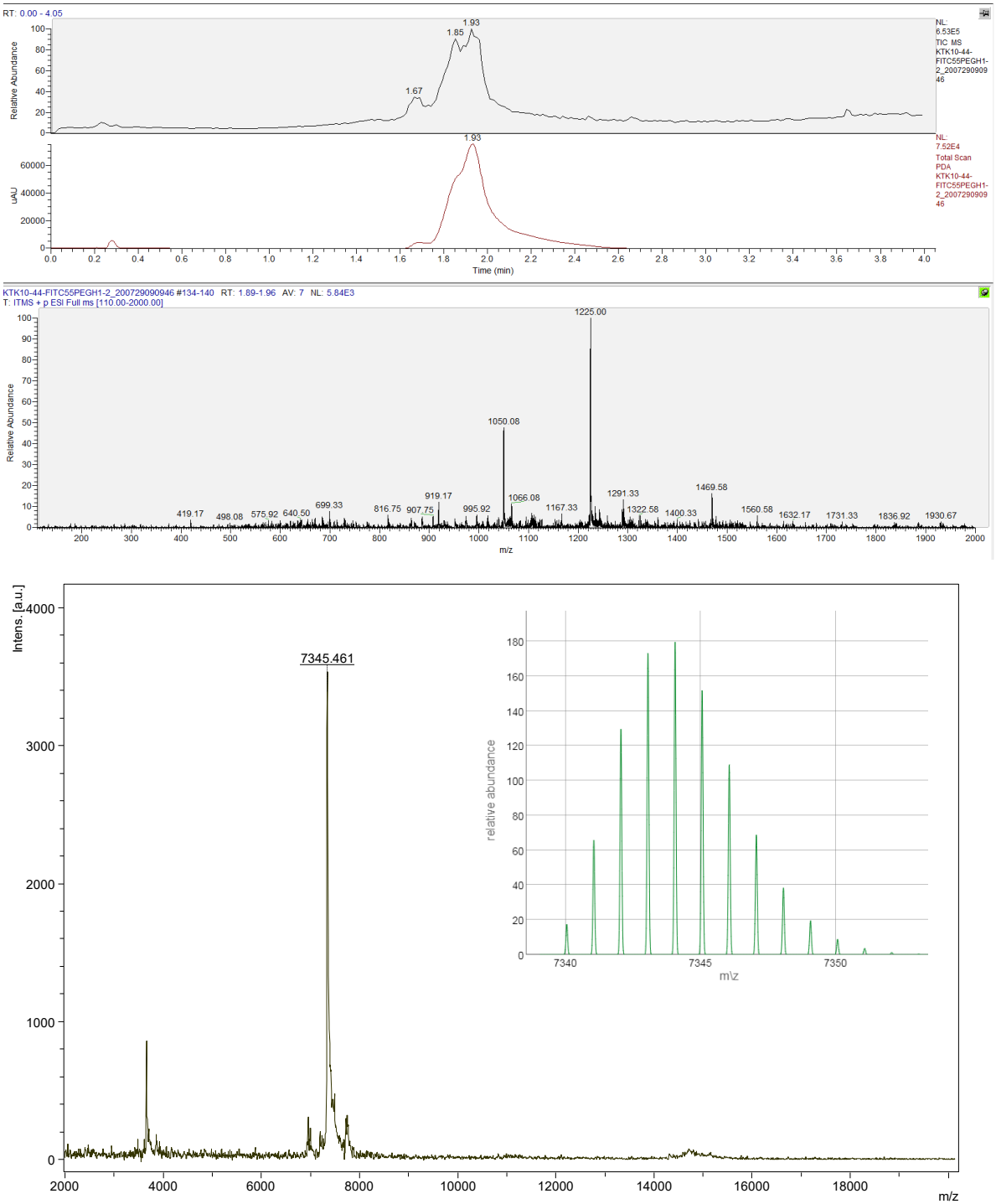

FpegH2 (FITC-peg-CGGCA-CATTC-TGCCG-CTAGT); Expected Mass for $C_{300}H_{410}N_{114}O_{100}S$: 7241.0222; isotopic mass range (green insert). LC-MS (ESI) RT= 1.87 min. m/z: 1449.9 $[M+5H]^{5+}$, 1208.5 $[M+6H]^{6+}$, 1035.9 $[M+7H]^{7+}$, 906.6 $[M+8H]^{8+}$, MALDI-TOF m/z found: 7245.1 $[M+H]^{+}$

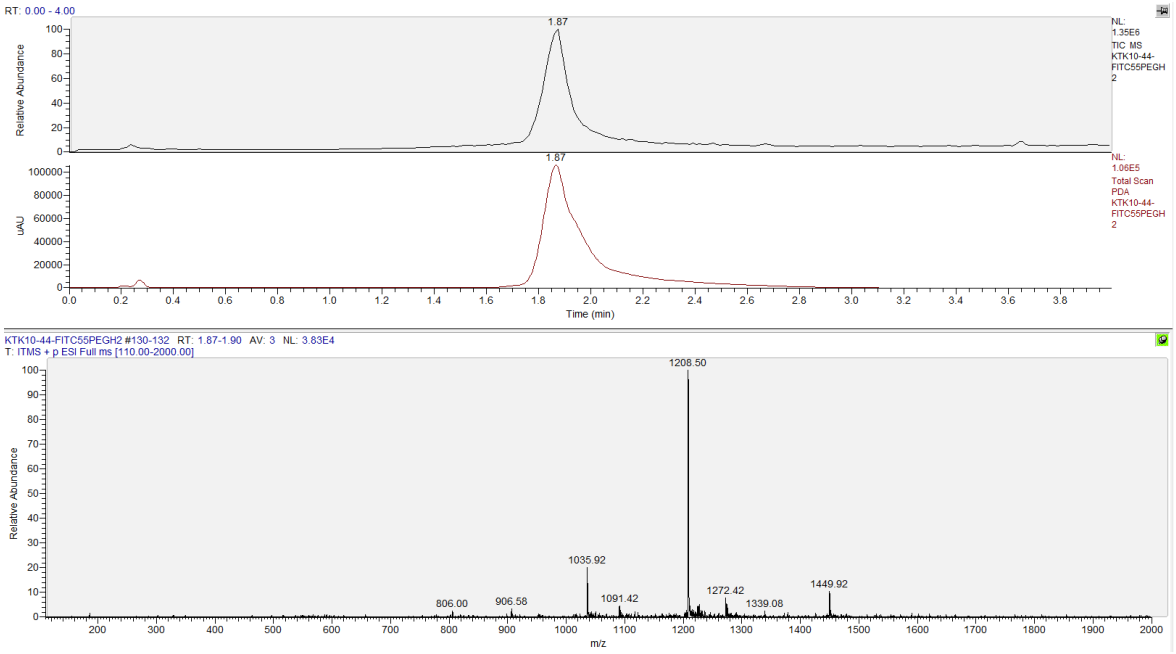

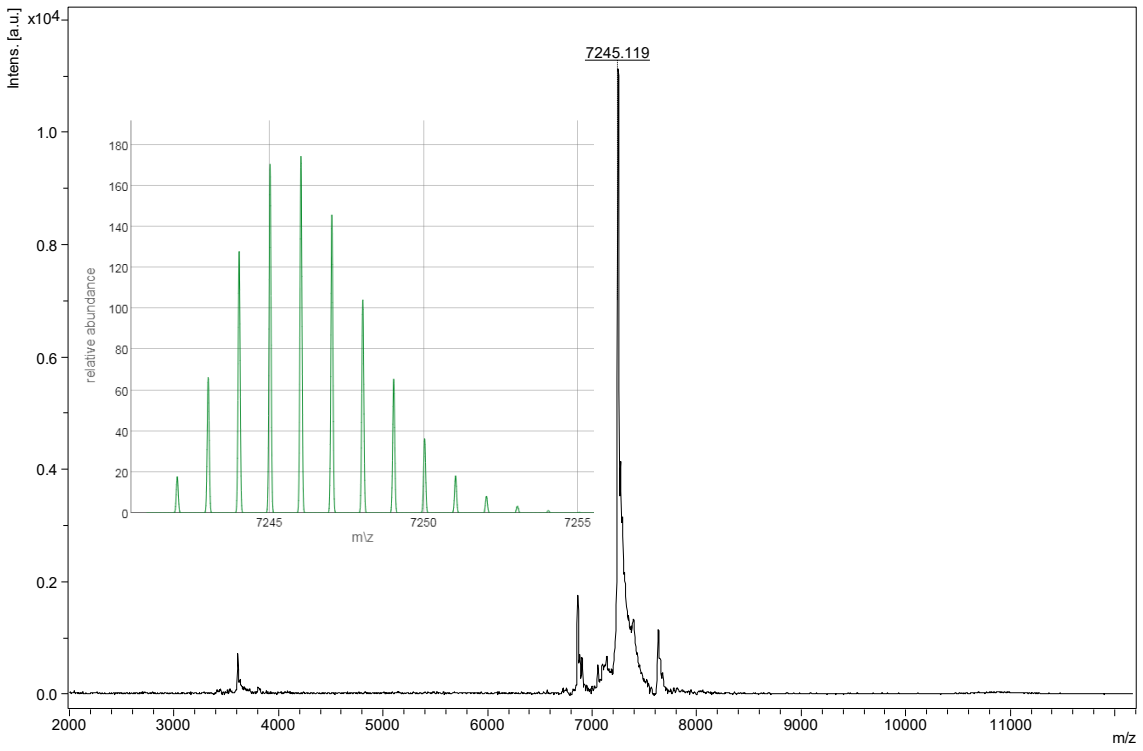

FpegI (FITC-peg-ACTAG-CGGCA-Lys-Ac); Expected Mass for $C_{172}H_{230}N_{66}O_{53}S$: 4099.7052; isotopic mass range (green insert). LC-MS (ESI) RT= 1.76 min. m/z: 1368.3 $[M+3H]^{3+}$, 1026.5 $[M+4H]^{4+}$, 821.3 $[M+5H]^{5+}$, 684.7 $[M+6H]^{6+}$, MALDI-TOF m/z found: 4101.9 $[M+H]^{+}$

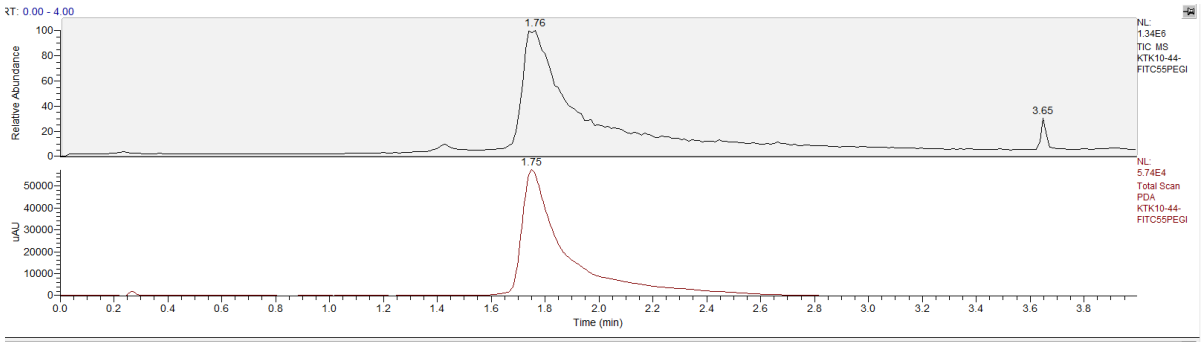

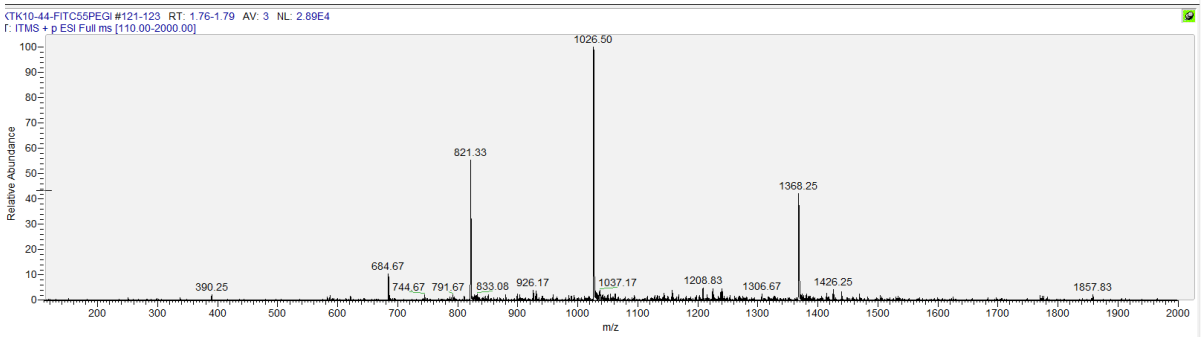

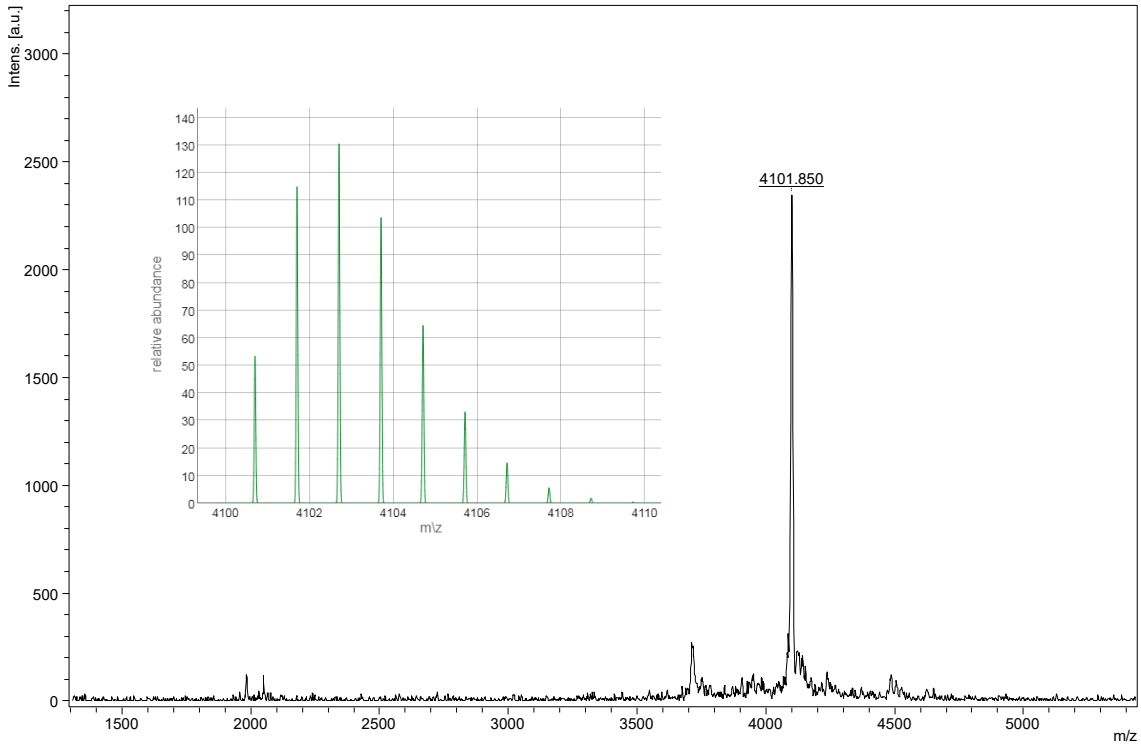

pegH1 (NH_2-peg-G<u>A</u><u>A</u><u>T</u>G-<u>T</u><u>G</u><u>C</u><u>C</u><u>G</u>-A<u>C</u><u>T</u><u>A</u>G-<u>C</u><u>G</u><u>G</u><u>C</u><u>A</u>); Expected Mass for $C_{281}H_{397}N_{123}O_{91}$: 6950.0219; isotopic mass range (green insert). LC-MS (ESI) RT= 1.61 min. m/z: 1739.4 $[M+4H]^{4+}$, 1391.9 $[M+5H]^{5+}$, 1160.3 $[M+6H]^{6+}$, 994.9 $[M+7H]^{7+}$, MALDI-TOF m/z found: 6956.6 $[M+H]^{+}$

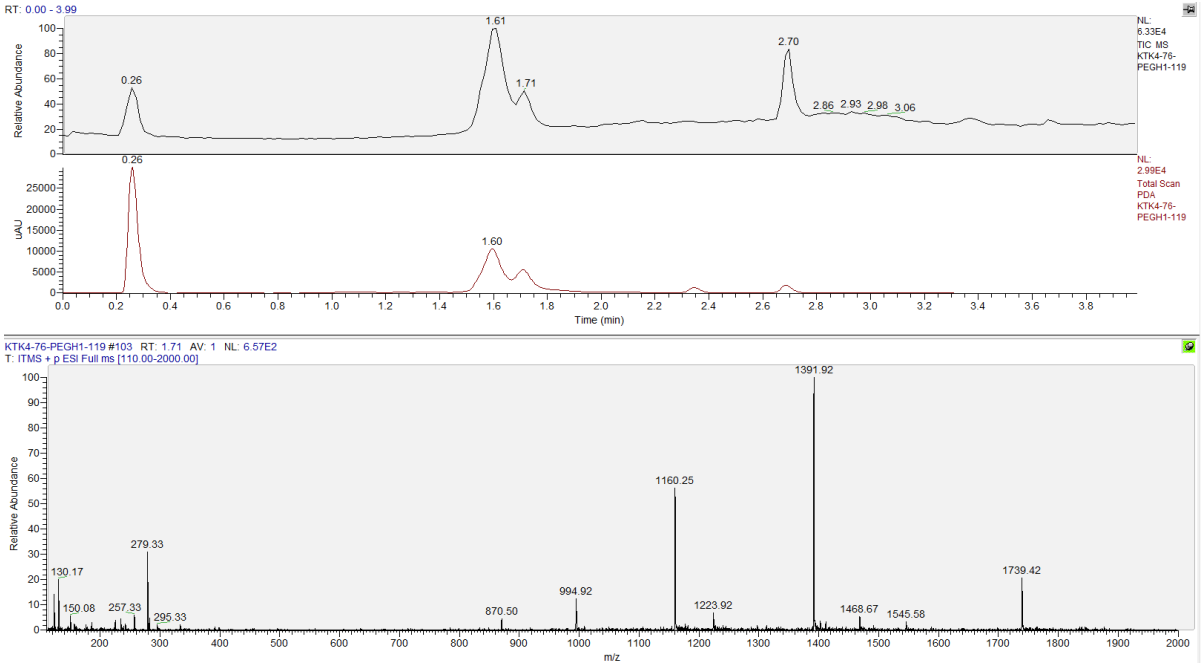

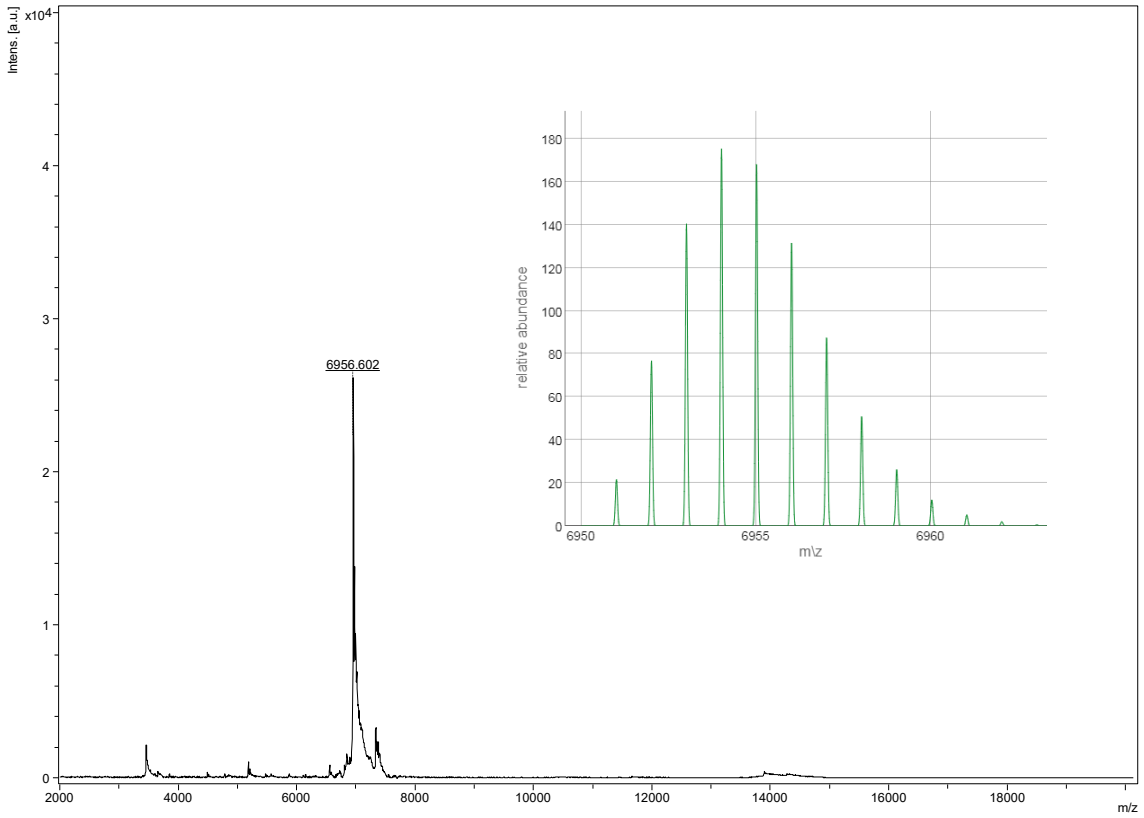

pegH2 (NH_2-peg-C<u>G</u><u>G</u><u>C</u>A-<u>C</u>A<u>T</u><u>T</u><u>C</u>-T<u>G</u><u>C</u><u>C</u>G-<u>C</u>T<u>A</u><u>G</u><u>T</u>); Expected Mass for $C_{279}H_{399}N_{113}O_{95}$: 6851.9864; isotopic mass range (green insert). LC-MS (ESI) RT= 1.61 min. m/z: 1715.0 $[M+4H]^{4+}$, 1372.3 $[M+5H]^{5+}$, 1144.0 $[M+6H]^{6+}$, 980.8 $[M+7H]^{7+}$, MALDI-TOF m/z found: 6858.5 $[M+H]^{+}$

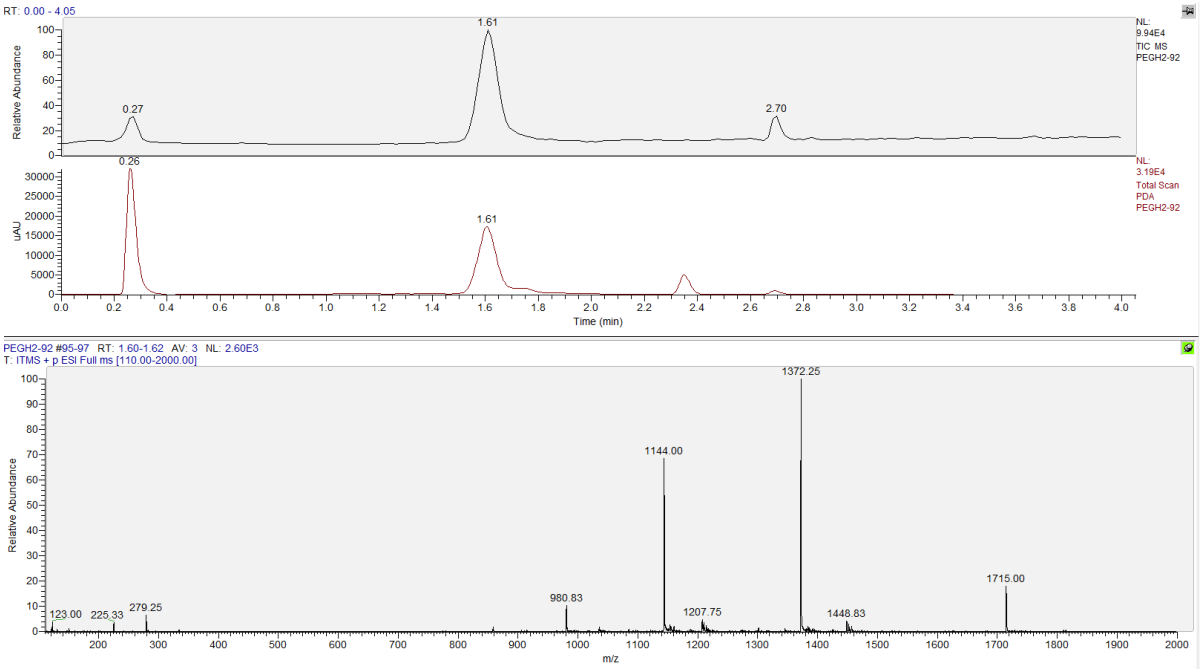

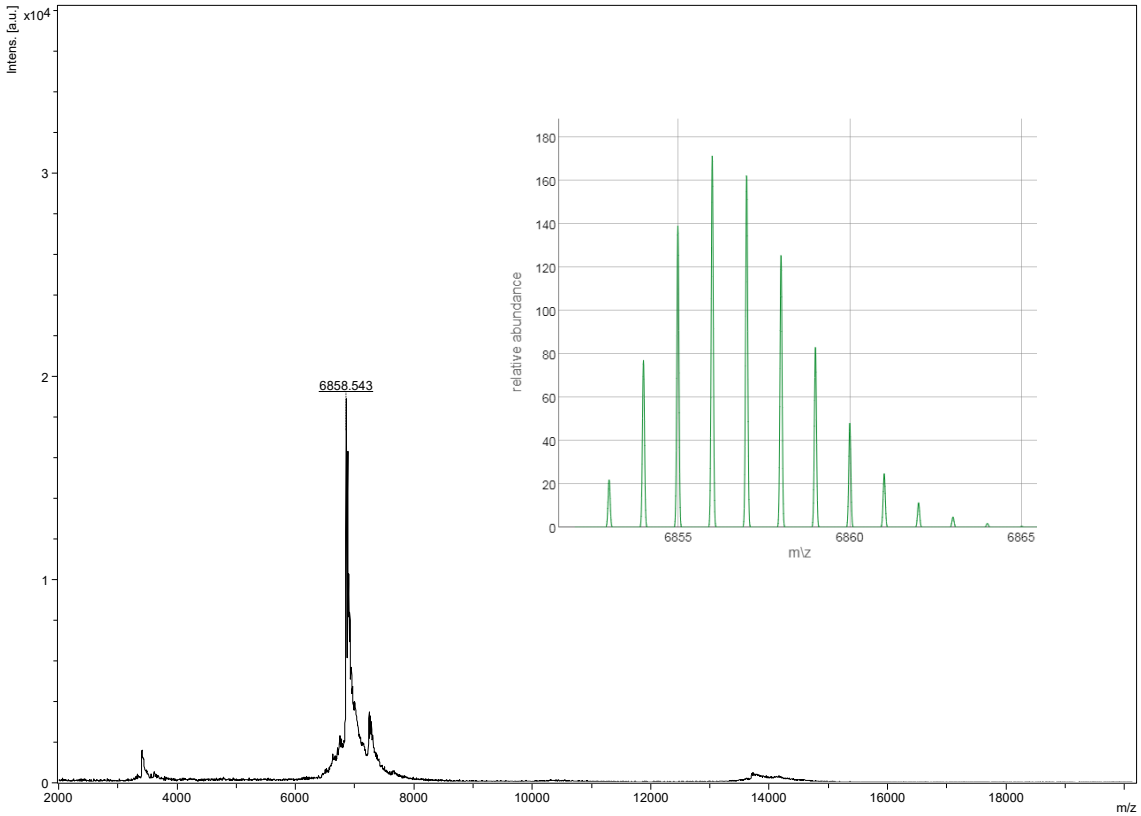

Cy3pegI (cy3-peg-A<u>C</u>T<u>A</u>G-<u>C</u>G<u>G</u>C<u>A</u>); Expected Mass for $C_{172}H_{238}N_{65}O_{47}^{+}$: 3965.8232; isotopic mass range (green insert). LC-MS (ESI) RT= 2.02 min. m/z: 1323.3 $[M+2H]^{3+}$, 992.8 $[M+3H]^{4+}$, 794.4 $[M+4H]^{5+}$, 662.3 $[M+5H]^{6+}$, MALDI-TOF m/z found: 3967.3 $[M]^{+}$

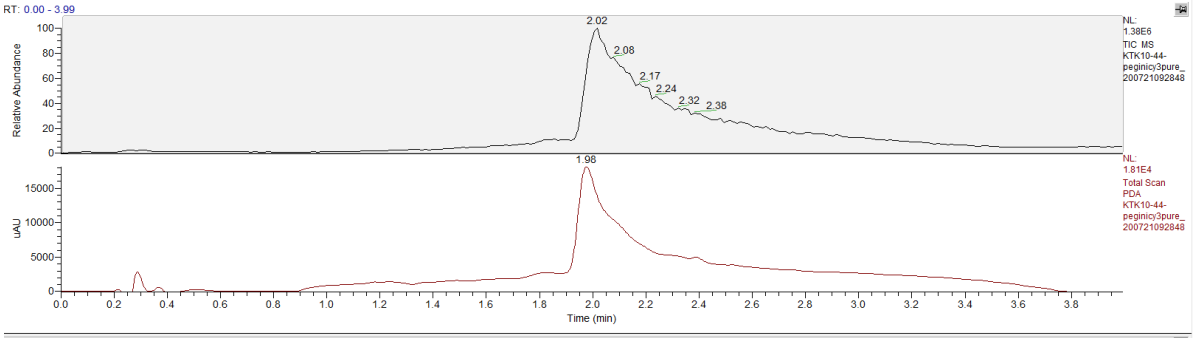

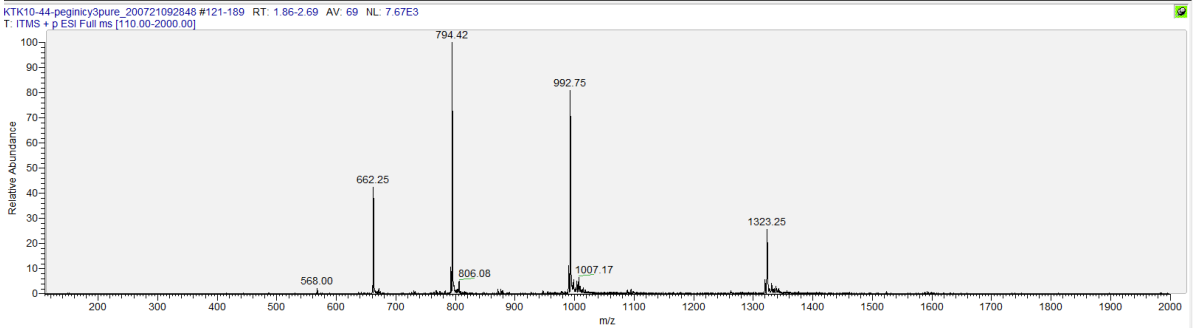

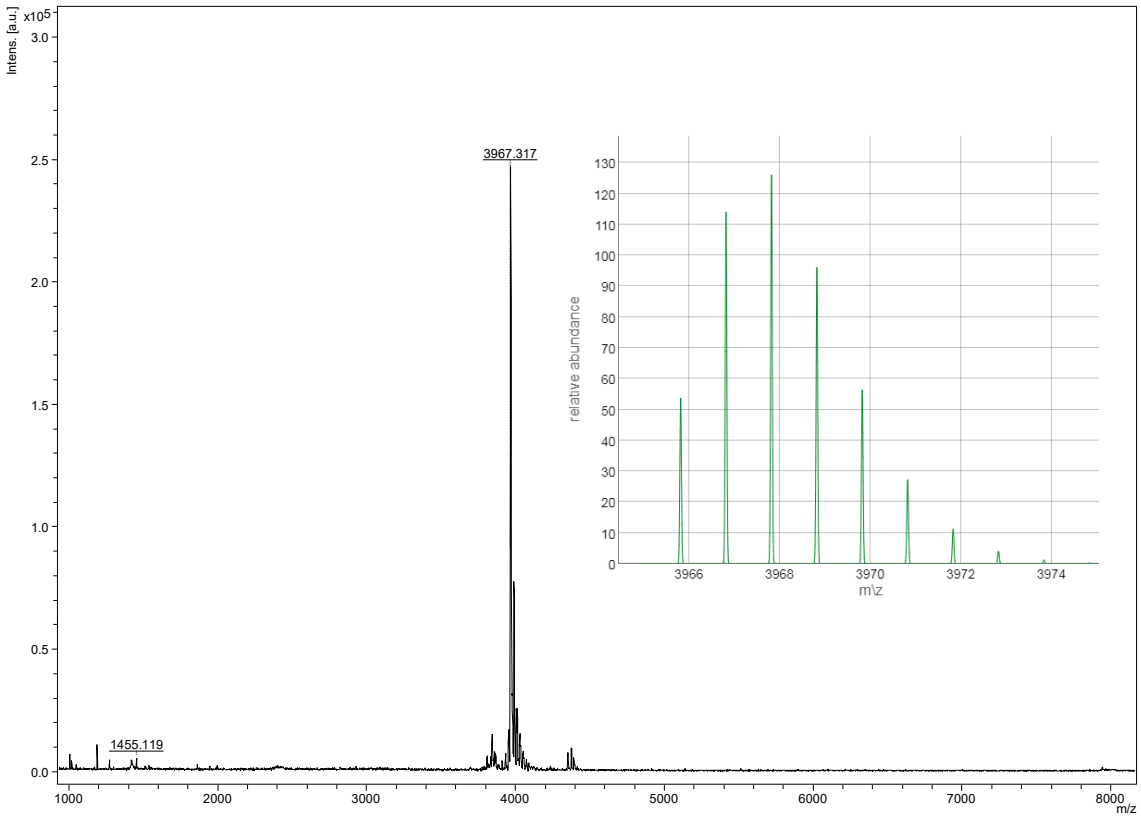

Cy3pegH2 (cy3-peg-CGGCA-CATTC-TGCCG-CTAGT); Expected Mass for $C_{308}H_{432}N_{115}O_{96}^{+}$: 7277.2457; isotopic mass range (green insert). LC-MS (ESI) RT= 1.92 min. m/z: 1456.9 $[M+4H]^{5+}$, 1214.3 $[M+5H]^{6+}$, 1041.0 $[M+6H]^{7+}$, MALDI-TOF m/z found: 7282.7 $[M]^{+}$

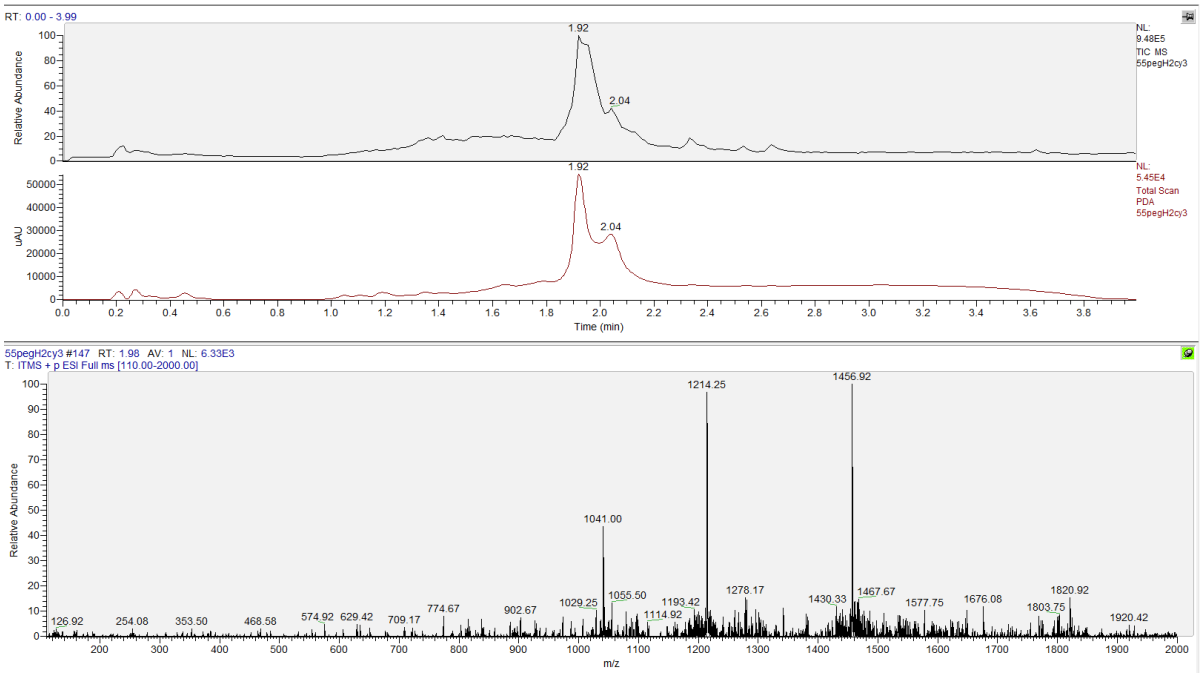

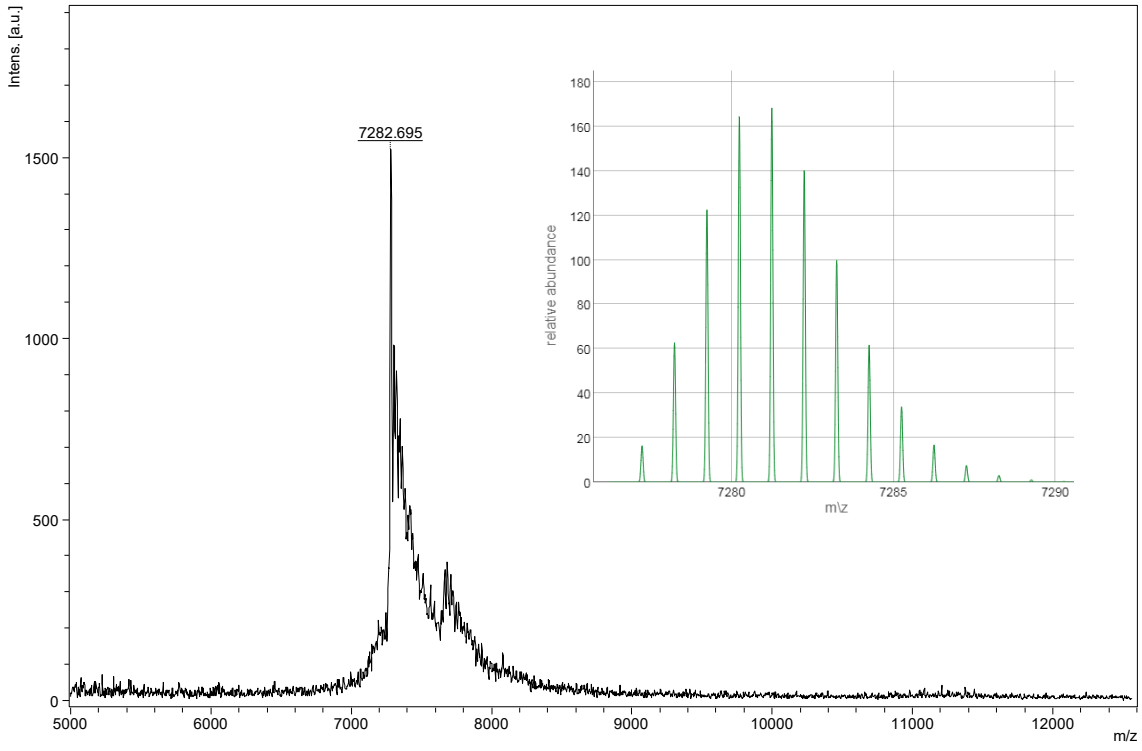

pegI (NH_2-peg-A<u>C</u>T<u>A</u>G-<u>C</u>G<u>G</u>C<u>A</u>); Expected Mass for $C_{143}H_{205}N_{63}O_{46}$: 3540.5639; isotopic mass range (green insert). LC-MS (ESI) RT= 1.76 min. m/z: 1182.0 $[M+3H]^{3+}$, 886.6 $[M+4H]^{4+}$, 709.5 $[M+5H]^{5+}$, MALDI-TOF m/z found: 3543.1 $[M+H]^{+}$

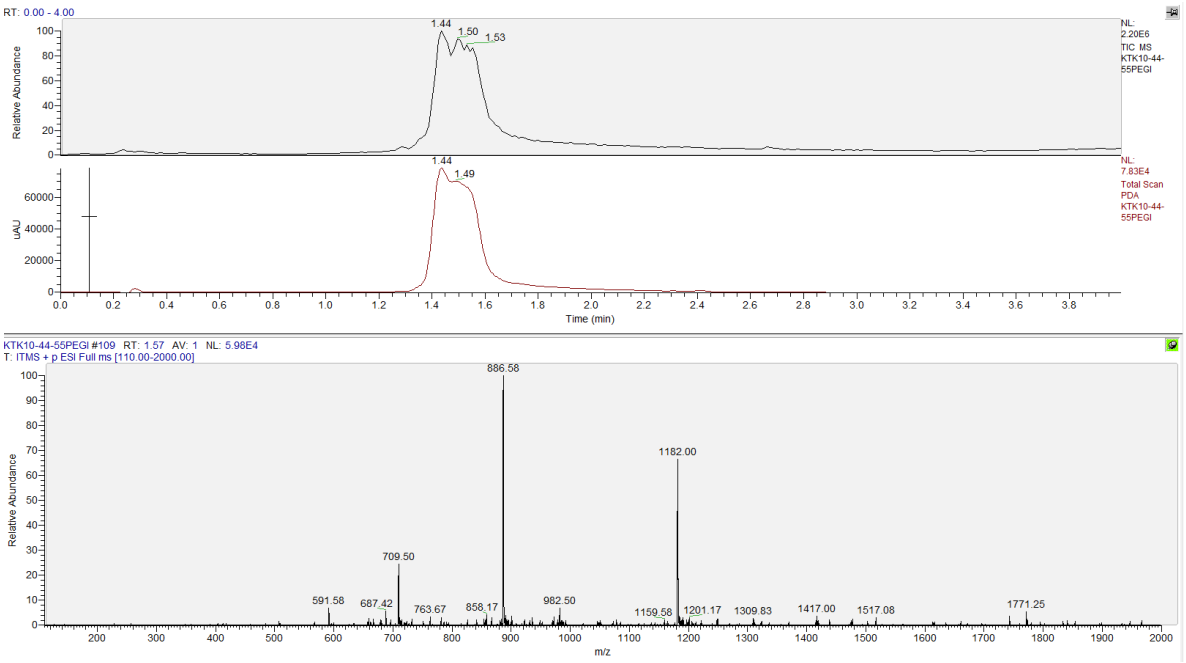

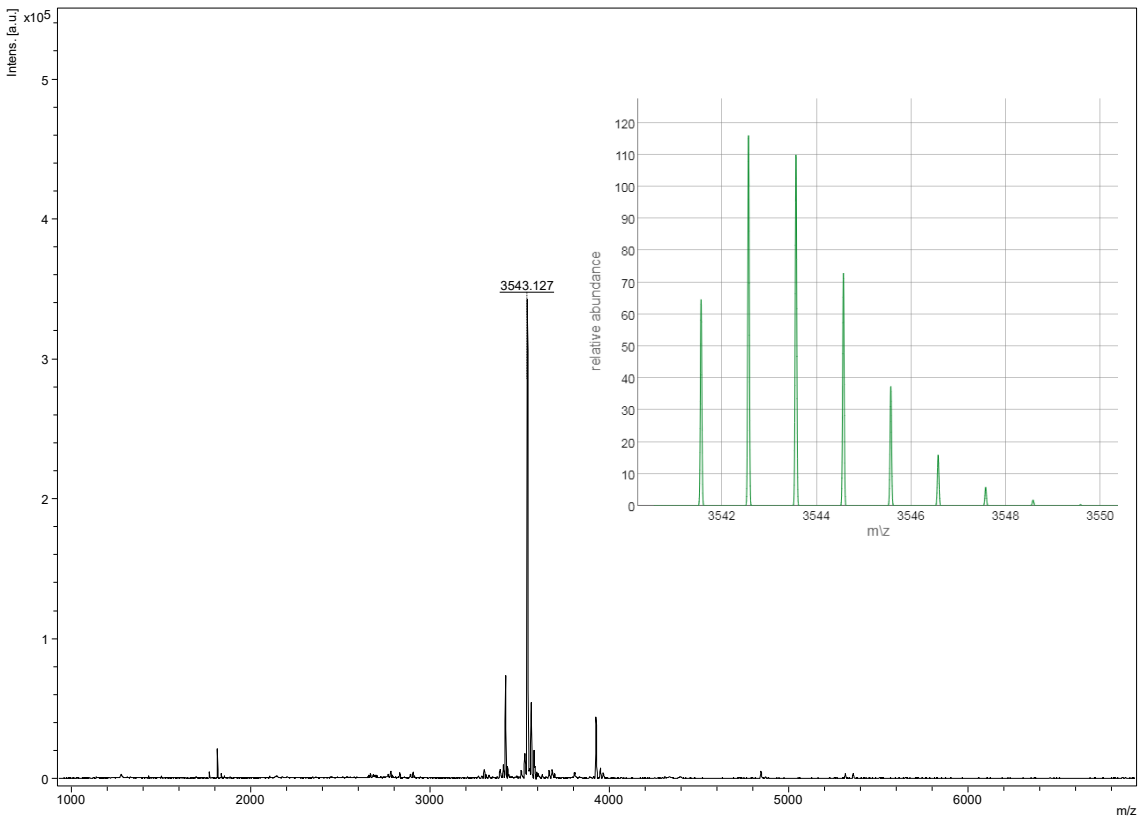

BpegI (Biotin-peg-peg-peg-peg-peg-ACTAG-CGGCA); Expected Mass for $C_{177}H_{263}N_{69}O_{60}S$: 4346.9370; isotopic mass range (green insert). LC-MS (ESI) RT= 1.56 min. m/z: 1450.8 $[M+3H]^{3+}$, 1088.3 $[M+4H]^{4+}$, 870.3 $[M+5H]^{5+}$, MALDI-TOF m/z found: 4350.0 $[M+H]^{+}$

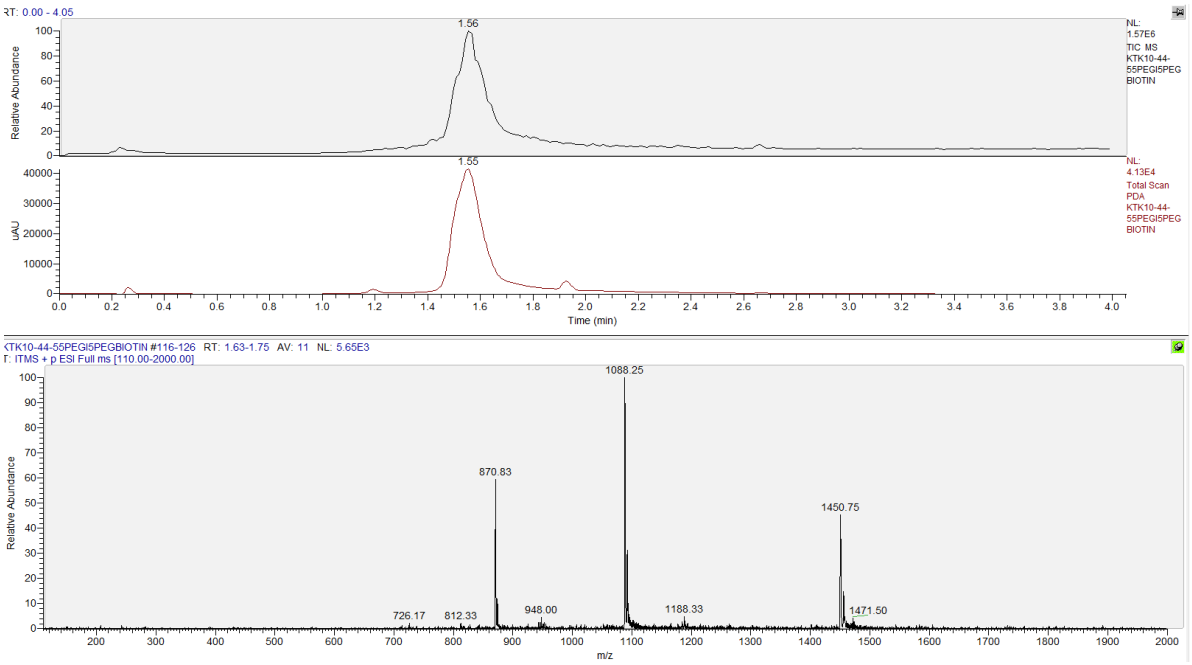

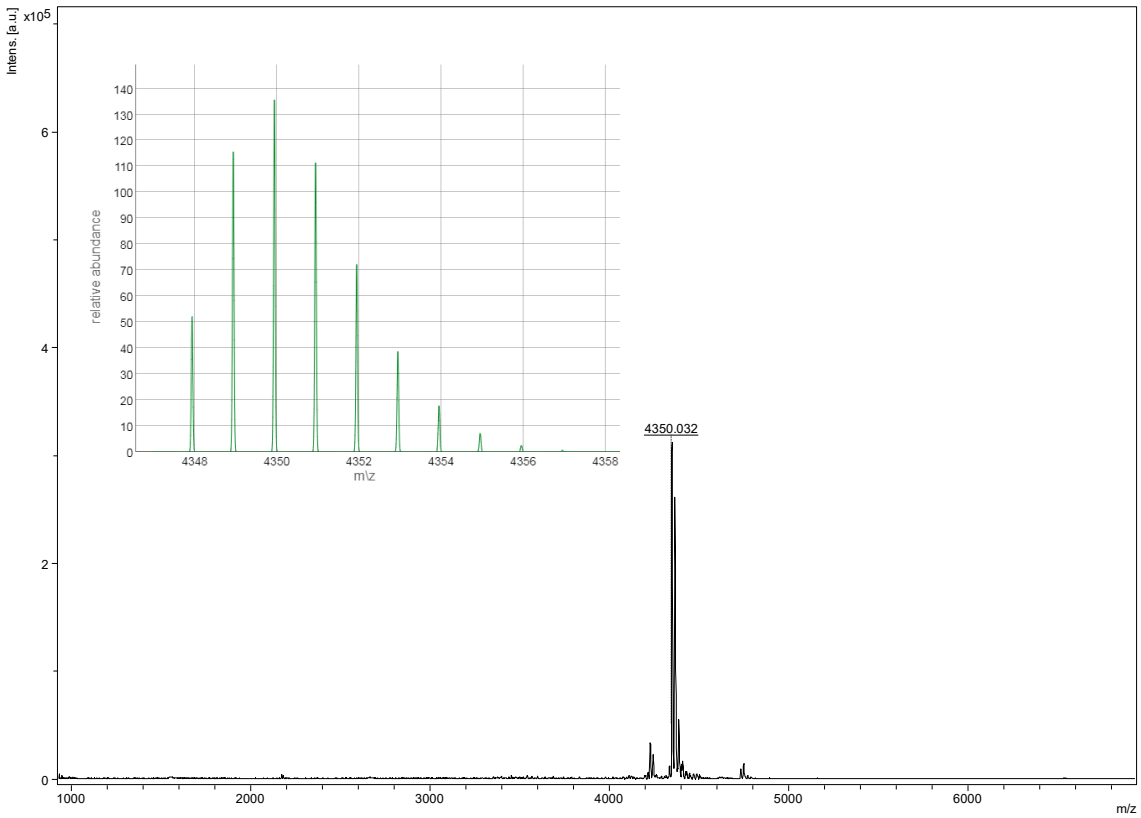

FBpegI (Biotin-peg-peg-Lys(FITC)-peg-ACTAG-CGGCA); Expected Mass for $C_{192}H_{264}N_{70}O_{60}S_2$: 4557.9300; isotopic mass range (green insert). LC-MS (ESI) RT= 1.71 min. m/z: 1526.3 $[M+4H]^{3+}$,1145.1 $[M+4H]^{4+}$, 916.5 $[M+5H]^{5+}$, MALDI-TOF m/z found: 4563 $[M+H]^{+}$

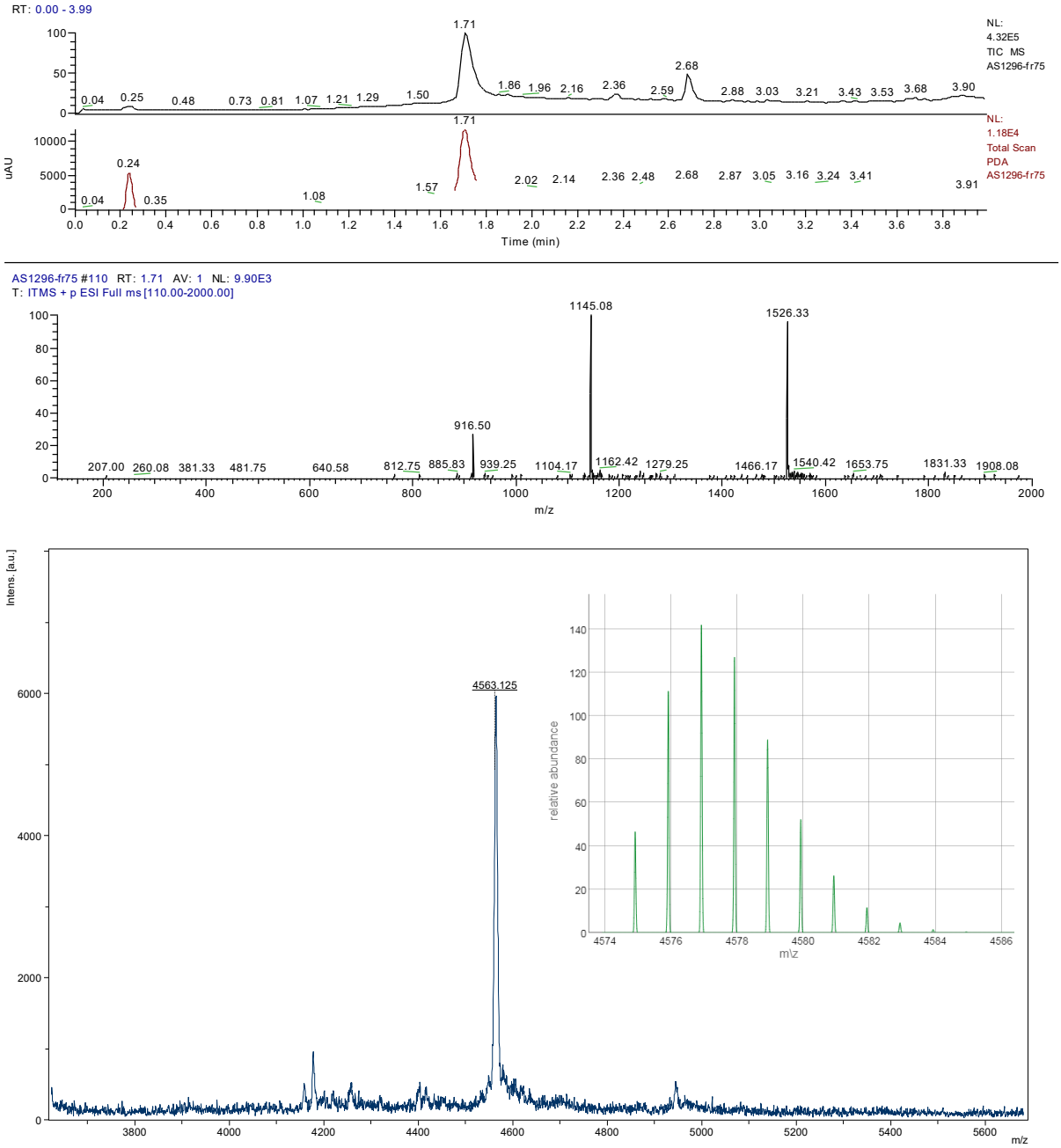

Ref1 (NH_2-peg-AGTCTCAGTGTCAACGTACG); Expected Mass for $C_{281}H_{399}N_{117}O_{93}$: 6900.0098; isotopic mass range (green insert). LC-MS (ESI) RT= 1.62 min. m/z: 1727.1 $[M+4H]^{4+}$, 1381.8 $[M+5H]^{5+}$, 1151.7 $[M+6H]^{6+}$, 987.5 $[M+7H]^{7+}$, MALDI-TOF m/z found: 6905.6 $[M+H]^{+}$

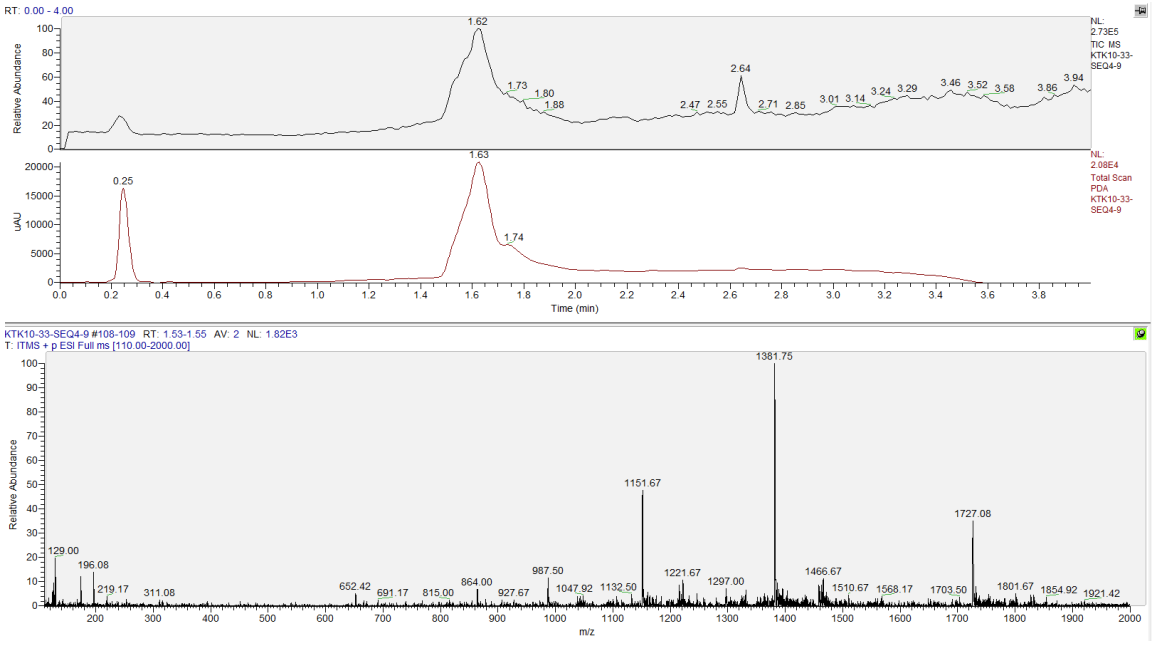

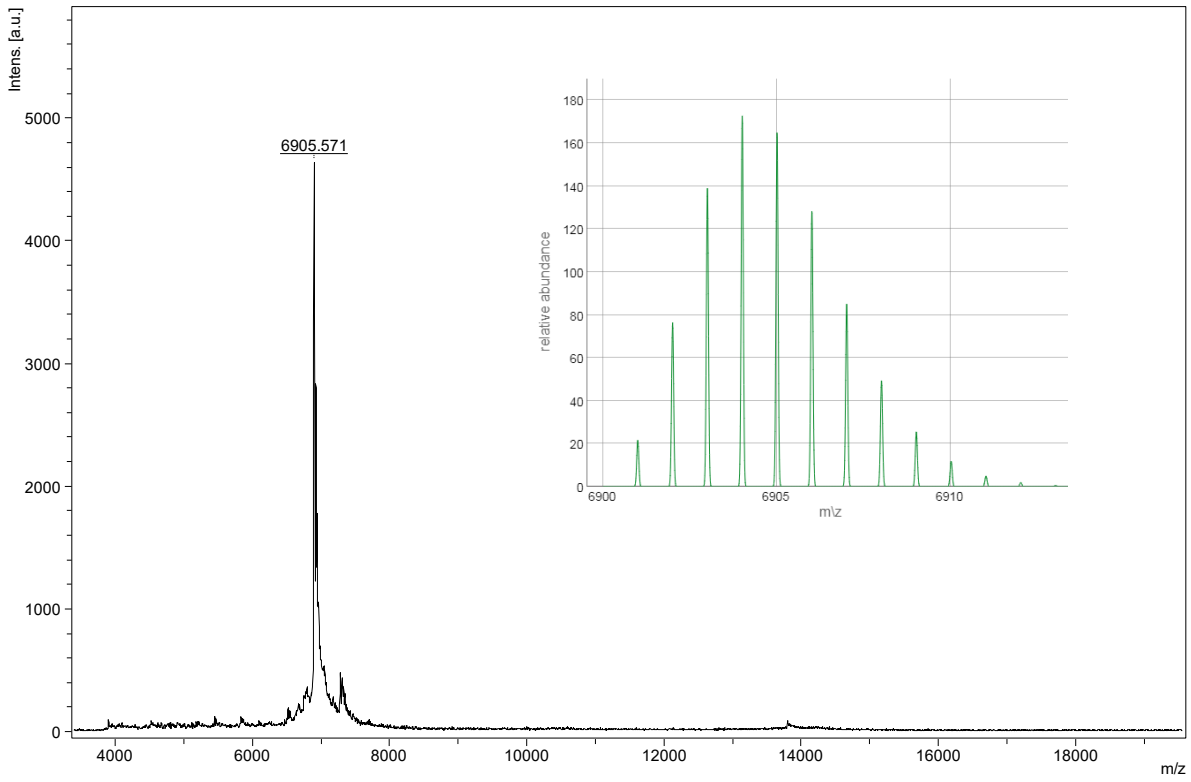

Ref2 (NH_2-peg-CGTACGTTGACACTGAGACT); Expected Mass for $C_{281}H_{399}N_{117}O_{93}$: 6900.0098; isotopic mass range (green insert). LC-MS (ESI) RT= 1.61 min. m/z: 1726.6 $[M+4H]^{4+}$, 1381.7 $[M+5H]^{5+}$, 1151.7 $[M+6H]^{6+}$, 987.3 $[M+7H]^{7+}$, MALDI-TOF m/z found: 6904.4 $[M+H]^{+}$

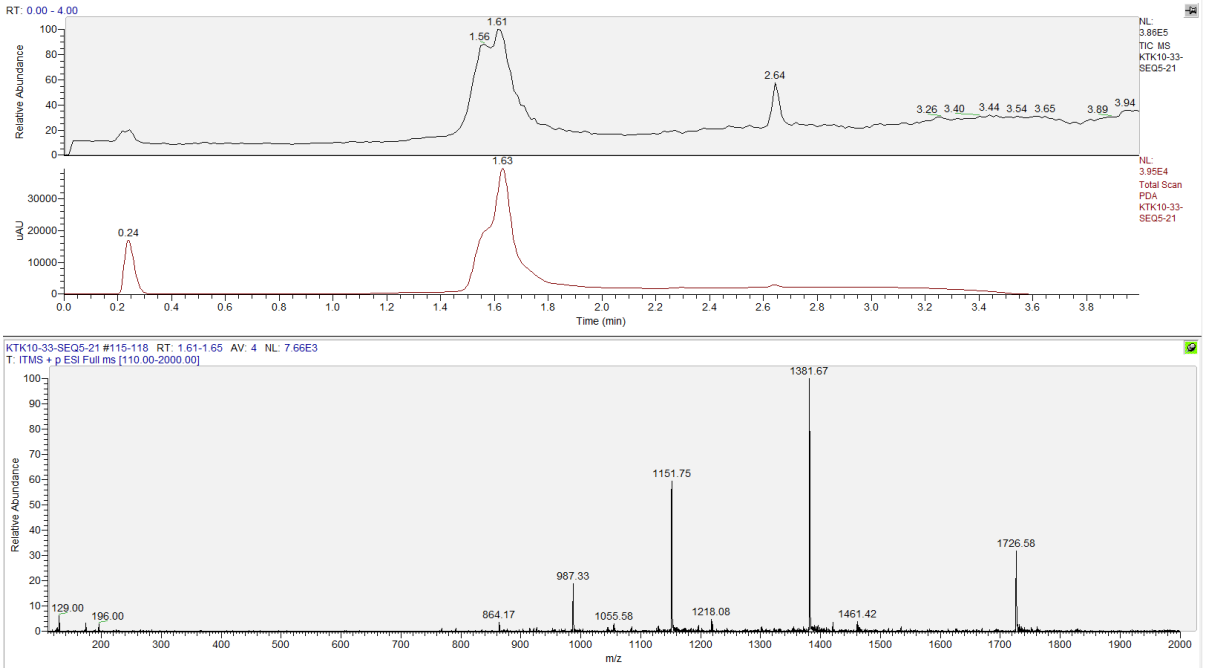

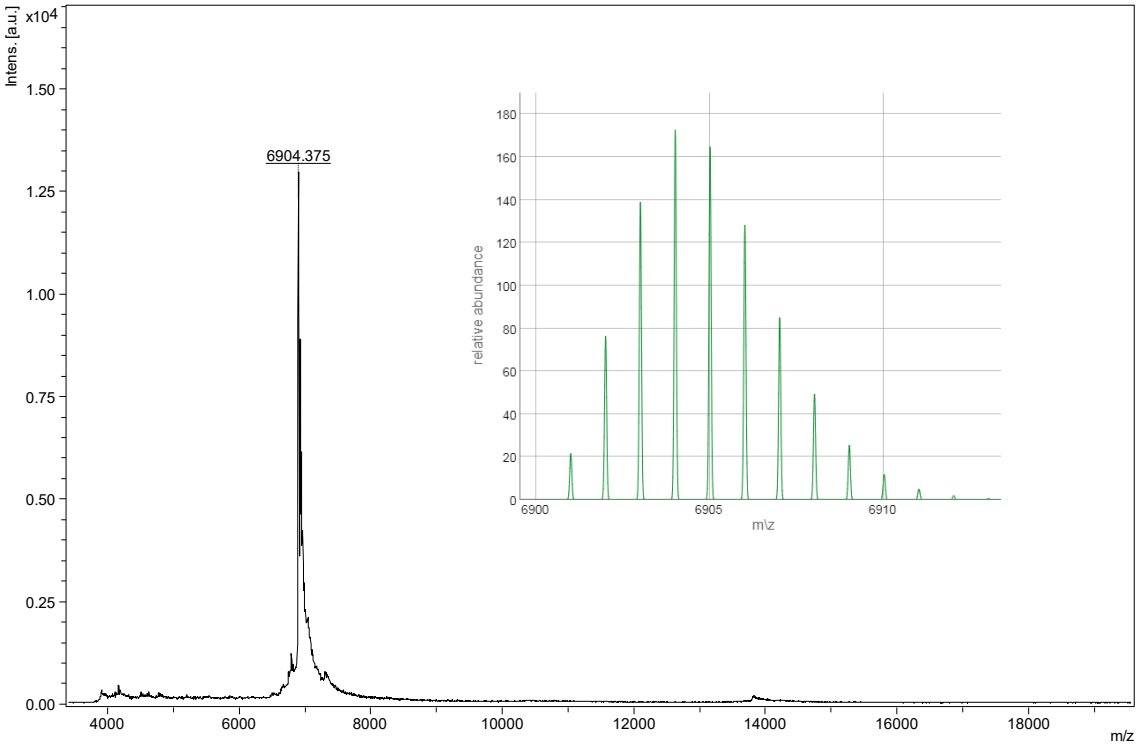

Ref3 (NH_2-peg-AGTCTCAGTG); Expected Mass for $C_{144}H_{207}N_{59}O_{49}$: 3546.5520; isotopic mass range (green insert). LC-MS (ESI) RT= 1.46 min. m/z: 1775.2 $[M+2H]^{2+}$, 1183.7 $[M+3H]^{3+}$, 888.2 $[M+4H]^{4+}$, 710.7 $[M+5H]^{5+}$, MALDI-TOF m/z found: 3548.1 $[M+H]^{+}$

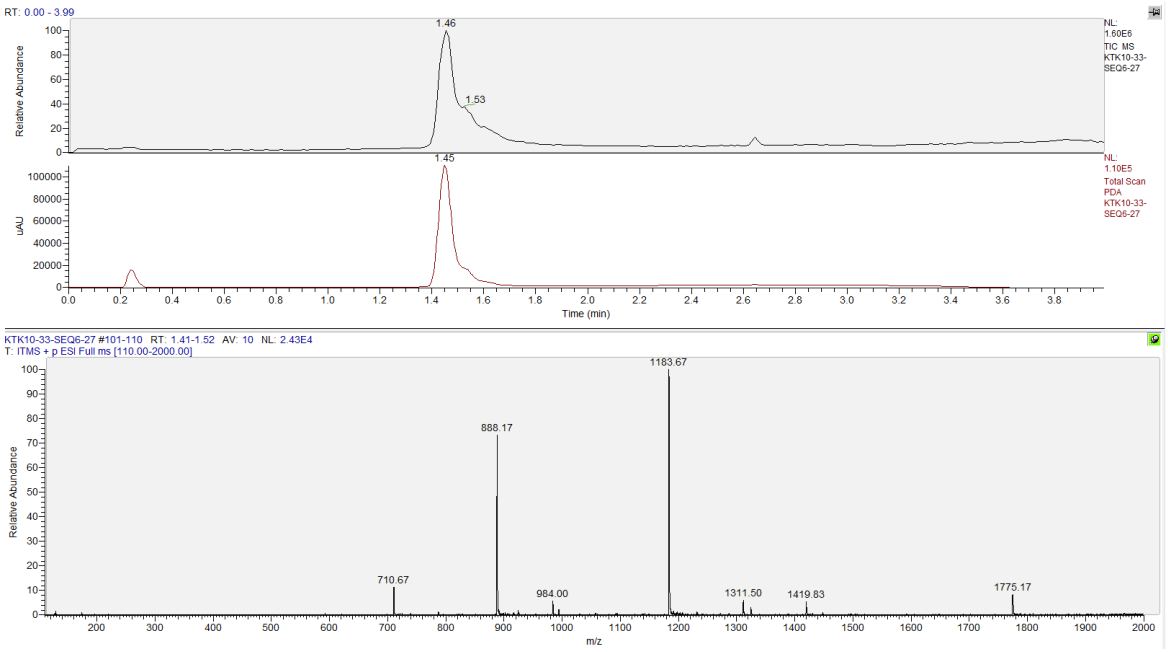

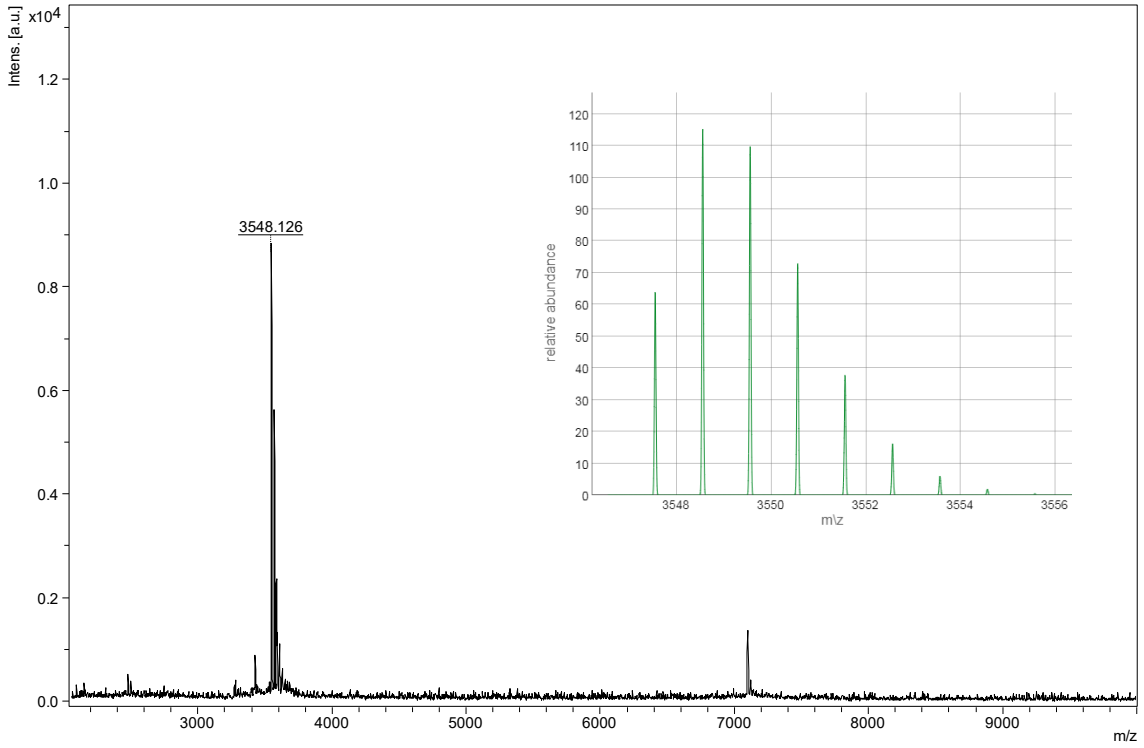

Ref4 (NH_2-peg-C<u>A</u>C<u>T</u>G<u>A</u>G<u>A</u>C<u>T</u>); Expected Mass for $C_{143}H_{206}N_{60}O_{47}$: 3515.5574; isotopic mass range (green insert). LC-MS (ESI) RT= 1.46 min. m/z: 1759.2 $[M+2H]^{2+}$, 1173.3 $[M+3H]^{3+}$, 880.3 $[M+4H]^{4+}$, 704.3 $[M+5H]^{5+}$, MALDI-TOF m/z found: 3518.2 $[M+H]^{+}$

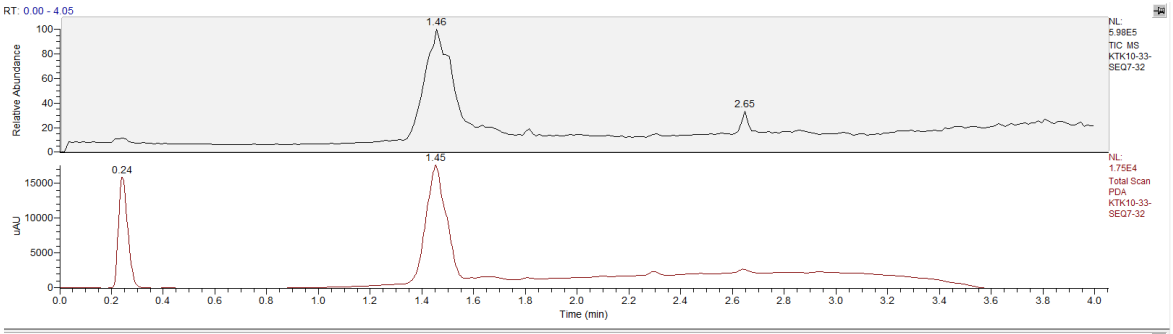

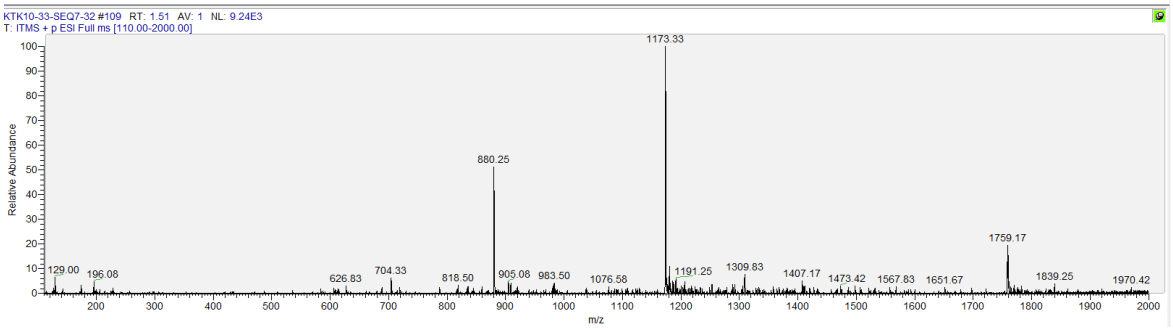

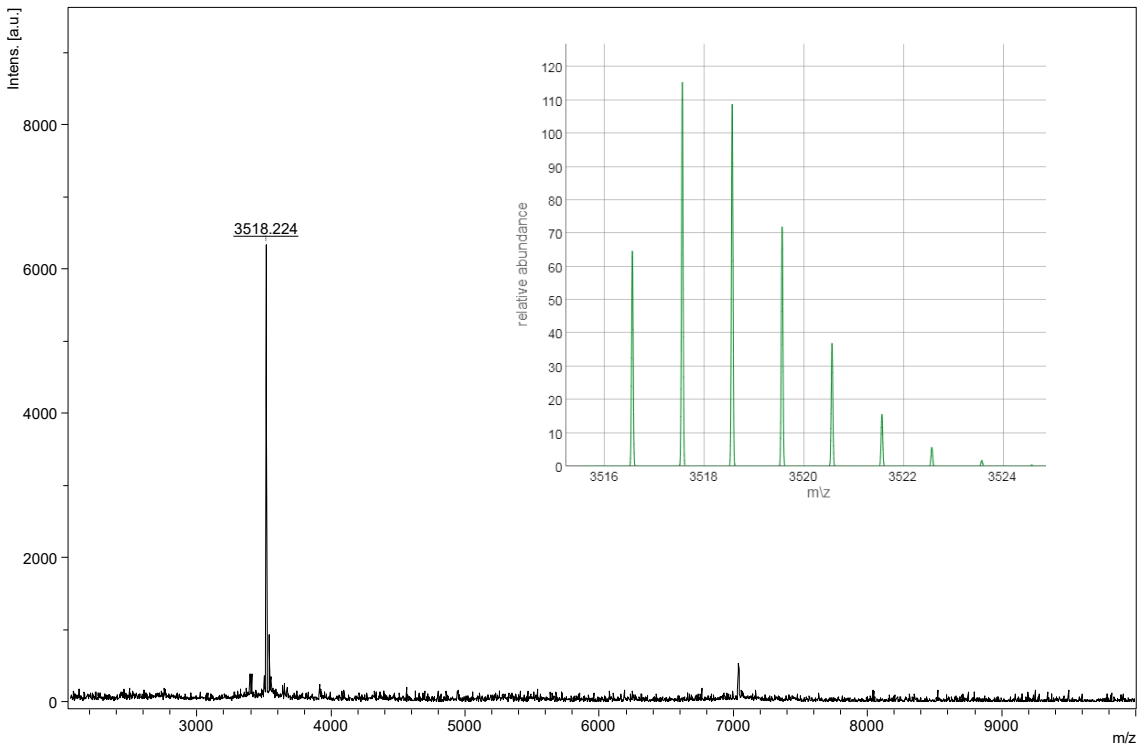

Ref5 (NH_2-peg-G<u>A</u>T<u>G</u>C<u>T</u>); Expected Mass for $C_{89}H_{130}N_{36}O_{31}$: 2198.9703; isotopic mass range (green insert). LC-MS (ESI) RT= 1.35 min. m/z: 1467.2 $[2M+3H]^{3+}$, 1100. $[M+2H]^{2+}$, 734.42 $[M+3H]^{3+}$, 551.0 $[M+4H]^{4+}$, MALDI-TOF m/z found: 2201.1 $[M+H]^{+}$

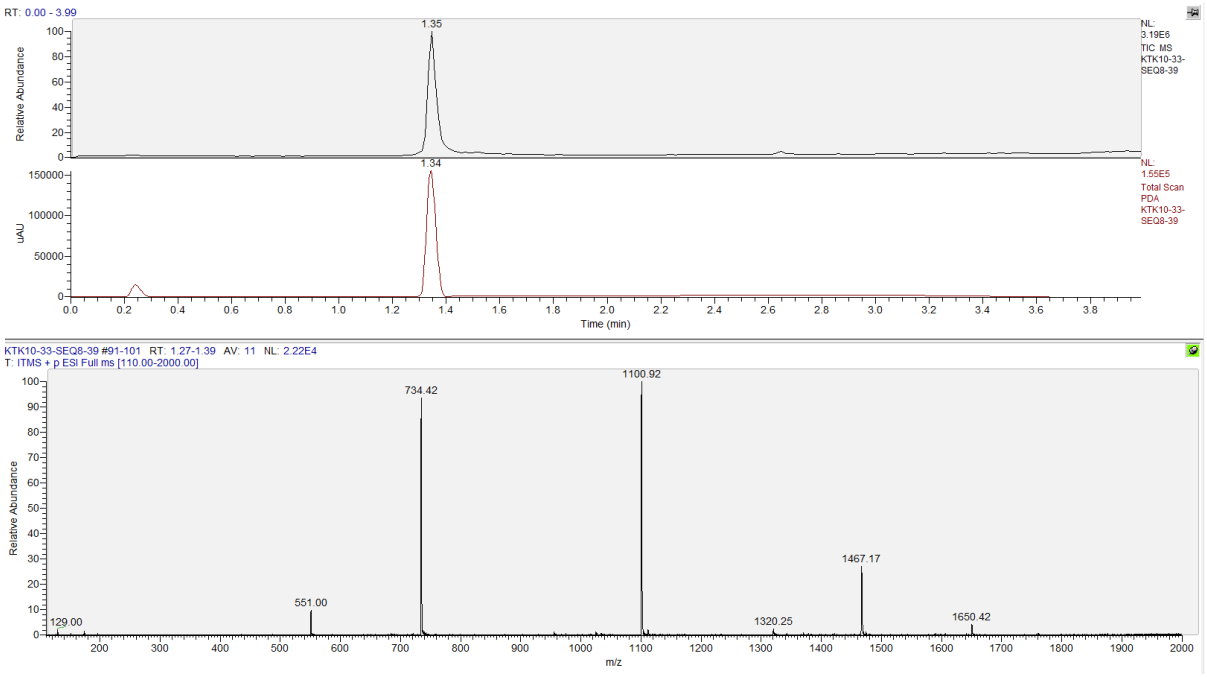

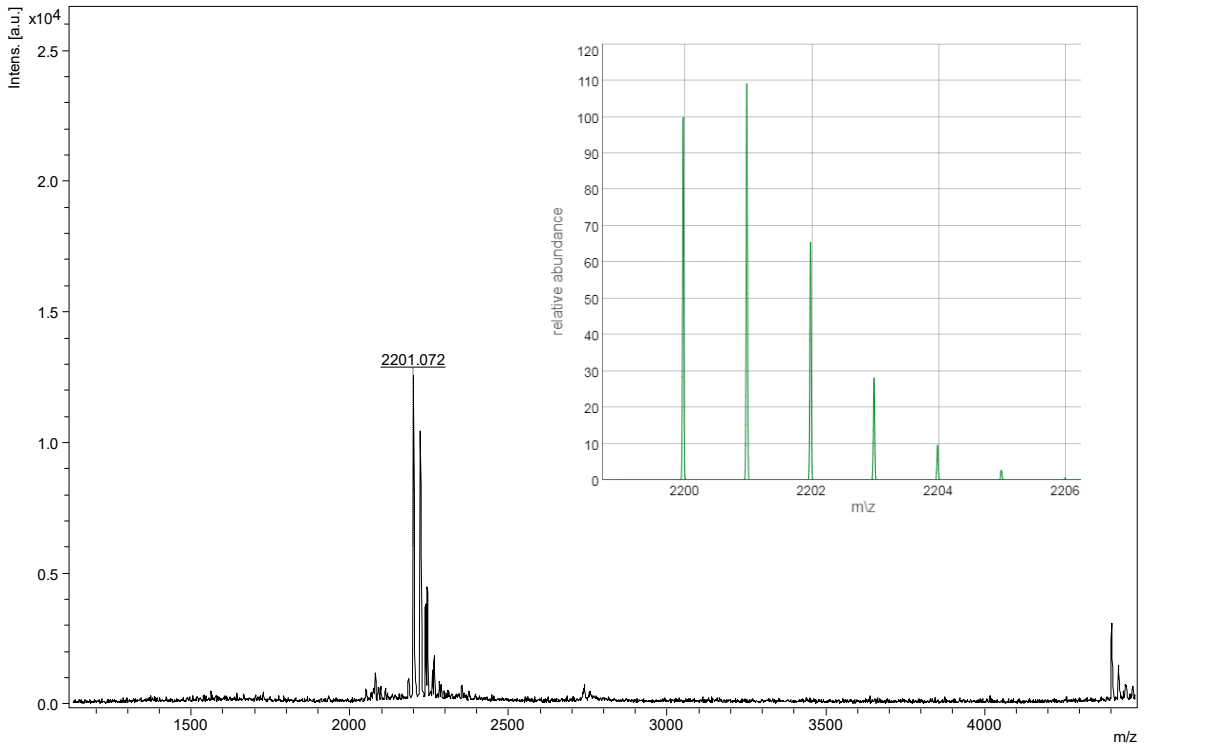

Ref6 (NH_2-peg-A<u>G</u>C<u>A</u>T<u>C</u>); Expected Mass for $C_{88}H_{129}N_{37}O_{29}$: 2167.9757; isotopic mass range (green insert). LC-MS (ESI) RT= 1.29 min. m/z: 1446.8 $[2M+3H]^{3+}$, 1085.5 $[M+2H]^{2+}$, 724.0 $[M+3H]^{3+}$, 543.3 $[M+4H]^{4+}$, MALDI-TOF m/z found: 2169.8 $[M+H]^{+}$

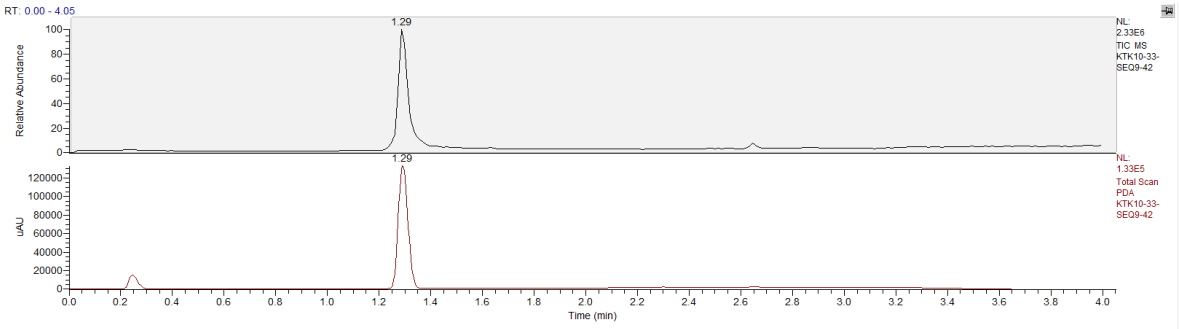

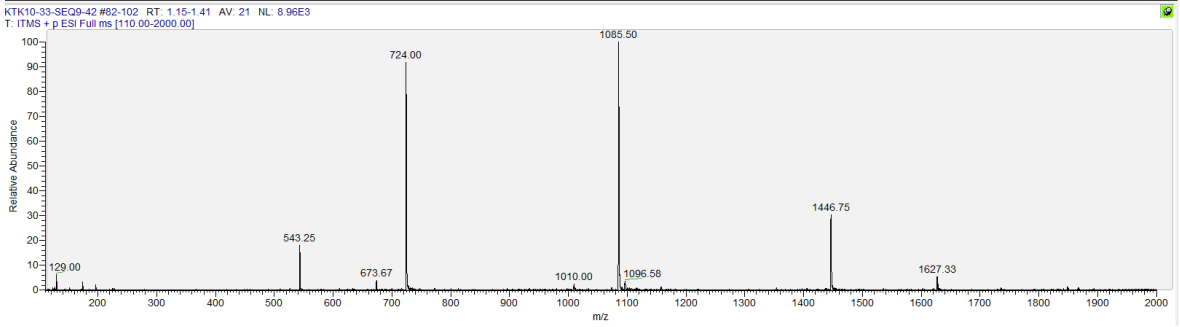

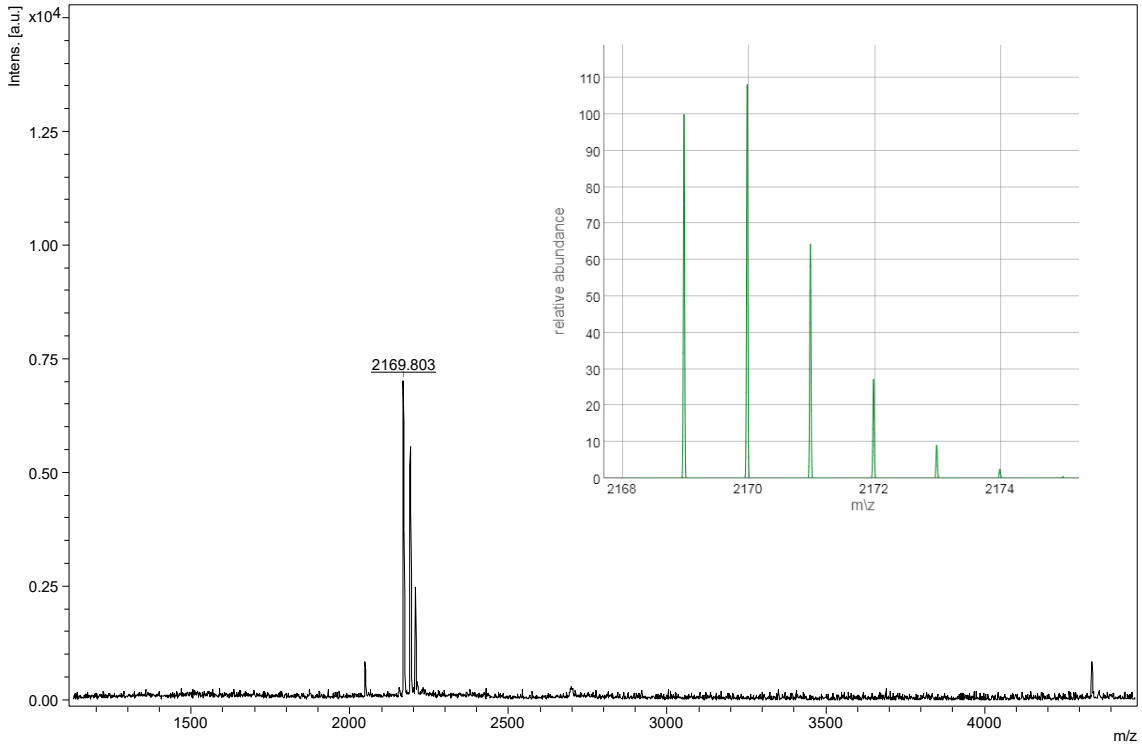

DpegH1 (Dabcyl-peg-GAATG-TGCCG-ACTAG-CGGCA); Expected Mass for $C_{296}H_{410}N_{126}O_{92}$: 7201.1277; isotopic mass range (green insert). LC-MS (ESI) RT= 2.09 min. m/z: 1442.2 $[M+5H]^{5+}$, 1201.8 $[M+6H]^{6+}$, 1030.5 $[M+7H]^{7+}$, 901.8 $[M+8H]^{8+}$, MALDI-TOF m/z found: 7204.7 $[M+H]^{+}$

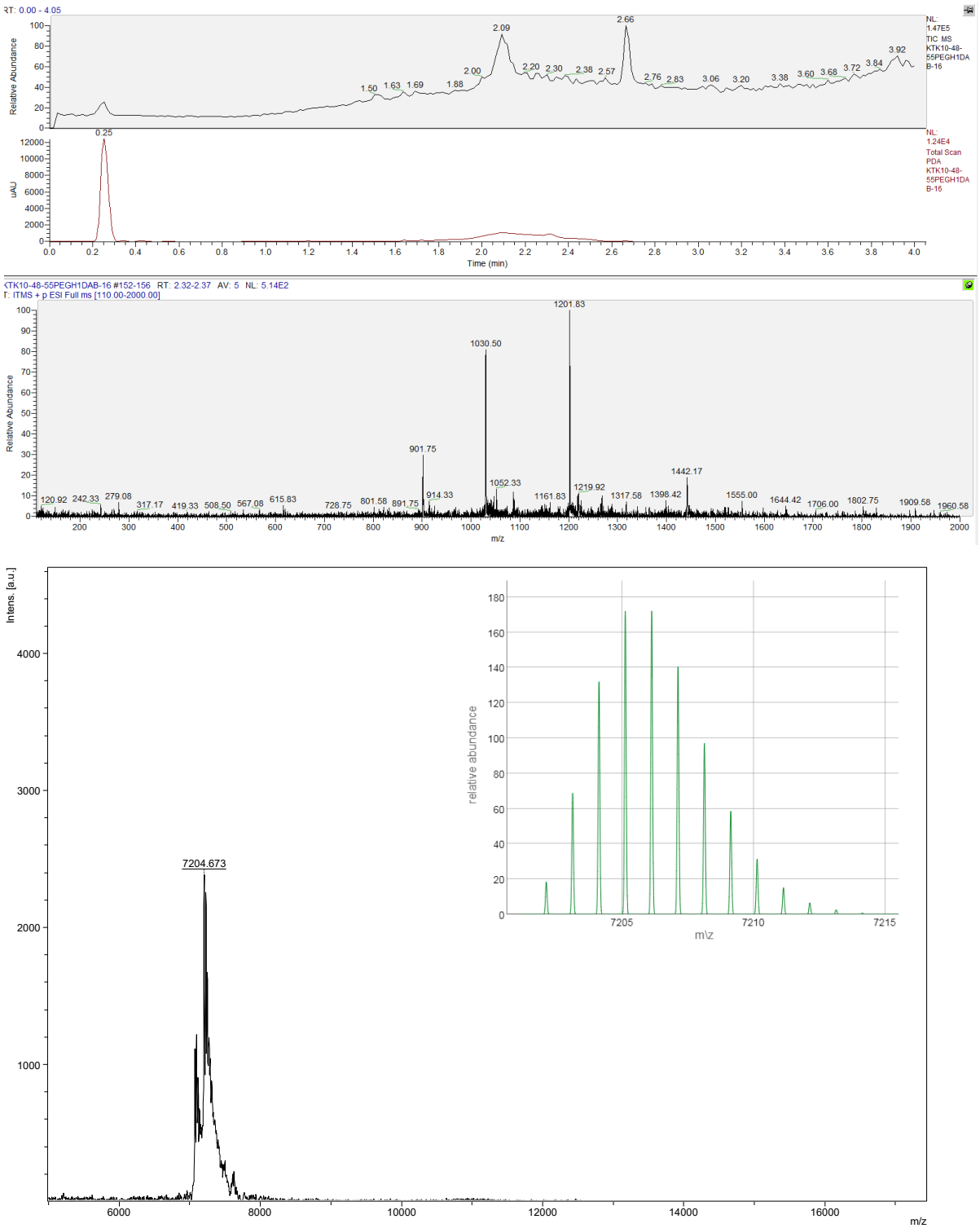

DpegH2 (Dabcyl-peg-CGGCA-CATTC-TGCCG-CTAGT); Expected Mass for $C_{294}H_{412}N_{116}O_{96}$: 7103.0923; isotopic mass range (green insert). LC-MS (ESI) RT= 1.96 min. m/z: 1422.3 $[M+5H]^{5+}$, 1185.5 $[M+6H]^{6+}$, 1016.3 $[M+7H]^{7+}$, 889.3 $[M+8H]^{8+}$, MALDI-TOF m/z found: 7106.8 $[M+H]^{+}$

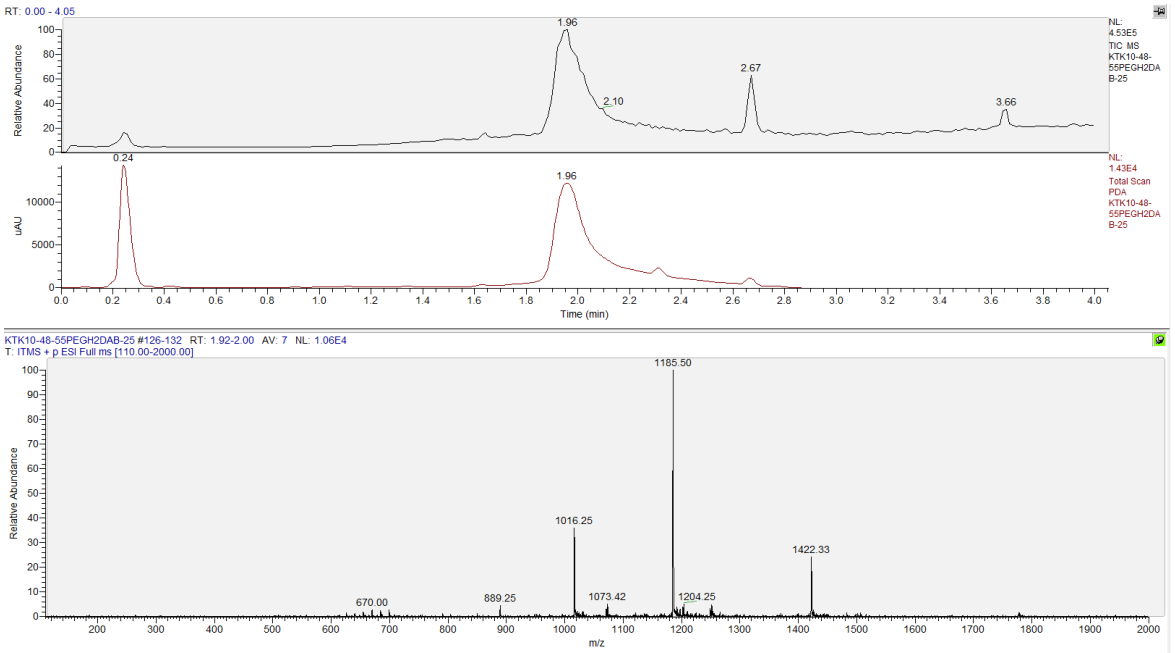

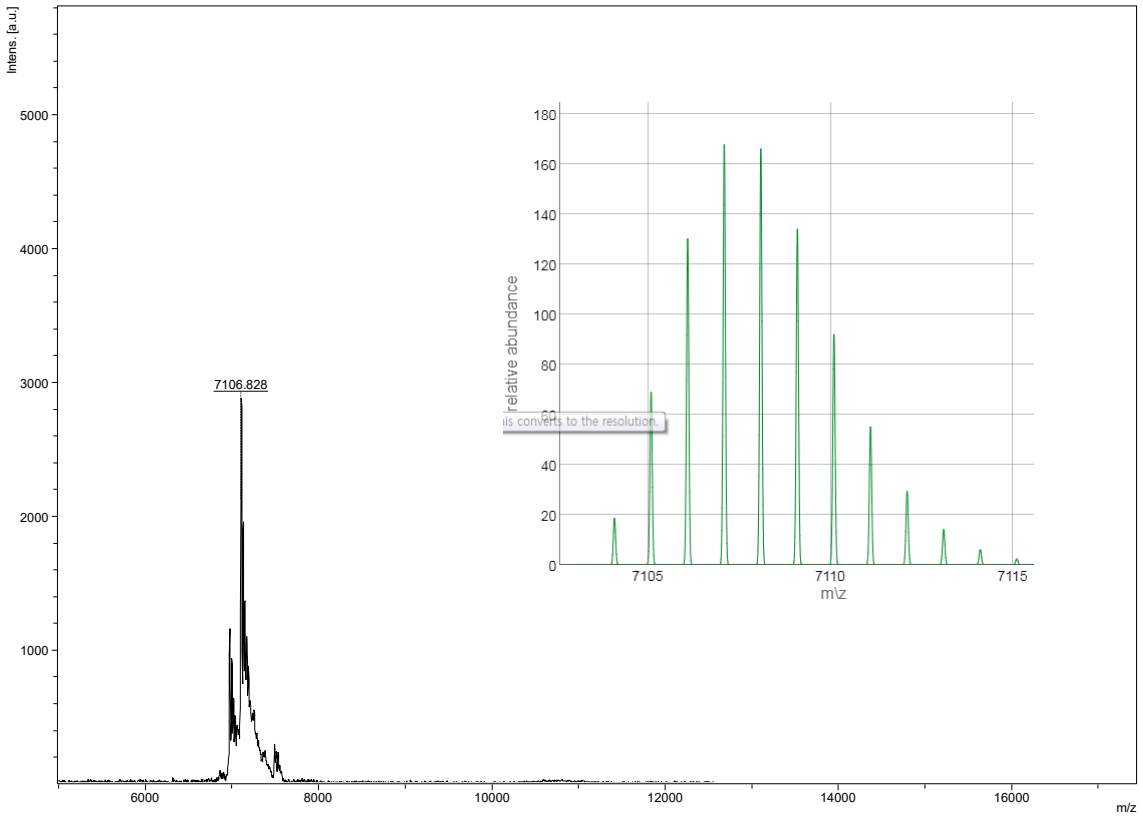

pegIF (Ac-ACTAG-CGGCA-Lys-peg(FITC)); Expected Mass for $C_{172}H_{230}N_{66}O_{53}S$: 4099.7052; isotopic mass range (green insert). LC-MS (ESI) RT= 1.77 min. m/z: 1368.0 $[M+3H]^{3+}$, 1026.5 $[M+4H]^{4+}$, 821.6 $[M+5H]^{5+}$, 684.6 $[M+6H]^{6+}$, MALDI-TOF m/z found: 4103.0 $[M+H]^{+}$

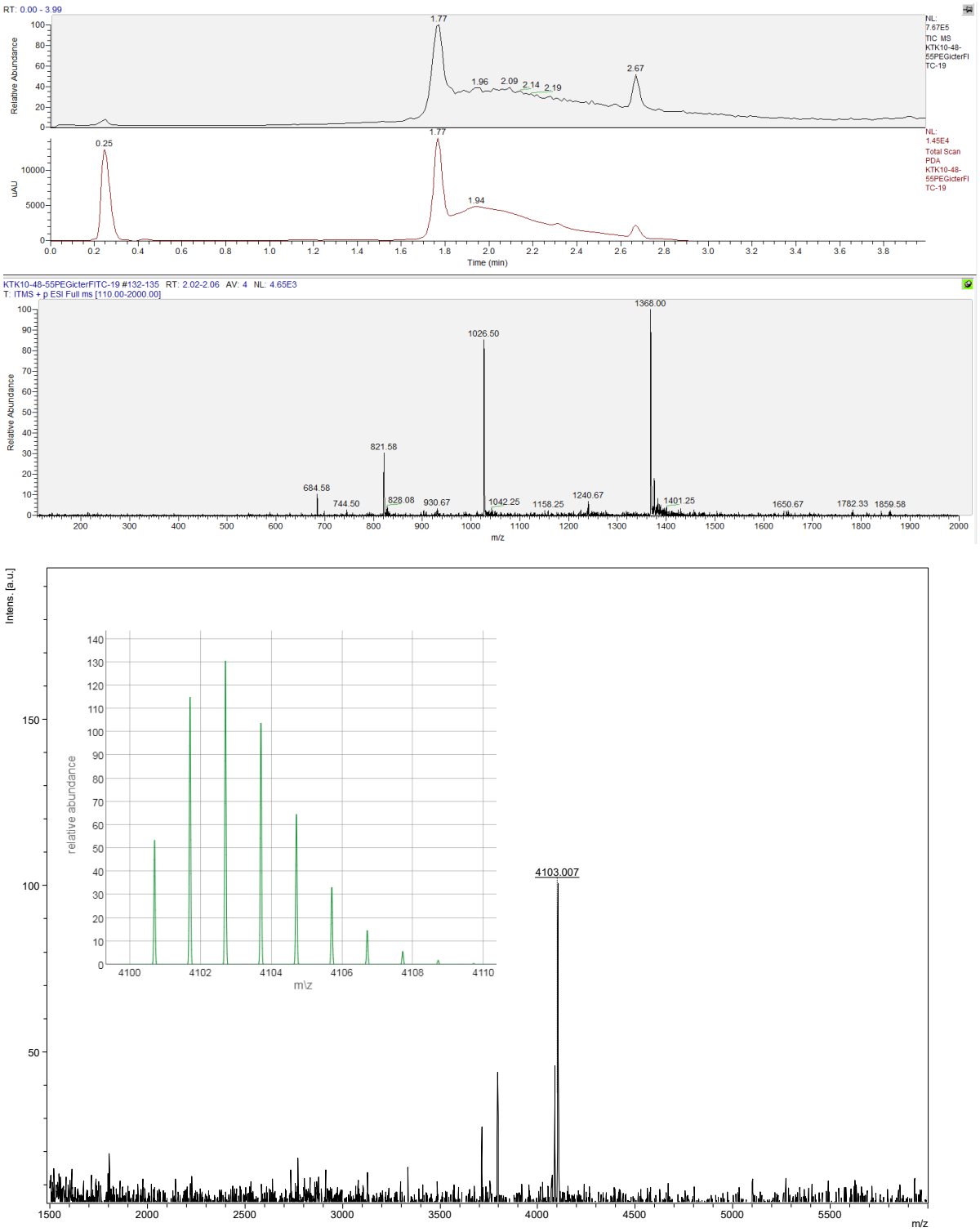

LpegI (ligand-Lys(Cy3)-peg-ACTAG-CGGCA); Expected Mass for $C_{226}H_{316}N_{87}O_{69}S_4^+$: 5480.2770; isotopic mass range (green insert). LC-MS (ESI) RT= 2.01 min. m/z: 1828.0 $[M+2H]^{3+}$, 1371.7 $[M+3H]^{4+}$, 1097.3 $[M+4H]^{5+}$, 914.8 $[M+5H]^{6+}$, MALDI-TOF m/z found: 5484.0 $[M]^+$

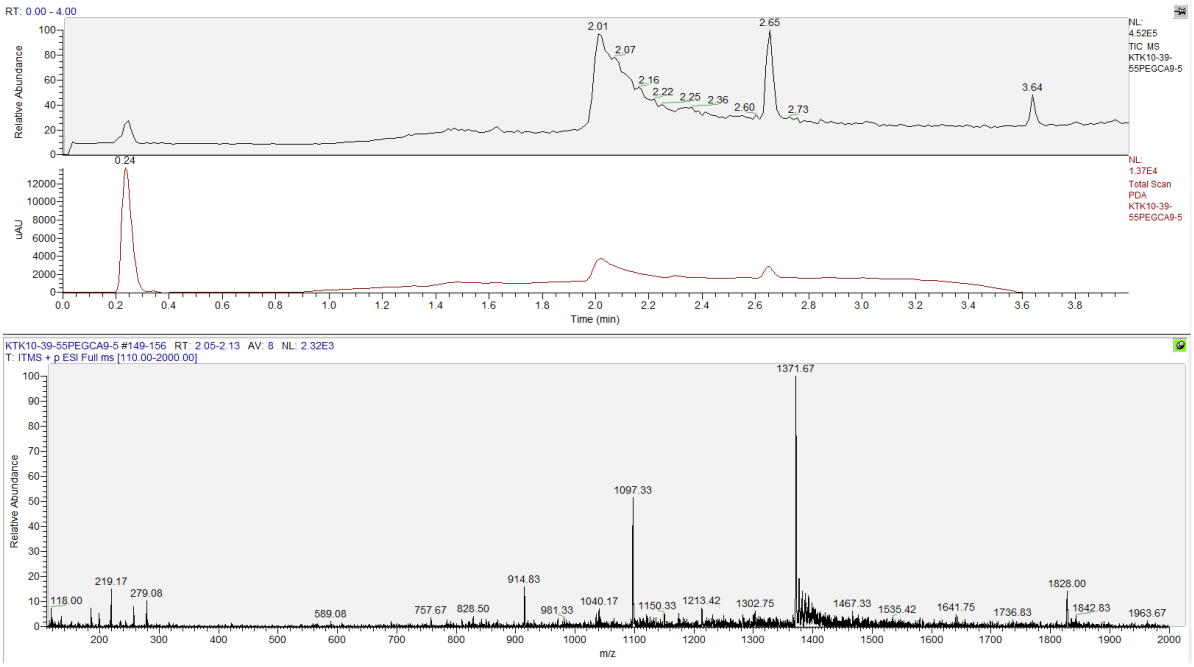

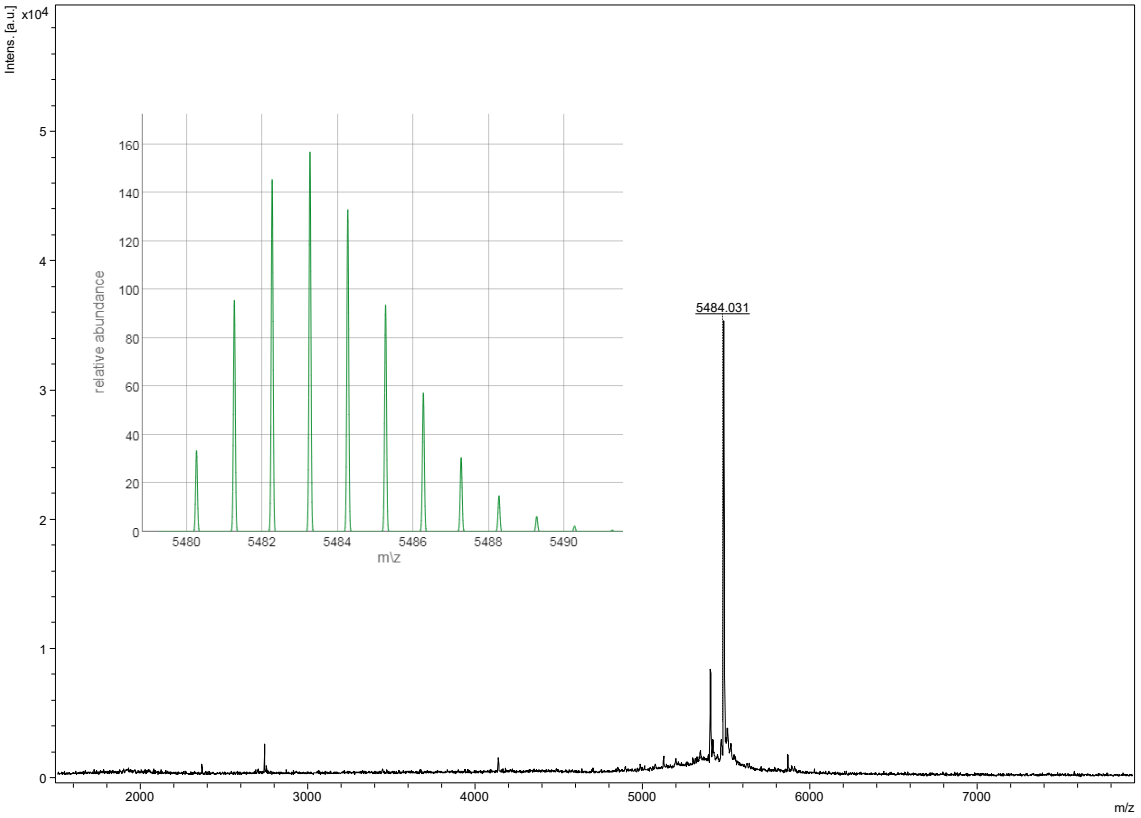

References

(1) Kim, K. T.; Angerani, S.; Chang, D.; Winssinger, N. *J. Am. Chem. Soc.* **2019**, *141*, 16288.

Supplementary Materials of Chapter IV

Materials and Methods

General Methods

All reagents and solvents were purchased from commercial sources and were used without further purification. Anhydrous solvents were obtained by passing them through commercially available alumina columns (Innovative Technology, Inc., ® VA). All the reactions were carried out under nitrogen. Reverse phase column chromatography was performed using Isolera Biotage using SNAP Cartridge KP-C18-HS of 60 g or 12 g. HPLC purification was performed with an Agilent Technologies 1260 infinity HPLC using a ZORBAX 300SB-C18 column (9.4 x 250 mm). NMR spectra were recorded on Bruker 300 UltraShield for 300 MHz, Bruker AVANCE 3 HD for 400 MHz and Bruker 500 UltraShield for 500 MHz using $CDCl_3$, DMSO-*d6*, acetone-*d6* and Methanol-*d*4 as reference solvent. LC-MS spectra were recorded using a DIONEX Ultimate 3000 UHPLC coupled with a Thermo LCQ Fleet Mass Spectrometer System (electrospray ionization (ESI)) operated in positive mode. MALDI-TOF mass spectra were measured using a Bruker Daltonics Autoflex spectrometer. Fluorescence and luminescence intensities were measured using a Molecular Devices Spectra Max M5. Automated solid phase synthesis was carried out on an Intavis AG Multipep RS instrument. Fluorescence imaging was carried out using a Leica SP8. Cell counting and imaging of cells was carried out using a Molecular Devices™ ImageXpress Micro (IXM) XL automated microscope. Furimazine,[1] 4-(bromomethyl)pyridine hydrobromide,[2] 3-azidopropyl trifluoromethanesulfonate,[3] bis(2,2′-bipyridine)-(5-amine-phenanthroline)ruthenium bis-(hexafluorophosphate),[4] benzyl guanine,[5,6] and 3,5-disulfobenzoic acid sodium salt[7] were prepared according to cited procedures. Methotrexate was synthesized from 2,4-diamino-6-(hydroxymethyl)pteridine as previously described.[8,9] SNAP-Pro_{30}-NLuc-cpDHFR plasmid was a kind gift from Kai Johnsson and was expressed and purified as previously described.[10]

Calculation of Förster distance between Nanoluc and $Ru(bpy)_2phen$

$$\boldsymbol{R_0 = 0.211\left(\kappa^2 n^{-4} Q_D J(\lambda)\right)^{\frac{1}{6}}}$$

Orientation factor (κ^2) and refractive index (*n)* was assumed to have a value of 2/3 and 1.36 respectively.[11] Quantum yield of NanoLuc (Q_D) has been reported as 0.28.[12] The spectral overlap integral between the luminescence spectrum of SNAP-Pro_{30}-NLuc-cpDHFR and the absorption spectrum of $[Ru(bpy)_2phen\text{-}NH_2]^{2+}$ ($J(\lambda)$) was calculated as 4.041 x 10^{12} M^{-1} cm^{-1} $(nm)^4$ using a|e software from Fluortools.[13]

R_0 = 16.4±0.9 Å

Calculation of energy transfer efficiency

$$\boldsymbol{E_{RET} = 1 - \left(\frac{I_{DA}}{I_D}\right)}$$

I_{DA} = donor emission in the presence of acceptor.
I_D = donor emission in the absence of acceptor.

Formula used as described.[11]

Calculated E_{RET} for NLuc - ruthenium = 0.64±0.08

Luminescence Spectra of SNAP-Pro30-NLuc-cpDHFR labeled with or without linker in presence or absence of methotrexate. Luminescence spectra of constructs were obtained by adding furimazine (10 μM) to a solution of labeled or unlabeled sensor protein constructs (1 nM) in HEPES (50 mM), NaCl (50 mM)(pH 7.2) buffer with or without methotrexate (100 μM). Spectra were measured with a step size of 2 nm and an integration time of 50 ms.

Procedure for automated PNA synthesis,[14] **Mtt deprotection, Fmoc deprotection, purification**. According to the methods described in chapter I.

Procedure for the templated unmasking of rhodamine by LUPIN. The templated reactions were carried out in a 96 well black plates in 50 mM HEPES, 50 mM NaCl (pH 7.2) at 25 °C. The stock solutions of PNA probes (in deionized water or DMSO), LUPIN construct, and sodium ascorbate were diluted in the reaction buffer and then added to wells (100 μL/well). The reactions were initiated by the addition of 2 μL of an ethanolic solution of furimazine (5 mM)(final concentration 100 μM). Each experiment was performed in triplicates. The concentration of released rhodamine by LUPIN was calculated from the fluorescence (ex: 490 nm; em: 530 nm; cutoff: 515 nm) using a standard curve prepared with free rhodamine, ascorbate (10 mM), and furimazine (100 μM).

Procedure for the templated unmasking of PNA-drug conjugates. The template reactions to release drugs were performed as follows: solutions of PNA-Ru (10 μM) and PNA-PyDrug (Drug: Duocarmycin-OMe or Ibrutinib) (100 μM) in PBS (10 mM, pH 7.4) with sodium ascorbate (10 mM) were mixed in an Eppendorf. Samples were injected into LC-MS at 0, 1 or 2 min irradiation time points. Samples were irradiated with a collimated LED light (455 nm, 1W: Thorlabs, part number M455L2-C1 – www.thorlabs.com). Areas under the curve for the chromatograms were calculated using Thermo Xcalibur Qual Browser. This integration was used to estimate a yield understanding that this method underestimates the actual yield since the product has a lower absorption coefficient than the starting material.

Synthesis of BG-(Ru)(PNA)-MTX. **BG-(Ru)(PNA)-MTX** was synthesized as shown in Supplementary Figure 1 by general methods described above. Specific reactions not included in the general methods are described below.
i) Ruthenium coupling: the Mtt was removed with a solution of HOBt in a 1:1 mixture of HFIP and DCE (200 μL) and the resin was washed with DMF and CH_2Cl_2. In a separate Eppendorf, bis(2,2′-bipyridine)-(5-amine-phenanthroline)ruthenium bis-(hexafluorophosphate) (8.3 mg, 11 μmol, 5.0 equiv) and triphosgene (3.26 mg, 11 μmol, 5.0 equiv) were added in 100 μL DCE, then DIPEA (19.2 μL, 0.11 mmol, 50 equiv) was added and kept for a few minutes until the solution became clear, the solution was added to the resin and swirled for 10 h. The resin was washed with DMF and DCM.
ii) Coupling of benzyl guanine to linker: to the purified linker in DMF was added BG-GLA-NHS (1.5 eq.) and DIPEA (5 eq.) and the reaction was left for 12 hours after which **1** was isolated

via RP-HPLC. **BG-(Ru)(PNA)-MTX** was dissolved in DMSO and stored in aliquots (0.4 mM) at -80 °C.

Preparation of ruthenium derivative

PNAs (5 mg 0.44 mmol/g, 2.2 μmol) with Lysine in the N-terminus were treated with 20% piperidine in DMF (200 μL, 30 min). The Mtt was removed with a solution of HOBt in a 1:1 mixture of HFIP and DCE (200 μL) and the resin was washed with DMF and CH_2Cl_2. In a separate Eppendorf, bis(2,2′-bipyridine)-(5-amine-phenanthroline)ruthenium bis-(hexafluorophosphate) (8.3 mg, 11 μmol, 5.0 equiv) and triphosgene (3.26 mg, 11 μmol, 5.0 equiv) were added in 100 μL DCE, then DIPEA (19.2 μL, 0.11 mmol, 50 equiv) was added and kept for a few minutes until the solution became clear, the solution was added to the resin and swirled for 10 h. The resin was washed with DMF and CH_2Cl_2. The resin was suspended in TFA (200 μL) for 2 h. The solution was filtered and the product precipitated with diethyl ether (2 mL, 10 times of the volume of TFA). The precipitate was pelleted by centrifugation and the supernatant was removed. The pellet was washed with diethyl ether then dissolved in 400 μL H_2O for HPLC purification as described in the general technique for PNA purification.

Preparation of PNA-Pyridinium derivatives. PNAs (5 mg 0.44 mmol/g, 2.2 μmol) with N-terminal Lysine were treated with a solution of 20% piperidine in DMF (200 μL, 30 min), then capped with a solution of Ac_2O (5.3 equiv) and 2,6-lutidine (6.4 equiv) in DMF (150 μL). Mtt group was removed with a solution of HOBt in a 1:1 mixture of HFIP and DCE (200 μL) for 3 x 3 min. The resin was then treated with a pre-activated (5 min) solution of 4-pentynoic acid (5 equiv), HATU (4 equiv), DIPEA (5 equiv) and 2,6-lutidine (7.5 equiv) for 60 min in NMP. After the reaction, the resin was washed with DMF and CH_2Cl_2. A solution of small molecule (**S19**, **S20**, **S21**, **S22**) (1.5 equiv in 200 μL NMP) was added to the resin followed by a solution of sodium ascorbate in H_2O (16.6 μL, 198 mg/mL, 16.5 μmol, 7.5 equiv), a solution of $CuSO_4$ in H_2O (4.2 μL, 21.4 mg/mL 0.55 μmol, 0.25 equiv) and TBTA (0.6 mg, 0.5 equiv). After 16 hours, the resin was washed with H_2O (6 x 250 μL), DMF (6 x 250 μL), and CH_2Cl_2 (6 x 250 μL). The resin was suspended in TFA (200 μL) for 2 h; the solution was filtered and the product precipitated with diethyl ether (2 mL, 10 times of the volume of TFA). The precipitate was pelleted by centrifugation and the supernatant was removed. The pellet was washed with diethyl ether, then dissolved in 400 μL H_2O for HPLC purification as described in the general technique for PNA purification.

Preparation of sulfonated PNA-Pyridinium derivatives. PNAs (5 mg 0.44 mmol/g, 2.2 μmol) with N-terminal Lysine were treated with a solution of HOBt in a 1:1 mixture of HFIP and DCE (200 μL) for 3 min (x 3) and then the resin was washed and treated with a pre-activated (5 min) solution of 4-pentynoic acid (5 equiv), HATU (4 equiv), DIPEA (5 equiv) and 2,6-lutidine (7.5 equiv) for 20 min in NMP twice. After the reaction, the resin was washed with DMF and CH_2Cl_2. The Fmoc group was removed with a solution of 20% piperidine in DMF (200 μL, 30 min). 3,5-disulfobenzoic acid (11 μmol, 5 equiv), HATU (4 equiv), DIPEA (5 equiv) and 2,6-lutidine (7.5 equiv) in 150 μL of DMF was added to the resin and swirled for 1 hour. After washings with H_2O, DMF and CH_2Cl_2, a solution of small molecule (**S29, S30**) (1.5 equiv in 200 μL of NMP) was added to the resin followed by a solution of sodium ascorbate in H_2O (16.6 μL, 198 mg/mL, 16.5 μmol, 7.5 equiv), a solution of $CuSO_4$ in H_2O (4.2 μL, 21.4 mg/mL

0.55 μmol, 0.25 equiv) and TBTA (0.6 mg, 0.5 equiv). After 16 hours, the resin was washed with H_2O (6 x 250 μL), DMF (6 x 250 μL), and CH_2Cl_2 (6 x 250 μL). The resin was suspended in TFA (200 μL) for 2 h; the solution was filtered and the product precipitated with diethyl ether (2 mL, 10 times of the volume of TFA). The precipitate was pelleted by centrifugation and the supernatant was removed. The pellet was washed with diethyl ether, then dissolved in 400 μL H_2O for HPLC purification as described in the general technique for PNA purification.

Labeling of SNAP-Pro30-NLuc-cpDHFR with BG-(Ru)(PNA)-MTX. An aliquot of **BG-(Ru)(PNA)-MTX** (4 μM) was added to an Eppendorf tube containing a solution of SNAP-Pro30-NLuc-cpDHFR (1 μM) in HEPES (50 mM) NaCl (50 mM) (pH 7.2). The solution was left shaking at room temperature for 1 h. The labeling was monitored and confirmed via MALDI-TOF. Labeled proteins were purified using an Ultra-centrifugal filter device with a 30 kDa MWCO (0.5 mL), performing three exchanges of 450 μL HEPES (50 mM) NaCl (50 mM) (pH 7.2) to remove excess amounts of **BG-(Ru)(PNA)-MTX**. Subsequent experiments, however, showed that non-covalently linked **BG-(Ru)(PNA)-MTX** had no effect. SNAP-Pro30-NLuc-cpDHFR labeled with **BG-(Ru)(PNA)-MTX** and purified via spin filtration showed no difference in performance in comparison with the product of a crude reaction mixture. The experiments depicted in Figure 2 were performed with material obtained via spin filtration while those illustrated in Figures 4 and 5 were conducted with crude reaction mixture.

Representative conditions for LUPIN release. Furimazine (100 μM) was added to a solution containing SNAP-Pro30-NLuc-cpDHFR labeled with **BG-(Ru)(PNA)-MTX** (10 nM), PNA-PyRho (**17**)(5 μM), and NaAsc (10 mM) in HEPES (50 mM) NaCl (50 mM) (pH 7.2). The rhodamine fluorescence generated was quantified by comparison with free rhodamine standard curves to estimate the concentration of rhodamine released.

Luminescence Spectra of SNAP-Pro30-NLuc-cpDHFR labeled with or without linker in presence or absence of methotrexate. Luminescence spectra of constructs were obtained by adding furimazine (10 μM) to a solution of labeled or unlabeled sensor protein constructs (1 nM) in HEPES (50 mM), NaCl (50 mM)(pH 7.2) buffer with or without methotrexate (100 μM). Spectra were measured with a step size of 2 nm and an integration time of 50 ms.

Cell culture

MCF-7 and SKBR3 cell lines were obtained from the American Type Culture Collection (ATCC) and expanded following their instructions. MCF-7 cells were maintained in Dulbecco's modified Eagle medium (DMEM, Gibco) supplemented with 10% FCS and 1% pen-strep antibiotic at 37 °C under 5% CO_2 in a humidified incubator. SKBR3 cells were grown in Real McCoy's medium containing 10% FCS and 1X Pen-Strep. All cell lines were regularly tested for mycoplasma contamination by staining with Hoechst 33342.

Ibrutinib competition in SKBR3 cells. $5x10^3$ SKBR3 cells were seeded in glass bottom dishes and grown for 24 hours in a humidified incubator at 37 °C, 5% CO_2. Cells were then washed twice with DPBS containing magnesium and calcium. To the control cells, PNA-Py-Ibrutinib (**18**, 10 μM) in HBSS (0.1% BSA; with magnesium and calcium), incubated for 2 hours

at room temperature, was added to the cells and incubated for 30 minutes at 37 °C and 5% CO_2. The same was repeated for the LUPIN release, where PNA-Py-Ibrutinib (**18**, 10 μM), SNAP-(Ru-PNA-Mtx)NLuc-cpDHFR, 10 nM), sodium ascorbate (10 mM), and furimazine (100 μM) in HBSS (0.1% BSA; with magnesium and calcium), incubated for 2 hours at room temperature, was added to the cells and incubated for 30 minutes at 37 °C and 5% CO_2. After 30 minutes, Ibrutinib-Cy3 (**20**, 50 nM) was added and the cells were further incubated for 30 minutes at 37 °C and 5% CO_2 after which the cells were washed twice with DPBS (with magnesium and calcium) and once with DMEM(-)(no phenol red). The cells were then imaged using a Leica SP8 fluorescent microscope with filter settings for Cy3 in the Leica software. Images were analyzed by image J.

Duocarmycin-OMe and PNA-Py^{2}Duo Toxicity in MCF-7 cells. MCF-7 cells were seeded into 96-well plates (10^4 cells/well) and allowed to adhere overnight. Media was replaced with Duo-OMe (**24**) and PNA-Py^{2}Duo (**23**) at different concentrations in Leibovitz's medium (Gibco) and cells were incubated at 37 °C under 0% CO_2 in humidified incubator for 3 h. The cells were then washed three times with DMEM; fresh media (DMEM, no phenol-red) was replaced and the cells were incubated for additional 72 h at 37°C, 5% CO_2. 10 µL of Hoechst 33342 from a 5 µg/mL stock in PBS was added to each well and incubated for 15 min at 37 °C. Fluorescence images were acquired using a HTS IXM microscope and subsequent image analysis and nuclei count was achieved by using MetaXpress® software. Drug effect was expressed as normalized nuclei count. 50% nuclei count was obtained from sigmoidal curve fits of normalized nuclei count vs. concentration data using GraphPad Prism 7. All experiments were conducted in triplicates, with error bars representing the standard error of the mean.

Lupin release of Duocarmycin-OMe in MCF-7 cells. MCF-7 cells (10^4 cells/well) were seeded in 96 well plates and left for 24 hours. Cell media was aspirated and replaced with Leibovitz's medium, containing various concentrations of PNA-Py^{2}Duo (**23**) (0-250 μM) and furimazine (0-100 μM). Sodium Ascorbate was used at a concentration of 1 mM and SNAP-(Ru-PNA-Mtx)NLuc-cpDHFR was used at a concentration of 10 nM. The plates were then incubated at 37°C for 3 hours with no CO_2 after which the cells were gently washed repeatedly with DMEM, containing 10% FCS, 1X pen-strep and no phenol red and placed in the incubator (37°C, 5% CO_2). After 72 hours Hoechst 33342 stain was added at a concentration of 5 μg / μL followed by incubation for 30 min at 37 °C and 5% CO_2. Bright field and fluorescence images were then acquired with the IXM system with DAPI settings at 37 °C and 5% CO_2. Excitation = 100 ms. Objective 20x. Fluorescence images were analyzed using MetaXpress® software by using a nuclei count protocol were the particle mask size was width = 10 μm; height = 25 μm; fluorescence cutoff threshold = 1000. Each well was analyzed by the acquisition of matrix of images covering the well.

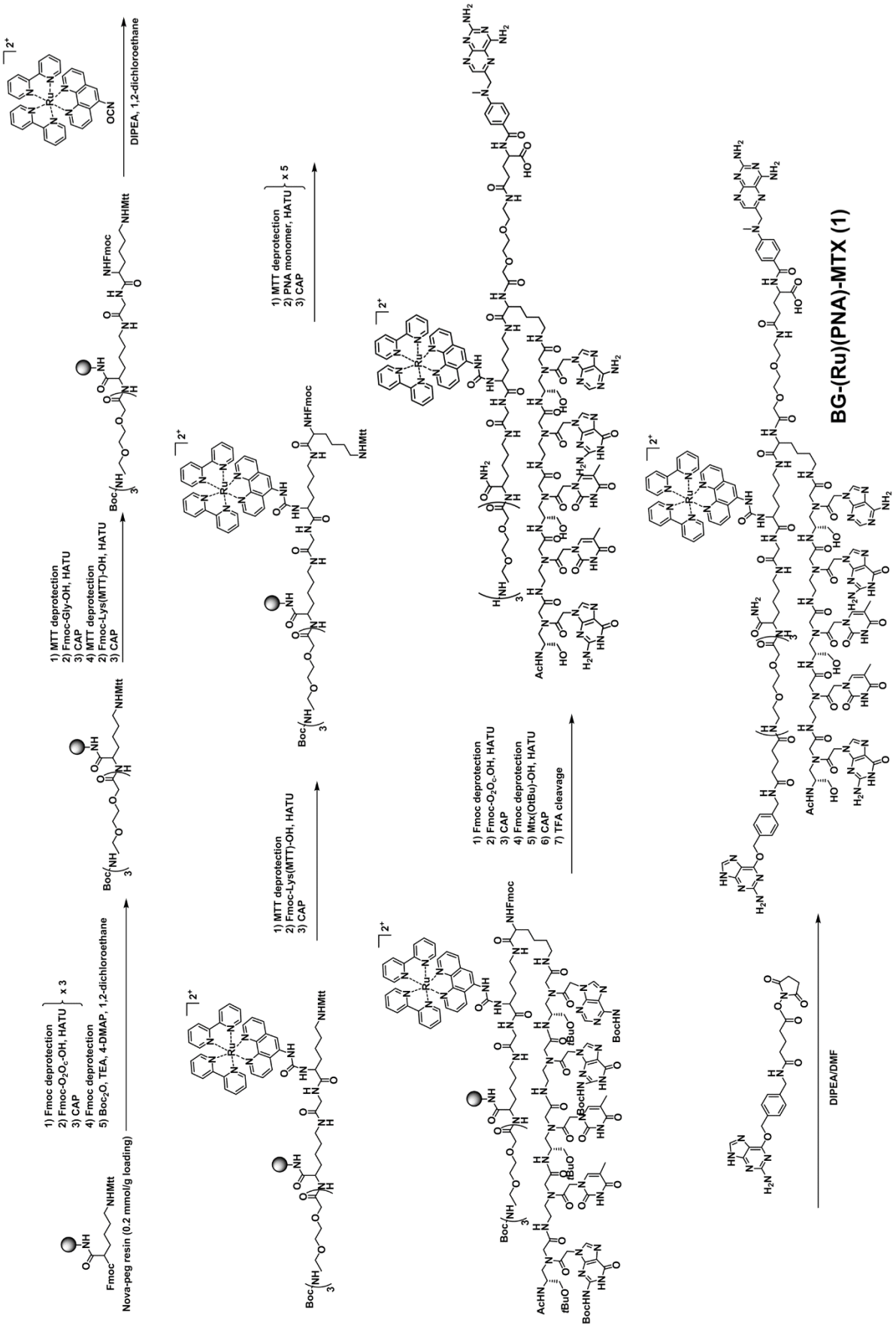

Figure IV-S1. Synthetic overview of **BG-(Ru)(PNA)-MTX** (**16**).

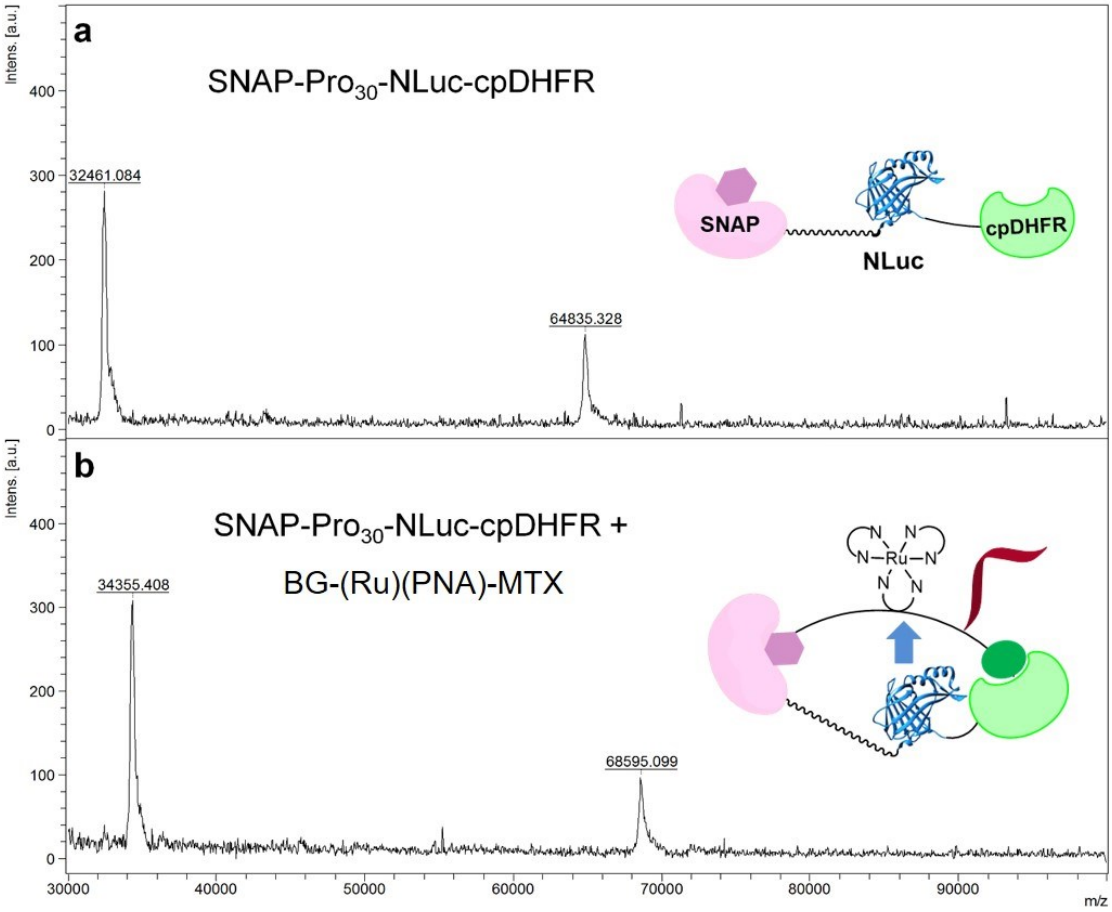

Figure IV-S2. MALDI-TOF spectra of SNAP-Pro$_{30}$-NLuc-cpDHFR before (**a**) and after (**b**) labelling with **BG-(Ru)(PNA)-MTX**.

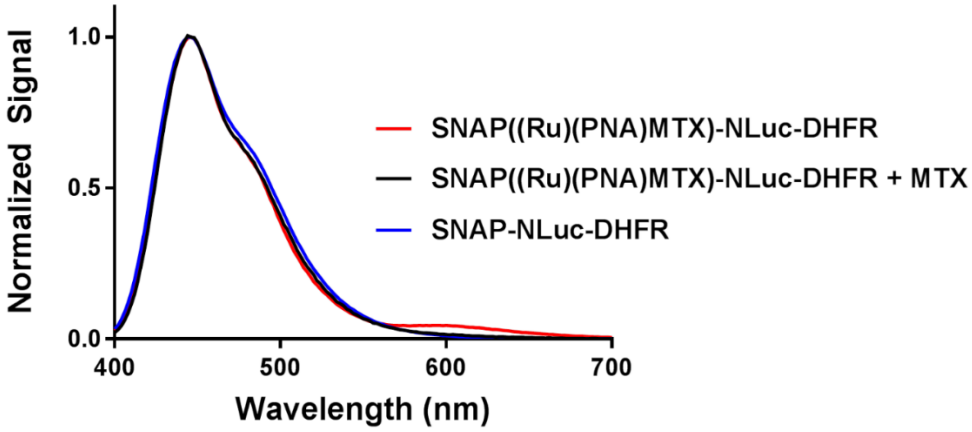

Figure IV-S3. Normalized luminescence spectra of SNAP-Pro$_{30}$-NLuc-cpDHFR labeled with BG-(Ru)(PNA)-MTX (red); unlabeled (blue) or labeled with 100 μM methotrexate (black).

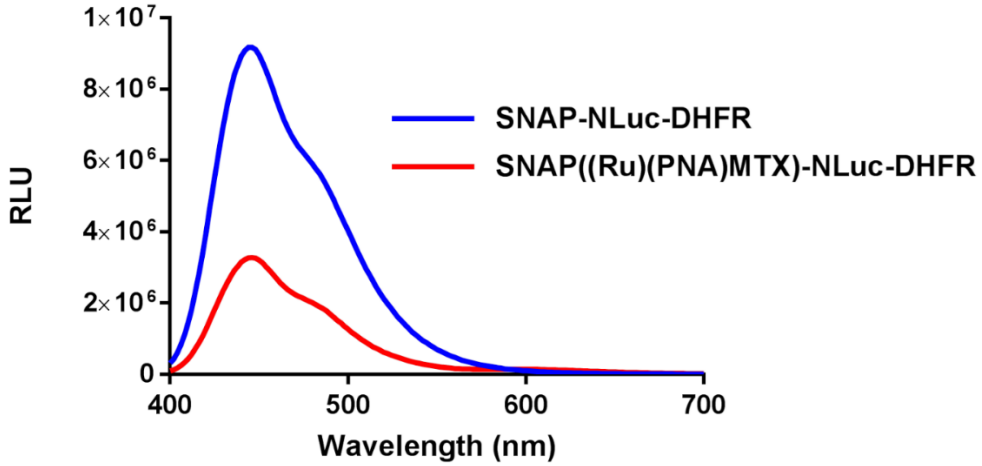

Figure IV-S4. Luminescence spectra of SNAP-Pro_{30}-NLuc-cpDHFR with or without labeling with BG-(Ru)(PNA)-MTX.

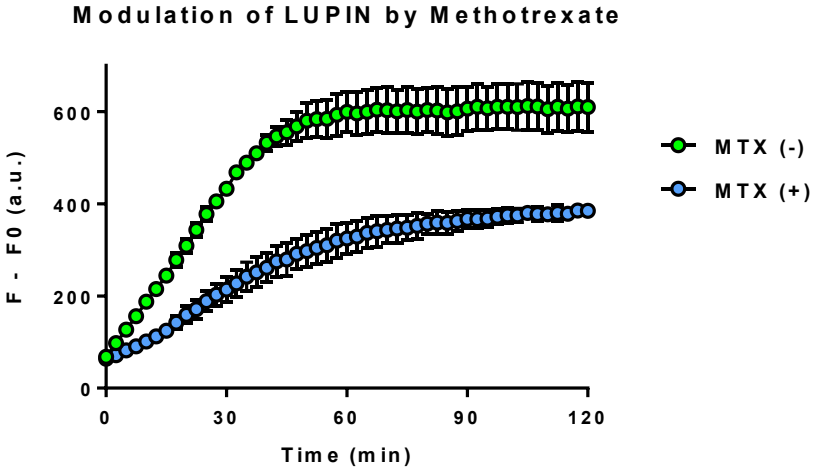

Figure IV-S5. Effect of methotrexate concentration on kinetics of LUPIN system. Methotrexate competes with the methotrexate on **BG-(Ru)(PNA)-MTX** of the LUPIN sensor, leading to more of the protein construct being in an open conformation, decreasing the BRET efficiency, leading to reduced reaction rate and yield. Conditions: SNAP-Pro_{30}-NLuc-cpDHFR labeled with **BG-(Ru)(PNA)-MTX** (10 nM), sodium ascorbate (10 mM), PNA-PyRho (**17**, 2.5 µM), and furimazine (100 µM) in HEPES (50 mM) NaCl (50 mM)(pH 7.2).

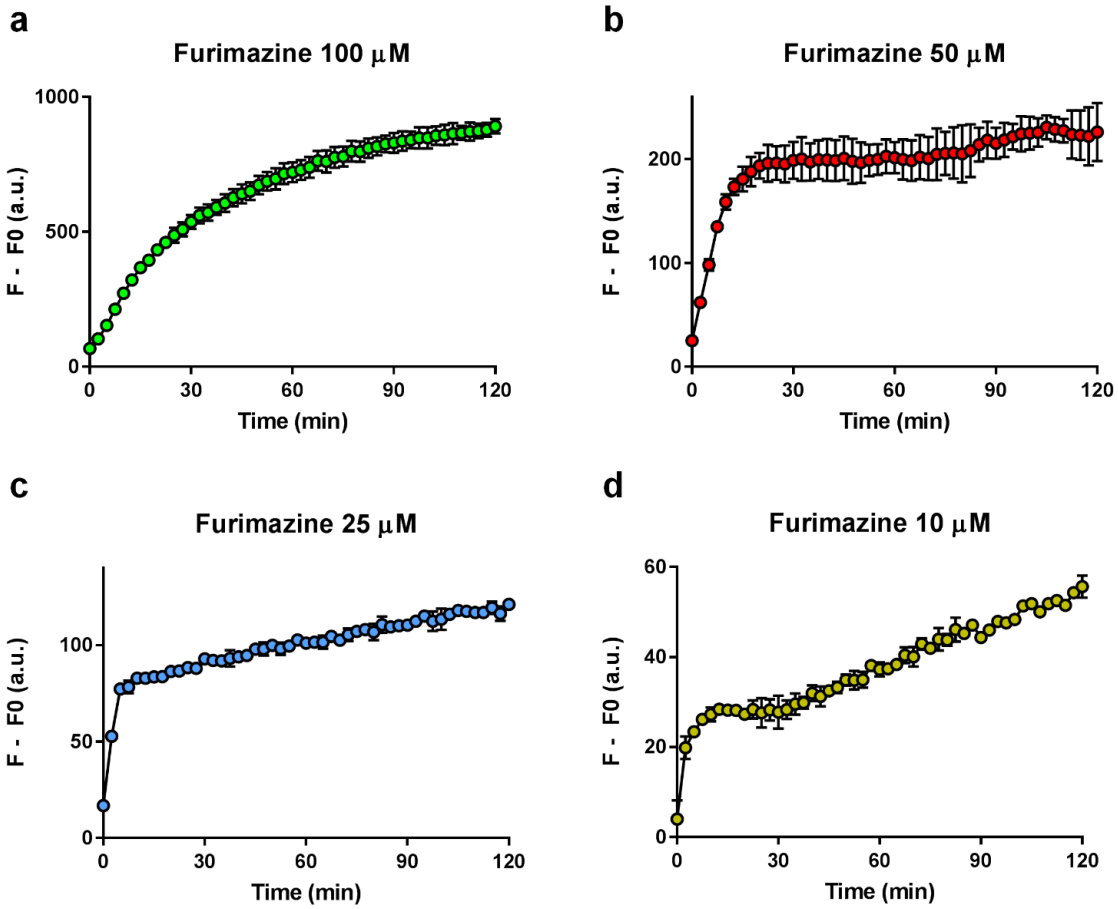

Figure IV-S6. Effect of furimazine concentration on kinetics of LUPIN system. Conditions: SNAP-Pro_{30}-NLuc-cpDHFR labeled with **BG-(Ru)(PNA)-MTX** (10 nM), sodium ascorbate (10 mM), PNA-PyRho (**17**, 5 µM), in Leibovitz's L-15 medium at 37 °C.

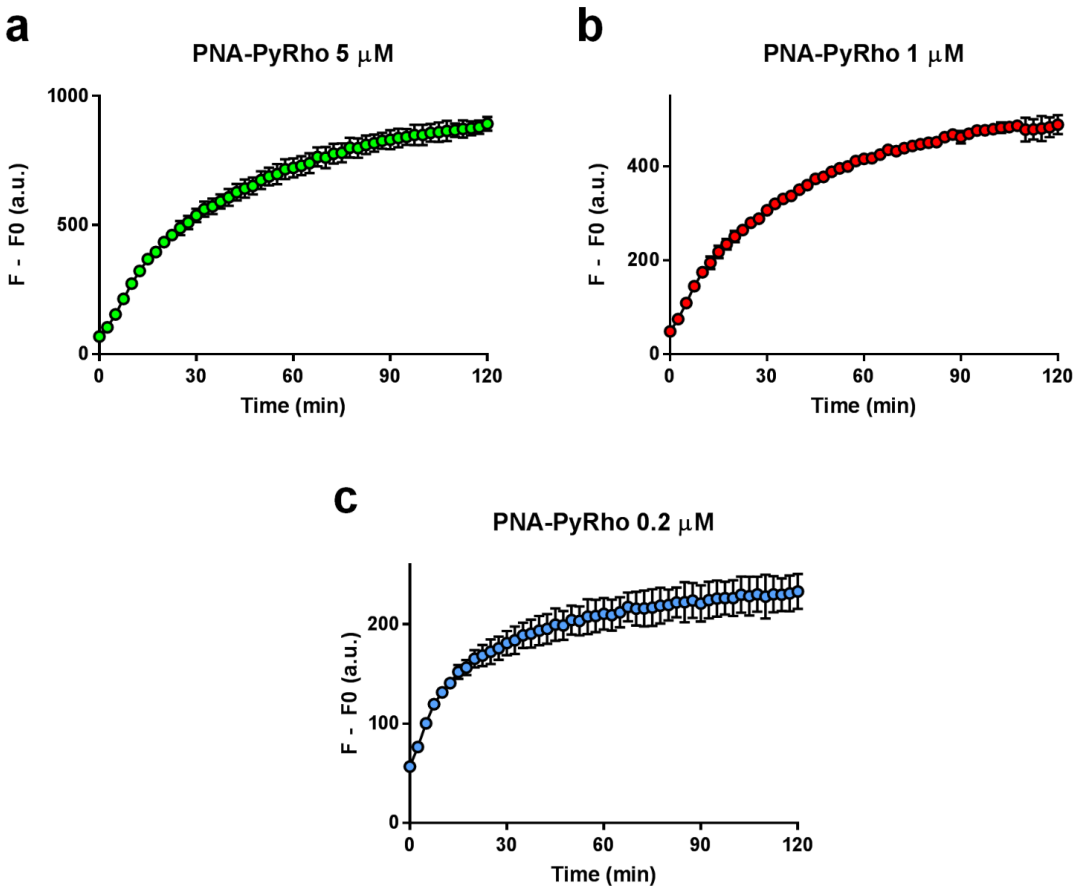

Figure IV-S7. Effect of PNA-PyRho (**17**) concentration on kinetics of LUPIN system. Conditions: SNAP-Pro_{30}-NLuc-cpDHFR labeled with **BG-(Ru)(PNA)-MTX** (10 nM), sodium ascorbate (10 mM), furimazine (100 μM), in Leibovitz's L-15 medium at 37 °C.

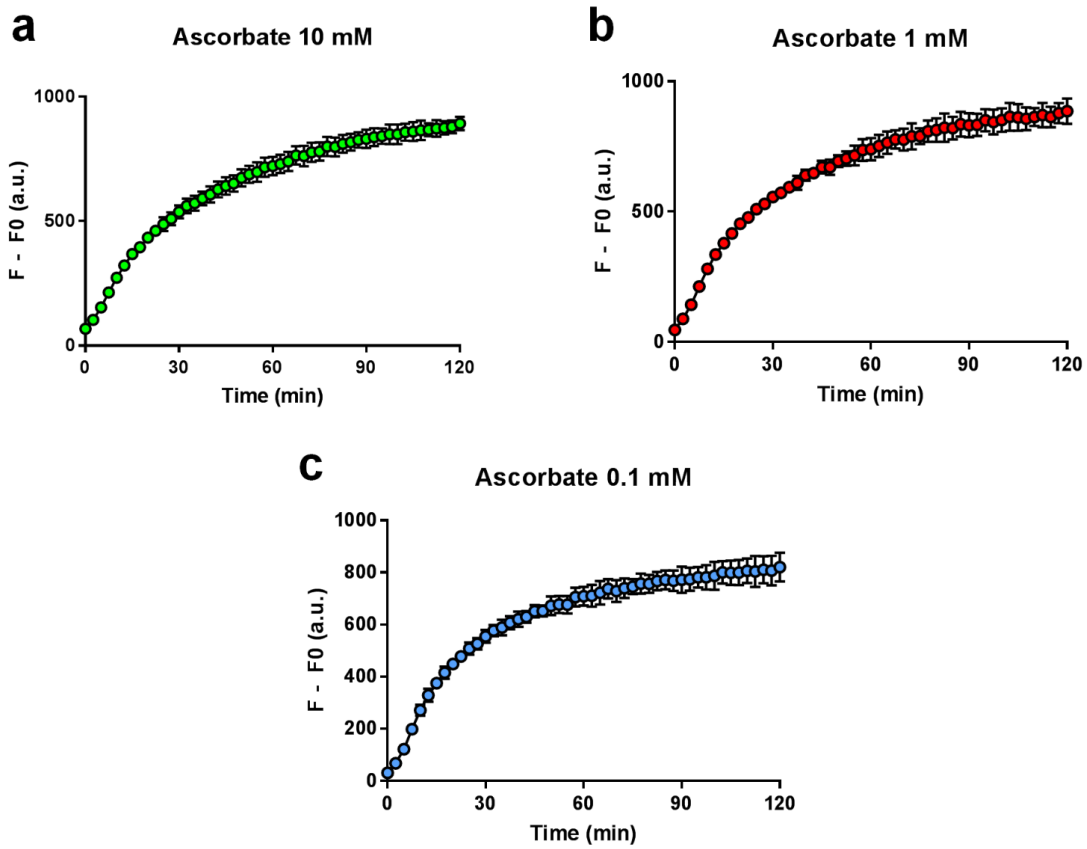

Figure IV-S8. Effect of ascorbate concentration on release kinetics of rhodamine with LUPIN system. Conditions: SNAP-Pro_{30}-NLuc-cpDHFR labeled with **BG-(Ru)(PNA)-MTX** (10 nM), PNA-PyRho (**17**) (5 μM), furimazine (100 μM), in Leibovitz's L-15 medium at 37 °C.

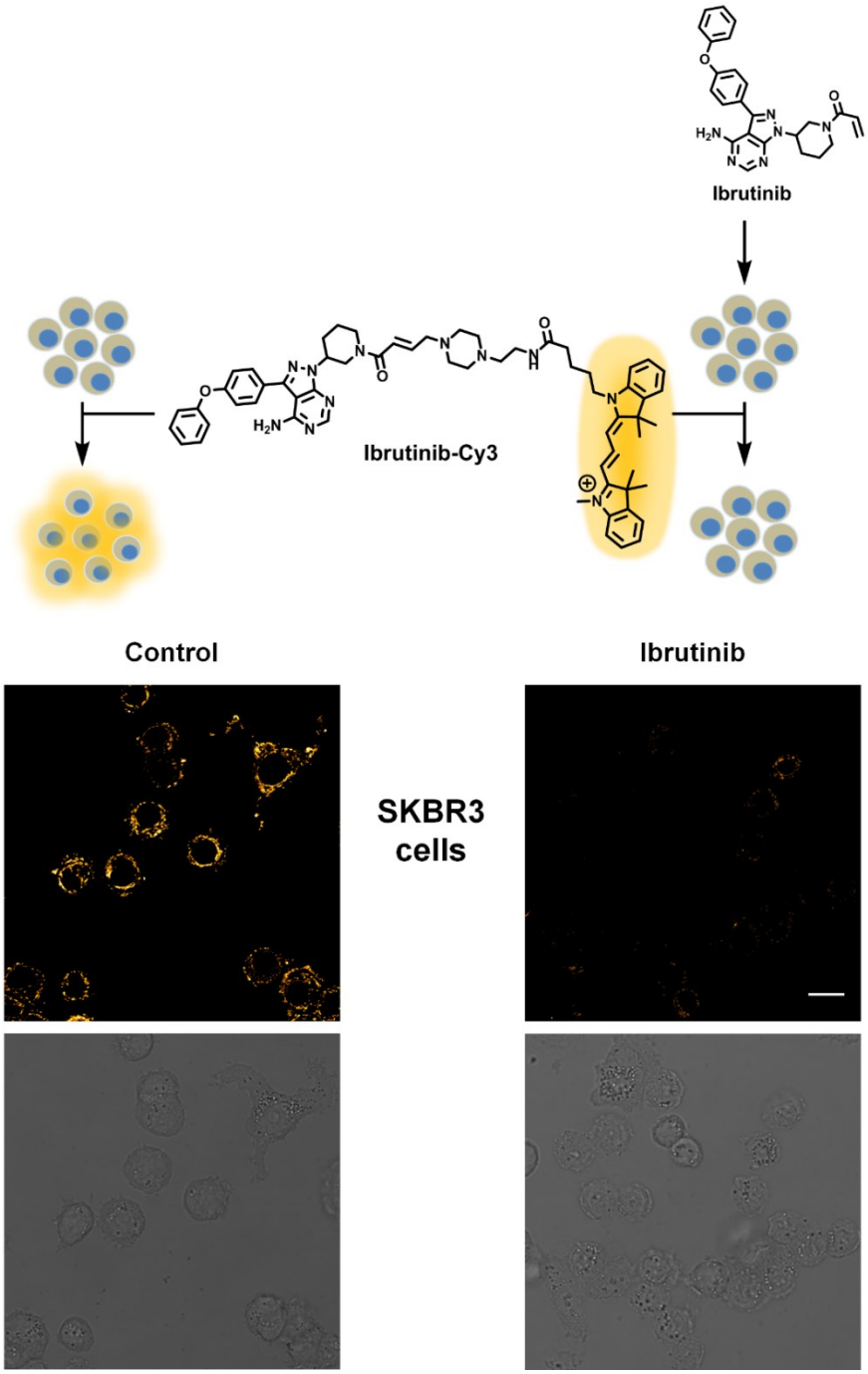

Figure IV-S9. Competition of free Ibrutinib versus Ibrutinib-Cy3 in SKBR3 cells. SKBR3 cells were incubated with Ibrutinib (1 μM) for 30 min, followed by Ibrutinib-Cy3 (**20**) (50 nM) for 30 min after which the cells were imaged. In the control experiment the cells were exposed to Ibrutinib-Cy3 (**20**) (50 nM) for 30 mins, followed by imaging. Scale bar: 20 μm.

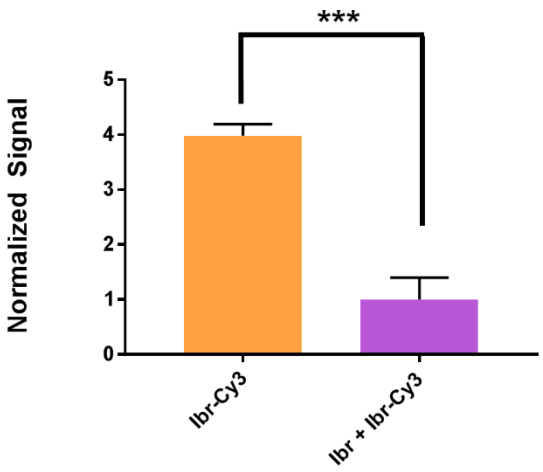

Figure IV-S10. Relative quantification of fluorescence in SKBR3 cells. Average fluorescence was measured and normalized to SKBR3 cell populations exposed to Ibrutinib and Ibrutinib-Cy3 (**20**). N = 7. Statistics calculated using a two-tailed *t*-test with unequal variances (Welch´s unpaired *t*-test). *** p<0.01.

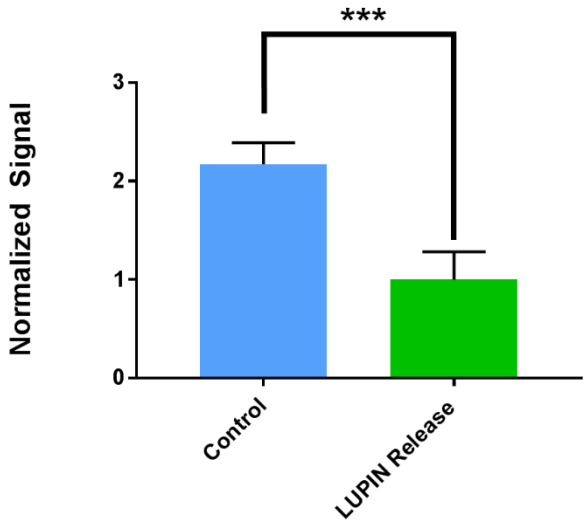

Figure IV-S11. Relative quantification of LUPIN release of Ibrutinib in SKBR3 cells. Average fluorescence was measured and normalized to SKBR3 cell populations exposed to LUPIN release of Ibrutinib and Ibrutinib-Cy3 (**20**). Control cell population was exposed to PNA-PyIbr (**18**) and Ibr-Cy3 (**20**). N = 9. Statistics calculated using a two-tailed *t*-test with unequal variances (Welch´s unpaired *t*-test). *** p<0.01.

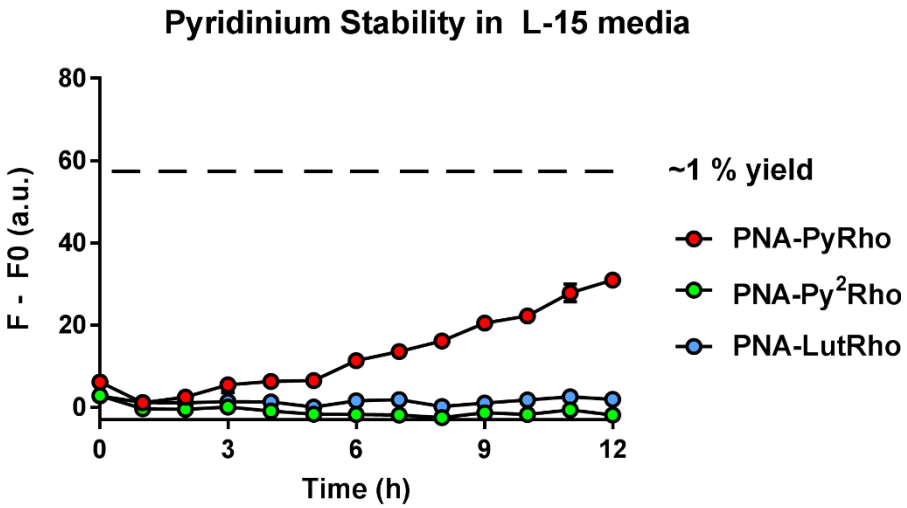

Figure IV-S12. Linker stability in Leibovitz's L-15 media. PNA-Rhodamine conjugates with different reductive linkers (PNA-pyRho **17,** PNA-LutRho **21,** PNA-py^{2}Rho **22**) (1 μM) were incubated in L-15 media at 37°C for 12 h. Release kinetics were compared to internal free rhodamine standards.

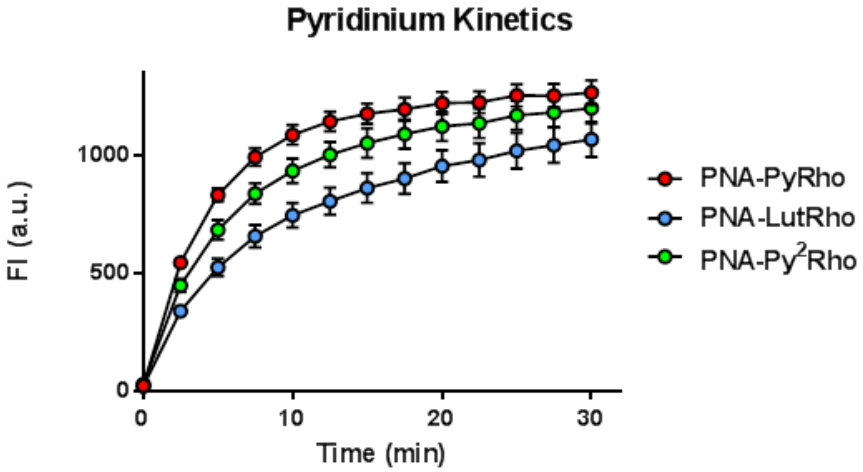

Figure IV-S13. Release kinetics of PNA-rhodamine conjugates with 3 different reductive linkers. Conditions: PNA-Linker-Rhodamine (PNA-pyRho **17,** PNA-LutRho **21,** PNA-py^{2}Rho **22**) (1 μM), PNA-Ru (**S17**) (0.1 μM), sodium ascorbate (10 mM) in PBS 1X (pH 7.4). Irradiation with 1W LED (455 nM) for 30 min.

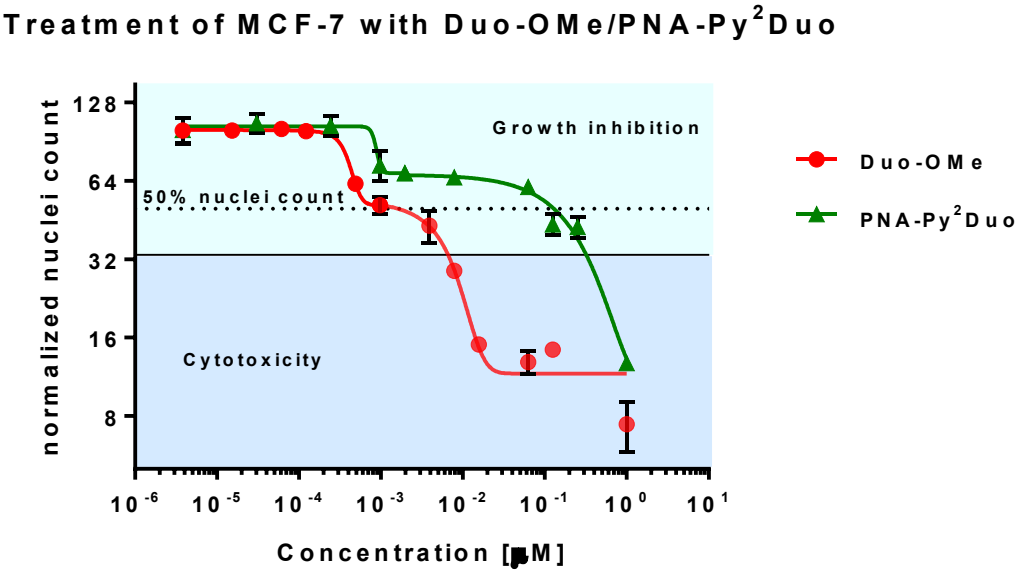

Figure IV-S14. Dose response curves for MCF-7 cells after 3 h treatment with Duo-OMe (**24**), PNA-Py^{2}Duo (**23**) and 72 h incubation. Relative toxicity was then evaluated via Hoechst staining, fluorescence imaging and nuclei count for each condition. X and Y-axis logarithmic scale. Cell population doubling time is 29 hours (based on ATCC website); change of background colour corresponds to the cell count estimated at the start of the experiment. The experiments were run in triplicates. Error bars indicate standard error of the mean.

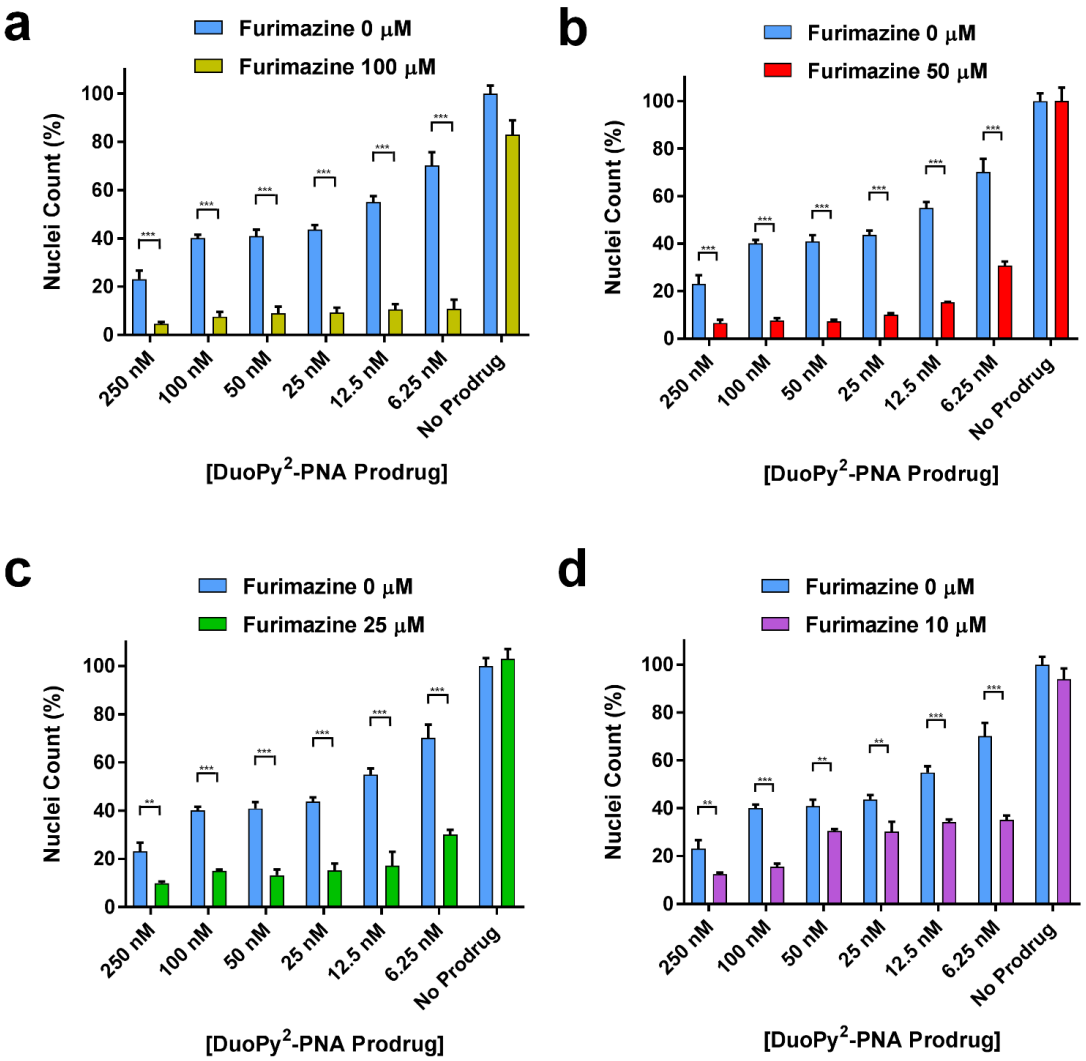

Figure IV-S16. Duo-OMe (**24**) release by LUPIN in MCF-7 cell culture. MCF-7 cells were exposed to release reaction for 3 hours after which the media was replaced and the cells were left to grow for 72 hours. Relative toxicity was then evaluated via Hoechst staining, fluorescence imaging and nuclei count for each condition. Conditions: SNAP-Pro_{30}-NLuc-cpDHFR labeled with **BG-(Ru)(PNA)-MTX** (10 nM), 1 mM Ascorbate, PNA-Py^2Duo (**23**) (0-250 nM), and furimazine (**a**, 100 μM; **b**, 50 μM; **c**, 25 μM; **d**, 10 μM) in Leibovitz's medium at 37°C. The data is the average of three independent experiments run in triplicates. Error bars show ± 1 standard deviation from the mean. Statistics calculated using a two-tailed *t*-test with unequal variances (Welch´s unpaired *t*-test).** $p<0.05$; *** $p<0.01$.

PNA sequences

Sequence: BG-$(PEG)_3$-Lys-Gly-Lys(Ru)-Lys(A*GT*TG*)-PEG-MTX (**16**)

Chemical Formula: $C_{175}H_{222}N_{62}O_{44}Ru^{2+}$, Expected Mass: 3997.61, **LC-MS (ESI^+)** RT= 1.49 min. *m/z* found: 1333.1 $[M]^{3+}$, 1000.3 $[M+H]^{4+}$, 800.6 $[M+H]^{5+}$, 667.1 $[M+H]^{6+}$; **MALDI-TOF** calculated *m/z*: 3998.611 (100%), *m/z* found: 3999.8 $[M+H]^+$.

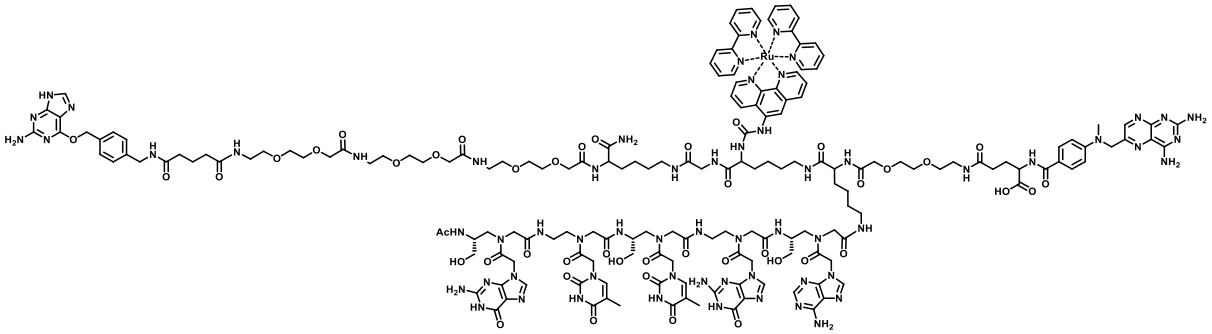

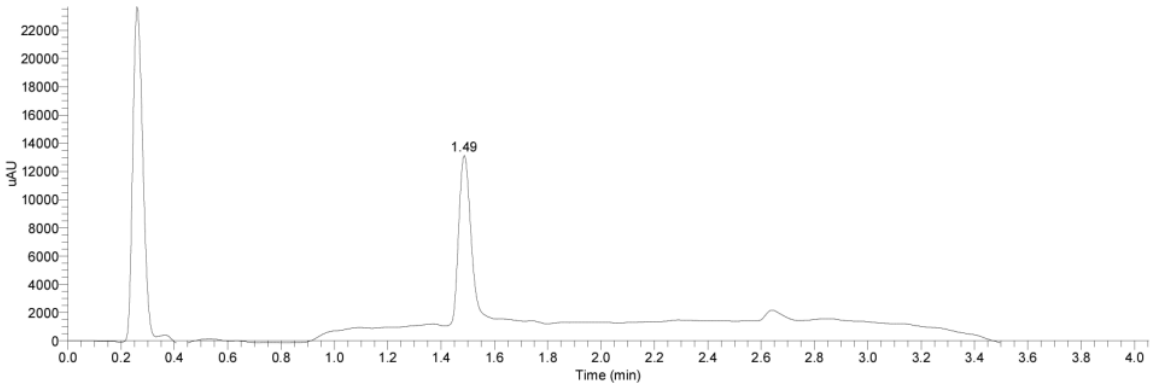

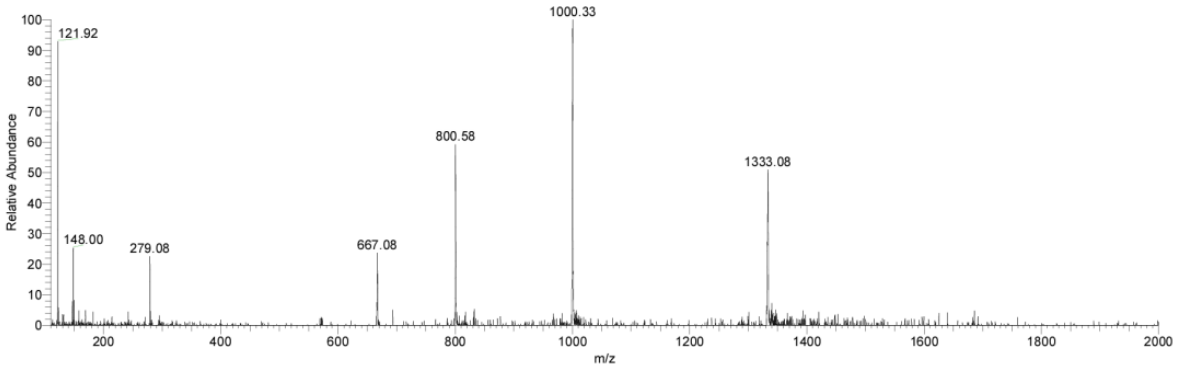

Sequence: Lys-C*AA*CT*-Pyridinium-Rhodamine (PNA-PyRho) (**17**)

Chemical Formula: $C_{101}H_{121}N_{38}O_{26}^{+}$, Expected Mass: 2281.32, **LC-MS (ESI^{+})** RT= 1.58 min. *m/z* found: 1142.17 $[M+H]^{2+}$, 761.9 $[M+H]^{3+}$, 571.8 $[M+H]^{4+}$; **MALDI-TOF** calculated *m/z*: 1852.834 (100%), *m/z* found: 1852.9 $[M - Rhodamine]^{+}$.

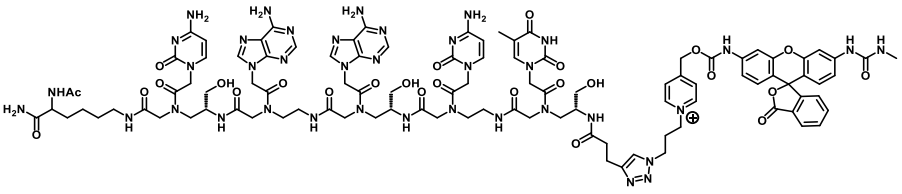

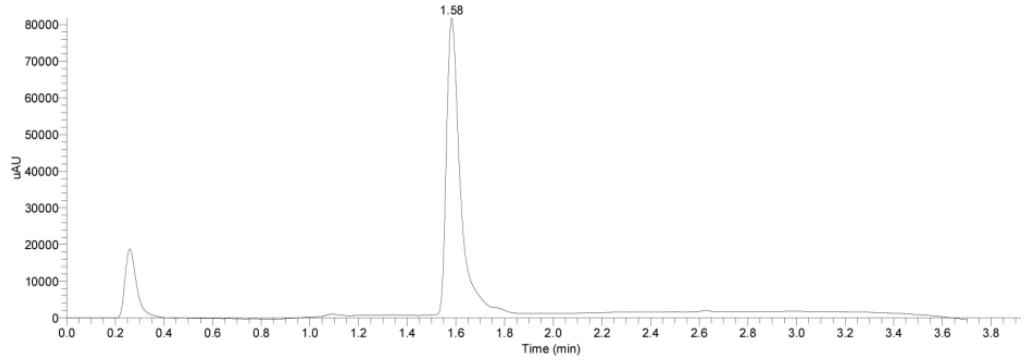

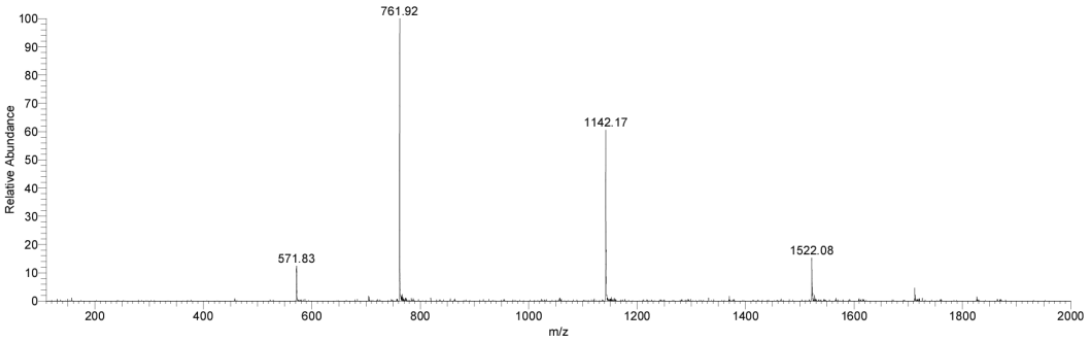

Sequence: Lys-CAA*CT*-Pyridinium-Ibrutinib (PNA-PyIbr) (**18**)

Chemical Formula: $C_{104}H_{128}N_{41}O_{24}^{+}$, Expected Mass: 2335.01, **LC-MS (ESI^{+})** RT= 1.77 min. *m/z* found: 1168.2 $[M+H]^{2+}$, 779.3 $[M+H]^{3+}$; **MALDI-TOF** calculated *m/z*: 1852.834 (100%), *m/z* found: 1853.8 $[M+H\text{-Ibrutinib}]^{+}$.

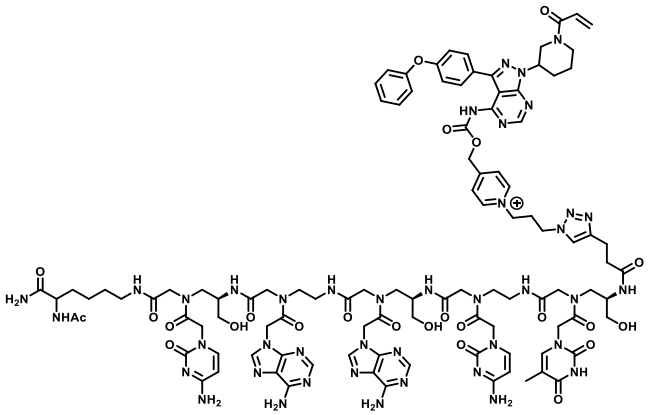

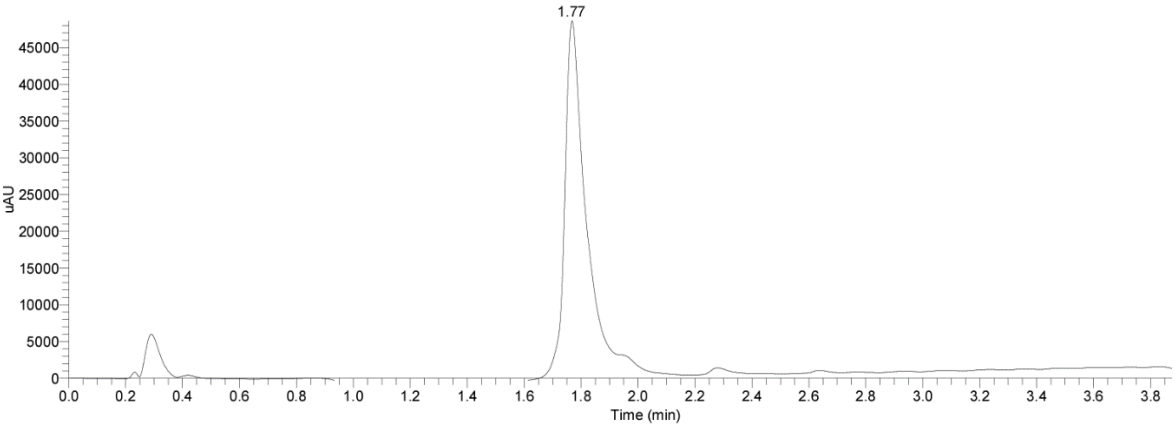

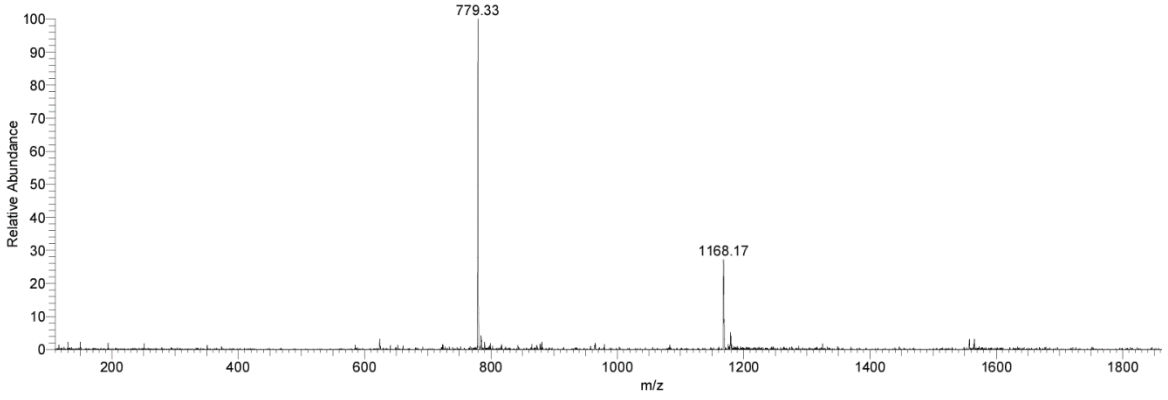

Sequence: Lys-CAA*CT*-Pyridinium-Duocarmycin (PNA-PyDuo) (**19**)

Chemical Formula: $C_{106}H_{125}ClN_{37}O_{29}S_2^+$, Expected Mass: 2478.85, **LC-MS (ESI$^+$)** RT= 1.99 min. *m/z* found: 1240.9 $[M+H]^{2+}$, 827.6 $[M+H]^{3+}$; **MALDI-TOF** calculated *m/z*: 2074.764 (100%), *m/z* found: 2073.5 $[M - Duocarmycin]^+$.

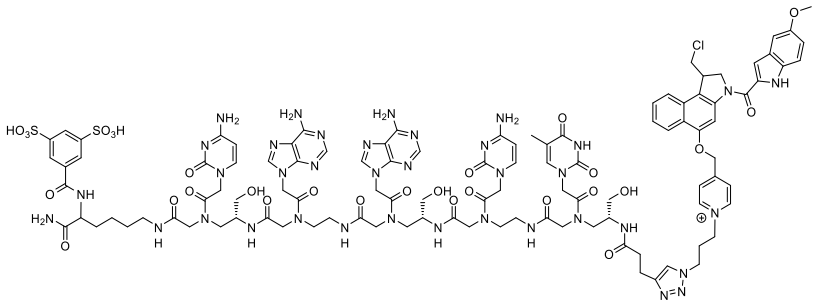

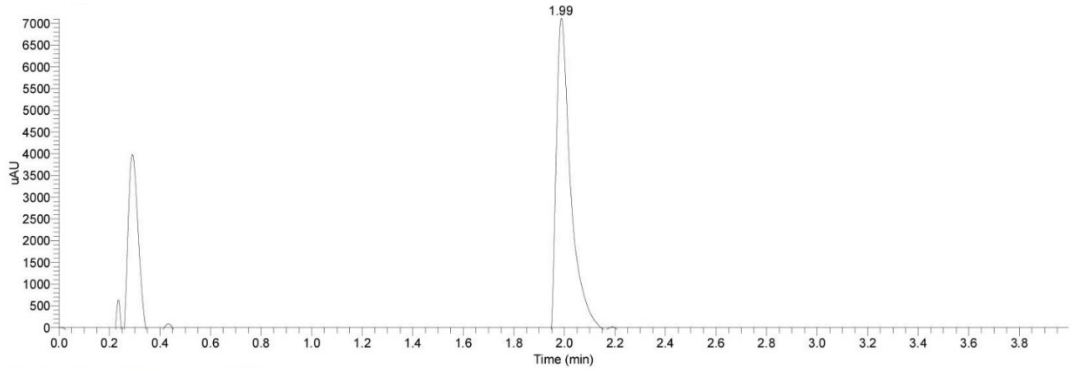

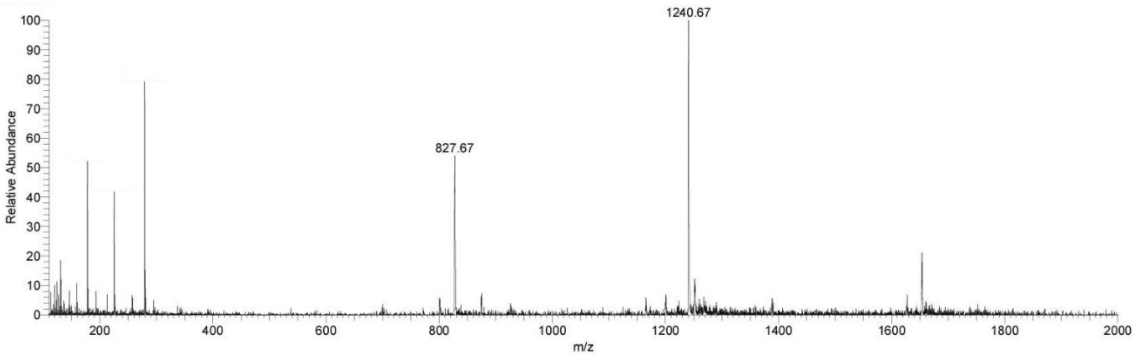

Sequence: Lys-C*AA*CT*-Lutidinium-Rhodamine (PNA-LutRho) (**21**)

Chemical Formula: $C_{103}H_{125}N_{38}O_{26}^{+}$, Expected Mass: 2309.96, **LC-MS (ESI^{+})** RT= 1.63 min. *m/z* found: 1156.0 $[M+H]^{2+}$, 771.2 $[M+H]^{3+}$, 578.8 $[M+H]^{4+}$; **MALDI-TOF** calculated *m/z*: 1880.866 (100%), *m/z* found: 1880.7 $[M - Rhodamine]^{+}$.

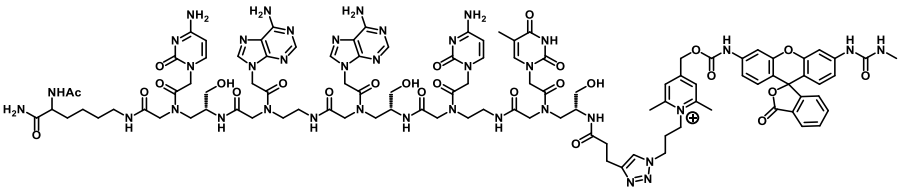

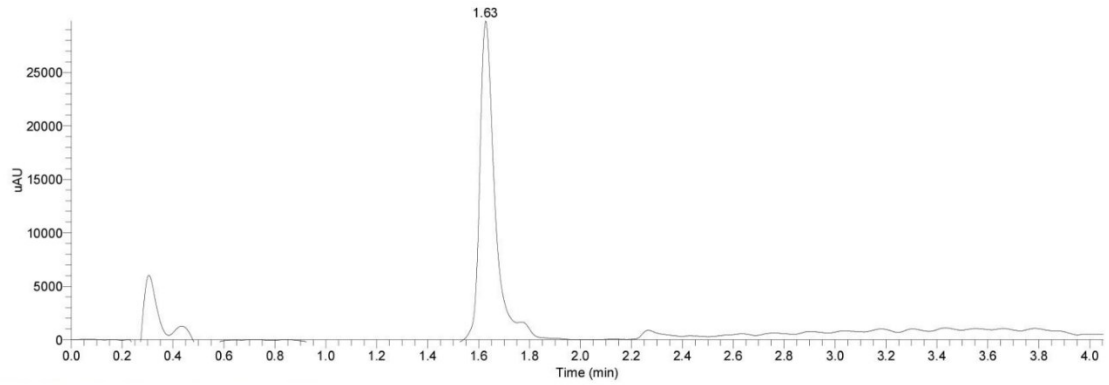

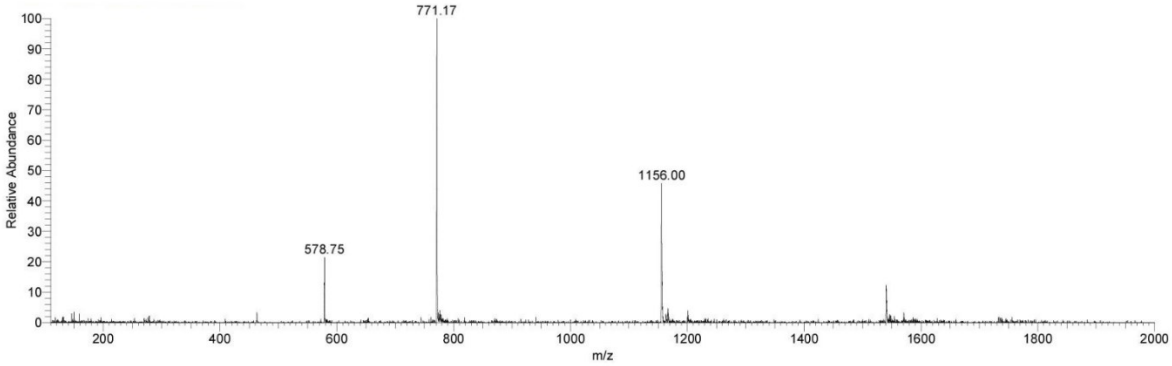

Sequence: Lys-C*AA*CT*-SecondaryPyridinium-Rhodamine (PNA-Py^{2}Rho) (**22**)

Chemical Formula: $C_{103}H_{125}N_{38}O_{26}^+$, Expected Mass*:* 2309.96, **LC-MS (ESI$^+$)** RT= 1.60 min. *m/z* found: 1156.0 $[M+H]^{2+}$, 771.2 $[M+H]^{3+}$, 578.7 $[M+H]^{4+}$; **MALDI-TOF** calculated *m/z*: 1880.866 (100%), *m/z* found: 1880.8 $[M - Rhodamine]^+$.

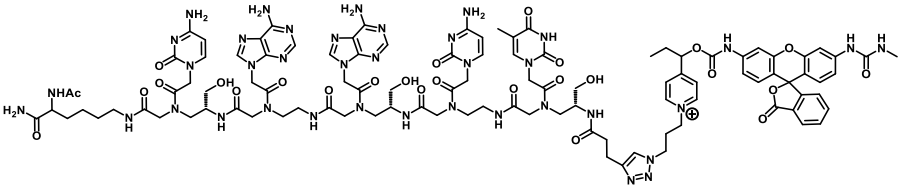

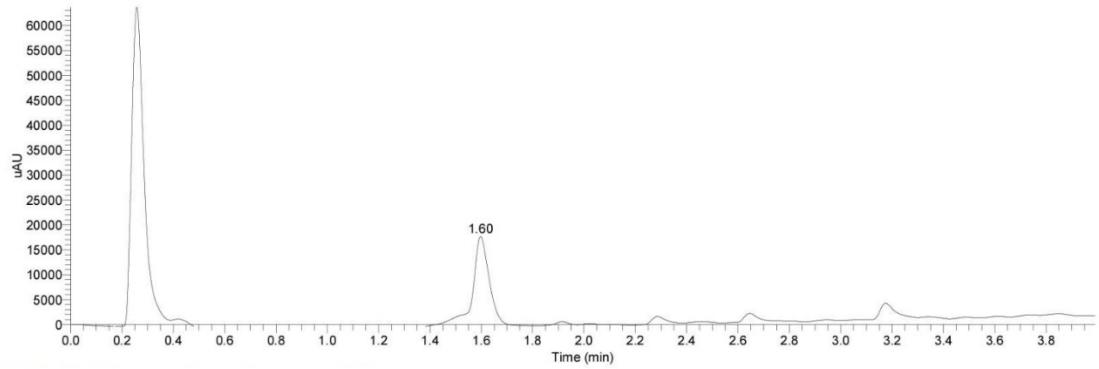

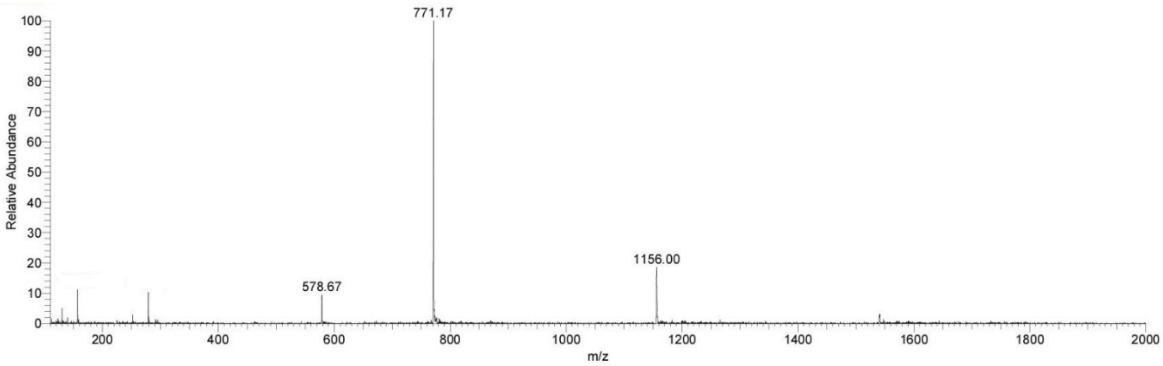

Sequence: Lys-CAA*CT*-SecondaryPyridinium-Duocarmycin (PNA-Py^{2}Duo) (**23**)

Chemical Formula: $C_{108}H_{129}ClN_{37}O_{29}S_2^+$, Expected Mass: 2506.88, **LC-MS (ESI$^+$)** RT= 2.10 min. *m/z* found: 1254.8 $[M+H]^{2+}$, 837.1 $[M+H]^{3+}$; **MALDI-TOF** calculated *m/z*: 2102.795 (100%), *m/z* found: 2102.7 $[M - Duocarmycin]^+$.

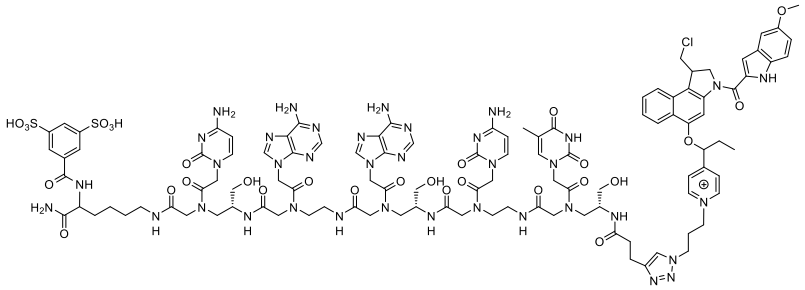

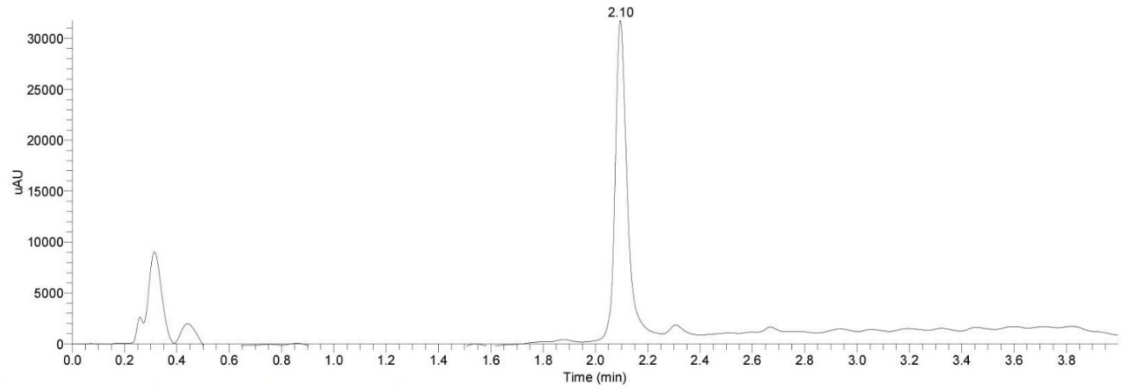

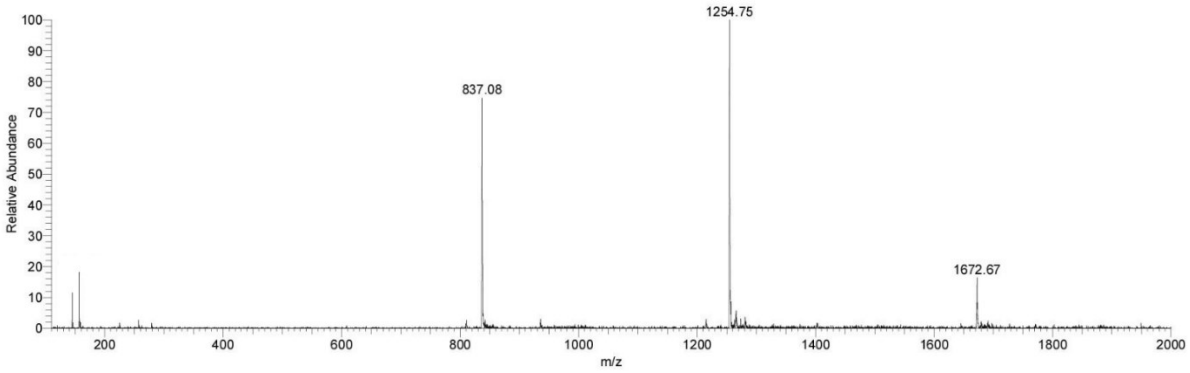

Sequence: (Ru)-Lys-A*GT*TG* (**S17**)

Chemical Formula: $C_{100}H_{119}N_{39}O_{21}Ru^{2+}$, Expected Mass: 2259.78, **LC-MS (ESI$^+$)** RT= 1.27 min. *m/z* found: 1130.1 $[M]^{2+}$, 753.7 $[M]^{3+}$, 565.8 $[M+H]^{4+}$, 452.8 $[M+H]^{5+}$; **MALDI-TOF** calculated *m/z*: 2260.789 (100%), *m/z* found: 2262.1 $[M+H]^+$.

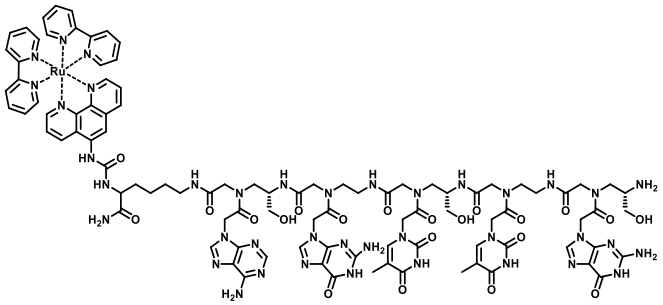

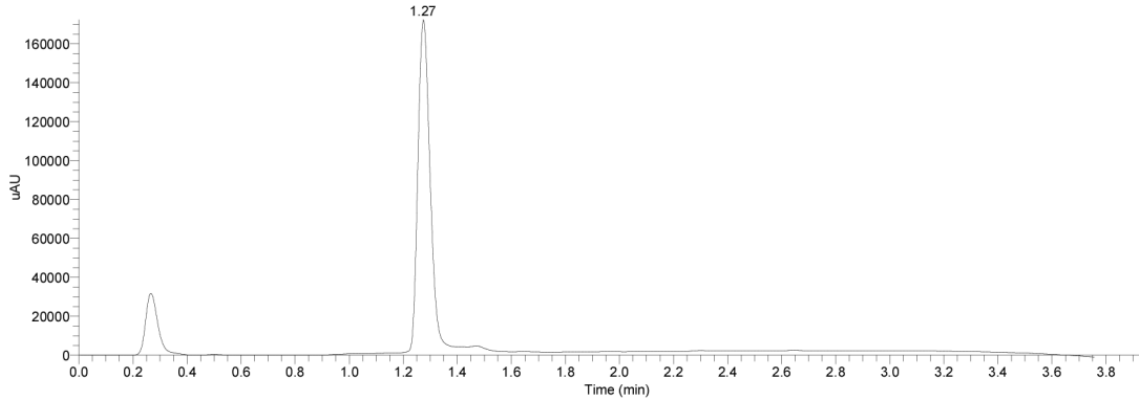

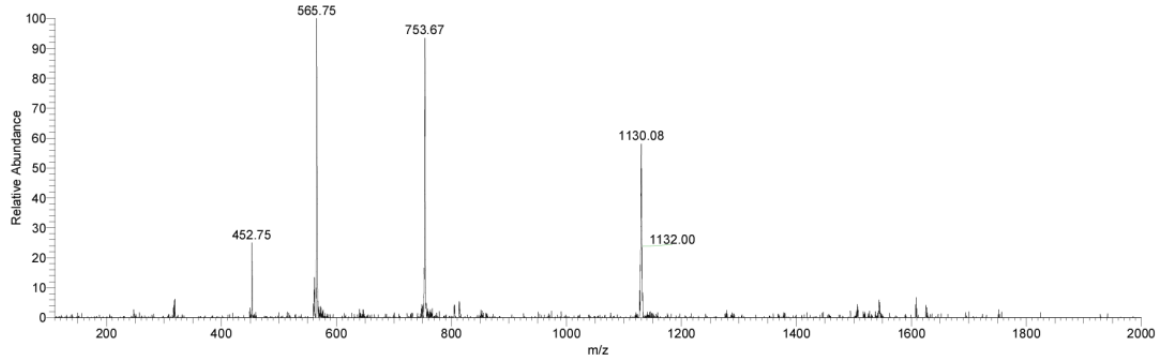

Synthesis of small molecules.

Synthesis of N_3-Pyridinium-Rhodamine (N_3PyRho) (S18)

Methylurea-Rhodamine was prepared as previously described.[15]

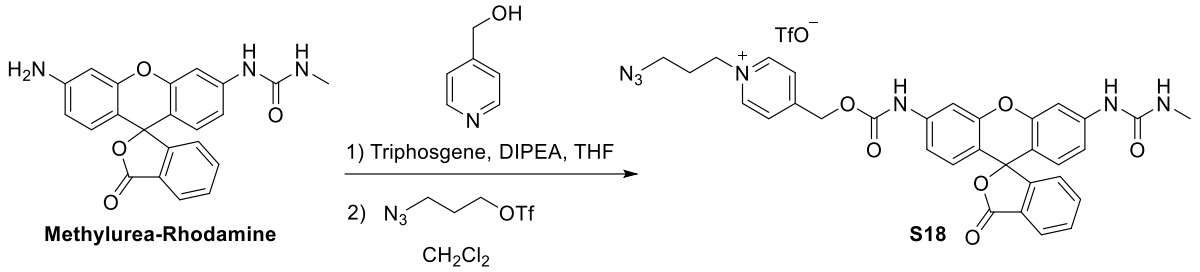

To a solution of methylurea-rhodamine (50 mg, 0.13 mmol, 1 equiv) in dry THF (3 mL) under nitrogen at 0 °C was added triphosgene (19.3 mg, 0.07 mmol, 0.5 equiv), followed by slow addition of DIPEA (70 µL, 0.39 mmol, 3 equiv) dropwise. Upon addition of DIPEA the solution became colorless and the formation of the isocyanate was monitored via LC-MS by taking small aliquots of the reaction mixture and quenching in MeOH before injection into the LC-MS. 4-pyridine-methanol (43 mg, 0.39 mmol, 3 equiv) was then added and the reaction was heated at 60 °C overnight under nitrogen. The reaction mixture was then concentrated, dissolved in DMSO, loaded and purified using reverse phase Biotage Isolera ONE equipped with a Biotage SNAP Cartridge KP-C18-HS. The desired fractions were combined and concentrated to yield pyridine-rhodamine-methylurea. The solid was dissolved in dichloromethane, cooled to -78°C, azidopropyl trifluoromethanesulfonate (1.1 equiv) was added and the reaction was allowed to warm up to room temperature slowly. The reaction was monitored via LC-MS and once all the starting material had been consumed the reaction mixture was concentrated, dissolved in H_2O and DMSO and purified via RP-HPLC to give the desired N_3PyRho (**S18**) compound as a dark red solid. **^{1}H NMR** (500 MHz, Acetone-*d6)* δ 9.18 (d, *J* = 6.3 Hz, 2H), 8.26 (d, *J* = 6.2 Hz, 2H), 7.98 (d, *J* = 7.5 Hz, 1H), 7.82 (d, *J* = 2.0 Hz, 1 H), 7.79 (td, *J* = 1.2 Hz, 7.5 Hz, 1H), 7.72 (td, *J* = 1.0 Hz, 7.6 Hz), 7.66 (d, *J* = 2.2 Hz, 1H), 7.29 (d, *J* = 7.7 Hz, 1H), 7.22 (dd, *J* = 2.2 Hz, 8.8 Hz, 1H), 7.13 (dd, *J* = 2.1 Hz, 8.8 Hz, 1H), 6.74 (d, *J* = 8.7 Hz, 1H), 6.62 (d, *J* = 8.6 Hz) 5.53 (s, 2H), 4.94 (t, *J* = 7.3 Hz, 2H), 3.61 (t, *J* = 6.4 Hz, 2H), 2.72 (s, 3H), 2.43 (m, 2H). **^{13}C NMR** (126 MHz, Acetone-*d6*) δ 169.66, 158.82, 154.04, 152.80, 152.58, 145.79, 136.18, 130.84, 129.48, 128.86, 127.66, 126.29, 125.46, 125.00, 115.26, 115.18, 115.09, 115.01, 114.86, 111.81, 106.80, 105.52, 105.46, 83.47, 64.54, 60.00, 48.77, 31.06, 26.51. Expected mass: 606.21 **LC-MS (ESI$^+$)**. RT= 1.95 min. *m/z* found: 606.3 $[M]^+$, 303.8 $[M]^{2+}$.

Synthesis of Propyl-Pyridinium-Rhodamine (PrPyRho (S19))

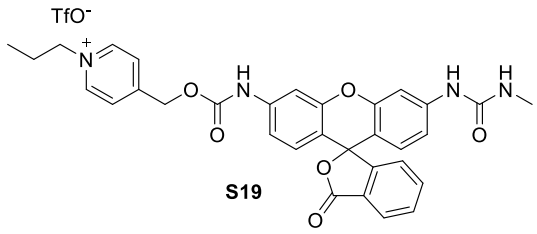

PrPyRho was synthesized using the same method as for N_3PyRho, using propyl trifluoromethansulfonate instead of azidopropyl trifluoromethansulfonate. **^{1}H NMR** (500 MHz, MeOD) δ 8.96 (d, *J* = 6.8 Hz, 2H), 8.11 (d, *J* = 6.3 Hz, 2H), 8.02 (dt, *J* = 7.6, 1.0 Hz, 1H), 7.78 (td, *J* = 7.5, 1.2 Hz, 1H), 7.72 (td, *J* = 7.5, 1.0 Hz, 1H), 7.67 (d, *J* = 2.2 Hz, 1H), 7.62 (d, *J* = 2.1 Hz, 1H), 7.24 – 7.19 (m, 1H), 7.10 (dd, *J* = 8.7, 2.2 Hz, 1H), 6.89 (dd, *J* = 8.7, 2.2 Hz, 1H), 6.71 (d, *J* = 8.7 Hz, 1H), 6.64 (d, *J* = 8.6 Hz, 1H), 5.54 (s, 2H), 4.58 (t, J = 7.4 Hz, 2H), 2.78 (s, 3H), 2.05 (h, *J* = 7.4 Hz, 2H), 1.02 (t, *J* = 7.4 Hz, 3H). **^{13}C NMR** (126 MHz, MeOD) δ 171.37, 159.28, 158.46, 154.41, 154.32, 153.30, 153.17, 145.75, 143.89, 142.29, 136.73, 131.28, 129.61, 129.30, 127.85, 126.38, 125.91, 125.16, 115.62, 115.53, 114.89, 113.12, 107.14, 106.71, 64.88, 64.00, 26.78, 25.72, 10.70. Expected mass: 565.21. **LC-MS (ESI$^+$)** RT= 1.96 min. *m/z* found: 565.4 $[M]^+$, 283.4 $[M+H]^{2+}$. **HRMS**: 565.20441 (± 6.70 ppm).

Synthesis of Secondary-Pyridinium-Rhodamine (N_3Py^2Rho) (S20)

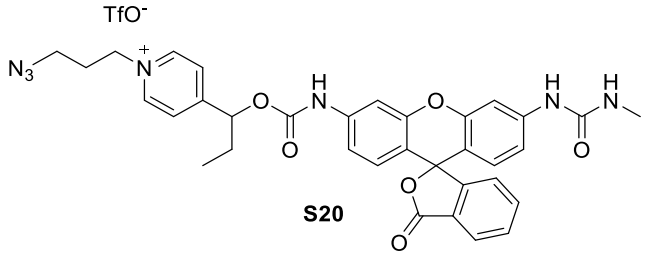

N_3Py^2Rho was synthesized using the same method as for N_3PyRho, using 1-(pyridin-4-yl)propan-1-ol instead of 4-pyridine methanol.

^{1}H NMR (400 MHz, MeOD) δ 8.87 (d, *J* = 6.5 Hz, 2H), 8.03 (d, *J* = 6.4 Hz, 2H), 7.92 (d, *J* = 7.6 Hz, 1H), 7.67 (t, *J* = 7.4 Hz, 1H), 7.64 – 7.59 (m, 1H), 7.57 – 7.55 (m, 1H), 7.49 (d, *J* = 2.0 Hz, 0.5H), 7.42 (d, *J* = 2.1 Hz, 0.5H), 7.10 (dd, *J* = 7.6, 3.4 Hz, 1H), 6.99 (dd, *J* = 8.7, 2.2 Hz, 0.5H), 6.93 (dd, *J* = 8.7, 2.2 Hz, 0.5H), 6.78 (dd, *J* = 8.6, 2.2 Hz, 1H), 6.58 (d, *J* = 8.7 Hz, 1H), 6.53 (d, *J* = 8.7 Hz, 1H), 5.81 – 5.76 (m, 1H), 4.60 (t, *J* = 7.2 Hz, 2H), 3.41 (t, *J* = 6.3 Hz, 2H), 2.24 – 2.13 (m, 2H), 1.98 – 1.86 (m, 2H), 0.97 (t, *J* = 7.3 Hz, 3H). **^{13}C NMR** (126 MHz, MeOD) δ 163.18, 158.46, 154.40, 153.17, 146.23, 143.88, 142.28, 136.71, 131.28, 130.80, 129.58, 129.29, 127.85, 126.31, 125.90, 125.16, 115.60, 113.11, 107.08, 106.69, 76.92, 60.21, 31.19, 30.03, 28.13, 26.77, 9.79. Expected mass: 634.24. **LC-MS (ESI$^+$)** RT= 2.13 min. *m/z* found: 634.3 $[M]^+$, 317.8 $[M+H]^{2+}$. **HRMS**: 634.23676 (± 6.52 ppm).

Synthesis of Lutidinium-Rhodamine (N_3LutRho) (S21)

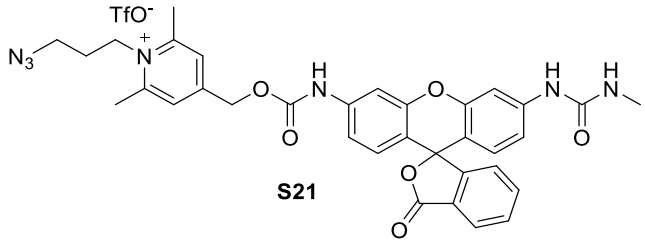

S21

N_3LutRho was synthesized using the same method as for N_3PyRho, using (2,6-dimethylpyridin-4-yl)methanol instead of 4-pyridine methanol.

Expected mass: 634.24. **LC-MS (ESI$^+$)** RT= 2.11 min. *m/z* found: 634.3 $[M]^+$, 317.8 $[M+H]^{2+}$.

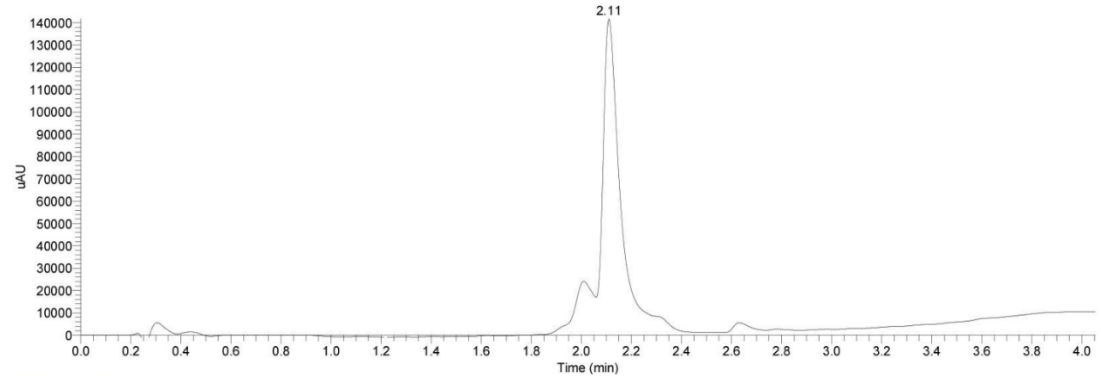

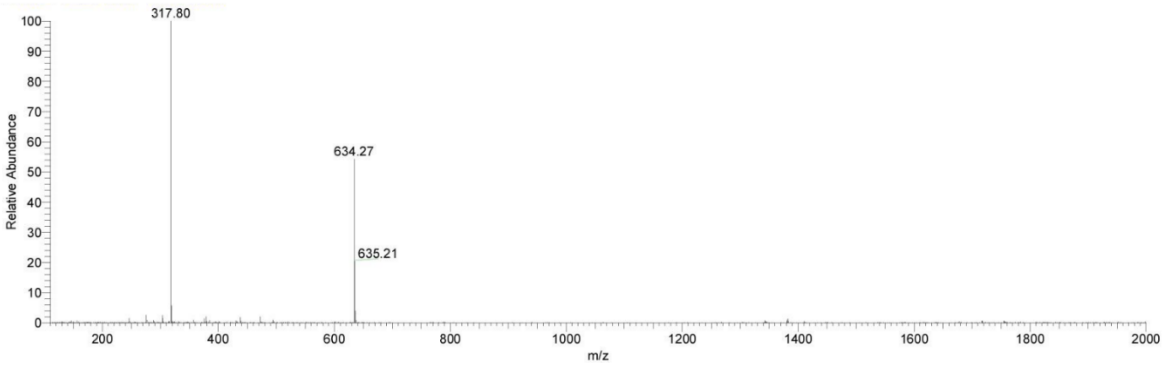

Synthesis of Pyridinium-Ibrutinib derivative (N_3PyIbr) (S22)

Ibrutinib (racemic) was synthesized according to a previously reported procedure.[16, 17]

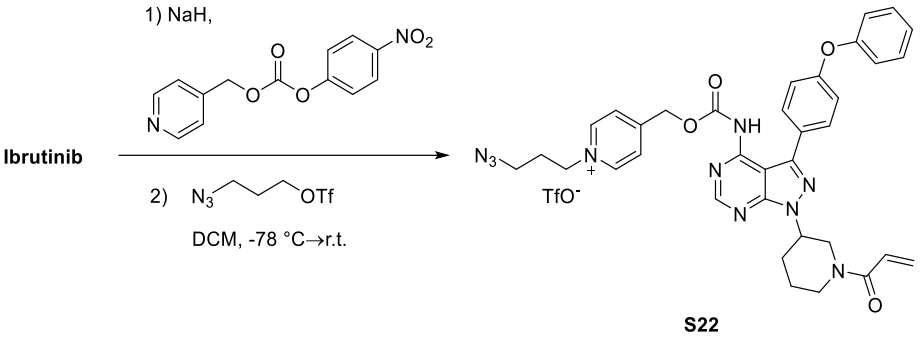

S22

NaH (60% dispersion in mineral oil) (2 mg, 0.09 mmol, 4 equiv) was dissolved in DMF (2.3 mL) and stirred for 15 minutes at room temperature. Ibrutinib (10 mg, 0.023 mmol, 1 equiv) was added to the previous suspension at 0 °C and the mixture was stirred for 1 hour before the addition of 4-nitrophenyl(pyridin-4-ylmethyl)carbonate (13 mg, 0.046 mmol, 2 equiv). The mixture was allowed to reach room temperature and stirred overnight. The mixture was poured into 50 mL of water and extracted with EtOAc (3 x 15 mL); the organic layers were combined, washed with brine (20 mL), dried over Na_2SO_4 and concentrated. The crude product (10 mg) was used in the next step without further purifications.

The crude residue was dissolved in CH_2Cl_2 (1.7 mL) and cooled to -78 °C. 3-azidopropyl trifluoromethanesulfonate (5 mg, 0.0174 mmol, 1 equiv) was added dropwise; the mixture was allowed to reach room temperature and stirred for 3 hours. The solution was then concentrated and purified by RP-HPLC. **S22** was obtained as a pale yellow solid. **^{1}H NMR** (500 MHz, Chloroform-*d*, rotamers) δ 9.05 – 8.98 (m, 2H), 8.48 – 8.39 (m, 1H), 8.02 – 7.89 (m, 3H), 7.44 – 7.32 (m, 2H), 7.20 – 7.02 (m, 6H), 6.68 – 6.49 (m, 1H), 6.35 – 6.23 (m, 1H), 5.78 – 5.62 (m, 1H), 5.36 (s, 2H), 4.98 – 4.87 (m, 1H), 4.82 (t, *J* = 7.1 Hz, 2H), 4.63 – 4.54 (m, 0.5H), 4.25 – 4.15 (m, 0.5H), 4.09 – 3.97 (m, 1H), 3.83 – 3.73 (m, 0.5H), 3.50 (t, *J* = 5.9 Hz, 2H), 3.47 – 3.37 (m, 0.5H), 3.30 – 3.19 (m, 1H), 2.99 – 2.87 (m, 0.5H), 2.46 – 2.34 (m, 1H), 2.34 – 2.22 (m, 2H), 2.07 – 1.99 (m, 1H), 1.80 – 1.65 (m, 1H), 0.91 – 0.78 (m, 1H). **^{13}C NMR** (126 MHz, $CDCl_3$) δ 165.92, 161.43, 158.62, 157.51, 156.66, 153.92, 144.95, 130.80, 130.11, 130.08, 128.46, 127.60, 127.15, 125.95, 125.77, 124.09, 120.07, 119.49, 119.38, 118.81, 115.17, 64.60, 59.47, 54.11, 53.01, 50.12, 47.78, 46.25, 46.07, 42.33, 30.48, 30.30, 25.32, 23.96, 20.30. Expected mass: 659.28, **LC-MS (ESI$^+$)** RT= 2.36 min. *m/z* found: 659.3 $[M]^+$. **HRMS**: 659.27936 (± 6.58 ppm).

Synthesis of Ibrutinib-Cy3 conjugate (Ibr-Cy3) (20)

Intermediate **S23** was synthesized as previously described.[16, 18]

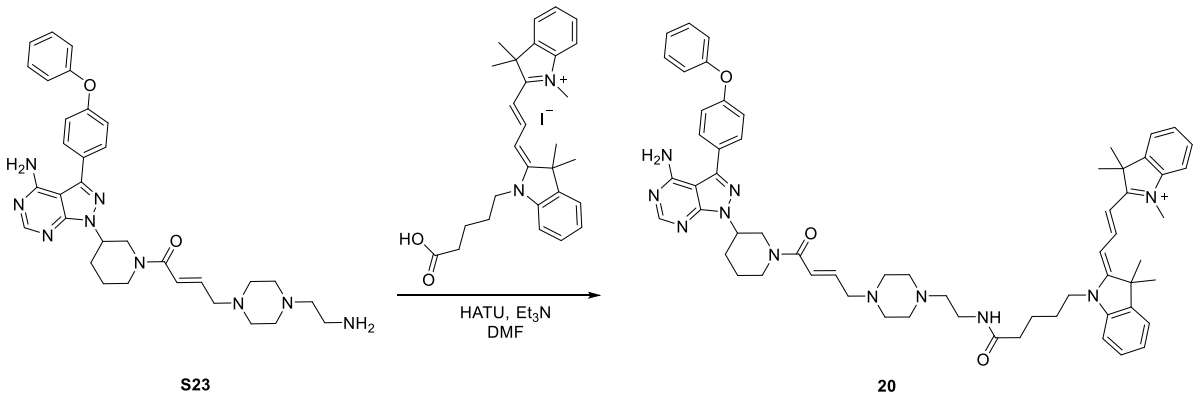

S23 **20**

To a solution of Cy3-COOH (7.4 mg, 0.013 mmol, 1 equiv) in DMF (1 mL) was added HATU (4.7 mg, 0.012 mmol, 0.92 equiv) and Et_3N (7 µl, 0.05 mmol, 3.8 equiv) and the reaction was stirred at room temperature for 10 minutes after which **S23** (5.8 mg, 0.01 mmol, 0.76 equiv) was added in DMF and the reaction was stirred at room temperature for 1 hour. The reaction mixture was then diluted in water and purified by RP-HPLC giving Ibr-Cy3 (1.1 mg) as a dark red solid. Expected mass: 1006.58, **LC-MS (ESI$^+$)** RT = 2.37 min. *m/z* found: 1006.8 $[M]^+$, 504.0 $[M+H]^{2+}$.336.3 $[M+2H]^{3+}$. **MALDI-TOF** calculated *m/z*: 1006.581 (100%), *m/z* found: 1006.711 $[M]^+$. **HRMS**: 1006.57654 (± 4.86 ppm).

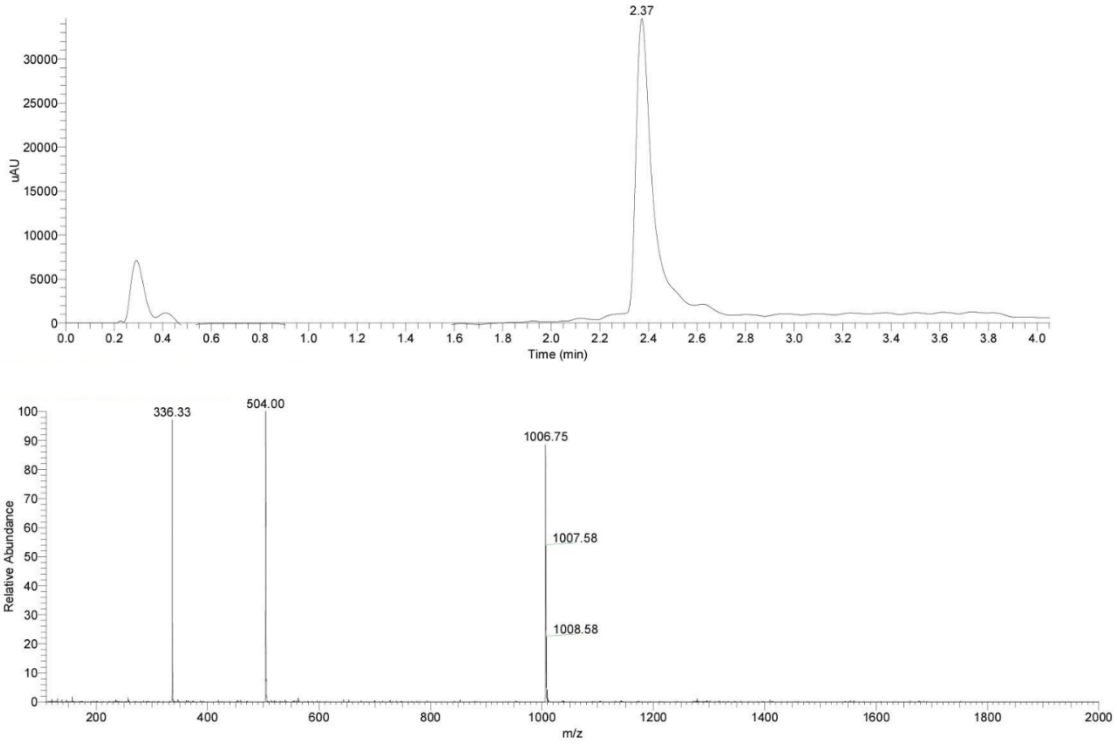

Synthesis of Duocarmycin derivative (Duo-OMe)

Derivative **S24** was synthesized according to a previously reported procedure.[19]

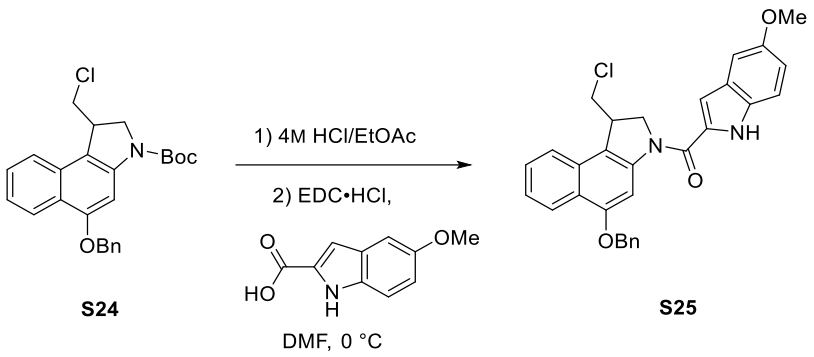

S24 (5 mg, 0.012 mmol, 1 equiv) was treated with 4 M HCl/EtOAc (0.3 mL) at room temperature and stirred for 1 hour. Then the mixture was concentrated and dried under vacuum. The residue was dissolved in DMF (0.5 mL) and cooled to 0 °C. 5-methoxy-1H-indole-2-carboxylic acid (2.5 mg, 0.012 mmol, 1 equiv) and EDC·HCl (6.8 mg, 0.035 mmol, 3 equiv) were added and the mixture was stirred at 0 °C for 2 hours. Then the mixture was diluted with $NaHCO_3$ saturated solution (10 mL) and extracted with EtOAc (3 x 5 mL). The organic layers were combined, washed with brine (2 x 5 mL), dried over Na_2SO_4 and concentrated. The crude was purified by preparative TLC on silica gel (Hexane/EtOAc 2:1) affording **S25** as yellow oil (4 mg, 65%). **^{1}H NMR** (400 MHz, Chloroform-*d*) δ 9.33 (s, 1H), 8.36 (dd, *J* = 8.3, 1.0 Hz, 1H), 8.19 (s, 1H), 7.73 (dd, *J* = 8.3, 0.9 Hz, 1H), 7.62 – 7.52 (m, 3H), 7.48 – 7.32 (m, 5H), 7.15 (d, *J* = 2.3 Hz, 1H), 7.07 (dd, *J* = 2.3, 0.9 Hz, 1H), 7.03 (dd, *J* = 8.9, 2.4 Hz, 1H), 5.32 (q, *J* = 11.5 Hz, 2H), 4.84 (dd, *J* = 10.8, 1.9 Hz, 1H), 4.70 (dd, *J* = 10.8, 8.3 Hz, 1H), 4.16 (ddt, *J* = 9.9, 8.3, 2.8 Hz, 1H), 4.05 – 3.95 (m, 1H), 3.88 (s, 3H), 3.55 – 3.43 (m, 1H). **^{13}C NMR** (126 MHz, $CDCl_3$) δ 160.75, 156.00, 154.91, 142.25, 136.86, 131.35, 130.70, 129.93, 128.76, 128.51, 128.21, 128.02, 127.76, 124.27, 123.91, 123.85, 122.30, 117.04, 116.51, 112.81, 106.28, 102.66, 98.47, 77.42, 77.36, 77.16, 76.91, 70.56, 55.88, 55.39, 46.20, 43.38. Expected mass: 496.16 **MS (ESI$^+$)** *m/z* found: 497.3 $[M+H]^+$.

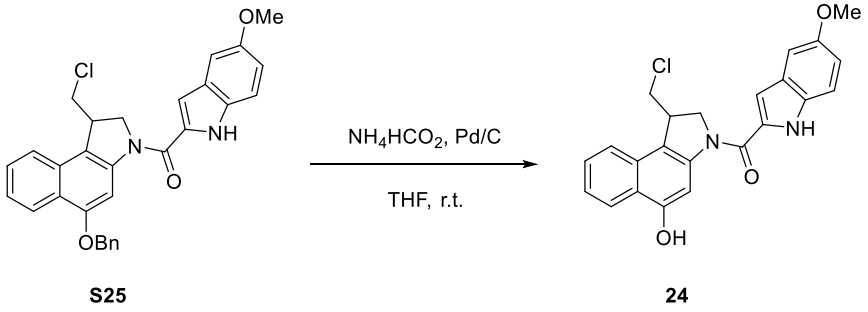

S25 (4 mg, 0.008 mmol, 1 equiv) was dissolved in THF (170 µL). Pd/C 10% (2.5 mg) was added under stirring and a 25% (w/w) aqueous solution of NH_4HCO_2 (15 µL, 8 equiv) was added dropwise. After stirring for 2 hours at room temperature, the mixture was filtered through Celite and washed with Et_2O. The filtrates were dried over Na_2SO_4 and concentrated. The residue was purified by RP-HPLC affording **Duo-OMe** (**24**) as a white foam (1.5 mg, 46%). **^{1}H NMR** (500 MHz, DMSO-d_6) δ 11.60 (d, *J* = 2.2 Hz, 1H), 10.44 (s, 1H), 8.11 (dd, *J* = 1.3 Hz, 1H), 7.97 (s, 1H), 7.85 (d, *J* = 8.4 Hz, 1H), 7.52 (ddd, *J* = 8.4, 6.8, 1.3 Hz, 1H), 7.42 – 7.31 (m, 2H), 7.16 (d, *J* = 2.4 Hz, 1H), 7.10 (d, *J* = 2.2 Hz, 1H), 6.91 (dd, *J* = 8.9, 2.4 Hz, 1H), 4.79 (dd,

J = 10.9, 8.9 Hz, 1H), 4.55 (dd, *J* = 10.9, 2.1 Hz, 1H), 4.26 – 4.18 (m, 1H), 4.02 (dd, *J* = 11.1, 3.2 Hz, 1H), 3.85 (dd, *J* = 11.1, 7.5 Hz, 1H), 3.78 (s, 3H).**^{13}C NMR** (126 MHz, DMSO) δ 160.14, 154.13, 153.86, 142.31, 131.57, 131.03, 129.91, 127.50, 127.34, 123.16, 123.11, 122.79, 122.13, 115.46, 114.96, 113.18, 105.30, 102.09, 100.35, 55.28, 55.03, 47.62, 41.23. Expected mass: 406.11, **LC-MS (ESI$^+$)** RT= 2.78 min. *m/z* found: 407.2 $[M+H]^+$.

Synthesis of Secondary-Pyridinium-Duocarmycin derivative (N_3Py^2Duo-OMe) (S29)

Compound **S26** was synthesized according to a previously reported procedure.[19]

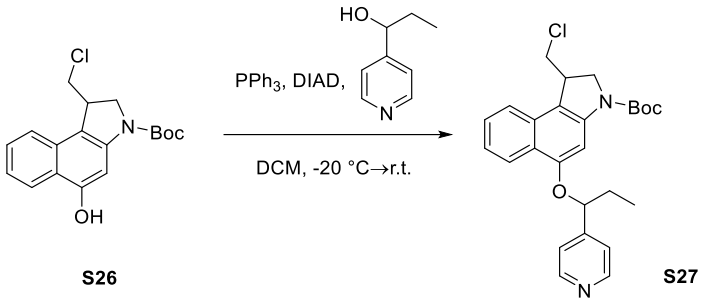

S26 **S27**

S26 (70 mg, 0.21 mmol, 1 equiv), 1-(pyridin-4-yl)propan-1-ol (58 mg, 0.42 mmol, 2 equiv) and PPh_3 (125 mg, 0.46 mmol, 2.2 equiv) were dissolved in CH_2Cl_2 (4 mL) in and the mixture was cooled to -20 °C. After the dropwise addition of DIAD (83 µL, 0.42 mmol, 2 equiv), the mixture was allowed to reach room temperature and stirred for 2 hours. Then the mixture was concentrated over silica and purified by flash chromatography on silica gel (Hexane/EtOAc 5:1) affording **S27** as a pale yellow solid (58 mg, 61%). **^{1}H NMR** (400 MHz, Chloroform-*d*) δ 8.58 – 8.52 (m, 2H), 8.39 (d, *J* = 8.4 Hz, 1H), 7.67 – 7.60 (m, 1H), 7.56 – 7.49 (m, 1H), 7.44 – 7.36 (m, 1H), 7.33 (s, 1H), 5.41 (s, 1H), 4.26 – 4.14 (m, 1H), 4.11 – 3.98 (m, 1H), 3.97 – 3.82 (m, 2H), 3.45 – 3.29 (m, 1H), 2.16 – 1.99 (m, 2H), 1.53 (s, 9H), 1.07 (td, *J* = 7.4, 5.4 Hz, 1H). **^{13}C NMR** (126 MHz, $CDCl_3$) δ 154.62, 152.50, 150.08, 130.51, 127.86, 123.47, 123.46, 122.69, 122.07, 121.33, 98.00, 97.93, 79.55, 53.15, 46.60, 46.47, 41.79, 30.85, 28.59, 28.58, 28.33, 9.96, 9.85. Expected mass: 452.19 **MS (ESI$^+$)** *m/z* found: 453.2 $[M+H]^+$.

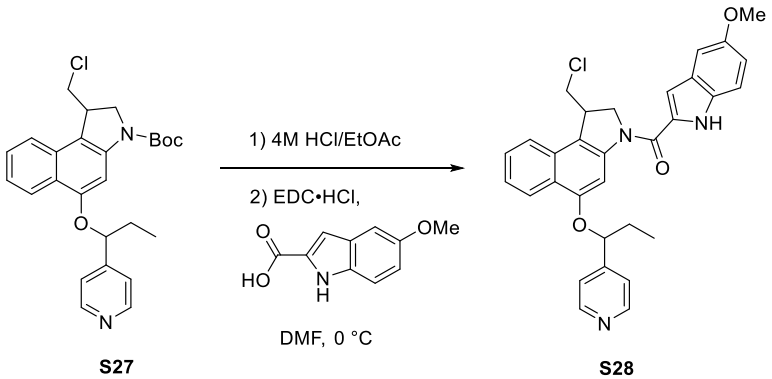

S27 **S28**

S27 (15 mg, 0.033 mmol, 1 equiv) was treated with 4 M HCl/EtOAc (0.5 mL) at room temperature and stirred for 1 hour. Then the mixture was concentrated and dried under vacuum. The residue was dissolved in DMF (1.0 mL) and cooled to 0 °C. 5-methoxy-1H-indole-2-carboxylic acid (6.3 mg, 0.033 mmol, 1 equiv) and EDC·HCl (20 mg, 0.099 mmol, 3 equiv) were added and the mixture was stirred at 0 °C for 2 hours. Then the mixture was

diluted with $NaHCO_3$ saturated solution (10 mL) and extracted with EtOAc (3 x 5 mL). The organic layers were combined, washed with brine (2 x 5 mL), dried over Na_2SO_4 and concentrated. The crude was purified by flash chromatography on silica gel (Hexane/EtOAc from 6:4 to 2:8) affording **S28** as a white solid (13 mg, 75%). **^{1}H NMR** (500 MHz, Chloroform-*d*) δ 9.22 (s, 1H), 9.18 (s, 1H), 8.66 – 8.56 (m, 1H), 8.52 (d, *J* = 5.3 Hz, 1H), 8.49 – 8.39 (m, 1H), 7.96 (s, 1H), 7.74 – 7.70 (m, 1H), 7.61 – 7.56 (m, 1H), 7.51 – 7.45 (m, 1H), 7.39 (d, *J* = 5.2 Hz, 1H), 7.35 (d, *J* = 8.9 Hz, 1H), 7.31 (s, 1H), 7.13 – 7.10 (m, 1H), 7.05 – 6.97 (m, 2H), 5.42 – 5.37 (m, 1H), 4.79 – 4.72 (m, 1H), 4.68 – 4.57 (m, 1H), 4.16 – 4.04 (m, 1H), 3.99 – 3.92 (m, 1H), 3.87 (d, *J* = 1.4 Hz, 3H), 3.48 – 3.37 (m, 1H), 2.19 – 2.12 (m, 1H), 2.09 – 2.02 (m, 1H), 1.14 – 1.05 (m, 3H). **^{13}C NMR** (126 MHz, $CDCl_3$) δ 160.65, 160.62, 154.89, 154.51, 154.48, 150.45, 150.35, 150.28, 150.26, 142.13, 131.30, 130.66, 130.57, 130.03, 128.45, 128.07, 128.04, 124.40, 124.34, 123.87, 123.60, 122.46, 121.33, 121.18, 117.01, 116.47, 112.76, 106.27, 106.14, 102.64, 102.62, 99.87, 99.81, 80.06, 55.88, 55.38, 55.22, 46.18, 46.04, 43.36, 43.23, 31.06, 30.82, 10.09, 10.00. Expected mass: 525.18 **MS (ESI$^+$)** *m/z* found: 526.3 $[M+H]^+$.

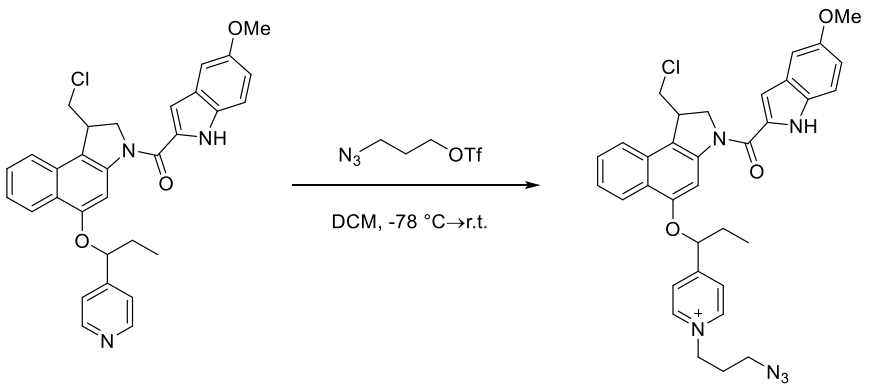

S28 **S29**

S28 (5 mg, 0.01 mmol, 1 equiv) was dissolved in CH_2Cl_2 (300 µL) and cooled to -78 °C. Then 3-azidopropyl trifluoromethanesulfonate (2.3 mg, 0.01 mmol, 1 equiv) was added dropwise. The mixture was stirred at -78 °C for 10 minutes; then it was allowed to reach room temperature and stirred for additional 2 hours. The mixture was concentrated and the residue was purified by RP-HPLC affording N_3Duo-OMe (**S29**) as a pale yellow foam (2.55 mg, 35%). Pair of diastereomers (60:40 ratio): **^{1}H NMR** (400 MHz, Chloroform-*d*) δ 10.42 (s, 0.3H), 10.21 (s, 0.5H), 9.12 (d, *J* = 5.9 Hz, 2H), 8.42 (dd, *J* = 8.3, 3.0 Hz, 1H), 8.05 (d, *J* = 5.7 Hz, 1H), 7.90 (d, *J* = 5.7 Hz, 1H), 7.80 – 7.73 (m, 1H), 7.72 – 7.61 (m, 2H), 7.55 (ddd, *J* = 8.2, 6.8, 1.2 Hz, 1H), 7.38 (d, *J* = 8.9 Hz, 0.6H), 7.34 (d, *J* = 9.0 Hz, 0.4H), 7.13 (d, *J* = 2.4 Hz, 0.6H), 7.09 (d, *J* = 2.4 Hz, 0.4H), 7.01 – 6.85 (m, 2H), 5.61 – 5.51 (m, 1H), 4.92 – 4.74 (m, 2H), 4.74 – 4.67 (m, 1H), 4.65 – 4.53 (m, 1H), 4.21 – 4.12 (m, 0.6H), 4.10 – 3.97 (m, 0.8H), 3.95 – 3.87 (m, 0.6H), 3.88 (s, 1.8H), 3.85 (s, 1.2H), 3.57 – 3.49 (m, 0.6H), 3.47 – 3.33 (m, 2.4H), 2.35 – 2.21 (m, 2H), 2.22 – 2.09 (m, 2H), 1.25 – 1.15 (m, 3H). **^{13}C NMR** (126 MHz, $CDCl_3$) δ 162.35, 162.24, 161.09, 154.79, 154.69, 153.12, 152.95, 145.37, 141.81, 141.65, 131.99, 131.82, 130.40, 130.26, 130.19, 130.09, 128.46, 128.39, 128.14, 127.96, 125.81, 125.50, 124.89, 124.80, 123.26, 123.20, 123.14, 123.11, 122.68, 117.74, 117.63, 116.92, 116.76, 113.43, 113.32, 106.36, 106.19, 102.28, 102.14, 100.79, 100.43, 79.32, 59.23, 59.17, 55.82, 55.80, 55.40, 55.10, 47.86, 47.79, 46.46, 45.89, 43.20, 42.93, 30.75, 30.71, 30.40, 30.34, 10.06, 10.02. Expected mass: 609.24, **LC-MS (ESI$^+$)** RT= 2.68 min. *m/z* found: 609.5 $[M]^+$. **HRMS**: 609.23328 (± 6.92 ppm).

Synthesis of Pyridinium-Duocarmycin derivative (N_3PyDuo-OMe) (S30)

Primary pyridinium derivatives were synthesized according to the synthetic strategy used for the secondary Py derivatives and using 4-pyridinemethanol as pyridine source.

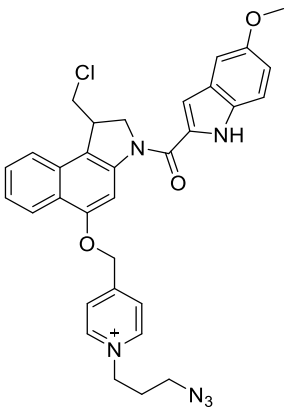

S30

^{1}H NMR (400 MHz, DMSO-d_6) δ 11.56 (d, *J* = 2.2 Hz, 1H), 9.16 – 9.07 (m, 2H), 8.44 – 8.34 (m, 3H), 8.12 (s, 1H), 7.99 (d, *J* = 8.3 Hz, 1H), 7.65 (ddd, *J* = 8.3, 6.8, 1.3 Hz, 1H), 7.52 (ddd, *J* = 8.3, 6.8, 1.1 Hz, 1H), 7.41 (d, *J* = 8.9 Hz, 1H), 7.19 – 7.11 (m, 2H), 6.93 (dd, *J* = 8.9, 2.5 Hz, 1H), 5.71 (s, 2H), 4.85 (dd, *J* = 11.0, 9.2 Hz, 1H), 4.70 (t, *J* = 7.2 Hz, 2H), 4.60 (dd, *J* = 11.0, 2.3 Hz, 1H), 4.39 – 4.29 (m, 1H), 4.07 (dd, *J* = 11.1, 3.2 Hz, 1H), 3.95 (dd, *J* = 11.1, 6.6 Hz, 1H), 3.79 (s, 3H), 3.50 (t, *J* = 6.5 Hz, 2H), 2.23 (p, *J* = 6.8 Hz, 2H). **^{13}C NMR** (126 MHz, DMSO) δ 160.33, 156.73, 153.92, 153.37, 144.89, 142.20, 131.64, 130.77, 129.75, 127.97, 127.52, 125.24, 124.31, 123.18, 122.77, 122.32, 117.70, 115.64, 113.22, 105.57, 102.10, 98.72, 67.40, 58.21, 55.29, 55.13, 47.75, 47.59, 41.07, 29.70. Expected mass: 581.20, **LC-MS (ESI$^+$)** RT= 2.49 min. *m/z* found: 581.4 $[M]^+$.

NMR spectra:

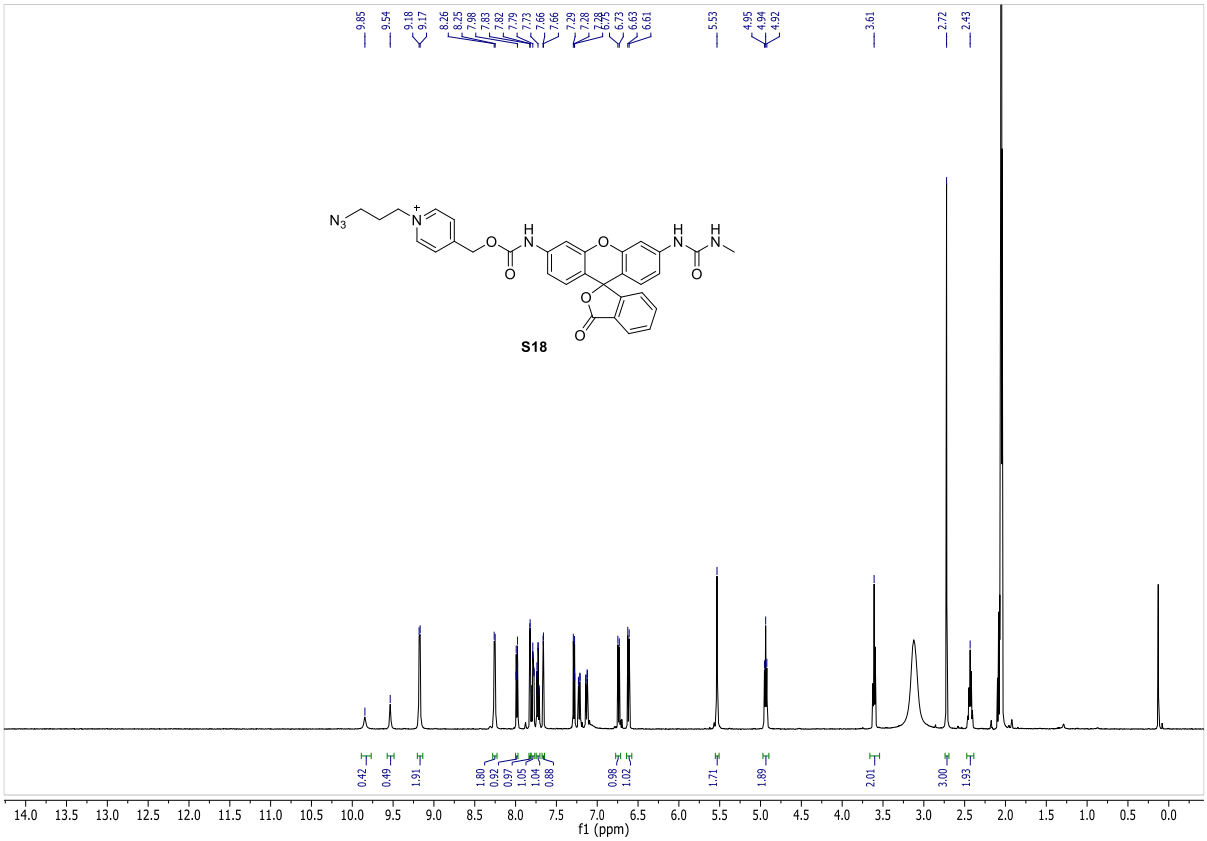

^{1}H NMR of compound **S18**.

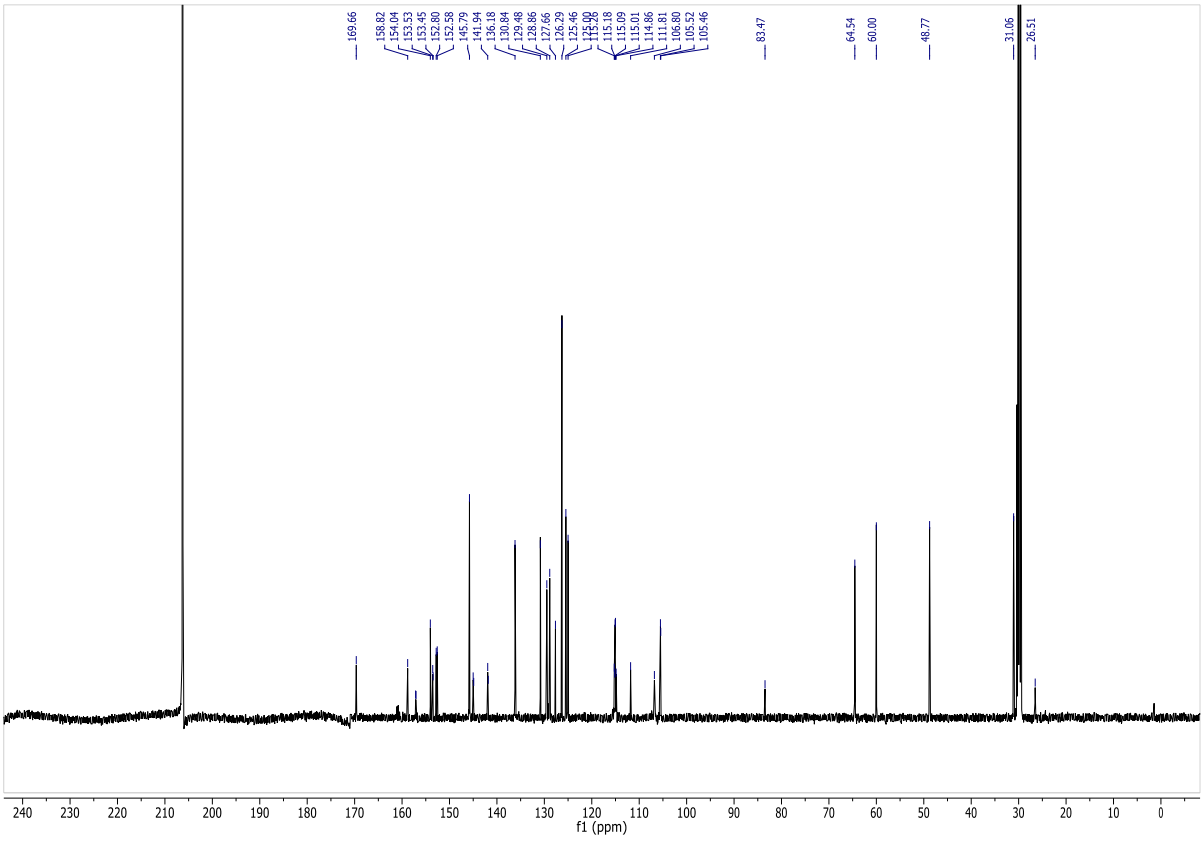

^{13}C NMR of compound **S18**.

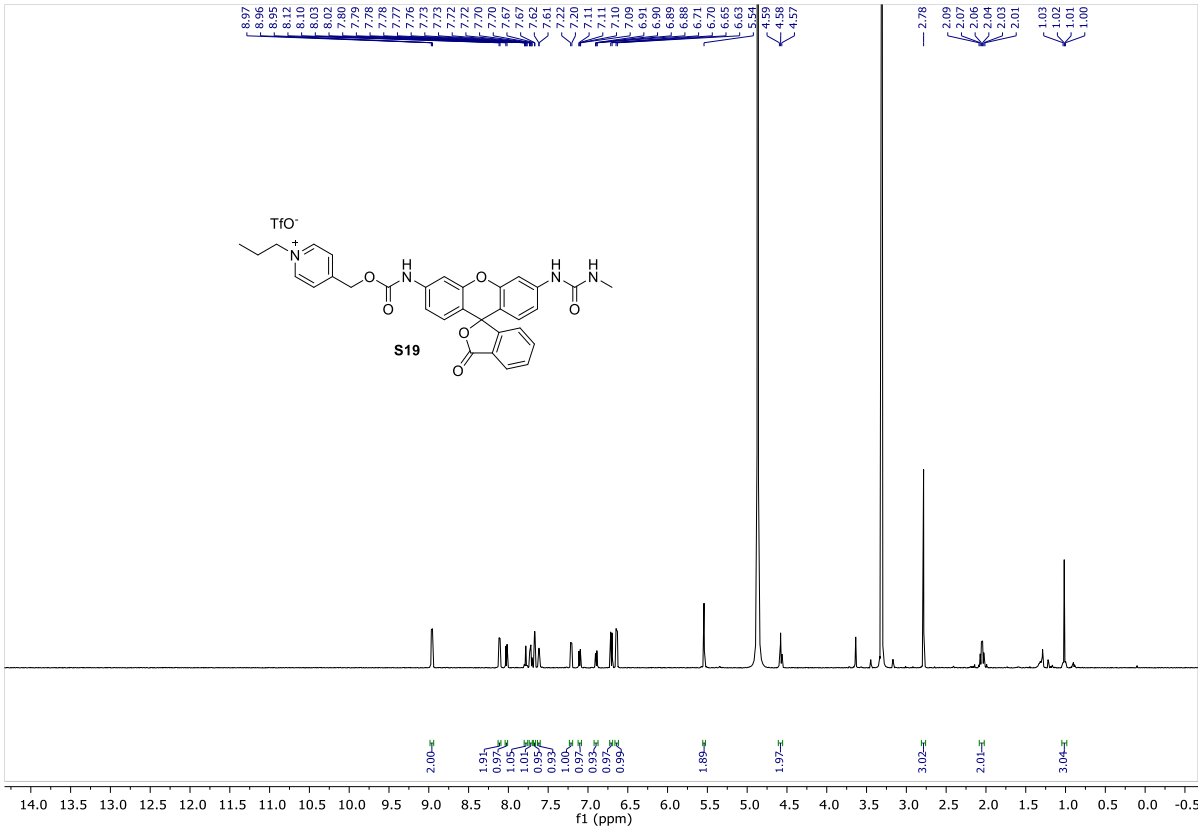

^{1}H NMR of compound **S19**.

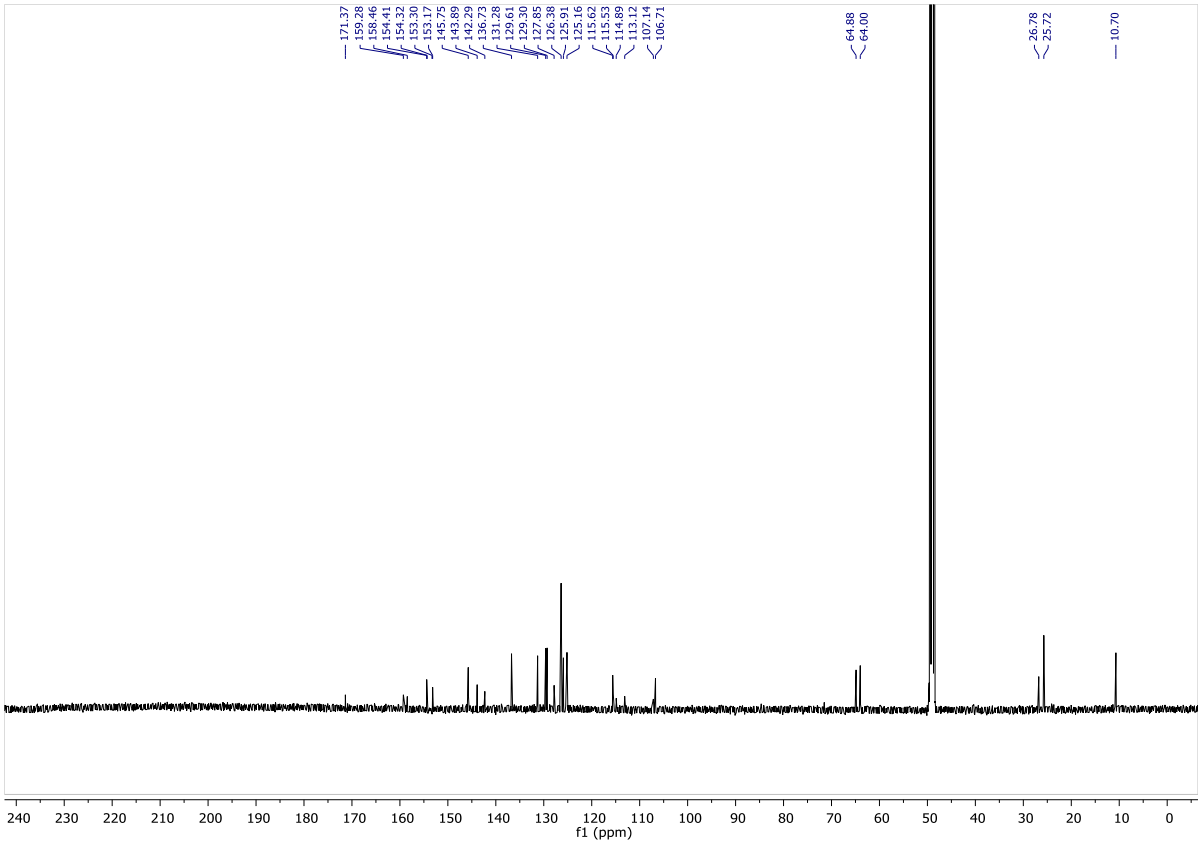

^{13}C NMR of compound **S19**.

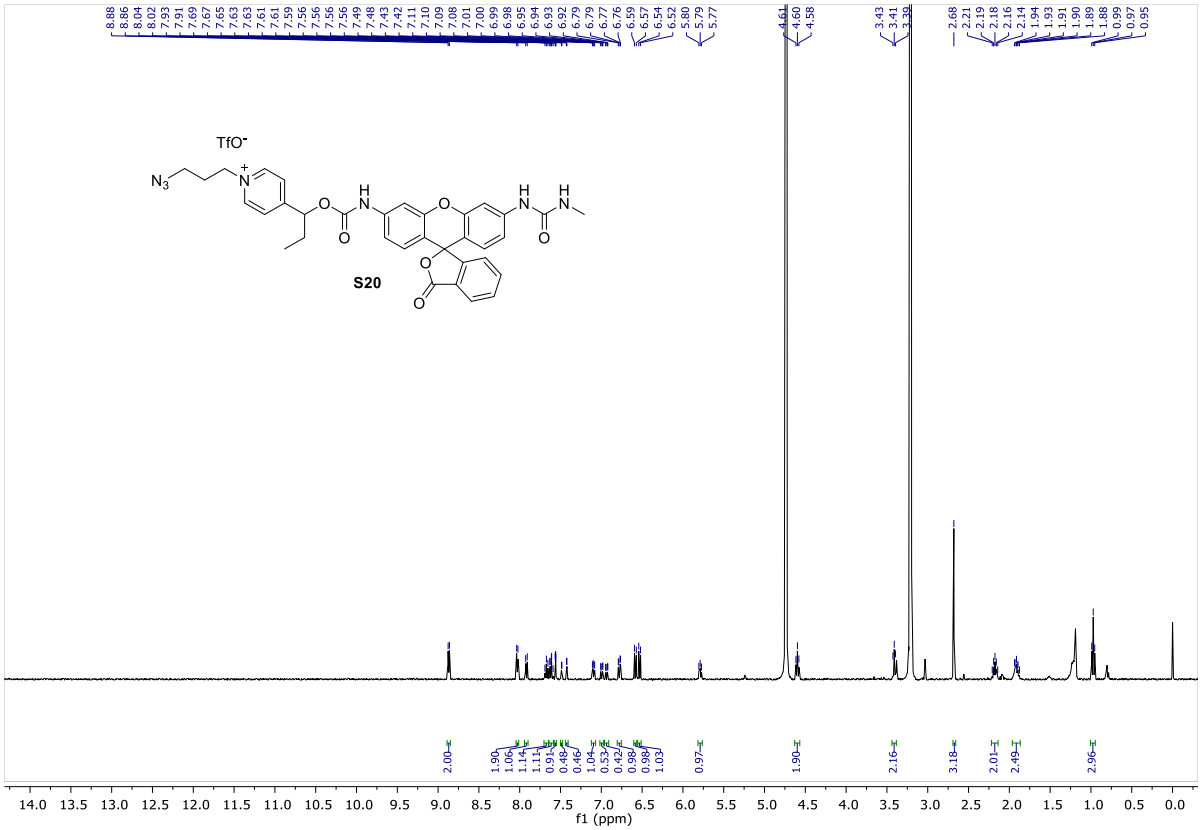

^{1}H NMR of compound **S20**.

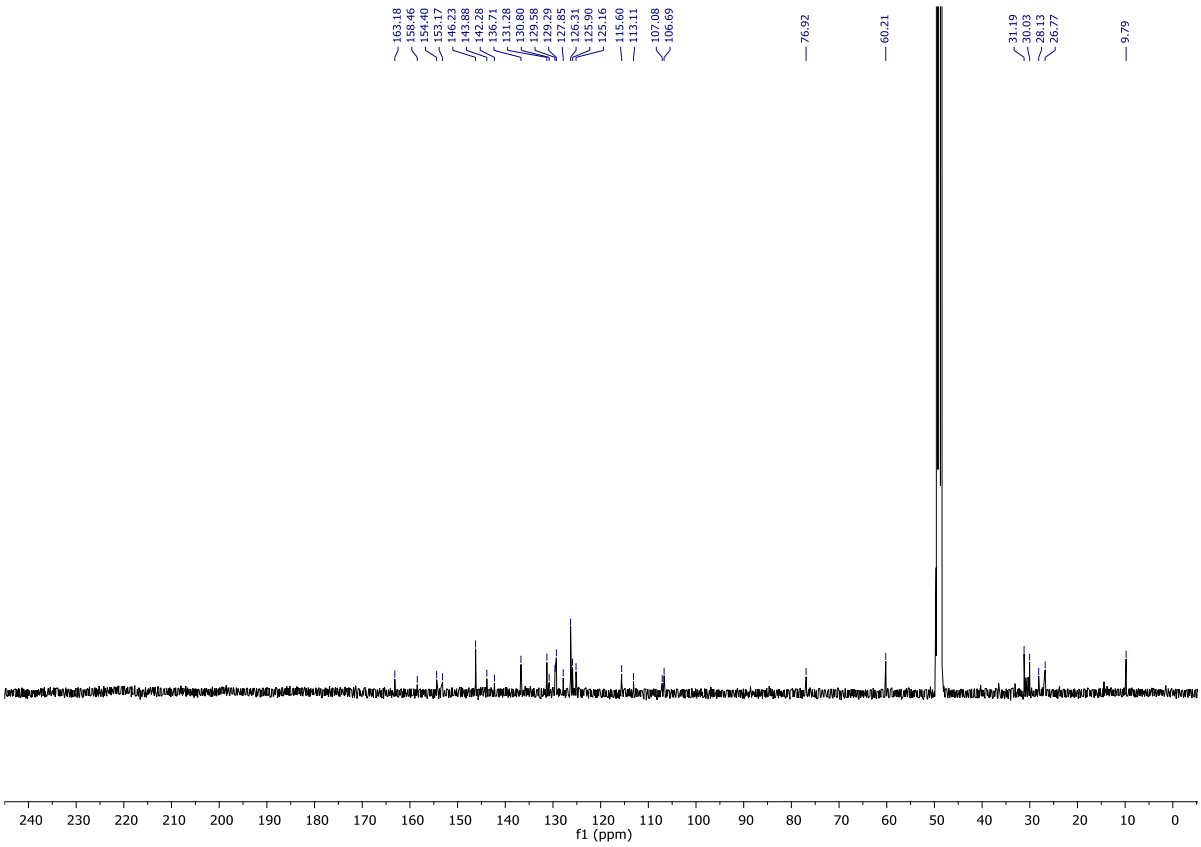

^{13}C NMR of compound **S20**.

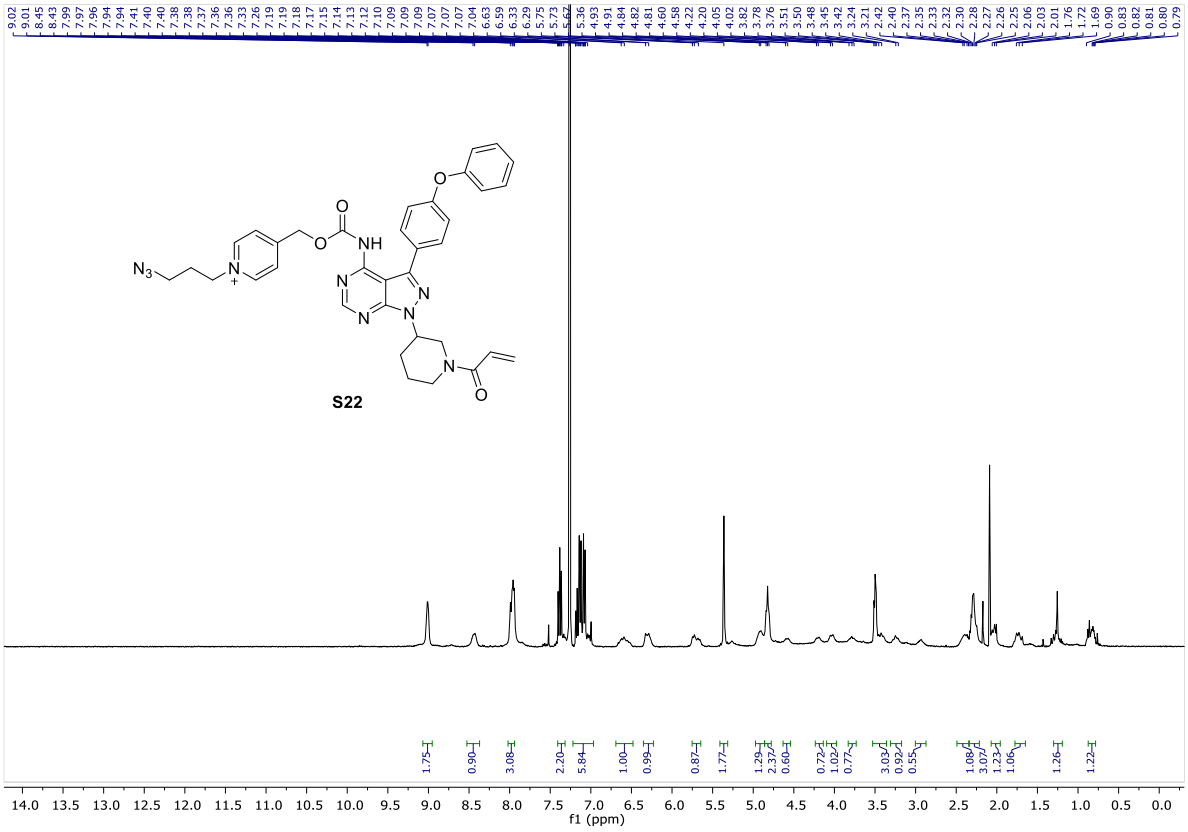

^{1}H NMR of compound **S22**.

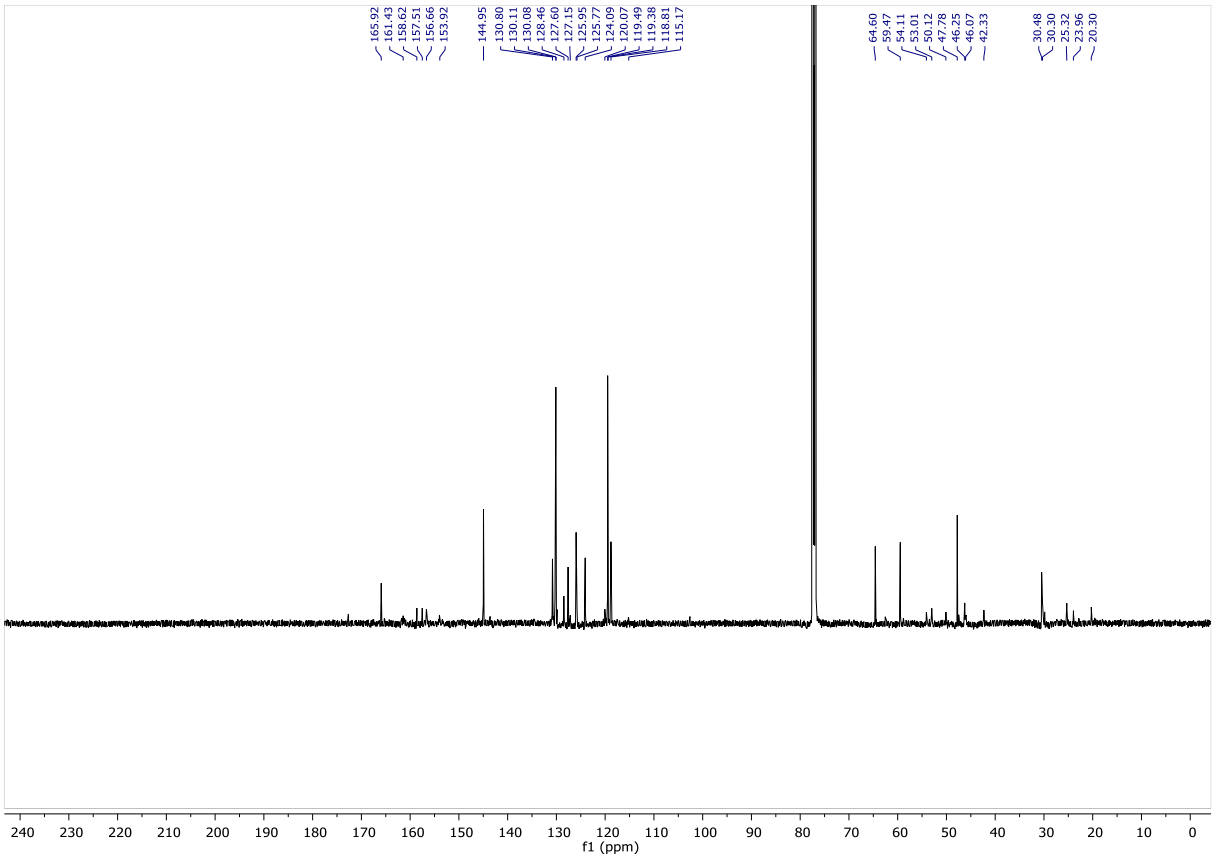

^{13}C NMR of compound **S22**.

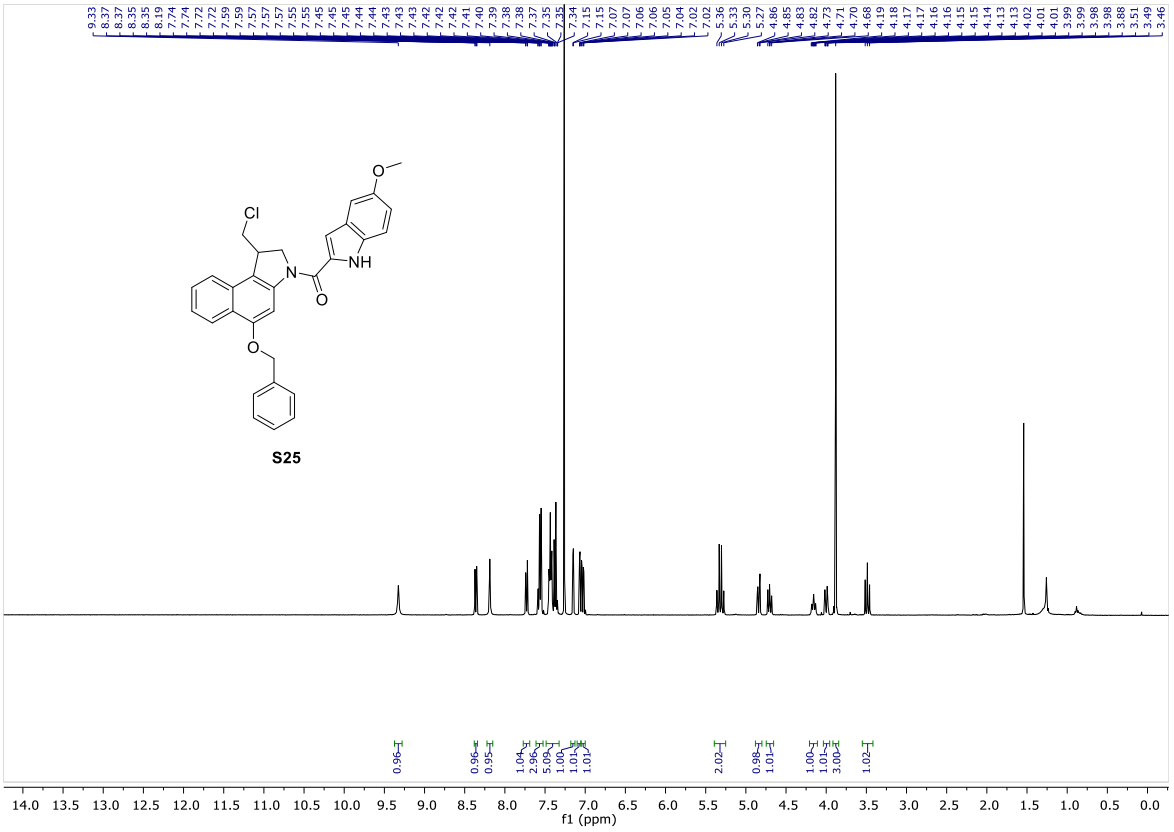

^{1}H NMR of compound **S25**.

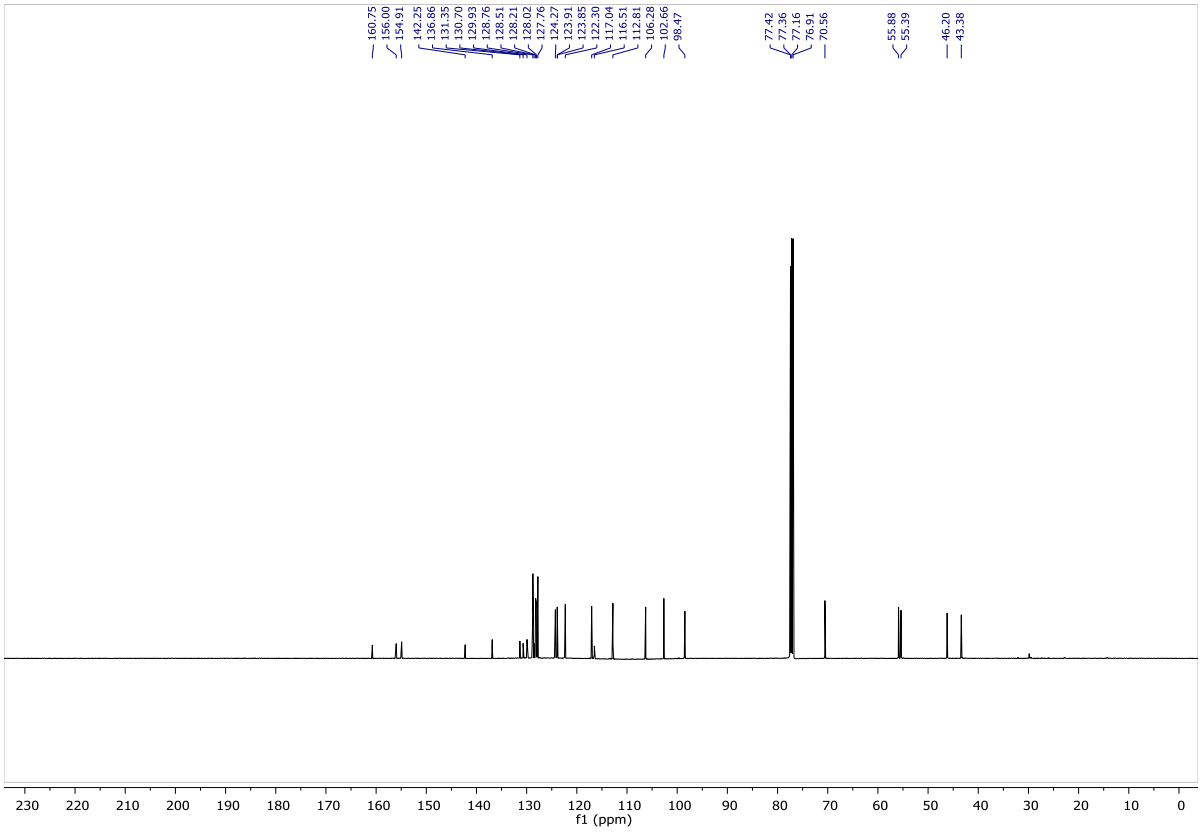

^{13}C NMR of compound **S25**.

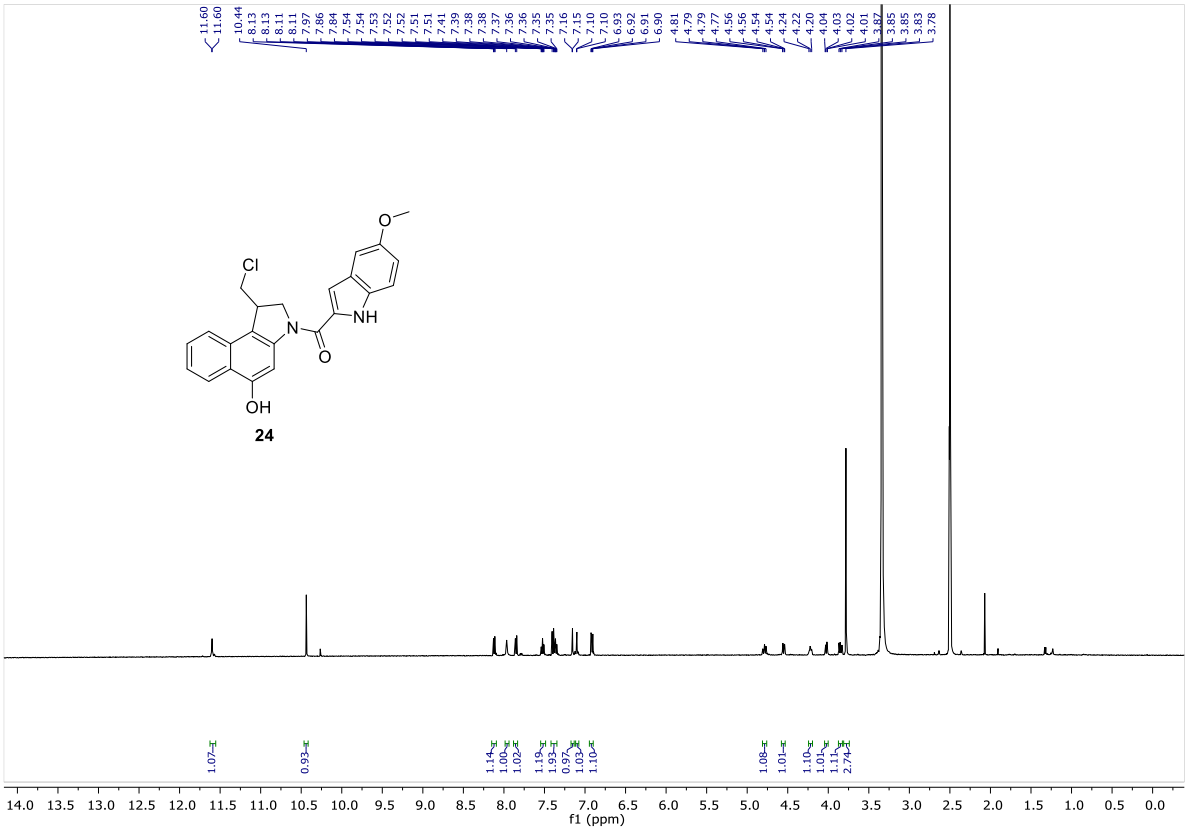

^{1}H NMR of compound **24**.

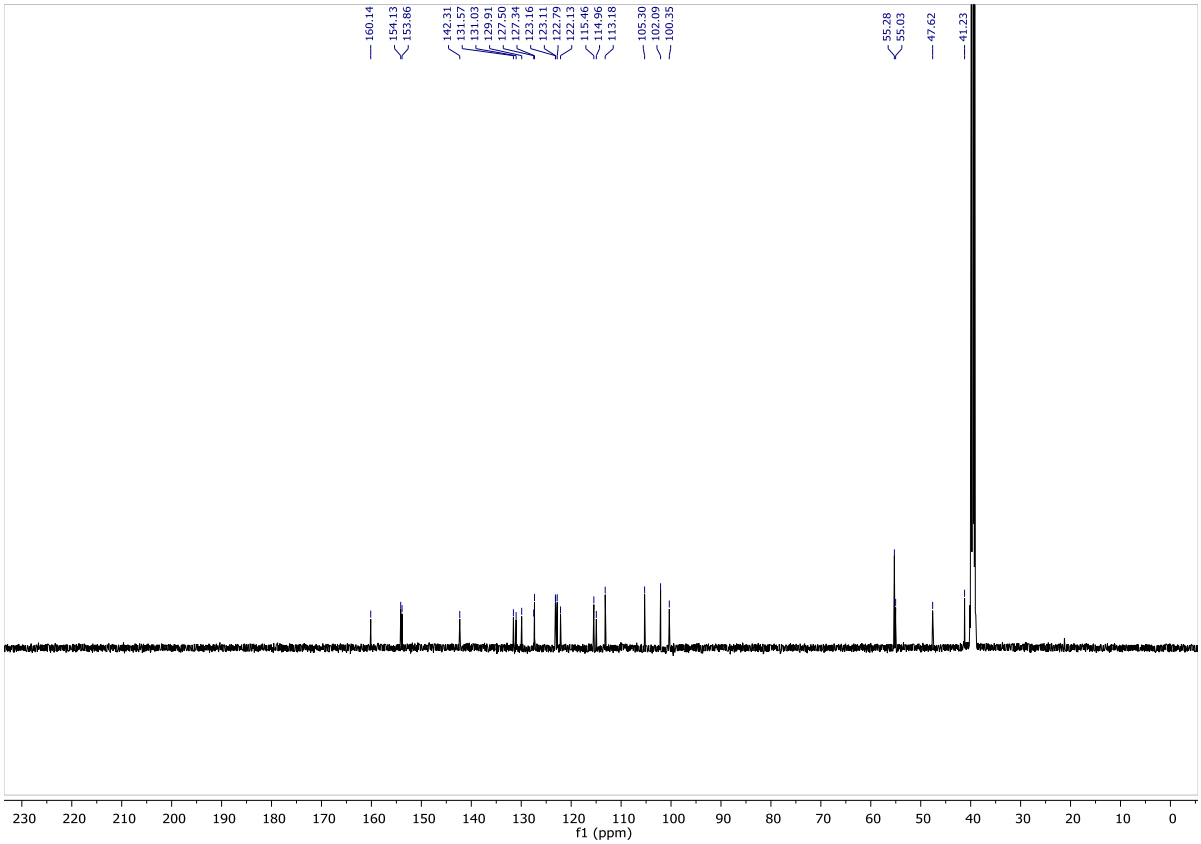

^{13}C NMR of compound **24**.

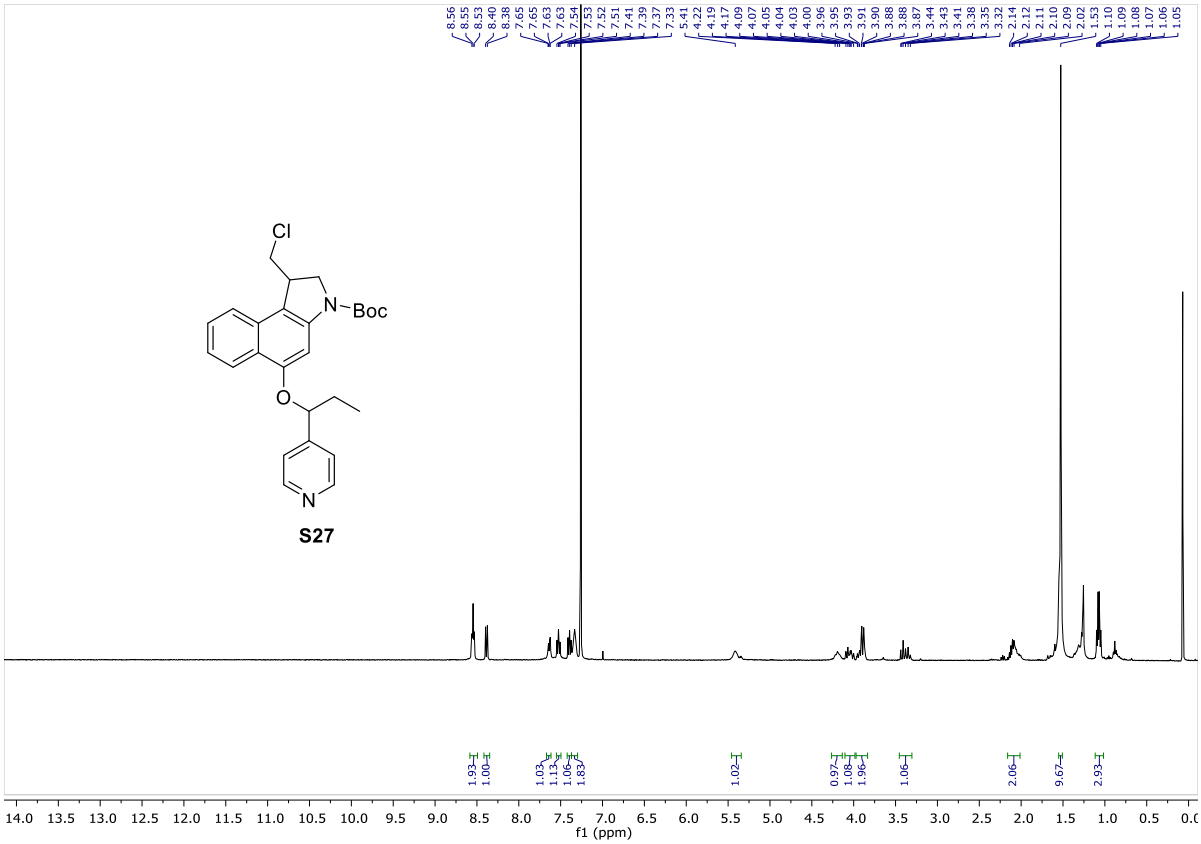

^{1}H NMR of compound **S27**.

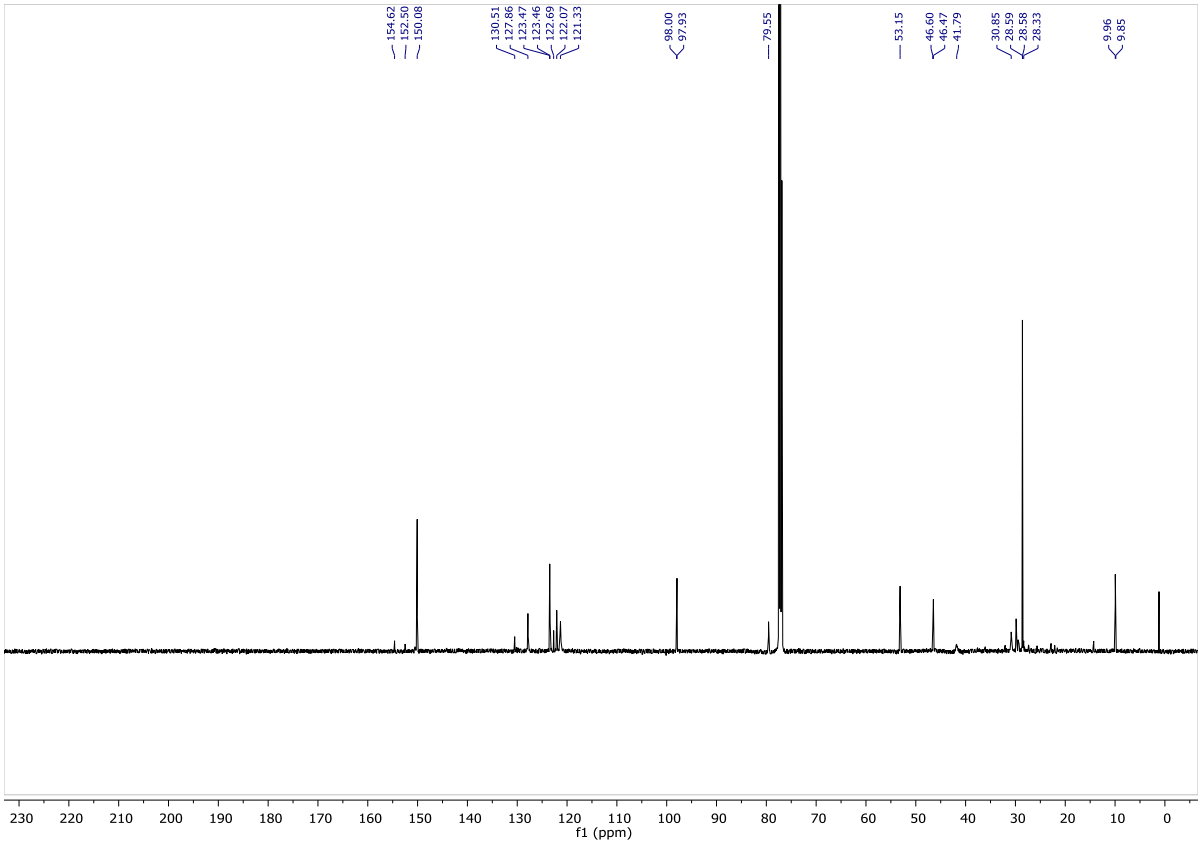

^{13}C NMR of compound **S27**.

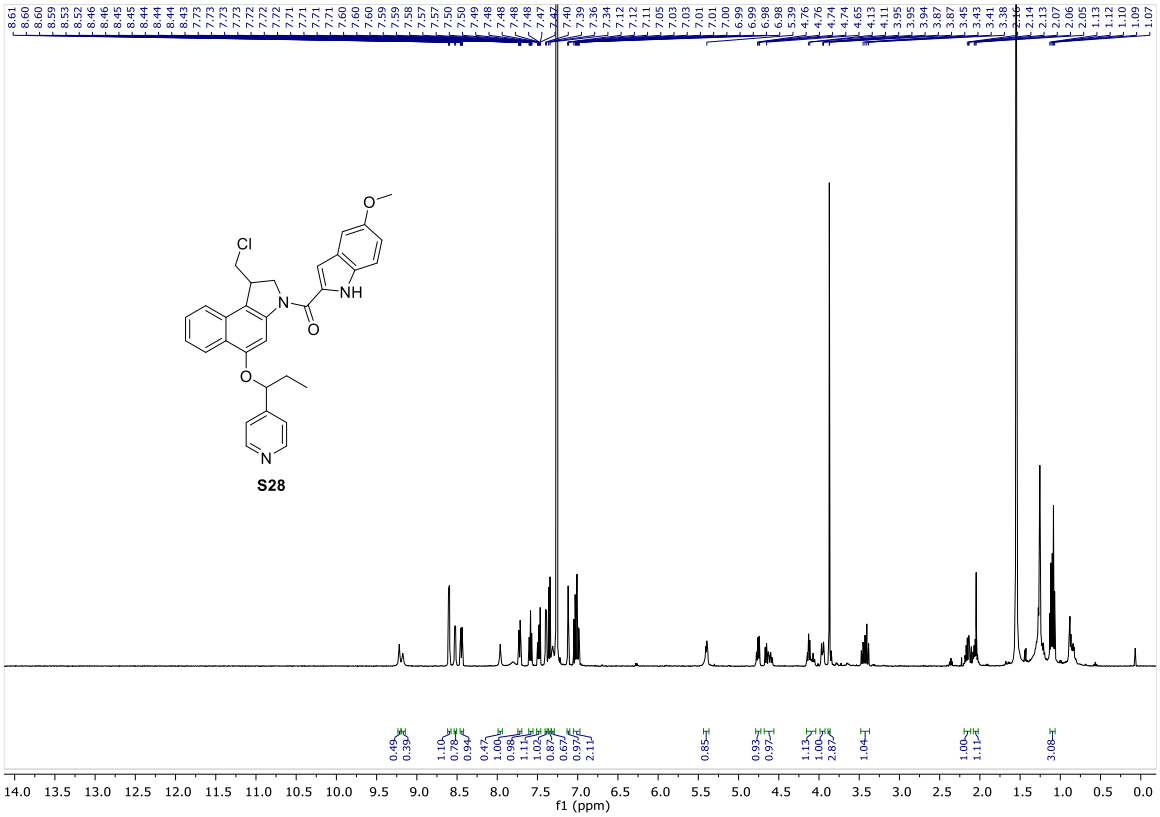

^{1}H NMR of compound **S28**.

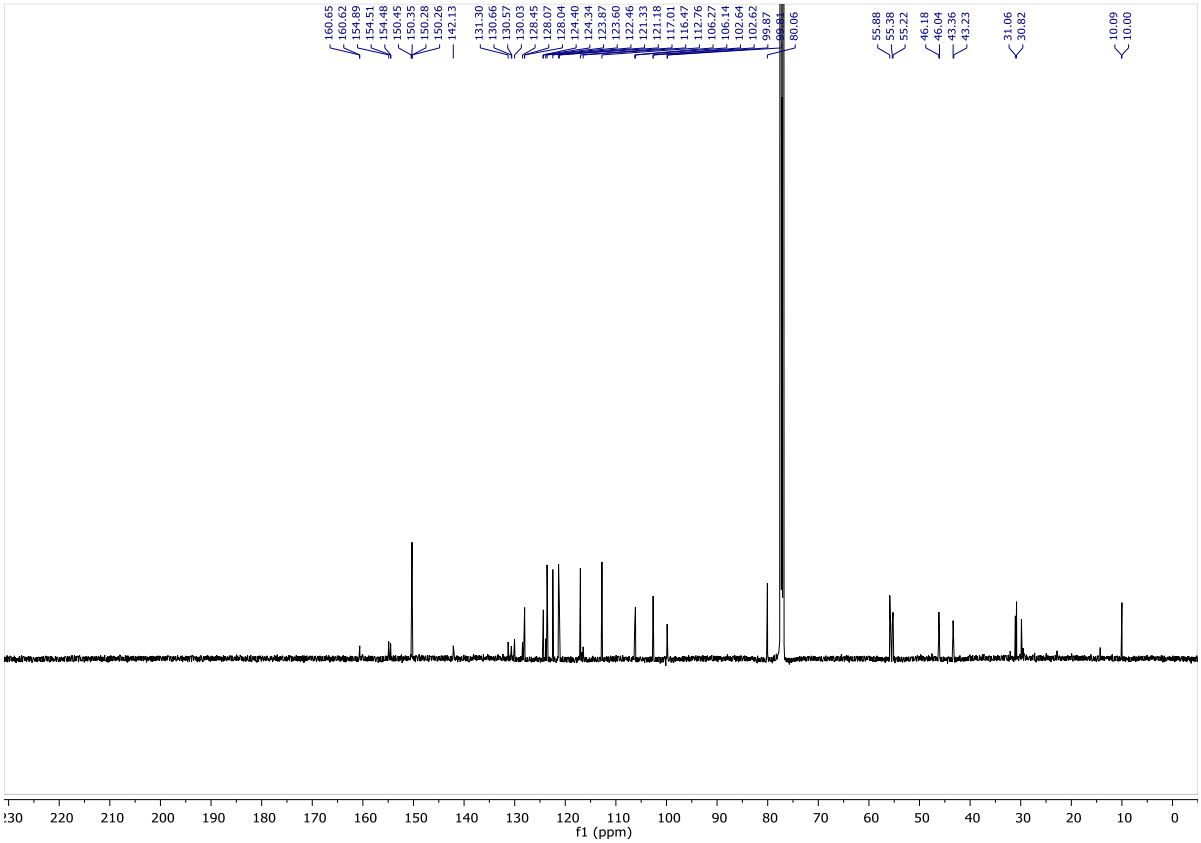

^{13}C NMR of compound **S28**.

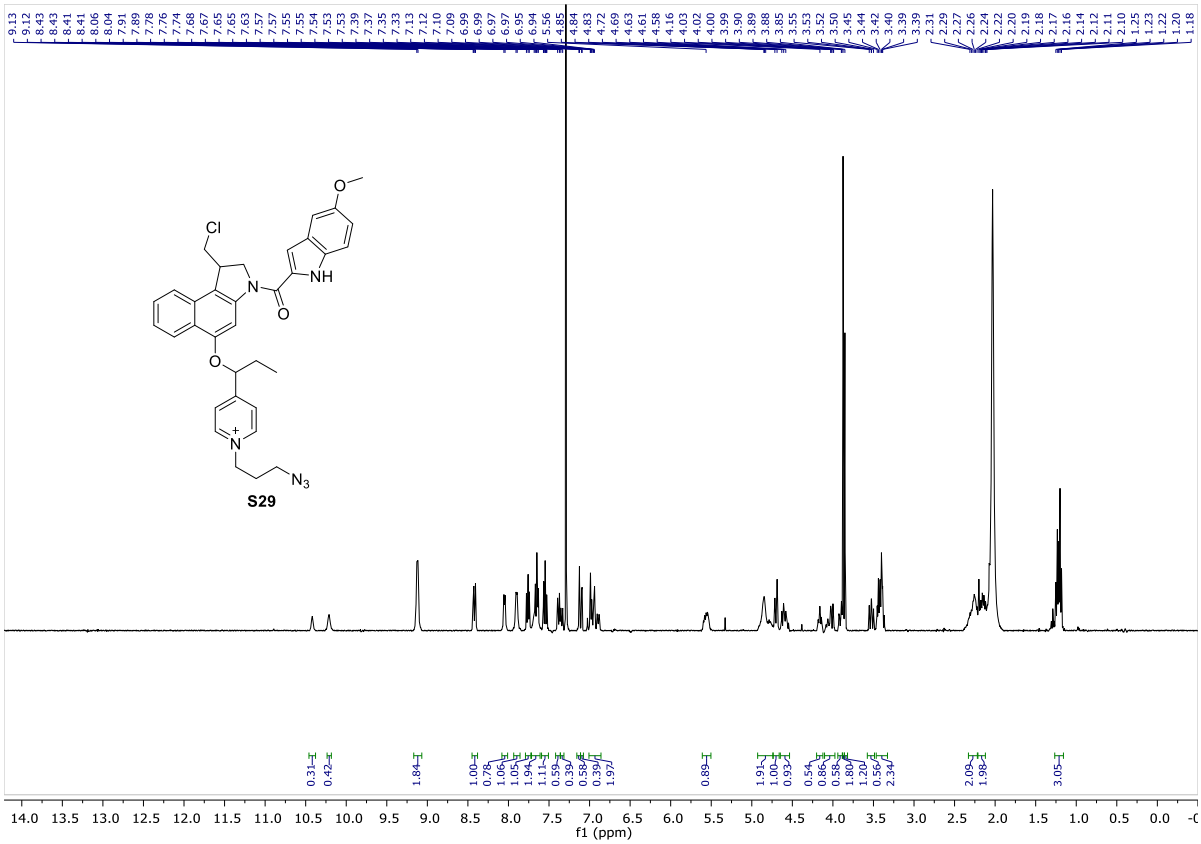

^{1}H NMR of compound **S29**.

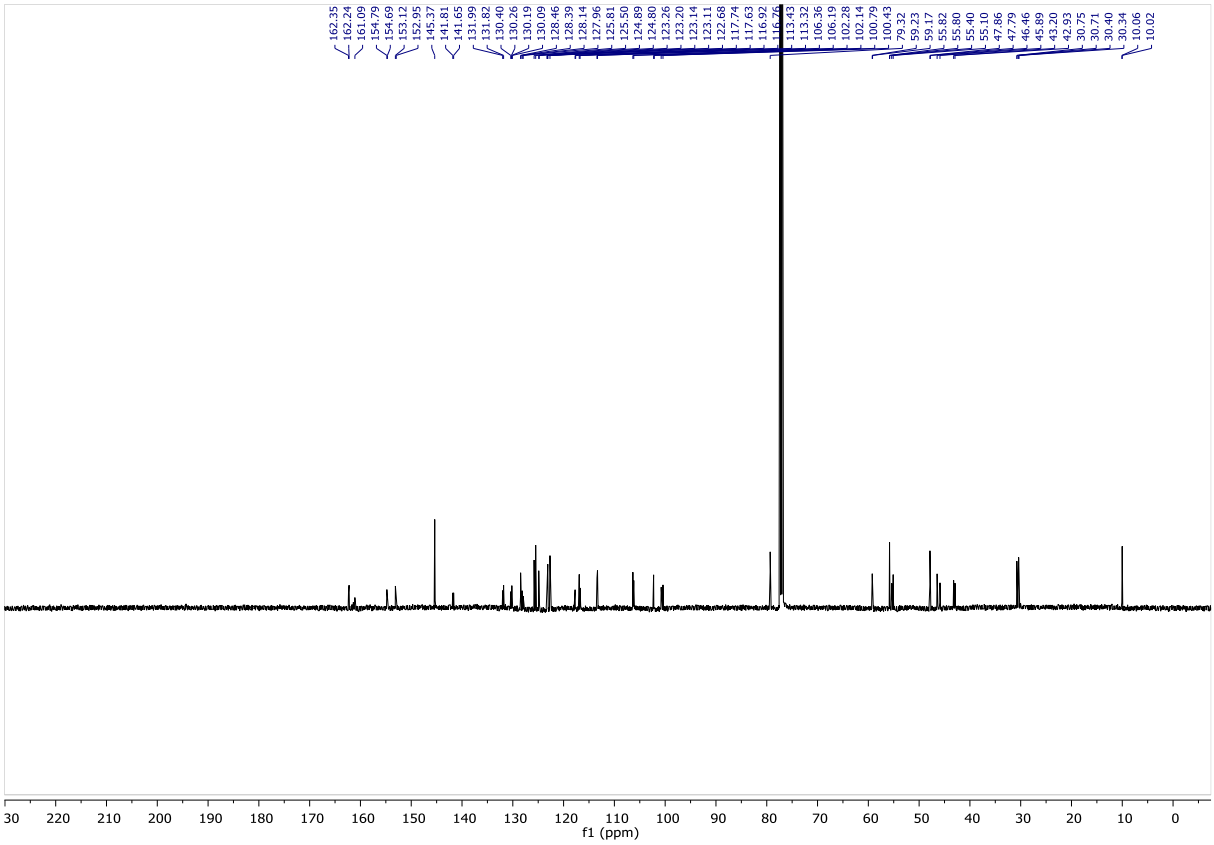

^{13}C NMR of compound **S29**.

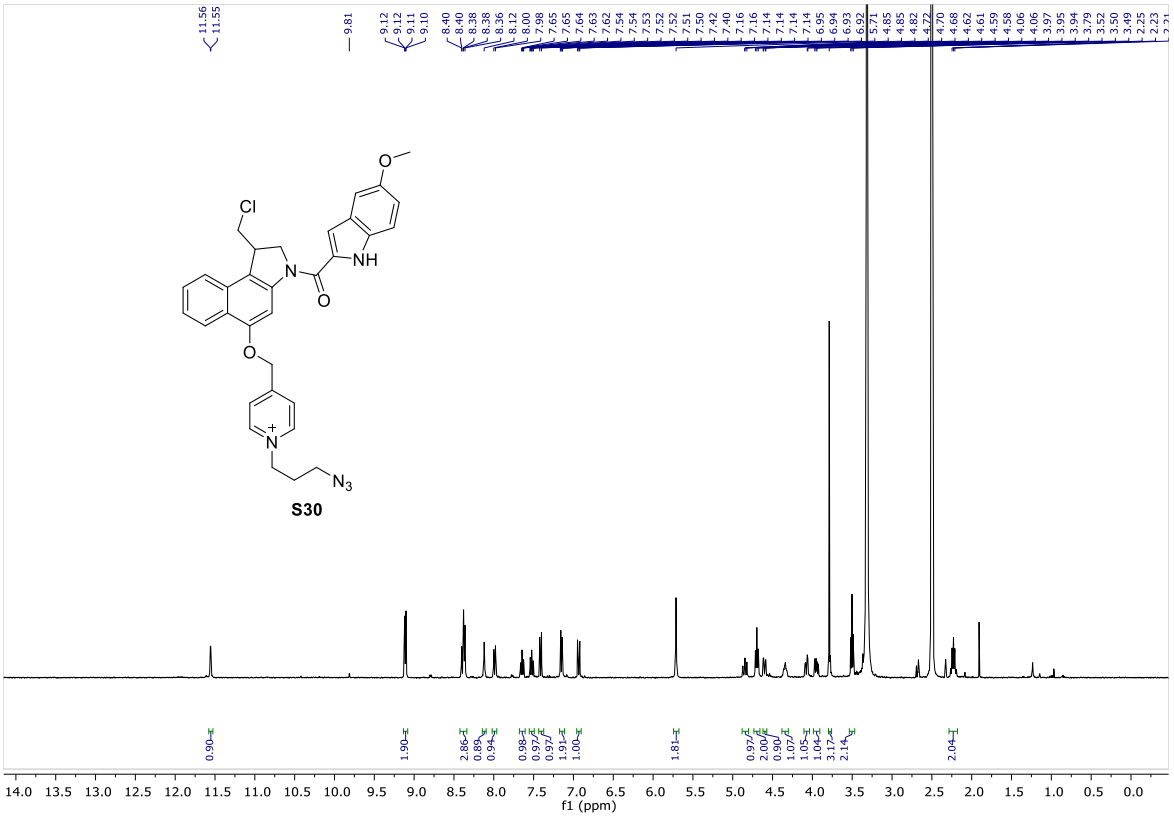

^{1}H NMR of compound **S30**.

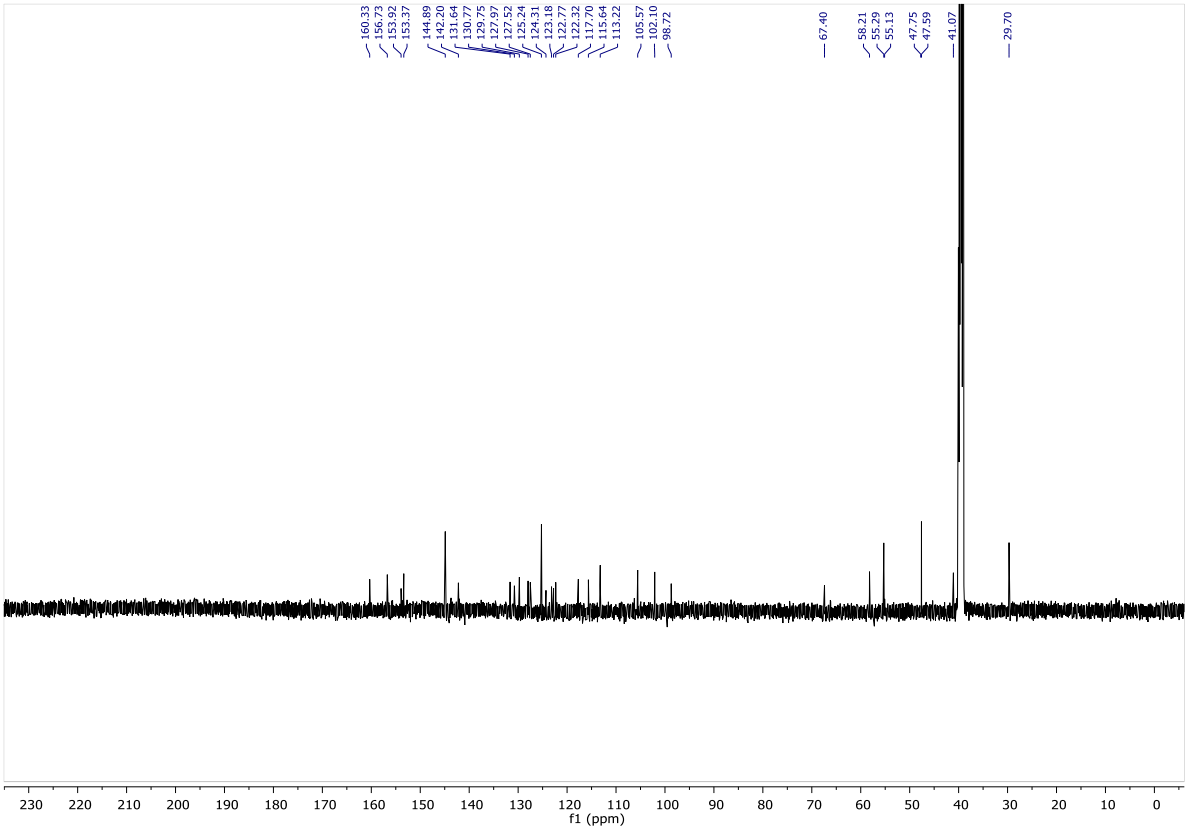

^{13}C NMR of compound **S30**.

References

1. Hall, M.P. et al. Engineered Luciferase Reporter from a Deep Sea Shrimp Utilizing a Novel Imidazopyrazinone Substrate. ACS Chemical Biology 7, 1848-1857 (2012).

2. Liu, Z.Z. et al. Semiconductor quantum dots photosensitizing release of anticancer drug. Chem. Commun. 47, 1482-1484 (2011).

3. Kramer, J.R. & Deming, T.J. Preparation of Multifunctional and Multireactive Polypeptides via Methionine Alkylation. Biomacromolecules 13, 1719-1723 (2012).

4. Lou, K. & Lovell, J.F. A quenched binuclear ruthenium(II) dimer activated by another photosensitizer. Chem. Commun. 50, 3231-3233 (2014).

5. Keppler, A. et al. A general method for the covalent labeling of fusion proteins with small molecules in vivo. Nat Biotechnol 21, 86-89 (2003).

6. Lemercier, G., Gendreizig, S., Kindermann, M. & Johnsson, K. Inducing and sensing protein--protein interactions in living cells by selective cross-linking. Angew Chem Int Ed Engl 46, 4281-4284 (2007).

7. Winkler, D.E. & Whetstone, R.R. Some Observations on the Pechmann Reaction1. The Journal of Organic Chemistry 26, 784-787 (1961).

8. Kralovec, J. et al. Synthesis of methotrexate-antibody conjugates by regiospecific coupling and assessment of drug and antitumor activities. Journal of Medicinal Chemistry 32, 2426-2431 (1989).

9. Francis, C.L. et al. Total Synthesis of Methotrexate-γ-TRIS-Fatty Acid Conjugates. Australian Journal of Chemistry 55, 635-645 (2002).

10. Griss, R. et al. Bioluminescent sensor proteins for point-of-care therapeutic drug monitoring. Nat Chem Biol 10, 598-603 (2014).

11. Lakowicz, J.R. Principles of Fluorescence Spectroscopy, Edn. 3rd. (Springer, 2006).

12. Suzuki, K. et al. Five colour variants of bright luminescent protein for real-time multicolour bioimaging. Nat Commun 7, 13718 (2016).

13. UV-Vis-IR Spectral Software 1.2, Fluortools, www.fluortools.com

14. Chouikhi, D. et al. Expanding the Scope of PNA-Encoded Synthesis (PES): Mtt-Protected PNA Fully Orthogonal to Fmoc Chemistry and a Broad Array of Robust Diversity-Generating Reactions. Chem. Eur. J. 18, 12698-12704 (2012).

15. Gorska, K., Manicardi, A., Barluenga, S. & Winssinger, N. DNA-templated release of functional molecules with an azide-reduction-triggered immolative linker. Chemical Communications 47, 4364-4366 (2011).

16. Liu, N. et al. Direct and two-step bioorthogonal probes for Bruton's tyrosine kinase based on ibrutinib: a comparative study. Organic & Biomolecular Chemistry 13, 5147-5157 (2015).

17. WO2016/079693 A Process For The Preparation Of Ibrutinib.

18. Machleidt, T. et al. NanoBRET--A Novel BRET Platform for the Analysis of Protein-Protein Interactions. ACS Chem Biol 10, 1797-1804 (2015).

19. Tietze, L.F. et al. Asymmetric synthesis and biological evaluation of glycosidic prodrugs for a selective cancer therapy. ChemMedChem 3, 1946-1955 (2008).

Supplementary Materials of Chapter V

Supplementary Figures

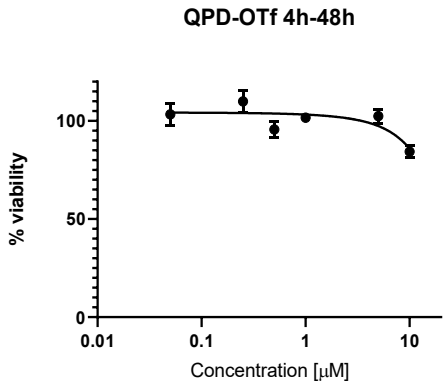

Figure V-S1. WST-1 viability assay in MCF-7 cells. Cells were treated with QPD-OTf for 4 hours; washed, incubated for 48 hours, then WST-1 assay was performed. Experiments were performed in triplicates; curve fitting was performed with GraphPad 8; data are presented as mean value +/- the standard deviation (SD).

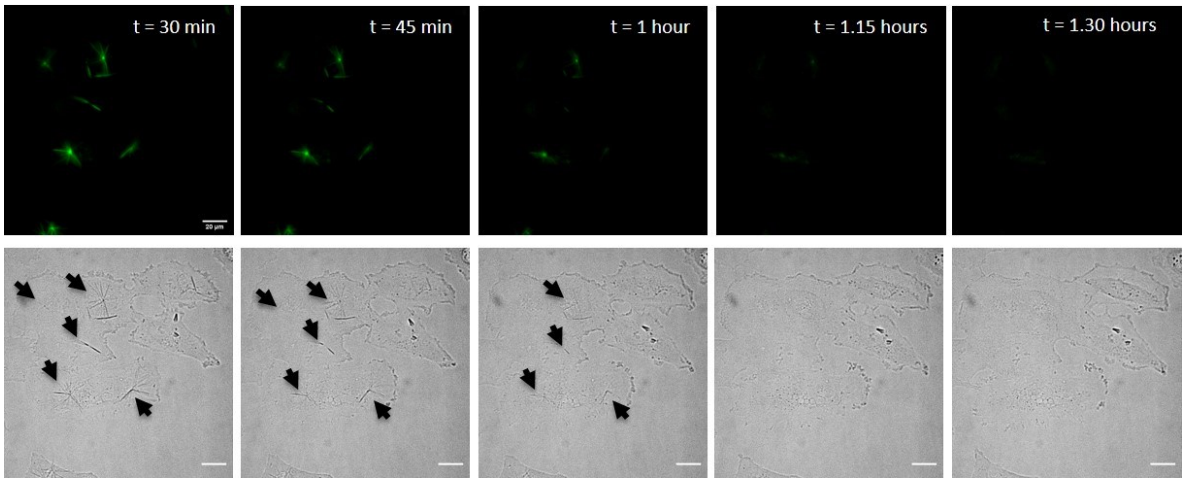

Figure V-S2. Crystals wash out. HeLa cells treated with QPD-OTf (20 μM, 1.5 hours), washed and imaged over time to observe crystal disappearance. Green: crystals (top); bright field images (bottom); black arrows indicate the position of crystals. Labels refer to the time after wash out. Scale bar 20 μm.

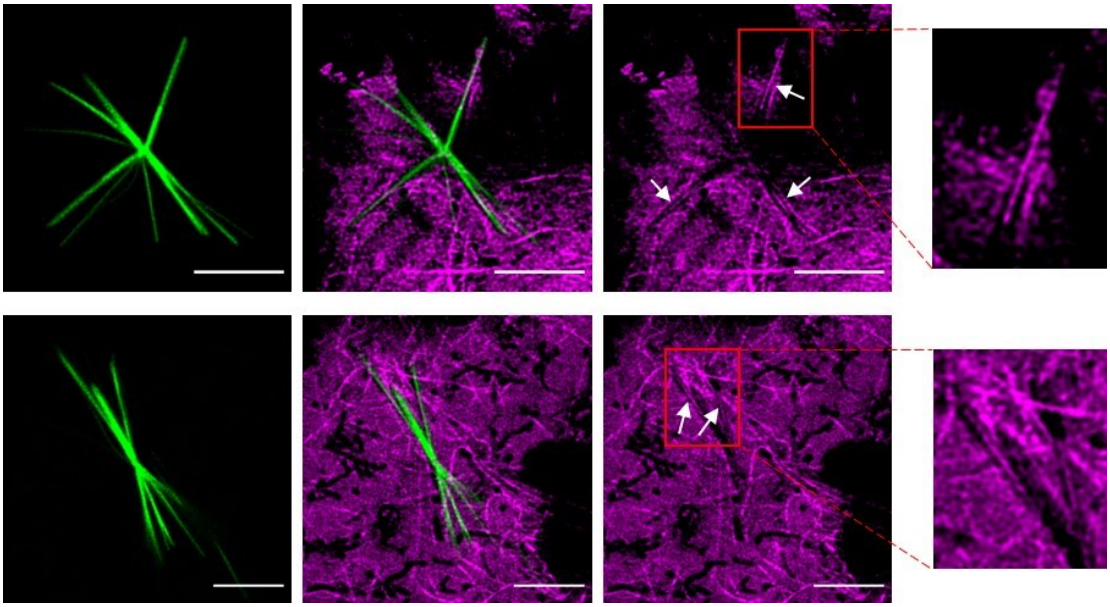

Figure V-S3. Colocalization of crystals with MTs. Super-resolution images of HeLa-GFP-Tubulin treated with QPD-OTf (20 μM; 2 hours); white arrows indicate MTs colocalization with crystals; red boxes indicate the portion of image zoomed-in (GFP-Tubulin: magenta; crystal: green). Scale bar 5 μM.

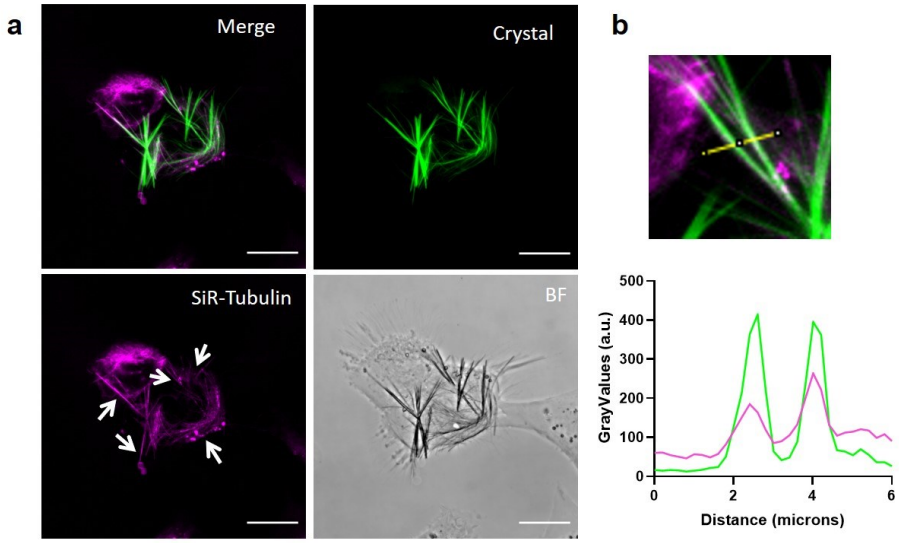

Figure V-S4. Colocalization of crystals with SiRTubulin staining. a) Tubulin staining in live U2OS cells treated with QPD-OTf; white arrows indicate colocalization with crystals (SiR-Tubulin: magenta; crystal: green). b) Plot profiles of tubulin channel and QPD channel (SiR-Tubulin: magenta; crystal: green; yellow line represents the section plotted in the graph) (a.u. represent arbitrary units). Scale bar 20 μM.

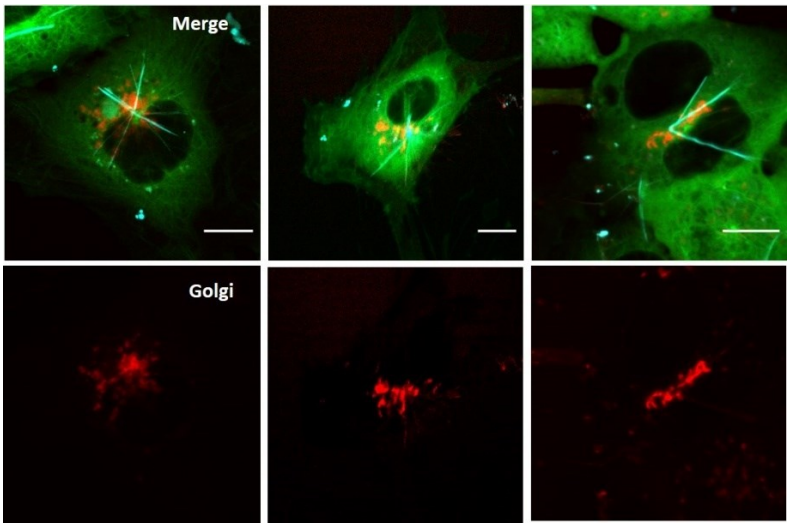

Figure V-S5. Colocalization of the center of crystals with Golgi apparatus. PTK2-GFP-Tubulin cells were transfected with mCherry-Giantin plasmid and treated with QPD-OTf (20 μM, 2 hours). Green: tubulin; cyan: crystals; red: Golgi. Scale bar 10 μM.

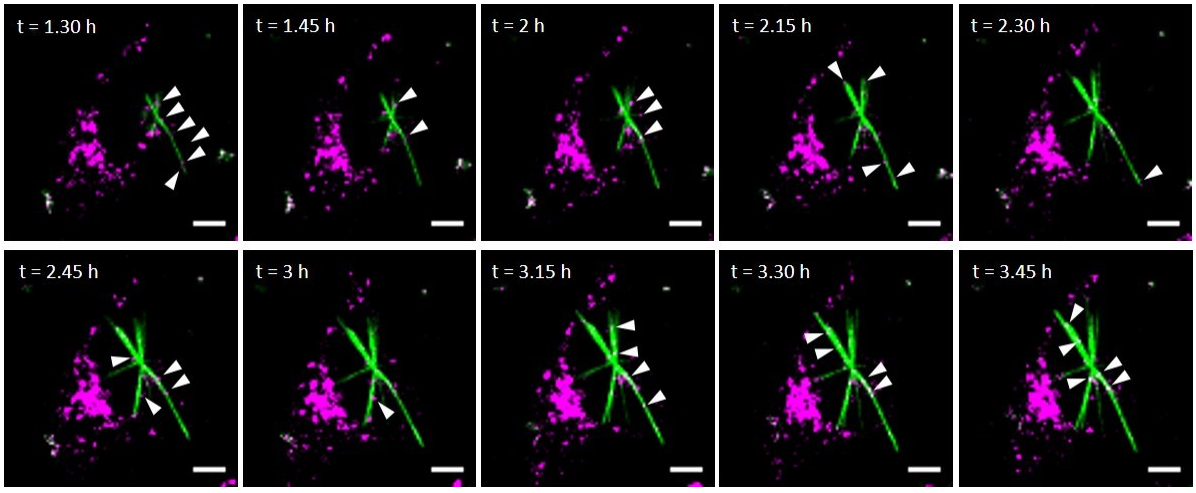

Figure V-S6. Crystal growth in U2OS cell over in relation to Golgi vesicle transport. U2OS cells transfected with mCherry-Giantin plasmid and treated with QPD-OTf (20 μM). White arrowheads indicate Golgi vesicles along crystal filaments. Green: crystal; magenta: Golgi. Scale bar 5 μM.

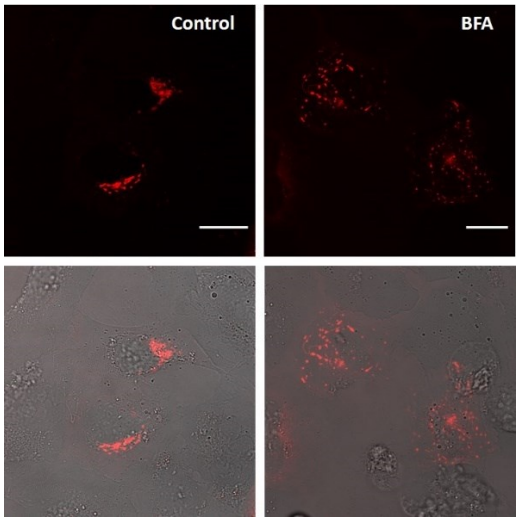

Figure V-S7. Imaging of Golgi apparatus in cells treated with BFA. U2OS cells were transfected with mCherry-Giantin plasmid before (Control) and after (BFA) treatment with Brefeldin A (20 μM, 4 hours). Red: Golgi. Scale bar 20 μM.

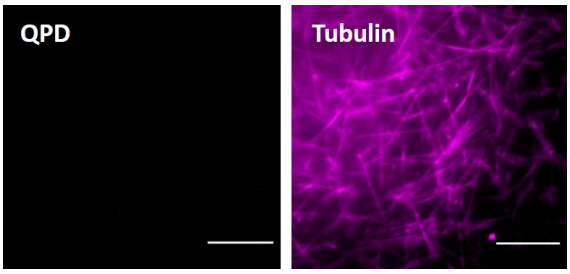

Figure V-S8. QPD-OTf treated MTs in vitro. TIRF images of QPD-OTf treated MTs (20 μM, 2 hours). Magenta: tubulin. Scale bar 10 μM.

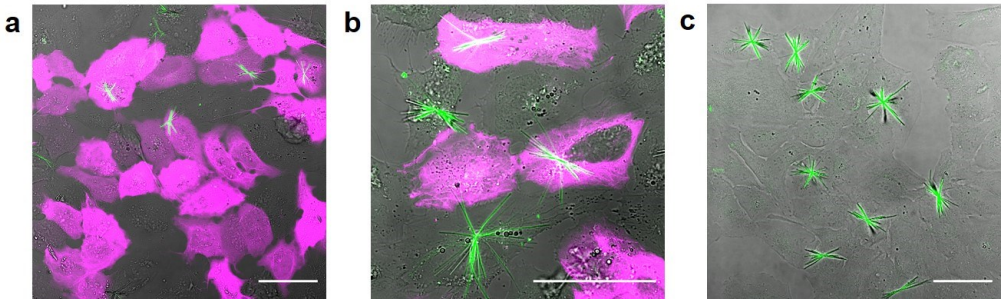

Figure V-S9. Imaging of transfected truncated kinesin in QPD-OTf treated U2OS. a) Merge image of U2OS cells transfected with Kin330-GFP plasmid and treated with QPD-OTf (20 μM, 2.5 hours); green: crystals, magenta: kin330-GFP. b) Merge image of U2OS cells transfected with Kin560-GFP plasmid and treated with QPD-OTf (20 μM, 2.5 hours); green: crystals, magenta: Kin560-GFP. c) Control: U2OS cells treated with QPD-OTf (20 μM, 2.5 hours); green: crystals. Scale bar: 50 μm.

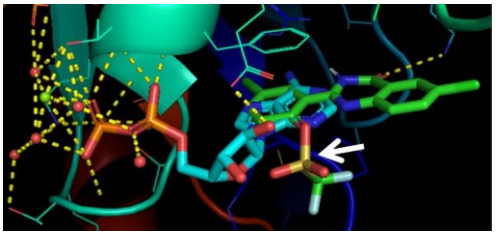

Figure V-S10. QPD-OTf docking into the ATP binding site of Eg-5. Superposition of QPD-OTf (green) and ADP (cyan). White arrow indicates the triflate group of QPD-OTf.

Materials and methods

Chemical reactions were performed in anhydrous conditions under N_2. All reagents and solvents were purchased from commercial sources and were used without any further purification. Anhydrous solvents were obtained by passing them through commercially available alumina column (Innovative Technology, Inc., ® VA). Synthesized compounds were characterized using ^{1}H, ^{13}C, ^{19}F NMR, recorded on AVANCE 3 HD for 400 MHz using Acetone-d_6, as solvent, with residual solvent peaks (δ = 2.05 ppm; δ = 29.84 ppm). LC-MS spectra were recorded by using a DIONEX Ultimate 3000 UHPLC coupled with a Thermo LCQ Fleet Mass Spectrometer System (electrospray ionization (ESI)) operated in positive mode (condition for elution gradient: 0 min, A:B = 100:0; 4 min, A:B = 10:90; solution A: 0.01% aqueous TFA solution; solution B, 0.01 % TFA in HPLC grade acetonitrile; flow rate: 0.750 mL/min.). Transmitted light imaging was performed using an EVOS XL Core Imaging System with a 20X objective. Fluorescence imaging was carried out using a Leica SP8 with LIGHTNING module, a Zeiss LSM700 or a Zeiss LSM710 2P microscope with 63X objectives. All images were analyzed with Image J (Fiji). FIB-SEM rendering was performed with Imaris. pSF-mCherry-SNAP-Giantin plasmid was a kind gift of Howard Riezman's lab (University of Geneva, Switzerland). Docking calculations were performed with Autodock Vina. Data plotting was performed using GraphPad Prism8.

Synthesis of 4-chloro-2-formylphenyl trifluoromethanesulfonate

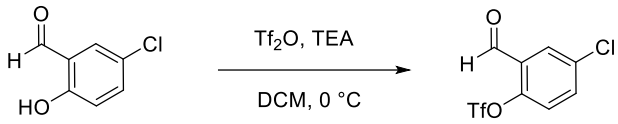

5-chloro-2-hydroxybenzaldehyde (300 mg, 1.92 mmol, 1 eq) was dissolved in dry DCM (5 mL) and cooled to 0 °C and trimethylamine (535 µL, 3.84 mmol, 2 eq) was added. After 5 min triflic anhydride (320 µL, 1.92 mmol, 1 eq) was added dropwise and the mixture was stirred at 0 °C for 2 hours. Then the mixture was diluted with H_2O (50 mL) and extracted with AcOEt (3x10 mL). The organic layers were combined, washed with brine, dried over Na_2SO_4 and concentrated under reduced pressure. The crude product was used in the next step without further purifications.

Synthesis of QPD-OTf.

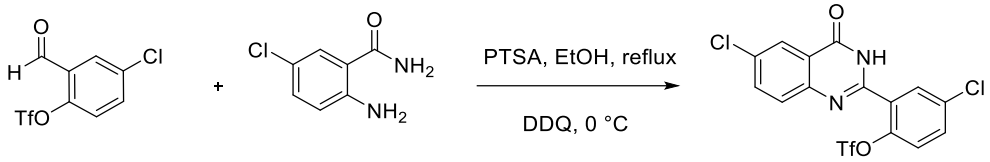

4-chloro-2-formylphenyl trifluoromethanesulfonate (300 mg, 1.04 mg, 1 eq), 2-amino-5-chlorobenzamide (177 mg, 1.04 mmol, 1 eq), *p*-toluensulfonic acid (59 mg, 0.3 mmol, 0.3 eq) were suspended in EtOH (2.6 mL). The mixture was heated to reflux and stirred for 2 hours. The the mixure was cooled to 0 °C and 2,3-Dichloro-5,6-dicyano-1,4-benzoquinone (236 mg, 1.04 mmol, 1 eq) was added portion wise; the mixture turns to green, then to brown with a white precipitate. The suspension was diluted with cold EtOH (5 mL) and centrifuged. The white solid was washed twice with cold EtOH and dried under vacuum. The crude residue was purified by flash chromatography on silica gel (Pentane/EtOAc 9:1 to 6:4). Fractions containing the desired product were collected and dried under reduced pressure to afford QPD-OTf (360 mg, 80% yield). LC-MS (ESI^+): RT= 2.92 min. m/z found: 438.9 $[M+H]^+$. HRMS (m/z): $[M+H]^+$ calcd. for $C_{15}H_8Cl_2F_3N_2O_4S^+$, 438.9528; found: 438.9534. ^1H NMR (400 MHz, Acetone-d_6): δ 11.69 (s, 1H), 8.18 (dd, *J* = 2.5, 0.5 Hz, 1H), 8.13 (d, *J* = 2.6 Hz, 1H), 7.89 (dd, *J* = 8.8, 2.5 Hz, 1H), 7.85 (dd, *J* = 8.9, 2.6 Hz, 1H), 7.82 (dd, *J* = 8.8, 0.5 Hz, 1H), 7.68 (d, *J* = 8.9 Hz, 1H). ^{13}C NMR (101 MHz, Acetone-*d*6): δ 161.12, 149.43, 148.04, 146.44, 135.74, 134.91, 133.57, 132.29, 130.97, 130.23, 126.10, 125.55, 123.89, 120.99, 117.81. ^{19}F NMR (282 MHz, Acetone-*d*6): δ -75.10.

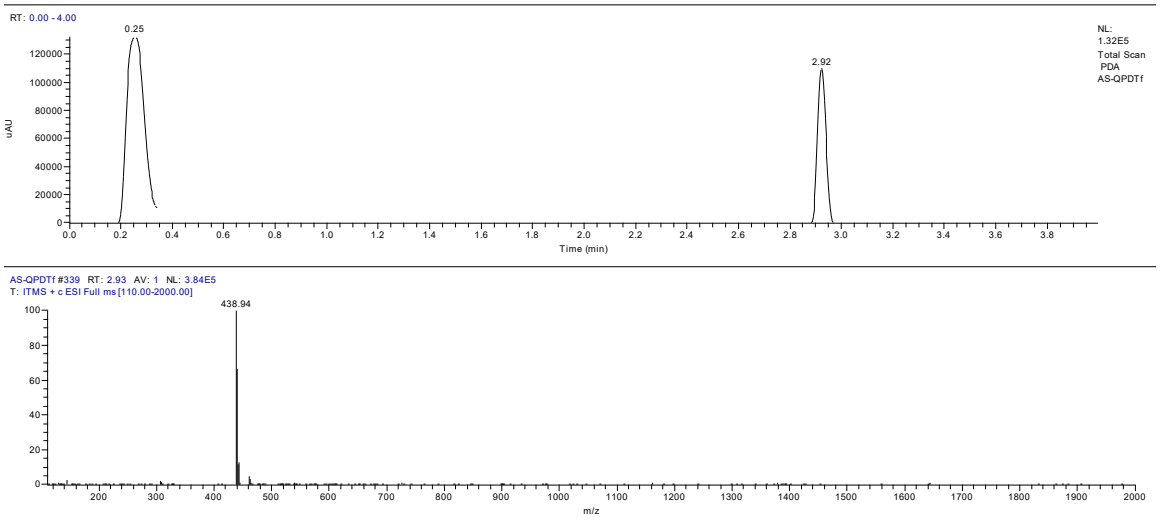

LC-MS trace of QPD-OTf.

Cell culture

U2OS, HeLa, HEK293T, MCF-7, RAW246.7 cell lines were obtained from the American Type Culture Collection (ATCC) and cultured according to their instructions. U2OS cells were grown in McCoy's 5A (modified) medium (Gibco) containing 10% FCS and 1% pen-strep at 37 °C under 5% CO_2 in a humidified incubator. Stable expressing GFP-Tubulin Ptk2 cells (kind gift from Franck Perez) were cultured in alpha-MEM (Gibco) containing 10% FCS and 1% pen-strep at 37 °C under 5% CO_2 in a humidified incubator. GFP-Tubulin CRISPR knock-in Hela cells (by C. Aumeier) were cultured in DMEM (Gibco) containing 10% FCS and 1% pen-strep at 37 °C under 5% CO_2 in a humidified incubator. Cells were regularly tested for mycoplasma contamination by staining with Hoechst 33342.

Crystal formation in cells

QPD-OTf (20 μM) was added to cells in DMEM (-) without additives and incubated at 37 °C, 5% CO_2 from 20 min to 4 hours. Crystals can be easily detected by a 20X objective. Super-resolution imaging was performed using adaptive deconvolution with Leica SP8 LIGHTNING with a 63X objective.

QPD-OTf in Zymosan stimulated RAW246.7 cells

RAW246.7 were seeded into 3.5 cm glass bottom dishes with 10 mm microwell (Mattek); cells were incubated in DMEM medium at 37 °C under 5% CO_2 in a humidified incubator for 16 hours. Then media was removed, cells were washed twice with DPBS (Ca^{2+}, Mg^{2+}) and IgG-opsonized Zymosan A particles (20 μL) + QPD-OTf (20 μM) was added to cells in DMEM (-) (no additives). Cells were incubated at 37 °C under 5% CO_2 and imaged at different time points with a Zeiss LSM710 2P microscope.

Fixed cells imaging of QPD-OTf treated cells

U2OS cells were grown in DMEM medium + 10% FBS to 50% confluency on 12 mm glass slides (seeded the day prior). Cells were treated for 24 hours with QPD-OTf (20 μM). After 24 hours, cells were fixed with MeOH fixation at -20 degrees Celsius for 5 minutes. Then the coverslips were washed for 30 minutes in PBS. Primary antibody staining was performed with 1:1000 dilution of DM1-alpha raised in mouse (T6199) and 1:1000 phalloidin raised in rabbit for 1 hour. Coverslips were washed in PBS for 30 minutes. Secondary antibody staining was performed with 1:400 dilution of anti-mouse ALEXA-488 and 1:400 dilution of 1:400 anti-rabbit ALEXA-568. Coverslips were washed in PBS for 30 minutes. Then coverslips were placed over DABCO mounting medium containing DAPI and imaged with a LSM700 microscope.

Live cell imaging of QPD-OTf treated cells

PTK2-GFP-Tubulin or HeLa-GFP-Tubulin cells ($2x10^5$) were seeded into 3.5 cm glass bottom dishes with 10 mm microwell (Mattek); cells were incubated in culture medium at 37 °C under 5% CO_2 in a humidified incubator for 24 hours. Then media was removed, cells were washed twice with DMEM (-) (no additives) and QPD-OTf (20 μM) was added to cells in DMEM (-) (no additives). Cells were incubated at 37 °C under 5% CO_2 for 2 hours or for 20 min (early stage crystals). Cells were washed twice with DMEM (-) and imaged with a LEICA SP8 microscope or with a LIGHTNING module for super-resolution images.

SiR-Tubulin staining in QPD-OTf treated cells

U2OS cells ($2x10^5$) were seeded into 3.5 cm glass bottom dishes with 10 mm microwell (Mattek); cells were incubated in McCoy's 5A medium at 37 °C under 5% CO_2 in a humidified incubator for 16 hours. Then media was removed, cells were washed twice with DMEM (-) (no additives) and QPD-OTf (20 μM) was added to cells in DMEM (-) (no additives). Cells were incubated at 37 °C under 5% CO_2 for 4 hours. After washing twice with DMEM (-) (no additives), SiR-Tubulin (1 μM) was added and cells were incubated for 45 min at 37 °C under 5% CO_2. Cells were washed twice with DMEM (-) and imaged with a LEICA SP8 microscope.

Sample Preparation for FIB-SEM

HeLa cells were grown on MatTek glass coverslips for 2 days. Cells were then washed x 3 with Hank's Balanced Salt solution and QPD-OTf (20 μM) in DMEM without serum was added. Cells were then incubated for 4 hours at 37° C with 5% CO_2. Cells were then washed with Hank's Balanced Salt solution, fixed, and processed as previously described[1] with some differences. After dehydration the MatTek glass coverslip was removed from the plastic by using propylene oxide. The removed glass coverslip was then rinsed in 100% ethanol followed by immersion in mixtures of Durcupan ACM and ethanol with the following ratios: 25/75 for 1.5 hours, 50:50 for 1.5 hours; 75/25 overnight. The sample was then immersed in 100% Durcupan ACM for 4-5 hours with replacement of fresh Durcupan every hour. The glass coverslip was then removed and excess Durcupan was removed using filter paper. The coverslip was then placed in an oven at 60 degrees Celsius for 10 minutes, after which the sample was placed vertically in a 50 mL Falcon tube in folded filter papers and centrifuged for 15 minutes at 37° C and 750 RCF. The glass coverslip was then placed in an oven at 60 degrees Celsius under vacuum and left to polymerize over 2 days. The sample was then placed on a sample stub by an adhesive carbon dot, sputter coated with 50 nm gold, and painted with silver paint, followed by drying under vacuum.

FIB-SEM

Datasets were acquired using a Zeiss Crossbeam 540 (Carl Zeiss Microscopy GmbH, Jena, Germany). Platinum and Carbon was deposited over the region of interest and the run was setup and controlled by Atlas5 software (Fibics) SEM settings: 1.5 kV; 2.5 nA; Milling probe: 300 pA. The Slice thickness and the voxel size was set to 5 nm. The total volume acquired was: 16.36 x 9.87 x 7.31 μm (XYZ) and 23.5 x 9.60 x 7.47 μm (XYZ).

FIB-SEM Data Analysis, Segmentation and Rendering

The FIB-SEM datasets were aligned using Atlas5 software (Fibics). The data was then imported into Fiji software2 and binned 3X, to 15 x 15 x 15 nm isotropic voxels. Segmentation of structures of interest was performed using the Pixel Classification module in the Ilastik software package (Ilastik.org). The probability maps were then imported into Imaris (Bitplane.com) and surfaces were generated around fully segmented structures. Images and videos were rendered using Imaris. Crystal cross-sections based on surface renderings were measured in Imaris.

MTs stabilization with Taxol in live U2OS cells

U2OS cells ($2x10^5$) were seeded into 3.5 cm glass bottom dishes with 10 mm microwell (Mattek); cells were incubated in McCoy's 5A medium at 37 °C under 5% CO_2 in a humidified incubator for 24 hours. Then media was removed, cells were washed twice with DMEM (-) (no additives), Taxol (1 μM) was added to cells in DMEM (-) (no additives) and cells were

incubated at 37 °C under 5% CO_2 for 1 hour. QPD-OTf (20 μM) was then added and cells were incubated at 37 °C under 5% CO_2 for 4 hours. Cells were imaged with a 20X objective on an EVOS XL Core.

MTs depolymerisation on ice in live U2OS cells

U2OS cells ($2x10^5$) were seeded into 3.5 cm glass bottom dishes with 10 mm microwell (Mattek); cells were incubated in McCoy's 5A medium at 37 °C under 5% CO_2 in a humidified incubator for 24 hours. Then media was removed, cells were washed twice with DMEM (-) (no additives) and put on ice for 1 hour. QPD-OTf (20 μM) was then added and cells were incubated on ice for 4 hours. Cells were imaged with a 20X objective on an EVOS XL Core. Control cells were washed with with DMEM (-) (no additives) and incubated with QPD-OTf (20 μM) at 37 °C under 5% CO_2 for 4 hours.

Transient transfection with mCherry-Giantin plasmid

U2OS or PTK2-GFP-Tubulin cells ($1.5x10^5$) were seeded into 3.5 cm glass bottom dishes with 10 mm microwell (Mattek); cells were incubated in culture medium at 37 °C under 5% CO_2 in a humidified incubator for 24 hours. pSF-mCherry-SNAP-Giantin plasmid (kind gift of Riezman's lab; University of Geneva, Switzerland) was transfected with FugeneHD reagent in Optimem (100 μL); cells were incubated at 37 °C under 5% CO_2 for 24 hours. Cells were washed twice with DMEM (-) (no additives) and QPD-OTf (20 μM) was added to cells in DMEM (-) (no additives). Cells were incubated at 37 °C under 5% CO_2 for 3 hours. Cells were washed twice with DMEM (-) and imaged with a LEICA SP8 microscope.

Brefeldin A treatment in live U2OS cells

U2OS cells ($2x10^5$) were seeded into 3.5 cm glass bottom dishes with 10 mm microwell (Mattek); cells were incubated in McCoy's 5A medium at 37 °C under 5% CO_2 in a humidified incubator overnight. Then media was removed, cells were washed twice with DMEM (-) (no additives), Brefeldin A (20 μM) was added to cells in DMEM (-) (no additives) and cells were incubated at 37 °C under 5% CO_2 for 4 hours. Then media was replaced with fresh one containing Brefeldin A (20 μM) and QPD-OTf (20 μM) and cells were incubated at 37 °C under 5% CO_2 for 2.5 hours. Cells were washed twice with DMEM (-) and imaged with a LEICA SP8 microscope. The same protocol was used for cells transfected with mCherry-Giantin plasmid.

Kinesore + QPD-OTf treatment in live cells

U2OS or PTK2-GFP-Tubulin cells ($1.5x10^5$) were seeded into 3.5 cm glass bottom dishes with 10 mm microwell (Mattek); cells were incubated in culture medium at 37 °C under 5% CO_2 in a humidified incubator for 24 hours. Then media was removed, cells were washed twice with DMEM (-) (no additives), Kinesore (100 μM) + QPD-OTf (20 μM) were then added to cells in Ringer's buffer and cells were incubated at 37 °C under 0% CO_2 for (1.5 hours for PTK2; 2 hours for U2OS). Cells were imaged with a LEICA SP8.

Kinesore treatment in live cells

U2OS cells ($1.5x10^5$) were seeded into 3.5 cm glass bottom dishes with 10 mm microwell (Mattek); cells were incubated in culture medium at 37 °C under 5% CO_2 in a humidified incubator for 24 hours. Then media was removed, cells were washed twice with DMEM (-) (no additives), Kinesore (100 μM) was added to cells in Ringer's buffer and cells were incubated at 37 °C under 0% CO_2 for 1.5 hours. Cells were imaged with a LEICA SP8.

Tubulin purification from bovine brain and tubulin labelling

Tubulin was purified from fresh bovine brain by two cycle of polymerisation and depolymerisation as previously described (Castoldi & Popov, 2003). A first polymerisation-depolymerisation cycle was performed in High-Molarity PIPES buffer [1 M PIPES-KOH at pH 6.9, 10 mM $MgCl_2$, 20 mM EGTA, 1.5 mM ATP and 0.5 mM GTP] supplemented with 1:1 glycerol and Depolymerisation buffer [50 mM MES-HCl at pH 6.6 and 1 mM $CaCl_2$] respectively. A second polymerisation-depolymerisation cycle was then performed: polymerisation in High-Molarity PIPES buffer and depolymerisation in 0.25X BRB80 complete after 15 min with 5X BRB80 to reach 1X BRB80 [80 mM PIPES at pH 6.8, 1 mM $MgCl_2$ and 1 mM EGTA] respectively.

Labelled tubulin with ATTO-488, ATTO-565, or ATTO-647 (ATTO-TEC GmbH) and biotinylated tubulin were prepared as previously described (Hyman et al., 1991) with slight modification. Tubulin was polymerised in Glycerol PB solution [80 mM PIPES-KOH at pH 6.8, 5 mM $MgCl_2$, 1 mM EGTA, 1 mM GTP and 33 % (v/v) glycerol] for 30 min at 37 °C and layered onto cushions of 0.1 M NaHEPES at pH 8.6, 1 mM $MgCl_2$, 1 mM EGTA and 60 % (v/v) glycerol followed by centrifugation. Pellet was resuspended in Resuspension buffer [0.1 M NaHEPES at pH 8.6, 1 mM $MgCl_2$, 1 mM EGTA, 40% (v/v) glycerol] and incubated 10 min at 37 °C with 1/10 volume of 100 mM ATTO-488, -565, or -647 NHS-fluorochrome or incubated 20 min at 37 °C with 2 mM Biotin reagent. Labelled tubulin was sedimented onto cushions of BRB80 supplemented with 60 % glycerol, resuspended in BRB80, and a second polymerisation-depolymerisation cycle was performed before use. Labelling ratio was 13 % for ATTO-565

Flow chamber

Slides and coverslips were cleaned by two successive incubations and sonication: sonicated for 40 min in 1 M NaOH, rinsed in bidistillated water, sonicated in ethanol (96 %) for 30 min and rinsed in bidistillated water. Slides and coverslips were dried with an air gun, placed into a Plasma cleaner (Electronic Diener, Plasma surface technology) for plasma treatment, followed by 2 days incubation with tri-ethoxy-silane-PEG (Creative PEGWorks) or a 1:5 mix of tri-ethoxy-silane-PEG-biotin and tri-ethoxy-silane-PEG at 1 mg/ml in 96 % ethanol and 0.02 % HCl, with gentle agitation at room temperature. Slides and coverslips were then washed in ethanol (96 %), and bidistillated water, dried with air gun and stored at 4 °C. Flow chamber was assembled by fixing with double tap a tri-ethoxy-silane-PEG treated slide with a 1:5 mix of tri-ethoxy-silane-PEG-biotin and tri-ethoxy-silane-PEG treated coverslip.

Microtubule seeds were prepared at 10 µM tubulin concentration (20 % ATTO-647-labelled tubulin and 80 % biotinylated tubulin) in BRB80 supplemented with 0.5 mM GMPCPP (Jena Bioscience) for 1 hour at 37 °C. Seeds were incubated with 1 µM Paclitaxel (Sigma) for 45 min at 37 °C, centrifuged (50.000 rpm at 25 °C for 15 min), resuspended in BRB80 supplemented with 1 µM Paclitaxel and 0.5 mM GMPCPP and stored in liquid nitrogen.

To observe precipitation of QPD in presence of stabilised microtubule seeds, we injected seeds in BRB80 supplemented with 20 µM QPD, 0.2 % BSA and anti-bleaching buffer (10 mM DTT, 0.3 mg/mL glucose, 0.1 mg/mL glucose oxidase, 0.02 mg/mL catalase, 0.125 % methyl cellulose (1500 cP, Sigma), 1 mM GTP, 2.7 mM $MgCl_2$ and 2.7 mM AMP-PMP), inside the flow chamber. No precipitation was observed after 2 hours under the microscope.

To study the precipitation of QPD in presence of dynamic microtubules we polymerised microtubules from seeds in BRB80 supplemented with 14 µm unlabelled tubulin, 20 µM QPD

and 1 mM GTP at 37 °C in an Eppendorf-tube. For direct observation of precipitation, we polymerised microtubules from microtubule seeds in the flow chamber. The Flow chamber was prepared by injecting successively 50 µg/mL neutravidin (ThermoFisher), BRB80, GMPCPP microtubule seeds, and washed with BRB80 to remove unattached seeds. Microtubule polymerised from the seeds with 12 µM tubulin (20 % Atto-565 labelled) in BRB80 supplemented with an anti-bleaching buffer [10 mM DTT, 0.3 mg/mL glucose, 0.1 mg/mL glucose oxidase, 0.02 mg/mL catalase, 0.125 % methyl cellulose (1500 cP, Sigma), 1 mM GTP] and 0.2% BSA. The chamber was incubated for 15 min at 37 °C for polymerisation. The chamber sealed for imaging of microtubule dynamics and QPD precipitation at 37 °C of microtubule dynamics. Images were recorded every 3 min for 2 hours.

TIRF Imaging

Microscopy imaging was realized with an Axio Observer Inverted TIRF microscope (Zeiss, 3i) and a Prime BSI (Photometrics). A 100X objective (Zeiss, Plan-Apochromat 100X/1.46 oil DIC (UV) VIS-IR) were used. SlideBook 6 X64 software (version 6.0.17) was used to record time-lapse imaging. For in vitro, microscope stage conditions were controlled with the Chamlide Live Cell Instrument incubator (37 °C).

Transient transfection with Kin330-GFP/Kin560-GFP

U2OS cells ($1.5x10^5$) were seeded into 3.5 cm glass bottom dishes with 10 mm microwell (MatTek); cells were incubated in culture medium at 37 °C under 5% CO_2 in a humidified incubator for 24 hours. Kin330-GFP or Kin560-GFP plasmid was transfected with FugeneHD reagent in Opti-Mem (100 µL); cells were incubated at 37 °C under 5% CO_2 for 24 hours. Cells were washed twice with DMEM (-) (no additives) and QPD-OTf (20 µM) was added to cells in DMEM (-) (no additives). Cells were incubated at 37 °C under 5% CO_2 for 3 hours. Cells were washed twice with DMEM (-) and imaged with a LEICA SP8 microscope.

Kinesin-1 knockdown

HeLa-GFP-Tubulin cells ($7.5 x10^4$) were seeded into 6 well plates; cells were incubated in culture medium at 37 °C under 5% CO_2 in a humidified incubator overnight. Then media was replaced with fresh one and cells were transfected with AllStars Negative Control siRNA or with a combination of four siRNA duplexes against Kif5B subunit of kinesin-1 (GeneSolution siRNA, Quiagen) at a final concentration of 10 nM in Lipofectamine RNAiMAX. Cells were incubated 37 °C under 5% CO_2 in a humidified incubator for 72 hours. Cells were washed with DMEM (-) (no additives), incubated with QPD-OTf (20 µM) and imaged after 2 hours.

Western Blot

To HeLa-GFP-Tubulin transfected with siRNA was added lysis buffer and cells were let 5 min on ice before being scraped. The cell lysate was transferred into eppendorf tubes and incubated on ice for 30 min, and then centrifuged at 14000 g at 4 °C for 20 min. An aliquot of the supernatant was mixed with Laemli buffer (5x) and loaded on 8% acrylamide gel. Proteins were transferred onto PVDF membrane and blocked in 5% BSA in TBST buffer for 1 hour at r.t.. The membrane was incubated with anti-UKHC (kinesin) primary antibody (1: 1000) or anti α-tubulin primary antibody (1:1000) in 5% dehydrated milk in TBST buffer at 4 °C overnight. The membrane was washed with TBST buffer (3x10 min) and incubated with secondary HRP antibody (1:10000) in 5% dehydrated milk in TBST buffer for 1 hour at r.t. The membrane was

washed with TBST buffer (3x10 min). The membrane was then rinsed several times with a mixture of peroxide/luminol solution and chemiluminescent signal was acquired.

In vitro precipitation of QPD

20 µM QPD was precipitated in Eppendorf-tubes at room temperature for 6 hours in BRB80 in presence of different combinations of unlabeled 14 µM tubulin, 150 nM kinesin-1, 2.7 mM AMP-PNP, 2.7 mM ATP, 1 mM GTP. Samples were visualized under a 366 nm lamp. The content of samples containing fluorescent precipitate was imaged by a LEICA SP8 microscope.

rKin430 expression and purification

All in vitro experiments were performed with truncated, kinesin-1 construct, rKin430-EGFP (referred as kinesin-1 in the text). The rKin430 plasmid (a kind gift of Stefan Diez's laboratory) was expressed and purified as previously described (Rogers et al., 2001). *E.coli* BL21(DE3)[pLysS] expressing rKin430 were lysed in a Lysis buffer [50 mM Na-Phosphate buffer at pH 7.5, 300 mM KCl, 10 % Glycerol, 1 mM $MgCl_2$, 20 mM ß-Mercaptoethanol, 0.2 mM ATP, 30 mM imidazole and protease inhibitors cocktail tablets (Roche)]. The cleared lysate was loaded into a pre-equilibrated HisTrap column (GE Healthcare 1mL HisTrap column) using an ÄKTA Pure Protein Purification System (GE Healthcare). After predefined washes, protein was eluted with Elution buffer [50 mM Na-Phosphate buffer at pH 7.5, 300 mM KCl, 10 % Glycerol, 1 mM $MgCl_2$, 0.2 mM ATP, 300 mM imidazole and 10 % (w/v) sucrose]. A dialysis was performed overnight to exchange the Elution buffer 20 mM NaHEPES at pH 7.7, 150 mM KCl, 1 mM $MgCl_2$, 0.05 mM ATP, 1 mM DTT and 20 % (w/v) Sucrose. Protein concentration was measured by Bradford method and the concentration was adjusted to 1.2 µg/µL using Centrifugal filter Amicon 30K (Millipore). Protein was aliquoted and stored in liquid nitrogen.

Molecular docking

Docking calculations were performed with Autodock4 Vina.[2] Receptor (PDB structure: 3J8Y for kinesin-1, 4AP0 for Eg5) and ligand preparation were performed in AutodockTools1.5.6. Results were displayed with PyMOL2.

NMR spectra

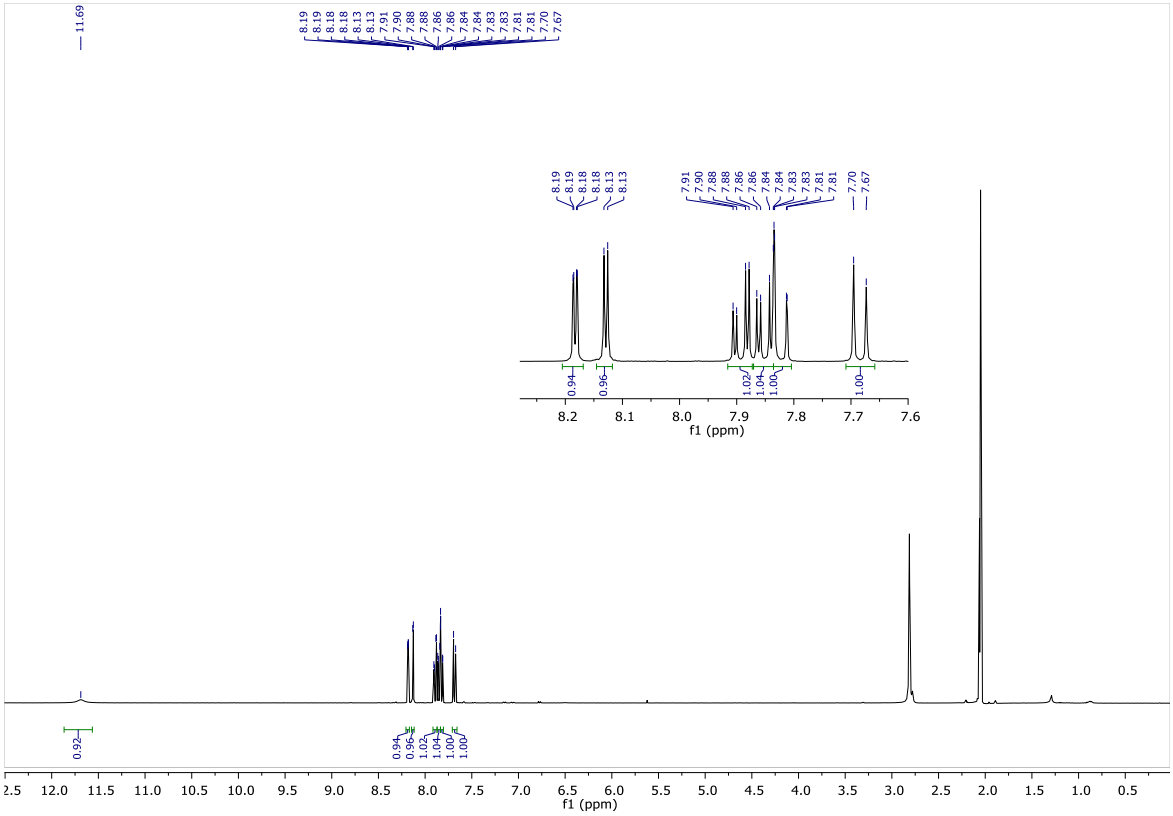

^{1}H NMR of **QPD-OTf** in acetone-*d6*

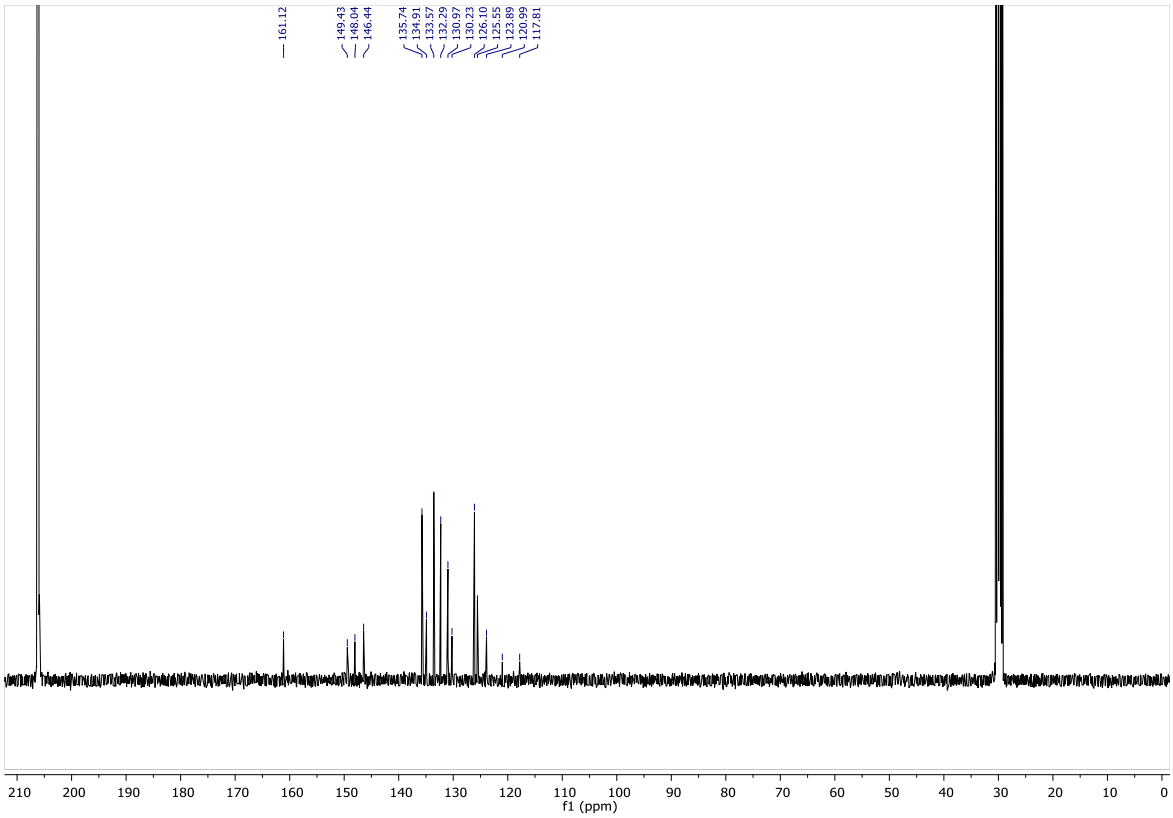

^{13}C NMR of **QPD-OTf** in acetone-*d6*

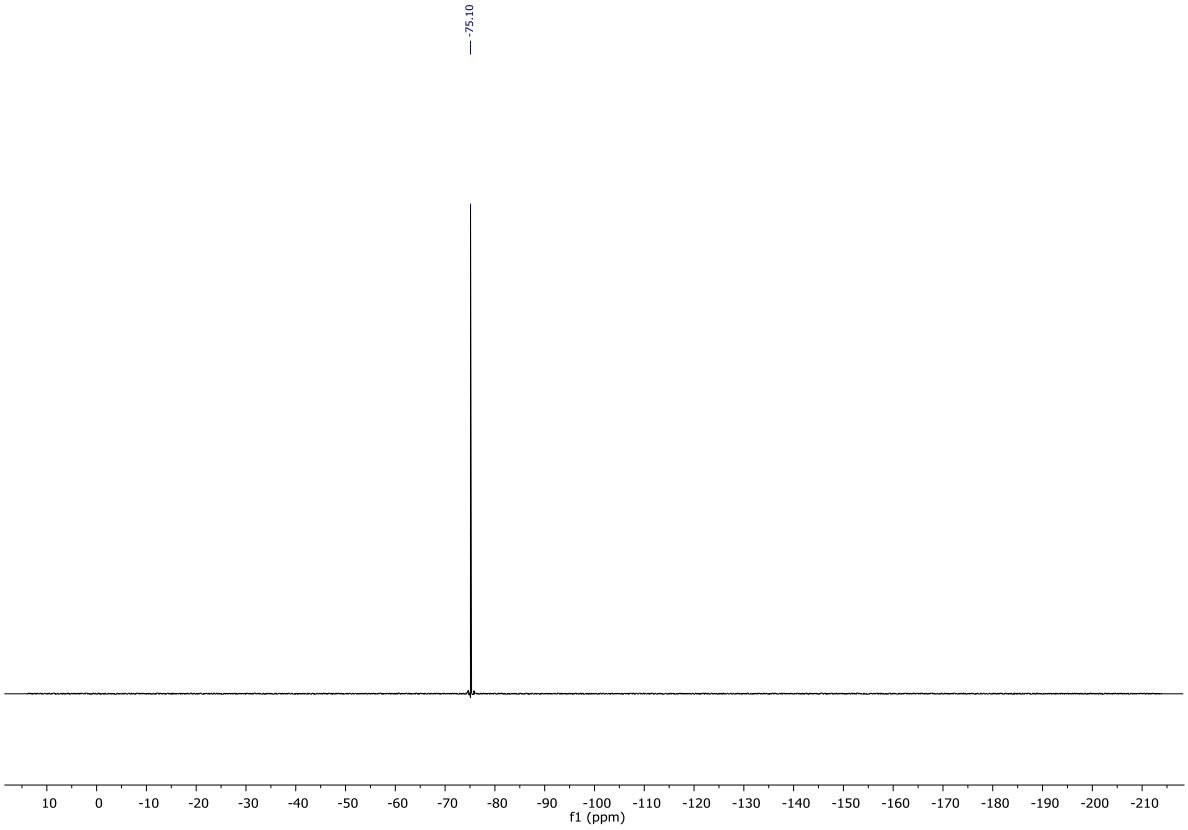

^{19}F NMR of **QPD-OTf**.

Supplementary References

1. Bleck, C.K.E., Kim, Y., Willingham, T.B. & Glancy, B. Subcellular connectomic analyses of energy networks in striated muscle. Nat Commun 9, 5111 (2018)

2. O. Trott, A. J. Olson, AutoDock Vina: improving the speed and accuracy of docking with a new scoring function, efficient optimization and multithreading, Journal of Computational Chemistry 31 (2010) 455-461.

Acknowledgements

First, I would like to thank Professor Nicolas Winssinger for the possibility to carry out my PhD in his group; these five years have been extremely enriching, both scientifically and personally. Thank you for giving me the chance to be involved in multidisciplinary projects, because it allowed me to learn and measure myself out of my confidence zone. Thank you for pushing me to always do better, because this motivated me to improve and persevere. Thank you for being always available for discussion, I will make treasure of the knowledge you shared; your passion for science has really been inspiring.

I would like to thank all the past and present members of the Winssinger lab for all the moments spent in and out of the lab; you have been my family for five years and I am thankful to have met each of you. A special thank to the people that welcomed me at the beginning of my PhD and helped me to get acquainted with the lab: Roman, Eric, Marcello,Takuya, Dalu, Lluc, Jacques, Bala, Pierre; without your support I would have probably not survived the first months. I want to thank Roman, for all the chemistry advice, and for his entertaining personality; your feisty comments always made me smile. I want to particularly thank Eric, for his infinite patience, and for staying close to me even from very far away; it has been a pleasure to work with you. Marcello, for being my Italian brother. Dalu, for your kind spirit. I would like to thank Kitae, for the very nice collaboration during these years. Thanks Lluc, for being the guy you can always have a nice chat with. Thanks to Miryam, for having shared six months of happy moments. Then I want to thank my desk neighbours: Yev, you really made my days in the lab sweeter, and Heng, for standing me during this last year. Many thanks also to Rémi, for his contagious optimism; Pramod, for all the chats in between experiments; Victoria, for her friendship; Emma, for being my source of wisdom. And many thanks also to the more recently arrived Arthur, Elsa, Jelena, Milly, Mateusz, Francesco. Thank you to Sofia and Patrick, for organizing the group and making the lab run smoothly.

I would like to thank the Matile group, that “adopted” me since the first days: you have the power to make everyone feel comfortable in your company; I will never forget the joyful moments spent with you. In particular, thank you to Javier and Antoine, for being by my side when I needed it; to Yoann, Lucia, Rémi, for all the cheerful moments; to Inga and Andrea, for your congeniality.

Voglio ringraziare particolarmente l’Italian team del gruppo Mazet: mi avete fatto sempre sentire a casa. Un ringraziamento speciale a Daniele, amico sincero, per essermi stato sempre vicino durante questi anni; grazie per essere stato l’esempio da seguire.
Grazie a Ciro, con la sua personalità pungente; grazie Michele, per avere sempre la battuta pronta. Grazie a Simone, per avere sempre una parola gentile.

I would like to thank Charlotte Aumeier for her precious help with the kinesin project. Thanks also to Nikolai, standing my impatient requests about experiments.

Un pensiero anche agli ex-colleghi e amici di Milano, che per primi mi hanno inculcato la passione per la ricerca, e alle amiche della 5F; anche se abbiamo preso strade diverse è sempre bello rincontrarsi per condividere le nostre esperienze.

I would like to thank Tina and Naomi, for having hosted me in their house for almost five years. I will always be thankful for your kindness.

Per finire vorrei ringraziare la mia famiglia, che ha sempre sostenuto le mie scelte. Grazie per esserci sempre, per aver sempre creduto in me, per essere sempre entusiasti per i miei piccoli successi e per rassicurarmi sulle mie incertezze. Siete la mia forza, vi voglio bene.